



electronics

Special Issue Reprint

Antenna Designs for 5G/IoT and Space Applications, 2nd Edition

Edited by
Faisal Tubbal, Ladislau Matekovits and Raad Raad

mdpi.com/journal/electronics



Antenna Designs for 5G/IoT and Space Applications, 2nd Edition

Antenna Designs for 5G/IoT and Space Applications, 2nd Edition

Guest Editors

Faisal Tubbal

Ladislau Matekovits

Raad Raad



Basel • Beijing • Wuhan • Barcelona • Belgrade • Novi Sad • Cluj • Manchester

Guest Editors

Faisal Tubbal
School of Electrical,
Computer and
Telecommunication
Engineering
University of Wollongong
Wollongong
Australia

Ladislau Matekovits
Department of Electronics
and Telecommunications
Politecnico di Torino
Torino
Italy

Raad Raad
School of Electrical,
Computer and
Telecommunication
Engineering
University of Wollongong
Wollongong
Australia

Editorial Office

MDPI AG
Grosspeteranlage 5
4052 Basel, Switzerland

This is a reprint of the Special Issue, published open access by the journal *Electronics* (ISSN 2079-9292), freely accessible at: www.mdpi.com/journal/electronics/special_issues/995F17HW88.

For citation purposes, cite each article independently as indicated on the article page online and using the guide below:

Lastname, A.A.; Lastname, B.B. Article Title. <i>Journal Name</i> Year , <i>Volume Number</i> , Page Range.
--

ISBN 978-3-7258-3632-1 (Hbk)

ISBN 978-3-7258-3631-4 (PDF)

<https://doi.org/10.3390/books978-3-7258-3631-4>

© 2025 by the authors. Articles in this book are Open Access and distributed under the Creative Commons Attribution (CC BY) license. The book as a whole is distributed by MDPI under the terms and conditions of the Creative Commons Attribution-NonCommercial-NoDerivs (CC BY-NC-ND) license (<https://creativecommons.org/licenses/by-nc-nd/4.0/>).

Contents

About the Editors	vii
Preface	ix
Dimitrios G. Arnaoutoglou, Tzichat M. Empliouk, Theodoros N. F. Kaifas, Michael T. Chryssomallis and George Kyriacou A Review of Multifunctional Antenna Designs for Internet of Things Reprinted from: <i>Electronics</i> 2024 , <i>13</i> , 3200, https://doi.org/10.3390/electronics13163200	1
Tale Saeidi and Saeid Karamzadeh Enhancing CubeSat Communication Through Beam-Steering Antennas: A Review of Technologies and Challenges Reprinted from: <i>Electronics</i> 2025 , <i>14</i> , 754, https://doi.org/10.3390/electronics14040754	34
Yuanming Xiao, Lianxing He and Xiaoli Wei Dual-Band Dual-Circularly Polarized Shared-Aperture Phased Array for S-/C-Band Satellite Communications Reprinted from: <i>Electronics</i> 2025 , <i>14</i> , 387, https://doi.org/10.3390/electronics14020387	74
Peter Miklavčič and Boštjan Batagelj A New Sum-Channel Radiating Element for a Patch-Monopole Monopulse Feed Reprinted from: <i>Electronics</i> 2024 , <i>13</i> , 3187, https://doi.org/10.3390/electronics13163187	87
Luis Inclán-Sánchez Performance Evaluation of a Low-Cost Semitransparent 3D-Printed Mesh Patch Antenna for Urban Communication Applications Reprinted from: <i>Electronics</i> 2023 , <i>13</i> , 153, https://doi.org/10.3390/electronics13010153	97
Syed Salman Kabir, Mehedi Hassan Khan and Saeed I. Latif A Multi-Band Circularly Polarized-Shared Aperture Antenna for Space Applications at S and X Bands Reprinted from: <i>Electronics</i> 2023 , <i>12</i> , 4439, https://doi.org/10.3390/electronics12214439	123
Gia Khanh Tran and Takuma Okada Design of Antenna Polarization Plane for Concurrent Uplink/Downlink Drone Networks Reprinted from: <i>Electronics</i> 2023 , <i>12</i> , 3045, https://doi.org/10.3390/electronics12143045	134
Junho Yeo and Jong-Ig Lee Gain Enhancement of Microstrip Patch Array Antennas Using Two Metallic Plates for 24 GHz Radar Applications Reprinted from: <i>Electronics</i> 2023 , <i>12</i> , 1512, https://doi.org/10.3390/electronics12071512	152
Hassan Sani Abubakar, Zhiqin Zhao, Boning Wang, Saad Hassan Kiani, Naser Ojaroudi Parchin and Bandar Hakim Eight-Port Modified E-Slot MIMO Antenna Array with Enhanced Isolation for 5G Mobile Phone Reprinted from: <i>Electronics</i> 2023 , <i>12</i> , 316, https://doi.org/10.3390/electronics12020316	170
Sherif A. Khaleel, Ehab K. I. Hamad, Naser Ojaroudi Parchin and Mohamed B. Saleh Programmable Beam-Steering Capabilities Based on Graphene Plasmonic THz MIMO Antenna via Reconfigurable Intelligent Surfaces (RIS) for IoT Applications Reprinted from: <i>Electronics</i> 2022 , <i>12</i> , 164, https://doi.org/10.3390/electronics12010164	181

Atta Ullah, Naser Ojaroudi Parchin, Ahmed S. I. Amar and Raed A. Abd-Alhameed
Eight-Element Antenna Array with Improved Radiation Performances for 5G Hand-Portable
Devices
Reprinted from: *Electronics* **2022**, *11*, 2962, <https://doi.org/10.3390/electronics11182962> **201**

**Gyoungdeuk Kim, Myeongha Hwang, Hyunmin Jeong, Chul-Min Lim, Kyoung Youl Park
and Sangkil Kim**
Design of a Flat-Panel Metasurface Reflectarray C-Band Antenna
Reprinted from: *Electronics* **2022**, *11*, 2729, <https://doi.org/10.3390/electronics11172729> **221**

About the Editors

Faisal Tubbal

Faisal Tubbal achieved his educational milestones in the field of telecommunication engineering. He obtained his B.E. degree from the College of Electronic Technology in Tripoli, Libya, in 2004. Continuing his academic journey, he completed an M.S. degree in telecommunication engineering from University of Wollongong, in Wollongong, Australia, in 2012, followed by an M.S. degree in engineering management in 2013. Finally, in 2017, he successfully obtained his Ph.D. degree in telecommunication engineering from the same university. Faisal began his professional journey as a researcher at the Libyan Centre for Remote Sensing and Space Science in Tripoli, Libya. In 2012, he joined the University of Wollongong as an academic assistant at the School of Electrical, Computer, and Telecommunication Engineering. In recognition of his contributions, since 2017, Faisal has served as a unit Convenor at the School of Computing, Engineering, and Mathematics at Western Sydney University, Australia. Currently, he holds the positions of lecturer, Labs Manager, and Work Integrated Learning Coordinator at the School of Computer, Electrical and Telecommunication Engineering (SECTE) within the University of Wollongong. As a researcher and author, Faisal has authored two edited books and three book chapters and has published over 65 articles in esteemed conferences and journals. His research interests encompass various areas, including antenna designs for CubeSat applications, wearable antennas, antennas for medical applications, antenna designs using metamaterials, wireless power transfer using Rectenna technology, and metasurface antennas. Dr. Faisal Tubbal's dedication and expertise have been recognized through prestigious awards. He received the Vice-Chancellor's Awards for Outstanding Contribution to Teaching and Learning (OCTAL) in both 2016 and 2021. He is also honored as a Fellow at the Wollongong Academy for Tertiary Teaching and Learning Excellence (WATTLE).

Ladislau Matekovits

Ladislau Matekovits received a degree in electronic engineering from Institutul Politehnic din București, Romania, and a Ph.D. degree in electronic engineering from Politecnico di Torino, Italy, in 1992 and 1995, respectively. Since 1995, he has been with the Department of Electronics and Telecommunications, Politecnico di Torino, where in 2014 he was appointed as Associate Professor. Beginning on July 1, 2009, for two years, he has been a Marie Curie Fellow at Macquarie University, Sydney, NSW, Australia. Since 2020, he has been an Honorary Professor at Polytechnic University of Timisoara, Romania.

His main research activities concern the numerical analysis of large arrays and active and passive metamaterials for cloaking applications. Different optimization techniques have also been considered. In the last few years, bio-electromagnetic aspects have also been contemplated, as, for example, the design of implantable antennas and the development of nano-antennas, for example, for drug delivery applications. He has published 450+ papers, including 140+ journal contributions, and delivered seminars on these topics all around the world. Prof. Matekovits has been invited to serve as Research Grant Assessor for government funding calls (Romania, Italy, Croatia, Kazakhstan, and Iceland) and as International Expert in PhD thesis evaluation by several Universities. Prof. Matekovits has been a recipient of various awards in international conferences, including the 1998 URSI Young Scientist Award, the Barzilai Award 1998 (Young Scientist Award, granted every two years by the Italian National Electromagnetic Group), and the Best AP2000 Oral Paper on Antennas, ESA-EUREL Millennium Conference on Ant. and Propag.

He was a recipient of the Motohisa Kanda Award 2018, for the most cited paper of the IEEE Tr. on EMC in the past five years; he received the 2020 Outstanding Associate Editor Award for the IEEE AWPL. He serves as an Associated Editor of the IEEE Tr. AP, IEEE ACCESS, and IET MAP.

Raad Raad

Raad Raad received a Bachelor of Engineering degree (Hons.) in electrical engineering and a master's degree from the Switched Networks Research Centre, University of Wollongong, Wollongong, NSW, Australia, in 1997, and a Ph.D. degree in neuro-fuzzy logic admission control in cellular mobile networks in 2006. Since 2004, he has been with the School of Electrical, Computer and Telecommunications Engineering, University of Wollongong, where he works as the Deputy Head of the school. His current research interests include wireless communications, CubeSat, the IoT, and antenna design. He received an Australian Postgraduate Award that was matched by Telstra Research Laboratories. He received a scholarship from the Motorola Australian Research Centre in the later part of his degree.

Preface

The evaluation of wireless communication and satellite technology has increased interest in advanced antenna design. This reprint presents cutting-edge research contributions that address challenges in antenna designs for 5G/IoT and space applications. The increasing need for low-profile and high-performance antennas in advanced communication networks, such as 5G, CubeSats, IoT, and body area networks, highlights the need for innovative antenna designs and enhanced integration techniques.

This collection of research articles provides engineers, researchers, and industry professionals with insights into the latest advancements in antenna technology. The topics covered include phased array antennas for satellite communications, multifunctional antenna designs for the Internet of Things, metasurface-based antennas, 3D-printed antennas for urban applications, MIMO antenna arrays for 5G mobile devices, polarization control for drone networks, gain enhancement techniques for radar applications, reconfigurable intelligent surfaces (RISs) for beam-steering in IoT applications, and advanced antenna technologies for CubeSat communication. By presenting these enhancements, we wish to inspire future investigations and additional research in this field. We thank all the contributing authors for their valuable work, the reviewers for their thoughtful feedback and insightful reviews, and the editorial team for their support.

Faisal Tubbal, Ladislau Matekovits, and Raad Raad

Guest Editors

Article

A Review of Multifunctional Antenna Designs for Internet of Things

Dimitrios G. Arnaoutoglou , Tzichat M. Empliouk , Theodoros N. F. Kaifas, Michael T. Chryssomallis and George Kyriacou *

Department of Electrical and Computer Engineering, Democritus University of Thrace, 67100 Xanthi, Greece; darnout@ee.duth.gr (D.G.A.); templiou@ee.duth.gr (T.M.E.); tkaifas@ee.duth.gr (T.N.F.K.); mchryso@ee.duth.gr (M.T.C.)

* Correspondence: gkyriac@ee.duth.gr

Abstract: The Internet of Things (IoT) envisions the interconnection of all electronic devices, ushering in a new technological era. IoT and 5G technology are linked, complementing each other in a manner that significantly enhances their impact. As sensors become increasingly embedded in our daily lives, they transform everyday objects into “smart” devices. This synergy between IoT sensor networks and 5G creates a dynamic ecosystem where the infrastructure provided by 5G’s high-speed, low-latency communication enables IoT devices to function more efficiently and effectively, paving the way for innovative applications and services that enhance our awareness and interactions with the world. Moreover, application-oriented and multifunctional antennas need to be developed to meet these high demands. In this review, a comprehensive analysis of IoT antennas is conducted based on their application characteristics. It is important to note that, to the best of our knowledge, this is the first time that this categorization has been performed in the literature. Indeed, comparing IoT antennas across different applications without considering their specific operational contexts is not practical. This review focuses on four primary operational fields: smart homes, smart cities, and biomedical and implantable devices.

Keywords: Internet of Things; multifunctional antennas; 5G systems



Citation: Arnaoutoglou, D.G.; Empliouk, T.M.; Kaifas, T.N.F.; Chryssomallis, M.T.; Kyriacou, G. A Review of Multifunctional Antenna Designs for Internet of Things. *Electronics* **2024**, *13*, 3200. <https://doi.org/10.3390/electronics13163200>

Academic Editors: Raad Raad, Ladislau Matekovits and Faisal Tubbal

Received: 5 July 2024

Revised: 5 August 2024

Accepted: 9 August 2024

Published: 13 August 2024



Copyright: © 2024 by the authors. Licensee MDPI, Basel, Switzerland. This article is an open access article distributed under the terms and conditions of the Creative Commons Attribution (CC BY) license (<https://creativecommons.org/licenses/by/4.0/>).

1. Introduction

Around the world, technology is advancing at a pace that surpasses anything previous generations could have imagined. Today, wireless communication has transformed from a privileged good to a necessary need in developed countries. To further increase the quality of life, a trend has emerged that exploits mobile communication protocols to interconnect more and more devices [1]. For this revolution to materialize, there is a need to establish a way to ensure that everything is connected to everything else. The Internet of Things (IoT) encapsulates this vision by integrating a diverse range of systems. Some popular examples include intelligent homes, industrial applications, advanced farming techniques, urban innovations, and the smart energy grid [2].

The IoT is an extensive network that connects a wide array of devices, enabling them to exchange data with one another at relatively high speeds [2]. For this vast network to function, these devices must incorporate some form of communication system, whether wired or wireless. Wired communication is generally preferred due to its high data transfer rates, low latency, reliability in packet delivery, and efficient power consumption. However, the necessity of physical connections makes it impractical for many applications, limiting its appeal. On the other hand, wireless communication offers flexibility and adaptability, allowing devices to be placed in various environments without the need for complex installation procedures. The goal is to make it available anywhere and at any time. Despite these advantages, wireless communication faces reliability issues. The quality of a wireless link

between two devices can be influenced by several factors, including range, environmental conditions (such as humidity and proximity to the ground), interference, and more. These factors can lead to increased data loss, jamming, connection drops, high latency, and even loss of control over the devices [2]. Therefore, there is a pressing need to develop more reliable and efficient wireless communication methods while also minimizing the power consumption of the devices involved.

The wireless connection of two devices involves communication via electromagnetic (EM) waves that can be divided into two major categories: optical and microwave links. Optical systems utilize EM waves in the infrared or visible light spectrum, enabling high data transmission rates. However, optical communication is primarily limited to line-of-sight (LoS) applications because light cannot penetrate obstacles like walls and can be disrupted by weather and environmental conditions. In contrast, microwaves, while they are relatively immune to weather and environmental conditions, allow the penetration of signals through various objects, facilitating non-line-of-sight (non-LoS) communication. Within microwave systems, antennas play a crucial role in wireless communication. Antennas are capable of emitting or receiving EM waves from their radiating surface, efficiently converting them to or from electrical currents, thereby enabling the exchange of information over distances without the need for physical connections.

Designing antennas for IoT applications presents unique challenges due to the diverse requirements of each application field (such as vehicle-to-vehicle communications (V2V), biomedical implants, smart sensors, etc.). A versatile antenna designed for IoT purposes must tackle several objectives, including easy deployment, minimal physical size, and the capability to efficiently receive a wideband response. Often, these demands are met by designing antennas that are omnidirectional or quasi-isotropic and support multiple polarizations, often in the form of printed antennas [3], especially for smart home applications. Depending on the specific application, more specialized antenna types may be necessary. For instance, durable antennas are essential for use in harsh environmental conditions (e.g., agricultural fields), whereas biomedical applications may require antennas that are more flexible and efficient to be placed in a patient and immersed in the highly lossy human body [4]. In scenarios requiring high data throughput, antennas capable of wideband, dual-band, or even multi-band operation become critical. For 5G and future generations where space-division multiple access (SDMA) is utilized, antennas with reconfigurable radiation patterns that can produce non-overlapping multi-beams while operating within a specific communication protocol are prioritized [5]. Additionally, the EM link may need to exhibit different polarizations, such as linear and circular-elliptical (right- or left-hand rotating). This feature calls for multi-polarized IoT antennas to allow parallel simultaneous propagation of orthogonal signals, increasing the communication capacity. These situations underscore the need to develop novel antennas or re-engineer existing ones to enhance the designer's toolkit. The goal is to accommodate a broader range of applications while also enabling precise adjustments to optimize critical performance indicators of the antenna.

In recent years, a growing number of innovative antenna designs have been introduced in the academic literature, targeting one or more of the above objectives to ensure their compatibility with IoT devices. Various methods are employed in the design and optimization of these antennas, including characteristic mode analysis [6,7], full-wave solvers [8], equivalent circuits [9], and analytical solutions [10]. Currently, the most common approach involves using numerical full-wave electromagnetic or multiphysics solvers. This process starts with a basic antenna structure, such as a rectangular patch antenna, which is then modified through the addition of slots, new elements, or even a complete redesign [11]. Subsequently, parametric or optimization methods are applied to fine-tune the antenna's performance to meet specific operational criteria. Once the design is finalized, a prototype is manufactured and tested under small-signal conditions to evaluate its S-parameters, radiation pattern, and efficiency [8].

The effectiveness of an antenna is typically assessed based on its size, bandwidth, axial ratio (for circularly polarized antennas), reconfigurability, and manufacturability.

Recent reviews on IoT antennas classify them based on attributes such as reconfigurable properties [12], design methodology [8], type [13], bandwidth [14], and the kinds of tunable elements utilized [15]. Occasionally, review papers introduce new metrics to facilitate a more equitable comparison among different antenna designs. One such metric, the axial-to-impedance bandwidth ratio, was proposed to evaluate an antenna's capability to function as circularly polarized (CP) throughout its entire operational bandwidth [15]. This metric and similar others aim to quantify the performance and suitability of antennas for specific applications.

The term "IoT" includes a wide range of applications, each with its unique requirements, making it overly simplistic to presuppose that any IoT antenna is suitable for all IoT applications. When an antenna is identified as suitable for IoT, it is essential to specify its operational domain. For instance, a wideband, high-gain, and beamforming-capable antenna might be ideal for IoT applications in 5G networks but less suitable for others [4]. Therefore, comparing IoT antennas across different applications without considering their specific operational contexts is impractical.

To address this issue, we undertake a comprehensive review of IoT antennas, categorizing them based on their field of operation within IoT. This approach requires selecting the most representative categories of IoT applications, considering the unique nature of each application and the specific antenna characteristics it demands. This review focuses on four primary operational fields: biomedical and implantable devices, smart homes, and smart cities. It is important to note that even within these categories, there are sub-categories with vastly different requirements (for example, the differences between implantable and wearable antenna specifications). This review represents the first attempt, to the authors' knowledge, to compare IoT antennas based on characteristics tailored to specific applications, providing a clear understanding of how antenna designs can meet the diverse needs of the IoT landscape.

2. Materials and Methods

2.1. Biomedical Devices

The Medical Internet of Things (Medical IoT) represents a groundbreaking integration of medical devices with individuals, utilizing wireless communication to enable the exchange of healthcare data, facilitate remote patient monitoring, and significantly improve the quality of life for patients [4]. This innovation not only promises to enrich lives but also aims to enhance the quality of care and introduce cost efficiencies within healthcare institutions. The implementation of the Medical IoT in the healthcare sector is rapidly expanding on a global scale, though it encounters a variety of obstacles that need to be addressed to widen its application. These challenges include, but are not limited to, scalability, mobility, cost, complexity, management, trust, security, and interoperability.

Medical IoT applications can range from simple biological metrics, such as blood pressure [6] or temperature [16], to more complex measurements like the concentrations of certain substances [17]. The devices responsible for this monitoring need to be sufficiently small to be implantable [6], ingestible in the form of a capsule [18], or wearable [16]. Beyond the real-time wireless monitoring of various physiological parameters, a variety of emerging applications have been highlighted in recent studies. These include:

- The management/treatment of brain disorders [19] through brain-computer interfaces (BCIs) that enable direct communication between the brain and an external device [20,21];
- The Tongue Drive System (TDS), which allows for control of devices through tongue movements [22];
- Leadless pacemakers that provide cardiac rhythm management without the need for wired leads [23];
- Neurostimulators that deliver electrical stimulation to targeted areas of the brain or nervous system [24];

- Techniques for imaging blood vessels to support diagnosis and treatment planning [25];
- Drug delivery systems designed to release medications in a controlled manner at targeted locations within the body [26].

These advancements illustrate the broad and evolving scope of the Medical IoT in enhancing healthcare delivery and patient care.

2.1.1. Challenges of Ingestible and Implantable Antennas

In recent years, there has been a rapid development of wearable sensors and transmitters, making them an easily accessible and commercially available option where simple patch antennas are sufficient [4]. Different examples of biomedical antennas are presented in Figure 1. However, IoT antennas for implantable and ingestible devices present a significant challenge for the designer. The human body is conductive and presents high dielectric constants [27], primarily due to its water content and the electrodes. This electromagnetically hostile environment complicates the development of miniature and efficient antennas capable of penetrating human tissue to transmit data to an external receiver when the sensor is located inside the patient's body. For these applications, the antenna must achieve high efficiency, operate at low frequencies, and have a small footprint.

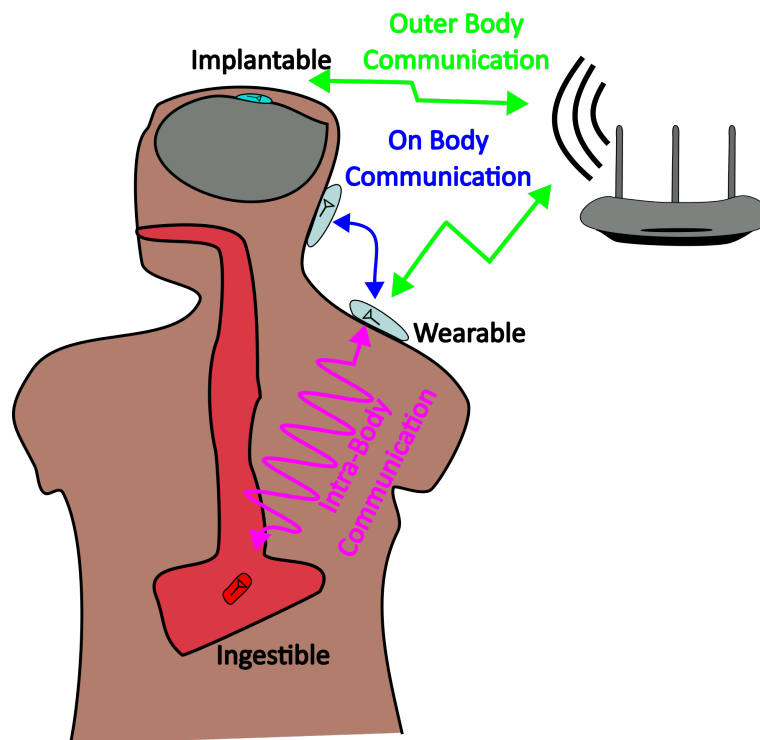


Figure 1. Architecture of communication systems involving implantable, ingestible, and wearable antennas.

High efficiency is crucial for these devices as their power supply is limited; they either use small batteries, which cannot be frequently replaced, or rely on energy harvesting or wireless power transfer techniques [4]. Additionally, to ensure that the signal can be transmitted outside of the human body, operating at a longer wavelength is beneficial, as it facilitates easier signal transmission through heterogeneous human tissues. Moreover, given the requirement for these devices to be implanted or ingested, it is imperative that the antennas have a low profile to fit within the confined spaces of a small capsule [18] or implantable device [28]. Based on the application, the size and the shape of the implantable antenna may differ, but in most cases, a few dozen mm^3 of volume is needed for their placement inside the human body. On the other hand, the data rate is not deemed a critical

factor for these types of devices, as the data collection from measurements is expected to occur at relatively low sampling frequencies (less than 1 Hz), focusing instead on the reliable transmission of crucial health metrics. As a result, electrically small antennas have become increasingly attractive for such applications [4].

Designing electrically small antennas presents significant challenges, primarily due to their extremely low efficiency, often a result of the platform effect seen in printed structures, and the complexity of their operation in the near field, which complicates the analysis [4]. Furthermore, due to their low operating frequencies, their bandwidth is limited to low-data-rate applications. The preferred operating frequency for most implantable antennas falls within the free bands allocated for industrial, scientific, and medical (ISM) applications (433, 915, and 2450 MHz). Among the various designs, printed planar loop antennas are the most commonly utilized for these applications [19,29]. These antennas are favored for their compact size and high efficiency, attributed to their primary excitation of magnetic fields, which are more capable of penetrating the highly dielectric and lossy human tissue compared to electric fields. This makes printed loop antennas particularly well suited for implantable devices, where efficient communication through human tissue is essential. On the other hand, in a conformal configuration, the antenna is wrapped inside the device package to minimize the occupied space while maintaining a large electrical size [30]. This structure is observed in capsule-like ingestible antennas (endoscopy). Their cylindrical shape is optimal, providing a smooth curvature for antenna wrapping [31]. However, in recent years, different types of magnetoelectric antennas have been proposed to achieve low operating frequencies while maintaining a low footprint ($<10 \text{ mm}^3$) in order to fit inside leadless pacemakers and brain devices [32,33].

2.1.2. Planar Loop Antennas

A novel rectangular loop implantable antenna design featuring three concentric loops was introduced, utilizing an I-shaped ground to significantly enhance tuning across operational bands [34]. Polydimethylsiloxane (PDMS) was chosen as the material for both the substrate and superstrate due to its favorable properties for implantable medical devices. The performance and safety of the overall antenna structure were evaluated using realistic human scalp phantom models and a homogeneous skin box to closely mimic the conditions of implantation. The simulation studies of this antenna design indicated that it operates effectively around 5.8 GHz. Concerning safety, the specific absorption rate (SAR), which measures the rate at which energy is absorbed by the human body when exposed to an RF field, was found to be 0.28 W/kg for the skin box and 0.26 W/kg for human scalp phantoms. The safety levels based on Institute of Electrical and Electronics Engineers (IEEE) and Federal Communications Commission (FCC) standards [35] are 1.6 W/kg and 2 W/kg when 1 g and 10 g of head tissue is exposed to EM radiation. It is important to note that these limits are valid for the RF frequency range of 100 kHz–300 GHz. This demonstrates the antenna's suitability for safe use within the specified operational parameters (1 mW input power). The transmitting system is powered by a battery source, which limits the operational period, particularly for cranial implants. Additionally, while selecting a high operating frequency can reduce the size of the system compared to other designs, it also results in a decreased gain of -32 dB . This reduction in gain confines the system's application primarily to shallow implants, where such low gain is less critical.

To further simplify the RF transceiver circuitry and eliminate the need for Baluns (balance to unbalance converters) required by single-ended antennas, differential loop antennas have been introduced as a solution [18,36]. These antennas feature an inductively coupled feed structure alongside dual-band meandered radiators, achieving a -10 dB impedance fractional bandwidth of 10.2% with the circular-shaped foldable circuitry frequently used in commercial ingestible capsules. Utilizing a realistic phantom for testing at 2.45 GHz, the antenna demonstrated a gain of -27.9 dB , indicating potential suitability for applications in wireless ingestible capsule technology. However, the frequency of operation was adjusted due to the structural complexity, which may be attributed to the flexibility of the foam. This

raises concerns about the behavior of the system when inserted inside the human body. Furthermore, such antennas present high reactive impedance due to the inductive coupling, making the matching between the antenna and chip a complex procedure.

2.1.3. Meander Antennas

Meandered patch radiators are an innovative approach to minimizing antenna size, particularly effective in scenarios requiring biocompatible materials. Such antennas are normally placed inside a plastic capsule in the shape of a pill in order to be swallowable (Figure 2). In one specific design [21], alumina serves as the dielectric substrate. This antenna incorporates a defected ground structure and a shorting pin to optimize its performance. It is strategically positioned between the cortical bone and dura layer within a seven-layer human brain phantom to assess its effectiveness in facilitating the transmission of neural signals to external devices or computers, a key function in the brain-computer Interface (BCI). The SAR was determined to be an enormous value of 682 W/kg when averaged for a 1 g tissue sample and 77.1 W/kg averaged over a 10 g tissue sample for 1 W power input. These findings demand that to avoid harmful effects on human brain tissue the antenna can safely operate at input power levels of 25 μ W and 3.24 μ W, respectively, much smaller than the expected power around 1 mW. The SAR limit is the same as defined earlier.

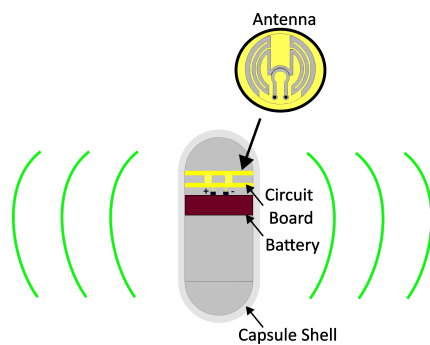


Figure 2. Differentially fed antenna enclosed in a capsule shell for ingestible wireless capsules.

A dual-band meandered patch antenna design is demonstrated in [37]. This miniaturized antenna, with dimensions of $5 \times 5 \times 0.635 \text{ mm}^3$, displayed a wideband response, namely, 300 MHz in the 1.4 GHz band and 380 MHz in the 2.45 GHz band. Its meander-shaped microstrip patch configuration not only provides a low-profile form factor but also simplifies integration with other circuits. The meandered slots play a critical role in tuning the antenna, enhancing its bandwidth, and minimizing its size. To achieve further size reduction, a material with a high relative permittivity ($\epsilon_r = 10.2$) was chosen for the antenna's substrate (Rogers RT/Duroid 6010). Additionally, the introduction of ground slots adds a parasitic element that boosts the antenna's radiation efficiency to a total of 1%. The proposed antenna's functionality in wireless bio-telemetry applications is demonstrated through the use of a pair of wireless transceivers. This setup highlights the antenna's capability for sustainable and stable wireless data transmission, achieving a high data rate of 2 Mb/s over a distance of up to 20 cm when the receiver is placed on the body surface.

2.1.4. Various Antenna Types

In the realm of antenna design, especially for applications requiring operation within or around the human body, a variety of innovative electrical structures have been explored and documented in the literature. Some indicative examples include planar inverted-F antennas (PIFAs) [38,39], dielectric resonator antennas (DRAs) [40], metamaterial-based antennas [41], and Vivaldi antennas [42]. Each of these designs offers unique advantages for specific applications, addressing different challenges related to size, efficiency, and bandwidth.

In particular, the Vivaldi antenna [42], when embedded vertically against the dura mater within a skull phantom, demonstrates particularly noteworthy performance characteristics. This configuration results in increased radiation gain directed toward the end-fire orientation of about 30% with respect to the conventional antenna, namely, with an average gain of -15.7 dBi across a wide bandwidth range from 3 to 5 GHz. This extensive bandwidth may go underutilized because even the most bandwidth-intensive modulation schemes used in such applications will not exceed 100 MHz. However, this antenna can offer versatility in its frequency of operation, particularly if certain frequencies experience high attenuation. Furthermore, a link budget analysis of this skull-embedded Vivaldi antenna underscores its potential for reliable wireless communication within the challenging harsh environment of the human body. The analysis indicates that effective communication can be maintained over a distance of 10.8 cm between the two antennas (receiver and transmitter), even with a transmitted power as low as -25 dBm [42]. Another advantage of the antenna is the low SAR, which permits higher power input in comparison with previously mentioned antennas (5 mW).

2.1.5. Magnetolectric Antennas

A novel class of antennas, particularly suitable for low-frequency (LF) applications where compact size and device integration are critical has been gaining attention. For example, the absorption of LF magnetic fields in human tissue is notably lower, enhancing the suitability of antennas generating dominant magnetic fields for use in or near the human body. These antennas exploit magnetolectric (ME) coupling and electromechanical resonance (EMR) to address the limitations traditionally associated with conventional electric field antennas, particularly in terms of efficiency and miniaturization, for very high frequency (VHF) and ultrahigh-frequency (UHF) applications. Unlike conventional EM antennas that resonate based on electromagnetic properties, LF ME antennas operate by resonating at the mechanical frequency of their physical structure, which allows for a significant reduction in their overall size.

In ME or multiferroic or mechanical antennas, a low-frequency AC magnetic field (H_{AC}) interacts with a magnetostrictive layer, causing a periodic rotation of magnetic domains and a shift in domain boundaries [43]. This interaction generates a mechanical strain, which, when transferred to an acoustically coupled piezoelectric layer, results in electrical polarization (or the reverse process, depending on the operation mode). Acoustically driven antennas can operate at resonant wavelengths that are up to 10^5 times smaller than their electrical counterparts, providing a substantial advantage in terms of miniaturization and efficiency for specific applications. It is important to note that the term high efficiency is denoted for ME when compared with the same dimensions of electric current-based antennas at the same frequency. This means that the efficiency may not be high as compared to conventional antennas, but their size is smaller while keeping the efficiency at acceptable levels.

One of the standout features of acoustic antennas is their real resonant impedance, while electrically small antennas of similar size present high reactance [43]. Notably, high real input impedance means that the antenna can accept and then radiate a significant amount of power. On the contrary, high input reactance causes the reflection of the power fed to the antenna. This unique operation mechanism allows LF ME antennas to achieve remarkable miniaturization and higher efficiency compared to embedded traditional EM antennas. Moreover, ME antennas can possess the dual functionality of wireless energy harvesting and sensing at different frequencies, expanding their utility beyond data transfer [44]. This dual capability, combined with their compact size and acceptable efficiency (0.5%), positions ME antennas as a promising solution for advancing the functionality and performance of a wide range of low-frequency applications, including those in the medical field.

Despite the above benefits, it is important to note that the radiation efficiency of acoustic antennas can vary widely depending on how the acoustically driven antenna is

implemented [45]. While the impedance characteristics are a common trait among most acoustic antennas, leading to enhanced matching efficiency, the specific design and fabrication of an acoustically driven antenna play a crucial role in determining its overall radiation efficiency.

A groundbreaking development in ME antenna technology involves a self-biased, miniaturized LF ME antenna, as proposed in [46]. This antenna operates at an electromechanical resonant frequency of 49.9 kHz, and its volume has been significantly reduced to only 1.75 mm³, making it substantially smaller than comparable EM antennas. The design features a piezoelectric layer sandwiched between two magnetostrictive layers, effectively leveraging the magnetoelectric effect for signal generation and reception. The performance of this antenna was evaluated both in air and within a specially optimized three-layered (skin, fat, and muscle) human tissue-mimicking phantom as a function of the frequency, to explore its potential for deep-body communication applications. In tests, the maximum received power was recorded at 20 nW in air and 8 nW in the phantom media at a distance of 1.2 m from the source. Notably, this ME antenna exhibits a significantly lower path loss of only 0.57 dB/m, compared to antennas operating at higher frequencies. In such cases, due to low operating frequency, the data rate is limited as in the case of [47], where for a center frequency of 274 kHz a rate of 220 kbps was achieved. However, in the tests, vibrations due to the body were not taken into consideration, which eventually will degrade the efficiency of the antenna.

In a similar approach to advance implantable medical devices, an ME antenna described in [44] has been integrated within a CMOS energy harvester chip. This combination aims to establish a wireless communication link specifically designed for fully integrated implantable devices, targeting the dual objectives of energy harvesting and signal transmission. The system is designed to perform two critical functions: first, to receive pulse-modulated power from a nearby transmitter, enhancing the device's operational longevity without the need for physical connections; and second, to accurately sense and transmit low-magnitude neural signals, facilitating advanced medical monitoring and therapeutic interventions. A piezoelectric layer made of aluminum nitride (AlN) was connected via epoxy with a magnetostrictive layer composed of iron gallium boron (FeGaB). The antenna operates at two different frequencies, corresponding to its width and thickness resonances, which are optimized for the specific requirements of neural implant applications.

To evaluate the efficacy of ME antennas, a wireless test platform was developed in [44], serving as a valuable tool for neural implant design and testing, as seen in Figure 3. This setup includes an RF measuring system to test the ME antenna behavior, while coils are used to produce AC and DC magnetic fields. In more detail, the DC magnetic field is needed to bias the magnetostrictive material, and the AC low-frequency magnetic field is sensed through the antenna. An RF signal is transmitted through software defined radio (SDR), which is collected from the antenna acting as a harvesting device, and measured using a spectrum analyzer. Finally, the SDR can receive an RF signal from the ME, which carries the information about the intensity of the low-frequency magnetic field. Utilizing this platform, the integrated system demonstrated its capability by successfully transmitting a magnetically modulated action potential waveform. Neuronal activity generates small transient currents that produce small neural magnetic fields (NMFs) [48]. The ME antenna is capable of detecting these NMF signals due to its low operating frequency. The test configuration was developed to simulate the magnetic field generated by brain activity using Helmholtz coils activated by an SDR. To achieve a realistic testing environment, the ME antenna was stimulated with neural action potentials to facilitate magnetic modulation of low-frequency signals. This setup reproduces the action potential's voltage waveform, generating a corresponding magnetic field. The process activates the ME antenna, enabling it to perform wireless sensing and data transmission over a 63.63 MHz frequency link. The received signal was then processed utilizing the microprocessor of the SDR to estimate the action potential.

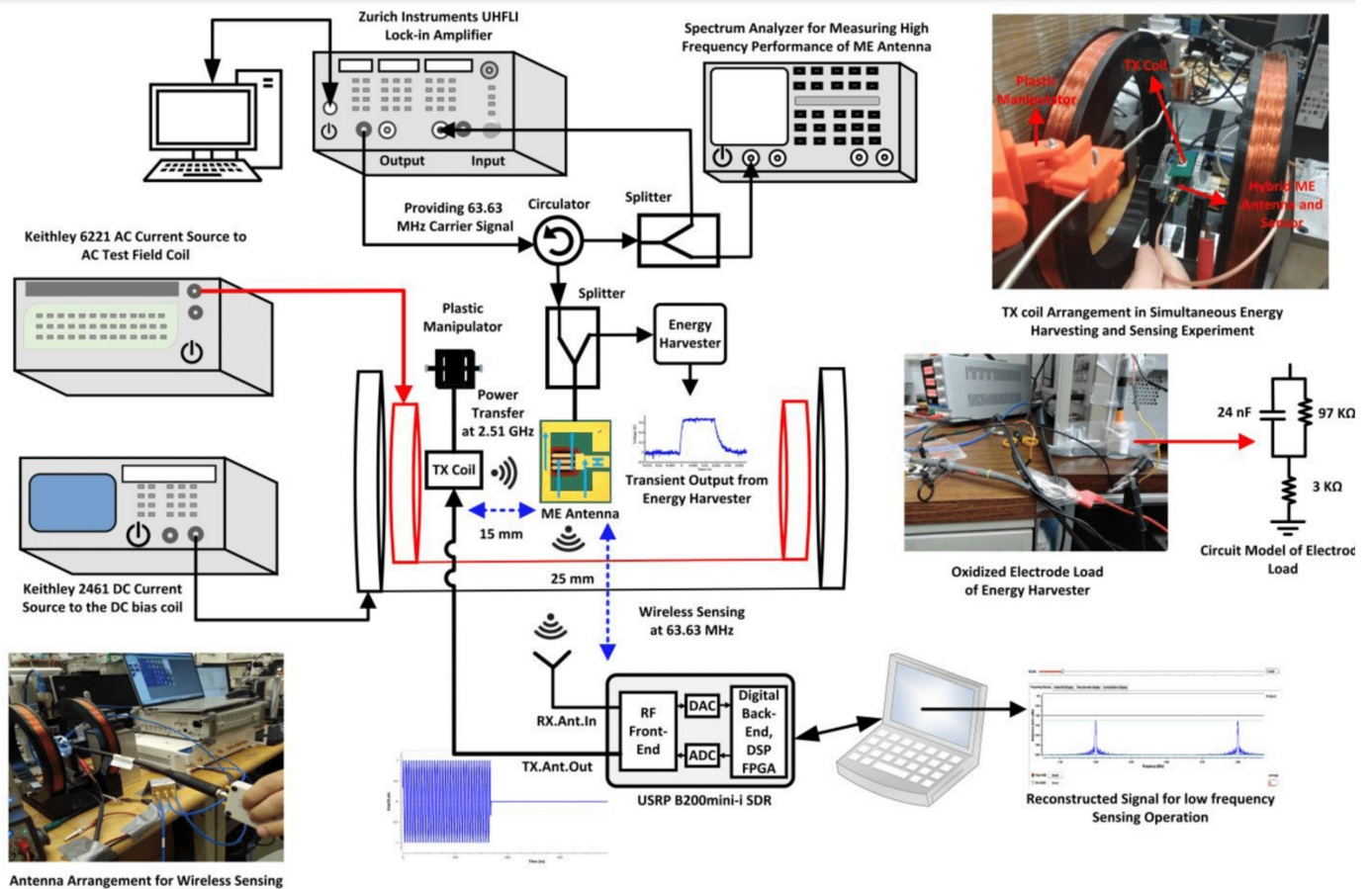


Figure 3. Measurement setup for simultaneous magnetic field sensing and energy harvesting of a magnetolectric antenna presented in [44].

2.1.6. Discussions and Perspectives through Interdisciplinary Collaborations

The aforementioned antennas are summarized in Table 1, which displays their most crucial parameters for these applications. It is evident that there is a trade-off between the size of the antenna and its gain, as electrically smaller antennas typically present low efficiency. Furthermore, in many cases, the operational bandwidth of the antenna is not mentioned, indicating a small bandwidth that leads to low data rates. To increase the data rate, multiple-band planar inverted-f antennas (PIFAs) have been investigated by different researchers [38,39]. To further increase the gain and the antenna efficiency metamaterials may be used, as seen in [41]. Another way to enhance the efficiency and minimize the volume of the structure is by exploiting magnetolectric (ME) materials, though this approach sacrifices bandwidth. In magnetolectric antennas, radiation is achieved through the acoustic resonance of the antenna, which induces magnetic oscillations. This phenomenon is utilized to surpass the radiation bounds defined by Chu–Harrington’s limit, particularly originating from the distance between the ground plane and the radiator [49]. It is important to highlight that this behavior is observed for general electrically small antennas due to the longer wavelengths. Despite these advantages, the efficiency of magnetolectric antennas remains poor due to acoustic mismatches between the piezoelectric and magnetostrictive materials, as well as the low piezoelectric and piezomagnetic coefficients. In summary, the concept of magnetolectric antennas appears to be more appealing at radio frequencies than in the microwave region based on current data.

Table 1. Comparison table of different antenna designs for implantable and ingestible devices.

Antenna	Gain (dBi)	Size (mm ³)	Q	Frequency	Reference
Meandered Patch	−32.1/−31.5	5 × 5 × 0.635	4.05/6.45	1.4/2.45 GHz	[37]
Dif. Meandered Patch	−27.9	25 × 11 × 11	10	2.45 GHz	[18]
Impl. Vivaldi	−15.7	44	2	4 GHz	[42]
Rectangular Loop	−32	5 × 7 × 0.3	5.9	5.9 GHz	[34]
Meandered Patch	−28.65	6 × 9.55 × 0.2	5.21	2.4 GHz	[21]
Dif. Meandered Loop	−28.6	25 × 11 × 11	19.6	2.45 GHz	[36]
Diel. Resonator	−25.7	3 × 4.7 × 1	-	2.45 GHz	[19]
Metamaterial	−15.2	8 × 8 × 0.15	-	2.45 GHz	[41]
Conformal Loop	−28.9/−18.6	28 × 9 × 9	-	0.434/2.45 GHz	[29]
PIFA	−33.6/−21/−15.49/−10.25	154	3.19/2.25/8.33/14	0.403/0.915/1.4/2.45 GHz	[39]
PIFA	−45.6/−27.6/−25.4	11 × 20.5 × 1.8	-	0.403/0.902/2.45 GHz	[38]
ME	−18.1	0.2 × 0.05 × 0.001	632	2.53 GHz	[50]
ME Disc	−15.59	0.2 × 0.2 × 0.001	16	2.49 GHz	[51]
Self-biased ME	−61	3.5 × 5 × 0.025	1970	49.9 kHz	[46]

The most challenging task in designing wearable, and especially implantable, antennas is that they primarily operate in the near field due to the highly lossy dielectric medium of the human body. This medium absorbs electromagnetic waves, significantly affecting antenna performance. Therefore, designing an effective implantable or ingestible antenna requires precise measurements within the human body to verify its operation and ensure reliable communication. However, for practical and ethical reasons human test subjects (clinical trials) cannot be used in the initial stages of design. Consequently, phantoms made from materials that mimic human tissue, such as minced meat or agarose gel [37] or an agarose matrix [52], are used for testing. These phantoms allow researchers to simulate the electromagnetic environment of the human body, providing valuable insights into antenna performance without the need for live human trials. By using these realistic models, engineers can refine antenna designs to enhance their efficiency, safety, and effectiveness before moving on to more advanced testing stages.

However, actual clinical trials to fully validate a device's functionality are performed in very few cases after the initial design stage. In this context, the optimal development and exploitation of antennas and wireless communication systems for biomedical devices cannot be achieved solely by engineers. Close collaboration with medical doctors and other healthcare professionals is essential to ensure continuous dialogue and bidirectional feedback throughout the design process. Such collaboration ensures that antenna designs meet both technical and clinical requirements, addressing practical healthcare challenges and patient needs.

Although the importance of interdisciplinary collaboration is well understood, related efforts often lack systematic organization. This can lead to communication gaps and misaligned priorities between engineers and medical professionals. Establishing structured frameworks for collaboration, such as interdisciplinary teams and regular meetings, can enhance the integration of medical insights into the engineering design process. By fostering a more organized and collaborative approach, the development of biomedical devices can better align with the realities of clinical practice, ultimately improving patient outcomes and advancing the field of medical technology.

In addition, implantable or wearable antennas and devices require complicated and miniaturized mechanical designs, and any materials used must be biocompatible. This issue can greatly benefit from recent advancements in 3D printing if they are appropriately directed through feedback from scientists developing antennas or biomedical devices. This perspective was emphasized a decade ago by organizations and universities, such as in the MIT white paper [53]. To our knowledge, this enlightening idea is not yet widely established. Organizing interdisciplinary committees at each university, possibly managed by national forums, could be a good approach.

2.2. Smart Home Appliances

Smart homes represent the combination of IoT technology with residential living, offering the ability to remotely control various home functions via a smartphone or computer [54]. This integration has led to remarkable progress in making our living spaces more comfortable, secure, energy-efficient, and convenient. By incorporating an array of technologies such as sensors, interactive interfaces, monitoring systems, and intelligent appliances, smart homes are interconnected environments that facilitate both automated and manual management of domestic activities [54]. These technologies, controlled by advanced information and communication systems and enhanced by machine learning algorithms, allow smart homes to analyze the behaviors and preferences of their inhabitants. This capability enables the home environment to adapt its operations to the specific needs and habits of its residents, thereby elevating their overall quality of life. Furthermore, smart homes are adept at optimizing energy consumption, ensuring that appliances and other household features operate more efficiently [55]. This not only contributes to a healthier and more eco-friendly living space but also promotes a more sustainable approach to residential living.

2.2.1. Antenna Specifications

To ensure connectivity among various sensors and actuators within a household, the development of novel multifunctional antennas is critical. Given the requirement for all devices within a home to be interconnected, there are primarily two antenna design strategies to consider, as illustrated in Figure 4. One approach involves antennas that generate multiple beams, adaptively steering their main beam toward other IoT devices. Alternatively, antennas can be designed with omnidirectional or nearly isotropic radiation patterns to ensure comprehensive coverage across the entire household space. Examples of omnidirectional and isotropic radiation patterns are depicted in Figure 5, for which the radiation is emitted almost in every direction. However, in such cases the antenna gain is minimized, decreasing the covering range of the antenna, so an appropriate analysis must be performed to ensure the entire coverage of a home. While a hybrid of these approaches is also feasible [56], this review will focus on the latter strategy. This decision is based on the assumption that many wireless sensors may lack the size or power capabilities to support multi-beam functionality.

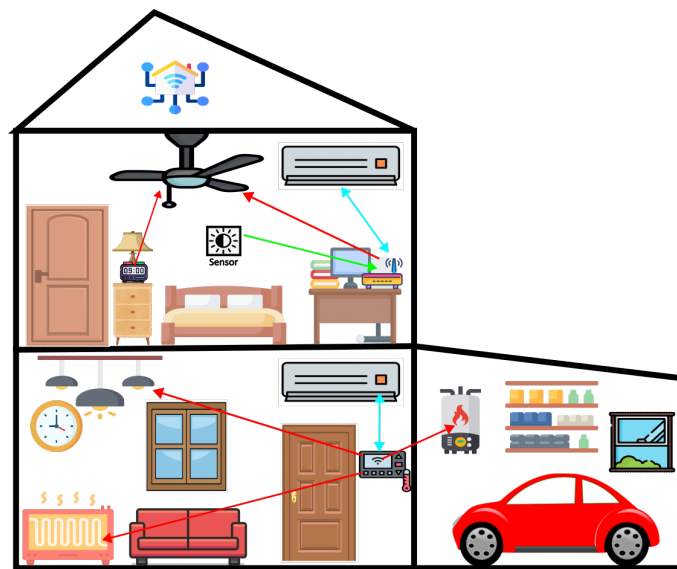


Figure 4. Typical smart home architecture denoting the antenna utilization. Arrows denote some of the plethora of possible communication lines.

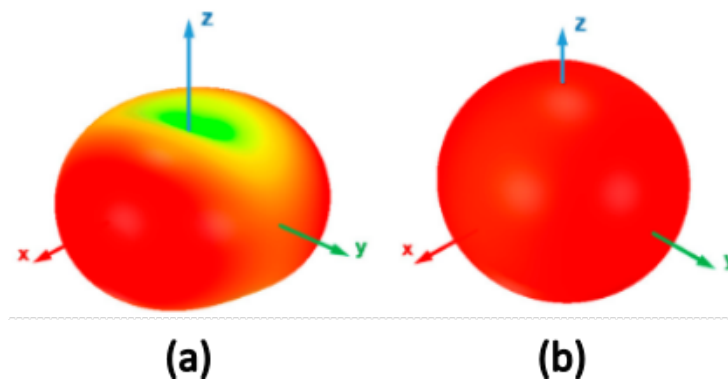


Figure 5. Radiation pattern of (a) an omnidirectional and (b) an isotropic antenna.

Regarding operating frequencies, most smart home applications use widely adopted communication protocols such as Wi-Fi, Bluetooth, and Zigbee, which operate in the ISM bands. The prevalence of these technologies is due to their mass production capabilities, cost-effectiveness, and ease of programming for IoT devices. Additionally, these protocols support high data rates within the small, controlled environment of a home network. Consequently, the majority of IoT antennas currently operate within the Wi-Fi bands. However, there have been research efforts to explore mmWave wireless systems, which offer higher data rates and reduced interference from crowded Wi-Fi bands, as well as miniaturized sizes [57]. Despite these advancements, commercial availability of mmWave systems remains limited. In this review, we will not limit our discussion to Wi-Fi bands but will also cover the entire sub-6 GHz band and some millimeter-wave (mmWave) bands. This broader scope aims to provide readers with a comprehensive view of emerging technologies, extending beyond commercially available bands. The primary goal of this review is to highlight multifunctional antennas that could potentially be used in future IoT devices. Additionally, many of the presented devices can be appropriately tuned to operate in the desired frequency bands, even if those frequencies are not currently licensed for use.

Non-directive antennas, therefore, are required to offer multi-polarization capabilities to cope with the polarization mismatch due to the highly reflective environment of modern homes. Notably, wave reflection is expected to alter the orientation of the electric field, thus causing a change in its polarization. This is very well understood in free space propagation, where a horizontally polarized wave may generate both horizontal and vertical fields when it is reflected at an obstacle. Thus, the multi-polarization feature is essential for maintaining reliable communication. Additionally, it is usually preferred for frequency-agile antennas to operate in different frequency bands of 5G because wideband behavior is difficult to achieve [15]. Such flexibility in antenna design is crucial for achieving comprehensive connectivity within smart homes, enhancing the integration and functionality of IoT devices.

Incorporating antennas with versatile polarization capabilities into communication systems necessitates meeting two key criteria: (i) the antenna must possess a structure capable of supporting multiple polarizations, and (ii) it requires a sophisticated feeding network designed to excite or receive the specific polarization needed at any given time. Achieving these requirements using only passive elements presents significant challenges, leading to the proposal of electrically and mechanically reconfigurable antennas as a solution [15]. Reconfigurability in antennas allows for adjustments in the electrical size and/or shape of the antenna, thereby controlling its operational characteristics, such as frequency, polarization, and radiation pattern. The polarization of an antenna is fundamentally linked to its physical configuration, as the direction of surface currents on its radiating elements is influenced by the shape of the antenna radiator and the manner in which it is excited. Recall that the electric field of the generated wave retains a direction (polarization) parallel (or following) to that of its source electric current density. An antenna can shift its polarization sensing between different types, such as from linear (LP) to circular (CP), or from RHCP

to LHCP, and so on [58]. A simple example is depicted in Figure 6, where a cross-dipole antenna can be operated in three polarization configurations.

Various methods exist for tuning antenna characteristics, including mechanical adjustments (e.g., motor-based steerable systems) [59], pumping liquid metals into special hollow cavities to alter substrate permittivity and permeability [60], and the use of photoconductive switches activated by laser light on semiconductor materials [61]. However, electrical tunability remains particularly attractive for sub-6 GHz integrated antennas. The ease with which electronic components can be integrated into antenna systems allows for efficient and effective modification of antenna properties. This form of reconfigurability at RF often employs electronic switches, such as PIN diodes and varactor diodes, to alter an antenna's operational characteristics [12].

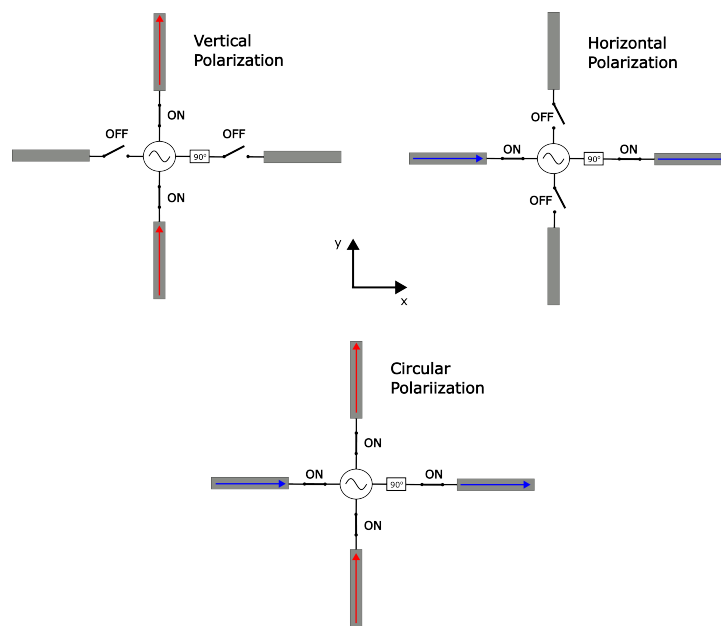


Figure 6. Simple switchable polarization cross-antenna configuration enabled by electronically controlled RF switches.

2.2.2. Characteristic Mode Analysis as IoT Design Tool

The design process of reconfigurable antennas presents a complex challenge that requires the utilization of various techniques to transform a conventional antenna into a multifunctional one. The literature highlights a diversity of methodologies, each bearing unique characteristics tailored to specific design goals. Notably, there has been a growing trend in recent years towards the use of characteristic mode analysis (CMA) in antenna design [62]. CMA is valued for its effectiveness as a design tool, primarily because it provides direct insights into the radiating behavior of antennas. This facilitates a more systematic and informed approach to design, as opposed to relying solely on the engineer's experience or trial and error. CMA can be particularly effective in determining the optimal locations for excitation on the radiator. In this context, CMA emerges as a powerful technique, equipping designers with a deeper understanding of the antenna's operational mechanisms and allowing for the strategic manipulation of its properties to achieve desired reconfigurability and functionality.

Various CMA-based antenna designs have been proposed for the IoT [6,7,63–65]. A notable example of leveraging CMA is presented in the design of an electronically reconfigurable 6-port dual-band dual-mode microstrip ring antenna (Figure 7) [7]. The design process, facilitated by CMA, identified two non-conventional higher-order modes suitable for operation within two sub-6 GHz frequency bands. The selection of these modes capitalized on the natural orthogonality of the characteristic modes. This orthogonality translated into achieved isolation exceeding 37 dB in both bands, negating the need for

complex decoupling strategies typically required to mitigate interference between multiple ports. To enable dynamic switching between the two identified operational modes, an integrated electronically reconfigurable matching network was developed, incorporating six PIN diodes and six varactor diodes. The antenna displayed a peak gain of 4.7 dB for both modes and radiation efficiency values of 44.3% and 64% at the two frequency bands, respectively. Unfortunately, the radiation pattern exhibits nulls in certain directions due to the selected characteristic mode, deviating from the desired quasi-isotropic pattern. Additionally, the selected modes differ by only about 300 MHz, which is insufficient for IoT devices that may need to switch between different Wi-Fi bands, such as 2.4 GHz and 5 GHz.

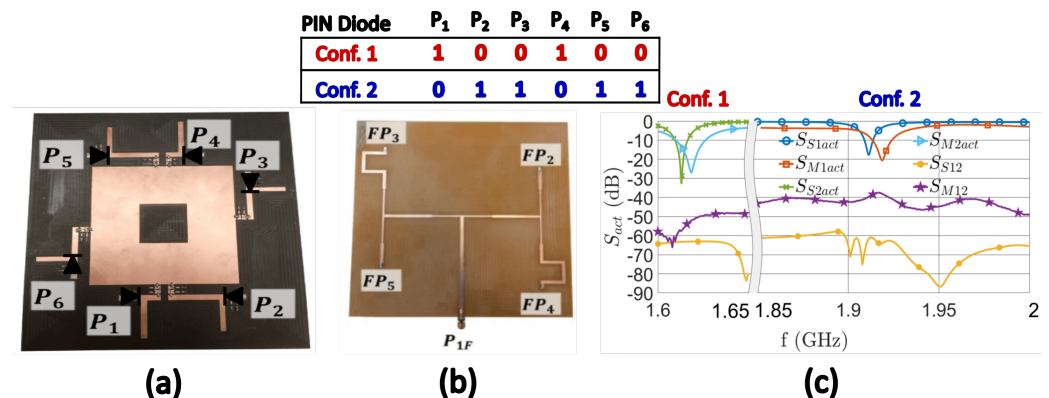


Figure 7. (a) A 6-port reconfigurable dual-band dual-mode microstrip ring antenna designed exploiting characteristic mode analysis; (b) its feeding network and (c) scattering parameters [7].

Two LP states is not quite enough for a polarization-agile antenna, due to the use of CP waves in an increasing number of applications to mitigate mismatch losses. For this purpose, a linear array employing square patch slotted elements was introduced in [6]. This innovative design (Figure 8) facilitates LP, RHCP, and LHCP by exploiting two LP orthogonal modes that possess equal modal significance and a 90° angle difference at 2.4 GHz. A strategically designed simple feeding network incorporating PIN diodes is employed to excite the various combinations of these two modes, depending on the state of excitation chosen. Notably, a common bandwidth (with $|S_{11}| \leq -10$ dB) that accommodates all three polarization states has been identified within the range of 2.25 to 2.55 GHz, equating to a 12.5% fractional bandwidth and 3 dB gain BW range from 2.25 to 2.7 GHz in the LP state. The axial ratio of the LHCP and RHCP states maintained values below 3 dB in their operation bands. The 1×4 antenna array showed measured maximum gains of 7.2 dBi for LP and 9.78 dBi and 9.8 dBi for LHCP and RHCP states, respectively. However, such a directive radiation pattern without the ability to manipulate its beam orientation, has questionable usability in IoT appliances. However, it can indeed be used when “Things” are placed at known angular directions, as in that case they may offer a more efficient link.

An alternative approach to achieving triple polarization involves using metasurfaces (MSs) as polarization transformation components [66] or even purely as metantennas [63]. An innovative solution features a miniaturized reconfigurable tri-polarization metantenna [63], which uniquely serves as the antenna radiator aperture itself, rather than as an auxiliary component. This metantenna (Figure 9) is composed of windmill-like units derived from square patch units, with design optimization based on characteristic mode analysis (CMA). This approach leads to a significant 46% reduction in size compared to traditional designs, while the radiation pattern presents only one wide beamwidth front lobe due to the ground plane. The metantenna shows remarkable maximum impedance bandwidths of 24.6% (ranging from 3.24 to 4.15 GHz) for circular polarization (CP) and 24.1% (spanning 3.26 to 4.05 GHz) for linear polarization (LP), accompanied by a peak gain of 5.25 dBi. However, to properly bias the diodes, a complex external network is required. A clever way to mitigate this was proposed in [66], where the authors managed to bias

the diodes without using a self-bias network, significantly reducing the complexity of the overall structure, as seen in Figure 10. A notable implementation involves leveraging a metasurface to significantly enhance the CP bandwidth while also enabling LP operation, with a microstrip patch serving as the main radiator. The measurements from this design confirm an impressive overlapped bandwidth of 12.4% and a broadside gain exceeding 5.8 dBi for all polarization states. These examples highlight the versatility and effectiveness of employing metasurfaces in developing antennas capable of supporting multiple polarization states.

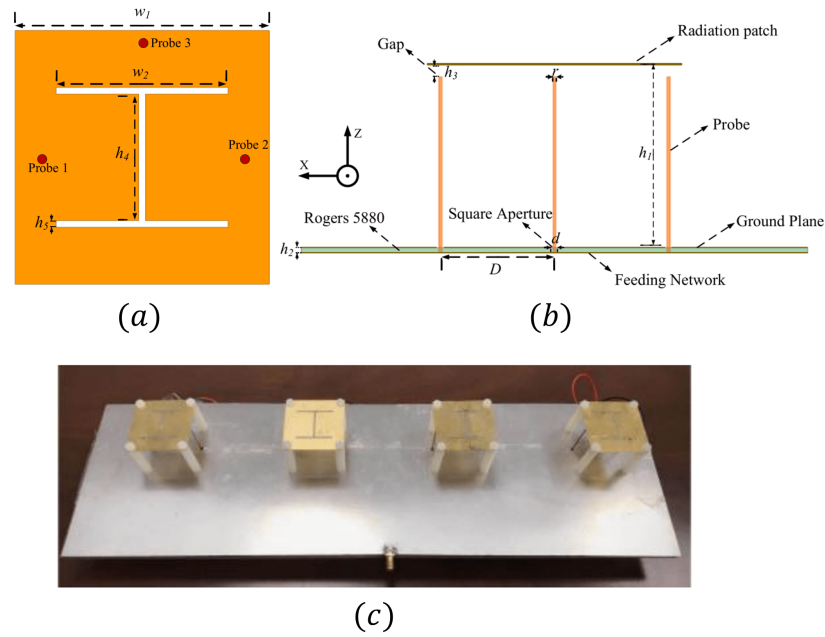


Figure 8. Geometrical configuration of multi-polarization slotted patch antenna in (a) top and (b) side views, designed based on CMA [6]. (c) Photograph of fabricated prototype [6].

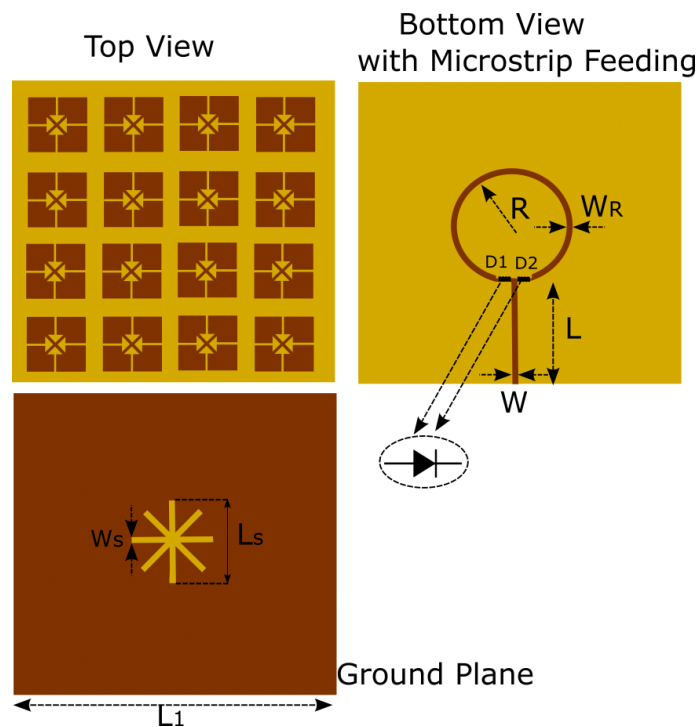


Figure 9. Tri-polarized metantenna designed based on CMA [63].

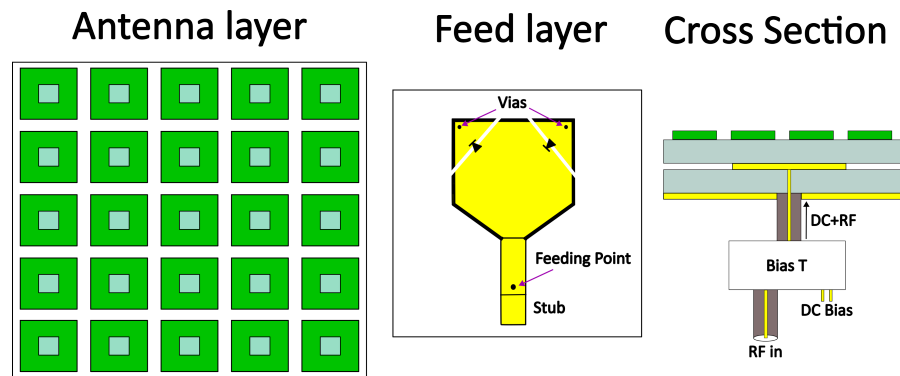


Figure 10. Triple-polarized metasurface antenna [66].

2.2.3. Alternative Methods for Agile Antennas

Microfluidically polarization-tunable probe-fed patch antennas represent a fascinating advancement in antenna technology, as detailed in [67]. The proposed design is presented in Figure 11. This functionality is achieved through the alternative insertion or removal of metallic ink within 3D-printed channels made of polylactic acid (PLA), demonstrating the potential of integrating microfluidic systems with an antenna. For the second antenna discussed in [67], both polarization states exhibit stable reflection coefficients, with a fractional bandwidth of 9.6% (ranging from 4.48 to 4.93 GHz) and a 3 dB axial ratio bandwidth (ARBW) of 5.2% (spanning 4.48 to 4.72 GHz). The design incorporates slots etched into the top copper layer of the patch antenna, with fluidic channels filled with EGaIn (eutectic gallium–indium) liquid metal ink serving as switching elements. These elements can create open or shortcircuit electrical connections, enabling the antenna’s polarization reconfigurability. Additionally, two slots are etched on a diagonally fed patch antenna to excite two modes, TM_{10} and TM_{01} , simultaneously, contributing to the antenna’s ability to support multiple polarizations effectively. This tuning mechanism is quite intriguing, but it is challenging to incorporate into a fully integrated system due to the complex process required to pump fluid in and out of the cavity.

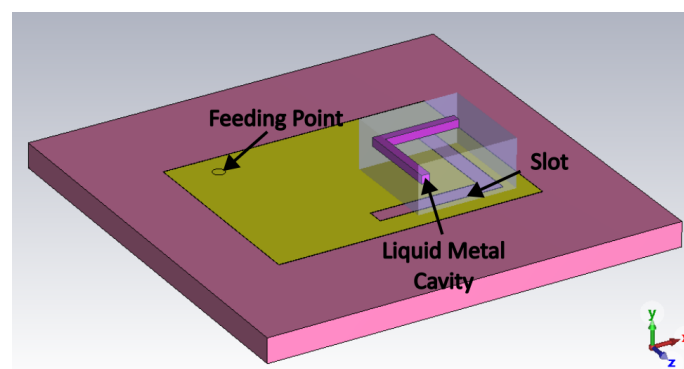


Figure 11. Double CP antenna manufactured by 3D printing and tuned through metallic ink [67].

Quad-polarized antennas represent a significant advancement in antenna technology, offering support for four distinct polarizations [68–71]. To approximate an all-polarization-capable antenna, it is essential to accommodate both right-hand circular polarization (RHCP) and left-hand circular polarization (LHCP), as well as two linear polarizations, typically horizontal polarization (HP) and vertical polarization (VP). This capability ensures that any arbitrarily polarized wave can be detected with minimal efficiency degradation.

A noteworthy antenna design is proposed in [69], featuring a 1×4 crossed inverted-V antenna array combined with a dual-Butler-matrix-based feed network (Figure 12). This setup facilitates both polarization diversity and beam-steering capabilities. The crossed inverted-V array incorporates a planar director to boost antenna gain. The outputs from

the dual-Butler-matrix network are connected to each pair of the gain-enhanced inverted-V antenna elements. Additionally, the dual Butler matrix is integrated with a polarization mode selection switch matrix. This polarization selector, comprising a simple switch matrix, allows the RF signal to be directed into a single or both Butler matrices with a relative phase difference. This arrangement enables the generation of quad-polarization based on the switching operations performed. Excluding the contributions of the dual Butler matrix, the measured gain averages 12.8 dBi across all polarizations. However, the beamforming capabilities of the antenna are limited due to the use of a 4×4 Butler matrix, which only covers the azimuth range between -30° and $+30^\circ$. Additionally, the occupied volume of the entire structure poses a challenge, especially due to its height when integrated into an IoT device.

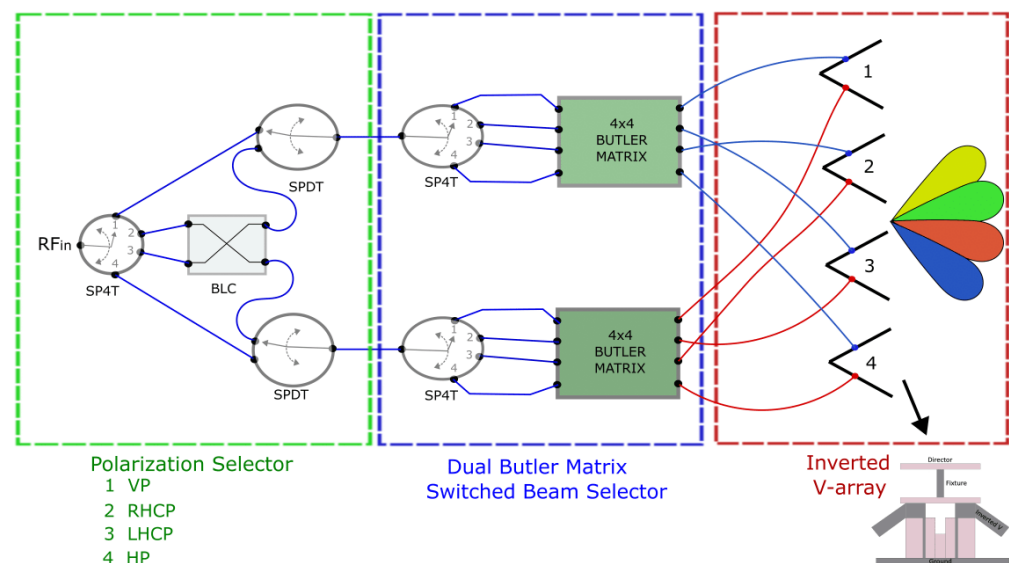


Figure 12. Configuration of inverted-V antenna array fed by a dual Butler matrix, enabling beam or polarization switching [69].

There are cases where antennas with four linear polarizations (LPs) are referred to as quad-polarized [72]. In the design proposed by Takato et al. (Figure 13), a stacked structure is employed that passively receives four distinct linear polarizations without relying on diodes for tuning. This design consists of a three-stacked element configuration. The bottom patch is dedicated to orthogonal-polarized elements, while the upper patch is rotated at a 45° angle to facilitate slant-polarized elements. A significant feature of this design is the reduction in mutual coupling between the two antenna layers. This is achieved through the introduction of side walls on the upper element and conductor posts. These components not only maintain the necessary distance between the two antenna layers but also serve as an electrical shield for the feeding cable to the upper antenna. This effectively mitigates potential interference and preserves the integrity of the signal transmission. The tuning in this antenna design can only be accomplished mechanically, requiring an electronically controlled rotor system. The large size and complexity of this system make it impractical for IoT applications, where compactness and simplicity are often critical requirements.

In the realm of advanced antenna design, the pursuit of multi-polarization capabilities has led to the exploration of innovative configurations that extend far beyond conventional solutions. Such approaches involve the use of high-order-mode cavity-fed patch antenna arrays (Figure 14) [73], which leverage the electric field distribution of high-order modes to achieve diverse polarization states. Similarly, high-order cavity-based resonant circular slot arrays [74] and orthogonally placed bowtie antennas with double printed rings [75] may be employed.

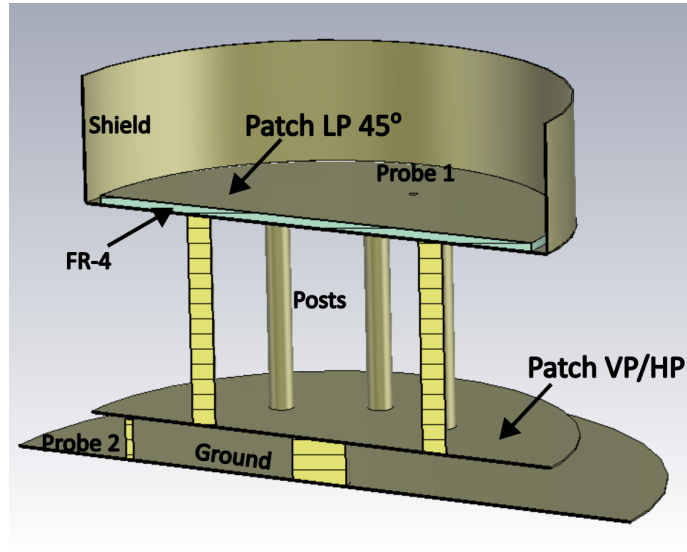


Figure 13. Mechanically tuned quad-polarized stacked patch antenna [72].

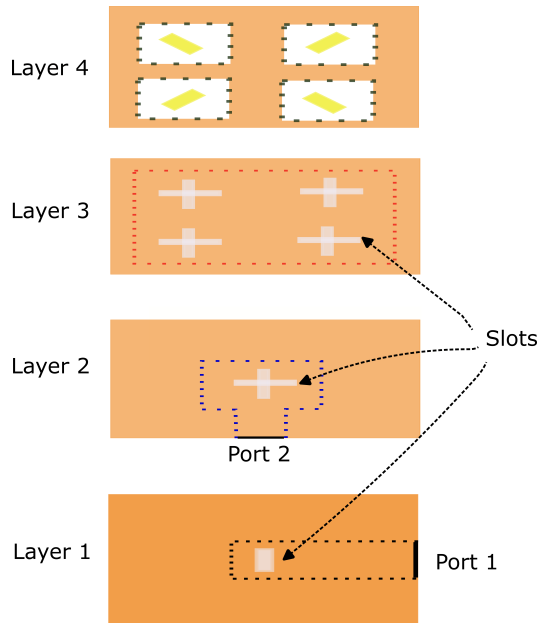


Figure 14. Multi-polarized high-order-mode cavity-fed antenna 2×2 sub-array [73].

A particularly interesting design feature is exhibited by a 16-switchable linear polarization sectioned circular stacked antenna, which operates within a reconfigurable frequency band ranging from 1.84 GHz to 2.64 GHz [76]. A schematic of this circular antenna is presented in Figure 15, along with its biasing network. This antenna employs an odd–even strategy to manage polarization states, with diode control facilitated by a field-programmable gate array (FPGA) coupled with the biasing network. This sophisticated control mechanism allows for significant reductions in linear polarization (LP) mismatching loss and equips the antenna with robust anti-interference capabilities, making it well suited for operation in modern, electromagnetically complex environments. The reconfiguration behavior of this antenna is achieved through the strategic distribution of PIN diodes across the slots on both patch surfaces. By activating different groups and numbers of sector patches, the effective current paths within the antenna are altered, thereby adjusting its operating frequency band.

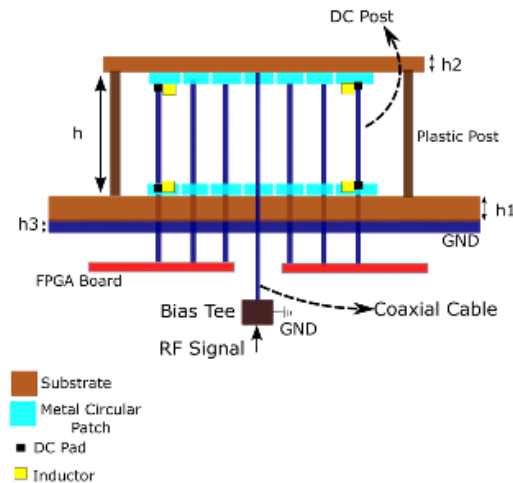


Figure 15. Multi-polarized circular section stacked antenna, switched by digitally driven (FPGA) PIN diodes [76].

A quite intriguing and smart realization of an all-polarization reconfigurable antenna (Figure 16) was introduced in [77]. The patch antenna is capable of altering its polarization states among arbitrary LPs, LHCP, and RHCP. The core of this design is a truncated square patch antenna featuring two isolated H-shaped aperture-coupling feeds, tailored for operation at 2.45 GHz. This configuration enables the antenna to operate in two orthogonal CP modes with minimal cross-talk. The mechanism for achieving polarization reconfigurability in this antenna involves the selective excitation of one of two feeding microstrip lines. Port 1 generates LHCP and port 2 RHCP; this means with the appropriate use of variable attenuators someone can generate only one. Furthermore, by simultaneously exciting both feeding microstrip lines with equal amplitudes—but with differing initial phases (phase shifters)—the antenna can produce different LP modes. Remarkably, the orientation of the LP mode’s polarization plane can be steered to any desired azimuth direction, offering unprecedented control over the antenna’s polarization state. Simulated and measured performance metrics for this antenna demonstrate its efficacy, with a consistent peak gain of approximately 6.8 dBi at 2.45 GHz. Moreover, the antenna’s impedance-matched bandwidth, which spans from 2.25 to 2.60 GHz, fully accommodates all polarization states without compromise.

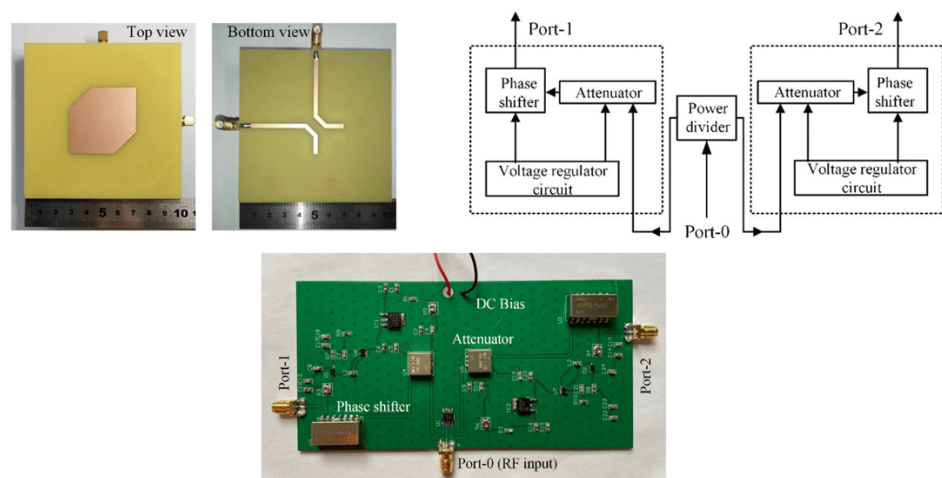


Figure 16. Configuration of the dual-circularly polarized square patch element: top layer and bottom layer along with the feeding network [77].

2.2.4. Recent Feedback on Smart Homes

In Table 2, the characteristics of various IoT antennas for smart home applications are displayed. Different methodologies have been implemented to ensure multi-polarization-capable antennas while maintaining small footprints. One group of antennas capable of integrating into the smallest devices operates in the millimeter-wave spectrum, using either cavities or frequency-selective surfaces to increase their directivity (gain) and form narrow-beamwidth main lobes in the radiation pattern. Cavity-backed antennas are a solution for the next generation of IoT devices, offering higher data rates due to their large bandwidth, compact structures, and increased efficiency.

Table 2. Comparison of different antenna designs for smart home appliances.

Antenna Type	Max Gain (dBi)	Size (cm ²)	Rad. Pattern	Polar. (States)	Frequency	FBW (%)	Ref.
Ring Patch	4.7	20.45 × 20.45	Omnidirec.	LP(1)	1.6 * GHz	0.5/1	[7]
Slotted Patch	9.8	35 × 10.5	Directive	LP(1), CP(2)	2.4 GHz	12.5	[6]
Metasurface	5.8	3.75 × 3.75	Front Lobe	LP(1), CP(2)	5.2 GHz	12.4	[66]
Windmill Metantenna	5.25	4.8 × 4.8	Front Lobe	LP(1), CP(2)	3.65 GHz	24.1	[63]
Microfluid	7.3	4 × 4	Front Lobe	CP(2)	4.6 * GHz	5.2	[67]
Crossed Inverted F	12.8	18.5 × 15	BF (−30°:30°)	LP(2), CP(2)	5.8 GHz	15.7	[69]
Crossed Inverted F	7.6	5.3 × 5.3	Front Lobe	LP(4)	3.4 GHz	5	[72]
High-Order Cavity	25	10.4 × 10.4	Directive	LP(4), CP(2)	38.5 GHz	13.3	[73]
High-Order Cavity	16.8	6.1	Directive	LP(5)	28.8 GHz	<0.1	[74]
Crossed Bowtie Dipole	6.6	9.5 × 9.5	Front Lobe	LP(3), CP(2)	2.7 GHz	37.1	[75]
Circular Sectoroid	4.7	92.25	Front Lobe	LP(16)	2.2 * GHz	35	[76]
Truncated Patch	6.8	10 × 10	Directive	All	2.45 GHz	12.8	[77]

BF: beamforming; * frequency-agile antenna.

However, this feature is not always desirable in smart home applications because IoT devices must communicate with different “Things” that may be placed in arbitrary directions. Highly directive antennas require a beamforming network to ensure a reliable link between nearby devices. Various solutions to this problem have been partially proposed in different works [78–82], but we are quite far from establishing a holistic, commercially ready cavity-backed antenna along with its feeding network. In addition, cavity-backed antennas operate at millimeter range preferably in the ISM band, but currently, there is only one below 100 GHz (24.1 GHz). The previously presented millimeter antennas do not belong in that band, meaning that more research is needed towards exploiting this specific band for smart home communications.

Therefore, we believe that in the coming years more researchers will propose novel electronically reconfigurable compact beamforming networks for smart home appliances. In this direction, metasurfaces and frequency-selective surfaces [83–87] can either enhance the beam-steering capabilities of the antenna or enable multi-polarization reception, albeit with the drawback of increasing the volume of the structure.

In the sub-6 GHz region, implementing a cavity-backed or metasurface antenna array is challenging due to the longer wavelengths in this band, making them unsuitable for small IoT devices. As explained previously, a quasi-isotropic radiation pattern is a more realistic option to meet this requirement. As depicted in Table 2, most radiation patterns show a main front lobe with almost no back lobe due to the ground plane. Therefore, there is a need for multi-polarization antennas with nearly isotropic radiation patterns. In this context, monopole antennas [88–92] exhibit omnidirectional or quasi-isotropic radiation patterns and operate in multiple bands [90]. They can also be printed on flexible substrates to wrap around any IoT device [56,92].

The smart home industry has already attracted major companies and seems too large to be driven solely by individual efforts. However, many innovative devices and antennas are initially inspired, developed, and published by university researchers. These innovations are then often modified and exploited by industry research and development departments. Consequently, smart home research evolves slowly and lacks a clear direction, which is often unfair to university researchers who do not fully benefit from their creations. To address this issue, a framework for collaboration between businesses and universities is needed.

Such a framework could be established through a state-issued open memorandum of understanding. Within this framework, multinational and domestic firms could announce their technical needs regarding the next generation of smart home facilities through white papers. This would motivate researchers worldwide to devise more advanced antennas and devices to optimally support smart home environments. In turn, national organizations should implement mechanisms to ensure researchers benefit from their inventions. While patenting is one such mechanism, it is often too expensive and complicated for individual researchers, resulting in most patents being monopolized by multinational firms rather than universities. A more accessible system that encourages collaboration and rewards innovation could help balance the relationship between academia and industry, ensuring that university researchers receive fair recognition and benefits for their contributions to smart home technology.

2.3. Smart Cities

Smart cities harness technology and data to significantly improve the quality of life for their citizens by enhancing efficiency, promoting sustainability, and encouraging economic growth [93]. By integrating a network of interconnected technologies, these cities enable real-time data collection and analysis, which, in turn, allows for informed decision making and optimal resource utilization. Through the incorporation of sensors, IoT devices, artificial intelligence (AI), and machine learning, smart cities can efficiently manage and improve various urban services, such as transportation, energy usage, waste management, and public safety. The transition to smart cities requires significant investments in infrastructure and innovation, but the benefits are manifold. For residents, it means living in environments that are safer, more convenient, and more responsive to their needs. For businesses, it opens up new opportunities for growth and innovation. In terms of the environment, smart cities promise reduced pollution and more sustainable living practices. Ultimately, the goal of smart cities is to create more resilient and adaptable urban spaces that can rise to the challenges of the 21st century. By minimizing the environmental impact of urban living and fostering economic development, smart cities aim to redefine what it means to live in urban areas, making them better places for future generations.

In this context, the demand for highly directive antennas becomes evident, driven by the unique challenges and opportunities presented by urban environments. Unlike the more confined spaces of homes, where omnidirectional antennas might suffice, smart cities require a more strategic approach to signal transmission due to their large scale and the longer distances between sensors and base stations. Directive antennas, especially those with electronically controllable beamforming capabilities, emerge as optimal solutions in this setting. Beamforming allows for focused signal coverage, directing power efficiently towards intended targets or users rather than dispersing it indiscriminately. This targeted approach not only conserves energy but also enhances the quality of communication, leveraging the urban landscape's potential for line-of-sight (LoS) connections. These LoS pathways between sensors or between sensors and base stations minimize latency and ensure high-quality signal transmission, which is crucial for the stable operation of smart city infrastructure.

2.3.1. Challenges for Next-Generation Smart City Antennas

For smart city applications, planar antenna arrays with high gain are preferred because they can significantly extend signal coverage without increasing power consumption. These advanced antenna systems feature beam steering, which allows for signal direction adjustments, enhancing their utility. Beam steering can be limited to a single plane, such as the azimuth, or it can encompass both planes (azimuth and elevation) for comprehensive 3D spatial scanning. Although the size of the antennas is a secondary concern compared to their performance capabilities, minimizing their footprint remains a design objective to ensure seamless integration into the urban landscape without being obtrusive. Size miniaturization is particularly important for IoT devices. Typically, such antenna systems are

placed near highly populated metropolitan areas on rooftops, buildings, and lighting poles, so selecting appropriate dimensions is crucial. Moreover, the ability to reconfigure polarization and frequency is essential for IoT devices spread across smart cities. These features ensure that the communication infrastructure can adapt to diverse and changing demands, accommodate various devices and technologies, and make the system indispensable for the efficient and flexible operation of smart city networks.

In contrast to smart home antennas, which primarily operate within the ISM bands using well-established protocols such as ZigBee, Bluetooth, and Wi-Fi for short-range communication within a house [94], smart cities require solutions that can handle longer distances between sensors and more challenging environmental conditions. To address these needs, it has been proposed that IoT devices utilize the 5G spectrum for long-range communications [95]. Currently, the 5G spectrum covers almost the entire sub-6 GHz region as well as millimeter-wave bands (26–28 GHz). Looking forward, Beyond 5G is expected to expand to include additional millimeter-wave bands [96], while early 6G systems will utilize the FR3 band (7–24 GHz) [97,98]. For distances shorter than 1 km, millimeter-wave bands are preferred due to their capability to provide higher data rates [99]. Considering these factors, both lower and higher bands of the 5G spectrum will be utilized for future fully connected IoT networks, depending on the specific topology and requirements of the deployment.

In the early stages of steerable antenna development, largely driven by radar system applications, mechanical mechanisms were used to rotate antennas and point beams in various directions. These systems were capable of controlling the main beam's direction in both azimuth and elevation angles, setting the groundwork for advanced directional communication. However, in the context of smart cities, mechanically steered antennas pose significant challenges due to their large size and maintenance demands, making them less feasible for urban deployment.

The trend toward electronically steerable antennas has been motivated by the need for more compact, rapidly adjustable, and energy-efficient solutions [100]. These antennas replace mechanically controlled parts with electronic components, enabling rapid changes in beam direction without any physical movement of the antenna structure itself. Printed multifunctional antenna arrays have emerged as a potent solution, meeting the demanding requirements of IoT devices in smart cities and supporting space-division multiple access (SDMA) or even MIMO (multiple-input multiple-output) communications. A linear antenna array allows beam steering within a two-dimensional plane (θ), while a planar array enables three-dimensional space steering (θ, ϕ) by feeding each element with the appropriate phased current [10]. The phase or time delay of the input current to each antenna element is critical for determining the direction of the main beam. Additionally, the uniform amplitude distribution feeding the array elements may also be adjusted to reduce the side lobe level (SLL), thereby minimizing interference between different antenna systems.

While the theoretical foundations for antenna arrays have been well established for decades [10], the challenge today lies in designing the individual antenna elements and their associated feeding networks. Explicitly, the design challenges that an antenna engineer usually faces are:

- Most antennas and feeding networks suffer from narrow band response, limiting the applications.
- In uniform arrays, the distance of the elements (d) limits the operation bandwidth due to beam squint ($d = \lambda_{min}/2, \lambda_{min} = c_0/f_{max}$).
- To efficiently steer the beam in space (3D) huge planar arrays are normally needed, which significantly increases the size and the complexity (feeding network) of the system.
- To adaptively steer an antenna demands huge computational resources (usually incorporating a microprocessor in the device), making it more power hungry while increasing latency.

- Off-the-shelf electronically tunable elements (e.g., phase shifter) are limited in the market and when they are found their tunability is small.
- All-polarization arrays are difficult to develop due to the complexity of the array's elements and feeding network.

Research is increasingly focused on developing novel structures that integrate the antenna array with its feeding network. The goal is to achieve electronic tunability through the incorporation of nonlinear elements, thereby enhancing the functionality and adaptability of antenna systems for the complex needs of modern smart cities.

Achieving continuous electronic scanning in antenna arrays poses significant challenges and is typically viable for arrays with a limited number of elements, often in conjunction with software-defined radio (SDR) or cognitive radio (CR) [56,101,102]. These cutting-edge technologies enable dynamic adjustment and optimization of the radio's operating parameters to meet specific needs or adapt to changing environmental conditions. Despite the potential for continuous scanning, in many practical scenarios, antenna arrays are operated with a predefined set of beams, utilizing either analog [103] or digital [104] control methods. This selective approach is particularly relevant for smaller antenna arrays, which tend to have relatively wide beamwidths. Such beamwidths limit the precision with which the antenna can steer its beam, making it challenging to achieve the level of accuracy required for certain applications, such as space-division multiple access (SDMA) or direction of arrival (DoA). In such applications, a beamwidth of -3 dB around 20° is demanded, while the acceptable overlapping beams $\Delta G = -3$ dB need to be at $\Delta\theta = 20^\circ$. Consequently, the diversity in radiation pattern states available for selection is directly related to the complexity of the antenna's feeding network and the number of controllable elements within the system, such as PIN diodes or RF switches.

2.3.2. State-of-the-Art Compact Antennas

In [9], a simplified unique single-fed four-faced cubical array with slotted inset-fed patch antenna designed for operation at 2.45 GHz is introduced. This antenna, structured as a cube and referred to as a $4 \times 2 \times 1$ antenna array (Figure 17), incorporates four RF switches, located at each arm of the four faces. These switches play a critical role in selective pattern reconfigurability choosing from six different azimuth states. A significant advantage of this design is its ability to switch beam while maintaining stability in the reflection coefficient. This offers full 360° azimuth coverage by six beams with average $HPBW = 50^\circ$ in azimuth. On the other hand, this specific design was originally intended for CubeSat applications. However, it can also be utilized in IoT applications as a gateway in a local area network to receive signals from all directions.

In contrast, another study [105] presents a low-profile, compact 16×16 antenna array that offers reconfigurability in frequency, radiation pattern, and polarization but at the expense of a complicated system. This advanced antenna design features a square patch element loaded with four capacitors and four switchable feeding ports, all controlled by an FPGA. The innovative aspect of this design lies in its frequency adjustability, which ranges from 1.35 to 2.19 GHz, achieved by selecting capacitance values between 0.31 and 3.14 pF. Additionally, by setting specific coding patterns for the digital radiating elements, the antenna can produce various radiation beams embodying three distinct LP states ($0, 45, 90^\circ$). This level of versatility and control, however, necessitates the use of 64 PIN diodes and 64 tunable capacitors, underscoring the complexity and advanced nature of the antenna's design. However, the 12 different radiation pattern states present peculiar behavior such as the creation of multiple front lobes and randomness in beam steering on the azimuth and elevation planes.

A dual-polarized frequency-reconfigurable patch antenna array designed for millimeter-wave (mmWave) frequencies was investigated in [106]. The use of varactor diodes, strategically positioned at the four corners of the square patch antenna, allows for dynamic adjustment of the antenna's operational frequency. This design enables the antenna array to be tuned across a broad frequency range from 23.2 to 30.2 GHz, at millimeter range,

simply by varying the capacitance of the varactor diodes. A key feature of the proposed antenna array is its exceptional isolation capabilities—achieving over 20 dB isolation between orthogonally polarized antenna elements and more than 15 dB isolation between antenna elements with the same polarization. This high level of isolation is critical for reducing interference and improving the quality of signal transmission and reception in densely populated frequency bands. Additionally, the antenna array exhibits impressive gain performance, with peak gains ranging from 8.9 to 10.5 dBi across its tunable frequency range. The beamforming capability of this 1×8 uniform linear array further enhances its utility in advanced communication systems. By feeding the different ports with appropriate phase differences, the array can continuously steer its main beam across a wide azimuth angular range, from -60° to 60° , with a mean $HPBW = 30^\circ$. However, this property was estimated using the antenna element radiation pattern with the use of the analytical array factor without any numerical validation and prototype implementation of its feeding network.

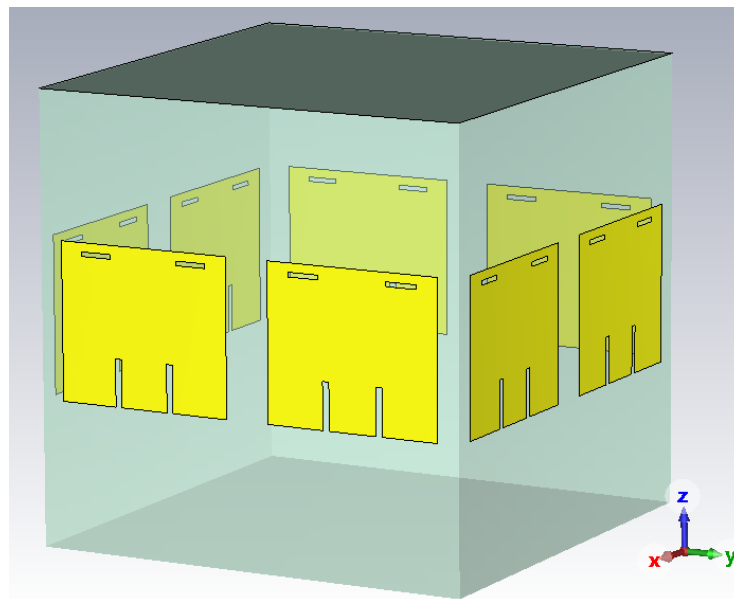


Figure 17. Designed cubical array along with the printed slotted patch antenna (radiated element) [9].

In contrast with the previously referred to antennas, a 1×4 CP patch array antenna was introduced in [103] for the higher bands of 5G. This antenna employs an ortho-hexagonal patch element, incorporating three groups (comprising in total six elements) of parasitic patches and varactor diodes to facilitate continuous tuning in frequency and switching polarization reconfiguration between LHCP and RHCP. Further enhancing the antenna's reconfigurability, four switchable feeding probes, each one integrated with a designed single-pole four-throw (SP4T) switch, are employed to feed each element. This setup permits feeding the array's ports with different initial phases. Consequently, by appropriately switching the feeding probes for the four elements, the radiation beam of the antenna array can be dynamically reconfigured among five distinct beam states (-40° , -20° , 0° , 20° , 40°), while presenting a beamwidth of 22° .

Electronically steerable parasitic array radiators (ESPARs) represent a significant category of antenna arrays that blend active and passive (parasitic) antenna elements. By switching these elements between the ON and OFF states, ESPARs achieve a reconfigurable behavior, notably in their beam-switching capabilities [107]. A key characteristic of classical ESPAR antennas is the incorporation of varactor diodes at the base of the parasitic elements [107]. This is normally achieved utilizing a variable reactive load, as depicted in Figure 18. The adapted voltage-controlled reactances of these diodes are adapted at producing varied antenna radiation patterns, enabling dynamic beam steering. As such, ESPARs are an attractive option for applications requiring directional communication capabilities

but are constrained by budget and complexity considerations. Some notable examples of ESPAR designs include:

1. A fan-shaped patch antenna system capable of producing four end-fire beams [104];
2. A 14-beam slot-based cylindrical cavity antenna, which exemplifies the use of ESPARs in more complex configurations, offering a higher number of beam directions for enhanced coverage and flexibility [108];
3. A 12-beam metasurface-based antenna, complemented by a reflector made of an artificial magnetic conductor reflector [107].

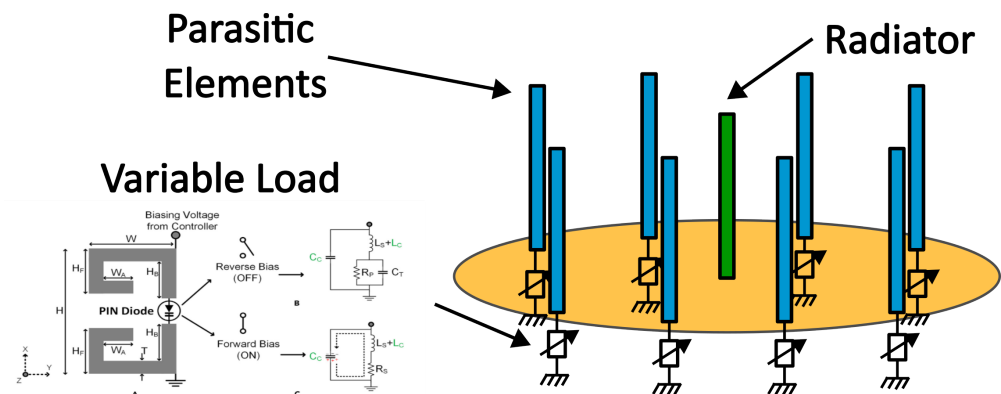


Figure 18. An electronically steerable parasitic array radiator (ESPAR) antenna, where the variable load is implemented with an electronically activated capacitive load loop [107].

In recent advancements within antenna technology, efforts have been directed towards developing compact antenna arrays capable of performing beamforming in three-dimensional space. One notable contribution in this area is the development of a polarization-reconfigurable slot-ring phased array antenna designed specifically for C-band applications [109]. This antenna demonstrates operational capabilities across a frequency range from 5.42 to 7.87 GHz, achieving a significant 37% fractional bandwidth along with a gain of 7.6 dBi. The strategic placement of the microstrip line diagonally within the perimeter of a single antenna element enhances the antenna's performance and facilitates scalability. A 2×2 array configuration was realized with an element spacing of $0.5\lambda_0$. This compact array is uniquely capable of supporting vertical, horizontal, or circular polarization, a flexibility achieved by feeding each antenna element port with the appropriate phase shift of the antenna elements. To excite horizontal LP, the second and fourth elements must present at 180° with respect to the first and third. Moreover, the array demonstrates the ability to perform beam scanning across a range of $\pm 30^\circ$ with a beamwidth of 60° . The main drawback of ESPAR antennas is their large volume requirement, which necessitates designing radomes to protect the antenna from harsh environmental conditions.

Expanding upon the versatility seen in reconfigurable antennas, a novel non-uniform all-polarization 2×2 array featuring Γ -dipoles (Figure 19) is introduced in [56], offering an innovative solution as well as advanced beamforming capabilities. This design uniquely incorporates Γ -dipoles arranged and rotated in such a way that the array mirrors the polarization agility of a crossed-dipole in each corner, enabling it to adapt to a wide range of polarization requirements. The clever positioning and orientation of the Γ -dipoles provide the array with a remarkable beamforming versatility. When operating near the broadside orientation (normal to the array's surface), and with appropriate phasing, the array mimics the behavior of a uniform planar array. This configuration facilitates conventional beamforming techniques. Conversely, when operating near the end-fire orientation (parallel to the array's surface), the array's behavior transitions to that of a uniform circular array. This shift not only showcases the array's flexible beamforming capabilities but also highlights its adaptability to different operational modes based on orientation. One of the most striking features of this antenna array is its physical flexibility. The array can be curved or

even distorted to conform to the surface of the package of an IoT device it serves, while maintaining nearly identical operational behavior but losing some of its beamforming capabilities. However, for future work an appropriate feeding network must be developed to fully harness the benefits of the proposed antenna.

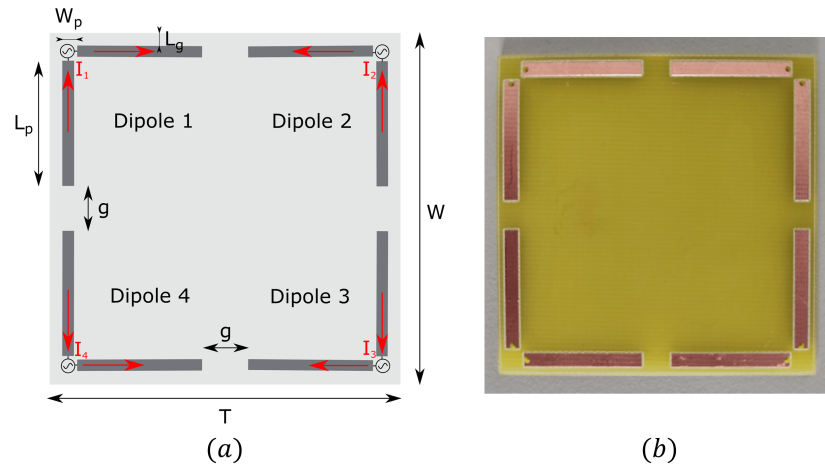


Figure 19. (a) Schematic and (b) fabricated all-polarization Γ -dipole array [56].

An attempt to further minimize the antenna’s footprint was investigated in [110] where a multi-sectoral annular antenna with electrical length $0.018\lambda_0$ was designed, as depicted in Figure 20a. This antenna employs slits and vias as methods for enhancing mutual coupling, resulting in a simplified configuration. By feeding the antenna’s sectors through different ports, the design supports digital beamforming techniques, allowing for dynamic adjustment of the antenna’s directional pattern. One of the standout features of this antenna is its ability to produce various polarization states with different radiation patterns (Figure 20c), including both LP and CP. Despite its innovative design and impressive efficiency and gain—up to 78% and 4.62 dBi, respectively—the antenna faces challenges in terms of its impedance bandwidth and return loss. These limitations suggest areas for further research and development, as overcoming these obstacles could significantly enhance the antenna’s applicability and performance in real-world scenarios. A challenging feature of this non-uniform array is the implementation of its controllable feeding network. This has not been presented yet but it is expected to be feasible based on a low-cost software-defined radio or even a dedicated chip.

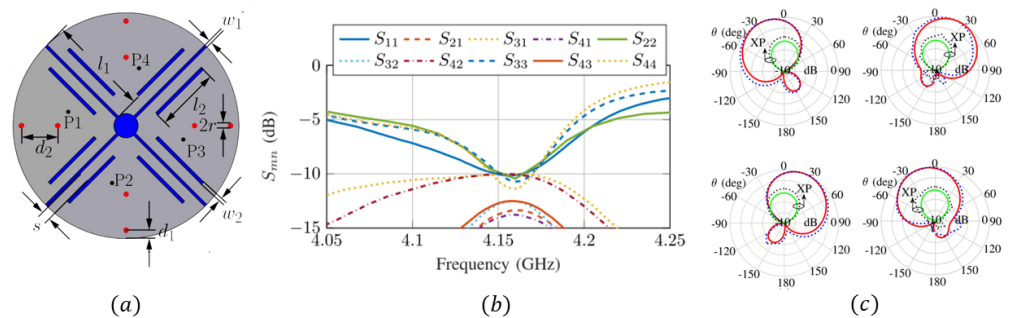


Figure 20. (a) Top view of multi-sectoral annular antenna: (b) measured S-parameters and (c) beam-steering capabilities [110].

2.3.3. Necessity of Integrated Social–Technical Systems—Smart Cities

The properties of the presented antennas are summarized in Table 3. In the literature, two major methodologies for designing antenna arrays are proposed: designing only the phased array or designing the array with the beamforming/feeding network. In the first approach [56,103,110], the design techniques are presented along with results such as angle

coverage, polarization, and gain. The beam coverage is then estimated by feeding each port with the appropriate phase-shifted current. This technique saves researchers a lot of trouble, as they only need to devise a design plan for the antenna, leaving the feeding network for a future phase. However, this methodology is impractical for real-life applications, where the realization of smart cities demands all-in-one wireless systems capable of being integrated into each IoT device. These elements need to incorporate both the antenna and an electronically reconfigurable feeding network (controlled by a microprocessor or microcontroller) capable of steering the main lobe and enabling space-division multiple access (SDMA). The biggest challenge in this direction is the electronically tunable feeding network and its integration with the microcontroller.

Table 3. Comparison table of different antenna designs for smart city antennas.

Antenna Array	Max. Gain (dBi)	No. Beams	Angle Cover.	Polar. (No)	Freq.	FBW * (%)	Freq. Reconf.	Ref.
Cubical	5.6	6	360°	LP(1)	2.45 GHz	2	No	[9]
Planar	15.28	12	60°	LP(3)	1.8 GHz	46	Yes	[105]
Linear	10.8	Cont.	120°	LP(2)	27 GHz	26	Yes	[106]
Ortho-hexagonal	10.8	5	100°	CP(2)	2.58 GHz	33	Yes	[103]
Fan shaped	3.9	4	360°	N/A	2.4 GHz	12.5	No	[104]
Cylindrical	4.29	14	6	LP (1)	2.44 GHz	3	No	[108]
ESPAR	4.29	12	360°	LP (1)	2.65 GHz	1	No	[107]
Slot ring	7.6	Cont.	60°	LP(2), CP(2)	6.65 GHz	37	No	[109]
Γ-Dipole	6.87	Cont.	60°	ALL	2.5 GHz	9.6	No	[56]
Annular	4.62	Cont.	60°/90°	LP (3), CP(2)	4.16 GHz	<1	No	[110]

* For frequency-reconfigurable antennas the tuning range is presented.

In most cases in the literature, due to the limitation of tunable components, only a finite number of desirable beams (states) can be issued to cover all the space [9]. Despite these efforts, in the future, the next-generation of the IoT will demand versatile antenna systems, permitting a main lobe scanning along every azimuth and elevation angle in real time. Following this path, adaptive continuous beamforming networks have emerged, targeting full control of currents' amplitude and phase [111–114]. Despite these efforts, such networks generally have a small number of ports ($N = 4$). Therefore, there is still a long way to go and there is a need for fully adaptive beamforming networks for large phased arrays to pave the way for establishing cognitive radio.

Despite significant efforts to develop smart city technologies, there remains a lack of essential dialogue between all stakeholders, including the citizens themselves. Although the concept of a “smart” city is widely discussed, many cities still fail to utilize available technologies effectively, leaving them “dumb” in aspects such as street lighting and wireless metering. What is missing is an integrated systems approach that ensures fairness and equity for all stakeholders through open dialogue. A promising initiative could begin with local universities taking the lead in addressing city officials and councils, while actively involving citizen organizations. This collaborative platform would allow citizens to voice their requests, while university engineers propose technical solutions that can be modified for implementation by municipal authorities. Additionally, ideas for addressing the economic and financial dimensions of smart city projects, such as crowdfunding or projecting future cost savings to benefit citizens, could be presented and discussed by the forum.

Engineers play a crucial role in the development of novel, low-cost, and highly efficient integrated electronic systems, where the RF front end, antennas, and digital processing units are implemented on the same chip (system on a chip). These compact systems need to be deployable in various parts of the city, such as traffic lights, rooftops, and electric poles, to provide seamless wireless communication between different IoT devices, ensuring the convenience and safety of citizens. An important lesson from wired digital communications (DSL, ADSL, and VOIP) is that their success lies in backward compatibility, meaning they all build upon the same infrastructure (copper lines). Building on this concept, antennas and electronic devices should, at least in their initial implementation, focus on retrofitting

existing infrastructure to make it “smart”. This approach allows for gradual integration of new technologies while leveraging existing resources, making the transition to smart cities more efficient and cost effective.

3. Conclusions

This report has provided a comprehensive overview of various antenna designs, tailored to meet the diverse requirements of the Internet of Things (IoT). We categorized these antennas based on their suitability for different IoT applications, highlighting the evolution and specialization within the field.

In biomedical applications, including in-body monitoring and actuation, the focus has been on developing compact and efficient antennas that can be implanted or encapsulated. Electrically small antennas with meandered or loop structures have become prevalent due to their favorable size and performance characteristics. More recently, there has been growing interest in magnetoelectric antennas, which offer unique advantages in terms of miniaturization and efficiency at lower frequencies. However, their adoption has been limited by poor radiation characteristics and sensitivity to vibrations.

In the context of smart homes, all-polarization antennas with frequency agility have been identified as promising solutions for enhancing the connectivity of household appliances. The tunability of these antennas can be achieved through various means, including nonlinear electrical elements like PIN diodes and varactors, as well as innovative materials such as liquid metal. However, the latter is not yet suitable for integrated devices.

For smart city applications, pattern-reconfigurable antennas are highlighted for their ability to provide high gain and support space-division multiple access, which is essential for efficient data traffic management between the multiple IoT sensors and actuators in metropolitan areas. Despite advancements, achieving electronically controlled continuous steering of the antenna’s beam poses significant design challenges, with beam-switching methods remaining the most commonly explored technique in the literature.

As the field of antennas continues to evolve, the drive toward multifunctional designs is becoming increasingly important for commercial use as the era of the IoT rapidly approaches. Industries demand antennas that can accommodate the specific needs of various applications—from biomedical devices to smart home systems—creating an overwhelming need for innovative solutions. This pursuit of multifunctionality not only challenges traditional antenna concepts but also opens up new avenues for research and development of novel designs. To fully achieve these targets, it is essential to foster synergy between engineers and non-engineers. Collaborative efforts with experts in fields such as biology, healthcare, urban planning, and user experience design are crucial to ensure that antenna designs are not only technically sound but also aligned with the practical and social needs of users. By integrating diverse perspectives and expertise, the development of IoT antennas can better address real-world challenges and enhance the functionality and adaptability of IoT systems.

Author Contributions: Conceptualization, G.K. and M.T.C.; methodology, D.G.A.; validation T.M.E.; formal analysis, D.G.A. and T.N.F.K.; investigation, D.G.A., T.N.F.K. and T.M.E.; resources, D.G.A.; data curation, M.T.C.; writing—original draft preparation, D.G.A. and T.M.E.; writing—review and editing, D.G.A., G.K. and M.T.C.; visualization, D.G.A. and M.T.C.; supervision, G.K. and M.T.C. All authors have read and agreed to the published version of the manuscript.

Funding: This research received no external funding.

Data Availability Statement: The original contributions presented in the study are included in the article, further inquiries can be directed to the corresponding author.

Conflicts of Interest: The authors declare no conflict of interest.

References

1. Bahalul Haque, A.K.M.; Oahiduzzaman Mondol Zihad, M.; Rifat Hasan, M. 5G and Internet of Things—Integration Trends, Opportunities, and Future Research Avenues. In *5G and Beyond*; Bhushan, B., Sharma, S.K., Kumar, R., Priyadarshini, I., Eds.; Springer Nature: Singapore, 2023; pp. 217–245. [CrossRef]
2. Chan, R.; Yan, W.K.; Ma, J.M.; Loh, K.M.; Yu, T.; Low, M.Y.H.; Yar, K.P.; Rehman, H.; Phua, T.C. IoT devices deployment challenges and studies in building management system. *Front. Internet Things* **2023**, *2*, 1254160. [CrossRef]
3. Roges, R.; Malik, P.K. Planar and printed antennas for Internet of Things-enabled environment: Opportunities and challenges. *Int. J. Commun. Syst.* **2021**, *34*, e4940. [CrossRef]
4. Kiourti, A.; Nikita, K.S. A Review of In-Body Biotelemetry Devices: Implantables, Ingestibles, and Injectables. *IEEE Trans. Biomed. Eng.* **2017**, *64*, 1422–1430. [CrossRef] [PubMed]
5. Dai, L.; Wang, B.; Ding, Z.; Wang, Z.; Chen, S.; Hanzo, L. A Survey of Non-Orthogonal Multiple Access for 5G. *IEEE Commun. Surv. Tutorials* **2018**, *20*, 2294–2323. [CrossRef]
6. Li, K.; Shi, Y.; Shen, H.; Li, L. A Characteristic-Mode-Based Polarization-Reconfigurable Antenna and its Array. *IEEE Access* **2018**, *6*, 64587–64595. [CrossRef]
7. Russo, N.E.; Zekios, C.L.; Georgakopoulos, S.V. A CMA-Based Electronically Reconfigurable Dual-Mode and Dual-Band Antenna. *Electronics* **2023**, *12*, 3915. [CrossRef]
8. Tubbal, F.; Matekovits, L.; Raad, R. Antenna Designs for 5G/IoT and Space Applications. *Electronics* **2022**, *11*, 2484. [CrossRef]
9. Alkurt, F.; Unal, E.; Palandoken, M.; Abdulkarim, Y.; Hasar, U.C.; Karaaslan, M. Radiation pattern reconfigurable cubical antenna array for 2.45 GHz wireless communication applications. *Wirel. Netw.* **2022**, *29*, 235–246. [CrossRef]
10. Balanis, C.A. *Antenna Theory: Analysis and Design*; JOHN WILEY & SONS: Hoboken, NJ, USA, 2005.
11. Huang, B.B.; Liu, N.W. A Low-Profile Circularly Polarized Antenna Array for Beam Steering. In Proceedings of the TENCON 2022—2022 IEEE Region 10 Conference (TENCON), Hong Kong, China, 1–4 November 2022; pp. 1–3. [CrossRef]
12. Subbaraj, S.; Thomas, S.B. Reconfigurable Antennas and Their Practical Applications—A Review. *Radio Sci.* **2023**, *58*, e2023RS007656. [CrossRef]
13. Kumar, S.; Dixit, A.S.; Malekar, R.R.; Raut, H.D.; Shevada, L.K. Fifth Generation Antennas: A Comprehensive Review of Design and Performance Enhancement Techniques. *IEEE Access* **2020**, *8*, 163568–163593. [CrossRef]
14. Dahri, M.H.; Jamaluddin, M.H.; Abbasi, M.I.; Kamarudin, M.R. A Review of Wideband Reflectarray Antennas for 5G Communication Systems. *IEEE Access* **2017**, *5*, 17803–17815. [CrossRef]
15. Alhamad, R.; Almajali, E.; Mahmoud, S. Electrical Reconfigurability in Modern 4G, 4G/5G and 5G Antennas: A Critical Review of Polarization and Frequency Reconfigurable Designs. *IEEE Access* **2023**, *11*, 29215–29233. [CrossRef]
16. Kim, S.; Park, J.; So, S.; Ahn, S.; Choi, J.; Koo, C.; Joung, Y.H. Characteristics of an Implantable Blood Pressure Sensor Packaged by Ultrafast Laser Microwelding. *Sensors* **2019**, *19*, 1801. [CrossRef] [PubMed]
17. Kaefer, K.; Krüger, K.; Schlapp, F.; Uzun, H.; Celiksoy, S.; Flietel, B.; Heimann, A.; Schroeder, T.; Kempfski, O.; Sönnichsen, C. Implantable Sensors Based on Gold Nanoparticles for Continuous Long-Term Concentration Monitoring in the Body. *Nano Lett.* **2021**, *21*, 3325–3330. [CrossRef] [PubMed]
18. Wang, H.; Feng, Y.; Guo, Y.X. Design of a Miniaturized Ingestible Antenna with Complex Input Impedance for Biotelemetry Applications. In Proceedings of the 2022 Asia-Pacific Microwave Conference (APMC), Yokohama, Japan, 29 November–2 December 2022; pp. 37–39. [CrossRef]
19. Ma, S.; Björninen, T.; Sydänheimo, L.; Voutilainen, M.H.; Ukkonen, L. Double Split Rings as Extremely Small and Tuneable Antennas for Brain Implantable Wireless Medical Microsystems. *IEEE Trans. Antennas Propag.* **2021**, *69*, 760–768. [CrossRef]
20. An, H.; Nason-Tomaszewski, S.R.; Lim, J.; Kwon, K.; Willsey, M.S.; Patil, P.G.; Kim, H.S.; Sylvester, D.; Chestek, C.A.; Blaauw, D. A Power-Efficient Brain-Machine Interface System with a Sub-mw Feature Extraction and Decoding ASIC Demonstrated in Nonhuman Primates. *IEEE Trans. Biomed. Circuits Syst.* **2022**, *16*, 395–408. [CrossRef] [PubMed]
21. Mainul, E.A.; Hossain, M.F. Design of a Compact Implantable Antenna in Seven-layer Brain Phantom for Brain-machine Interface Applications. In Proceedings of the 2021 International Conference on Electronics, Communications and Information Technology (ICECIT), Khulna, Bangladesh, 14–16 September 2021; pp. 1–4. [CrossRef]
22. Kong, F.; Zada, M.; Yoo, H.; Ghovanloo, M. Triple-Band Transmitter with a Shared Dual-Band Antenna and Adaptive Matching for an Intraoral Tongue Drive System. In Proceedings of the 2018 IEEE International Symposium on Circuits and Systems (ISCAS), Florence, Italy, 27–30 May 2018; pp. 1–5. [CrossRef]
23. Faisal, F.; Zada, M.; Yoo, H.; Mabrouk, I.B.; Chaker, M.; Djeraji, T. An Ultra-Miniaturized Antenna with Ultra-Wide Bandwidth for Future Cardiac Leadless Pacemaker. *IEEE Trans. Antennas Propag.* **2022**, *70*, 5923–5928. [CrossRef]
24. Feng, Y.; Li, Y.; Li, L.; Ma, B.; Hao, H.; Li, L. Tissue-Dependent Co-Matching Method for Dual-Mode Antenna in Implantable Neurostimulators. *IEEE Trans. Antennas Propag.* **2019**, *67*, 5253–5264. [CrossRef]
25. Ullah, S.; Yoo, H. High-Resolution Implantable Microcoil Antennas for Blood-Vessel Imaging in High-Field MRIs. *IEEE Trans. Antennas Propag.* **2021**, *69*, 2560–2570. [CrossRef]
26. Khan, A.N.; Wen, D.; Liu, Y.; Sukhorukov, G.; Hao, Y. An Ultrawideband Conformal Antenna for Implantable Drug Delivery Device. In Proceedings of the 2020 14th European Conference on Antennas and Propagation (EuCAP), Copenhagen, Denmark, 15–20 March 2020; pp. 1–3. [CrossRef]

27. Gabriel, C.; Gabriel, S. Compilation of the Dielectric Properties of Body Tissues at RF and Microwave Frequencies; Internet Document. 1996. Available online: <http://safeemf.iroec.fir.cnr.it> (accessed on 8 August 2024).
28. Panunzio, N.; Ligresti, G.; Losardo, M.; Masi, D.; Mostaccio, A.; Nanni, F.; Tartaglia, G.; Marrocco, G. Cyber-Tooth: Antennified Dental Implant for RFID Wireless Temperature Monitoring. In Proceedings of the 2021 IEEE International Conference on RFID Technology and Applications (RFID-TA), Delhi, India, 6–8 October 2021; pp. 211–214. [CrossRef]
29. Nikolayev, D.; Skrivervik, A.K.; Ho, J.S.; Zhadobov, M.; Sauleau, R. Reconfigurable Dual-Band Capsule-Conformal Antenna Array for In-Body Bioelectronics. *IEEE Trans. Antennas Propag.* **2022**, *70*, 3749–3761. [CrossRef]
30. Wang, Y.; Yan, S.; Huang, B. Conformal Folded Inverted-F Antenna with Quasi-Isotropic Radiation Pattern for Robust Communication in Capsule Endoscopy Applications. *IEEE Trans. Antennas Propag.* **2022**, *70*, 6537–6550. [CrossRef]
31. Basir, A.; Cho, Y.; Shah, I.A.; Hayat, S.; Ullah, S.; Zada, M.; Shah, S.A.A.; Yoo, H. Implantable and Ingestible Antenna Systems: From imagination to realization [Bioelectromagnetics]. *IEEE Antennas Propag. Mag.* **2023**, *65*, 70–83. [CrossRef]
32. Yousaf, M.; Mabrouk, I.B.; Faisal, F.; Zada, M.; Bashir, Z.; Akram, A.; Nedil, M.; Yoo, H. Compacted Conformal Implantable Antenna with Multitasking Capabilities for Ingestible Capsule Endoscope. *IEEE Access* **2020**, *8*, 157617–157627. [CrossRef]
33. Basir, A.; Yoo, H. A Quadband Implantable Antenna System for Simultaneous Wireless Powering and Biotelemetry of Deep-Body Implants. In Proceedings of the 2020 IEEE/MTT-S International Microwave Symposium (IMS), Los Angeles, CA, USA, 4–6 August 2020; pp. 496–499. [CrossRef]
34. Janapala, D.K.; Moses, N.; Bhagavathsingh, J. Compact size antenna for skin implantable medical devices. *Int. J. Microw. Wirel. Technol.* **2023**, 1–10. [CrossRef]
35. IEEE C95. 1-2019; IEEE Standard for Safety Levels with Respect to Human Exposure to Electric, Magnetic, and Electromagnetic Fields, 0 Hz to 300 GHz. BOG/ICES—International Committee on Electromagnetic Safety: New York, NY, USA 2019; pp. 1–312. [CrossRef]
36. Wang, H.; Feng, Y.; Guo, Y. A Differentially Fed Antenna with Complex Impedance for Ingestible Wireless Capsules. *IEEE Antennas Wirel. Propag. Lett.* **2022**, *21*, 139–143. [CrossRef]
37. Zhang, J.; Das, R.; Hoare, D.; Wang, H.; Ofiare, A.; Mirzai, N.; Mercer, J.; Heidari, H. A Compact Dual-Band Implantable Antenna for Wireless Biotelemetry in Arteriovenous Grafts. *IEEE Trans. Antennas Propag.* **2023**, *71*, 4759–4771. [CrossRef]
38. Pournoori, N.; Sydänheimo, L.; Rahmat-Samii, Y.; Ukkonen, L.; Björninen, T. Small Triple-Band Meandered PIFA for Brain-Implantable Biotelemetric Systems: Development and Testing in a Liquid Phantom. *Int. J. Antennas Propag.* **2021**, *2021*, 6035169. [CrossRef]
39. Kumar, R.; Singh, S.; Singh Chauhan, A.P. Multiband antenna design based on Gosper fractal for implantable biomedical devices. *Int. J. Microw. Wirel. Technol.* **2022**, *14*, 970–980. [CrossRef]
40. Shanmughavel, S.; Sona, S. Design of PET Substrate Based Independently Controllable Triangular DRA for Implantable Devices. In Proceedings of the 2023 International Conference on Emerging Research in Computational Science (ICERCS), Coimbatore, India, 7–9 December 2023; pp. 1–4. [CrossRef]
41. Shaw, T.; Mandal, B.; Mitra, D.; Rangaiah, P.K.; Perez, M.D.; Augustine, R. Metamaterial integrated highly efficient wireless power transfer system for implantable medical devices. *AEU-Int. J. Electron. Commun.* **2024**, *173*, 155010. [CrossRef]
42. Sapari, L.; Hout, S.; Chung, J.Y. Brain Implantable End-Fire Antenna with Enhanced Gain and Bandwidth. *Sensors* **2022**, *22*, 4328. [CrossRef] [PubMed]
43. Cui, Y.; Wang, C.; Song, X.; Wu, M.; Zhang, Q.; Yuan, H.; Yuan, Z. A survey of mechanical antennas applied for low-frequency transmitting. *iScience* **2023**, *26*, 105832. [CrossRef] [PubMed]
44. Das, D.; Xu, Z.; Nasrollahpour, M.; Martos-Repath, I.; Zaeimbashi, M.; Khalifa, A.; Mittal, A.; Cash, S.S.; Sun, N.X.; Shrivastava, A.; et al. Circuit-Level Modeling and Simulation of Wireless Sensing and Energy Harvesting with Hybrid Magnetolectric Antennas for Implantable Neural Devices. *IEEE Open J. Circuits Syst.* **2023**, *4*, 139–155. [CrossRef] [PubMed]
45. Hassanien, A.E.; Breen, M.; Li, M.H.; Gong, S. A theoretical study of acoustically driven antennas. *J. Appl. Phys.* **2020**, *127*, 014903. [CrossRef]
46. Mukherjee, D.; Mallick, D. A self-biased, low-frequency, miniaturized magnetolectric antenna for implantable medical device applications. *Appl. Phys. Lett.* **2023**, *122*, 014102. [CrossRef]
47. Hosur, S.; Karan, S.K.; Priya, S.; Kiani, M. Short-Range Communication for Small Biomedical Implants using Magnetolectric Effect. In Proceedings of the 2023 IEEE International Symposium on Circuits and Systems (ISCAS), Monterey, CA, USA, 21–25 May 2023; pp. 1–5. [CrossRef]
48. Nunez, P.; Srinivasan, R. A theoretical basis for standing and traveling brain waves measured with human EEG with implications for an integrated consciousness. *Clin. Neurophysiol. Off. J. Int. Fed. Clin. Neurophysiol.* **2006**, *117*, 2424–2435. [CrossRef] [PubMed]
49. Yao, Z.; Wang, Y.E.; Keller, S.; Carman, G.P. Bulk Acoustic Wave-Mediated Multiferroic Antennas: Architecture and Performance Bound. *IEEE Trans. Antennas Propag.* **2015**, *63*, 3335–3344. [CrossRef]
50. Nan, T.; Lin, H.; Gao, Y.; Matyushov, A.; Yu, G.; Chen, H.; Sun, N.; Wei, S.; Wang, Z.; Li, M.; et al. Acoustically actuated ultra-compact NEMS magnetolectric antennas. *Nat. Commun.* **2017**, *8*, 296. [CrossRef] [PubMed]
51. Li, N.; Li, X.; Xu, B.; Zheng, B.; Zhao, P. Design and Optimization of a Micron-Scale Magnetolectric Antenna Based on Acoustic Excitation. *Micromachines* **2022**, *13*, 1584. [CrossRef] [PubMed]

52. Lodi, M.B.; Makridis, A.; Kazeli, K.; Samaras, T.; Angelakeris, M.; Muntoni, G.; Fanti, A.; Mazzarella, G. A methodology for the measurement of the specific absorption rate of magnetic scaffolds. In Proceedings of the 2023 24th International Conference on Applied Electromagnetics and Communications (ICECOM), Dubrovnik, Croatia, 27–29 September 2023; pp. 1–4. [CrossRef]
53. MIT. MIT White Papers. Available online: <https://connection.mit.edu/white-papers> (accessed on 27 July 2024).
54. Chakraborty, A.; Islam, M.; Shahriyar, F.; Islam, S.; Zaman, H.; Hasan, M. Smart Home System: A Comprehensive Review. *J. Electr. Comput. Eng.* **2023**, *2023*, 7616683. [CrossRef]
55. Athanasiadis, C.L.; Pippi, K.D.; Papadopoulou, T.A.; Korkas, C.; Tsaknakis, C.; Alexopoulou, V.; Nikolaidis, V.; Kosmatopoulos, E. A Smart Energy Management System for Elderly Households. In Proceedings of the 2022 57th International Universities Power Engineering Conference (UPEC), Istanbul, Turkey, 30 August–2 September 2022; pp. 1–6. [CrossRef]
56. Arnaoutoglou, D.G.; Kyriakou, A.A.G.; Kaifas, T.N.F.; Sirakoulis, G.C.; Kyriacou, G.A. An All-Polarization, Beamforming, and DoA Ready, Γ -Dipole Antenna Array. *IEEE Trans. Antennas Propag.* **2024**, *72*, 2323–2336. [CrossRef]
57. Mazaheri, M.; Ruiz, R.; Giustiniano, D.; Widmer, J.; Abari, O. Bringing Millimeter Wave Technology to Any IoT Device. In Proceedings of the 29th Annual International Conference on Mobile Computing and Networking, 2–6 October 2023; Association for Computing Machinery: New York, NY, USA, 2023.
58. Hu, R.; Lin, W.; Yun, X.; Xu, D.; Zhang, B.; Zeng, Z. A High-Gain Ultra-Compact ME Antenna Design for Portable RF Wireless Communication. In Proceedings of the 2022 IEEE 9th International Symposium on Microwave, Antenna, Propagation and EMC Technologies for Wireless Communications (MAPE), Chengdu, China, 26–29 August 2022; pp. 165–168. [CrossRef]
59. Vaquero, Á.F.; Teixeira, J.; Matos, S.A.; Arrebola, M.; Costa, J.R.; Felício, J.M.; Fernandes, C.A.; Fonseca, N.J.G. Design of Low-Profile Transmitarray Antennas with Wide Mechanical Beam Steering at Millimeter Waves. *IEEE Trans. Antennas Propag.* **2023**, *71*, 3713–3718. [CrossRef]
60. Wang, C.; Yeo, J.C.; Chu, H.; Lim, C.T.; Guo, Y.X. Design of a Reconfigurable Patch Antenna Using the Movement of Liquid Metal. *IEEE Antennas Wirel. Propag. Lett.* **2018**, *17*, 974–977. [CrossRef]
61. Selvam, Y.P.; Sangamithira, N.; Karuppasamy, T.; Puvvadi, M.; Jayapalan, A. Optically Reconfigurable Slotted Waveguide Antenna Array for 5G Applications. In Proceedings of the 2023 International Conference on Computer Communication and Informatics (ICCCI), Coimbatore, India, 23–25 January 2023; pp. 1–4. [CrossRef]
62. Elias, B.B.Q.; Soh, P.J.; Al-Hadi, A.A.; Akkaraekthalin, P.; Vandenbosch, G.A.E. A Review of Antenna Analysis Using Characteristic Modes. *IEEE Access* **2021**, *9*, 98833–98862. [CrossRef]
63. Huang, H.; Wen, H. Miniaturized reconfigurable tri-polarization metantenna based on characteristic mode analysis with high-aperture efficiency. *Int. J. RF Microw. Comput.-Aided Eng.* **2021**, *31*, e22867. [CrossRef]
64. Molins-Benlliure, J.; Antonino-Daviu, E.; Cabedo-Fabrés, M.; Ferrando-Bataller, M. Design Procedure for 5G/IoT Multiple-Port Cavity-Backed Antennas. In Proceedings of the 2021 15th European Conference on Antennas and Propagation (EuCAP), Dusseldorf, Germany, 22–26 March 2021; pp. 1–5. [CrossRef]
65. SR, V.K.; Venkatesh, T.; Rajanna, P.K.T. Characteristic Mode Analysis of Polarization Reconfigurable Compact Metasurface Antenna for sub-6GHz 5G Application. In Proceedings of the 2023 3rd International Conference on Mobile Networks and Wireless Communications (ICMNWC), Tumkur, India, 4–5 December 2023; pp. 1–6. [CrossRef]
66. Tran, H.H.; Park, H.C. Wideband Reconfigurable Antenna with Simple Biasing Circuit and Tri-Polarization Diversity. *IEEE Antennas Wirel. Propag. Lett.* **2019**, *18*, 2001–2005. [CrossRef]
67. Kiani, H.; Chatzichristodoulou, D.; Nadeem, A.; Quddious, A.; Shoab, N.; Vryonides, P.; Anagnostou, D.E.; Nikolaou, S. Microfluidically Frequency & Polarization Reconfigurable Patch Antennas. In Proceedings of the 2022 16th European Conference on Antennas and Propagation (EuCAP), Madrid, Spain, 27 March–1 April 2022; pp. 1–5. [CrossRef]
68. Kim, J.H.; Joo, C.H.; Ahn, S.H.; Lee, W.S. A quadruple-polarized reconfigurable antenna for 915 MHz ISM band applications. In Proceedings of the 2018 IEEE International Conference on Consumer Electronics (ICCE), Las Vegas, NV, USA, 12–14 January 2018; pp. 1–2. [CrossRef]
69. Dong, H.J.; Kim, Y.B.; Lee, H.L. Reconfigurable Quad-Polarization Switched Beamforming Antenna With Crossed Inverted-V Array and Dual-Butler Matrix. *IEEE Trans. Antennas Propag.* **2022**, *70*, 2708–2716. [CrossRef]
70. Liu, M.; Zhai, Z.J.; Lin, F.; Sun, H.J. Wideband Quad-Polarization-Reconfigurable Bidirectional Antenna With a Simple Wideband Switchable Feeding Network. *IEEE Antennas Wirel. Propag. Lett.* **2023**, *22*, 1346–1350. [CrossRef]
71. Row, J.S.; Wei, Y.H. Wideband Reconfigurable Crossed-Dipole Antenna with Quad-Polarization Diversity. *IEEE Trans. Antennas Propag.* **2018**, *66*, 2090–2094. [CrossRef]
72. Takato, S.; Arai, H.; Moon, Y.C.; Kim, D.Y. Decoupling Design of Quad-Polarization Overlay Antenna Element with a Stacked Structure. *IEEE Antennas Wirel. Propag. Lett.* **2023**, *22*, 1336–1340. [CrossRef]
73. Zhao, W.; Li, X.; Qi, Z.; Zhu, H. High-Order-Mode Cavity Fed Antenna Arrays for Diverse Polarizations With Compact Size, High Gain, and High Efficiency. *IEEE Trans. Antennas Propag.* **2022**, *70*, 1045–1056. [CrossRef]
74. Chen, S.L.; Liu, Y.; Zhu, H.; Chen, D.; Guo, Y.J. Millimeter-Wave Cavity-Backed Multi-Linear Polarization Reconfigurable Antenna. *IEEE Trans. Antennas Propag.* **2022**, *70*, 2531–2542. [CrossRef]
75. Tran, H.H.; Nguyen-Trong, N.; Le, T.T.; Park, H.C. Wideband and Multipolarization Reconfigurable Crossed Bowtie Dipole Antenna. *IEEE Trans. Antennas Propag.* **2017**, *65*, 6968–6975. [CrossRef]
76. Guo, P.; Zhong, W.; Chen, S.L.; Chen, D.; Liu, Y. A Novel Programmable Stacked Patch Antenna with the Diversity of Sixteen Linear Polarizations and Four Frequency Bands. *IEEE Trans. Antennas Propag.* **2023**, *71*, 1035–1040. [CrossRef]

77. Wang, S.; Yang, D.; Geyi, W.; Zhao, C.; Ding, G. Polarization-Reconfigurable Antenna Using Combination of Circular Polarized Modes. *IEEE Access* **2021**, *9*, 45622–45631. [CrossRef]
78. Mohamed, I.M.; Sebak, A.R. 60 GHz 2-D Scanning Multibeam Cavity-Backed Patch Array Fed by Compact SIW Beamforming Network for 5G Applications. *IEEE Trans. Antennas Propag.* **2019**, *67*, 2320–2331. [CrossRef]
79. Li, Q.; Hirokawa, J.; Tomura, T.; Takahashi, Y.; Kita, N.; Fonseca, N.J.G. A Two-Dimensional 6×4-Way Hollow Waveguide Beam-Switching Matrix. *IEEE Access* **2023**, *11*, 74239–74249. [CrossRef]
80. Zhu, H.; Peng, J.; Gao, C.; Qian, Z. A Two-Dimensional Beam Scanning 60 GHz Antenna Array Based on SIW Butler Matrix. In Proceedings of the 2023 Cross Strait Radio Science and Wireless Technology Conference (CSRSWTC), Guilin, China, 10–13 November 2023; pp. 1–3. [CrossRef]
81. Li, Q.; Hirokawa, J.; Tomura, T.; Fonseca, N.J.G. Two-Dimensional One-Body 3 × 3-Way Hollow-Waveguide Nolen Matrix Using a Two-Plane Unequal Division Coupler. *IEEE Trans. Microw. Theory Tech.* **2024**, *72*, 376–390. [CrossRef]
82. Wang, D.; Xu, K.D.; Cao, Y.; Guo, C.; Yan, S. A Butler Matrix-Based Multibeam W-Band Slot Antenna Array Fabricated by Metal Additive Manufacturing Technology. *IEEE Trans. Antennas Propag.* **2024**, *72*, 5349–5354. [CrossRef]
83. Ji, L.Y.; Guo, Y.J.; Qin, P.Y.; Gong, S.X.; Mittra, R. A Reconfigurable Partially Reflective Surface (PRS) Antenna for Beam Steering. *IEEE Trans. Antennas Propag.* **2015**, *63*, 2387–2395. [CrossRef]
84. Dutta, R.K.; Jaiswal, R.K.; Saikia, M.; Srivastava, K.V. Beam-Forming Antenna Based on Electrically Reconfigurable Frequency Selective Surface. In Proceedings of the 2022 IEEE Microwaves, Antennas, and Propagation Conference (MAPCON), Bangalore, India, 12–16 December 2022; pp. 511–515. [CrossRef]
85. Ali, H. Spherical Active Frequency-Selective Surface for 3-D Beam-Scanning Antenna. In Proceedings of the 2024 18th European Conference on Antennas and Propagation (EuCAP), Glasgow, UK, 17–22 March 2024; pp. 1–4. [CrossRef]
86. Chen, Y.; Chernogor, L.F.; Zheng, Y.; Jin, Z.; Sun, Z.; Yao, Z.; Wang, C.; Liu, T. Dual-Band Dual-Polarized Antenna Based on TDLS Metasurface for 4G/5G Base Station Applications. *IEEE Trans. Circuits Syst. II Express Briefs* **2024**, *71*, 577–581. [CrossRef]
87. Vinod, G.V.; Khairnar, V.V. A Wideband Beam Steering and Beamwidth Reconfigurable Antenna Using Coding Metasurface. *IEEE Access* **2024**, *12*, 97143–97153. [CrossRef]
88. Raza, M.U.; Zhang, Z.; Liu, T.; Shoukat, M.U.; Niaz, A.; Luo, K. Flexible Monopole Antenna for IoT Applications: A Survey. In Proceedings of the 2021 7th International Conference on Computer and Communications (ICCC), Chengdu, China, 10–13 December 2021; pp. 2154–2159. [CrossRef]
89. Bhardwaj, S.; Malik, P.; Islam, T.; Gehlot, A.; Das, S.; Asha, S. A Printed Monopole Antenna for Next Generation Internet of Things: Narrow-Band Internet of Things (NB-IoT). *Prog. Electromagn. Res. C* **2023**, *138*, 117–129. [CrossRef]
90. Muzaffar, S.; Turab, D.; Zahid, M.; Amin, Y. Dual-Band UWB Monopole Antenna for IoT Applications. *Eng. Proc.* **2023**, *46*, 29. [CrossRef]
91. Yahya, M.S.; Soeung, S.; Singh, N.S.S.; Yunusa, Z.; Chinda, F.E.; Rahim, S.K.A.; Musa, U.; Nor, N.B.M.; Sovuthy, C.; Abro, G.E.M. Triple-Band Reconfigurable Monopole Antenna for Long-Range IoT Applications. *Sensors* **2023**, *23*, 5359. [CrossRef] [PubMed]
92. Li, J.; Huang, J.; He, H.; Wang, Y. An Ultra-Thin Multi-Band Logo Antenna for Internet of Vehicles Applications. *Electronics* **2024**, *13*, 2792. [CrossRef]
93. Gracias, J.S.; Parnell, G.S.; Specking, E.; Pohl, E.A.; Buchanan, R. Smart Cities—A Structured Literature Review. *Smart Cities* **2023**, *6*, 1719–1743. [CrossRef]
94. Singh, P.; Goswami, P.K.; Sharma, S.; Goswami, G. Frequency Reconfigurable Multiband Antenna for IoT Applications in WLAN, Wi-Max, and C-Band. *Prog. Electromagn. Res. C* **2020**, *102*, 149–162. [CrossRef]
95. Syed, A.S.; Sierra-Sosa, D.; Kumar, A.; Elmaghaby, A. IoT in Smart Cities: A Survey of Technologies, Practices and Challenges. *Smart Cities* **2021**, *4*, 429–475. [CrossRef]
96. Doré, J.B.; Belot, D.; Mercier, E.; Bicaïs, S.; Gougeon, G.; Corre, Y.; Miscopein, B.; Ktéas, D.; Strinati, E.C. Technology Roadmap for Beyond 5G Wireless Connectivity in D-band. In Proceedings of the 2020 2nd 6G Wireless Summit (6G SUMMIT), Levi, Finland, 17–20 March 2020; pp. 1–5. [CrossRef]
97. Kim, H.; Kim, J.; Oh, J. Communication A Novel Systematic Design of High-Aperture-Efficiency 2D Beam-Scanning Liquid-Crystal Embedded Reflectarray Antenna for 6G FR3 and Radar Applications. *IEEE Trans. Antennas Propag.* **2022**, *70*, 11194–11198. [CrossRef]
98. Empliouk, T.; Kapetanidis, P.; Arnaoutoglou, D.; Kolitsidas, C.; Lialios, D.; Koutinos, A.; Kaifas, T.N.F.; Georgakopoulos, S.V.; Zekios, C.L.; Kyriacou, G.A. Compact, Ultra-Wideband Butler Matrix Beamformers for the Advanced 5G Band FR3—Part I. *Electronics* **2024**, *13*, 2763. [CrossRef]
99. NYBSYS. Low to High 5G Bands Explained. Available online: <https://nybsys.com/5g-bands/> (accessed on 27 July 2024).
100. Chaloun, T.; Boccia, L.; Arnieri, E.; Fischer, M.; Valenta, V.; Fonseca, N.J.G.; Waldschmidt, C. Electronically Steerable Antennas for Future Heterogeneous Communication Networks: Review and Perspectives. *IEEE J. Microwaves* **2022**, *2*, 545–581. [CrossRef]
101. Liu, T.Y.; Row, J.S. A scanning phased array based on a polarization reconfigurable antenna with compact aperture size. *Int. J. RF Microw. Comput.-Aided Eng.* **2021**, *31*, e22902. [CrossRef]
102. Kim, B.; Park, J.; Choi, D.; Hong, W. A Software-Defined Reconfigurable Phased-Array Architecture for Beyond 5G Applications. In Proceedings of the 2021 International Conference on Microwave and Millimeter Wave Technology (ICMMT), Nanjing, China, 23–26 May 2021; pp. 1–3. [CrossRef]

103. Hu, J.; Yang, X.; Ge, L.; Guo, Z.; Hao, Z.C.; Wong, H. A Reconfigurable 1×4 Circularly Polarized Patch Array Antenna With Frequency, Radiation Pattern, and Polarization Agility. *IEEE Trans. Antennas Propag.* **2021**, *69*, 5124–5129. [CrossRef]
104. Santamaria, L.; Ferrero, F.; Staraj, R.; Lizzi, L. Electronically Pattern Reconfigurable Antenna for IoT Applications. *IEEE Open J. Antennas Propag.* **2021**, *2*, 546–554. [CrossRef]
105. Wu, J.; Lu, X.; Wang, W.; Han, J.; Xu, G.; Huang, Z. Design of a Compact Polarization-Agile and Frequency-Tailored Array Antenna with Digital-Controllable Radiation Beams. *IEEE Trans. Antennas Propag.* **2022**, *70*, 813–822. [CrossRef]
106. Chen, Q.; Ala-Laurinaho, J.; Khripkov, A.; Ilvonen, J.; Moreno, R.M.; Viikari, V. Varactor-Based Frequency-Reconfigurable Dual-Polarized mm-Wave Antenna Array for Mobile Devices. *IEEE Trans. Antennas Propag.* **2023**, *71*, 6628–6638. [CrossRef]
107. Singh, V.; Khalily, M.; Tafazolli, R. A metasurface-based electronically steerable compact antenna system with reconfigurable artificial magnetic conductor reflector elements. *iScience* **2022**, *25*, 105549. [CrossRef] [PubMed]
108. Santamaria, L.; Ferrero, F.; Staraj, R.; Lizzi, L. Slot-Based Pattern Reconfigurable ESPAR Antenna for IoT Applications. *IEEE Trans. Antennas Propag.* **2021**, *69*, 3635–3644. [CrossRef]
109. Hasan, Z.; Gong, X. Design of A Reconfigurable-Polarization Slot-Ring Phased Array Antenna. In Proceedings of the 2023 IEEE International Symposium on Antennas and Propagation and USNC-URSI Radio Science Meeting (USNC-URSI), Portland, OR, USA, 23–28 July 2023; pp. 91–92. [CrossRef]
110. Zandamela, A.; Marchetti, N.; Ammann, M.J.; Narbudowicz, A. Pattern and Polarization Diversity Multisector Annular Antenna for IoT Applications. *IEEE Trans. Antennas Propag.* **2023**, *71*, 7241–7249. [CrossRef]
111. Palazzi, V.; Mezzanotte, P.; Roselli, L. A Novel Agile Phase-Controlled Beamforming Network Intended for 360° Angular Scanning in MIMO Applications. In Proceedings of the 2018 IEEE/MTT-S International Microwave Symposium—IMS, Philadelphia, PA, USA, 10–15 June 2018; pp. 624–627. [CrossRef]
112. Wei, Z.; Zhu, X.; Chi, P.L.; Xu, R.; Yang, T. A Fully Reconfigurable 1×4 Filtering Beamforming Network With Continuous Phase and Amplitude Control. *IEEE Trans. Microw. Theory Tech.* **2024**, *72*, 348–362. [CrossRef]
113. Wang, X.Z.; Chen, F.C.; Chu, Q.X. A Compact Broadband 4×4 Butler Matrix with 360° Continuous Progressive Phase Shift. *IEEE Trans. Microw. Theory Tech.* **2023**, *71*, 3906–3914. [CrossRef]
114. Yu, D.; Liu, H.; Li, S.; Wang, Z.; Fang, S. Control-Relaxed Wideband 2×4 Nolen Matrix with 360° Continuously Tuned Differential Phase. *IEEE Trans. Circuits Syst. II Express Briefs* **2024**, *71*, 1979–1983. [CrossRef]

Disclaimer/Publisher’s Note: The statements, opinions and data contained in all publications are solely those of the individual author(s) and contributor(s) and not of MDPI and/or the editor(s). MDPI and/or the editor(s) disclaim responsibility for any injury to people or property resulting from any ideas, methods, instructions or products referred to in the content.

Review

Enhancing CubeSat Communication Through Beam-Steering Antennas: A Review of Technologies and Challenges

Tale Saeidi ^{1,2,*}  and Saeid Karamzadeh ^{3,4,*} 

¹ WiSAR Lab, Atlantic Technological University (ATU), F92 FC93 Letterkenny, Ireland

² Electrical and Electronics Engineering Department, Faculty of Engineering and Natural Sciences, İstinye University, 34396 Istanbul, Turkey

³ Millimeter Wave Technologies, Intelligent Wireless System, Silicon Austria Labs (SAL), 4040 Linz, Austria

⁴ Electrical and Electronics Engineering Department, Faculty of Engineering and Natural Sciences, Bahçeşehir University, 34349 Istanbul, Turkey

* Correspondence: tale.saeidi@atu.ie (T.S.); saeid.karamzadeh@silicon-austria.com (S.K.)

Abstract: With their compact design and versatility, CubeSats have emerged as critical platforms for advancing space exploration and communication technologies. However, achieving reliable and efficient communication in the dynamic and constrained environment of low Earth orbit (LEO) remains a significant challenge. Beam-steering antenna systems offer a promising solution to address these limitations, enabling adaptive communication links with improved gain and coverage. This review article provides a comprehensive analysis of the state-of-the-art in CubeSat communication, concentrating on the latest developments in beam-steering antennas. By synthesizing the findings from recent studies, the key challenges are highlighted, including power constraints, miniaturization, and integration with CubeSat platforms. Furthermore, this paper investigates cutting-edge techniques, such as phased array systems, metasurface-based designs, and reconfigurable antennas, which pave the way for enhanced performance. This study can serve as a resource for researchers and engineers, offering insights into current trends and future opportunities for advancing CubeSat communications through innovative antenna systems.



Academic Editors: Raad Raad,
Ladislau Matekovits and Faisal
Tubbal

Received: 14 January 2025

Revised: 8 February 2025

Accepted: 12 February 2025

Published: 14 February 2025

Citation: Saeidi, T.; Karamzadeh, S. Enhancing CubeSat Communication Through Beam-Steering Antennas: A Review of Technologies and Challenges. *Electronics* **2025**, *14*, 754. <https://doi.org/10.3390/electronics14040754>

Copyright: © 2025 by the authors. Licensee MDPI, Basel, Switzerland. This article is an open access article distributed under the terms and conditions of the Creative Commons Attribution (CC BY) license (<https://creativecommons.org/licenses/by/4.0/>).

Keywords: CubeSat communications; beamforming antennas; leaky wave antenna; metasurface

1. Introduction

Medium Earth orbit (MEO) satellites typically weigh between 500 and 1000 kg, carry out at a height above sea level of 900 km, follow an orbit synchronized with the Sun's position, and have elevated levels of power consumption, at around 8 kW. They have a lifespan of approximately four years and come with a hefty price tag of USD 50 to 100 million. As a result, only large companies and government organizations with significant financial resources have been able to build and operate these large satellites. MEO satellites support Earth observation, weather forecasting, mobile networks, and scientific research. A notable example is Formosat-2, the first remote sensing and scientific observation satellite in a sun-synchronous orbit, developed and deployed by Taiwan's National Space Program Office (NSPO). Figure 1 shows a general concept of CubeSat communications (Figure 1).

Traditional satellites use large medium-gain antennas, like horn antennas with precise pointing systems, for ground communication. In contrast, CubeSats offer low-cost alternatives that are accessible to the public. These small, lightweight satellites operate in low Earth orbit (LEO) and utilize readily available, commercial off-the-shelf (COTS) components. Three typical CubeSat configurations of varying sizes exist, such as 10 cm³ for

a 1U CubeSat, $10 \times 10 \times 20 \text{ cm}^3$ for a 2U CubeSat, and $10 \times 10 \times 30 \text{ cm}^3$ for a 3U CubeSat (Figure 2). They weigh between 1 and 6 kg and have low power requirements of around 2 W. The Tokyo Tech 1U CubeSat, CUTE-I, is a prominent example of CubeSat technology. Developed by TIT, in 2003, it weighs 1 kg and operates in LEO at an altitude of 820 km. They created it for communication and sensing operations [1].

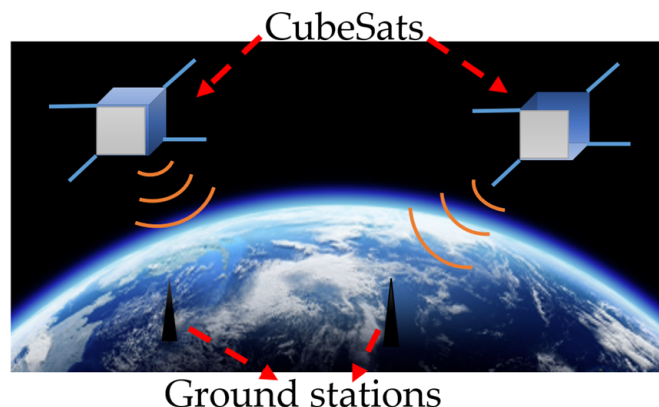


Figure 1. CubeSat communications.



Figure 2. CubeSat designs: (left) 1U; (middle) 2U; (right) 3U [1].

The Telemetry, Tracking, and Communications (TTC) subsystem is critical to a CubeSat, ensuring reliable communication with the ground station for continuous data exchange. The subsystem's antenna facilitates the transmission of telemetry and scientific data, such as images, while also receiving commands. Designing CubeSat antennas is challenging due to stringent constraints on size (1U), weight (under 1.3 kg), and power consumption (but to a lesser extent, at 2 W) while still requiring great gain and broad BW [2].

Traditional CubeSat communication systems often rely on omnidirectional mono or dipole antennas that operate in the UHF or S-band frequencies. Although relatively simple and robust, they offer limited gain and directivity, resulting in lower data rates and increased susceptibility to interference. As mission requirements evolve to demand higher data throughput and more robust communication links, there is a pressing need to enhance the performance of CubeSat antenna systems.

Beam-steering and beamforming technologies have emerged as promising solutions for these challenges. Beam steering involves directing the antenna's main lobe toward a specific direction without physically moving the antenna. At the same time, beamforming utilizes multiple antenna elements to electronically shape and control the radiation's pattern. These techniques can significantly improve communication performance by increasing antenna gain, enhancing link reliability, and reducing interference.

Modern antenna design improvements have resulted in the development of various beam-steering and beamforming systems suitable for CubeSats. For instance, metasurface-based antennas have been explored for their ability to steer beams passively, offering an ideal compact and power-efficient solution for the constrained CubeSat environment. These antennas utilize engineered surfaces to manipulate electromagnetic waves, enabling beam-steering capabilities without the need for complex feeding networks or mechanical parts [3]. In addition, implementing beam-steering and beamforming systems in CubeSats is challenging. The limited size and power availability necessitate highly efficient and miniaturized components. Thermal management becomes critical as active components may generate heat that must be dissipated within the small satellite body. Additionally, the complexity of integrating these advanced antenna systems with existing CubeSat platforms requires careful consideration to ensure compatibility and reliability.

Despite these challenges, the potential benefits of enhanced communication capabilities make the pursuit of beam-steering and beamforming technologies for CubeSats a worthwhile endeavor. As the demand for more sophisticated CubeSat missions continues to grow, developing and implementing advanced antenna systems will be crucial in expanding the horizons of small satellite applications.

Paper Contributions

This review paper makes a distinct and valuable contribution to the field of CubeSat communication by focusing on the advancements in beam-steering antenna systems, addressing critical challenges such as power efficiency, miniaturization, and integration with CubeSat platforms. Our paper delves deeper into the specific context of CubeSat communication in low Earth orbit (LEO). It also adequately addresses dynamic beam-steering technologies' unique demands and opportunities, such as phased array systems, metasurface-based designs, and reconfigurable antennas. By synthesizing recent research, our review paper investigates the critical gap in beam-steering technology for CubeSats, offering a more targeted and up-to-date analysis of beam-steering antennas tailored to CubeSat communication. This includes highlighting innovative approaches that enhance gain, coverage, and adaptability in constrained environments. In terms of the focus of this review paper, other review papers have discussed the types of antennas used for satellite and CubeSat communications. For instance, Reference [1] is primarily a general survey of planar antennas for pico-satellites, emphasizing their fundamental characteristics. It is also essential for understanding planar antenna designs. However, it does not sufficiently explore the specific requirements and potential of dynamic beam-steering technologies, particularly in the context of CubeSat communications, which is the primary focus of our paper. Our paper, therefore, not only builds upon but also surpasses the foundational insights provided in [1], serving as a modern resource for researchers and engineers seeking to advance CubeSat communication through cutting-edge beam-steering antenna technologies. In addition, Reference [2] reviews antennas designed for CubeSats, providing a broad overview of such designs, covering various types and their fundamental characteristics. It also serves as a valuable resource for understanding the general landscape of CubeSat antennas. However, the authors do not focus on an analysis of beam-steering technologies, which are critical for enabling adaptive communication links with improved gain and coverage. Furthermore, they do not extensively explore emerging techniques, such as phased array systems, metasurface-based designs, and reconfigurable antennas, which are at the forefront of recent advancements in CubeSat communication and the focus of our paper. Our paper addresses these gaps by offering a more focused and up-to-date synthesis of the state-of-the-art developments in beam-steering antennas, highlighting their unique demands, opportunities, and potential to overcome LEO communication challenges.

The structure of this review paper is organized as follows: In-depth explanations of CubeSat communications, applications, challenges, and techniques are provided in Sections 1 and 2. Then, the general aspects of antennas utilized for CubeSats are assessed in Section 3. Next, Section 4 presents in-depth information on antennas used for beam steering, and several industry cases studies are provided in Section 5. Finally, Sections 6 and 7 discuss and conclude the review.

2. CubeSat Antennas, Challenges, and Requirements

Various research efforts have explored different frequencies, techniques, materials, and dimensions to address the challenges and limitations in designing high-performance antennas for CubeSats. CubeSat antennas must meet specific requirements to be suitable for space communications. CubeSats are limited by size and weight, typically within $10 \times 10 \times 10 \text{ cm}^3$ units (1U) or multiples. Antennas need to be compact and lightweight to adhere to these limits. Deployable structures are often used for more extensive or higher-gain antennas. They must be securely deposited, compacted during the process, and efficiently positioned once in orbit. CubeSats typically operate within designated frequency bands, such as VHF, UHF, S-band, or X-band. The antenna must be adjusted to operate within the target frequency band and comply with ITU and other international standards for satellite communications. Depending on the mission, the antenna may require omnidirectional coverage—especially for low Earth orbit (LEO) missions—to maintain connectivity regardless of the satellite’s orientation. Alternatively, directional antennas with high-gain patterns may be used to focus energy for enhanced communication reliability [4].

Other critical design considerations can be addressed as follows:

Polarization: circular polarization (CP) is often preferred due to its resistance to orientation mismatches, although linear polarization may also be employed with precise alignment;

High efficiency: the antenna must maximize limited power resources onboard;

Sufficient bandwidth: it should support the necessary communication protocols, including telemetry, commands, and data downlinks;

Low-power operation: since CubeSats have constrained power budgets, the antenna must perform efficiently with limited power;

Environmental resilience: antennas must withstand extreme temperature variations and radiation in space, ensuring long-term operational reliability;

Structural durability: The design should be able to endure launch vibrations and shocks. Deployable antennas, in particular, must have reliable mechanisms for flawless operation in microgravity and vacuum conditions;

Multifunctionality: antennas may need to support multiple tasks, such as data transmission, telemetry, and intersatellite communication;

Minimal interference: designs should avoid disrupting other onboard systems;

Cost-effectiveness: manufacturing must be affordable, as CubeSat missions often operate within strict budgets.

Considering these requirements and the techniques to improve them, the following research on antenna design was performed and proposed for CubeSat and satellite communications.

3. Antennas with General Aspects Utilized for CubeSat

This section depicts all recent antennas designed and used for CubeSat communications and applications. All relevant aspects of antennas designed for this purpose, such as the working band, polarization, dimensions, and materials, were considered in the analysis of each work.

3.1. Planar Phased Patch Antennas and Their Arrays

Reference [5] investigated the design and feasibility of a reconfigurable phased antenna array to enhance CubeSat operations in the Ka-band. The proposed design enables dynamic beam steering, improving the gain and allowing for high-data-rate communication links for advanced CubeSat missions. The antenna's reconfigurability allows for the adaptability of the radiation patterns, making it suitable for multi-ground-station communication and intersatellite links. Operating in the Ka-band provides broader bandwidths and higher data rates, which is ideal for Earth observation and scientific data transmission applications. However, the study acknowledges the challenges of integrating such systems into CubeSats, including the high power demands, precise pointing accuracy requirements, and the complexity of controlling multiple antenna elements. Additionally, Ka-band communication is more susceptible to atmospheric attenuation, impacting performance. Despite these challenges, the feasibility analysis highlights the potential of phased arrays to meet CubeSat size, weight, and power (SWaP) constraints through careful design and optimization, offering a promising approach to extending CubeSat communication capabilities.

Reference [6] presents the development of a compact microstrip antenna array tailored for fifth-generation (5G) CubeSat applications. The proposed design features 16 miniaturized patch antennas arranged in a 4×4 configuration, utilizing a feeding network on a Rogers TMM10 substrate. This configuration achieves a low-profile structure suitable for the limited space available on CubeSats. The antenna array operates effectively within the frequency range of 3.46 GHz to 3.54 GHz, making it compatible with 5G communication standards. Both simulation and experimental results demonstrate the antenna's high gain and performance, indicating its potential for enhancing data transmission capabilities in CubeSat missions. The study underscores the importance of integrating efficient, low-profile antenna systems in small satellite platforms to meet the growing demand for high-speed communication.

Reference [7] explores the integration of phased array microstrip patch antennas into structural panels of satellites. This multifunctional approach aims to optimize the limited space in small satellites by combining structural and communication functions. The study evaluates the feasibility of embedding these antennas within composite panels of carbon-fiber-reinforced polymers (CFRPs) and aluminum, focusing on maintaining the structural integrity while ensuring effective communication capabilities. The embedded phased array design offers advantages such as a reduced payload volume and enhanced system integration, which are critical for small satellite missions. However, the challenges include managing the potential electromagnetic interference between the antenna and composite materials, ensuring that the panel's structural properties are not compromised. The research concludes that with careful design and material selection, embedding phased array patch antennas within satellite structures is a viable solution to enhance the functionality and efficiency of small satellites.

Reference [8] addressed the challenge of enhancing data transmission rates for CubeSats, which are often limited by power constraints and low-gain antennas. The authors propose a low-power, electrically steered, S-band phased array antenna system designed to increase CubeSat communications' adequate isotropic radiated power (EIRP), thereby enabling higher data rates. The prototype developed in this study features an active phased array with beam-steering capabilities, allowing for directional communication without the need for mechanical movement. This design is particularly advantageous for CubeSats, offering a compact, power-efficient solution to improve the downlink capacity. The research includes constructing and testing the prototype in an anechoic chamber, demonstrating its potential to significantly enhance CubeSat communication performance.

In Ref. [9], CubeSats, which are a type of nano-satellite, offer a cost-effective platform for space missions that now support applications involved in Earth observation, remote sensing, deep space exploration, and intersatellite communication. Advancements in antenna technology have driven their development to meet diverse mission requirements. Despite their potential, CubeSats face challenges such as limited data rates. Transceivers with elevated gain and data rates are currently being developed to address these challenges. Circularly polarized (CP) antennas are essential for reliable communication, mitigating issues like antenna misalignment and atmospheric Faraday rotation. Among the various antenna types, microstrip patch antennas are the most versatile for CubeSat missions because of their low profile, light weight, cost-effectiveness, and integration issues. Microstrip patch arrays deliver high gain and are CP, which are crucial for high-data-rate downlinks. Designing CP microstrip arrays involves techniques like sequential feeding with a 90° phase shift between elements. While practical, this method adds design complexity and potentially leads to signal loss.

The SPORT is a CubeSat mission jointly developed by Brazil and the United States to study space weather. The SPORT CubeSat uses an X-band radio for downlink communications, featuring a custom-designed circularly polarized antenna positioned on the nadir side to face Earth consistently. This low-cost antenna meets specific size and reliability requirements for consistent communication as the CubeSat rises from the horizon. In the communication link, transmitted power experiences losses due to device imperfections, atmospheric attenuation, antenna polarization mismatches, and path losses, which are calculated using the Friis transmission equation. The receiver antenna also introduces noise due to environmental interference and heat generated by resistance and internal components. The SNR, the proportion of received power to noise, must exceed a threshold for reliable communication. A link margin above 0 dB indicates a successful signal reception, with an ideal margin exceeding 3 dB. The SNR maximum depends on the required BER and the modulation technique employed [10].

Reference [11] presents a compact UHF multi-band RHCP quadrifilar antenna devised for CubeSat communications, operating in the LoRa bands. The antenna employs two FR4-epoxy substrates linked by shorting pins, with a ceramic insertion in between and screws for mechanical robustness against launch vibrations. By utilizing parasitic elements, it achieves a multi-band functionality, while its quadrifilar structure ensures effective RHCP radiation, mitigating alignment issues with terrestrial stations. Measurements in the anechoic chambers showed a 2.3 dBic gain at 870 MHz and 1.1 dBic at 920 MHz, featuring an AR < 3 dB across a 120° aperture beamwidth. The antenna demonstrated successful real-world application in a 3U CubeSat launched with validated ground-to-space communications. However, the challenges included reduced gain when integrated into the CubeSat due to chassis-induced vertical currents, a modest fractional bandwidth of 7.8%, and a suboptimal RF performance by the FR4 material despite its mechanical advantages. Overall, the design offers a robust solution for CubeSat communications, with potential areas for improvement including the material and integration effects.

Reference [12] presents a transparent microstrip GPS antenna designed for CubeSat applications, utilizing transparent conductive materials to maintain optical transparency while ensuring RF functionality. The design employs a microstrip patch configuration with materials like ITO (indium tin oxide) or AgHT (silver halide transparent) conductors, which allow for integration with solar panels, optimizing the utilization of space on CubeSats. The findings highlight an adequate GPS signal reception, compact size, and low-profile design, making it suitable for CubeSat deployment. However, challenges such as high resistive losses, reduced conductivity compared to traditional metals, and fabrication complexities impact the efficiency, gain, and durability in space conditions. Additionally,

while the design supports GPS reception, it is not optimized for beam steering or dynamic beamforming, limiting its applicability for advanced CubeSat communication systems requiring directional adaptability and high-gain performance.

A 1U CubeSat, which is a 100 mm cube, is built to support multiple functions. CubeSat satellites require antennas for TT&C, downlinking data, receiving signals, and facilitating intersatellite cross-links. The available area for antenna allocation in the minor CubeSat is $100 \times 100 \text{ mm}^2$, necessitating compact and lightweight antennas. CubeSat VHF–UHF antennas typically use deployable linear wire designs, mainly dipoles and their variations. Conversely, the machine-driven arrangement of these antennas introduces the danger of assignment collapse, as several small satellite missions have encountered issues due to these mechanical components. Many CubeSats operate within the VHF and UHF frequency bands [13].

Maintaining a communication link during the CubeSat maneuvers is crucial, and the challenge lies in achieving superior gain with compact patch antenna arrays fitted within the constrained space of the CubeSat. Reference [14] introduced a four-element antenna array for CubeSat cross-linking, with each element featuring two $14 \times 14 \text{ mm}^2$ transparent patch antennas mounted on a 1U CubeSat's sides. To ensure circular polarization, each patch is cropped. The authors simulated four arrays of patch antennas by applying a T-junction PD to feed them with sequential phase rotation. Every component has dimensions of $83 \text{ mm} \times 69 \text{ mm} \times 1 \text{ mm}$. A simulated S_{11} of -17 dB (with solar cells) and a 10.20% bandwidth, ranging from 4.78 to 5.3 GHz, are achieved. In contrast, without solar cells, an S_{11} of -21.5 dB at 5.1 GHz, with a bandwidth of 8.43%, was obtained [14].

In Ref. [15], a high-performance four-element patch antenna array tailored for a 3U CubeSat was suggested. This antenna is planned for attachment to one side ($100 \times 100 \text{ mm}^2$) of a 3U CubeSat, and it is specifically designed for Earth observation purposes. The primary goal is to enhance the gain of the antenna and attain circular polarization (CP) by positioning each adjacent pair of patches at a 90° angle and powering them through a Wilkinson power divider. This setup enhanced the signal strength and improved the isolation among ports, leading to optimal input impedance matching. It achieved a simulated gain, S_{11} , and BW of 8.22 dBi, -45 dB at 2.45 GHz, and 2.05 to 3.15 GHz, respectively.

In Ref. [16], researchers developed an antenna for 3U CubeSat communication. The main design featured a transparent quartz substrate with square mesh lines arranged on a square ground plane. A significant challenge in this design was addressing the non-linear correlation between the copper meshed lines due to diminished radiation efficiency and gain. It achieved a transparency of 90%, a BW of 1.65%, an efficiency of 85.9%, an S_{11} of -14.5 dB , and a total gain of 5.3 dBi at 2.43 GHz ($28.44 \times 43.7 \text{ mm}^2$ dimensions). A notable benefit of this design is its high transparency, enabling it to be positioned over solar cells, allowing sunlight to pass through. This approach effectively halves the required area, since the antenna and solar panels occupy the same space. However, the transparency of the antenna is poor at lower frequencies (below 2.4 GHz).

Reference [17] introduced a design for a CP, meshed antenna suitable for 1U CubeSats. The antenna has compact dimensions of $24.1 \times 24.8 \text{ mm}^2$ and operates at 2.45 GHz. Both the bandwidth and overall gain were enhanced when it was seamlessly integrated with a solar cell. CP was achieved by orthogonally exciting the antenna through two terminals, with the feed network positioned below the solar cell. This configuration improves the performance while maintaining a high transparency, as the meshed lines are placed on glass, allowing sunlight to pass through to the solar cells. This integration is significant for maximizing the space for solar cells, thereby increasing the satellite's power budget for its subsystems.

Both simulated and measured reflection coefficients were reported, with values of -18 dB (1.35% bandwidth) and -19 dB (2.45% bandwidth) at 2.385 GHz, respectively.

In Ref. [18], a patch antenna array designed for intersatellite communication on a 1U CubeSat was introduced. The configuration consisted of a 3×3 array comprising nine identical subarrays, with each subarray made up of 2×2 rectangular patch elements connected sequentially. CP was achieved by orienting every two elements within the 2×2 subarrays orthogonally. Operating at 5.8 GHz, the antenna array demonstrated a measured reflection coefficient of -21 dB and a simulated total gain of 6.98 dBi, though it featured a narrow bandwidth of 1.20%. A key advantage of this design was beam steered by modifying the feeding angles. This enhances communication between CubeSats and ground stations, particularly during maneuvers, adjusting the consistency and adaptability of the communication system. A high-gain F-shaped patch antenna was developed for a 3U CubeSat, designed to operate at 2.45 GHz (S-band). The antenna had dimensions of 100×100 mm². This innovative approach minimized the physical size by effectively extending the electrical length of the radiating patch. To increase the bandwidth around the two bands, two arms were utilized. The F-shaped patch antenna also obtained a wide BW and boosted the gain when assessed against other types of patches. However, a significant limitation was its lack of durability, as the reliance on shorting pins between the upper patch and ground plane posed potential challenges to its robustness in practical applications (Figure 3) [19].

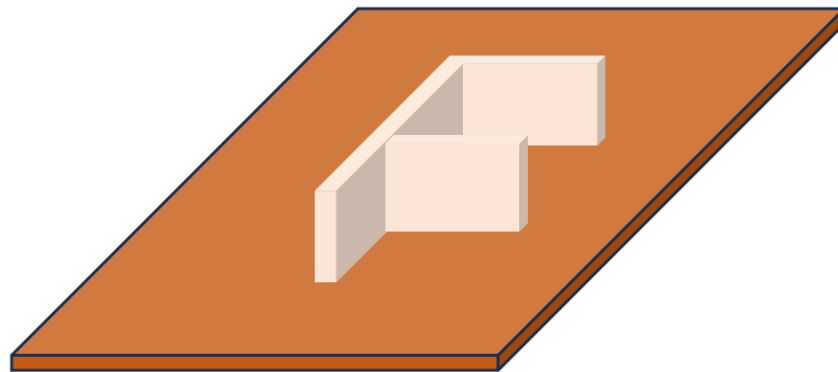


Figure 3. A metal-only wideband patch antenna designed for a CubeSat [19].

In Ref. [20], researchers developed a 16×16 array for CubeSat communications, considering the 6U. It incorporates two layers folded into a compact 2U volume, supported by four deployable formations, and is designed to operate at 3.6 GHz. A key benefit of this design is its ability to minimize the usage of space while folded, leaving extra space for solar panels and other components on the 6U CubeSat. Once in orbit, the patch antenna array expands to improve communication. The results indicate an impressive gain of 30.5 dBi, highlighting the antenna's efficiency in transmitting data. However, the design faces a critical limitation due to its reliance on a complex deployment mechanism. Any failure in deployment could lead to mission failure, emphasizing the need for highly reliable disposition systems.

Reference [21] introduced a CP two-band transmitter for CubeSat communications on three units. Designed for communication with ground stations, the antenna operates in the following two distinct bands: L-band and S-band. The design positions the antenna on one side of the CubeSat, with dimensions of 100×100 mm². The -27 dB and -40 dB S_{11} with BWs of 9.55% and 9.66% were obtained for the lower and upper bands, demonstrating strong performances at both operating frequencies. However, the design has certain drawbacks. The ground plane measures 110×110 mm², exceeding the CubeSat face's

dimensions of $100 \times 100 \text{ mm}^2$. Furthermore, the antenna lacks the ability to beam steer, making it challenging to maintain communication links during CubeSat maneuvers.

In the study conducted in Ref. [22], a broad-spectrum, compact stacked-patch antenna was created for communications with a 3U CubeSat. This antenna operates within the S-band range and measures $100 \times 100 \text{ mm}^2$ in size. A slot-coupled, strip-line feed structure was employed as a key design component. Metallic enclosures surround the uneven strip-line feeding network to enhance the antenna's efficiency. This arrangement is crucial, as it creates a cavity that improves the electric field distribution, strengthening the link between the emitting element and excitation structure through the nearby electromagnetic field. Its gain improved by up to 9 dBi, and the radiation to backward was steered forward. The study reported an extensive 32.6% BW covering the frequency range of 0.8 GHz. This configuration effectively maximizes the CubeSat's available space while ensuring robust satellite communications.

The primary drawback of current works that operate in the S-band frequency range is their relatively larger dimensions, especially when they form an array [23]. To resolve this problem, the authors of Ref. [24] developed a foldable microstrip patch antenna featuring a fractal layout for 1U CubeSats. The novel implementation of a Koch snowflake fractal design enabled the antenna's miniaturization while preserving a high gain, low reflection coefficient, extensive bandwidth, and efficient impedance matching. The authors also suggest a simple method for deploying the fractal antenna. The antenna displayed a low reflection coefficient of -28 dB at 2.3 GHz and offered a wide bandwidth of 28.7%. It attained a moderate gain of 4.39 dBi at the same frequency. The main benefit of this antenna was its compact dimensions, measuring only $60 \text{ mm} \times 26.3 \text{ mm} \times 0.02 \text{ mm}$. However, its key drawback was its omnidirectional radiation pattern, which leads to reduced gain.

In Ref. [25], an array of circularly polarized slot antennas was proposed to facilitate CubeSats communication. The design featured a single-slot array element functioning within the C-band, incorporating four slots and measuring $70.5 \text{ mm} \times 23.5 \text{ mm}$. To enhance the radiation efficiency and minimize losses, an SIW structure was implemented, with four slots strategically placed on the upper copper layer. The primary concept involved mounting two SIW slots on both sides of the CubeSat's walls, allowing for sufficient room to integrate solar panels or additional components. This configuration plays a key role in conserving power while directing the antenna beam effectively, ensuring a stable link despite variations in the CubeSat's orientation. The simulated and experimental results demonstrated gains of 5.08 dBi and 4.98 dBi at 5 GHz, respectively. The fabricated antenna exhibited an S_{11} of -17 dB with a limited 1.99% BW. Additionally, the design supports beam-steering capabilities.

A cavity-backed slot antenna concept tailored to CubeSat communications is presented in Ref. [26], and it operates in the UHF band (485 and 500 MHz). The design features a looped meander-line slot that wraps around and is affixed to four faces of a 1.5U CubeSat situated between the solar panels. Circular polarization (CP) was achieved by feeding each neighboring loop section with a phase shift of 90° , ensuring reliable signal transmission regardless of the CubeSat's orientation. Additionally, the operational frequency can be tuned for uplinks/downlinks by adjusting the meandered segments' lengths. However, a key limitation of this design is its relatively low gain.

In Ref. [27], the authors introduced a dipole antenna set with 3×1 arrays designed for CubeSat communications (1U). The central objective is to enhance the gain, directionality, and BW while eliminating the need to deploy. A major benefit of this design is its capacity to electronically direct the beam, providing adaptable and dependable communication links. The proposed antenna was installed on a GND layer with dimensions of $80 \times 80 \text{ mm}^2$, with each dipole measuring enough spacing between them. The antenna achieved a

5.03 dBi gain, -27.35 dB for S_{11} , and a 4.8% BW. Nevertheless, its primary drawback is its considerable size, occupying substantial areas on the CubeSat— $80\text{ mm} \times 80\text{ mm}$ on each side. Its large dimensions potentially limit the space available for other components.

In Ref. [28], a compact planar dipole antenna with a square form for 1U CubeSats was designed to incorporate four array elements linked through a phase-shifting network. To maintain a balanced power distribution, a balun was positioned beneath each dipole. This configuration produced circular polarization (CP), ensuring a stable communication link even as the CubeSat reoriented in space. It had compact dimensions of $55\text{ mm} \times 55\text{ mm}$ and exhibited bidirectional radiation. It achieved a broad bandwidth of 33.46% and a 3.49 dBi gain. The primary benefit of this design is its small size coupled with a wide bandwidth. Regarding the bandwidth, the antenna in Ref. [28] outperformed the dipole antenna. Nonetheless, a major limitation is the relatively low gain, which might constrain the communication range or performance compared to higher-gain designs.

Another major limitation is the complexity of the deployment mechanisms. Among the designs, the one in Ref. [29] distinguishes itself by having achieved the highest gain of 48.7 dBi in the Ka-band (34.2–34.7 GHz), exceeding the gains of other systems.

The researchers introduced an X-band CP 2×2 annular array of patches developed for a 1U CubeSat. The main innovation involves grounding by short-circuiting it to the GND layer with six pins to accomplish CP. Furthermore, the array elements are energized by a ring resonator positioned at the array's center, which is connected to all four patches via strips. It employs a sequential phase feeding network, yielding a broad BW of 16.97% and a total gain of 13 dBi. However, the researchers only presented simulation results for this design [30].

In Ref. [31], the authors present a transparent dual-band patch antenna array designed for a 3U CubeSat, operating at frequencies of 8 GHz and 11.2 GHz. The innovative aspect of this design is the implementation of a transparent patch on a glass substrate, allowing it to be placed above solar cells. This configuration maximizes the space available for solar cells while enabling sunlight to reach them. The antenna consists of an $8\text{ mm} \times 8\text{ mm}$ top patch layer for the 11.2 GHz frequency, which is fed via two probes from a coupler at the bottom layer. Beneath this, a $6.3\text{ mm} \times 6.3\text{ mm}$ patch serves the 8 GHz frequency and is fed from the top patch layer. A dual-band coupler provides two inputs with a 90° phase shift, facilitating both right-hand circular polarization (RHCP) and left-hand circular polarization (LHCP). However, the proposed antenna has notable limitations, such as exceptionally high reflection coefficients of -19 dB at 8 GHz and -15.5 dB at 11.2 GHz. These values indicate that a significant amount of power is reflected rather than radiated into space, which can impact the overall efficiency of the communication link. To mitigate this, shorting walls and pins can reduce the antenna size without compromising performance aspects like gain, bandwidth, and impedance matching.

Ref. [32] introduced a multifunctional, high-gain, and circularly polarized (CP) transparent subarray patch antenna tailored for CubeSat remote sensing applications. Operating in the X-band, the antenna has a compact size of $10\text{ mm} \times 10\text{ mm}$. The design comprises a 2×2 subarray with two layers and a cross-slot etched into the bottom ground plane. The authors utilize the Fabry–Perot cavity approach and a parallel sequential rotation feeding network technique to achieve CP and enhance antenna performance. The feeding network is an unequal power divider with four output ports with a $50\ \Omega$ impedance, providing a 90° phase delay between ports in an anticlockwise direction. The antenna is constructed using a combination of indium tin oxide (ITO) and copper (Cu)-coating layers on a transparent polyethylene terephthalate (PET-G) substrate, ensuring high transparency and good conductivity. This design allows for the solar panel to be placed between the TMM10i and PET-G substrates, maximizing the space for solar cells on the CubeSat and

facilitating better energy harvesting. The authors report simulated and measured reflection coefficients of -25 dB and -18 dB at 10 GHz, respectively, with a wide -10 dB bandwidth of 40% (covering 8–12 GHz). Additionally, when the solar cell was integrated with the antenna design, it achieved a high measured gain of 15 dB at 10 GHz. This innovative approach enhances the communication capabilities and optimizes the power efficiency for CubeSat missions.

Reference [33] presents a high-gain X-band patch array antenna design for small satellites, including CubeSats, to achieve enhanced aperture efficiency and low sidelobe levels for circular polarization (CP). The proposed antenna measures $100\text{ mm} \times 100\text{ mm}$ and operates within the 7.52 to 8.82 GHz frequency range. It features a 4×4 patch array comprising 16 stacked CP patch elements, contributing to its high aperture efficiency. The authors employed unequal 1–16 series parallel power dividers for the antenna feed to minimize sidelobe levels. Additionally, each of the 16 driven patch elements includes a slot and two truncated corners to facilitate CP radiation. The antenna demonstrated measured reflection coefficients of -15 dB and -12 dB at frequencies of 7.7 GHz and 8.6 GHz, respectively. It also provided a measured -10 dB bandwidth of 15.85%, an impressive gain of approximately 20.03 dBi, a low sidelobe level of -20 dB, and an aperture efficiency of 86.5%.

Reference [34] outlines the creation of a deployable high-gain antenna for the Mars CubeSat. The antenna is an innovative crumpled reflectarray engineered to be tailored within a 6U CubeSat (8.425 GHz). With RHCP, it achieved a 29.2 dBic gain. A significant benefit of the design is its compact stowage, occupying only about 4% of the available spacecraft payload volume and weighing less than 1 kg.

In Ref. [35], an antenna was implemented on a $40 \times 40\text{ mm}^2$ PCB and operated in the X-band. HFSS 2013 software was used for the evaluations. The antenna incorporates circular and rectangular slot structures to enhance the BW and achieve dual resonance. Measured values for an S_{11} of -17.14 dB and -14.29 dB, consistent radiation efficiency of 78.85%, and 4.31 gain dBi were obtained. The impedance BW of the proposed design was recorded at 1.59 GHz.

A miniature pentagonal patch antenna was designed for dual-band operation at 7.6 GHz and 12 GHz, catering to satellite communication, 5G, and high-speed applications. Built on an FR4 substrate with dimensions of $16 \times 16\text{ mm}^2$ and a thickness of 0.8 mm, the antenna also cut the patch with four corner circles and a cross-shaped slot to enhance performance. A partial ground plane improved the BW and gain, achieving 7.13 dBi and 8.07 dBi peak gains at 7.6 GHz and 12 GHz, respectively. Its small size and wide BW make it suitable for C-, X-, and Ku-band applications, including satellite ground stations and remote sensing [36].

Various MPAs aimed at medical, wireless technology, and satellite communication applications. Antennas operating in the S-, C-, and X-bands were developed using FR4 and polyimide substrates. A bow-tie antenna was implemented for the S-band, while compact X-band antennas were analyzed for a fixed satellite service (FSS) within 7.89–10.49 GHz, achieving, again, up to 35 dB. Another design at 6 GHz was categorized in the C-band, while an X-band antenna utilized an SSR background for simulation. Fabrication used chemical etching, and the results were compared in terms of impedance, S_{11} , gain, and directivity. Additionally, the proposed antenna was evaluated as an array element to enhance the gain during transmission and reception [37].

A compact inverted S-shaped patch antenna was designed for three-band operation in the X-band. A fabricated prototype confirmed the design's performance, with measured BWs of 5.02%, 9.13%, and 3.79% for all bands. Elliptical slots in the ground plane enhanced the gain. The antenna showed strong agreement between simulations and measurements.

Its stable gain, omnidirectional radiation, and efficient performance made it suitable for X-band applications [38].

One project focused on designing and implementing a 2×2 antenna array for X-band radar applications. The compact design operates between 7.5 and 9.8 GHz, achieving a 12.5 dB peak gain with a directional radiation pattern. Stacked patches with an air gap enhance the impedance and bandwidth performance. FR4 and other substrates were initially used for their availability and affordability. Simulations and analyses were conducted using HFSS software [39].

A compact dual-frequency microstrip antenna was designed for S- and X-band operations. Utilizing a 1:3.3 frequency ratio saved space by using the S-band antenna as the ground plane for a 2×2 X-band array. Electromagnetic coupling enabled measured bandwidths of 13% at the S-band and 6.2% at the X-band ($|S_{11}| < -10$ dB), with the isolation exceeding 38 dB. The antenna achieved gains of 7.5 dBi at the S-band and 10.5 dBi at the X-band (Figure 4) [40].

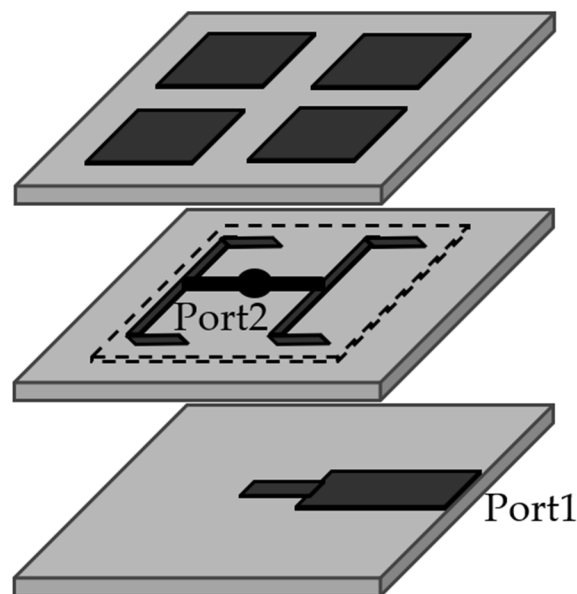


Figure 4. S-band antenna serving as the ground for an X-band array in a dual-frequency S-/X-band design [40].

A multi-band, crescent-shaped patch antenna was designed using five nested annular rings. Three rings were merged on the upper section, while two were positioned along the feed line. The key parameters were analyzed, including bandwidth, radiation pattern, gain, impedance, and return loss. The compact design achieved return losses of -33 dB at 3.1 GHz and 9.3 GHz. Simulated using ANSYS HFSS, the results showed strong agreement with the measurements. The X-band and WLAN bands offered 500 MHz and 4300 MHz bandwidths, making the antenna suitable for various applications (Figure 5) [41].

A rectangular, slot-loaded microstrip antenna with DGS was designed for multi-band operations, achieving high gain across the C-, X-, and Ku-bands. Simulated using HFSS 13.0, the antenna supports frequencies at 6.035 GHz (GNSS), 6.795 GHz (satellite TV), 7.46 GHz (long-distance communication), 8.505 GHz (radar), 11.45 GHz (space communication), 13.35 GHz (detector), 15.06 GHz (military), 17.24 GHz (aerospace), and 19.05 GHz (astronomical observation). Multi-band functionality was enabled by U-slot and rectangular slot cuttings, with no ground or patch modifications required for quad-band resonance. Additional slot adjustments extend operation to nine bands. The optimized slot dimensions enhance the gain, which reached up to 14.679 dB at higher frequencies [42].

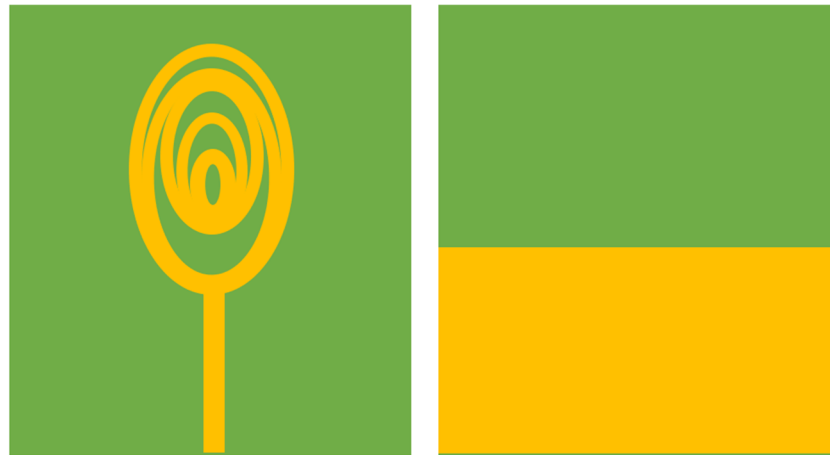


Figure 5. Design and fabrication of a crescent-shaped microstrip patch antenna with an annular ring structure for X-band applications and compact integration [41].

3.2. Dielectric Lenses, Reflectors, and Beam Control

A one-meter mesh reflector was devised to be compatible with 12U CubeSat telecommunications. This reflector is designed to work with NASA's DSN in the X-band and Ka-band frequencies. The following three categories of RHCP antennas are presented: only-X-band, only-Ka-band, and both X- and Ka-band operations [43].

Reference [44] proposed a compact, high-gain antenna designed for CubeSat applications. The use of a cavity-backed reflector enhances the gain. It ensures a directional radiation pattern, which is crucial for establishing efficient communication links, while the CPW-fed design simplifies integration with CubeSat circuitry and minimizes the system weight. Additionally, its low-profile and compact form factor aligns well with the space constraints of CubeSats. However, the design has several limitations for modern CubeSat communications. It lacks dynamic beam-steering capabilities, which are essential for handling frequent repositioning and enabling multi-ground-station or intersatellite links. The antenna is likely optimized for a single frequency band, limiting its support for the multi-band or wideband communications required in diverse CubeSat missions. Furthermore, the inclusion of a cavity-backed reflector, while effective for enhancing gain, poses scalability challenges for advanced systems like phased arrays or MIMO systems, which are becoming increasingly relevant. Finally, the antenna's fixed radiation parameters reduce its adaptability to dynamic and rapidly changing communication demands in low Earth orbit (LEO).

Parabolic antennas, recognized for their substantial dimensions, can deliver high gains surpassing 30 dBi across frequency ranges of 0.3–300 GHz [45]. They have recently attracted considerable interest for CubeSat missions in elevated orbits and deep space due to their ability to support long-range communications with enhanced gains. However, the primary obstacle is their bulky size, making their accommodation within a CubeSat's restricted space more challenging. Several reflector-based antenna configurations are recommended for CubeSat applications, offering high gains spanning 28–48.7 dBi, functioning across X-band and W-band frequencies. Despite these benefits, the considerable physical size of these antennas remains a significant drawback, consuming a large portion of a CubeSat's available surface area.

In Ref. [46], the challenges of limited storage volume and deployment complexity associated with reflector antennas are addressed by suggesting a CP, elevated gain feed horn antenna for CubeSat applications and operating in the W-band. The key innovation proposed is the use of a horn antenna to illuminate a reflector with an offset parabolic shape, integrating a polarizer with circular cavities that generate LHCP while shortening

the overall length compared to conventional polarizers. The resulting reflector antenna, with a diameter of 100 mm, was designed to fit within a 1U CubeSat. Together, both the horn and reflector antennas occupied the entire 1U CubeSat volume. The feed horn and parabolic reflector antennas were integrated within a 6U CubeSat model. The system achieved a 9.88% BW, demonstrating an LHCP gain of approximately 8.8 and 9.2 dBic. At the same time, the antenna with a reflector in an offset parabolic shape delivered exceptional right-hand circular polarization gains of around 33.77 and 34.36 dBic at 86 GHz and 83 GHz, respectively.

An ultra-compact, X-band deployable wrap-rib antenna was designed for space applications, particularly small satellites. The antenna employs a wrap-rib deployment mechanism, which allows it to remain compact during launch and expand in orbit, ensuring a balance between high gain, compact stowage, and structural stability. The design includes a parabolic reflector with a deployable rib structure, offering efficient X-band communication with improved directivity. The findings demonstrated successful deployment, stable radiation patterns, and enhanced gain, making it viable for deep-space and Earth observation missions. However, the reliance on mechanical deployment introduces potential failure points, increasing the risk of malfunction due to mechanical wear, space debris impact, or deployment errors. Additionally, the mechanically steered reflectors lack real-time electronic beam control, making them less suitable for dynamic CubeSat communication, which requires agile and adaptive beam-steering capabilities [47].

Reference [48] outlines a $1.5 \times 1.5 \text{ m}^2$ reflect array antenna that is designed to be stored within a cylinder with a 20 and 9 cm diameter and height, respectively. After deployment, the antenna offers a gain of 39.6 dB, and the reflect array's mass is 1.75 kg. The reflect array, composed of multiple crossed dipoles positioned 5 mm above a ground layer, is supported by thin composite face sheets, with collapsible "S"-shaped springs maintaining the spacing between the dipole layer and the ground plane. The structure, divided into concentric quartz-epoxy composite strips, is interconnected with sliding folds, allowing the strips to be compressed, star-folded, and wrapped, which enables the entire assembly to fit within a compact cylindrical volume. After the construction and testing of a full-scale prototype, it successfully demonstrated stowage within the specified volume while meeting all RF performance criteria, as verified by both pre- and post-deployment RF tests.

The authors of Ref. [49] introduced two innovative high-gain deployable reflect-array antennas for CubeSats. The first ISARA design was developed for 26 GHz and planned for employment in a 3U CubeSat. This antenna consists of three reflect-array panels measuring $33.9 \text{ cm} \times 8.26 \text{ cm}$. The second design features an antenna with a reflect array, crafted explicitly for station communication on the ground, and a 6U CubeSat (8.425 GHz). This antenna features three reflect arrays of $33.3 \text{ cm} \times 19.9 \text{ cm}$. The ISARA and MarCO antennas offer high gain (33 dBi) with very low stowed volumes, making them suitable for LEO and deep space use (0.38% BW at 8.425 GHz). The antennas are deployed once the CubeSat reaches orbit. The antenna that operates in the X-band provides a 28 dBi gain and a 1.19% BW. These designs deliver high-gain communication capabilities while maintaining compact form factors for space missions.

Reference [50], which was presented at the 2018 International Symposium on Space Terahertz Technology, discusses the design of a dielectrically embedded mesh lens intended for deployment on a 6U CubeSat. The primary objective is to observe the 556 GHz water emission line, a spectral feature inaccessible from ground-based observations due to atmospheric absorption. The proposed lens design aims to provide a significant effective collecting area at this frequency, enabling the CubeSat to detect and study water emissions in space. This approach offers a cost-effective solution for space-based water detection, leveraging the CubeSat platforms' compact and versatile nature.

In Ref. [51], a dielectrically embedded mesh lens composed of stacked printed circuit board (PCB) material layers with embedded copper elements was designed. The mesh lens consists of layers of dielectric material containing sub-wavelength-dimension metal elements arranged in a grid pattern, resulting in a flat and lightweight structure. This configuration is particularly advantageous for CubeSats with stringent size, weight, and power (SWaP) constraints. The design aims to provide a cost-effective solution for high-frequency applications, such as water detection in space missions, by leveraging the compact and efficient nature of the mesh lens. The study demonstrates the feasibility of this approach, offering a promising avenue for future CubeSat antenna designs.

Reference [52] introduces a novel antenna design intended for CubeSat applications. This design features a dielectrically embedded mesh lens composed of stacked printed circuit board (PCB) material layers with embedded copper elements. The mesh lens consists of layers of dielectric material containing sub-wavelength-dimension metal elements arranged in a grid pattern, resulting in a flat and lightweight structure. This configuration is particularly advantageous for CubeSats with stringent size, weight, and power (SWaP) constraints. The design aims to provide a cost-effective solution for high-frequency applications, such as water detection in space missions, by leveraging the compact and efficient nature of the mesh lens. The study demonstrates the feasibility of this approach, offering a promising avenue for future CubeSat antenna designs.

Reference [53], presented at the 31st Symposium on Space Terahertz Technology in 2020, discusses designing and testing a metamaterial flat lens operating at 20 GHz. This lens is intended as a low-frequency prototype to validate design procedures for higher-frequency applications, such as those operating at 600 GHz or above 1 THz. The lens is designed to transform a plane wave into the phase of a converging Gaussian beam, with a focal length of 1.5 cm and a diameter of 2.5 cm. The lens is fabricated using 11 RO3003 circuit board laminate layers with etched sub-wavelength-sized copper patterning. The study includes measurements and simulations to evaluate the lens's performance, aiming to achieve less than half a dB of loss, significantly better than that of a Fresnel zone plate lens. The successful design and testing of this prototype are expected to facilitate the development of metamaterial lenses for higher-frequency applications in space-based missions.

3.3. Leaky-Wave Antenna (LWA) Technology

In Ref. [54], a CP microstrip antenna was developed for S-band applications, focusing on ground and intersatellite communication. The antenna measured $80 \times 180 \text{ mm}^2$ in size. The design used a closed-loop traveling wave as the radiating element to achieve an optimal performance for either LHCP or RHCP. A two-terminal hybrid coupler was employed in the feeding mechanism, enabling control over the phase difference between the feeds. The desired polarization was obtained by feeding the antenna through ports 1 and 2 with equal magnitudes but distinct phase differences. Specifically, a quadrature phase difference of -90° produced RHCP, while a $+90^\circ$ phase difference resulted in LHCP. The simulated reflection coefficient was reported as -27 dB at 2.43 GHz, with a bandwidth of 16.05%. The measurements showed a reflection coefficient of -23.5 dB at 2.52 GHz and a bandwidth of 11.11%. The simulated gain at 2.45 GHz reached 7 dBi, while the measured gain was 5.2 dBi. This antenna design demonstrated adaptability and efficiency for CubeSat communications, effectively balancing compact dimensions with high performance.

A higher-order mode suppression technique for single- and dual-frequency microstrip antennas was proposed. The method integrates a microstrip filter within the antenna, simplifying the transmitter/receiver chain by eliminating the need for a separate filter. This technique leads to a higher-order mode suppression of 8 dB using a low-pass microstrip filter without affecting the resonance frequency and the antenna gain. A dual-frequency

antenna for the S- and X-bands was designed using this technique to obtain a bandwidth of 7% and a gain of 8 dBi for the S-band and a bandwidth of 10.5% and a gain of 11.5 dBi for the X-band. This antenna can be used for satellite applications [55].

Reference [56] presents the design of a miniaturized planar Yagi-Uda antenna tailored for integration with PicoSats and other small satellite missions. To address the space constraints inherent in small satellite platforms, the authors employed miniaturization techniques such as meandering and one-dimensional artificial dielectric concepts, effectively reducing the guided wavelength and enabling the antenna to fit within the limited footprint of small satellites. The antenna operates effectively within the frequency range of 3.46 GHz to 3.54 GHz, aligning with communication standards for small satellite missions. Both the simulation and experimental results demonstrate the antenna's high gain and performance, indicating its potential for enhancing data transmission capabilities in CubeSat missions. The study underscores the importance of integrating efficient, low-profile antenna systems to meet the growing demand for high-speed communications with small satellite platforms.

Reference [57] introduces a compact substrate-integrated waveguide (SIW) antenna designed for CubeSat applications. This antenna utilized middle-point feeding and shorting walls to achieve broadside radiation at two distinct frequencies, effectively transitioning from a dominant leaky wave at lower frequencies to a more uniform radiation pattern at higher frequencies. The dual-frequency operation enhances communication flexibility, allowing CubeSats to operate across multiple frequency bands. The antenna's compact structure is achieved through shorting walls and middle-point feeding, which reduces the overall size without compromising performance. This design is particularly advantageous for CubeSats with stringent size, weight, and power (SWaP) constraints. The antenna's broadside radiation pattern ensures efficient signal transmission and reception, crucial for maintaining reliable communication links in space. The study demonstrated that the proposed antenna meets the specific requirements of CubeSat missions, offering a viable solution for enhancing communication capabilities in small satellite platforms.

Reference [58] introduces a novel planar leaky-wave antenna (LWA) designed to enhance CubeSat communication capabilities. Using substrate-integrated waveguide (SIW) technology, the antenna features periodic fan-shaped slots etched on the SIW's surface, facilitating high-efficiency circular polarization (CP) radiation. This design is particularly advantageous for CubeSat applications, as it offers a compact and lightweight solution that meets the stringent size, weight, and power (SWaP) constraints typical of small satellite platforms. The antenna's high gain and broadside radiation pattern ensures reliable and efficient communication links, which are crucial for maintaining consistent data transmission during space missions. The study demonstrated that the proposed antenna design effectively addresses the communication challenges faced by CubeSats, providing a viable solution for future small satellite missions.

Reference [59], which was presented at the 2024 17th United Conference on Millimetre Waves and Terahertz Technologies (UCMMT), introduces an innovative antenna system designed to enhance communication capabilities for 3U CubeSats. This system integrated a planar leaky-wave antenna (LWA) with a reflectarray, aiming to achieve high gain and directivity within the compact constraints of CubeSat platforms. The LWA, based on substrate-integrated waveguide (SIW) technology, radiated in single-linear polarization and served as the feed for the reflectarray. A full-wave simulation was conducted to analyze the near-field radiation from the SIW LWA on a surface corresponding to the reflectarray, which was sized to fit within the 3U CubeSat's dimensions. This design approach optimizes the antenna's performance, ensuring efficient communication links for CubeSat missions.

Reference [60] presents the development of a high-gain, broadband, and circularly polarized Fabry–Perot cavity (FPC) antenna designed to enhance data transmission

capabilities for CubeSat and small satellite missions. The proposed antenna utilizes a spatially separated superstrate area excitation method to achieve broadband operations, which is crucial for accommodating the diverse communication requirements of CubeSats. The design aims to provide a compact and efficient solution that meets the stringent size, weight, and power (SWaP) constraints typical of small satellite platforms. The study includes detailed simulations and experimental validations to demonstrate the antenna's performance, highlighting its potential to support high-data-rate communication links in CubeSat applications. This advancement is significant for the small satellite community, as it addresses the growing demand for efficient and reliable communication systems in space missions.

Reference [61] introduces a cost-effective dual-polarized leaky-wave antenna (LWA) fabricated using 3D printing technology, offering broad beam-scanning capabilities and dual-polarized operations. While the design benefits from low-cost manufacturing and relatively high radiation efficiency, its reliance on frequency-dependent beam steering limits its suitability for CubeSat communications, for which a stable and predictable link performance is essential. Additionally, LWAs suffer from gain degradation and beam distortion at large steering angles, which can negatively impact a signal's integrity in dynamic satellite environments. Using 3D printed materials raises concerns about mechanical stability and long-term reliability in space conditions. In contrast, electronically controlled phased arrays or metasurface-based antennas provide more adaptive beamforming capabilities, making them better suited for CubeSat applications requiring precise and reliable communication links.

3.4. Hybrid Beamforming Techniques

In Ref. [62], the hybrid beamforming combines analog and digital processing to mitigate the high cost and power consumption associated with fully digital beamforming, which requires a dedicated radio-frequency (RF) chain for each antenna element. This technique leverages analog beamforming to manage a large number of antennas with fewer RF chains. In contrast, digital beamforming provides fine-tuned signal processing control, thereby balancing performance and hardware complexity. The proposed method in the paper addresses challenges such as hardware impairments and inter-user interference by optimizing the hybrid beamforming architecture, resulting in improved spectral efficiency and reduced computational complexity. However, the limitations include potential performance degradation due to analog hardware constraints and the need for precise calibration to maintain beamforming accuracy. In the context of CubeSat communications, hybrid beamforming offers significant advantages. CubeSats are constrained by size, weight, and power (SWaP) limitations, making deploying extensive RF chains impractical. By employing hybrid beamforming, CubeSats can utilize large antenna arrays to achieve the high-gain directional beams necessary for long-distance space communications while keeping the number of RF chains minimal to conserve power and space. This approach enhances data transmission rates and link reliability without imposing substantial hardware burdens, making it a viable solution for advanced CubeSat communication systems.

In Ref. [63], the authors suggest a two-band single monopole antenna to minimize the number of antennas needed for CubeSat communications. This antenna functions at VHF and UHF, simultaneously enabling data transmission and reception. The main idea is the use of a diplexer to manage uplink and downlink communications through a single antenna. The design incorporates a strip that attaches the antenna to the CubeSat's surface. The proposed deployable monopole antenna has several significant drawbacks. The primary issue is the potential for mechanical failure in the deployment system, which can lead to a loss of communication with the ground station and possibly result in mission

failure. Additionally, the relatively low gains of 2.06 dBi (uplink) and 3.35 dBi (downlink) restricts the antenna to short-range communications and lower data rates, which might not meet the requirements of specific CubeSat missions.

In Ref. [64], retractable dipole and monopole antennas work at dual frequencies within the VHF and UHF bands, optimizing transmission and reception while reducing the number of required antennas. By utilizing a single dual-frequency antenna instead of separate ones, the design effectively conserves space on a CubeSat, making it more efficient. The antennas are integrated with an LC circuit, leveraging the CubeSat's outer structure as a ground plane, particularly for the monopole configuration. When fully deployed, the dipole antenna spans 980 mm in length and exhibits 2.59 and 3.91 dBi directional gains. Additionally, it measures 313.5 mm in total length and demonstrates an exceptionally low reflection coefficient. The monopole antenna provides a superior gain, lower reflection coefficient, and more compact form factor than its dipole counterpart.

One paper aimed to design a practical shape for a microstrip patch antenna for the X-band (8 to 12 GHz) and Ku-band (12 GHz to 18 GHz). An artificial neural network was used to optimize the microstrip antenna's dimensions. The network inputs the different microstrip antenna parameters and delivers their dimensions in X-/Ku-band satellite communications. An error and validity analysis of the neural network results was conducted in MATLAB 2015. Finally, HFSS simulation software was used for the prototype of the microstrip antenna, which had the best antenna parameters compared with the actual value [65].

3.5. Metasurfaces and Advanced Materials

This section discusses metasurface antennas and advanced materials like metamaterials. Metasurface antennas utilize engineered subwavelength structures to manipulate electromagnetic waves, enabling beamforming, beam steering, and polarization control without traditional phase shifters or mechanical movement. These antennas offer high gain, low profile, and reconfigurable radiation patterns, making them attractive for advanced wireless and satellite communications. By adjusting the metasurface elements, they can dynamically steer beams, enhance directivity, or generate multiple beams efficiently. However, challenges such as lossy materials, fabrication complexity, and limited bandwidth must be addressed. Their potential in CubeSat communications lies in their ability to provide compact, low-power, and adaptive solutions, improving link reliability in space environments.

Reference [66] presents a semi-transparent meshed patch antenna with CP, which is designed for S-band CubeSat use at 2.25 GHz. A new method was introduced by integrating solar cells with an antenna, where these cells and glass served as the primary substrate materials. The authors integrated metamaterials featuring an RIS as a GND layer to improve the BW and performance. An 11.11% BW and an overall 3D gain of 4.87 dBi were obtained. The antenna in Ref. [66] demonstrated a broader -10 dB bandwidth. Nonetheless, it exhibited a decrease in gain compared to the other antennas discussed in the referenced studies.

Slot antennas generally comprise flat metal surfaces (plates) featuring cuts and operate within the 0.3–25 GHz range. Few slot antenna designs have been explicitly developed for CubeSats, mainly due to their provision of LP and little directivity, which lead to an insufficient signal and diminished gain. Several methods and strategies are suggested and applied to address these shortcomings. Among the slot antenna designs, the one in Ref. [67] is notable for its 9.71 dBi gain and 30.2% BW. Nevertheless, its major disadvantage is its larger size. Brief summaries of these works are presented in Tables 1 and 2.

Table 1. Proposed patch antennas designed for the CubeSat.

Ref.	Size (cm ²)	f _r (GHz)	BW (%)	Gain (dBi)	CubeSat Type	Deployable	Polarization	Application
[1]	N/A	7.4	16.21	7.2	1U	No	CP	Ground Communication
[2]	1.41 × 1.17	5.1	10.2	5.9	1U	No	CP	Intersatellite Communication
[9]	0.78 × 0.78	2.45	44.9	8.22	3U	No	CP	Earth Observation
[10]	0.23 × 0.35	2.43	1.65	5.3	1U, 2U, 3U	no	N/A	Ground Communication
[11]	0.19 × 0.20	2.45	2.45	4.8	1U	No	CP	Ground/Intersatellite Communication
[12]	1.93 × 1.93	5.8	1.2	6.98	1U	No	CP	Intersatellite Communication
[13]	2.13 × 2.13	8, 11.2	2.39, 3.22	6.45, 5.34	3U	No	Dual, CP	Educational Ground Communication
[14]	0.89 × 0.69	5.03 (C-band)	1.99	4.98	1U	No	LHCP	Intersatellite Communication
[15]	0.96 × 0.4	0.485/0.5 (UHF)	N/A	4	1.5U	No	CP	TT&C
[17]	0.76 × 0.127	2.45 (S-band)	4.45	8.62	2U	No	CP	Ground Communication
[18]	0.4 × 0.4	2.45 (S-band)	2.05	5.8	1U	No	CP	Ground/Intersatellite Communication
[43]	0.67 × 1.51	2.52	11.11	5.2	3U	No	CP	Ground/Intersatellite Communication

Table 2. Utilized planar antennas for CubeSat communication operations in the X-band.

References	Gain (dBi)	Efficiency (%)	CubeSat Unit	Polarization	Dimensions (mm × mm ²)	Feeding Tech	f _r (GHz)	Mass (kg)
[30]	<13	N/A	1	CP	N/A	coaxial probe	8.27	N/A
[31]	<7	N/A	3 × 1	CP	100 × 100	coaxial probe	8, 11.5	N/A
[32]	15	65	1	CP	<300	Fabry–Perot cavity	10	N/A
[33]	20	97.5	1	CP (RHCP)	100 × 100	unequal series parallel power dividers	8.2	N/A
[34]	29.2	45	6	CP (RHCP)	100 × 200 × 340	offset fed reflect array	8.425	<1
[35]	4.31	<78.8	N/A	N/A	40 × 40	coaxial probe	8–12	N/A
[36]	8.07	N/A	N/A	N/A	16 × 16	coaxial probe	7.6, 12	N/A
[37]	35	N/A	N/A	N/A	N/A	coaxial probe	7.89–10.49	N/A
[38]	<5.5	90.90	N/A	N/A	20 × 17.2	coaxial probe	9, 11	N/A
[39]	12.5	N/A	N/A	N/A	70 × 70	patch rod	8	N/A
[40]	10.5	N/A	N/A	N/A	95 × 95	coaxial probe	8.15	N/A
[41]	6.1	>80	N/A	N/A	35 × 33	coaxial probe	9.3	N/A
[42]	<10	>80	N/A	LP	27 × 22	coaxial probe	8.5, 10	N/A
[48]	39	N/A	3 × 2	N/A	1500 × 1500	diagonal cord feed	8.4	1.75
[55]	<11.5	N/A	N/A	N/A	49.6 × 53	PBG	2.5, 8	N/A

4. Antennas for Beam Steering and Beamforming

Beam steering and beamforming are related concepts in antenna systems, but their meanings and applications differ slightly. Beamforming is a signal-processing technique used to shape the radiation pattern of an antenna array to focus energy in a desired direction while minimizing interference in other directions. It involves adjusting the amplitude and phase of signals fed to or received from individual elements of an antenna array to create constructive interference in the desired direction and destructive interference elsewhere. Beamforming enhances signal strength and quality in a specific direction,

improving the communication range and reducing interference. On the other hand, beam steering is the ability to dynamically change the direction of the main lobe (i.e., focus) of an antenna's radiation pattern without physically moving the antenna. It involves electronically controlling the phase of signals in an antenna array to steer the beam in the desired direction. Beam steering allows for the flexible coverage of a specific area or tracking of a moving target, such as a satellite or mobile device, without mechanical movement (Figure 6).

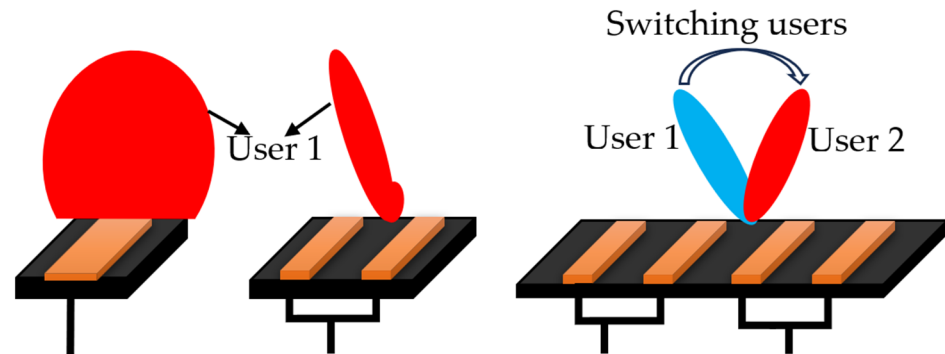


Figure 6. Beam steering with different feeds.

The feasibility of dynamic beam-steering in Low Earth Orbit (LEO) satellite communications is heavily impacted by power limitations. Directing communication beams toward ground targets demands precise antenna array control, which requires considerable power for signal transmission and steering operations. This challenge is particularly pronounced in small satellites like CubeSats, which have minimal energy resources due to their size. Consequently, the power used for beam-steering must be shared with other vital tasks, such as managing onboard systems and regulating thermal conditions. To tackle these constraints, researchers have introduced energy-efficient strategies that optimize beam handovers and switching within multi-LEO satellite networks, aiming to maximize power efficiency without compromising communication reliability [68].

Moreover, studies on beam scheduling and beamforming design under individual feed power limitations emphasize the difficulties in distributing power effectively across multiple beams. The goal is to optimize data rates while ensuring the overall power consumption remains within the designated limits [69]. In addition, beam-hopping techniques have been investigated as a solution to manage uneven traffic demands. These methods enable flexible adjustments in both time and power domains, ensuring that diverse communication needs are effectively met [70]. These methods highlight the importance of adequate power management to sustain dynamic beam-steering in LEO satellite systems with limited power resources. Additionally, artificial intelligence (AI) offers transformative potential by enabling real-time adaptability and optimizing antenna arrays. AI-driven solutions can enhance power allocation, minimize latency, and boost beamforming precision, ensuring optimal utilization of CubeSat energy reserves [71].

4.1. Beam-Steering/Beamforming Techniques and Their Possible Features for CubeSat Communications

By adjusting the phase and amplitude of signals at each antenna element in an array, beamforming enables enhanced signal strength, reduced interference, and better spectral efficiency. It is critical in modern communication systems like 5G networks, satellite communications, and radar systems. Beamforming can be categorized into analog beamforming (ABF), digital beamforming (DBF), and hybrid beamforming (HBF), each with distinct methodologies, advantages, and limitations.

In ABE, the signal phase and amplitude are controlled directly at the radio-frequency (RF) stage using analog devices such as phase shifters and attenuators. This technique generates a single beam by combining signals from all antennas before converting them to a baseband. It has several advantages, such as low complexity (simpler hardware implementation compared to digital systems, making it more cost-effective), power efficiency (consumes less power as it requires a single RF chain), and suitability for narrowband systems (well-suited for systems with limited bandwidth requirements). However, it also has some limitations like limited flexibility (generating only a single beam per array, restricting its capability to support multi-user scenarios), lack of interference mitigation (limited ability to perform complex spatial filtering, leading to a reduced performance in high-interference environments), and susceptibility to non-idealities (analog devices introduce phase errors and amplitude mismatches, impacting beamforming precision). The techniques utilized variable phase shifters for signal steering and employing RF combiners to merge signals from different antenna elements.

DBF operates at the baseband or intermediate frequency (IF) stage. Signals from each antenna element are individually digitized and processed using digital signal processing (DSP) algorithms, allowing for precise control over beam characteristics. Its advantages are high flexibility (it can generate multiple beams simultaneously, supporting multi-user scenarios), interference management (enables advanced signal processing techniques for interference suppression and null steering), and wideband support (capable of handling wideband signals, making it suitable for modern broadband communication systems). However, each antenna element requires a dedicated RF chain, ADC/DAC (analogue to digital/digital to analogue), and DSP unit. It consumes significantly more power due to the extensive hardware and processing requirements and the complex hardware and software integration. Its applied techniques include the application of advanced DSP algorithms, such as adaptive beamforming, minimum variance distortionless response (MVDR), and eigen-beamforming. Digital filters are usually used for beam steering and shaping.

HBF combines the principles of analog and digital beamforming to balance efficiency with hardware complexity. It employs analog beamforming at the RF stage and digital beamforming at the baseband stage. Its advantages are scalability (reduction in the number of required RF chains compared to digital beamforming while maintaining high performance), cost, and power efficiency (balances cost and power consumption by using fewer RF chains), and support for multi-user scenarios (can generate multiple beams with fewer resources than a fully digital system). Nevertheless, its performance is typically inferior to pure digital beamforming due to reduced flexibility in analog signal steering. It requires careful integration of analog and digital components, increasing the system's design complexity, and involve trade-offs in beam placement and resource allocation. The utilized technique is the decomposition of the beam-forming task into analog precoding and digital precoding. Moreover, low-dimensional digital beamformers can be combined with analog phase shifters or switches, and sparse array structures can reduce the complexity while maintaining performance.

Artificial intelligence (AI)-driven beam steering is emerging as a transformative approach in CubeSat communications, offering enhanced adaptability and efficiency in dynamic space environments. Traditional beam-steering methods, such as mechanical adjustments or predefined electronic configurations, often struggle to meet modern CubeSat missions' rapid and complex demands. By integrating AI, particularly machine learning algorithms, CubeSats can achieve real-time adaptive beamforming, optimizing signal directionality and strength in response to changing conditions. For instance, supervised learning algorithms have been proposed for real-time adaptive beamforming on multibeam satellites, enabling precise beam projection and dynamic adjustments to beamwidth and

sidelobe levels, thereby enhancing communication performance. The application of AI to beam steering also addresses the limitations of traditional mechanical systems, which can be bulky and slow to respond. AI algorithms can process vast amounts of data from onboard sensors to predict and react to environmental changes, such as satellite movement or signal interference, allowing for swift electronic adjustments without mechanical components. This capability particularly benefits CubeSats, for which size, weight, and power constraints are critical considerations. Research has demonstrated that AI-driven beam steering can effectively manage these constraints while maintaining high communication performance. Moreover, AI-driven beam steering facilitates the implementation of advanced communication techniques, such as multiple-input, multiple-output (MIMO) systems, by efficiently managing the complex signal processing tasks required for these technologies. This integration enhances the data throughput and link reliability, which are essential for the increasing demands of CubeSat applications. Studies have shown that AI algorithms can optimize the performance of MIMO systems in satellite communications, leading to significant improvements in data rates and connection stability. In addition to improving performance, AI-driven beam steering contributes to the resilience of CubeSat communication systems. By continuously learning and adapting to the space environment, AI algorithms can anticipate potential issues, such as signal blockages or degradations, and proactively adjust beam patterns to maintain optimal communication links. This initiative-taking approach reduces the risk of communication disruptions and enhances the overall reliability of CubeSat missions. Research in this area has highlighted the potential of AI to significantly increase the robustness of satellite communication systems through adaptive beam steering [72–74].

When beam steering and beamforming are discussed, signal processing should be considered an inevitable part. Signal-processing techniques are fundamental to CubeSat communications, enabling efficient data transmission within limited power and bandwidth constraints. Digital modulation schemes, such as phase shift keying (PSK) and frequency shift keying (FSK), are commonly employed to optimize the spectral efficiency and resilience to noise. Additionally, error correction codes like Reed–Solomon and convolutional codes enhance the data integrity by mitigating the signal degradation effects during transmission. Integrating software-defined radios (SDRs) allows for flexible implementation of these techniques, facilitating adaptability to various communication protocols and frequency bands. This flexibility is particularly advantageous for CubeSats operating in the crowded VHF and UHF bands, as it enables dynamic spectrum access and efficient utilization of available frequencies [75].

The advent of 5G technology has introduced opportunities to enhance CubeSat communications through advanced signal-processing techniques. One notable advancement is the utilization of millimeter-wave (mm-wave) frequencies, which offer significantly larger bandwidths than traditional frequency bands. Operating in the 30 to 100 GHz range, mmWave communications can support the high data rates essential for high-resolution Earth observation and real-time data relay applications. However, mmWave signals are susceptible to greater free-space path loss and atmospheric attenuation, necessitating sophisticated beamforming and beam-steering techniques to maintain reliable links [76,77].

Beyond 5G, research has explored the terahertz (THz) frequency spectrum (0.3 to 10 THz) to further augment communication capabilities. THz frequencies promise ultra-high data rates due to the vast available bandwidth, making them attractive for future CubeSat missions requiring substantial data throughput. Nevertheless, THz communications face challenges such as severe atmospheric absorption and a limited transmission range, which can be mitigated through advanced signal-processing techniques like adaptive modulation and coding and the development of high-gain directional antennas.

The integration of mmWave and THz technologies into CubeSat communications necessitates advancements in signal processing to address the challenges associated with high-frequency signal propagation. Techniques such as adaptive beamforming, which dynamically adjusts the directionality of the antenna array, can compensate for signal degradation and enhance link reliability. Implementing multiple-input, multiple-output (MIMO) systems can also exploit spatial diversity to improve data rates and link robustness. These approaches require sophisticated algorithms and real-time processing capabilities, underscoring the importance of high-performance onboard processing units in future CubeSat designs [78].

As mentioned before, beam steering and its techniques are slightly different. Beam steering is a pivotal technology in modern communication and radar systems, enabling the dynamic redirection of signal beams without needing mechanical movement. This capability is essential for applications such as 5G networks, satellite communications, and advanced radar systems, for which rapid and precise beam direction is crucial. Recent advancements have introduced innovative methods to enhance beam-steering performance, presenting unique challenges and outcomes. Two of the most common techniques that have been utilized to improve the performance of beamforming/ beam steering are applying metasurface and reconfigurable structures.

Metasurfaces are ultra-thin, two-dimensional structures composed of sub-wavelength-sized elements that can manipulate electromagnetic waves in a controlled manner. By engineering these elements, metasurfaces can modulate the amplitude, phase, and polarization of incident waves, enabling advanced wavefront-shaping capabilities. In beamforming and beam-steering applications, metasurfaces offer a low-profile alternative to traditional bulky components, allowing for precise control over the direction and shape of electromagnetic beams. This precision is achieved by designing specific phase gradients across the metasurface, facilitating the steering of beams without mechanical movement. The advantages of metasurfaces include their compactness, lightweight nature, and the potential for integration into various platforms, making them suitable for applications like wireless communications and optical systems. However, challenges such as fabrication complexity, sensitivity to fabrication errors, and potential limitations in bandwidth and efficiency need to be addressed. Ongoing research aims to overcome these limitations, with developments in tunable and reconfigurable metasurfaces showing promise for dynamic beamforming and beam-steering applications [79].

Metasurface structures have been used to improve beam steering. For instance, Ref. [80] employed a reflective metasurface technique, incorporating metal slots around the radiating patch to enhance the gain. A secondary metasurface antenna was also positioned 10 mm from the primary radiating antenna to further enhance the radiation and directivity. The design utilized a partial ground and line feeding with a conventional coplanar waveguide (CPW) technique to optimize the overall performance. A rectifier circuit was also integrated to convert the harvested electromagnetic energy into direct current (DC) output power. The proposed model achieved a gain of 8.1 dB, a backward radiation reduction to -13.1 dB, and a DC output power of 2.82 V. While the antenna demonstrated effective gain enhancement and beam-steering capabilities for RF energy harvesting, its suitability for dynamic beamforming or beam-steering applications is limited. The design focuses on static beam steering achieved through the fixed configuration of metasurfaces and metal slots. This static approach restricts the antenna's ability to adaptively steer beams in response to changing signal environments or target movements, a key requirement in advanced communication systems. Moreover, integrating multiple metasurface layers and the specific placement of components introduces fabrication complexities. It increases the overall size of the antenna system, potentially limiting its applicability in compact or

dynamically reconfigurable platforms. Therefore, while effective for enhancing the gain in RF energy harvesting, this design is not suitable for applications requiring agile and real-time beamforming or beam-steering capabilities.

Reference [81] introduced a metasurface antenna capable of electronic beam steering without mechanical movement. The design features an array of subwavelength resonators, each integrated with tunable elements, allowing for dynamic control over the phase and amplitude of emitted microwaves. This configuration enables rapid adjustments to the beam direction, enhancing imaging, radar, and wireless communications applications. The antenna's planar structure offers a compact, cost-effective alternative to traditional phased array systems. However, challenges such as the fabrication complexity, power consumption of tunable components, and potential limitations in bandwidth and efficiency affect the performance. Further research is necessary to optimize these aspects for practical deployment.

Reference [82] focuses on the application of Huygens' metasurfaces—ultra-thin structures capable of controlling electromagnetic wavefronts—to achieve precise antenna beamforming and beam steering. By engineering these metasurfaces, the authors demonstrated the ability to manipulate the direction and shape of antenna radiation patterns without relying on traditional bulky feeding networks. This approach offers a low-profile solution for directing electromagnetic beams, which is advantageous in various applications such as wireless communications and radar systems. The study highlights the potential of Huygens' metasurfaces to provide efficient and compact alternatives to conventional beamforming techniques.

Reference [83] introduces a metasurface-driven antenna system designed for three-dimensional beam steering in satellite communications. The system employed a pair of phase gradient metallic metasurfaces (PGMMs) operating in the Ku-band, engineered using a near-electric field phase transformation method. By independently rotating these PGMMs above a fixed-beam base antenna, the design achieves wide-angle beam steering in both the azimuth and elevation planes. The experimental results demonstrated effective beam scanning, with the elevation angles reaching $\pm 38^\circ$ and full 360° coverage in the azimuth plane. This approach offers a low-profile, passive solution for dynamic beam steering, eliminating the need for complex feeding networks or mechanical movement, which are common in traditional systems.

One notable development involved the use of metasurfaces for beam steering. A study published in Ref. [84] demonstrates beam steering by employing two vertically oriented metasurfaces. This method achieves precise control over beam direction by manipulating electromagnetic waves at the metasurface interface. The primary challenge in this approach is the complex fabrication and integration of metasurfaces into existing systems. However, the outcome showed significant potential for high-precision beam steering with minimal signal loss, indicating a promising avenue for future research.

Integrated optical beam-steering devices have been developed using switchable liquid crystal metasurfaces. A study available in Ref. [85] depicts a method employing holography techniques to calculate the required phases, enabling dynamic beam steering in optical systems. The challenges of this approach include the precise control of the liquid crystal properties and the integration into compact optical devices. The outcomes demonstrated ultrafast beam-steering capabilities, which could revolutionize applications in optical communications and beyond (Figure 7).

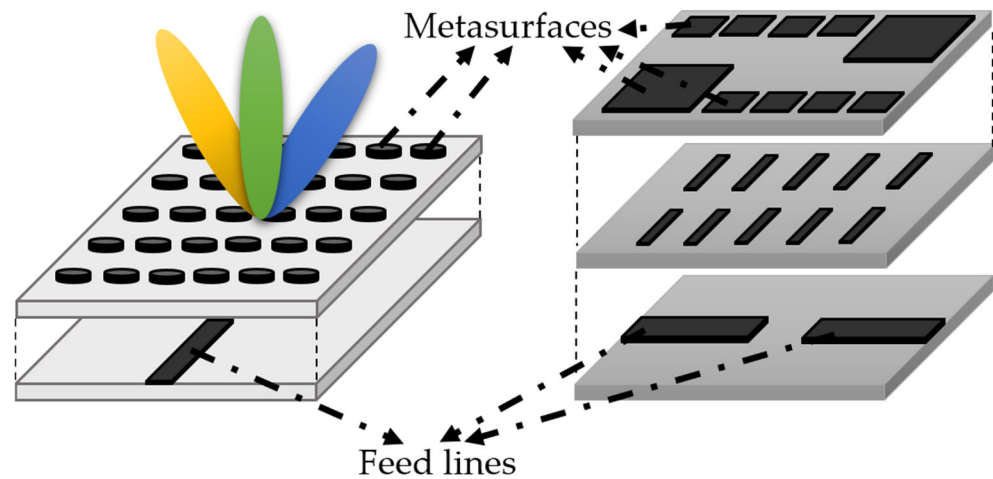


Figure 7. The design of metasurface antennas.

Reference [86] introduced a pattern-reconfigurable antenna that utilizes a metasurface for two-dimensional beam steering. The design integrates a reconfigurable metasurface with the antenna structure, enabling dynamic control over the radiation pattern in both the azimuth and elevation planes. This approach allows for efficient beam steering without the need for mechanical movement, offering potential advantages in applications such as wireless communications and radar systems. However, the available summary did not provide specific details regarding the operational frequency range, steering range, and the methods employed for reconfiguring the metasurface. Further information from the full text is necessary to comprehensively assess this design's performance and potential limitations.

Reference [87] presents a dual-port, dual-beam, and pattern-reconfigurable antenna capable of independent two-dimensional (2D) beam scanning. The antenna features two feeding ports that allow for the independent control of each beam, enhancing flexibility in beam directionality. This design enables dynamic beam switching, making it well-suited for applications requiring adaptive beamforming, such as satellite communications and wireless networks. The proposed antenna achieves efficient 2D beam scanning without requiring mechanical movement, reducing system complexity and improving reliability. However, the design introduces challenges related to the feed network's complexity and potential mutual coupling between the two beams. Additionally, the extent of the beam-scanning coverage and its adaptability in real-time environments require further evaluation. While promising for advanced communication systems, its feasibility for CubeSat integration depends on the size, power consumption, and reconfiguration speed.

Reference [88] proposes a low-cost multibeam switching antenna utilizing a reconfigurable hybrid metasurface for beamforming applications. The design integrates a hybrid metasurface with tunable elements, enabling beam switching without requiring complex phase-shifting networks. This approach enhances beamforming efficiency while maintaining a cost-effective and compact structure, making it suitable for wireless and satellite network applications. The proposed antenna achieves dynamic beam control with minimal power consumption, an advantage for power-constrained platforms like CubeSats. However, its reliance on discrete tuning elements introduces response-time limitations, potentially restricting real-time adaptability in highly dynamic environments. Additionally, practical implementation challenges, such as fabrication complexity and integration with existing satellite communication systems, must be addressed. While promising for adaptive beamforming, its scalability and performance under different operational conditions require further investigation.

Reference [89] proposes a beamforming technique for a linear antenna array using a reconfigurable frequency selective surface (FSS). The antenna comprises a 1×4 linearly polarized array fed by a power divider and a coaxial connector. A reconfigurable FSS superstrate was mounted above the antenna to control the radiation pattern dynamically. This configuration allows for adjustable beamforming, enhancing the antenna's adaptability in various communication scenarios. The reconfigurable FSS enables real-time pattern modification, offering potential benefits in flexible beam-steering applications. However, the complexity of integrating the FSS with the antenna array and the potential of an increased system size present challenges. Additionally, the performance of the reconfigurable FSS in terms of bandwidth and efficiency needs further evaluation to ensure its suitability for practical applications. While promising, the design's effectiveness in dynamic beamforming scenarios, such as those encountered in CubeSat communications, requires further investigation.

Reference [90] proposes a beam-reconfigurable multi-antenna system utilizing beam-combining technology to enhance UAV-to-everything (U2X) communications. The system integrates multiple antennas with phase control techniques to reconfigure radiation patterns, dynamically improving the communication reliability and coverage. The system enhances signal strength by employing beam-combining and mitigating interference, making it suitable for various UAV applications, including surveillance, disaster response, and remote sensing. This approach's key advantage is its adaptability to changing environments, ensuring stable connections despite UAV mobility. However, the implementation faces challenges such as increased system complexity, power consumption, and potential hardware limitations in real-time beam adjustments. While effective for UAV communications, its direct applicability to CubeSat beamforming requires further exploration, as CubeSats operate under stricter power and size constraints. Nonetheless, the study provides valuable insights into beam-reconfigurable designs that can be adapted for space-based communication networks.

Reference [91] introduces a pattern-reconfigurable integrated array antenna leveraging a coding metasurface. This design integrates a coding metasurface with an antenna array to achieve dynamic radiation pattern reconfiguration. By adjusting the coding sequences of the metasurface elements, the antenna can steer beams and modify radiation patterns without mechanical movement. This approach offers a low-profile and efficient solution for applications requiring adaptable beam steering, such as wireless communications and radar systems. However, the reliance on electronic reconfiguration introduces challenges related to control complexity and response time. Additionally, the performance in terms of bandwidth and efficiency under different operational conditions requires further evaluation to ensure its suitability for practical applications. While promising, the design's effectiveness in dynamic beamforming scenarios, such as those encountered in CubeSat communications, also requires further investigation.

Reconfigurable transmit array antennas have also garnered attention for their beam-steering capabilities. A comprehensive review in Ref. [92] highlights the recent developments and challenges associated with these antennas. The study discusses methods involving tunable materials and electronic components to achieve dynamic beam steering. The challenges include the complexity of the design and the potential increases in the system's cost. Despite these hurdles, the outcomes demonstrate enhanced beam-steering performance, making reconfigurable transmit array antennas a viable option for modern communication systems (Figure 8).

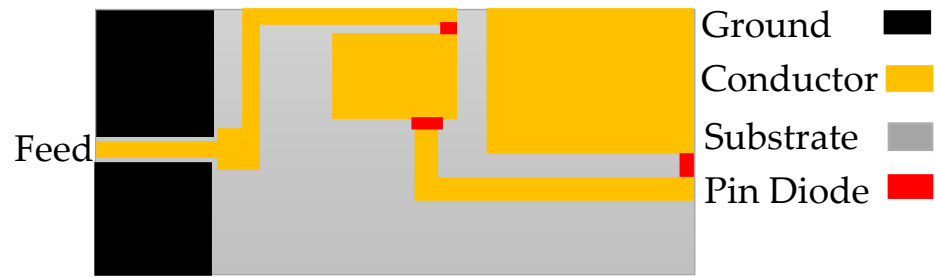


Figure 8. The design of a reconfigurable antenna.

Furthermore, in the realm of wireless applications, reconfigurable electromagnetic surfaces have been explored to enhance beam steering. For instance, the research published in Ref. [93] introduces an innovative approach using reconfigurable electromagnetic surfaces to achieve beam steering in reflectarray structures. The method involves electronically adjusting the surface properties to direct beams dynamically. The challenges with this technique include the need for sophisticated control algorithms and potential signal degradation. Nevertheless, the outcomes indicate improved beam steering flexibility and efficiency, significantly impacting future wireless communication technologies.

Metasurfaces and reconfigurable antennas offer precise beamforming and beam-steering without mechanical movement, making them ideal for modern communication systems. Various designs, including reflective, tunable, and Huygens' metasurfaces, enable wide-angle and adaptive beam control, benefiting CubeSats, UAVs, and optical systems. While these structures improve the compactness and efficiency, challenges like the fabrication complexity and bandwidth limitations remain. Advances in tunable materials and electronic control continue to enhance their adaptability, reinforcing their potential for next-generation wireless and satellite communications. In addition, metasurfaces and reconfigurable structures outperform traditional beam-steering methods like mechanical steering and phased arrays by offering compactness, low power use, and real-time beam control without moving parts. Unlike phased arrays, which require complex phase shifters, metasurfaces use subwavelength elements for precise wavefront control, reducing the system's complexity and cost. Reconfigurable designs further enhance adaptability to changing environments with minimal hardware modifications. These advantages make them ideal for CubeSats, UAVs, and next-generation wireless networks, for which the size, weight, and energy efficiency are crucial.

As a vital part of any communication system, antennas should be fully understood so that all of their requirements and characteristics can be used for CubeSat and satellite communications. The following section illustrates more passive antennas utilized for beam steering in CubeSat communications. A brief of some metasurface and reconfigurable antennas are presented in Table 3.

Table 3. Utilized metasurface and reconfigurable antennas for beam steering and beamforming.

Reference	Gain (dBi)	Efficiency (%)	Dimensions (mm × mm ²)	Technique	f _r (GHz)	Steering Range (°)
[80]	N/A	N/A	N/A	metasurface	12.5	10–23
[81]	<10	<90	120 × 229	SIW, Nyquist metasurface	9, 10	−75–75
[84]	N/A	N/A	<85 mm ²	IRS, metasurface	26.5–27	15–45
[82]	<8	<77	18 mm ²	Huygens' metasurface	10	N/A
[86]	N/A	N/A	N/A	partially reflecting surface	3.3–3.8	−40–40°
[87]	8	>80	80 mm ²	partially reflecting surface	3.6	−30–30°
[88]	7.32	80	58 × 49	hybrid metasurface	9.07–9.42	48°, 312°
[89]	10.7	N/A	131 × 131	reconfigurable FSS	5.5	−48–48°
[90]	5.8	76	<60 mm diameter	single-pole, double-throw	5–5.5	0, 90°

4.2. Passive Antennas for Beam Steering

Beam steering is a critical technology for modern communication systems, enabling high directional gain and interference mitigation by focusing transmitted or received energy in specific directions. Passive antennas, which do not rely on active electronic components such as amplifiers, are increasingly being explored for beam-steering applications in small satellite platforms, including CubeSats. These systems offer compact, lightweight, and energy-efficient alternatives to active beamforming systems, making them particularly attractive for space missions constrained by mass, volume, and power budgets. In CubeSat communications, achieving high data rates and reliable links over long distances are challenging due to their small form factor and limited power availability. Passive antennas designed for beam-steering can address these issues by enhancing signal directivity without adding complexity and power consumption to active elements. Despite their advantages, passive antennas for beam-steering face several challenges. Passive beamforming systems require meticulous design to achieve precise phase control and high efficiency. This often involves intricate geometries, tight tolerances, and advanced materials. In the harsh environment of space, passive antennas must withstand extreme temperatures, radiation, and mechanical stresses, which can degrade performance over time. Manufacturing compact and lightweight passive antennas with high precision is also challenging, especially when integrating them into the constrained volume of a CubeSat. Moreover, passive antennas can achieve beam steering; the range and accuracy of the steering are typically less flexible than active systems. To address these challenges, several innovative techniques have been developed, such as passive phased arrays that utilize time-delay elements or phase shifters to control the direction of the radiated beam. These systems achieve high gain and directivity, although their operational bandwidths often limit them. In the reflect arrays method, antennas combine the features of reflectors and arrays by using a flat panel of passive elements to reflect and steer the beam. Their planar structure is ideal for CubeSat integration. In addition, the metasurface technique, composed of subwavelength elements, enables beamforming through phase manipulation across the surface. These antennas offered ultrathin profiles and enhanced design flexibility. To overcome volume constraints, deployable passive antennas inspired by origami techniques have been developed, allowing for compact stowage during launch and deployment in orbit. Last but not least, using lightweight, radiation-hardened, and thermally stable materials can also improve the durability and performance of passive antennas in the space environment.

Recent antennas utilized for CubeSat communications, as well as explanations of their limitations, techniques, and outcomes, have been presented. It would be informative to consider several recent passive antennas for beam steering to investigate their challenges and methods, as well as explain how they can be used for CubeSat communications.

Reference [94] explores phased array antennas operating in the D-band frequency range (110–170 GHz), focusing on high-frequency performance. Microstrip-based techniques were used for compactness and integration. The antenna demonstrated the design feasibility of D-band phased array antennas, with notable gains of 26.75 dBi and beam-steering capabilities of -13.5 – 13.7° . It also addresses the need for miniaturization, which is crucial for high-frequency applications. Operating in D-band frequencies requires high precision of fabrication because of the small dimensions and tight tolerances, which are not always feasible in mass production. Microstrip antennas suffer significant losses at high frequencies, impacting the overall efficiency. The study explored beam steering but did not address real-world challenges, such as hardware implementation for real-time beam control. While simulations showed promising results, real-world environmental factors like interference, material imperfections, and atmospheric absorption in the D-band range limit performance.

In Ref. [95], a microstrip antenna array was designed and implemented to support beam steering, emphasizing compactness and low-profile characteristics at 2.4 GHz. It likely incorporated phase shifters and other techniques to achieve beam steering, enhancing the signal directionality for communication systems. The authors also included various configurations (e.g., linear and planar) to improve the gain and performance. They highlight an increased gain of up to 7 dBi and beam steering as significant benefits of using the microstrip antenna array. They also suggest that communication system applications, such as 4G and 5G networks or radar, require high data rates and precise signal directionality. However, the paper does not address challenges related to dielectric and conductor losses, especially for higher-frequency applications. The beam-steering technique, while helpful, can increase the design complexity, especially if implementing phase shifters or control systems. There was a limited discussion of real-world challenges like environmental interference, manufacturing tolerances, and system integration into commercial devices.

Reference [96] focuses on the K-band frequency range (~18–27 GHz) with microstrip technology, which is suitable for compact and planar systems. The authors employed phased array principles to achieve directional beam steering, improving antenna efficiency in high-frequency communication. They used series feed techniques to distribute power uniformly across array elements. They also demonstrated a gain of 7.6 dBi and a beam range of 30 degrees. However, the closely spaced elements in the array can lead to interference, reducing the overall efficiency. High-frequency designs, particularly in the K-band, are more susceptible to environmental factors like atmospheric attenuation.

Reference [97] focuses on scalable and integrated patch antennas for 28 GHz, a key frequency for 5G applications. It demonstrated an integrated beamforming solution for enhanced connectivity in automotive systems. It used high-efficiency power amplifiers in the antenna system to ensure effective signal transmission in 5G networks, offering maximum gains of 7.5 dBi and 21.8 dBi before and after amplifier integration. The proposed antenna system offers 5G signal coverage and capacity through beamforming and amplifier integration. It is tailored for high-speed and reliable communications in automotive environments, addressing challenges like Doppler effects. However, integrating power amplifiers with antennas can lead to thermal issues, especially in compact systems. Moreover, high-frequency signals, such as those at 28 GHz, are prone to attenuation due to weather conditions and obstacles.

In Ref. [98], a multibeam antenna at 38 GHz, a critical band for 5G communication, was designed. The array enhances spatial coverage using a folded Butler matrix for compact beam steering, which reduces the circuit area while achieving precise beam steering. It also focused on integrating multiple components into a package to save space, which is crucial for 5G mobile and IoT devices. An excellent beam-steering performance with low sidelobe levels was demonstrated, improving the signal quality and reducing the size by 53.5% compared to conventional Butler matrices and phased arrays, making it suitable for space-constrained applications. Four beams were measured at $\pm 36^\circ$ and $\pm 12^\circ$ and offered maximum gains of 19.8 and 21 dBi, respectively. However, the multi-folded design can introduce additional losses, which affect the overall efficiency.

In Ref. [99], antenna arrays were designed to operate at 28.8 GHz, focusing on miniaturization. The arrays adopt a linear arrangement to enable efficient beam-steering capabilities. The design also incorporates techniques for efficient energy usage, supporting a high-frequency performance while maintaining a small footprint. The antenna arrays demonstrate an enhanced gain of up to 9.19 dBi and directional beam steering. The results indicate their potential for deployment in 5G applications and beyond. However, the design does not support broader frequency ranges, limiting the flexibility.

Reference [100] presents a compact and lightweight multi-beam antenna system tailored for CubeSat applications operating in the Ka-band (26.5–40 GHz). The design incorporates a 3D printed dielectric lens to enhance beam directivity and a planar antenna array to generate multiple beams with a coverage of 14–18° for efficient connectivity. This approach enables passive beam steering, reducing the complexity and power consumption while maintaining high performance, such as a maximum gain of 16 dBi. Three-dimensional printing also lowers the manufacturing costs and facilitates scalability for CubeSat systems. However, the design faces challenges, such as sensitivity to manufacturing tolerances, limited adaptability to other frequency bands, and environmental factors like signal attenuation in adverse weather.

Reference [101] introduces a dual-band antenna design leveraging phase-gradient metascreens (PGMs) and near-field meta-steering capabilities. The design employs innovative dual-band, phase-gradient metascreen structures to achieve effective beam steering of $\pm 46^\circ$ and $\pm 51^\circ$ for near-field applications. These metascreens are designed to operate efficiently at two distinct frequency bands (11.57–11.97 GHz and 13.95–15.0 GHz), with independent beam-steering capabilities for each band. The PGMs were engineered to precisely control the electromagnetic wave propagation through phase adjustments across the metascreen surface. However, the approach relies on intricate multi-layer structures, which increase the manufacturing complexity and cost. Metal layers in the design introduce conductivity losses, impacting the overall system efficiency.

Reference [102] explores the design of a dual-band, shared-aperture antenna system at 3.2–3.45 GHz and 25.5–29.5 GHz, tailored for 5G technologies. This system integrates multiple antenna elements within a compact shared aperture, supporting dual-band operation and beam-steering capabilities. Beam steering of up to 112° in the sub-6 GHz band and up to 56° in the mm-wave band are achieved using an innovative phase-shifting network that facilitates precise control of the antenna beam across both frequency bands. The design prioritizes compactness and achieves a maximum efficiency of 78% and gain of 19.31 dBi, making it suitable for integration into modern 5G infrastructure.

Reference [103] proposes a hybrid reflectarray antenna combining passive and active unit cells for efficient two-directional beam steering in the coverage of -18° and 18° around 10.1 GHz. The active cells enable dynamic control of phase gradients, while passive cells ensure a lightweight and cost-effective design. Integrating active and passive unit cells for phase manipulation and phase-gradient control to direct beams toward two target directions offers a high efficiency of up to 69.5%. However, the design's complexity increases because of the integration of active and passive cells, and the scalability for multi-directional beam steering is limited.

Reference [104] introduces a low-profile, dual-band, and dual-circularly polarized folded transmit array antenna for independent beam control in the K- and Ka-bands (12 and 15 GHz). The design utilizes a unique folded transmit array mechanism and polarization control to steer beams independently at each band (up to 45°). The system provides high gains of 24.7 dB and 26.1 dB for the respective bands, with efficiencies exceeding 55%. These results highlight the antenna's effectiveness in modern applications like satellite communications and 5G networks, combining compactness with advanced polarization and beam control capabilities. However, its limitations include potential challenges in fabricating such intricate structures and maintaining high precision for dual-band beam control.

Reference [105] presents a design for a dual-band transmit array at 12.5 GHz and 14.25 GHz capable of generating orthogonally polarized contour beams (360° phase range), targeting advanced communication systems. The design utilizes independent phase compensation for each band, achieved through the design of high-precision elements,

polarization control, and a maximum gain of 25.3 dBi. Its limitations involve the complexity of fabrication and alignment, as well as challenges in maintaining the performance over wide angular ranges. The design holds promise for improving multifunctional antenna systems.

Ref. [106] presented a Fabry–Pérot-based, all-dielectric Huygens' structure for millimeter-wave beam steering with circular polarization. The design employs dielectric metasurfaces with tailored phase and amplitude responses to achieve compactness and efficient beam steering (360° phase coverage). It integrates well with 60 GHz slot antennas, achieving circular polarization with a gain of 34.13 dBi. While the design demonstrates effective beam steering and reduced cross-polarization, its limitations include fabrication complexity and potential performance sensitivity to dielectric material inconsistencies.

Reference [107] presents a method for achieving wide-angle beam steering with circular polarization in the Ka-band (29.5–30 GHz) using a plate lens antenna. The approach relies on the in-plane translation of a dielectric plate lens to steer the beam over a wide angular range while maintaining circular polarization (0° to 50°). The method demonstrates a high gain of 27.3 dBi and high beam quality. However, the mechanical translation of the lens introduces practical limitations, such as slower response times and potential wear-and-tear issues in dynamic systems compared to fully electronic beam steering. Additionally, the setup can be bulky and less suitable for highly compact or integrated applications.

Ref. [108] presented a high-gain aperture antenna using a leaky-wave antenna (LWA) array with substrate-integrated waveguide (SIW) technology designed for CubeSat applications. Operating at 28 GHz, the antenna achieves a gain of 15.2 dBi with a fixed radiation angle of -45° , while its compact design ($98.6 \times 16 \times 1.575$ mm³ per element) ensures integration within a 1U CubeSat. SIW enables a low-profile, efficient structure, making it suitable for space-constrained environments. However, its fixed radiation angle may limit communication flexibility, requiring satellite orientation adjustments, and the frequency-specific design at 28 GHz may necessitate modifications for different operational bands. Despite these limitations, the proposed antenna offers a promising solution for enhancing CubeSat communication with its high gain and compact form factor.

Reference [109] proposes a CubeSat microstrip antenna incorporating a metamaterial structure for LoRa communication at 924 MHz. The design utilizes a metamaterial layer to enhance the antenna's performance by improving the gain by up to 2.6 dBi while maintaining a compact form factor suitable for CubeSat applications. The authors demonstrate that the metamaterial structure effectively reduces the antenna's size while preserving its efficiency, making it ideal for low-power, long-range communications such as LoRa. However, while the antenna shows promise for CubeSat-based IoT and remote sensing applications, its suitability for beamforming or beam-steering tasks is limited. The passive nature of the metamaterial structure restricts dynamic beam control, making it less adaptable to varying communication conditions in low Earth orbit (LEO).

Reference [110] presents a compact phased array antenna for 5G millimeter-wave communication devices. The linear array comprises eight elements utilizing substrate-integrated waveguide technology, complemented by two rows of metasurfaces to enhance impedance matching and optimize the transition to free space. The antenna operates within the 26.5–29.5 GHz frequency range, achieving a maximum realized gain of approximately 12.5 dBi. It maintains a radiation efficiency exceeding 60% across this band. The design supports a wide scanning range, enabling effective beam steering for enhanced communication performance in 5G applications. Although the proposed metasurface-based phased array antenna offers excellent beam scanning and efficiency for 5G terrestrial networks, its reliance on high-frequency operation, power-hungry active beam steering, and structural limitations make it less suitable for CubeSat communications.

5. Industry and Study Cases of Antenna for CubeSats

CubeSats have become a popular platform for space missions due to their cost-effectiveness and versatility. A critical component of these small satellites is the antenna system, which ensures effective communication with ground stations. Several industry trials and studies have focused on developing and testing antennas tailored for CubeSats. Notable examples include the following:

X-Band CubeSat Communication System Development: This project focused on designing and testing a complete X-band communication system for CubeSats. It involved simulations, antenna analysis for the X- and S-bands, transceiver design, and optimization of space-to-ground links. The findings contribute to advancing NEN-compatible CubeSat communication systems [111].

A reflectarray antenna was designed and measured for a downlink antenna on the 2-by-3-unit surface of 6U and 12U CubeSats operating in the X-band frequency range (8.025 GHz to 8.4 GHz). A key design requirement is the minimization of the internal volume required to stow the antenna within the CubeSat. The resulting design involves a cavity feed that protrudes less than 4 mm into the CubeSat. This implies that there is still room for an entire unit of payload below the feed. The feed is linearly polarized, and to achieve the required RHCP for the downlink, the reflectarray is designed to generate circular polarization [112].

A novel mechanical beam-steering system was designed for integration with deployable antennas. It uses motors to control rods attached to a parabolic dish, with rod lengths determining the dish's orientation, stored in a codebook. It enables a high-gain deployable antenna for THz-band CubeSat links, achieving an over 40 dB gain across various angles. The design and development of the prototype are in progress [113].

The AcubeSAT mission, developed by SpaceDot at the Aristotle University of Thessaloniki, studies the effects of microgravity and radiation on eukaryotic cells. Its communication system features a 2.4 GHz S-band microstrip antenna and a deployable UHF antenna for telemetry and telecommand. Over three years, the antenna design evolved through multiple iterations with input from ESA experts. Initially, the team considered adapting the UPS at ADM but opted for an in-house design. They share insights into the development process, covering design considerations, ADM architecture, and key lessons learned. Environmental tests on the EQM were conducted, and future improvements are explored [114].

University of San Diego researchers developed and analyzed RF components for a phased array antenna designed for 1U CubeSats. The study assessed the viability of achieving high-speed, low-power, and cost-efficient communications. With a limited power budget of only a few watts and integration of low-power COTS components, a four-element phased array downlink system was deemed feasible. The system is theoretically capable of achieving an 11 Mb/s downlink speed, surpassing any previously deployed CubeSat, while maintaining low power consumption to sustain other onboard subsystems and sensors [115].

In 2022, the Get Away Special (GAS) team at Utah State University launched GASPACS to demonstrate inflatable structures in space. This project was part of NASA's CubeSat Launch Initiative, which funds and launches university and nonprofit satellites for research experiments [116].

SOURCE (Stuttgart Operated University Research CubeSat for Evaluation and Education), as a nanosatellite with dimensions of $10 \times 10 \times 36 \text{ cm}^3$, complies with the 3U+ CubeSat standard. It was developed in cooperation between KSat eV and the Institute of Space Systems (IRS) at the University of Stuttgart. As a student CubeSat, it is developed and operated exclusively by students under the supervision of the IRS. As part of the

“CubeSat Technology Internship” module, many students had the opportunity to gain practical experience over a semester and earn credit points for their participation in the project. In addition to supervising the project, the IRS offered numerous opportunities for testing and developing its components. Moreover, SOURCE was funded by ESA’s Fly Your Satellite! Program, which enabled students to learn development, testing, and documentation in accordance with the standards of the European Cooperation for Space Standardization (ECSS) [117].

6. Discussion and Future Directions

The evolution of CubeSat communication systems has necessitated significant advancements in antenna technologies, focusing on beamforming/beam-steering techniques that ensure efficient and reliable communication in resource-constrained environments. This review analyzes diverse approaches to passive antennas used for CubeSat communications, including planar phased patch antenna arrays, dielectric lenses, and leaky-wave antennas (LWAs), highlighting their respective merits and challenges in addressing the unique demands of CubeSat platforms.

A significant takeaway from the reviewed studies is the growing shift toward innovative design methodologies to achieve high gain, compact form factors, wide-angle beam steering, and efficient polarization. For instance, planar phased patch arrays, though offering rapid and precise electronic beam steering, face power consumption-, cost-, and complexity-related challenges. These issues became particularly pronounced in CubeSat platforms, for which size, weight, and power (SWaP) constraints are critical. Similarly, dielectric lenses provide high efficiency and excellent polarization but rely on mechanical steering mechanisms that can hinder the response speed and complicate system integration. UWB antennas are ideal for wideband applications but encounter difficulties achieving consistent gain and effective beam steering across their operating range.

To overcome these challenges, future research directions emphasize the need for hybrid systems that combine the strengths of multiple techniques. For example, integrating phased array principles with dielectric metasurfaces can mitigate power consumption issues while maintaining beam-steering capabilities. Similarly, using advanced materials, such as metamaterials or lightweight 3D printed dielectric structures, can facilitate the development of compact, efficient, and scalable antenna solutions. Emerging concepts, such as reconfigurable intelligent surfaces (RIS) and adaptive control algorithms, offer further opportunities to enhance beam-steering performance. RIS technology can dynamically manipulate electromagnetic waves to optimize beam steering in real-time, while adaptive algorithms can adjust beamforming parameters in response to changing link conditions and orbital dynamics. Together, these advancements hold the potential to unlock new levels of adaptability and efficiency in CubeSat communication systems.

By leveraging the natural beam-steering capabilities of LWAs, this configuration can provide an optimal balance between simplicity, functionality, and performance. The two-port design reduces the complexity of feeding networks. At the same time, the four-element array enhances the gain and directivity, which are critical for maintaining robust communication links in low Earth orbit (LEO). To address the limitations of traditional LWAs, such as bandwidth constraints and gain degradation at extreme angles, the integration of passive beam-steering networks and advanced materials, such as metamaterials, can be proposed. Metamaterials and gradient-index structures offer broader bandwidth and improved beam scanning capabilities, while 3D printed dielectric materials facilitate the creation of lightweight, customizable designs that integrate seamlessly into CubeSat architectures. Additionally, flexible and deployable materials are being explored to develop

antennas that can be stowed compactly during launch and deployed in orbit, maximizing the size and performance without exceeding launch constraints.

In addition, HBF techniques, which combine passive networks with frequency-tuned operations, represent a viable path forward, enabling multi-directional coverage and high gain without excessive power requirements. Moreover, metasurface-based LWAs can expand bandwidth and improve beam control, aligning with CubeSat SWaP requirements while enhancing the overall communication performance.

Adaptive control algorithms are emerging as a critical area of focus, offering the ability to dynamically optimize beam-steering parameters in real time. Algorithms powered by machine learning can analyze live data to adjust beam direction, enhance signal quality, and respond to disruptions caused by orbital motion or interference. These algorithms ensure robust and reliable communication links, even in challenging operational environments.

7. Conclusions

This review paper highlights advanced beamforming/beam-steering techniques for CubeSat communications, focusing on technologies like planar phased patch arrays, dielectric lenses, and leaky-wave antennas (LWAs). These approaches offer benefits such as high gain, compact design, wide-angle beam steering, and efficient circular polarization but face limitations like *phased arrays* (which provide rapid electronic beam steering but are costly, complex, and power-intensive), *dielectric lenses* (which deliver high efficiency but rely on slow mechanical steering and are challenging to integrate), and *leaky-wave antennas* (which enable frequency-based beam steering without complex circuitry but suffer from limited bandwidth, gain degradation, and open stopbands at large angles).

A two-port, four-element LWA is proposed as a viable solution for CubeSat communications, balancing simplicity, efficiency, and functionality. This design enhances gain and directivity while meeting size, weight, and power (SWaP) constraints, which are critical to CubeSats. However, limitations like bandwidth and beam control issues require advanced solutions. To address these challenges, integrating passive beamforming/beam-steering networks (e.g., Butler matrices and Rotman lenses) and advanced materials (e.g., metamaterials) can improve bandwidth, scanning range, and multi-beam operations. Hybrid beamforming/beam-steering techniques combining passive and frequency-tuned methods are recommended for efficient, multi-directional coverage.

This review paper remains limited regarding experimental feasibility, future directions, real-world mission tests, and experimental validation. However, the techniques and the state of the art discussed here can pave the way for reaching an effective experimental performance. For instance, phased array systems have been tested in some satellite missions, demonstrating their capability for rapid electronic beam steering. However, their high power consumption and complexity restrict widespread CubeSat adoption. Dielectric-lens-based antennas have shown high efficiency in lab environments, but their reliance on mechanical steering poses integration challenges for small satellites. LWAs, another promising technique offering frequency-dependent beam steering, have been experimentally validated in terrestrial applications. However, their space-based implementation is still in its early stages, with concerns over bandwidth and gain degradation at extreme angles. While some CubeSat missions have explored reconfigurable antennas and passive beamforming networks, comprehensive on-orbit demonstrations of metasurface-based designs and hybrid beamforming solutions remain scarce. Future work should focus on integrating these technologies into CubeSat platforms for real-world testing, ensuring their feasibility for Earth observation, intersatellite networking, and deep-space communications.

Author Contributions: T.S. investigated the CubeSat communications and the antennas utilized, as well as wrote the original draft of this review article. S.K. edited the article. All authors have read and agreed to the published version of the manuscript.

Funding: This work has been jointly supported by the European Space Agency, under contract number: 4000145253, and by Silicon Austria Labs (SAL), owned by the Republic of Austria, the Styrian Business Promotion Agency (SFG), the federal state of Carinthia, Upper Austrian Research (UAR), and the Austrian Association for the Electric and Electronics Industry (FEEL).

Data Availability Statement: The data are contained within the article.

Conflicts of Interest: The authors declare no conflicts of interest.

References

1. Tubbal, F.E.; Raad, R.; Chin, K.-W. A survey and study of planar antennas for pico-satellites. *IEEE Access* **2015**, *3*, 2590–2612. [CrossRef]
2. Abulgasem, S.; Tubbal, F.; Raad, R.; Theoharis, P.I.; Lu, S.; Iranmanesh, S. Antenna Designs for CubeSats: A Review. *IEEE Access* **2021**, *9*, 45289–45324. [CrossRef]
3. Nabeel, M.I.; Singh, K.; Afzal, M.U.; Thalakituna, D.N.; Esselle, K.P. Dual-Band Passive Beam Steering Antenna Technologies for Satellite Communication and Modern Wireless Systems: A Review. *Sensors* **2024**, *24*, 6144. [CrossRef] [PubMed]
4. Chen, Y.; Qi, D.; Li, C. A Deep Learning Framework for Evaluating the Over-the-Air Performance of the Antenna in Mobile Terminals. *Sensors* **2024**, *24*, 5646. [CrossRef]
5. Buttazzoni, G.; Comisso, M.; Cuttin, A.; Fragiaco, M.; Vescovo, R.; Gatti, R.V. Reconfigurable phased antenna array for extending cubesat operations to Ka-band: Design and feasibility. *Acta Astronaut.* **2017**, *137*, 114–121. [CrossRef]
6. Jiménez, D.A.; Reyna, A. Luz Idalia Balderas and Marco Antonio Panduro, Design of 4×4 Low-Profile Antenna Array for CubeSat Applications. *Micromachines* **2023**, *14*, 180. [CrossRef]
7. Platero, V.; Ferguson, P.; Jayaraman, R.; Isleifson, D. 2-In-1 smart panels: Embedding phased array patch antennas within satellite structures. *Acta Astronaut.* **2020**, *175*, 51–56. [CrossRef]
8. Klein, J.; Hawkins, J.; Thorsen, D. Improving CubeSat Downlink Capacity with Active Phased Array Antennas. In Proceedings of the 2014 IEEE Aerospace Conference, Big Sky, MT, USA, 1–8 March 2014.
9. Theoharis, P.I.; Raad, R.; Tubbal, F. High-Gain Circular Polarized Microstrip Patch Array for X-band CubeSat Applications. In Proceedings of the IEEE 15th International Conference on Signal Processing and Communication Systems (ICSPCS), Sydney, Australia, 13–15 December 2021; ISBN 978-1-6654-3699-1/21/\$31.00.
10. Baktur, R.; Oliveira, E.; Sato, L.S.; Swenson, C. An X Band Downlink Antenna for a CubeSat Mission. *Ursi Radio Sci. Lett.* **2022**, *4*, 4.
11. Nguyen, M.T.; Ferrero, F.; Trinh, L.-H. Compact UHF Circularly Polarized Multi-Band Quadrifilar Antenna for CubeSat. *Sensors* **2023**, *23*, 5361. [CrossRef]
12. Rabie, M.M.; El-Henawy, H.; El-Hefnawy, F.; Ibrahim, F. Transparent Microstrip GPS Antenna for Cubesat Applications. In Proceedings of the 17th International Conference on Aerospace Sciences & Aviation Technology (ASAT-17), Cairo, Egypt, 11–13 April 2017.
13. da Silva, W.G.; Campos, A.L.P.S.; Guerra, J.R.F. A Compact Dual-Band UHF Microstrip Patch Antenna for CubeSat Applications. *J. Commun. Inf. Syst.* **2021**, *36*, 166–172. [CrossRef]
14. Maged, M.A.; Elhefnawi, F.; Akah, H.M.; El-Hennawy, H.M. C-band transparent antenna design for intersatellites communication. *Int. J. Sci. Eng. Res.* **2018**, *9*, 248–252.
15. Nascetti, A.; Pittella, E.; Teo, P.; Pisa, S. High-gain S-band patch antenna system for earth-observation CubeSat satellites. *IEEE Antennas Wirel. Propag. Lett.* **2015**, *14*, 434–437. [CrossRef]
16. Neveu, N.; Garcia, M.; Casana, J.; Dettloff, R.; Jackson, D.R.; Chen, J. Transparent Microstrip Antennas for CubeSat Applications. In Proceedings of the IEEE International Conference on Wireless for Space and Extreme Environments, Baltimore, MD, USA, 7–9 November 2013; pp. 1–4.
17. Podilchak, S.K.; Comite, D.; Montgomery, B.K.; Li, Y.; Buendía, V.G.-G.; Antar, Y.M.M. Solar-panel integrated circularly polarized meshed patch for cubesats and other small satellites. *IEEE Access* **2019**, *7*, 96560–96566. [CrossRef]
18. Rodríguez-Orsorio, R.M.; Ramírez, E.F. A hands-on education project: Antenna design for inter-CubeSat communications [education column]. *IEEE Antennas Propag. Mag.* **2012**, *54*, 211–224. [CrossRef]
19. Abulgasem, S.; Tubbal, F.; Raad, R.; Theoharis, P.I.; Liu, S.; Khan, M.U.A. A wideband metal-only patch antenna for CubeSat. *Electronics* **2020**, *10*, 50. [CrossRef]

20. Warren, P.A.; Steinbeck, J.W.; Minelli, R.J.; Mueller, C. Large, Deployable S-Band Antenna for a 6U CubeSat. In Proceedings of the 29th AIAA Annual Conference on Small Satellites, Logan, UT, USA, 8–13 August 2015; pp. 1–7.
21. Yao, Y.; Liao, S.; Wang, J.; Xue, K.; Balfour, E.A.; Luo, Y. A new patch antenna designed for CubeSat: Dual feed, LS dual-band stacked, and circularly polarized. *IEEE Antennas Propag. Mag.* **2016**, *58*, 16–21. [CrossRef]
22. Veljovic, M.J.; Skrivervik, A.K. Aperture-coupled low-profile wideband patch antennas for CubeSat. *IEEE Trans. Antennas Propag.* **2019**, *67*, 3439–3444. [CrossRef]
23. Tubbal, F.E.; Raad, R.; Chin, K.-W.; Butters, B. S-Band Shorted Patch Antenna for Inter Pico Satellite Communications. In Proceedings of the 8th International Conference Telecommunication Systems, Services and Applications (TSSA), Kuta, Bali, Indonesia, 23–24 October 2014; pp. 1–4.
24. Palacios, O.F.G.; Vargas, R.E.D.; Perez, J.A.H.; Erazo, S.B.C. S-Band Koch Snowflake Fractal Antenna For CubeSats. In Proceedings of the IEEE ANDESCON, Arequipa, Peru, 19–21 October 2016; pp. 1–4.
25. Maged, M.A.; El-Hefnawi, F.; Akah, H.M.; El-Akhdar, A.; El-Hennawy, H.M.S. Design and realization of circular polarized SIW slot array antenna for cubesat intersatellite links. *Prog. Electromagn. Res. Lett.* **2018**, *77*, 81–88. [CrossRef]
26. Tariq, S.; Baktur, R. Circularly Polarized UHF Up- and Downlink Antennas Integrated with CubeSat Solar Panels. In Proceedings of the 2015 IEEE International Symposium on Antennas and Propagation & USNC/URSI National Radio Science Meeting, Vancouver, BC, Canada, 19–24 July 2015; pp. 1424–1425.
27. Liu, S.; Raad, R.; Chin, K.-W.; Tubbal, F.E.M. Dipole Antenna Array Cluster for CubeSats. In Proceedings of the 10th International Conference on Signal Processing and Communication Systems (ICSPCS), Surfers Paradise, Australia, 19–21 December 2016; pp. 1–4.
28. Lokman, A.H.; Soh, P.J.; Azemi, S.N.; Jamlos, M.F.; Al-Hadi, A.A.; Chalermwisutkul, S.; Kkaraekthalin, P. Compact Circularly Polarized S-Band Antenna for Pico-Satellites. In Proceedings of the 2017 International Symposium on Antennas and Propagation (ISAP), Phuket, Thailand, 30 October–2 November 2017; pp. 1–2.
29. Chahat, N.; Sauder, J.; Mitchell, M.; Beidleman, N.; Freebury, G. One meter deployable mesh reflector for deep-space network telecommunication at X-band and Ka-band. *IEEE Trans. Antennas Propag.* **2020**, *68*, 727–735. [CrossRef]
30. Lehmensiek, R. Design of a wideband circularly polarized 2_2 array with shorted annular patches at X-band on a CubeSat. In Proceedings of the 2017 International Symposium on Antennas and Propagation (ISAP), Phuket, Thailand, 30 October–2 November 2017; pp. 1–2.
31. Franzén, F.; Hultin, H.; Olsson, J. A Transparent Dual-Band CubeSat Antenna Based on Stacked Patches. Bachelor's Thesis, School of Electrical Engineering, KTH Royal Institute of Technology, Stockholm, Sweden, 2017.
32. Zarbakhsh, S.; Akbari, M.; Farahani, M.; Ghayekhloo, A.; Denidni, T.A.; Sebak, A.-R. Optically transparent subarray antenna based on solar panel for CubeSat application. *IEEE Trans. Antennas Propag.* **2020**, *68*, 319–328. [CrossRef]
33. Ta, S.X.; Le, V.D.; Nguyen, K.K.; Dao-Ngoc, C. Planar circularly polarized X-band array antenna with low sidelobe and high aperture efficiency for small satellites. *Int. J. RF Microw. Comput. Aided Eng.* **2019**, *29*, e21914. [CrossRef]
34. Hodges, R.E.; Chahat, N.; Hoppe, D.J.; Vacchione, J.D. A Deployable High-Gain Antenna Bound for Mars. *IEEE Antennas Propag. Mag.* **2017**, *59*, 39–49. [CrossRef]
35. Islam, M.M.; Islam, M.T.; Faruque, M.R.I.; Hueyshin, W. Design of an X-band microstrip patch antenna with Enhanced bandwidth. In Proceedings of the 2013 2nd International Conference on Advances in Electrical Engineering (ICAEE 2013), Dhaka, Bangladesh, 19–21 December 2013.
36. Zahid, M.; Taqdeer, M.M.; Amin, Y. A Compact Dual-Band Microstrip Patch Antenna for C- and X- and Ku-Band Applications. *Eng. Proc.* **2023**, *46*, 16. [CrossRef]
37. Raza, A.; Adnan, M.; Maryam, H.; Mukhtar, M. Microstrip patch antenna fabricated and simulated results for S-Band, C-band and X-band antenna for space and communication applications. *Braz. J. Dev.* **2024**, *10*, e70809.
38. Samsuzzaman, M.; Islam, M.T. Inverted S-Shaped Compact Antenna for X-Band Applications. *Sci. World J.* **2014**, *2014*, 604375. [CrossRef]
39. Ayush; Shakya, P.; Rashm, T.; Srivastava, T. 2×2 X-Band Microstrip Patch Array Antenna for Radar Application. *Glob. Sci. J.* **2022**, *10*, 1–2.
40. Mathur, P.; Kumar, G. Antenna at S-Band as Ground for Array at X-Band in Dual Frequency Antenna at S/X-Bands. *Prog. Electromagn. Res. Lett.* **2017**, *71*, 15–22. [CrossRef]
41. Aras, U.; Delwar, T.S.; Durgaprasadarao, P.; Sundar, P.S.; Ahammad, S.H.; Eid, M.M.A.; Lee, Y. Ahmed Nabih Zaki Rashed and Jee-Youl Ryu, Dual Features, Compact Dimensions and X-Band Applications for the Design and Fabrication of Annular Circular Ring-Based Crescent-Moon-Shaped Microstrip Patch Antenna. *Micromachines* **2024**, *15*, 809. [CrossRef]
42. Arockia, P.; Mercy, M.; Wilson, K.S.J. High Gain Miniaturized Multi-band Microstrip Patch Antenna Using Slot-Cutting Techniques for C, and X Band Applications. *PriMera Sci. Eng.* **2023**, *2*, 53–65.

43. Chahat, N.; Sauder, J.; Mitchel, M.; Beidleman, N.; Freebury, G. One Meter Deployable Mesh Reflector for Deep Space Network Telecommunication at X and Ka-Band. In Proceedings of the 13th European Conference on Antennas and Propagation (EuCAP 2019), Krakow, Poland, 31 March–5 April 2019.
44. Tubbal, F.E.; Raad, R.; Chin, K.-W. A Low Profile High Gain CPW-Fed Slot Antenna with a Cavity Backed Reflector for CubeSats. In Proceedings of the 2017 11th International Conference on Signal Processing and Communication Systems (ICSPCS), Surfers Paradise, Australia, 13–15 December 2017; pp. 1–4.
45. Rao, S.; Shafai, L.; Sharma, S.K. *Handbook of Reflector Antennas and Feed Systems. Applications of Reflectors*; Artech House: Boston, MA, USA, 2013; Volume 3.
46. Mishra, G.; Sharma, S.K.; Chieh, J.-C.S. A circular polarized feed horn with inbuilt polarizer for offset reflector antenna for W-band CubeSat applications. *IEEE Trans. Antennas Propag.* **2018**, *67*, 1904–1909. [CrossRef]
47. Zhang, H.; Wu, M.; Xiang, P.; Wu, D.; Yan, Z.; Cui, Q. Design, analysis, and test of an ultra-compact X-band deployable wrap-rib antenna. *Acta Astronaut.* **2025**, *228*, 918–930. [CrossRef]
48. Aya, M.; Sauder, J.; Hodges, R.E. *Large-Area Deployable Reflect Array Antenna for CubeSats*; California Institute of Technology: Pasadena, CA, USA, 2019.
49. Hodges, R.E.; Hoppe, D.J.; Radway, M.J.; Chahat, N.E. Novel Deployable Reflectarray Antennas for CubeSat Communications. In Proceedings of the 2015 IEEE MTT-S International Microwave Symposium, Phoenix, AZ, USA, 17–22 May 2015; pp. 1–4.
50. Whitton, J.D.; Mauskopf, P.D.; Goldsmith, P.F.; Davis, K.K.; Groppi, C.E. Dielectrically embedded mesh lens design for cubesat water detection. In Proceedings of the SPIE 10708, Millimeter, Submillimeter, and Far-Infrared Detectors and Instrumentation for Astronomy IX, Austin, TX, USA, 3 August 2018. 107083L. [CrossRef]
51. Whitton, J.D.; Mauskopf, P.D.; Goldsmith, P.F.; Davis, K.K.; Groppi, C.-P.E. Prototype Design of a Dielectrically Embedded Mesh Lens. In Proceedings of the 29th IEEE International Symposium on Space THz Technology (ISSTT2018), Pasadena, CA, USA, 26–28 March 2018.
52. Pisano, G.; Ng, M.W.; Ozturk, F.; Maffei, B.; Haynes, V. Dielectrically embedded flat mesh lens for millimeter waves applications. *Appl. Opt.* **2013**, *52*, 2218–2225. [CrossRef] [PubMed]
53. Whitton, C.; Groppi, C.; Mauskopf, P.; Siles, J.; Tang, A. Measurements and Simulations of a 20 GHz Metamaterial Lens. In Proceedings of the 31st Symposium on Space Terahertz Technology, ISSTT 2020, Tempe, AZ, USA, 8–11 March 2020; pp. 111–114.
54. Lobato-Morales, H.; Villarreal-Reyes, S.; Guerrero-Arbona, E.; Martinez-Aragon, E.; Chávez-Pérez, R.A.; Medina-Monroy, J.L.; Figueroa-Torres, C.A. A 2.45-GHz Circular Polarization Closed-Loop Travelling-Wave Antenna for CubeSats. In Proceedings of the International Conference on Electronics, Communications and Computing (CONIELECOMP) 2019, Cholula, Mexico, 27 February–1 March 2019; pp. 154–157.
55. Mathur, P.; Kumar, G. Dual-frequency microstrip antenna at S and X bands with higher-order mode suppression technique. *IET Microw. Antennas Propag.* **2018**, *12*, 583–587. [CrossRef]
56. Buendía, V.G.-G.; Podilchak, S.K.; Liberto, S.; Walkinshaw, T.; Constantinides, C.; Anagnostou, D.E.; Goussetis, G.; Van Der Vorst, M. Compact and Planar End-Fire Antenna for PicoSat and CubeSa Platforms to Support Deployable Systems. *IEEE Open J. Antennas Propag.* **2022**, *3*, 1341–1350. [CrossRef]
57. Kuznetsov, M.V.; Podilchak, S.K.; Poveda-Garc, M.; Hilario, P.; Alistarh, C.A.; Goussetis, G.; Gómez-Tornero, J.L. Compact Leaky-Wave SIW Antenna with Broadside Radiation and Dual-Band Operation for CubeSats. *IEEE Antennas Wirel. Propag. Lett.* **2021**, *20*, 2125–2129. [CrossRef]
58. Li, X.; Wang, J.; Goussetis, G.; Wang, L. Circularly Polarized High Gain Leaky-Wave Antenna for CubeSat Communication. *IEEE Trans. Antennas Propag.* **2022**, *70*, 7612–7624. [CrossRef]
59. Prado, D.R.; Poveda-García, M.; Goussetis, G.; Wang, L. Design of a Reflectarray Fed by a Planar Leaky-Wave Antenna for 3U CubeSats. In Proceedings of the 2024 17th United Conference on Millimetre Waves and Terahertz Technologies (UCMMT), Palermo, Italy, 21–23 August 2024.
60. De, R.; Abegaonkar, M.P.; Basu, A. A broadband circularly polarized Fab-ry Perot antenna with spatially separated superstrate area excitation for CubeSat applications. *Sci. Rep.* **2023**, *13*, 11224. [CrossRef]
61. García-Vigueras, M.; Menargues, E.; Debogovic, T.; de Rijk, E.; Mosig, J.R. Cost-effective dual-polarised leaky-wave antennas enabled by three-dimensional printing. *IET Microw. Antennas Propag.* **2017**, *11*, 1985–1991. [CrossRef]
62. Shim, S.-J.; Lee, S.; Lee, W.-S.; Ro, J.-H.; Baik, J.-I.; Song, H.-K. Advanced Hybrid Beamforming Technique in MU-MIMO Systems. *Appl. Sci.* **2020**, *10*, 5961. [CrossRef]
63. Leao, T.F.C.; Mooney-Chopin, V.; Trueman, C.W.; Gleason, S. Design and implementation of a diplexer and a dual-band VHF/UHF antenna for nano-satellites. *IEEE Antennas Wirel. Propag. Lett.* **2013**, *12*, 1098–1101. [CrossRef]
64. Schraml, K.; Narbudowicz, A.; Chalermwisutkul, S.; Heberling, D.; Ammann, M.J. Easy-to-Deploy LC-Loaded Dipole and Monopole Antennas for CubeSat. In Proceedings of the 1th European Conference on Antennas and Propagation (EuCAP 2017), Paris, France, 19–24 March 2017; pp. 2303–2306.

65. Ozkayaa, U.; Seyfia, L. Dimension Optimization of Microstrip Patch Antenna in X/Ku Band via Artificial Neural Network. *Procedia-Soc. Behav. Sci.* **2015**, *195*, 2520–2526. [CrossRef]
66. Ygnacio-Espinoza, A.; Penalozza-Aponte, D.; Alvarez-Montoya, J.; Mesco-Quispe, A.; Clemente-Arenas, M. Quasi-transparent meshed and circularly polarized patch antenna with metamaterials integrated to a solar cell for S-band CubeSat applications. In Proceedings of the International Conference on Electromagnetics in Advanced Applications (ICEAA), Cartagena, Colombia, 10–14 September 2018; pp. 605–608.
67. Tubbal, F.; Raad, R.; Chin, K.-W.; Matekovits, L.; Butters, B.; Dassano, G. A high gain S-band slot antenna with MSS for CubeSat. *Ann. Telecommun.* **2019**, *74*, 223–237. [CrossRef]
68. Chen, S.-H.; Shen, L.-H.; Feng, K.-T.; Yang, L.-L.; Wu, J.-M. Energy-Efficient Joint Handover and Beam Switching Scheme for Multi-LEO Networks. In Proceedings of the 2024 IEEE 99th Vehicular Technology Conference (VTC2024-Spring), Singapore, 24–27 June 2024.
69. Xv, H.; Sun, Y.; Zhao, Y.; Peng, M.; Zhang, S. Joint Beam Scheduling and Beamforming Design for Cooperative Positioning in Multi-beam LEO Satellite Networks. *IEEE Trans. Veh. Technol.* **2024**, *73*, 5276–5287. [CrossRef]
70. Gao, R.; Wang, K.; Lin, W.; Kang, H. Joint Beam-Hopping Pattern Scheduling and Power Allocation for LEO Satellite Network. In Proceedings of the 2024 IEEE Wireless Communications and Networking Conference (WCNC), Dubai, United Arab Emirates, 21–24 April 2024.
71. Shlezinger, N.; Ma, M.; Lavi, O.; Nguyen, N.T.; Eldar, Y.C.; Juntti, M. Artificial Intelligence-Empowered Hybrid Multiple-input/multiple-output Beamforming: Learning to Optimize for High-Throughput Scalable MIMO. *IEEE Veh. Technol. Mag.* **2024**, *19*, 58–67. [CrossRef]
72. Ortiz, F.; Vasquez-Peralvo, J.A.; Querol, J.; Lagunas, E.; Rios, J.L.G.; Mendonca, M.O.K.; Garces, L.; Baeza, V.M.; Chatzinotas, S. Supervised Learning Based Real-Time Adaptive Beamforming On-board Multibeam Satellites. In Proceedings of the 2024 18th European Conference on Antennas and Propagation (EuCAP), Edinburgh, UK, 17–22 March 2024.
73. Jahnavi, V.; Afrin, S.; Dheeraj, S.S.; Armaan, S.A.K.; Ramagiri, A.; Gottipat, S. Artificial Intelligence in Space-Limitations and its Solutions to Interplanetary CubeSats. In Proceedings of the 2023 International Conference on Innovative Data Communication Technologies and Application (ICIDCA), Uttarakhand, India, 14–16 March 2023.
74. Wang, J.; Manohar, V.; Rahmat-Samii, Y. Beam Steerable Reflectarray Enabling CubeSat Internet of Space: Conceptualization and Design (Invited Paper). In Proceedings of the 2020 14th European Conference on Antennas and Propagation (EuCAP), Copenhagen, Denmark, 15–20 March 2020.
75. Available online: <https://www.nasa.gov/smallsat-institute/sst-soa/soa-communications> (accessed on 12 February 2024).
76. Song, J.; Castellanos, M.R.; Love, D.J. *Key Technologies For 5G Wireless Systems. Part II Physical Layer Communication Techniques*; Cambridge University Press: Boston, MA, USA, 2017; pp. 188–213. [CrossRef]
77. Bing, L.; Gu, Y.; Hu, L.; Aulin, T.; Yin, Y.; Wang, J. QoS Provision for Industrial IoT Net-working: Multiantenna NOMA Based on Partial CSIT. *IEEE Trans. Ind. Inform.* **2024**, *20*, 8239–8250. [CrossRef]
78. Hong, W.; Jiang, Z.H.; Yu, C.; Hou, D.; Wang, H.; Guo, C. The Role of Millimeter-Wave Technologies in 5G/6G Wireless Communications. *IEEE J. Microw.* **2021**, *1*, 101–122. [CrossRef]
79. Hu, J.; Bandyopadhyay, S.; Liu, Y.-H.; Shao, L.-Y. A Review on Metasurface: From Principle to Smart Metadevices. *Front. Phys.* **2021**, *8*, 5860787. [CrossRef]
80. Kumar, M.V.; Sharma, D. A metasurface antenna with beam steering capabilities for radio frequency energy harvesting. *Comput. Electr. Eng.* **2024**, *118*, 109443. [CrossRef]
81. Boyarsky, M.; Sleasman, T.; Imani, M.F.; Gollub, J.N.; Smith, D.R. Electronically steered metasurface antenna. *Sci. Rep.* **2021**, *11*, 4693. [CrossRef]
82. Ataloglou, V.G.; Kim, M.; Eleftheriades, G.V. Huygens Metasurfaces for Antenna Beamforming and Beamsteering. In Proceedings of the 2022 16th European Conference on Antennas and Propagation (EuCAP), Dublin, Ireland, 27 March 2022.
83. Ahmed, F.; Singh, K.; Esselle, K.P.; Thalakituna, D. Metasurface-Driven Beam Steering Antenna for Satellite Communications. In Proceedings of the 2022 5th International Conference on Communications, Signal Processing, and their Applications (ICCSIPA), Cairo, Egypt, 27–29 December 2022.
84. Jahangiri, M.; Soleimani, H.; Soleimani, M. Beam steering by two vertically faced metasurfaces using polarization free unit cells with three operating modes. *Sci. Rep.* **2025**, *15*, 394. [CrossRef]
85. Ghafari, V.; Yousef, L. Integrated optical beam steering device using switchable nanoantennas and a reflective metalens. *Sci. Rep.* **2023**, *13*, 7099. [CrossRef] [PubMed]
86. Suryapaga, V.; Khairnar, V.V. Pattern reconfigurable antenna with two-dimensional beam steering capability using metasurface. *AEU Int. J. Electron. Commun.* **2024**, *177*, 155213. [CrossRef]
87. Zhang, Y.; Tang, S.; Rao, J.; Chiu, C.-Y.; Chen, X.; Murch, R. A Dual-Port Dual-Beam Pattern-Reconfigurable Antenna With Independent 2-D Beam-Scanning. *IEEE Trans. Antennas Propag.* **2024**, *72*, 7628–7643. [CrossRef]

88. Sheng, L.; Luo, Y.; Ning, G.; Meng, L.; Cao, W. A Low-Cost Multibeam Switching Antenna Using Reconfigurable Hybrid Metasurface for Beamforming Applications. *Micromachines* **2023**, *14*, 1631. [CrossRef] [PubMed]
89. Dutta, R.K.; Bandyopadhyay, B.; Jaiswal, R.K.; Srivastava, K.V. Beamforming of a Linear Antenna Array Using Reconfigurable Frequency Selective Surface. In Proceedings of the 2023 IEEE Microwaves, Antennas, and Propagation Conference (MAPCON), Ahmedabad, India, 11–14 December 2023.
90. Choi, Y.-S.; Park, J.-S.; Lee, W.-S. Beam-Reconfigurable Multi-Antenna System with Beam-Combining Technology for UAV-to-Everything Communications. *Electronics* **2020**, *9*, 980. [CrossRef]
91. Fan, Y.; Chen, J.; Mou, C. Pattern-reconfigurable integrated array antenna based on a coding metasurface. *Opt. Express* **2024**, *32*, 8816. [CrossRef]
92. Ali, Q.; Shahzad, W.; Ahmad, I.; Safiq, S.; Bin, X.; Abbas, S.M.; Sun, H. Recent Developments and Challenges on Beam Steering Characteristics of Reconfigurable Transmitarray Antennas. *Electronics* **2022**, *11*, 587. [CrossRef]
93. Beiranvand, B.; Mirzavand, R. Enhancing wireless applications through reconfigurable electromechanical reflectarray antenna design for beam steering. *Sci. Rep.* **2024**, *14*, 30140. [CrossRef]
94. Nissanov, U.; Singh, G. Beamforming D-band phased array microstrip antennas. *Sens. Int.* **2022**, *3*, 100196. [CrossRef]
95. Abbas, S.M.; Ali, R.L.; Nawaz, H.; Saleem, I.; Khan, S.A. Microstrip Antenna Array for Beamforming Systems. *J. Prz. Elektrotechniczny* **2012**, *88*, 170–173.
96. Yu, Z.; Feng, W.; Song, X. A beamforming microstrip array antenna for K-band applications. In Proceedings of the 2022 International Applied Computational Electromagnetics Society Symposium (ACES-China), Xuzhou, China, 9–12 December 2022.
97. Aluigi, L.; Orecchini, G.; Larcher, L. A 28 GHz scalable beamforming system for 5G automotive connectivity: An integrated patch antenna and power amplifier solution. In Proceedings of the 2018 IEEE MTT-S International Microwave Workshop Series on 5G Hardware and System Technologies (IMWS-5G), Dublin, Ireland, 30–31 August 2018; pp. 1–3. [CrossRef]
98. Cao, Y.; Chin, K.S.; Che, W.; Yang, W.; Li, E.S. A compact 38 GHz multi-beam antenna array with multi-folded Butler matrix for 5G applications. *IEEE Antennas Wirel. Propag. Lett.* **2017**, *16*, 2996–2999. [CrossRef]
99. Saeed, M.A.; Obi, E.R.; Nwajana, A.O. A Compact Linear Microstrip Patch Beamformer Antenna Array for Millimeter-Wave Future Communication. *Sensors* **2024**, *24*, 4068. [CrossRef] [PubMed]
100. Trzebiatowski, K.; Kalista, W.; Rzymowski, M.; Kulas, L.; Nyka, K. Multibeam Antenna for Ka-Band CubeSat Connectivity Using 3-D Printed Lens and Antenna Array. *IEEE Antennas Wirel. Propag. Lett.* **2022**, *21*, 2244–2248. [CrossRef]
101. Ahmed, F.; Afzal, M.U.; Esselle, K.P.; Thalakituna, D.N. Novel Dual-Band Phase-Gradient Metascreen and Dual-Band Near-Field Meta-Steering Antenna. *IEEE Trans. Antennas Propag.* **2024**, *72*, 2202–2216. [CrossRef]
102. Yang, G.; Zhang, S. Dual-band shared-aperture multiple antenna system with beam steering for 5G applications. *IEEE Trans. Circuits Syst. II Express Briefs* **2022**, *69*, 4804–4808. [CrossRef]
103. Nam, Y.H.; Kim, Y.; Lee, S.G.; Lee, J.H. Hybrid reflectarray antenna of passive and active unit cells for highly directive two-direction beam steering. *IEEE Access* **2022**, *11*, 6299–6304. [CrossRef]
104. Lei, H.; Liu, Y.; Jia, Y.; Yue, Z.; Wang, X. A low-profile dual-band dual-circularly polarized folded transmitarray antenna with independent beam control. *IEEE Trans. Antennas Propag.* **2021**, *70*, 3852–3857. [CrossRef]
105. Aziz, A.; Zhang, X.; Yang, F.; Xu, S.; Li, M. A dual-band orthogonally polarized contour beam transmitarray design. *IEEE Trans. Antennas Propag.* **2021**, *69*, 4538–4545. [CrossRef]
106. Emara, M.K.; Tomura, T.; Hirokawa, J.; Gupta, S. Fabry–Pérot-Based Compound All-Dielectric Huygens Structure for Circularly Polarized Millimeter-Wave Beamforming. *IEEE Antennas Wirel. Propag. Lett.* **2020**, *19*, 1784–1788. [CrossRef]
107. Lima, E.B.; Matos, S.A.; Costa, J.R.; Fernandes, C.A.; Fonseca, N.J. Circular polarization wide-angle beam steering at Ka-band by in-plane translation of a plate lens antenna. *IEEE Trans. Antennas Propag.* **2015**, *63*, 5443–5455. [CrossRef]
108. Li, X.; Wang, L.; Wang, J.; Goussetis, G. Conformal High Gain Aperture Antenna Based on Leaky-Wave Array for CubeSat Communication. In Proceedings of the 2020 International Symposium on Antennas and Propagation (ISAP), Osaka, Japan, 25–28 January 2021. [CrossRef]
109. Putra, N.A.H. Design of Cubesat Microstrip Antenna with Metamaterial Structure for LoRa Communication. In Proceedings of the 2021 IEEE International Conference on Aerospace Electronics and Remote Sensing Technology (ICARES), Bali, Indonesia, 3–4 November 2021.
110. Federico, G.; Hubrechsen, A.; Coenen, S.L.; Reniers, A.D.C.F.; Caratelli, D.; Smolders, A.B. A Wide-Scanning Metasurface Antenna Array for 5G Millimeter-Wave Communication Devices. *IEEE Access* **2022**, *10*, 102308–102315. [CrossRef]
111. Altunc, S.; Kegege, O.; Bundick, S.; Shaw, H.; Schaire, S.; Bussey, G.; Crum, G.; Burke, J.C. X-band CubeSat Communication System Demonstration. In Proceedings of the 29th Annual AIAA/USU Conference on Small Satellites, All Systems Go! Critical Pieces for Mission Success 2015, Logan, UT, USA, 12 August 2015; pp. 1–9.
112. Zhou, M.; Rubæk, T.; Ericsson, A.; Bilgic, M.M.; Jørgensen, E. Design and RF Testing of Reflectarray for Cubesat at X-band. In Proceedings of the 41st ESA Antenna Workshop on Large Deployable Antennas at ESA-ESTEC, Noordwijk, The Netherlands, 25–28 September 2023.

113. Alqaraghuli, A.J.; Singh, A.; Jornet, J.M. Novel CubeSat Combined Antenna Deployment and Beam Steering Method Using Motorized Rods for Terahertz Space Networks. In Proceedings of the 2021 IEEE Conference on Antenna Measurements & Applications (CAMA), Antibes Juan-les-Pins, France, 15–17 November 2021.
114. Bountzioukas, P.; Kikas, G.; Tsiolakis, C.; Stoupis, D.; Chatziargyriou, E.; Hatzopoulos, A.; Kourampa-Gottfroh, V.; Karakosta-Amarantidou, I.; Mavropoulos, A.; Komis, I.-N.; et al. The Evolution from Design to Verification of the Antenna System and Mechanisms in the AcubeSAT mission. In Proceedings of the 74th International Astronautical Congress (IAC), Baku, Azerbaijan, 2–6 October 2023.
115. LaCalli, K. Phased Helical Antenna Array for CubeSat Application. Bachelor's Thesis, The Faculty and the Honors Program of the University of San Diego, San Diego, CA, USA, 19 December 2016.
116. Available online: https://utahstatemagazine.usu.edu/research/get-away-special-team-is-using-cubesats-to-push-space-research-boundaries/?utm_source=chatgpt.com (accessed on 19 December 2024).
117. Available online: <https://ksat-stuttgart.de/projekte/source/> (accessed on 15 October 2019).

Disclaimer/Publisher's Note: The statements, opinions and data contained in all publications are solely those of the individual author(s) and contributor(s) and not of MDPI and/or the editor(s). MDPI and/or the editor(s) disclaim responsibility for any injury to people or property resulting from any ideas, methods, instructions or products referred to in the content.

Article

Dual-Band Dual-Circularly Polarized Shared-Aperture Phased Array for S-/C-Band Satellite Communications

Yuanming Xiao ^{1,2} , Lianxing He ^{1,2,*} and Xiaoli Wei ^{1,2}

¹ The Innovation Academy for Microsatellites, Chinese Academy of Sciences (IAMCAS), Shanghai 201304, China; xiaoyuanming20@mailsucas.ac.cn (Y.X.); weixl@alumni.shanghaitech.edu.cn (X.W.)
² University of Chinese Academy of Sciences, Beijing 100049, China
* Correspondence: 13816474811@139.com

Abstract: In this article, a novel method of achieving a single-layer, dual-band, dual-circularly polarized (CP) shared-aperture phased array antenna with wide beam scanning coverage is presented. The space antenna was designed to provide direct-to-cellular communications services at S-/C-bands with a frequency ratio of 1:1.8. Using novel ceramic substrates with high dielectric constants for antenna miniaturization, the optimum interelement spacing can be ensured in one single layer to meet the large-angle scanning demand. The CP characteristic of the phased array is improved by the sequential rotation technique. A prototype of phased array, which is composed of an 8 × 8 S-band Rx array and a 16 × 16 C-band Tx array, is fabricated to verify this design. The measured results show that the shared-aperture phased array can provide ±50° beam scanning coverage at both the S- and C-bands simultaneously to meet the direct-to-cellular communication demand in low earth orbit (LEO) satellites.

Keywords: satellite communication; shared-aperture array; dual-band; dual-circular polarized; single layer



Academic Editors: Djuradj Budimir, Ladislau Matekovits, Raad Raad and Faisal Tubbal

Received: 14 November 2024

Revised: 25 December 2024

Accepted: 29 December 2024

Published: 20 January 2025

Citation: Xiao, Y.; He, L.; Wei, X. Dual-Band Dual-Circularly Polarized Shared-Aperture Phased Array for S-/C-Band Satellite Communications. *Electronics* **2025**, *14*, 387. <https://doi.org/10.3390/electronics14020387>

Copyright: © 2025 by the authors. Licensee MDPI, Basel, Switzerland. This article is an open access article distributed under the terms and conditions of the Creative Commons Attribution (CC BY) license (<https://creativecommons.org/licenses/by/4.0/>).

1. Introduction

Commercial off-the-shelf cellular phones, or “stock” cellular phones, have a demand to establish connectivity directly with the satellite for voice, messaging, and basic web browsing services, especially outside the reach of traditional terrestrial mobile networks. Due to the limitation of terrestrial mobile terminals in gain and transmission power, a large aperture of phased array antenna for satellite payload is needed to improve the passive gain and realize direct-to-cellular communications. The space antenna with a large aperture should have the merits of a low-profile, shared aperture for RX/TX, be lightweight, and be deployable to meet the serious demands of limited space, weight, and power in a satellite platform.

This work has selected the S-/C-band for direct-to-cellular communications services, specifically 1.9–2 GHz and 3.4–3.6 GHz for the downlink and uplink, respectively. However, it is costly to support two separate downlink and uplink phase arrays simultaneously, especially for a satellite with limited space and resources. The shared-aperture antenna is thus an attractive candidate due to its compact space and cost-effective manufacture [1]. Circularly polarized (CP) antennas have many advantages [2,3] over linearly polarized antennas [4–6]. For example, due to its lower attenuation in complex climatic environments, the CP antenna could penetrate the ionosphere and overcome the Faraday Effect in the ionosphere between satellite and earth communications. Therefore, CP antennas have an important significance in direct-to-cellular communications.

Recently, different antennas for space applications with dual-band and dual-CP operation have been reported. A simple way to achieve dual-band dual-CP operation is to use a reflector and feed horn with dual-frequency dual-CP characteristics [7,8]. However, the reflector antenna is relatively too high and heavy for the application of the multi-satellite launch mode. Therefore, the planar phased array based on microstrip antenna technology is a better choice. In [9], this antenna is fed by microstrip lines with double orthogonal slits, and the circular-polarized radiation can be realized by tuning the quadrature slits with appropriate amplitude and phase. However, two orthogonal double-slit structures are too large and complicated to be arranged for dual-frequency dual-CP operation in the phased array normally with an elements space of half-wavelength. More commonly, dual-frequency, dual-CP performance is realized by multi-layer stacking [10–12] with two different elements for different frequencies, respectively. The multi-layer stacking structure can effectively improve the isolation between the two bands. However, the axial ratio (AR) and the gain of the lower frequency antenna are normally deteriorated due to the shielding of the upper layer. Moreover, multi-layer antennas are less stable than single-layer antennas and have the potential risk of delamination in the complex space environment, with alternate operation temperatures from -90°C to 90°C in low earth orbit (LEO) as an example.

Several antennas have also been proposed to achieve dual-frequency dual-CP through single-layer structures, such as monopole [13], slot [14], and patch [15]. However, these antennas have complex fed structures and are still difficult to form large arrays for the satellite payloads with direct-to-cellular communication capability. In design [13], two orthogonal E vectors with a 90-degree phase difference is excited in a planar monopole antenna for dual-CP operation. However, this monopole with a CPW ground is not suitable for working as a radiation element of a phased array. In design [14], a dual-CP, single-layer, full-metal slot array antenna in gap waveguide technology is proposed. However, this antenna has a complex fed structure and is too bulky to form a large direct-to-cellular communication payload, which is operated in the S-/C-band. An approach to implement the dual-band dual-CP array with a single-layer substrate is also reported in [15]; dual-CP operation is achieved by directly connecting two patches operating at 2 different frequencies and different polarizations. However, the maximum element spacing in high frequency is limited to avoid grating lobes in large scanning angles, which means that the element spacing in low frequency is very small under the same aperture, with the same element number for high- and low-frequency elements as shown in [14]. The gain of the low-frequency antenna array is thus sacrificed. Furthermore, the strong mutual coupling and poor isolation due to the small element spacing will greatly decrease the capability of wide-angle beam scanning in the low-frequency band. Ensuring a wide-angle beam scanning capability for both high- and low-frequency band operation simultaneously and arranging all the elements appropriately on one single-layer substrate is never a trivial task, especially under the limit of a special high-low-frequency ratio.

In this paper, a dual-band, dual-CP, shared-aperture phased array antenna is proposed for direct-to-cellular communications. The proposed shared-aperture array is composed of two separate antenna arrays with single-layer structures, viz., a 16×16 Tx antenna phased array with left-handed circular polarization (LHCP) and an 8×8 Rx antenna phased array with right-handed circular polarization (RHCP), respectively. To meet the demands of antenna element miniaturization and low profile of satellite payload antennas, radiation elements are optimized using ceramic substrates with appropriate dielectric constant and optimum interelement spacing on one single layer, to ensure a wide-angle beam scanning capability for both high- and low-frequency band operation without a grating lobe.

To the authors' best knowledge, it is the first time to achieve the large-angle beam scanning capability with $\theta \geq 50^\circ$ in the elevation plane for S-/C-band simultaneously in one single-layer shared-aperture array based on high dielectric ceramic antenna technology.

This article is organized as follows. Section 2 describes the configuration and design principles of the proposed dual-band, dual-CP phased array and elements. Section 3 presents simulation results and experimental results. Section 4 shows the performance of the proposed antenna array compared with other related works. Finally, the conclusion is shown in Section 5.

2. Configurations and Design Principles

2.1. Architecture of the Shared-Aperture CP Array

The array lattice arrangement is crucial to achieving a good radiation performance for a dual-band phased array [16]. Within the scanning range, the appropriate element arrangement should meet the demand of avoiding grating lobes first. In addition, the element spacing should be large enough to allow element implementation in engineering, which can effectively help to improve the isolation performance between co-frequency elements and different-frequency elements. To avoid the generation of grating lobes, the element spacing should meet the requirement as shown in the following expression:

$$d \leq \frac{\lambda}{1 + \sin \theta_0} \quad (1)$$

The maximum scanning angle is θ_0 . λ is the wavelength of the corresponding frequency in free space. The shared-aperture array has a small frequency ratio of about 1:1.8 between two operating bandwidths. To arrange as many elements as possible under the same aperture and avoid grating lobes, the element interval is chosen to be $d_s = 0.58 \lambda_s$ for the S-band array and $d_c = 0.52 \lambda_c$ for the C-band array, as shown in Figure 1a.

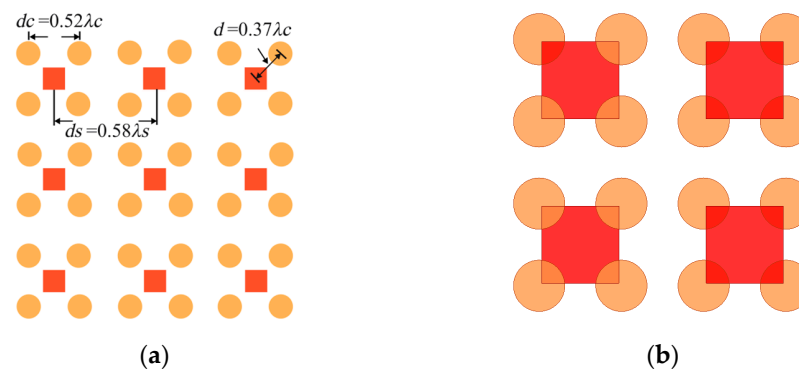


Figure 1. Shared-aperture phased array lattice (a) array lattice; (b) array lattice with traditional PCB substrate. (The yellow ones are C band elements and the red ones are S band elements).

One can see that the spacing d between the S-band and the C-band elements is only $0.37 \lambda_c$, and it is really difficult to implement both S- and C-band elements using one radio frequency (RF) printed circuit board (PCB) substrate with the same dielectric constant (normally with a dielectric constant less than 10) because the elements of high frequency are partially touched with the elements of low frequency already, as illustrated in Figure 1b. Two high-permittivity ceramic antenna elements are thus chosen to address this issue.

2.2. S-/C-Band Elements and Generation of CP

It is well known that increasing the dielectric constant of the substrate (while reducing the dimensions of the antenna) results in a narrower bandwidth [17]. At the same time, increasing the thickness of the substrate is helpful to increase the operating bandwidth

(by reducing the quality factor). To ensure the spacing between the two nearest elements is as large as possible, we truncated the ceramic substrate to a size that is slightly larger than the size of the printed patch, which shows an extra contribution to reduce the surface wave loss.

Figure 2 shows the configuration of the CP element for the C-band. The antenna is composed of a top circular metallic patch (radius R_p), a ceramic substrate (with a dielectric constant of 15, $\tan\delta = 2.2 \times 10^{-4}$, and thickness h of 6 mm), and a metal ground plane. Notably, a slot is cut on the top metallic patch, which produces the CP radiation characteristics and increases the bandwidth by changing the current flow path on the surface of the patch antenna (the slot is deviated from the y -axis by 45°). Furthermore, the slot also contributes to a further diminution of the antenna's overall dimensions, thereby enhancing its suitability for the compact layout of the array where space is also a limiting factor. The feed probe is offset from the Y -axis to ensure a good impedance match (the proposed antennas are all fed by coaxial cables). In order to ensure the flexibility of the sequential rotating installation of the above structure, the corners are cut on both sides of the patch and the ceramic substrate. Other detailed structural parameters of the element antenna are listed in the caption of Figure 2.

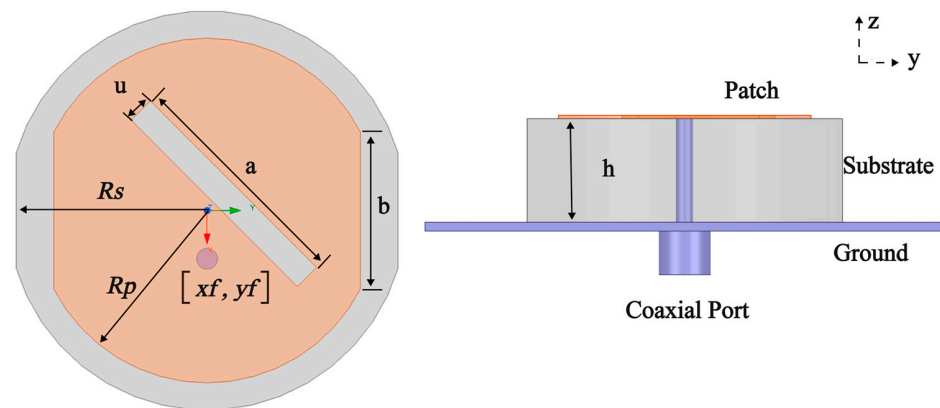


Figure 2. Geometry of the C-band antenna. Dimensions are $R_s = 9.5$, $R_p = 8.2$, $h = 6$, $a = 11.2$, $b = 7.5$, $u = 1.3$. (unit: millimeter).

The configuration of the S-band element is shown in Figure 3. The square substrate with the same dielectric constant as that of the C-band antenna element is adopted. The element incorporates four truncated corners, a design feature that helps in optimizing the radiation characteristics and impedance matching. A slot in the center of the metallic patch is used to increase impedance bandwidth and decrease the antenna size further (the slot is deviated from the y -axis by 45°).

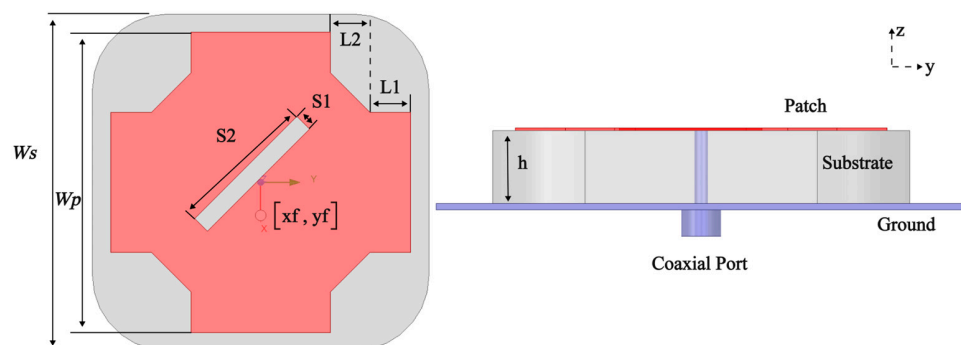


Figure 3. Geometry of the S-band antenna. Dimensions are $W_s = 32$, $W_p = 28$, $h = 6$, $S_1 = 1.7$, $S_2 = 13.5$, $L_1 = 3.8$, $L_2 = 3.7$. (unit: millimeter).

2.3. Array Design: Sequential Rotation

A good CP performance is essential for satellite communication, as the 3 dB AR bandwidth of the elements is comparatively a little narrow to meet the requirements of the application. The sequential rotation technique is used to increase the CP radiation performance and AR bandwidth of the phased array. The sequential rotation technique can disrupt the mutual coupling effect among array elements through rotation among them, thereby improving the antenna’s cross-polarization performance and axial ratio performance. For a four-element subarray, four elements are respectively rotated around the center in an anticlockwise or clockwise direction; the phases of these elements are set to 0° , 90° , 180° , and 270° , respectively, and RHCP or LHCP will be obtained. With this method, the AR bandwidth of the array can be greatly increased.

The basic principles of sequential rotation are shown in Figure 4. The C-band elements rotate in a clockwise direction to realize LHCP, while the S-band elements gradually increase the phase in an anticlockwise direction to realize RHCP within the same aperture.

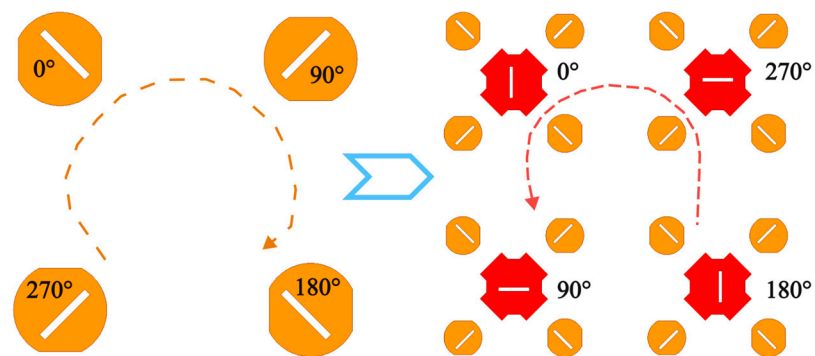


Figure 4. Principles of sequential rotation technique.

For brevity, the final layout of the proposed one-quarter subarray is shown in Figure 5. Due to the utilization of the as-proposed antenna element based on the ceramic dielectric substrate, it can be observed that the presence of air among the elements is also beneficial to the lightweight design of the antenna and offers more flexibility for antenna installation. Furthermore, the single-layer structure is not only conducive to the large-scale formation of phase arrays but also beneficial to the design of radio frequency feeding networks on satellite solar panels operating in space.

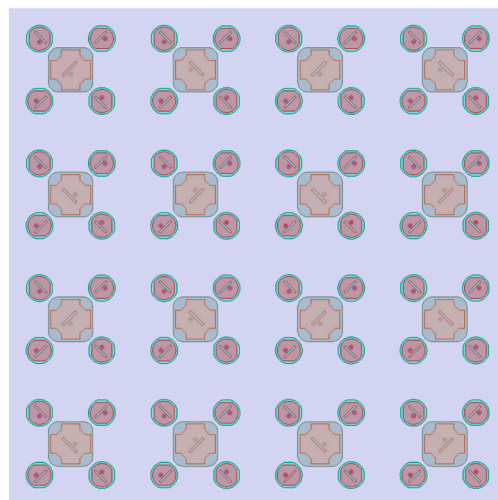


Figure 5. The final layout of the S-/C-band CP antenna subarray.

3. Results

The proposed antenna was simulated and well-optimized according to the required design specifications. This work was simulated and studied through the full-wave simulation software HFSS. Based on the simulated results, the prototype of a dual-band shared-aperture phased array antenna was developed. Then, the fabricated antenna array prototype was tested, and the measured results of the antenna array prototype were compared with the simulated results.

3.1. Simulated Results

To illustrate the operational mechanism of the element antennas, we performed the surface current distributions of two elements at specific time instances (e.g., phase = 0° and 90°) within a period, as shown in Figure 6. As shown in Figure 6a, the surface current direction of the S-band antenna element rotates in the anticlockwise direction, achieving RHCP radiation. On the other hand, the surface current direction of the C-band antenna element will rotate in the clockwise direction, and an LHCP radiation is thus achieved, as shown in Figure 6b.

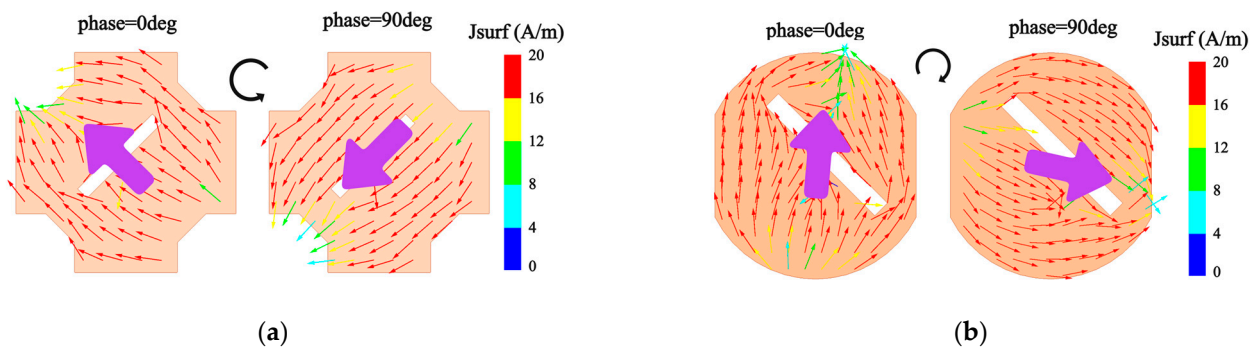


Figure 6. Simulated current distributions of (a) the S-band element at 1.975 GHz; (b) the C-band element at 3.55 GHz.

For the purpose of elucidating the operational mechanism of the offset of excitation, the surface electric field distributions of the S- and C-band antenna elements were investigated, as depicted in Figure 7. It is a well-established principle in the field of electromagnetics that a diminished electric field intensity correlates with a relatively reduced impedance value. Consequently, by positioning the probe in the vicinity of points characterized by lower electric field intensity, the attainment of favorable impedance matching conditions can be ensured. This approach is predicated on the fundamental understanding of the relationship between electric field characteristics and impedance behavior, thereby facilitating the optimization of antenna performance through precise manipulation of the probe location with respect to the electric field distribution. In Figure 7, it can be seen that the electric field intensities at the positions where the two probes are located are relatively weak, indicating that the antenna has a relatively good impedance matching at this time. For the S-band element antenna, the offset of the probe relative to the y -axis is 1.4 mm (millimeter); on the other hand, on the patch of the C-band element, the probe offset is about 2.3 mm.

The simulated S_{11} and the gain of the elements are shown in Figure 8. As shown in Figure 8a, the simulated -10 dB impedance bandwidth of the S-band antenna is about 6.6% from 1.91 GHz to 2.04 GHz. A simulated maximum gain of 6.76 dBi is attained at the center frequency of 1.97 GHz. The peak gain does not take into account the mismatch caused by reflection. The gain variation of the antenna is less than 0.1 dBi over the whole operation band. The simulated results of the C-band element are depicted in Figure 8b; the simulated S_{11} shows that the impedance bandwidth is about 10% from 3.37 to 3.73 GHz. A simulated

maximum gain of 6.84 dBi is achieved at a center frequency of 3.55 GHz. The peak gain is higher than 6.5 dBi with a variation of less than 0.2 dBi over the whole operation band. Notably, the reason that the impedance bandwidth in the C-band is higher than that in the S-band is its relatively greater thickness (the element in the C-band is $0.071 \lambda_c$, while that in the S-band is $0.04 \lambda_s$).

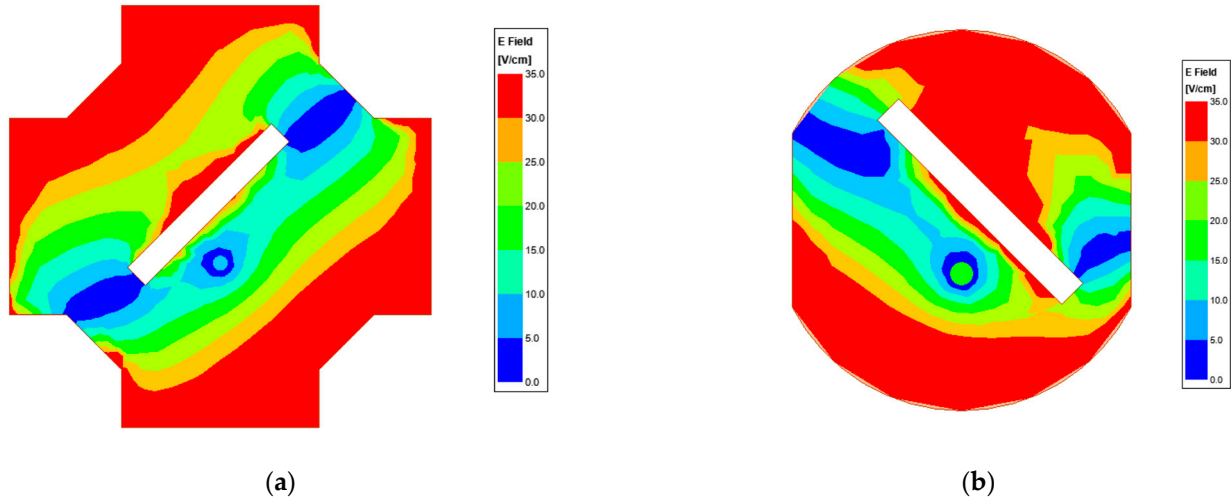


Figure 7. Simulated electric field distributions of (a) the S-band element at 1.975 GHz; and (b) the C-band element at 3.55 GHz.

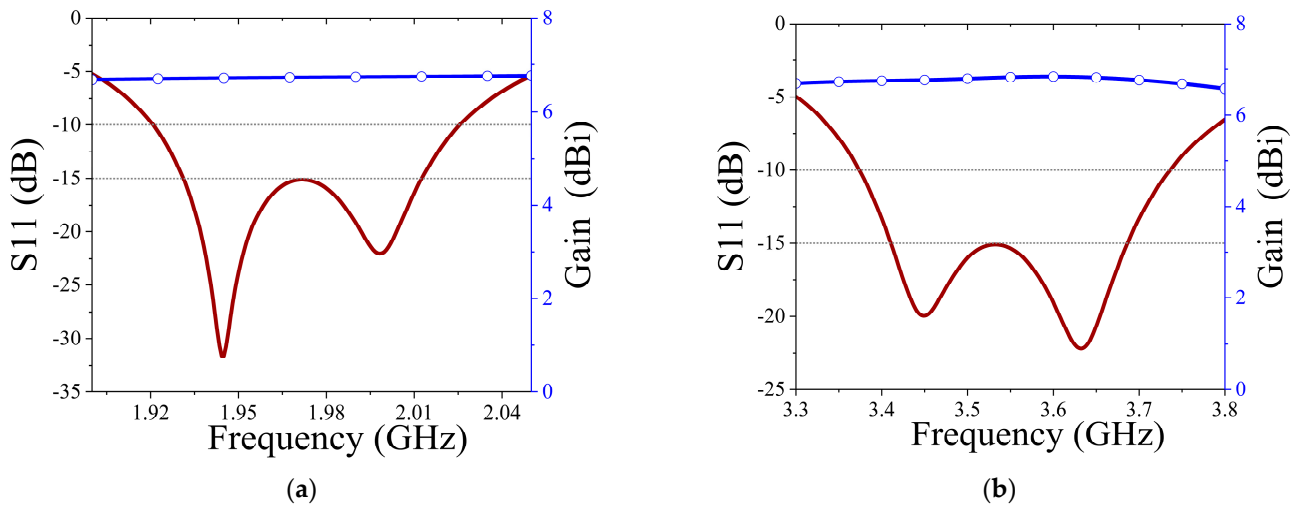


Figure 8. Simulated S_{11} and gains (a) the S-band antenna element; and (b) the C-band antenna element.

The simulated AR of the proposed shared-aperture array is shown in Figure 9; one can see that a good CP performance with AR less than 0.5 dB is obtained in the whole operating bands of S-/C-bands. For the proposed array, such excellent circular polarization performance within the two frequency bands benefits from the application of the sequential rotation technique.

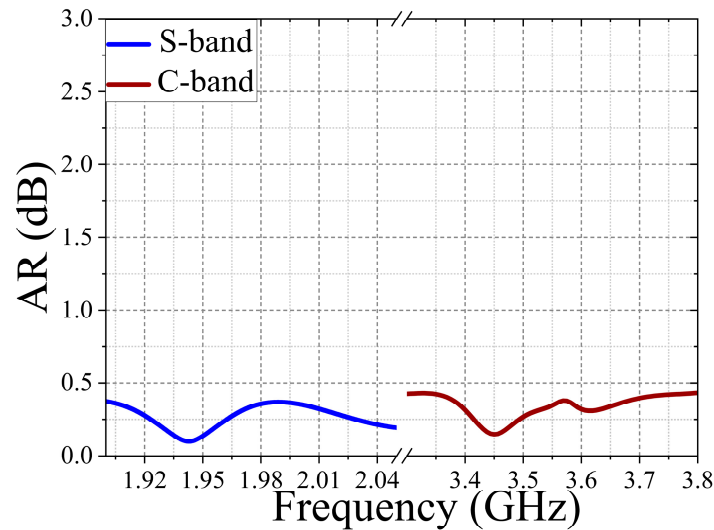


Figure 9. The simulated ARs of the S-/C-band CP antenna array.

3.2. Antenna Prototype Fabrication and Measurement

A prototype of the proposed shared-aperture phased array antenna is developed, and the scanning performance is measured in a near-field anechoic chamber, as shown in Figure 10. The excitation of each element by the coaxial Sub Miniature version A (SMA) is fed through the beam controller. The array scanning can be achieved by changing the phase difference of each element. Due to the limitations of test time and venue, the array performances at 1.97 GHz for the S-band and at 3.55 GHz for the C-band were tested. These measured results are sufficient to verify the design validity of the proposed phased array antenna.

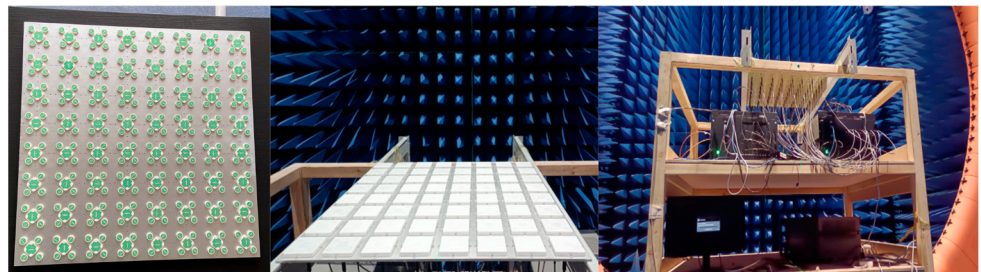


Figure 10. Prototype of the fabricated as-proposed antenna in a near-field anechoic chamber.

Figure 11a shows the simulation and measurement S_{11} of the proposed antenna array at the S-band. As shown, a good agreement between the simulated and measured is attained, showing a relative bandwidth of about 5.3% from 1.93 to 2.03 GHz with S_{11} less than -10 dB. The simulation and measurement S_{11} at the C-band are depicted in Figure 11b. The measurement agrees well with the simulated results, which show a relative bandwidth of about 11% from 3.36 to 3.75 GHz with S_{11} less than -10 dB.

The isolation between the nearest two different-frequency elements is shown in Figure 12. For the convenience of analysis, the port sequence is marked in Figure 12. P1 and P2 are two adjacent C-band ports, respectively, while P3 and P4 are two adjacent S-band ports, respectively. The simulated and measured isolations (S_{34} and S_{12}) between the nearest S-/C-band elements are higher than 20 dB across the operating S-band and C-band. Similarly, the simulated and measured isolations (S_{31} and S_{13}) between the S-band element and its nearest C-band elements are higher than 20 dB across the operating S-band and C-band. The results represent the proposed S-band and C-band antenna arrays that can effectively work at the same time without serious coupling and interference. In addi-

tion, the S_{11} and isolations of the proposed phased array were measured through a vector network analyzer, the Rohde & Schwarz ZNB 40.

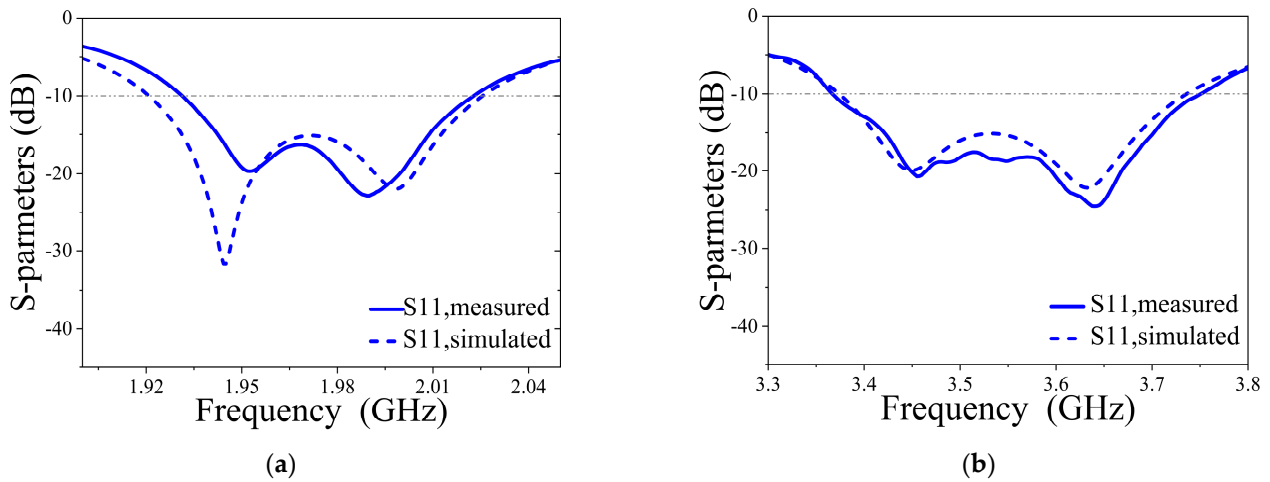


Figure 11. Simulated and measured S-parameters of the antenna (a) at S-band; and (b) at C-band.

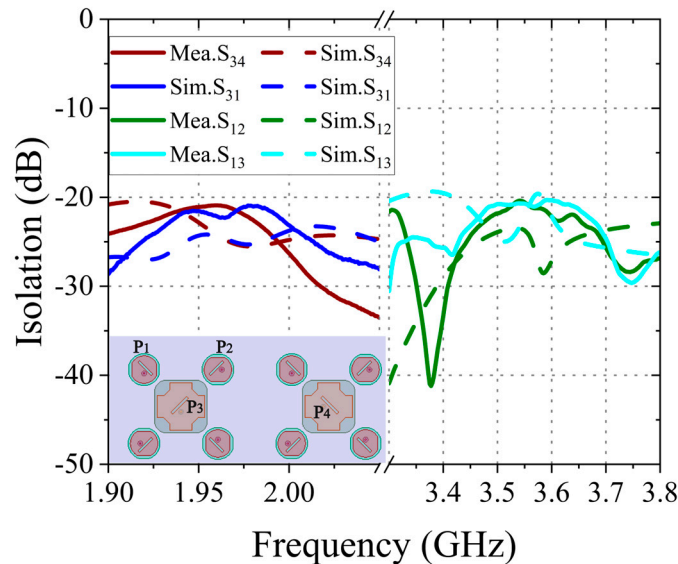


Figure 12. Simulated and measured isolations between the S-/C-band.

The simulated and measured normalized radiation pattern of the S-band array is shown in Figure 13. Notably, θ and φ are the scanning angles of the array (θ represents the elevation angle and φ represents the azimuth angle). In addition, the excitations of all ports are of equal amplitude, and the scanning of the array is achieved by changing the phase differences among the ports. A maximum gain drop of approximately 4.5 dB is observed when the scan angle is up to 50° ($\theta = 50^\circ, \varphi = 0^\circ$). As can be seen, an obvious grating lobe appeared when the array pattern pointed down to 50° as the element spacing is exactly 0.58λ at 1.97 GHz, which is close to the minimum spacing of generating grating lobes. Because the gain drop is less than 4.5 dB, the above grating lobe is still acceptable.

The simulated and measured radiation pattern of the C-band array at the center frequency of 3.55 GHz is shown in Figure 14a. The maximum gain drop of 3.4 dB is observed when the beam is scanning up to 50° ($\theta = 50^\circ, \varphi = 0^\circ$), the measurement result agrees well with the simulated results. Limited by the number of phase-shifter channels of the testing equipment, only the scanning properties of the 64-element subarray located in the center of the 256-element array are measured. However, the simulation results of the

256-element array at 3.55 GHz, as presented in Figure 14b, show that a larger phased array has a better scanning performance at a large angle with gain drops less than 3 dB. It means that a phased array can be extended to a larger array with better scanning performance in a larger aperture for direct-to-cellular communications.

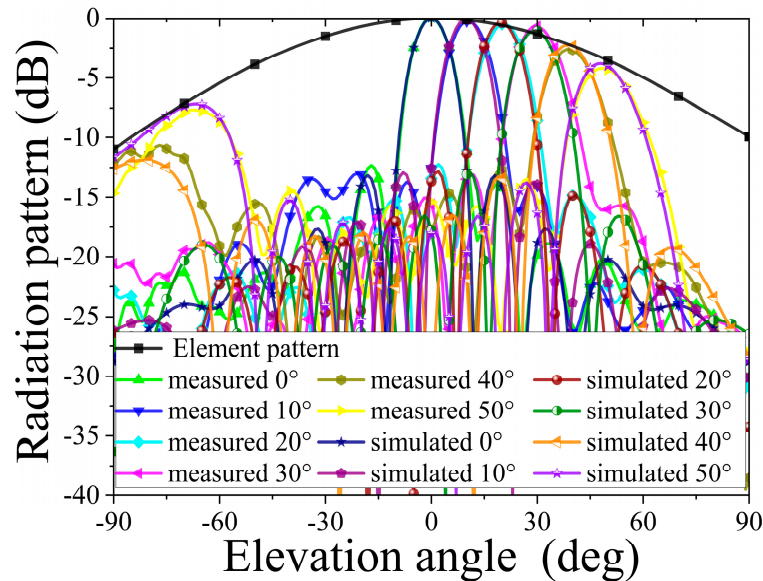


Figure 13. Simulated and measured radiation pattern of the S-band array at 1.97 GHz in $\varphi = 0^\circ$ plane when scanning to different angles.

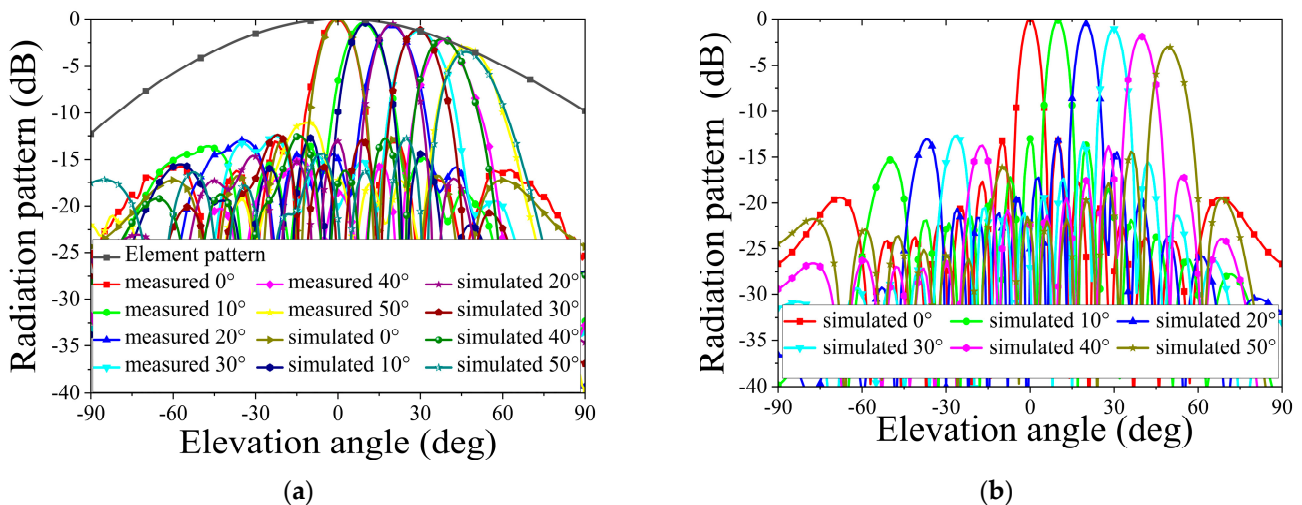


Figure 14. Array radiation patterns of the C-band array at 3.55 GHz in $\varphi = 0^\circ$ plane when scanning to different angles. (a) 64–element array; (b) 128–element array.

The simulated and measured AR at the different scanning angles of the S-/C-band phased array antennas are shown in Figures 15a and 15b, respectively. The AR values below 3 dB for both the S- and C-band are obtained with measured results a little higher than that of the simulation, which is probably caused by the phase errors imported by the phase-shifter channels of the test equipment. The good performance also demonstrates the enhancement of the circular polarization radiation performance of the array by the sequential rotation technique.

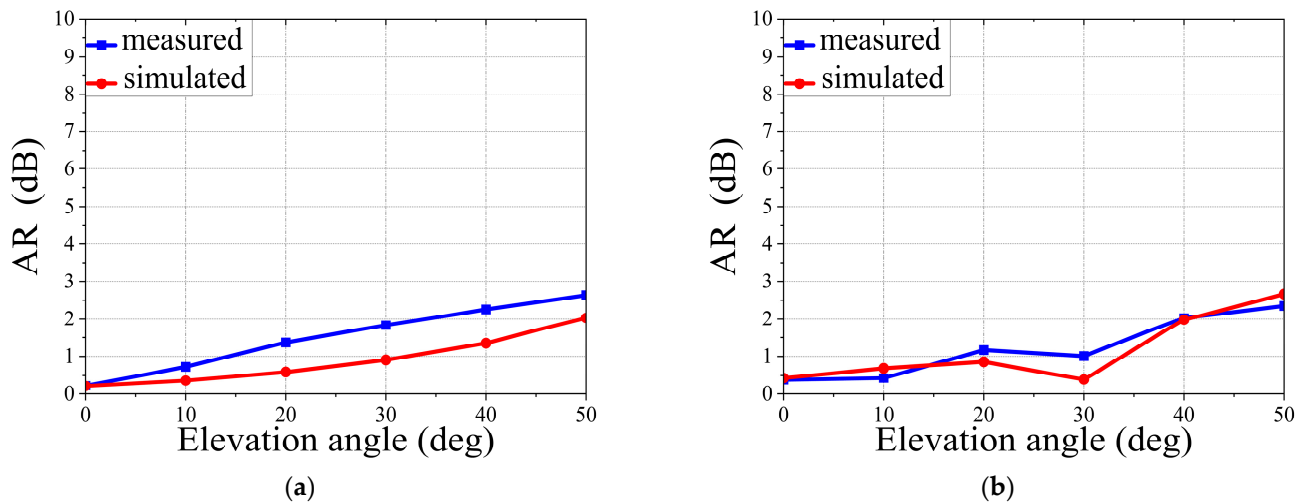


Figure 15. Simulated and measured AR at the different scanning directions (a) at 1.97 GHz; (b) 64-element array at 3.55 GHz.

The measured parameters of the proposed dual-band, dual-CP phased array are summarized in Table 1. It can be seen that the proposed array with a single-layer structure has achieved RHCP and LHCP operations, respectively, within the proposed operating frequency band. In addition, it can be observed that the proposed array has the ability to scan up to 50° in the elevation direction within two frequency bands, with sidelobe level suppressions of -12.5 dB and -13.1 dB, respectively. All the measured results effectively verified the validity of our design, which indicates that the large-scale, dual-band, dual-circular-polarization, shared-aperture antenna array can be realized on a single-layer structure.

Table 1. Comparison of measured parameters between two bands of the proposed antenna array.

Operating Frequency	S @ 1.975 GHz	C @ 3.55 GHz
Bandwidth (GHz)	1.93–2.03 (5.3%)	3.36–3.75 (11%)
Polarization	RHCP	LHCP
Element Spacing	0.58λ	0.52λ
Boresight Gain of 64-Elements Array (dB)	23.57	23.34
Scanning Range	$\pm 50^\circ$	$\pm 50^\circ$
$\theta = 50^\circ$ Side Lobe Level (dB)	-12.5	-13.1

4. Discussion

Table 2 gives a comparison between the proposed shared-aperture phased array antenna and other related works. For dual-band, dual-CP antenna arrays, some of them [18,19] can achieve large-angle scanning, but the phased array with a multi-layer structure is too complex and has the potential risk of delamination in a satellite environment (alternatively operated from -90°C to 90°C in LEO). A dual-band, single-layer, shared-aperture antenna array [15,20], is mainly composed of traditional PCB CP patch elements, and they are limited by the larger element spacing and cannot provide the capability of large-angle scanning. Our proposal, with a single-layer shared-aperture structure, can provide stable wide-angle scanning of larger than $\pm 50^\circ$ for S-/C-bands without a serious grating lobe. It is thus a potential good candidate for direct-to-cellular satellite payload.

Table 2. Comparison between the proposed antenna array and other works.

Works	Operation Bands	Frequency Ratio	Structure	Element Spacing	Scanning Range
[18]	K/Ka	1:1.5	Multi-layer	$0.49 \lambda / 0.53 \lambda$	$55^\circ / 60^\circ$
[19]	Ku/K	1:1.5	Multi-layer	$0.63 \lambda / 0.62 \lambda$	$26^\circ / 30^\circ$
[15]	X/Ku	1:1.46	Single-layer	$0.67 \lambda / 0.95 \lambda$	-
[20]	S/C	1:1.45	Single-layer	$0.57 \lambda / 0.81 \lambda$	-
Our work	S/C	1:1.8	Single-layer	$0.58 \lambda / 0.52 \lambda$	$50^\circ / 50^\circ$

5. Conclusions

In this paper, a novel S-/C-band RHCP/LHCP shared-aperture phased array with large-angle beam scanning is proposed. The proposed array, based on high-dielectric ceramic technology, is arranged in one single layer. The optimum interelement spacing is ensured by the miniaturization of the elements to provide wide-angle scanning of larger than $\pm 50^\circ$ for both high- and low-frequency bands without a serious grating lobe. The CP characteristic of the phased array is improved by the sequential rotation technique. The simulated and measured results show that the shared-aperture phased array can effectively operate at the S-band (from 1.93 to 2.03 GHz) and C-band (from 3.32 to 3.71 GHz) simultaneously with a large-angle beam scanning up to $\pm 50^\circ$ and a good CP performance with AR less than 3 dB. Furthermore, the as-proposed array is convenient for expanding to a larger aperture phased array for satellite payloads with direct-to-cellular communications capability.

Author Contributions: Conceptualization, Y.X. and L.H.; methodology, Y.X.; software, Y.X.; validation, Y.X., L.H. and X.W.; formal analysis, Y.X.; investigation, Y.X.; resources, Y.X.; data curation, Y.X.; writing—original draft preparation, Y.X., L.H. and X.W.; writing—review and editing, Y.X., L.H. and X.W.; visualization, Y.X., L.H. and X.W.; supervision, Y.X.; project administration, Y.X. and L.H.; funding acquisition, Y.X., L.H. and X.W. All authors have read and agreed to the published version of the manuscript.

Funding: This research was funded by the National Natural Science Foundation of China (grant number U21A20443).

Data Availability Statement: Data are contained within the article.

Conflicts of Interest: The authors declare no conflicts of interest.

References

- Shafai, L.L.; Chamma, W.A.; Barakat, M.; Strickland, P.C.; Seguin, G. Dual-band dual-polarized perforated microstrip antennas for SAR applications. *IEEE Trans. Antennas Propag.* **2000**, *48*, 58–66. [CrossRef]
- Sung, Y. Dual-Band Circularly Polarized Pentagonal Slot Antenna. *IEEE Antennas Wirel. Propag. Lett.* **2011**, *10*, 259–261. [CrossRef]
- Ko, S.T.; Park, B.C.; Lee, J.H. Dual-Band Circularly Polarized Patch Antenna with First Positive and Negative Modes. *IEEE Antennas Wirel. Propag. Lett.* **2013**, *12*, 1165–1168. [CrossRef]
- Imbriale, W.A.; Boccia, L. *Space Antenna Handbook*; Wiley Online Library: Hoboken, NJ, USA, 2012.
- Li, B.; Yin, Y.Z.; Hu, W.; Ding, Y.; Zhao, Y. Wideband Dual-Polarized Patch Antenna with Low Cross Polarization and High Isolation. *IEEE Antennas Wirel. Propag. Lett.* **2012**, *11*, 427–430.
- Bai, C.X.; Cheng, Y.J.; Ding, Y.R.; Zhang, J.F. A Metamaterial-Based S/X-Band Shared-Aperture Phased-Array Antenna with Wide Beam Scanning Coverage. *IEEE Trans. Antennas Propag.* **2020**, *68*, 4283–4292. [CrossRef]
- Peng, W.F.; Ye, W.J.; He, S.H. A novel dual-band and dual circular-polarization feed for paraboloidal reflector antenna. In Proceedings of the 2012 International Conference on Microwave and Millimeter Wave Technology (ICMMT), Shenzhen, China, 5–8 May 2012; pp. 1–3.
- Sarkar, S.; Gupta, B. A Dual-Band Circularly Polarized Antenna with a Dual-Band AMC Reflector for RFID Readers. *IEEE Antennas Wirel. Propag. Lett.* **2020**, *19*, 796–800. [CrossRef]

9. Mao, C.X.; Gao, S.; Wang, Y.; Chu, Q.X.; Yang, X.X. Dual-Band Circularly Polarized Shared-Aperture Array for C-/X -Band Satellite Communications. *IEEE Trans. Antennas Propag.* **2017**, *65*, 5171–5178. [CrossRef]
10. Nayeri, P.; Lee, K.F.; Elsherbeni, A.Z.; Yang, F. Dual-Band Circularly Polarized Antennas Using Stacked Patches with Asymmetric U-Slots. *IEEE Antennas Wirel. Propag. Lett.* **2011**, *10*, 492–495. [CrossRef]
11. Ye, S.; Geng, J.; Liang, X.; Guo, Y.J.; Jin, R. A Compact Dual-Band Orthogonal Circularly Polarized Antenna Array with Disparate Elements. *IEEE Trans. Antennas Propag.* **2015**, *63*, 1359–1364. [CrossRef]
12. Shavit, R.; Pazin, L.; Israeli, Y.; Sigalov, M.; Leviatan, Y. Dual frequency and dual circular polarization microstrip nonresonant array pin-fed from a radial line. *IEEE Trans. Antennas Propag.* **2005**, *53*, 3897–3905. [CrossRef]
13. Jou, C.F.; Wu, J.W.; Wang, C.J. Novel Broadband Monopole Antennas with Dual-Band Circular Polarization. *IEEE Trans. Antennas Propag.* **2009**, *57*, 1027–1034. [CrossRef]
14. Ferrando-Rocher, M.; Herranz-Herruzo, J.I.; Valero-Nogueira, A.; Baquero-Escudero, M. Dual-Band Single-Layer Slot Array Antenna Fed by K/Ka-Band Dual-Mode Resonators in Gap Waveguide Technology. *IEEE Antennas Wirel. Propag. Lett.* **2021**, *20*, 416–420. [CrossRef]
15. Zhang, J.D.; Wu, W.; Fang, D.G. Dual-Band and Dual-Circularly Polarized Shared-Aperture Array Antennas with Single-Layer Substrate. *IEEE Trans. Antennas Propag.* **2016**, *64*, 109–116. [CrossRef]
16. Sandhu, A.I.; Arnieri, E.; Amendola, G.; Boccia, L.; Meniconi, E.; Ziegler, V. Radiating Elements for Shared Aperture Tx/Rx Phased Arrays at K/Ka Band. *IEEE Trans. Antennas Propag.* **2016**, *64*, 2270–2282. [CrossRef]
17. Jackson, D.R.; Alexopoulos, N.G. Simple approximate formulas for input resistance, bandwidth, and efficiency of a resonant rectangular patch. *IEEE Trans. Antennas Propag.* **1991**, *39*, 407–410. [CrossRef]
18. Chang, X.; Wang, H.B.; Li, T.J.; Jin, S.C.; Liu, D.G.; Cheng, Y.J. Shared-Aperture Phased Array Antenna with Codesigned Near-Field Coupled Circular Polarizer Loaded for K/Ka-Band Wide-Angle Satellite Communication. *IEEE Trans. Antennas Propag.* **2022**, *70*, 7478–7490. [CrossRef]
19. Liu, W.; Cao, Y.; Chen, J.; Yan, S. Design of a Low-Profile Dual-Band Shared-Aperture Circularly Polarized Phased Array. *IEEE Antennas Wirel. Propag. Lett.* **2024**, *23*, 543–547. [CrossRef]
20. Zhang, J.D.; Zhu, L.; Liu, N.W.; Wu, W. Dual-Band and Dual-Circularly Polarized Single-Layer Microstrip Array Based on Multiresonant Modes. *IEEE Trans. Antennas Propag.* **2017**, *65*, 1428–1433. [CrossRef]

Disclaimer/Publisher’s Note: The statements, opinions and data contained in all publications are solely those of the individual author(s) and contributor(s) and not of MDPI and/or the editor(s). MDPI and/or the editor(s) disclaim responsibility for any injury to people or property resulting from any ideas, methods, instructions or products referred to in the content.

Article

A New Sum-Channel Radiating Element for a Patch-Monopole Monopulse Feed

Peter Miklavčič^{1,2} and Boštjan Batagelj^{1,*} ¹ Faculty of Electrical Engineering, University of Ljubljana, Tržaška Cesta 25, 1000 Ljubljana, Slovenia² Space-SI, Aškerčeva cesta 12, 1000 Ljubljana, Slovenia

* Correspondence: bostjan.batagelj@fe.uni-lj.si

Abstract: This article describes a new design for the sum-channel, circularly-polarized, radiating patch element of a multimode patch-monopole monopulse feed. Such feeds are suitable for the prime-focus illumination of a deep symmetric reflector. A relatively simple and compact feed design allows for a compact single-mirror antenna with monopulse tracking. The feed is about a wavelength in diameter, also making it suitable for illuminating smaller antennas, for example, in LEO-satellite ground (client) stations. The design applies a slotted circular patch as a circularly-polarized sum-channel element. The design variables are optimized mainly for the sum-channel aperture illumination efficiency in an S-band satellite ground station. After a few cut-and-try iterations, the final feed prototype was produced and measured. In addition to an additional degree of freedom in the geometry and potentially easier fabrication, the new sum-channel radiating-element shape allows for a slightly better monopulse channel isolation, and a higher radiation-pattern symmetry compared to the previous design.

Keywords: monopulse antenna; multimode antenna; prime-focus feed; circularly-polarized patch



Citation: Miklavčič, P.; Batagelj, B. A New Sum-Channel Radiating Element for a Patch-Monopole Monopulse Feed. *Electronics* **2024**, *13*, 3187. <https://doi.org/10.3390/electronics13163187>

Academic Editors: Raad Raad, Ladislav Matekovits and Faisal Tubbal

Received: 16 July 2024

Revised: 2 August 2024

Accepted: 7 August 2024

Published: 12 August 2024



Copyright: © 2024 by the authors. Licensee MDPI, Basel, Switzerland. This article is an open access article distributed under the terms and conditions of the Creative Commons Attribution (CC BY) license (<https://creativecommons.org/licenses/by/4.0/>).

1. Introduction

The patch-monopole monopulse feed [1] is a relatively simple and compact multimode feed design with a circular cavity that is approximately a wavelength in diameter. This type of monopulse feed is suitable as a prime-focus illumination of a rotationally-symmetric (deep) reflector, a single-reflector paraboloidal (parabolic) antenna [2,3]. It enables inexpensive monopulse antenna designs for stations that benefit from rapid and very accurate antenna pointing, such as LEO (low Earth orbit) satellite ground stations [4–6], as illustrated in Figure 1, ground stations of moving aerial or high-altitude platforms, long-distance links (for example, Lunar communications [7]), and similar.

The compactness of the design results in minimal antenna-aperture shading and makes the feed suitable also for small(est) prime-focus paraboloidal antennas, only a few wavelengths in size. The simplicity of the design results in a very manageable fabrication complexity and low production cost. The compact design makes the feed also suitable for mobile radars, aerial–platform communications, and similar applications where compact monopulse antennas are sought.

The main radiating element is a circularly-polarized patch exciting the TE_{11} mode (circular-waveguide equivalent) as the sum channel. The second radiating element is a linearly-polarized monopole exciting the TM_{01} mode (circular-waveguide equivalent) for the difference channel. The patch element in a relatively shallow cavity radiates like an open-ended (short) circular waveguide [8–10]. Two-dimensional monopulse operation requires a circularly-polarized incident wave, in contrast to the conventional monopulse design with an antenna array and a comparator network [11–15]. The tracking information is obtained by quadrature detection with the sum signal as the reference.

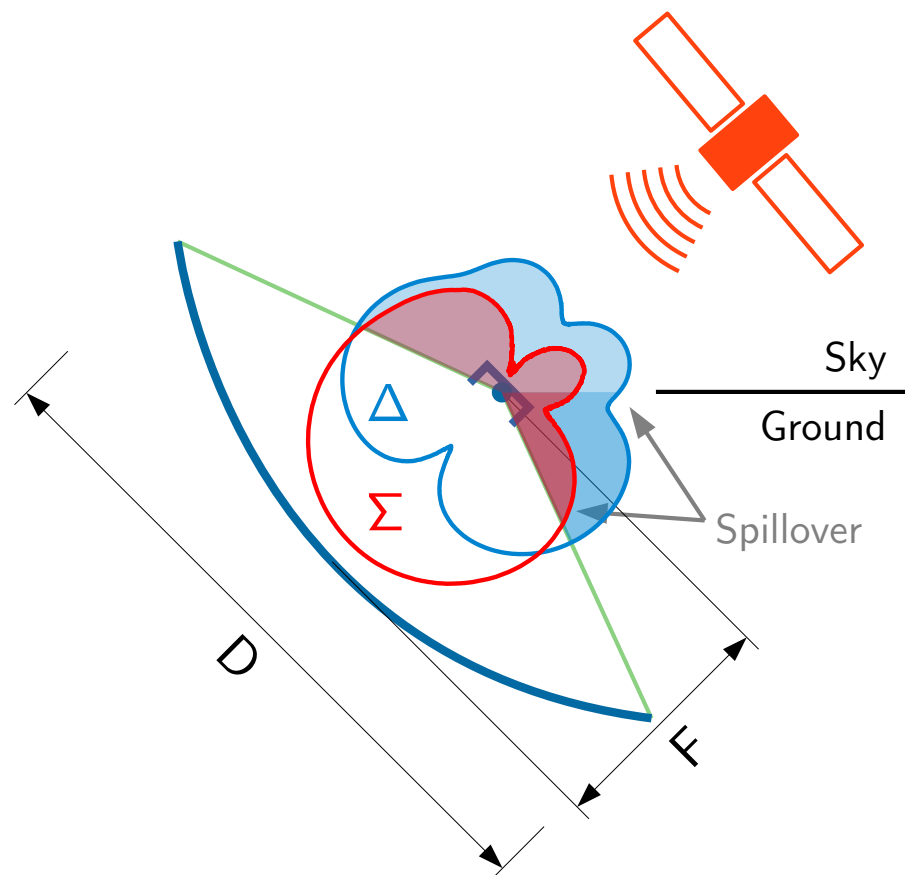


Figure 1. Illustration of the proposed feed in a satellite ground station with sum (Σ) and difference (Δ) beam marking.

This article briefly describes the research, development, and prototype measurements of a patch-monopole monopulse feed design with a novel, sum-channel, radiating patch element. The evolved design employs, as a circularly-polarized, sum-channel radiating element, a slotted circular patch [16–18] instead of an elliptical patch [18,19] or similar [20,21] from the previous design [1]. The slot allows for an additional separation of the sum-channel radiating element from the rest of the feed. The design variables are optimized mainly for good radiation properties, including the sum-channel aperture illumination efficiency in a typical satellite-receiving antenna (spillover illumination is minimized). The slot is designed so that the two fundamental modes of the patch are phase-shifted in quadrature for circular polarization. A technical drawing of the proposed design is shown in Figure 2.

As in the previous design, the sum-channel patch is left-handed-circularly polarized (LHCP) and it is optimized for a symmetric paraboloidal antenna with a focal-distance-to-diameter ratio $\frac{F}{D}$ of 0.4. The center frequency of operation is 2.21 GHz. Compared to the previous design, the new patch geometry provides an additional degree of freedom while the circular patch outline is somewhat simplified, allowing for a potentially easier fabrication. The new design shows a slightly improved monopulse channel isolation, and a high radiation-pattern symmetry.

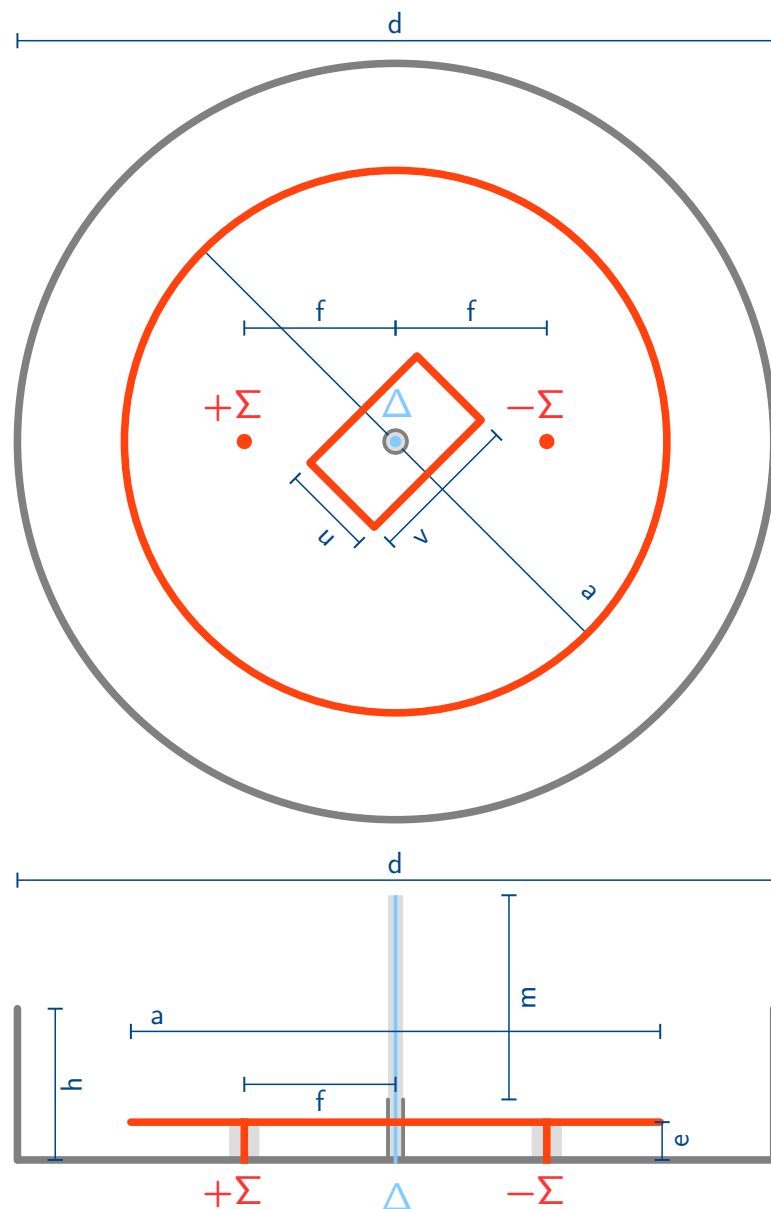


Figure 2. Top and side views of the proposed feed design with input ($\pm\Sigma$, Δ) and parameter (dimension) marking. The parameters include cavity diameter (d), cavity wall height (h), patch height above cavity floor (e), patch diameter (a), patch feedpoint offset (f), slot dimensions (u , v), and monopole length (m).

2. Materials and Methods

The main course of the research consisted of a study and review of the literature study, then the design synthesis, which was followed by a few prototype iterations to optimize the design. The initial patch dimensions can be obtained from resonance-frequency approximations [22]. Any general-purpose antenna-simulation software, employing, for example, the method of moments, suffices for simulating and optimizing such a feed. At the current stage of research, the feeding circuit consists of coaxial lines below the cavity floor, which complicates electromagnetic modeling of the whole structure. We only simulated the cavity part of the antenna for coarse-tuning of radiation properties, and the experimental work was mainly focused on prototype fabrication and measurements. The optimized physical and electrical dimensions (at 2.21 GHz) of the proposed monopulse feed design are shown in Table 1 and correspond to the marking in the technical drawing in Figure 2.

Table 1. Physical and electrical dimensions (at 2.21 GHz) of the proposed monopulse feed design.

Unit	d	h	e	a	f	u	v	m
mm	96.0	11.0	3.5	69.2	11.0	7.0	18.5	27.5
λ	0.71	0.08	0.03	0.51	0.08	0.05	0.14	0.20

The idea for prototype fabrication is the same as that of the design itself: simplicity and straightforwardness. Prototypes were fabricated manually, by using only some standard tools such as a ruler and compass, metal cutters, a drill, a soldering iron with approximately 50 watts of thermal power, standard tin and flux, etc. The used materials and components were also standard. The cavity and the patch element are both made from 0.4 mm thick brass sheet. The patch element is held up by the center conductors (and/or dielectric) of both sum-channel feedpoints, made from flanged SMA (SubMiniature version A) connectors. The monopole is easily made from a standard SMA cable connector with a flanged mount and a suitable coaxial cable (such as RG-405) with an outer cladding stripped to make a monopole. A fabricated prototype is shown in Figure 3.

**Figure 3.** A fabricated prototype of a patch-monopole monopulse feed.

The sum-channel patch requires a balanced feed for a symmetric, nonsquinted radiation pattern and least coupling to the difference channel. The prototype uses a simple balun made out of a parallel tee connection of coaxial cables that are $\frac{1}{2} \lambda$ and 1λ in length. The patch is best fed at a point where the impedance is around 100Ω [23]. A parallel connection of the two arms results in an impedance of around 50Ω . The monopole feedline is made for the best impedance matching of the difference channel. The length differences in the sum and difference channels manifest as an additional constant phase shift of the resulting monopulse ratio, which needs to be spatially aligned with the antenna (calibrated). The final feed prototype during radiation-pattern measurements, including the feeding circuit, is shown in Figure 4.

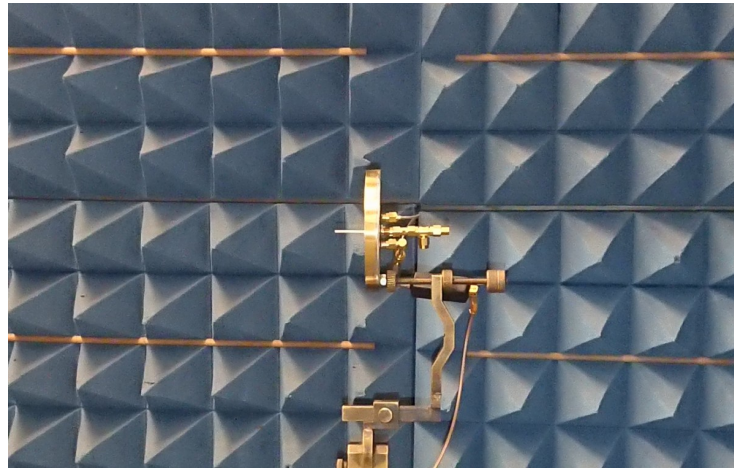


Figure 4. Patch-monopole monopulse feed final prototype during radiation-pattern measurements.

The radiation efficiency is expected to be high since the prototype is made out of good-conductivity metals and low-loss dielectrics: air in the cavity, PTFE (polytetrafluoroethylene, also known as Teflon) or PTFE-like in coaxial lines, etc. Simulations show a sum-channel radiation efficiency above 99% for an ideally-fed antenna and above 95%, including a simple coaxial network balun. The experimental verification [24] in a less-than-ideal reverberation chamber revealed a sum-channel radiation efficiency above 80%.

3. Results

3.1. Scattering Parameters

The scattering parameters were measured together with a simple feeding circuit: a coaxial sum-channel balun and a difference-channel monopole impedance-matching stub. The feeding circuit was only coarsely optimized with the conventional cut-and-try method, so only the measurements are provided in this subsection. The simulations indicated that the return loss is not a limiting factor of the design with a good feeding circuit, and confirmed that the patch impedance remains predictable [23]. The return loss frequency characteristic is shown in Figure 5. It indicates a nonideal sum-channel balun for matching the target frequency of 2.21 GHz. The crosstalk between the sum and difference channels of the measured prototype is around -35 dB in the band, and is also shown in Figure 6.

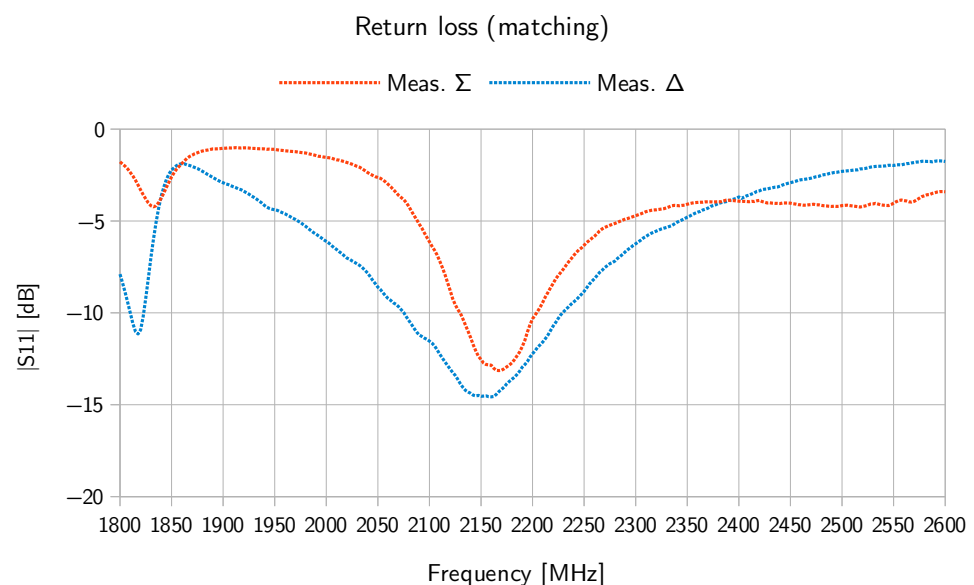


Figure 5. Return loss frequency characteristic measurement of both channels.

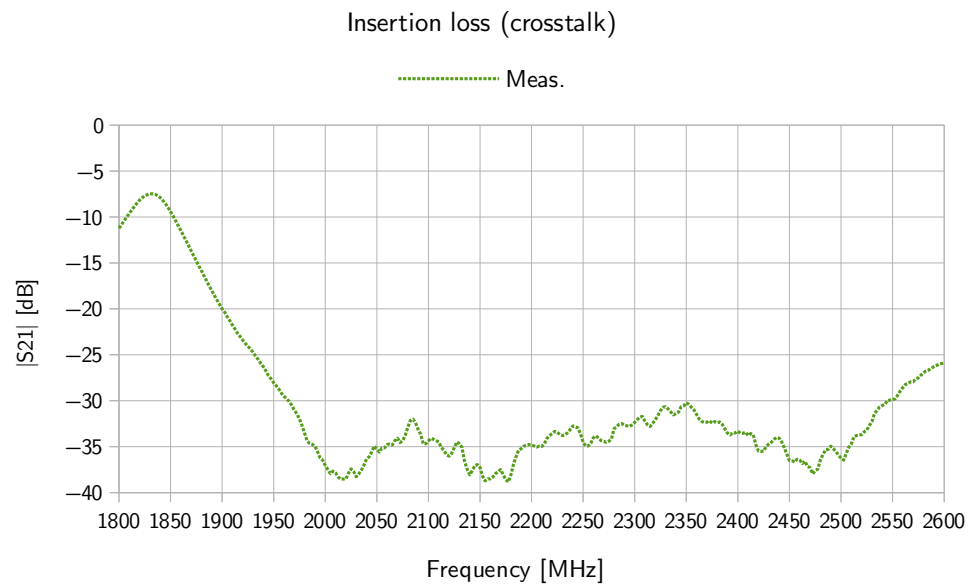


Figure 6. Crosstalk frequency characteristic measurement between the channels.

3.2. Radiation Parameters

The total sum-channel directivity of the proposed design at the center frequency of 2.21 GHz is simulated to be 8.9 dBi. Indoor laboratory measurements in a semi-anechoic space confirmed the simulation results within 0.4 dB of the difference in both radiation-pattern cross-sections (cuts), even with the nonideal balun. The radiation-pattern cuts of the sum channel are shown in Figure 7 and those of the difference channel are shown in Figure 8. The horizontal cut plane (mark *H*) is parallel to the line between the patch feed points, and the vertical cut plane (mark *V*) is perpendicular to them.

The patch has a bandpass frequency characteristic. The axial ratio is 0.1 dB at the center frequency, where the circular polarization is optimal, and the 3 dB bandwidth of the axial ratio is 32 MHz. The total directivity and the LHCP gain frequency characteristics are shown in Figure 9. As explained in Section 2, the radiation efficiency seems to be in the 80% to 90% range, resulting in a center-frequency LHCP realized gain value of around 8 dBi. The peak aperture illumination efficiency is calculated to be 75% at an $\frac{F}{D}$ ratio of 0.4. The difference radiation pattern, shown in Figure 8, exhibits a strong dip, suitable for tracking operation. A quick test of the monopulse operation of the feed with a transmitting circularly-polarized antenna and a vector voltmeter at the receiving side showed that the feed is working as expected.

The rotational symmetry of the sum-channel pattern at the reflector's edge is close to 0 dB according to the simulation results. The measurement results agree well, considering a semi-anechoic-only measurement space. The difference in both points of a cut intersecting the reflector's edge is 0.4 dB for both cuts. The values between both cuts differ by 1.3 dB, and, on average, the measurements correspond well to the simulation results at the reflector's edge. Backside radiation results are not accurate due to suboptimal measurement space and the effect of the mounting structure.

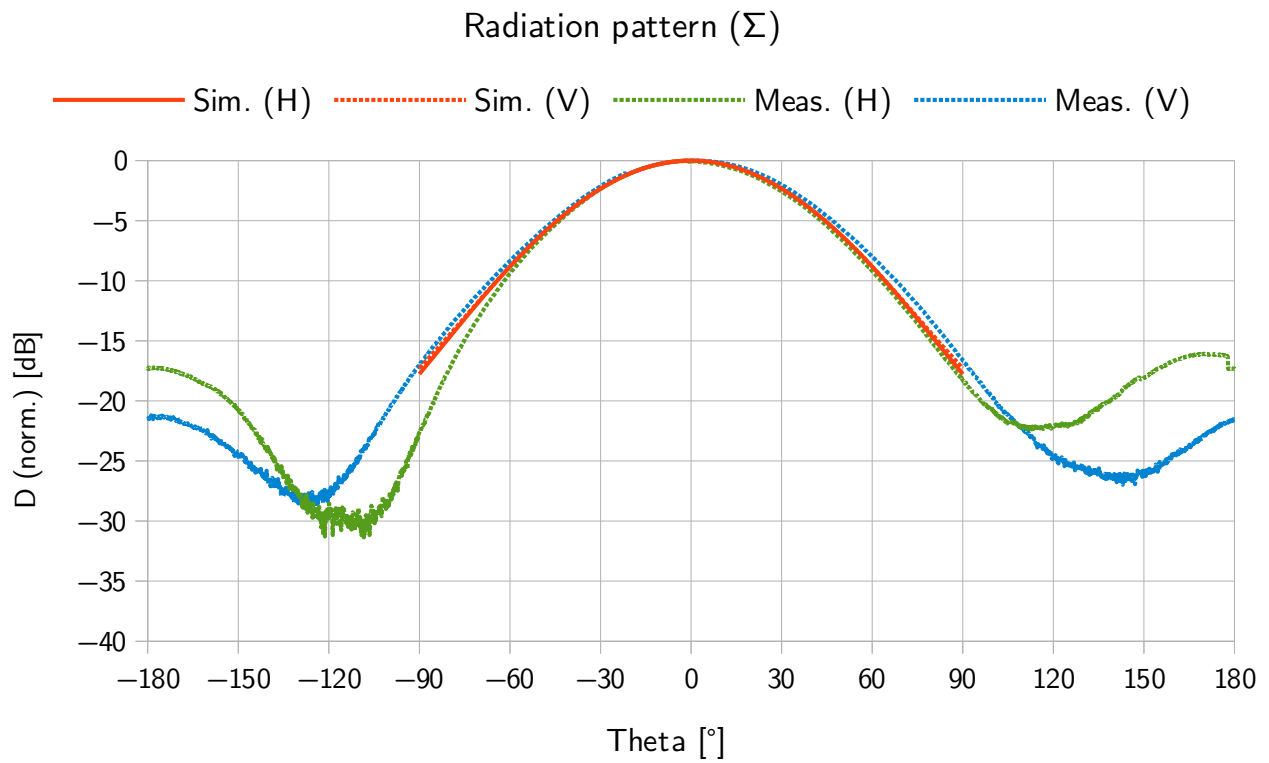


Figure 7. Radiation-pattern simulation and measurement results of the sum channel.

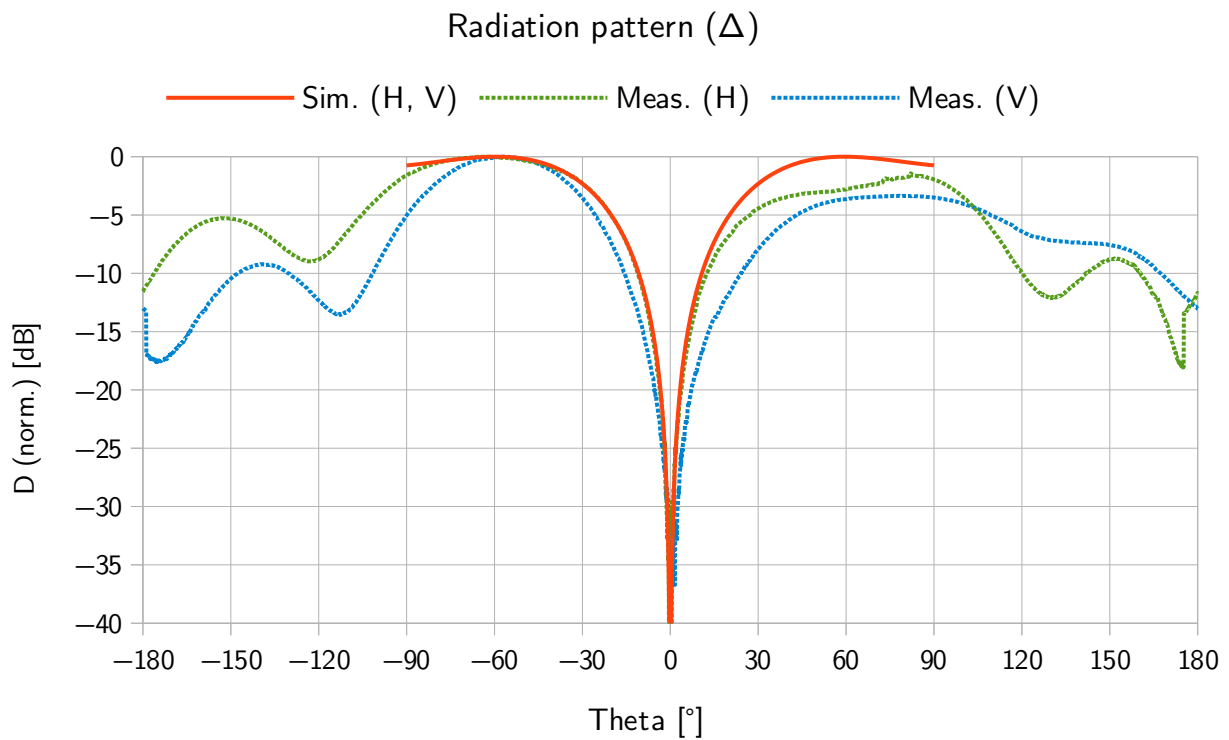


Figure 8. Radiation-pattern simulation and measurement results of the difference channel.

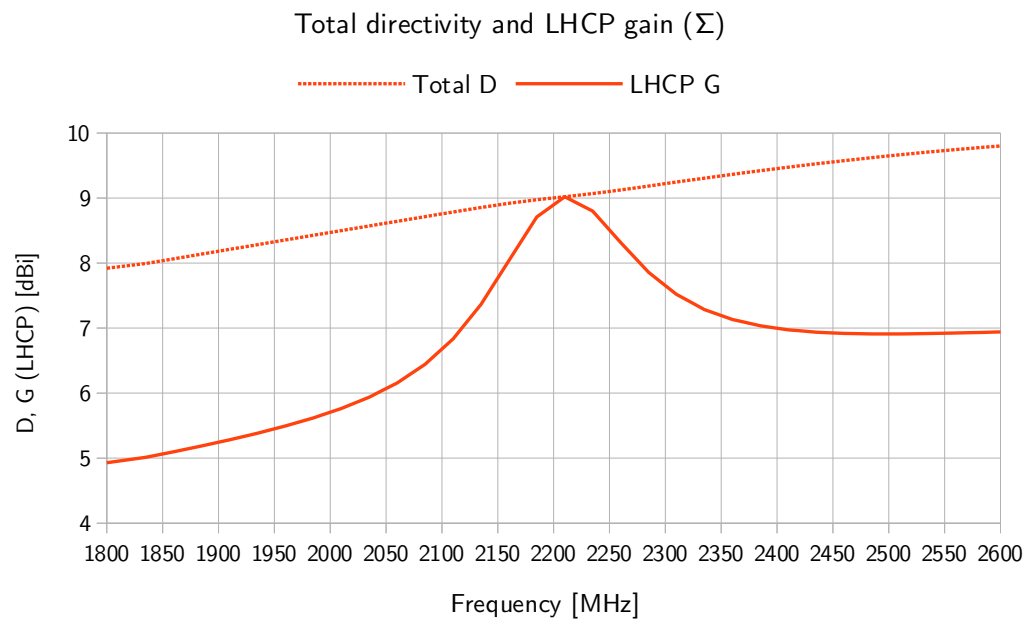


Figure 9. Sum-channel simulation results of total directivity and LHCP gain frequency characteristics.

4. Discussion

The radiation-pattern measurements correspond well to measurements at about the same solid angle as the illuminated reflector is located, so the taper efficiency is easily calculable. The spillover-efficiency calculation is more problematic, since spillover radiation measurements and simulation results are only rough approximations. The simulation model is too ideal and the measured weak backside-radiated power is sensitive to a nonideal measurement space, while also affected by the mechanical mounting structure, cabling, and a measurement probe (as seen in Figure 4). The same applies to determining the depth of the difference-channel minimum. The sum-channel radiation pattern tapers off by about 9 dB at the edge of the reflector. Including the edge attenuation due to the reflector shape (3 dB for $\frac{F}{D}$ of 0.4), the edge attenuation amounts to about 12 dB. There is still confidence in the results around the reflector's edge, where the spillover radiation is the strongest. The weaker side and back radiation affect the spillover-efficiency approximation less.

Compared to the elliptic-patch design [1], the diameter of the feed is slightly reduced, while the new design still increases the directivity. A feed of this size shades only 2% of the aperture area of a reflector that is only 5λ in diameter. More than the new patch shape, the narrowband design is responsible for the increased directivity, and also a shallower cavity, to a lesser extent. The feed design is optimized for a relatively narrowband sum channel to see the achievable efficiencies of such a design. The crosstalk between the channels of -35 dB is suitable for tracking operation. Since the tracking control loop is very slow compared to the sum-channel data rate, the difference channel is much less demanding in terms of bandwidth and the required signal-to-noise ratio.

For future work, a wideband optimization at a minimal and acceptable performance loss in the middle of the band should be tested with the design to find its practical limits. The feeding circuit elements could be integrated directly into the feed structure for an even more compact, repeatable, and integral solution. It should also be possible to scale the design to at least the X band, make a dual-polarization version of the design, or develop a simple radome for such a feed. Finally, it is impractical to wholly measure the feed in an indoor test space, and the final antenna efficiency, gain, and noise temperature can only be predicted. In the future, we will also focus on field-testing the feed, illuminating a real ground-station antenna.

5. Conclusions

The main contribution of this article is the introduction of a new sum-channel radiating element with a comparable shape complexity to the patch-monopole monopulse feed design. The new sum-channel patch shape allows for conductive separation of the patch to the other parts of the feed.

Both sum and difference channel radiation patterns are as expected in the design phase. The sum-channel center-frequency LHCP gain of the feed is around 8 dBi. The feed exhibits a somewhat narrowband sum-channel in the 30 MHz range as it is primarily optimized to test achievable efficiencies of the design. The sum-channel aperture illumination efficiency is 75% at a target $\frac{F}{D}$ ratio of 0.4. We were unable to measure radiation efficiency very well, but the design with low-loss dielectrics should not be problematic or limiting in this regard.

Author Contributions: Conceptualization, P.M.; methodology, P.M.; software, P.M.; validation, P.M. and B.B.; formal analysis, P.M.; investigation, P.M.; resources, B.B.; data curation, P.M. and B.B.; writing—original draft preparation, P.M.; writing—review and editing, P.M. and B.B.; visualization, P.M. and B.B.; supervision, B.B.; project administration, B.B.; funding acquisition, B.B. All authors have read and agreed to the published version of the manuscript.

Funding: This research was funded by the Slovenian Research and Innovation Agency under grant J2-50072 and research core fund P2-0246.

Data Availability Statement: Data are contained within the article.

Conflicts of Interest: Author Peter Miklavčič was employed by the company Space-SI. The remaining authors declare that the research was conducted in the absence of any commercial or financial relationships that could be construed as a potential conflict of interest.

References

- Miklavčič, P.; Vidmar, M.; Batagelj, B. Patch-monopole monopulse feed for deep reflectors. *Electron. Lett.* **2018**, *24*, 1364–1366. [CrossRef]
- Cutler, C.C. Parabolic-antenna design for microwaves. *Proc. IRE* **1947**, *11*, 1284–1294. [CrossRef]
- Rusch, W.V.T. The current state of the reflector antenna art-entering the 1990s. *Proc. IEEE* **1992**, *80*, 113–126. [CrossRef]
- Hawkins, G.J.; Edwards, D.J.; McGeehan, J.P. Tracking systems for satellite communications. *IEE Proc. Commun. Radar Signal Process.* **1988**, *135*, 393–407. [CrossRef]
- Patel, P.D. Inexpensive multi-mode satellite tracking feed antenna. *IEE Proc. H Microwaves Antennas Propag.* **1988**, *135*, 381–386. [CrossRef]
- Maral, G.; Bousquet, M.; Sun, Z. *Satellite Communications Systems: Systems, Techniques and Technology*, 5th ed.; John Wiley & Sons: Hoboken, NJ, USA, 2009.
- Farkasvölgyi, A.; Csurgai-Horváth, L.; Boháček, P. The evolution of lunar communication - From the beginning to the present. *Int. J. Satell. Commun. Netw.* **2023**, *3*, 200–216. [CrossRef]
- Hong, M.; Nyquist, D.; Chen, K. Radiation fields of open-cavity radiators and a backfire antenna. *IEEE Trans. Antennas Propag.* **1970**, *6*, 813–815. [CrossRef]
- Ehrenspeck, H.W. A new class of medium-size, high-efficiency reflector antennas. *IEEE Trans. Antennas Propag.* **1974**, *2*, 329–332. [CrossRef]
- Lee, C.S.; Lee, S.W.; Chuang, S.L. Plot of modal field distribution in rectangular and circular waveguides. *IEEE Trans. Microw. Theory Tech.* **1985**, *3*, 271–274. [CrossRef]
- Zhao, F.; Cheng, Y.J.; Kou, P.F.; Yao, S.S. A wideband low-profile monopulse feeder based on silicon micromachining technology for W-band high-resolution system. *IEEE Antennas Wirel. Propag. Lett.* **2019**, *8*, 1676–1680. [CrossRef]
- Li, S.; Zhang, Q.; Xu, Z.; Zhao, H.; Yin, X. Phase transforming based on asymmetric spoof surface plasmon polariton for endfire antenna with sum and difference beams. *IEEE Trans. Antennas Propag.* **2020**, *9*, 6602–6613. [CrossRef]
- Zhao, J.; Hao, L.; Li, H.; Tong, Z.; Li, T.; Wang, H.; Hu, B.; Zhou, Y.; Li, F.; Fu, C.; et al. A Novel Metasurface-Based Monopulse Antenna with Improved Sum and Difference Beams Radiation Performance. *Micromachines* **2022**, *11*, 1927. [CrossRef] [PubMed]
- Monebi, A.M.; Lee, C.-S.; Ahn, B.-C.; Choi, S.-G. Design of a Ku-Band Monopulse Antenna with a Truncated Reflector and an Open-Ended Waveguide Feed. *Sensors* **2023**, *1*, 118. [CrossRef]
- Monebi, A.M.; Otgonbat, D.; Ahn, B.-C.; Lee, C.-S.; Ahn, J.-H. Conceptual Design of a Semi-Dual Polarized Monopulse Antenna by Computer Simulation. *Appl. Sci.* **2023**, *5*, 2960. [CrossRef]
- Kerr, J.L. Microstrip polarization techniques. In Proceedings of the Antenna Applications Symposium, Urbana, IL, USA, 20–22 September 1978.

17. Kerr, J.L. Microstrip antenna developments. In Proceedings of the Workshop on Printed Circuit Antenna Technology, New Mexico State University, Las Cruces, NM, USA, 17–19 October 1979.
18. Carver, K.; Mink, J. Microstrip antenna technology. *IEEE Trans. Antennas Propag.* **1981**, *1*, 2–24. [CrossRef]
19. Irish, R.T. Elliptic resonator and its use in microcircuit systems. *Electron. Lett.* **1971**, *7*, 149–150. [CrossRef]
20. Squadrito, P.; Livreri, P.; Di Donato, L.; Squadrito, C.; Sorbello, G. A Telemetry, Tracking, and Command Antennas System for Small-Satellite Applications. *Electronics* **2019**, *8*, 689. [CrossRef]
21. Atif, A.; Majid, A.; Zahid, M.; Amin, Y. Circular Slotted Triangular Patch Antenna for 5.8 GHz ISM Band Applications. *Eng. Proc.* **2023**, *46*, 10. [CrossRef]
22. Shen, L.; Long, S.; Allarding, M.R.; Walton, M. Resonant frequency of a circular disc, printed-circuit antenna. *IEEE Trans. Antennas Propag.* **1977**, *4*, 595–596. [CrossRef]
23. Long, S.A., Shen, L.C., Walton, M.D.; Allarding, M.R. Impedance of a circular-disc printed-circuit antenna. *Electron. Lett.* **1978**, *21*, 684–686. [CrossRef]
24. Holloway, C.L.; Shah, H.A.; Pirkel, R.J.; Young, W.F.; Hill, D.A.; Ladbury, J. Reverberation chamber techniques for determining the radiation and total efficiency of antennas. *IEEE Trans. Antennas Propag.* **2012**, *4*, 1758–1770. [CrossRef]

Disclaimer/Publisher’s Note: The statements, opinions and data contained in all publications are solely those of the individual author(s) and contributor(s) and not of MDPI and/or the editor(s). MDPI and/or the editor(s) disclaim responsibility for any injury to people or property resulting from any ideas, methods, instructions or products referred to in the content.

Article

Performance Evaluation of a Low-Cost Semitransparent 3D-Printed Mesh Patch Antenna for Urban Communication Applications

Luis Inclán-Sánchez 

Department of Signal Theory and Communications, Universidad Carlos III de Madrid, 28911 Leganés, Spain; linclan@ing.uc3m.es

Abstract: This study explores the possibility of designing simple semitransparent antennas that allow for the passage of most visible light while maintaining good electromagnetic performance. We propose a substrateless metal mesh patch antenna manufactured using low-cost 3D printing and silver conductive paint. Our goal is to integrate numerous such radiators onto office building windows, preserving natural lighting with minimal visual impact, aiming to alleviate infrastructure congestion or improve antenna placement in sub-6 GHz frequency bands. In this paper, we conduct an analysis of the primary parameters influencing patches constructed with substrateless metal mesh wires, focusing on the grid topology and the width of the metallic wires, as well as their effects on antenna transparency and back radiation. Owing to the absence of a substrate, the antenna demonstrates minimal losses. Furthermore, in this study, we thoroughly investigate the effects of conductivity and roughness on surfaces printed with metallic paint. A prototype at 2.6 GHz is presented, achieving over 60% transparency, a 2.7% impedance-matching bandwidth, and a realized peak gain of 5.4 dBi. The antenna is easy to manufacture and cost-effective and considers sustainability. Its large-scale implementation can alleviate building infrastructure, enhancing radio connectivity in urban environments and offering new cost-effective and energy-efficient wireless solutions.

Keywords: optically transparent antenna; patch antenna; metal mesh; metal grid; 3D printing; substrateless antenna; low-cost antenna; surface roughness; effective conductivity; sustainable materials



Citation: Inclán-Sánchez, L. Performance Evaluation of a Low-Cost Semitransparent 3D-Printed Mesh Patch Antenna for Urban Communication Applications. *Electronics* **2024**, *13*, 153. <https://doi.org/10.3390/electronics13010153>

Academic Editors: Raad Raad, Ladislav Matekovits and Faisal Tubbal

Received: 7 December 2023
Revised: 25 December 2023
Accepted: 27 December 2023
Published: 29 December 2023



Copyright: © 2023 by the authors. Licensee MDPI, Basel, Switzerland. This article is an open access article distributed under the terms and conditions of the Creative Commons Attribution (CC BY) license (<https://creativecommons.org/licenses/by/4.0/>).

1. Introduction

We are witnessing rapid advancements in radio systems, primarily driven by the widespread implementation of 5G technology and strategic planning for the imminent era of 6G [1]. The increasing availability of frequency bands and the coexistence of diverse applications, including communications, sensors, vehicle guidance, and the Internet of Things (IoT), emphasize the growing need for versatile high-efficiency devices.

Within this landscape of multifaceted systems, each demanding exceptional capabilities in terms of latency, ubiquity, and low power consumption [1], it has become imperative to explore innovative approaches to radio device design. Prioritizing elements such as sustainable network development [2], energy efficiency, and minimization of visual or radioelectric impact is crucial. Ultimately, these systems must demonstrate economic viability and energy efficiency while reducing their environmental footprint during manufacturing and maximizing recyclability.

Another challenge arises from the vast number of devices that will need to coexist, motivating an increased need for adequate physical space to accommodate radio systems [1,3]. These locations must facilitate new applications while providing enough space for the multiple antennas and arrays necessary for configurations like massive MIMO. Additionally, they must adhere to rigorous security standards across all radio applications [1]. This approach relates to the concept of Smart Cities [4], integrating infrastructure and network capacity into urban planning from its inception [4] or improving connectivity [5] and

ultimately addressing the capacity and coexistence challenges of future 5G/6G wireless systems. In these Smart Cities, reconciling old and new networks is imperative, often requiring buildings and infrastructure to have additional access points, smart surfaces, antennas, and signal repeaters. An emerging possibility is the use of windows and architectural glass surfaces in buildings and vehicles as antenna locations to ensure enough physical space for radio systems. Seeking to maintain the use of natural light and minimize visual impact, there is substantial interest in designing optically transparent antennas that allow for the passage of most visible light [4,6].

The state of the art in transparent antenna design has utilized two main approaches [6]. The first involves designing the entire antenna using transparent materials. In this scenario, the antenna appears invisible, except for limitations in light transmission due to the materials used and non-transparent parts like connectors. Although it is feasible to create conductorless transparent antennas using only dielectric materials (DRA) [7], materials for transparent antennas typically fall into two categories: the substrate and the metallic parts. For substrates, materials like PET or PMMA plastics, glass, acrylic, and even water in transparent containers have been used [4,6,8–12]. Regarding the conductive sections, they are made from semiconductor films like transparent conductive oxides (TCOs) doped with conductive particles to enhance their electrical properties [13]. Research conducted using compounds such as ITO, AZO, AgHT, and ZnO aims to achieve high transparency with high electrical conductivity [4,6,14,15]. However, despite progress, these materials still experience greater losses and lack the efficiency of metals found in PCB-based electronics [6].

The second approach involves replacing the solid metal parts of the antenna with a metal mesh or grid [6,8,16,17]. The density of the mesh—or the spacing between the metal wires—must maintain electrical continuity (typically with periods between $\lambda/10$ and $\lambda/20$ [14]) yet be significantly larger than the wavelength for good optical transmission. As the ratio of holes to surface area increases, the antenna's transparency improves at the expense of electromagnetic performance [8,14]. Practically, this mesh remains visible, making the antenna truly semitransparent. Nevertheless, it retains utility by harnessing natural light or reducing visual impact. Previous studies have often employed micromeshes with thin metal wires—often micrometric [14] or even smaller [18]. This seems like an intermediate approach in which the layout of the mesh is less perceived by the naked eye but limits optical transmission according to its density. Overall, this mesh-based approach generally produces better-performing antenna designs [4,6]. In the state of the art, there are numerous mesh antennas with greater efficiency than those that use conductive films [6], even with performance close to their respective non-transparent designs, as is the case described below. Within the realm of mesh-type antennas, besides the aforementioned micromeshes, work has been conducted with larger-sized meshes where the grid or antenna design is notably visible. In this line, PCB techniques have been employed for the metallic parts, followed by cutting off the non-metallic part [17,19], including via laser cutting [20].

In any of these approaches, antenna manufacturing always involves the following stages: (1) manufacturing of conductive films, micro metal meshes, or macro grids using ink-jet processes, PVD, or PCB followed by cutting; (2) the production, purchase, and/or cutting of transparent materials used as substrates; (3) layer adherence through gluing or deposition processes on the material. This process resembles conventional printing technology, but the complexity of the stages and their integration increases.

Regarding the most common applications for transparent antennas, the initial use has been in communications, including integrating antennas into solar cell panels [21,22], vehicle windows or windshields [10], and device screens [23]. They have also been used in RFID applications, motion/presence control, and even smart glasses [24]. New application fields have recently emerged, such as in energy harvesting [25] and instruments for biological applications [26]. Furthermore, transparent versions of recent technologies are gradually emerging, as seen in [27] for SIW technology or in [28] for advanced absorbers. Transparent electronics are mentioned as an area of interest in radiocommunications, involving not

just antennas but also other elements like filters [4] or their combinations, giving rise to rectennas [25,29] or filtering antennas [30].

Patch antennas are the most used radiators in the design of transparent antennas, including examples of all the abovementioned approaches [8,11,15,17,30,31]. In this work, we develop the idea suggested in [32], proposing the creation of transparent mesh antennas using 3D printing. The metallic mesh is manufactured from conventional plastic filaments that are later metallized. Because the antenna can be made as one piece or in two easily joinable parts that include mechanical fastening posts, it is possible to create the antenna without a substrate. This idea was used in [33] to propose an optically semitransparent PIFA made in a grid and integrated into a low-coupling 2×2 MIMO configuration. Now, we propose the development of a low-cost, semitransparent 3D printed patch metallized with silver conductive paint (SCP). The most relevant aspects of the design, mesh topology, width of the metal wires, and the tradeoff between electrical behavior and transparency are analyzed. As the antenna does not have a substrate, it experiences fewer losses, which is mainly attributed to the effective conductivity and the surface roughness of the metallic grid elements. These aspects are studied throughout the paper, and some prototypes are characterized to demonstrate the possibility of designing a simple, cost-effective, semitransparent antenna with good radiation performance and advantages in terms of reduced material usage. Such antennas might be interesting for setting up transparent radiant systems and arrays for sub-6 GHz bands in 5G/6G applications. They offer the possibility of being integrated into office building windows, utilizing natural light, and minimizing visual impact to address space limitations, alleviate the capacity of new network infrastructure, or enable optimal antenna placement for specific wireless environments.

2. Semitransparent Mesh Patch Antenna

In this section, we first present the specific application intended for the semitransparent antenna, covering broader aspects related to energy efficiency and resource utilization. Subsequently, we provide detailed information about the mesh patch antenna proposed in this study and its key design aspects.

2.1. Urban Communication Applications: Optical Transparency and Efficient Resource Allocation

Figure 1 illustrates a typical scenario involving the integration of transparent antennas into the network infrastructure of a smart building. It exemplifies potential solutions for antenna systems integrated into existing structures, like older buildings with saturated infrastructure. Additionally, it showcases the strategic placement of these antennas, considering factors such as coverage from base stations, 5G point-to-point radio links, and the radio environment influenced by nearby building layouts.

As shown in Figure 1, the building's primary architectural surface is glass, offering a substantial area for deployment of antennas or large antenna arrays. Considering the dimensions of the windows, even at lower frequencies of 5G/6G, the space occupied by antennas would be minimal, likely positioned at the window's top or bottom, resulting in minimal visual impact. Furthermore, considering typical antenna array surface dimensions of 20–30 cm \times 50 cm for frequencies between 2 and 3 GHz, the shielding at optical frequencies would be practically imperceptible, preserving natural lighting. Figure 1 depicts a potential integration of multiple semitransparent antennas constructed with a metal mesh on a large window or glass facade of an office building. The intended application involves the deployment of a significant array of antennas, enabling the passage of most light with minimal visual impact while forming part of the building's radio infrastructure. Larger antennas for windows could correspond to frequencies below 6 GHz (sub-6 GHz bands). Thus, aside from the space they occupy, a desirable structural characteristic would be a lightweight design for proper attachment to architectural glass.

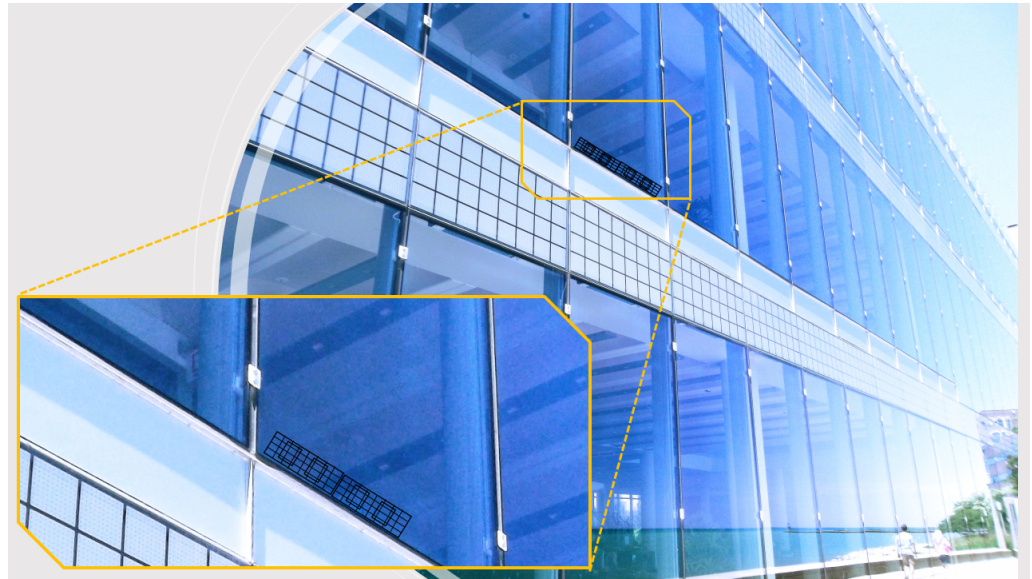


Figure 1. A potential urban application scenario featuring transparent antennas within a smart building. The zoomed-in view illustrates a potential array of semitransparent antennas constructed with metal mesh installed on the window of an office building.

The coexistence of numerous radio systems in urban environments, viewed from the perspective of Smart cities, presents multifunctional challenges with diverse objectives [4,34]. For instance, various wireless network systems coexist within different spatial coverage scales. For example, WiFi has limited coverage, whereas WiMAX and LTE cover broader areas. Different operating frequencies or requirements for power, latency, and data rates present significant variations. Systems like Bluetooth, operating at 2.4 GHz with a range of approximately 1–10 m and a data rate of 1 Mb/s, contrast with more demanding systems like LTE-A, operating at 2.5 GHz or 15 GHz with a coverage of 30 Km and data rates approaching 1 Gb/s in the downlink [34].

In addition to managing coverage and power needs, factors such as spectral efficiency within smart buildings and energy utilization are crucial [34,35]. Energy efficiency is pivotal in terms of network consumption and overall system balance, including buildings' thermal efficiency. Addressing sustainability involves considering waste generation, recycling, and the impact of electronics and network devices [36]. Balancing these aspects necessitates optimization of antennas and technology not only for electromagnetic performance but also for energy utilization, material recycling, manufacturing sustainability, and cost-effectiveness of the process, as depicted in Figure 2. One of the significant advantages of 3D printing lies in its positive impact on sustainability and material recycling. This technique reduces waste by enabling the reuse of surplus material or recycling defective products back into printable material. This ability to utilize and recycle materials, combined with manufacturing precision, aids in reducing the environmental footprint and promoting sustainable practices within the manufacturing industry. In this paper, we specifically utilize cost-effective 3D printing techniques to further explore these sustainability aspects.

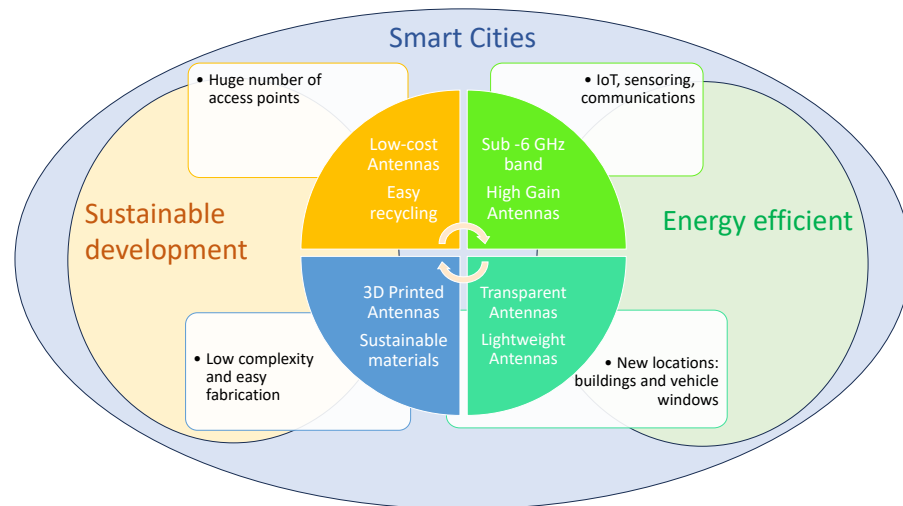


Figure 2. Conceptual scheme of the proposed work. The aim is a low-cost antenna solution operating within the sub-6 GHz band that is suitable for integration into building windows to deploy multiple elements, considering both energy efficiency and resource sustainability.

2.2. Semitransparent Mesh Patch Antenna Description

This section presents the design of a semitransparent antenna made with a metallic mesh. Figure 3 shows the proposed antenna, using the common approach of dividing the metallic surfaces into a grid from a solid metallic patch [4,14,17]. The discretization affects the ground plane and the patch differently, as observed in Figure 3, which also depicts the absence of the substrate and dielectric posts (see Figure 3c) that allow for the mechanical support of the structure. Within this section, we treat the metallic components of the antenna as a lossy conductor. The analysis was conducted using the silver parameters integrated into the CST Studio Suite 2021 simulator. The feeding line is also meshed, in this case using three metallic wires, as shown in Figure 3a, with a width of $w = 15.6$ mm to provide 50Ω .

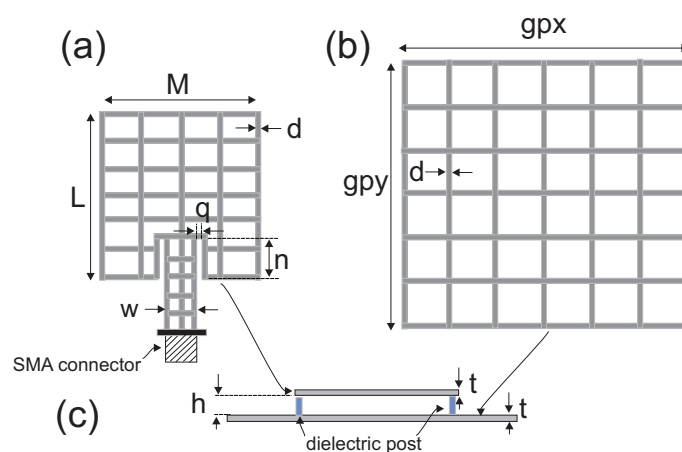


Figure 3. Description of the proposed semitransparent patch antenna and its main geometric parameters: (a) patch mesh; (b) ground-plane mesh; (c) side view with the air layer that replaces the dielectric substrate.

These mesh antennas require a small separation between grid elements compared to the working wavelength. To achieve high electromagnetic field shielding, a separation approximately 10 to 20 times smaller than λ_0 is necessary [14]. In our case, we verified that with larger distances, it is possible to achieve good antenna behavior, although perfect shielding may not be achieved. Our target frequency is 2.6 GHz, and we consider a ground-plane size of $0.56\lambda_0$. This size might seem relatively small, especially considering that a

patch antenna typically measures around $\lambda_0/2$ in its fundamental mode. However, we demonstrate that despite its size, it proves adequate to deliver good performance.

We simulated different spacings for the square ground plane of the antenna, as shown in Figure 4, which also includes the main geometric parameters considered for the antenna. As the patch is fed with an inset and considering that the feeding microstrip line is made with three wires, an odd number of elements in the grid is considered in that axis to maintain symmetry, while an even number is chosen in the perpendicular direction. Three transparency levels are compared, corresponding to three different grids: 7×8 metal wires (referred to as grid 1), 5×6 metal wires (grid 2), and 9×10 metal wires (grid 3). With these configurations, we have metallic element distances of $0.19\lambda_0 \times 0.16\lambda_0$ for grid 1, $0.23\lambda_0 \times 0.28\lambda_0$ for grid 2, and $0.14\lambda_0 \times 0.16\lambda_0$ for grid 3. Figure 4 shows the vertical component of the electric field in the antenna’s frequency range at 2.5 GHz, 2.6 GHz, and 2.7 GHz for the three grid sizes. The antenna’s mode is the fundamental TM_{10} , as shown in Figure 4, with a minimum field in the center and maxima at the ends of the cavity where the patch’s fringing fields are excited. It is observed that for all frequencies, as the grid becomes less dense, the electric field penetrates the ground plane to a greater extent. This clearly corresponds to an increasing level of back radiation as the ground-plane metal wires move farther away, as shown in Figure 5. Grid 3 exhibits lower levels of back radiation from the antenna in both planes. Furthermore, in Figure 5, we observe that at all three frequencies, the radiation patterns obtained for grid 1 are very similar to those of grid 3, with a slight increase in the back radiation as the frequency decreases. For the case with the least dense grid (grid 2 of 5×6 in Figure 5), the radiation patterns show a substantial increase in back radiation for both planes across the three frequencies.

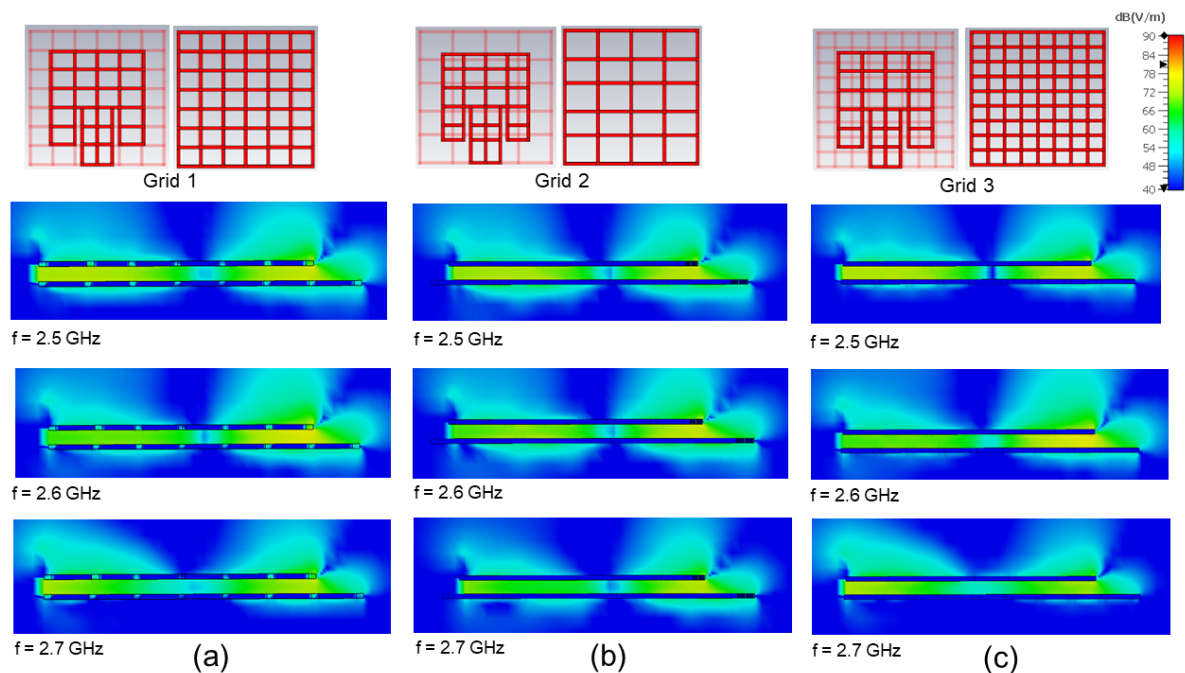


Figure 4. Side view of the $|E_z|$ electric field distribution evaluated for the antenna at different frequencies for the three considered cases of ground-plane metal mesh ($g_{px} = g_{py} = 64.4$ mm, $h = 3$ mm, $t = 1$ mm, $d = 1.5$ mm, $q = 1.9$ mm): (a) 7×8 wire mesh ($L = M = 45.2$ mm and $n = 16.3$ mm); (b) 5×6 wire mesh ($L = M = 42.4$ mm and $n = 16.2$ mm); (c) 9×10 wire mesh ($L = M = 45.5$ mm and $n = 16.3$ mm).

To choose the mesh topology, one must balance the antenna's electromagnetic behavior with the achievable level of transparency [4,14]. The transparency level, in our case, can be obtained from the following expression [20]:

$$t = 1 - \frac{\sum_{i=1}^n A_i}{A_t} \quad (1)$$

where the summation extends over the entire surface occupied by all metallic elements; A_i is the antenna (across both layers if they are not coincident); and A_t is the total area occupied by the antenna, which, in our case, is the total surface of the ground plane. Given that our antenna does not include a substrate, the only elements restricting light transmission in the optical range are its metallic wires (completely opaque in our case). It is clear that the transparency level of the proposed patch depends on the number of wires used for the ground plane and the patch's radiating layer, as well as their lengths and widths.

Given the intended application, the primary merit of the antenna we are considering is its gain. The antenna should exhibit sufficient efficiency for typical applications. It also needs to be planar for seamless integration into buildings. We chose a separation thickness of 3 mm between the ground plane and the patch ($h = 0.026\lambda_0$), making the antenna very flat (approximately 5 mm in total thickness), facilitating its placement on windows. The patch thickness influences its impedance bandwidth, resulting in a narrower bandwidth for the antenna. Transparent mesh-based antennas offer a tradeoff between their degree of transparency on one hand and their gain and resonance frequency on the other [4]. As transparency increases in the patch antenna, its gain decreases, as evidenced by the radiation patterns shown in Figure 5. The resonance frequency can be easily adjusted according to the element's size, but it is important to consider the significant relationship between the transparency and the front-to-back (FTB) ratio of the radiated power of the antenna [33]. There is no doubt that this ratio must be high to improve radio coverage while minimizing interference and exposure levels inside the building. Figure 6 analyzes these effects comprehensively for the three grids considered thus far.

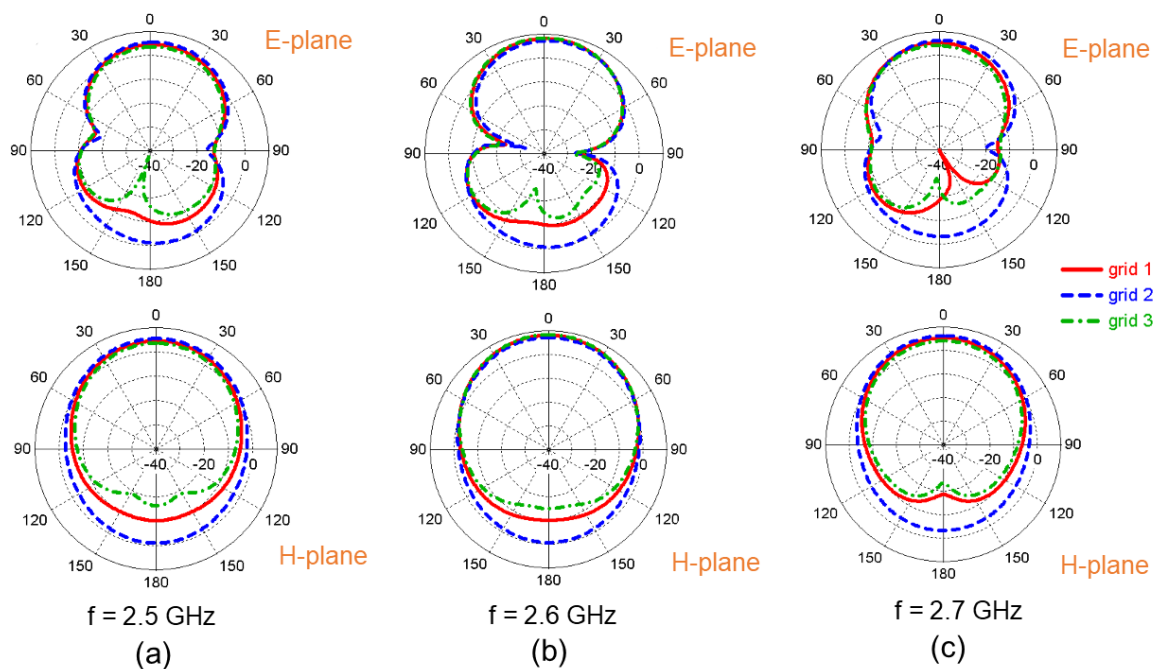


Figure 5. Simulated radiation patterns for the semitransparent antenna for the three ground planes in Figure 7: (grid 1) 7×8 wire mesh, (grid 2) 5×6 wire mesh, and (grid 3) 9×10 wire mesh at different frequencies. (a) $f = 2.5$ GHz; (b) $f = 2.6$ GHz; (c) $f = 2.7$ GHz.

The densest grid (grid 3) yields a gain of 8.3 dB at the working frequency, whereas for the intermediate grid (grid 1), the gain slightly reduces to 8.1 dB. In contrast, the grid with greater separation (grid 2) experiences a decrease in gain down to 7.3 dB at $f = 2.6$ GHz. It is also noticeable that in this case, although the antenna is matched to the frequency, the highest gain values occur at higher frequencies (2.8–2.9 GHz). The variation in the front-to-back ratio for the antenna relative to the ground plane is much more pronounced. At $f = 2.6$ GHz, simulation results show FTB values of 24 dB, 18.6 dB, and 8.5 dB for grid 3, grid 1, and grid 2, respectively, as seen in Figure 6. When comparing across grids, clearly, grid 3 and grid 1 offer similar gain values and an FTB increase slightly higher than 5 dB, which is acceptable to enhance transparency. However, when comparing grid 3 with grid 2, a significant decrease in gain is observed, and notably, a substantial increase in back radiation reduces the FTB from 24 dB to 8.5 dB. Clearly, grid 2 does not provide sufficient merit for the application.

In the following sections of this study, we analyze and design a semitransparent patch with an intermediate topology (grid 1), which offers very similar performance to the densely meshed patch but substantially improves its transparency. Applying the expression given by Equation (1), we obtain a transparency of $t = 60.2\%$ for the grid 1 topology with a wire width of $d = 1.5$ mm.

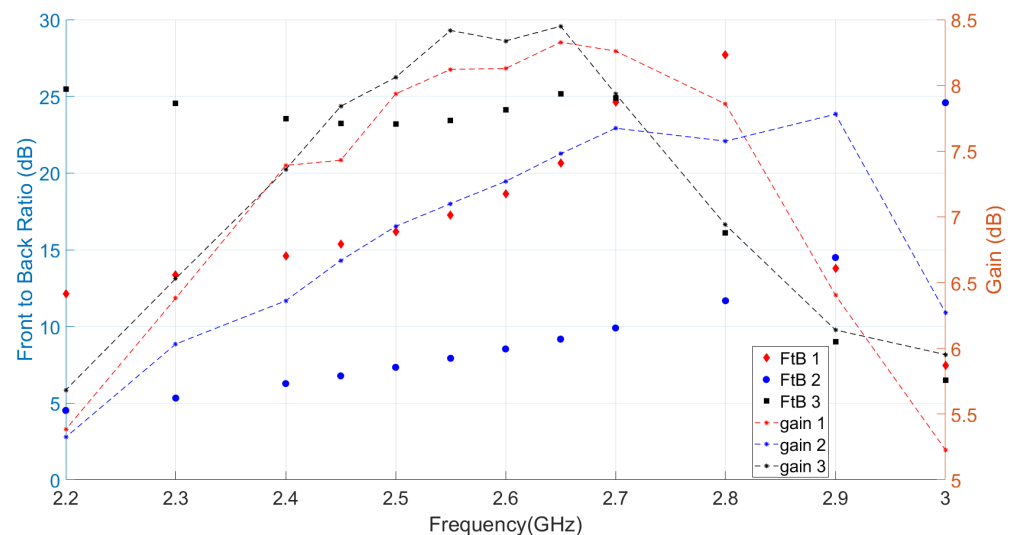


Figure 6. Front to back and gain evaluated for the proposed antenna as a function of frequency for the three ground planes in Figure 7: grid 1 (7×8 wires mesh with $L = M = 45.2$ mm and $n = 16.3$ mm); grid 2 (5×6 wires mesh with $L = M = 45.2$ mm and $n = 16.3$ mm); grid 3 (9×10 wires mesh with $L = M = 45.5$ mm and $n = 16.3$ mm).

Regarding the mesh design for patch metallization, our initial choice involved a 5×6 wire configuration. The odd count along the horizontal axis facilitated a wire placement at the center of the feeding point. Additionally, aligning the six wires along the vertical axis, with the lower plane housing the ground plane, helps to enhance the overall transparency, as discussed below. The spacing between elements within the patch mesh did not hinder the proper formation of the antenna cavity, as confirmed in Figure 4. Moving on to Figure 7, the observed $|E_y|$ electric field component aligns with the typical fringing field distribution of the patch. Symmetry and uniformity in the fringing field of the two edges of the resonant side for the patch were maintained for both grid 3 and grid 1, as shown in Figure 7a,b. However, the less dense grid showcased in Figure 7c resulted in a deterioration in both the distribution of the $|E_y|$ component and the current across the wires. Returning to the alignment between antenna layers and utilizing a specific grid similar to grid 1 for the ground plane shown in Figure 8 enables the alignment of wire positions for both the patch's meshed layer and the ground plane's meshed layer,

as depicted in Figure 8a,b. This alignment prevents direct visual obstruction through the antenna, enhancing overall transparency, as evidenced in Figure 8c for a manufactured prototype. However, establishing an exact patch size compromises grid uniformity, as evident in the prototype shown in Figure 8c. This slight irregularity, considering wire spacing concerning wavelength, has a minimal impact on the antenna’s response. For grid 1, the focal point from this point forward, this effect is minor and was taken into account in the simulations. In the final proposed patch design, besides the obtained gain and FTB values, it was confirmed that the cross-polar components of the radiation patterns remained consistently below -30 dB across all relevant frequencies.

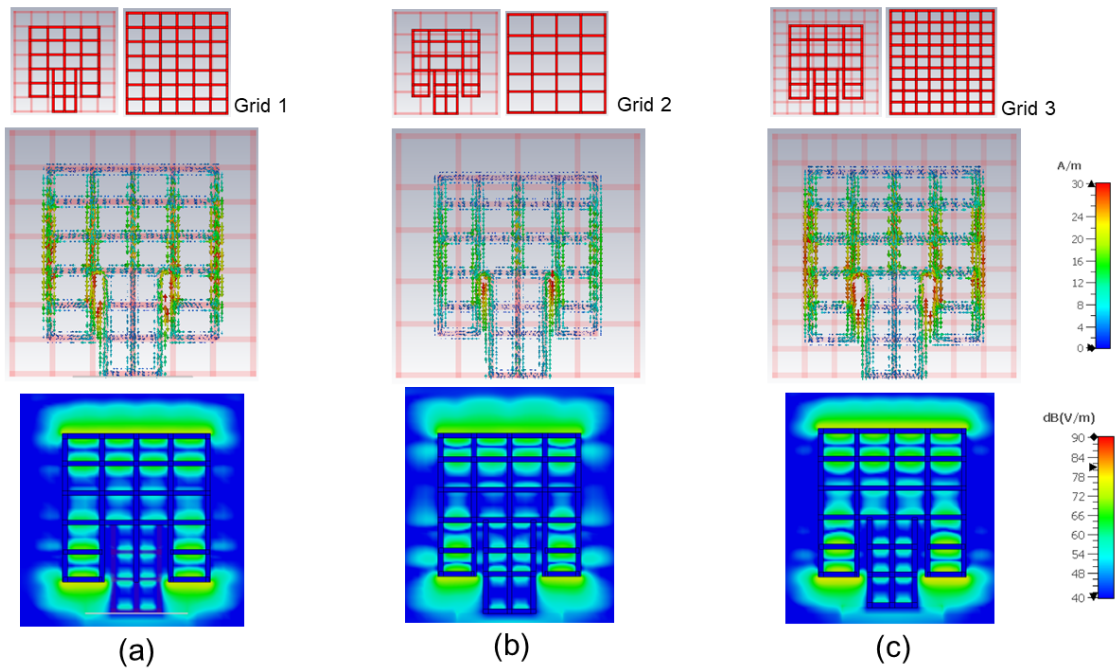


Figure 7. Surface current distribution (top) and $|E_y|$ field amplitude (lower) at $f = 2.6$ GHz for three types of meshed ground plane ($g_{px} = g_{py} = 64.4$ mm, $h = 3$ mm, $t = 1$ mm, $d = 1.5$ mm, $q = 1.9$ mm): (a) 7×8 wire mesh ($L = M = 45.2$ mm and $n = 16.3$ mm); (b) 5×6 wire mesh ($L = M = 42.4$ mm and $n = 16.2$ mm); (c) 9×10 wire mesh ($L = M = 45.5$ mm and $n = 16.3$ mm).

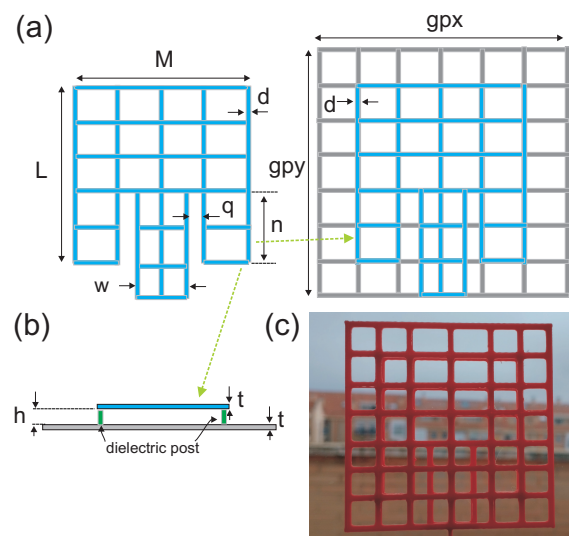


Figure 8. Scheme of the proposed configuration for the semitransparent patch: (a) mesh patch layer (left) and the patch overlaid on the ground plane (right); (b) side view of the antenna’s metal layers without a substrate; (c) back-view photo of a prototype to illustrate transparency.

It is clear that once we set the mesh design for both the patch and ground plane, we can change the antenna’s operating frequency by adjusting the patch size and tweaking the microstrip line’s position using the inset. The graph in Figure 9 shows how the antenna’s response varies depending on the patch size. For a patch measuring $L = M = 46.2$ mm, the antenna sits right at the target frequency of $f = 2.6$ GHz, with an impedance bandwidth ($|S_{11}| < -10$ dB) of 2.7%. At this frequency, the antenna size with this mesh setup is $0.4\lambda_0$, which is smaller than expected for a continuous patch. In these antennas, it is known that as the transparency increases (meaning the grid becomes less dense), the resonance frequency shifts to lower values. To maintain a specific operating range, we shrank the patch size as we increased transparency. This was evidenced in the values obtained for the antenna size as the grid became more transparent (Figure 4).

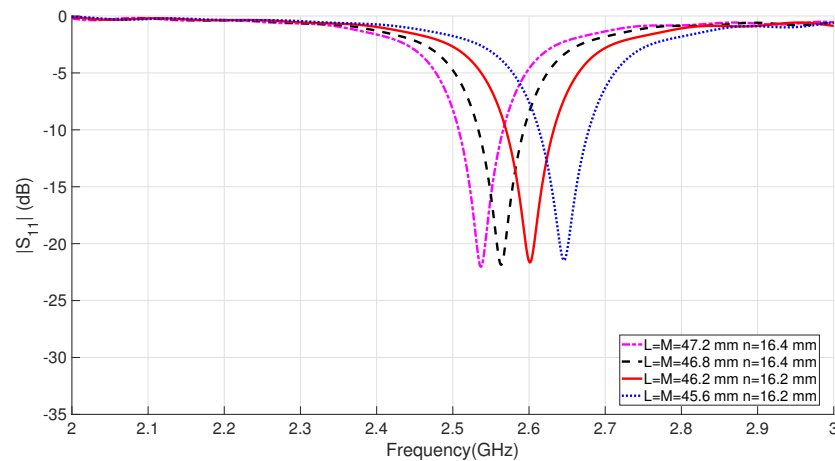


Figure 9. Simulated impedance response (S_{11}) of the proposed antenna for different sizes of the square patch considering the ground plane with 7×8 wire mesh, i.e., grid 1 ($g_{px} = g_{py} = 64.4$ mm, $h = 3$ mm, $t = 1$ mm, $d = 2$ mm, $q = 1.9$ mm, and $w = 15.6$ mm).

One last crucial aspect to explore in this section is the size of the metallic wires composing the antenna mesh. For simplicity, we assume that they are all uniform. Starting with wire thickness, taking into account the conductivity of silver, and assuming the conductor approximation described in Equation (2) (where f represents frequency and μ_0 stands for the permeability of free space and assuming $\mu_r = 1$ for the relative permeability of the conductor), we can calculate the skin depth at the antenna’s operating frequency of $f = 2.6$ GHz.

$$\delta_s = \sqrt{\frac{1}{\pi f \mu_0 \sigma}} \approx 9.87 \times 10^{-3} \sqrt{\frac{1}{\sigma}} \quad (2)$$

In this scenario, where $\delta_s = 1.25$ μm , we observe that the distance at which the field concentrates does not impose restrictions on the thickness of the wire layers. Although the wire thickness minimally affects the antenna’s response, its value is governed by mechanical requirements. As the antenna lacks a substrate and is 3D-printed using plastic materials, the wire thickness (denoted as ‘ d ’) must provide adequate mechanical stability and rigidity for suspension and placement in the window or final location. Printer tests indicated significantly improved rigidity for thicknesses above 0.8 mm. Therefore, for safety margins, a value of $t = 1$ mm was chosen throughout the research.

To understand the effect of metallic wire width on the antenna’s impedance response, Figure 10 depicts the variation in S_{11} for three different widths (d). It is evident from the antenna’s response that as the wire width decreases, the resonance shifts to lower frequencies, necessitating a smaller antenna to adjust its frequency. Naturally, a thinner ‘ d ’ would enhance transparency if maintaining the antenna’s size. However, as the patch size decreases, this effect would be partially or wholly offset, depending on the ‘ d ’ variation.

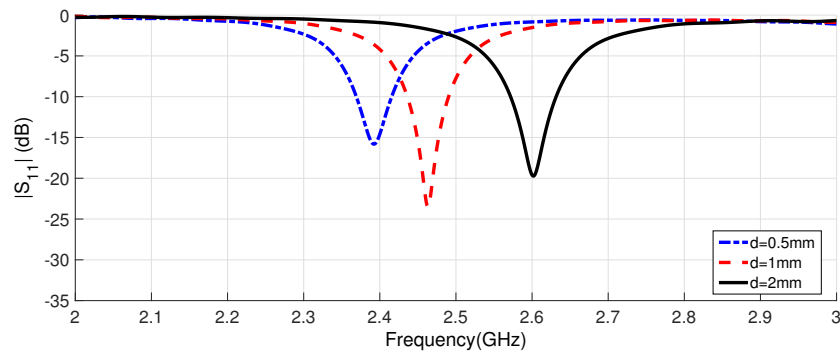


Figure 10. Simulated impedance response (S_{11}) of the proposed antenna for different widths (d) of mesh wires ($L = M = 46.2$ mm, $g_{px} = g_{py} = 64.4$ mm, $h = 3$ mm, $t = 1$ mm, $n = 16.3$ mm, $q = 1.9$ mm, and $w = 15.6$ mm).

Further exploring the impact of wire width on antenna gain, Figure 11 displays the antenna’s broadside gain for the same ‘ d ’ values as depicted in Figure 10. Reducing the wire width notably diminishes the antenna’s primary performance, decreasing from a maximum gain of 8.5 dB to 7.9 dB and 7.6 dB for $d = 2$ mm, $d = 1$ mm, and $d = 0.5$ mm, respectively. The maximum gain curves depicted in Figure 11 shift towards the left as the wire width decreases, which is consistent with the trend observed in the return losses shown in Figure 10.

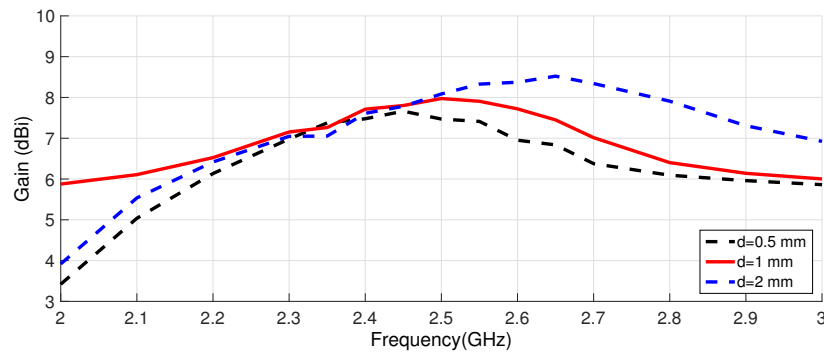


Figure 11. Simulated gain of the proposed antenna for different widths (d) of mesh wires ($L = M = 46.2$ mm, $g_{px} = g_{py} = 64.4$ mm, $h = 3$ mm, $t = 1$ mm, $n = 16.3$ mm, $q = 1.9$ mm, and $w = 15.6$ mm).

Considering the minor effect on transparency, the optimal choice to maintain the patch’s efficiency as a radiator is not to significantly reduce ‘ d ’; instead, opting for a value within the previously simulated higher range, i.e., $d = 2$ mm, seems more advantageous.

Table 1 indicates the values for the main geometric parameters for the designed semitransparent patch antenna. Numerical analysis suggests promising performance, with achieved gains exceeding 8 dB; good impedance matching within an FBW of 2.5–3%; and radiation patterns, FTB ratios, and cross polarizations similar to those of a non-transparent continuous patch.

Table 1. Parameters of the semitransparent patch antenna.

Parameter value (mm)	L	M	g_{px}	g_{py}	h
	46.2	46.2	64.4	64.4	3
Parameter value (mm)	t	d	q	n	w
	1	2	1.9	16.3	15.6

In the following section, we evaluate the performance achieved by our cost-effective design.

3. Performance Evaluation of the Antenna

This section details the manufacturing of prototypes, characterizes the final result of the printed and metallized parts of the proposed antenna using microscopy images, and analyzes the impact of the metallized surface on the performance of the semitransparent patch through simulation.

3.1. 3D Printing Low-Cost Fabrication

3D printing has revolutionized modern manufacturing by offering an innovative and versatile technique for creating three-dimensional objects from digital models. This is illustrated in Figure 12, where one of the semitransparent antenna models can be seen in Figure 12a, along with the result of printing semitransparent patch prototypes using different non-metallized materials in Figure 12b,c,d. This technique stands out for its relatively low cost compared to traditional manufacturing methods [37,38], as it minimizes material waste by building objects layer by layer, using only the precise amount of material required. Furthermore, 3D printing showcases an impressive diversity of available materials, ranging from plastics and resins to metals, ceramics, and even biodegradable materials, significantly expanding RF design possibilities and applications [39].

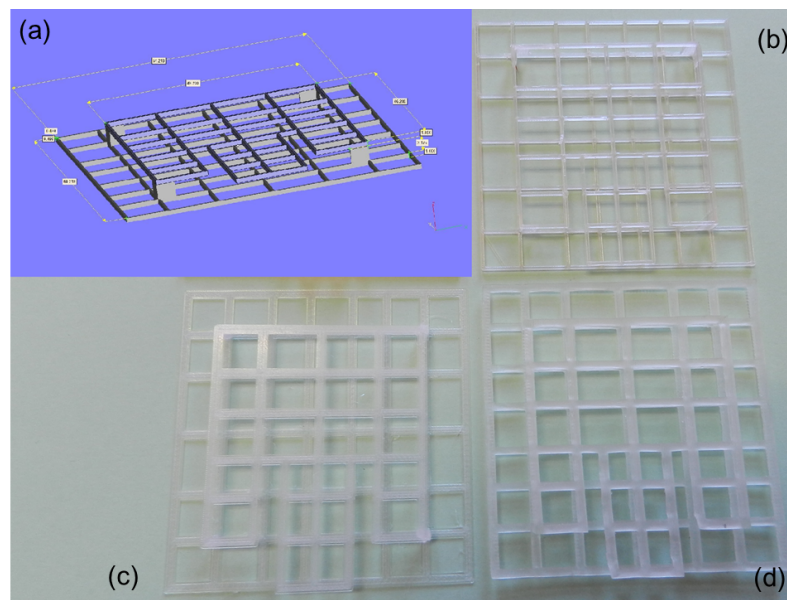


Figure 12. Illustrative stages of the 3D manufacturing process for the antenna: (a) model used for printing; (b) PETG prototype manufactured with $d = 0.5$ mm and $t = 1$ mm; (c) PETG prototype manufactured with $d = 2$ mm and $t = 0.4$ mm; (d) resin prototype manufactured with $d = 2$ mm and $t = 1$ mm.

From an antenna perspective, an issue that remains unresolved is the metallization of printed surfaces. On one hand, there is the possibility of printing using FDM diffusion techniques employing metallic filaments [39]. However, the final conductivity of presently accessible materials falls short, and published outcomes have been inefficient. Additional methodologies, such as metal diffusion or the utilization of conductive filament in conjunction with subsequent electroplating or electrodeposition, represent more advanced alternatives. However, these methods come with higher costs and limited accessibility in contrast to the approach expounded upon in this article. In our case, we chose to print using dielectric filaments (primarily PLA, PET, and ABS) and later metallize the surfaces using silver conductive paint (SCP). There is a wide range of manufacturing techniques and numerous dielectric materials available to carry out these printing processes, as detailed comprehensively in [40], the authors of which provide detailed information regarding the ranges they offer for tolerances in objects and, more importantly, their impact on surface

quality. Surface quality, in our case, affects the surface roughness level, which, alongside the conductivity of the metal layer covering the antenna's metallized elements, is the primary determinant of the patch's electrical performance.

The surface roughness in transmission lines impacts both losses and signal phase delay [41]. Consequently, patch antenna simulations often underestimate losses stemming from surface roughness, which is significant in our case due to the inherent inevitability of roughness in 3D printing. Assuming surface roughness as a random process, advanced models have recently been proposed to address this problem. In a physical approach with a clear practical focus aimed at simulation designs, the gradient model was proposed in [42]. This model calculates a conductivity gradient (perpendicular to the surface) based on the surface parameter (R_q), from which it derives a surface impedance, enhancing loss estimation. Additionally, it enables a more precise modeling of propagation delay in transmission lines or downshift of resonance frequencies in resonators [43]. R_q , known as the root mean square of measured microscopic peaks and valleys, given a roughness profile ($z(x)$) and its length (l_e), is determined according to

$$R_q = \sqrt{\frac{1}{l_e} \int_0^{l_e} z^2(x) dx} \quad (3)$$

This parameter is employed, in the case of lossy metals, by CST Microwave Studio to quantify the degree of surface roughness and introduce improvements in simulations by modeling surface impedance. To incorporate this effect into simulations and include it in the antenna gain analysis, we require an estimation of the magnitude of roughness on 3D-printed surfaces.

Table 2 details the characteristics of several manufactured prototypes, such as their manufacturing process, materials used, and printing layer thickness. It also indicates where prototype photographs appear, if available. Typical roughness values for these cases compiled from similar materials and thicknesses based on referenced studies are included in the table as R_a parameter ranges measured within this context. It is essential to note that these ranges are broad due to the dependence of surface roughness on multiple factors, including the orientation (deposition) angle [44]. For instance, factors like printing layer thickness, material properties, printing techniques, and printer settings contribute to this variability. In [40], the most significant factors affecting the surface roughness of PLA and ABS were identified, listed in order of importance: layer thickness, build orientation, printing speed, nozzle diameter, and temperature. However, the references consulted and their values included in Table 2 suggest that the roughness of printed plastic (PLA, ABS, and PET) surfaces typically falls between 0.1 and 0.3 times the printing thickness, reaching, at most, the thickness of the layer. To incorporate this effect into simulations using the commonly used R_a experimental parameter, it needs to correlate with the software's characteristic parameter for lossy metals (R_q). R_q represents the average roughness, which is the arithmetic average of the absolute values of the roughness profile ordinates, and is calculated as

$$R_a = \frac{1}{l_e} \int_0^{l_e} |z(x)| dx \quad (4)$$

The relationship between R_q and R_a varies depending on the surface roughness profile ($z(x)$) and may change based on the specific nature of the surface, the measurement technique employed, or the distribution of its irregularities. Generally, R_q tends to be smaller than R_a . It has been observed that R_a can typically exceed R_q by about 10% to 20% [40,44]. Commonly observed associations include $R_a = 1.1R_q$ and $R_a = 1.2R_q$; therefore, in our case, we consider these parameters as equivalent for the purposes of our qualitative analysis.

Table 2. Characteristic overview of 3D printing prototypes and comparison with the state-of-the-art roughness range (roughness data were extracted for a similar printed layer thickness).

Process	Material	Printed Layer	Photo	Range R_a (μm)			
AM	Filament	thickness	Figure	ref [40]	ref [44]	ref [45]	ref [46]
FDM	PLA	0.12 mm	Figure 13	5–10	-	6–22	-
FDM	ABS	-	-	6–15	11–18	-	7–20
FDM	PET	0.1 mm	Figure 12b,c	4–31	-	-	-
SLA/DLP	E-guard (resin)	0.1 mm	Figure 12d	5–30	-	-	-

Conductive paints and inks typically exhibit lower conductivity compared to the bulk material they contain [39]. Nevertheless, metallization using SCP has been successfully employed over the antenna in previous RF designs using methods such as airbrushing, paint-gun application, or manual brush application [37,38,47]. In this work, the antenna was hand-painted with a brush, applying a single layer on both sides of the conductive parts of the patch previously printed with dielectric filament. The paint was a commercial SCP containing approximately 40–50% silver by weight, along with other solvents, such as ethanol and acetone, as its main components [48]. Figure 13a depicts the 3D-printed parts of the antenna, patch, and ground plane in unpainted PLA, along with the paint used. The non-uniform configurations of the meshes for the ground plane and the patch, allowing them to visually overlap for improved transparency, are also detailed in Figure 13a. The final result of the antenna after paint application and assembly with adhesive is shown in Figure 13b. Obviously, soldering the connector is not feasible; hence, it is mounted onto the antenna using silver epoxy. The metallic paint used for manual metallization in some literature examples exhibits variable conductivity based on its composition and application. For instance, in [47], a stretchable silver conductive paste was used, yielding a conductivity value of $\sigma = 1.7 \times 10^4$ S/m for a paste layer with a thickness of 26.5 μm . Another hand-painted design is described in [38], where it was concluded that the manufacturer’s nominal conductivity of the paint ($\sigma = 1.3 \times 10^6$ S/m) did not significantly impact the antenna’s efficiency in the measurement. However, the surface layer’s conductivity was not experimentally characterized. In [37], similar SCP as in our case [48] was used to airbrush a 3D-printed filter prototype. Subsequently, in this study, the metallization was enhanced through an electroplating process, but before this, the estimated paint layer, with a thickness ranging between 10 and 20 μm , was experimentally characterized. Resistance was measured using probes at different distances across the dry paint layer, resulting in a DC conductivity value between $\sigma = 2.86 \times 10^5$ S/m and $\sigma = 5.7 \times 10^5$ S/m. This value might serve as a reasonable estimation for the conductivity range of our hand-painted surface for the metallic mesh.

Hand painting allows for greater control of strokes and details, resulting in a visible texture and brush marks on the surface, as can be seen in Figure 14. The paint was carefully applied, aiming for uniformity and complete coverage of the dielectric material surface. Figure 14a shows the detail of a semitransparent antenna prototype with a wire width of $d = 1$ mm in the center. For comparison, two prototypes are placed beside it; the thicker one on the left has a width of $d = 2$ mm, and the thinner one on the right has width of $d = 0.5$ mm. Transparency above 60% was achieved in all cases, with slightly higher values for prototypes with thinner wires. The result of the printing and metallization process appears reasonable at first sight, although slight brush marks and the roughness of the printed material persist, as shown in the detailed photos in Figure 14b,c. In the following section, we analyze the surface quality in greater detail using microscopic view analysis.

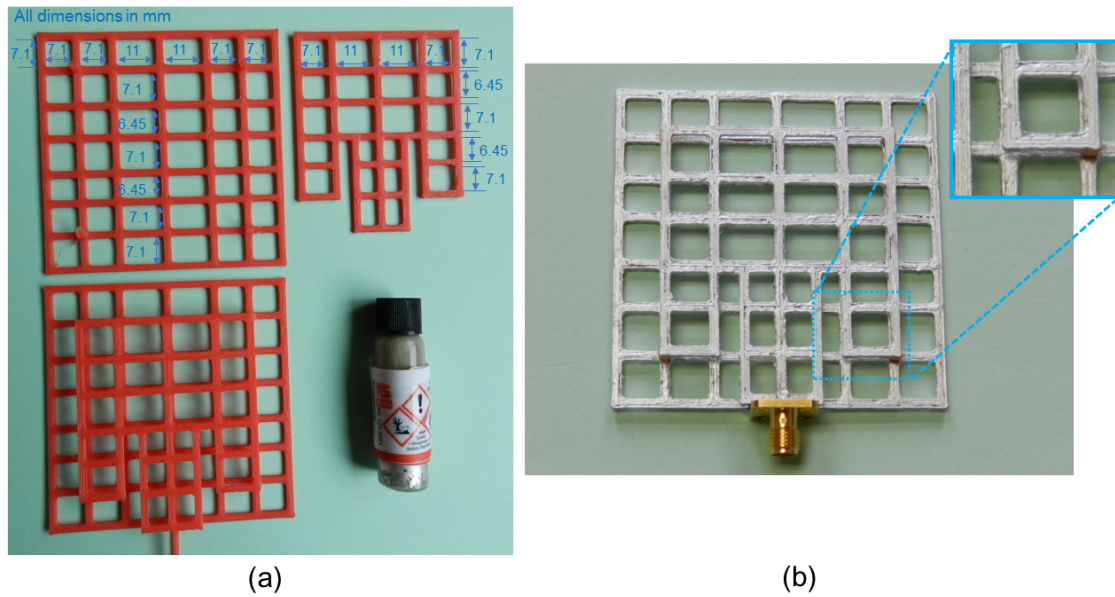


Figure 13. Photograph of the manufactured mesh antenna prototype: (a) 3D-printed PLA parts without metallization and the applied conductive paint (SCP), along with details depicting the non-uniform separation of the grid wires; (b) antenna metallized using the SCP and incorporating the SMA connector.

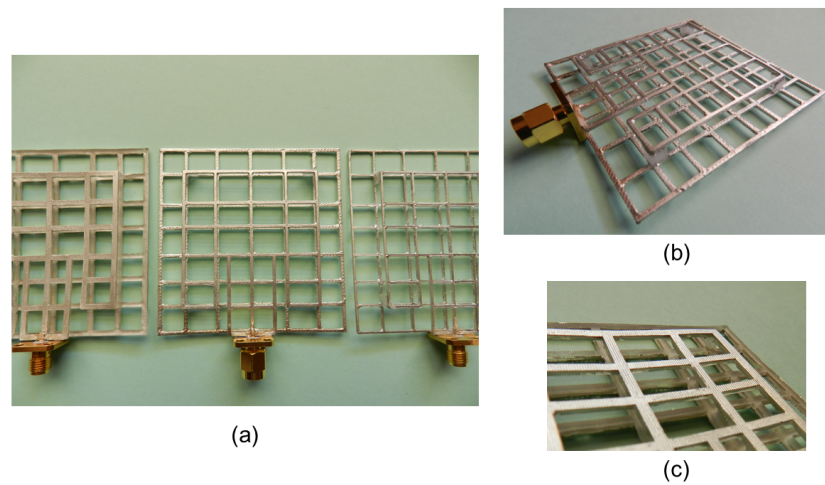


Figure 14. Photographs of manufactured prototypes. (a) With resin and a width of $d = 2$ mm (left); PET and a width of $d = 1$ mm (center); and PET and a width of $d = 0.5$ mm (right). (b) Perspective view of the mesh patch (PET and a width of $d = 1$ mm). (c) Surface detail (resin and a width of $d = 2$ mm).

3.2. Microscopic Characterization

We now describe the hand-painted surface of the two manufactured prototypes using a scanning electron microscope (SEM). Although the photographs presented Section 3.1 showed a uniformly painted surface at first glance, at the microscopic level, in Figure 15, we observe the roughness and small irregularities present on the surface of the 3D-printed material. Figure 15a,b display the prototype manufactured in PET using FDM with a width of $d = 1$ mm. In this case, small longitudinal grooves, paint burrs at the corners, and thin paint filaments protruding from the grid structure are evident. Another prototype, the resin antenna manufactured using SLA with a width of $d = 2$ mm, is shown unpainted in Figure 12d. Figure 15c displays its surface, showing significant structural roughness

in the transverse direction of the printed wires. The distance between peaks and valleys is clearly visible in Figure 15d, and although it was not quantified, it is observed to be significant compared to the width of the wires in the section. The SCP layer microscopically exhibits a fairly regular granular appearance of silver particles, although changes in particle density are evident in Figure 15b,d, with areas changing color due to the absence of silver. Irregularities in the 3D-printed surface due to the filament—not the paint—are also visible in Figure 15c.

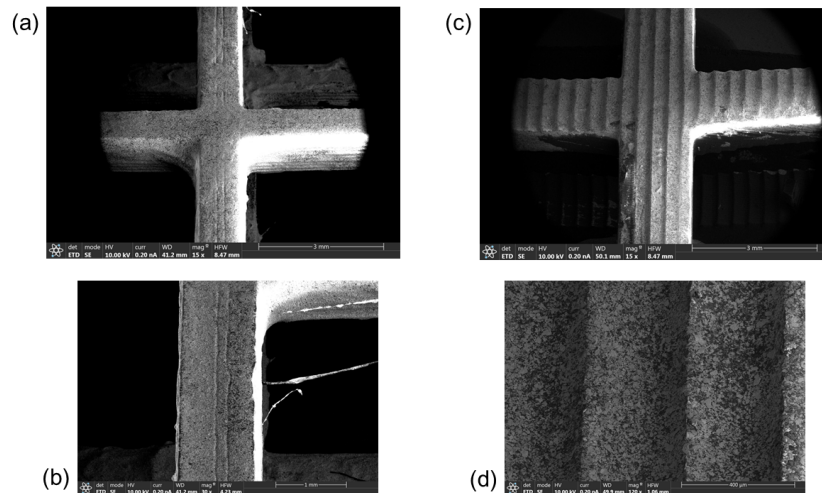


Figure 15. SEM images of two antenna prototypes. (a) Detail of a wire crossing printed with PET and a width of $d = 1$ mm; (b) zoomed-in view of a wire printed with PET and a width of $d = 1$ mm. (c) Detail of a wire crossing printed with resin and a width of $d = 2$ mm; (d) zoomed-in view of a wire printed with resin and a width of $d = 2$ mm.

In the literature, numerous studies have been conducted on the surface characteristics and properties of silver paint or ink. For instance, the authors of [49] delved into the mechanical and conductive properties of silver paint for applications in textile electronics, while the electrical and morphological properties of a hand-painted electrode using silver nanowires are described in [50]. Once applied, silver paint can undergo a thermal curing process, as exemplified in [47], where a sample was subjected to a $110\text{ }^{\circ}\text{C}$ temperature for 15 min. The curing and sintering processes of metal powder or paint substantially enhance the final conductivity of the metallized surface. However, the process temperature limits the use of plastic materials—particularly low-cost materials—in 3D printing of the structure to be metallized [49]. In our case, the paint was air-dried at room temperature, which evidently limited the final outcome. Silver in the paint is commonly found in the form of small particles or colloidal suspensions, and temperature influences the formation of silver flakes due to the chemical reaction between its components. SEM images presented in Figure 16 depict the formation of silver flakes on the surfaces of both prototypes, stratifying to form the paint layer. The size of these flakes varies; in Figure 16a, the detail shows sizes ranging from $2\text{--}3\text{ }\mu\text{m}$ up to $15\text{--}20\text{ }\mu\text{m}$. This morphological analysis of the surface demonstrates continuity through the contact of these flakes, which facilitates current transport across the surface. Nonetheless, manual application of the paint and the absence of curing reduce the aggregation of silver flakes, leading to a decrease in the effective conductivity of the surface [49]. In Figure 16c, areas with a lower density of silver particles are uniformly distributed. Additionally, in Figure 16a, some particle aggregates are surrounded by areas not covered by paint, forming islands that decrease metal connectivity, thereby negatively impacting electron transport and effective conductivity [51]. Figure 16b illustrates the basic chemical composition analysis of the two marked areas comprising the silver island: one with a high silver content (Ag) and the other with compounds from the material used for 3D printing (for example, O or C). Finally, in Figure 16d, the irregular coating applied

by the brush at the interface between two differently elevated zones on the surface is visible. These irregularities stem from the hand-painting process with a brush, unlike other techniques like airbrushing that achieve greater uniformity.

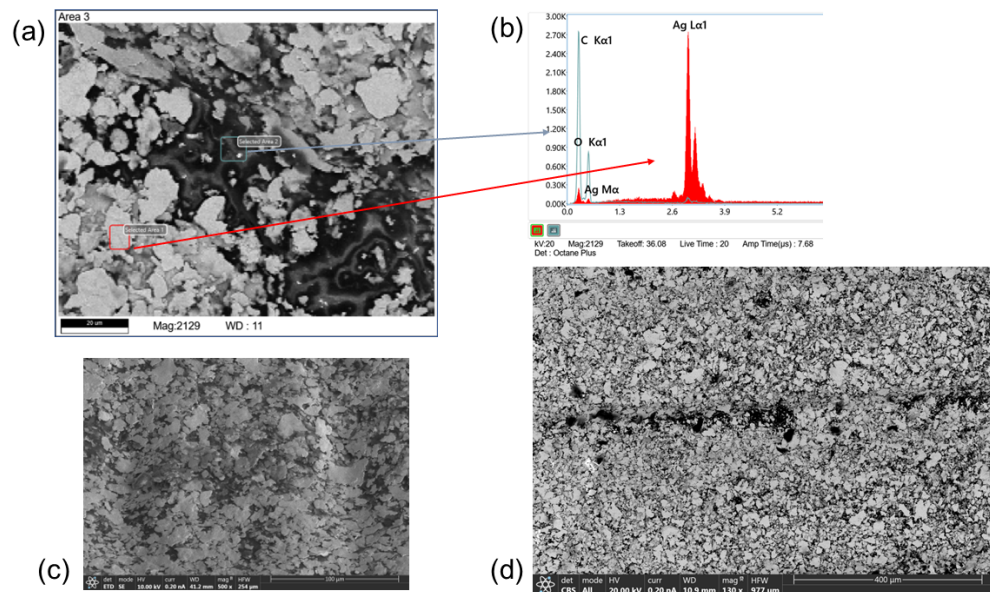


Figure 16. SEM images of the prototypes: (a) formation of silver islands with areas lacking a metal layer; (b) elemental SEM analysis of material composition; (c) silver flakes on the surface; (d) non-uniformities in the SCP layer.

Considering these factors, it is reasonable to anticipate a lower conductivity level on the surface compared to the measurement reported in [37]. This is attributed to both the brush application and the observed lack of connectivity in the SEM images of the surface. Starting from the approximate values measured in [37] ($\sigma = 2.8 - 5.7 \times 10^5$ S/m), establishing an upper limit, it seems reasonable to incorporate lower conductivity values into our numerical analysis of the antenna. Therefore, broad range of conductivity values between $\sigma = 5 \times 10^5$ S/m and $\sigma = 1 \times 10^4$ S/m is considered. In the subsequent section, we explore the impact on the antenna parameters by integrating the electrical characteristics and the degree of surface roughness into the simulation model.

3.3. Antenna Response Analysis: Surface Roughness and Conductivity

Figure 17 illustrates the simulated radiation efficiency for the proposed antenna concerning frequency, considering various conductivities and levels of roughness. The efficiency achieved with ideal smooth metal (upper continuous traces) shows values above 95% in the antenna's frequency range of interest (2.5–2.7 GHz) for $\sigma = 6.3 \times 10^7$ S/m (in blue), which represents the ideal limit for silver. However, reducing conductivity to more realistic values within the measured range [37] results in a drop in the antenna's efficiency drops to around 85% for $\sigma = 5 \times 10^5$ S/m (in red). Introducing different degrees of roughness alongside decreased conductivity significantly reduces the antenna efficiency. For a conductivity of $\sigma = 5 \times 10^5$ S/m, with roughness values (R_q) of 10 μm , 25 μm , 50 μm , and 100 μm , radiation efficiencies of 78.6%, 64.5%, 49.7%, and 36% are obtained, respectively. These R_q values correspond to 0.1, 0.25, 0.5, and 1 times the thickness of the printed layer. This range aligns with observed values in the state of the art for low-cost 3D-printed materials like PLA, ABS, and PET, including the absolute thickness limit of the printed layer [40]. In our case, we found that in contrast to maximum height, the distance between valleys and peaks is much less than 0.5 of the printed layer thickness for FDM with PET and of that order, at most, for the SLA-manufactured resin prototype. Therefore, considering the surface is smoothed by the SCP layer, the roughness in terms of R_a or R_q

should be significantly lower—approximately within 0.1 times the layer thickness for the 3D-printed dielectric material. However, in our case, there exists the inherent roughness of the silver flake layer, which, although not continuous, exhibits irregularities of that magnitude, as observed in Figure 16.

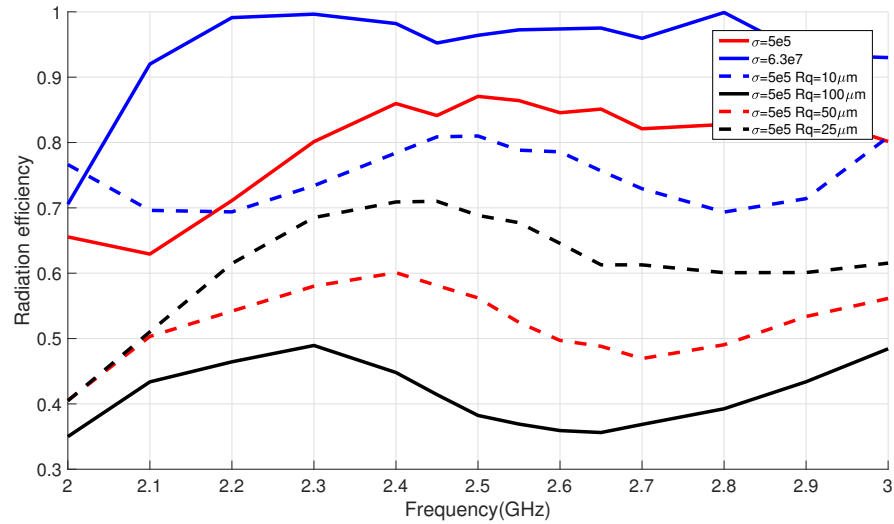


Figure 17. Simulated radiation efficiency calculated as a function of the conductivity of the metallic material of the antenna and the roughness of the surface: (smooth surfaces in continuous trace at the top of the figure) ($L = M = 46.2$ mm, $g_{px} = g_{py} = 64.4$ mm, $h = 3$ mm, $t = 1$ mm, $n = 16.3$ mm, $q = 1.9$ mm, and $w = 15.6$ mm).

To analyze the impact of surface roughness on impedance matching of the antenna, Figure 18 presents the simulated S_{11} parameter for the same roughness parameter (Rq) values. For the simulations, a conductivity of $\sigma = 5 \times 10^5$ S/m was selected, which falls within the likely range of values measured for this type of metallic ink [37]. This level of conductivity is sufficiently high to disregard dielectric and polarization effects, ensuring the continued validity of the approximation provided by Equation (2) [52]. According to this expression, the skin depth in this case is $\delta_s = 14 \mu\text{m}$, aligning with typical thicknesses for this type of metallic ink [37,38,47]. The antenna is well matched for smooth cases and for Rq values below $25 \mu\text{m}$. The figure demonstrates the shift towards lower frequencies in the antenna’s operating band as the degree of roughness (Rq) increases [41].

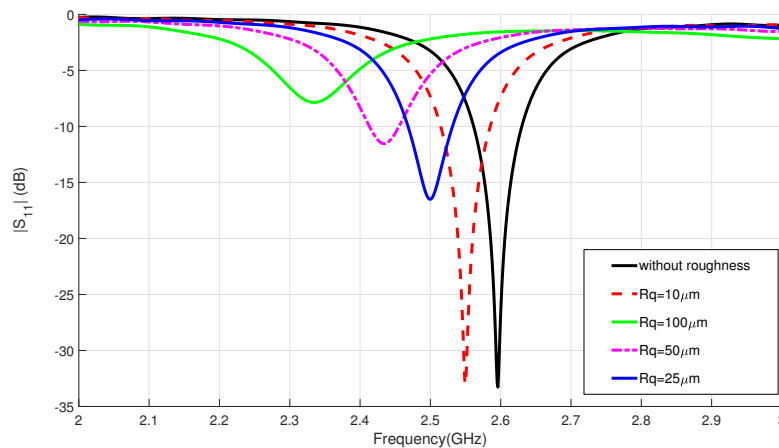


Figure 18. Simulated impedance response (S_{11}) of the proposed antenna for different surface roughness values of metallic material with a conductivity of $\sigma = 5 \times 10^5$ S/m.

Finally, Figure 19 includes the proposed antenna's gain vs. frequency across the entire range of conductivities and three roughness values, extending to the lowest surface print quality level at $R_q = 50 \mu\text{m}$. The combined effect of reduced conductivity and increased roughness significantly impacts the antenna's performance, reducing its theoretical gain. On one hand, the a conductivity decrease by two orders of magnitude results in a reduction in antenna gain from 7.6 dBi, 6.8 dBi, and 5.9 dBi for $R_q = 10 \mu\text{m}$, $R_q = 25 \mu\text{m}$, and $R_q = 50 \mu\text{m}$ to 6 dBi, 5.5 dBi, and 4.6 dBi, respectively. On the other hand, increased R_q at all conductivities also leads to reduced antenna gain. For instance, there is a reduction from 7.1 dBi for $\sigma = 5 \times 10^5 \text{ S/m}$ and $R_q = 10 \mu\text{m}$ to 5.5 dBi for the same conductivity with $R_q = 50 \mu\text{m}$. Moreover, this rise in roughness in simulations causes a shift in the frequency of the antenna's maximum gain towards lower frequencies. It is evident that controlling the final quality of the 3D-printed surface, particularly by limiting R_q and ensuring sufficient effective conductivity, is critical in achieving a high gain in semitransparent mesh antennas.

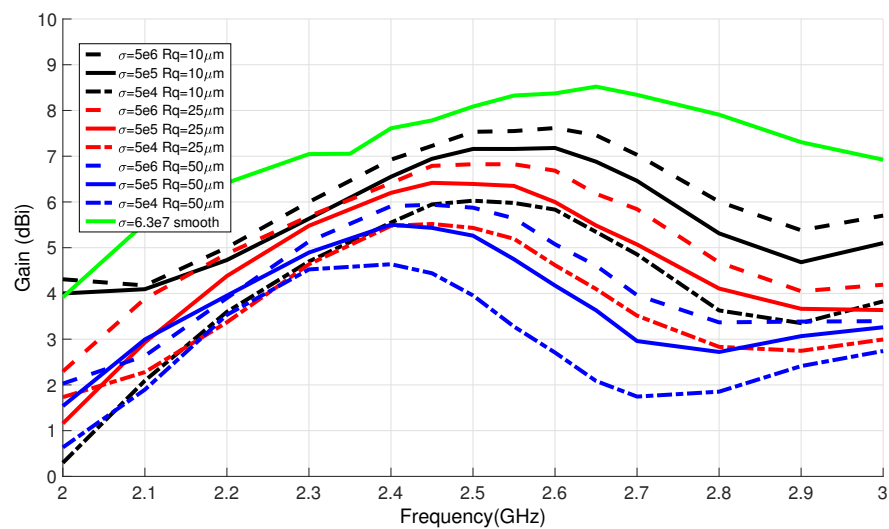


Figure 19. Simulated gain for the semitransparent antenna under different values of conductivity and roughness of the metal surface.

4. Results and Discussion

4.1. Experimental Results

To verify the performance of the proposed antenna with the parameters listed in Table 1, its impedance response and gain were measured in an anechoic chamber. Figure 20 presents a comparison between the experimentally observed realized gain and simulations for different surface conductivity and roughness values. Meanwhile, both simulation and measurement results for impedance matching are included in Figure 21. The measured antenna exhibits an operational frequency centered at $f_c = 2.64 \text{ GHz}$, with a bandwidth of $|S_{11}| < -10 \text{ dB}$ of 2.7%. Simulated matching curves show good agreement with the measurement for smooth cases (with ideal conductivity and with the conductivity measured in [37]), as well as for cases with low roughness ($R_q = 10 \mu\text{m}$ and $R_q = 5 \mu\text{m}$) and high conductivity ($\sigma = 5 \times 10^5 \text{ S/m}$ and $\sigma = 1 \times 10^5 \text{ S/m}$). For higher roughness values or for low roughness combined with lower conductivities, the simulated response reduces its matching and shifts towards lower frequencies. Regarding the gain, the proposed antenna reaches a peak of 5.4 dBi at a frequency of 2.64 GHz. It can be stated that the comparison of the measurement aligns well with the levels and responses of simulations for lower material conductivity values ($\sigma = 5 \times 10^5 \text{ S/m}$ and $\sigma = 1 \times 10^5 \text{ S/m}$) and low roughness levels around $R_q = 10 \mu\text{m}$.

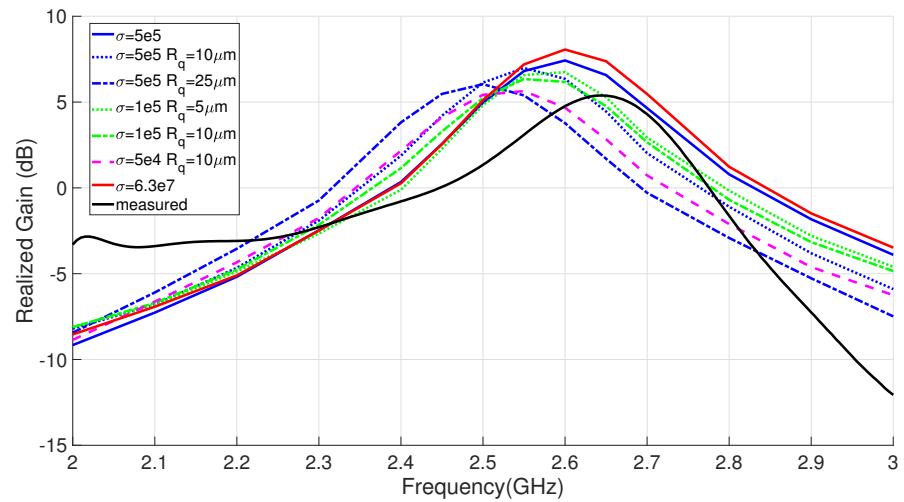


Figure 20. Realized gain for the manufactured semitransparent mesh antenna and for simulations accounts for various conductivity and surface roughness values on the metallic surfaces ($L = M = 46.2$ mm, $g_{px} = g_{py} = 64.4$ mm, $h = 3$ mm, $t = 1$ mm, $n = 16.3$ mm, $q = 1.9$ mm, and $w = 15.6$ mm).

Table 3 presents a summary comparing the impedance, radiation efficiency, and realized gain results. Considering the cost-effectiveness of the 3D printing manufacturing process, the antenna’s mesh components were metallized by hand-painting with a brush, and metallic adhesive was used for connector attachment, showcasing satisfactory performance in terms of S_{11} and realized gain for the proposed semitransparent patch. The calculated optical transparency derived from Equation (1) for the antenna with $d = 2$ mm exceeds 60%. This transparency result is depicted in the accompanying photographs included in Figure 22.

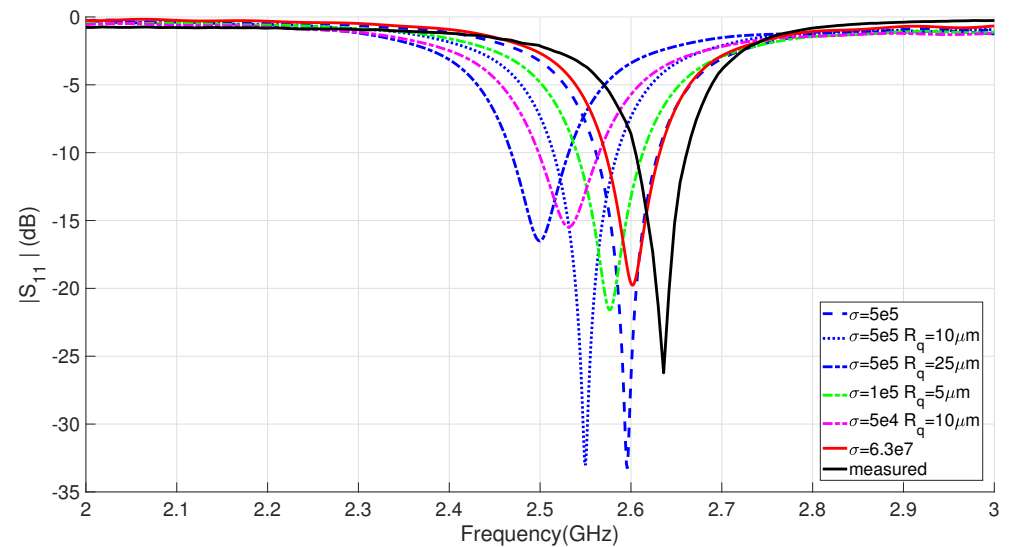


Figure 21. $|S_{11}|$ for the manufactured semitransparent mesh antenna and for simulations accounts for various conductivity and surface roughness values on the metallic surfaces ($L = M = 46.2$ mm, $g_{px} = g_{py} = 64.4$ mm, $h = 3$ mm, $t = 1$ mm, $n = 16.3$ mm, $q = 1.9$ mm, and $w = 15.6$ mm).

Table 3. Semitransparent antenna performance comparison between simulated and measured results.

Case	Material		Impedance BW			Radiation			
	Model	σ (S/m)	Rough. Rq μm	f_c (GHz)	RL (10dB)	RL (6dB)	f_r (GHz)	Peak R.Gain (dB)	3 dB BW%
sim lossy	6.3e7	smooth	2.6	2.31%	4%	2.605	8	8.8%	98.2%
sim lossy	5e5	smooth	2.6	2.7%	4.8%	2.6	7.4	8.1%	84.5%
sim lossy	5e5	10	2.55	2.74%	4.7%	2.55	7	8.6%	78.6%
sim lossy	5e5	25	2.5	2.52%	4.6%	2.5	6.1	8.7%	64.5%
sim lossy	1e5	5	2.57	2.9%	5%	2.56	6.3	8.6%	70.7%
sim lossy	5e4	10	2.53	2.4%	5.1%	2.58	5.6	6.2%	59.7%
mea PET + SCP	-	-	2.64	2.7%	3.9%	2.64	5.4	7.6%	-

4.2. Discussion

This study demonstrates the feasibility of designing an antenna with high optical transparency, as shown in Figure 22, utilizing 3D printing for its structure and applying low-cost techniques and materials for fabrication and metallization. Measurements of the proposed mesh patch antenna showcase its favorable performance relative to similar antennas, as detailed in Table 4. This research highlights the potential for advanced designs and applications in sub-6GHz bands for 5G/6G, allowing for integration in windows and glass surfaces without the limitations of surface restrictions or element count, presenting advantages in various RF systems within urban environments, such as improved gain, beamforming capabilities, MIMO arrays, etc.



Figure 22. Photographs of prototypes placed on a window to showcase their transparency, manufactured with: (a) PET and widths of $d = 0.5$ mm (left) and $d = 1$ mm (center); with resin and a width of $d = 2$ mm (right); (b) PLA and a width of $d = 2$ mm (left); and PET and a width of $d = 0.5$ mm (right).

Outlined below are some of the advantages offered by these cost-effective antennas:

1. The antenna's design allows for the passage of most visible light, harnessing natural light and minimizing visual impact.
2. The absence of a substrate enables manufacturing using various 3D printing materials, avoiding electrical losses inherent in substrates, reducing economic costs, and eliminating waste and recycling expenses. Furthermore, the lack of a substrate facilitates airflow, potentially lessening wind load or enhancing cooling.
3. The choice of 3D printing material for the antenna, whether metallic for optimized radiation efficiency or as a structural component later metallized with a low-cost dielectric, depends on factors such as material sustainability and recyclability. For

instance, PLA filament sourced from renewable sources like corn starch or sugarcane is considered more environmentally friendly than ABS derived from non-biodegradable fossil fuels [40].

4. The antenna's construction involves meshing its metallic parts, significantly reducing material usage and coupled with the absence of a substrate, implementing a mass reduction technique that drastically decreases its weight, aligning with current research trends [53].
5. The 3D printing technique enables consideration of material and electrical properties as additional parameters in the structure's design. This facilitates the elimination of conductive parts from ground planes, reducing mutual coupling, which is a substantial advantage in MIMO implementations [33].

In this research, we systematically evaluated the impact of the design and manufacturing process on antenna performance, particularly focusing on the surface quality of 3D-printed parts and low-cost metallic coatings (using paint or ink). The results indicate that despite cost limitations, the performance of the semitransparent antenna remains compatible with demanding applications in frequency bands below 6 GHz. However, due to limitations of metallized wires (width, surface quality, and manufacturing), obtaining antennas with both good performance and transparency greater than 50% above these frequencies is challenging. With the hand-painting method used in this work, it was observed that reducing the width of the wires to values below 1.25 mm rapidly affected the matching and gain of the manufactured prototypes, deteriorating their performance. Enhancing the smoothness and conductivity of printed surfaces, potentially through electroplating processes, could yield comparable gains to metallic PCB-based patches, even in designs at frequencies exceeding 10 GHz. A limited increase in transparency is also feasible by reducing the width of the metallic wires if effective conductivity is increased and the quality of 3D-printed surfaces is enhanced. Finally, it is important to note that when conductivity values are below $\sigma = 1 \times 10^5$ S/m, the skin depths obtained from Equation (2) exceed 30 μm , typically surpassing the thickness of the metallic paint layers. As a result, the electric field would penetrate significantly into the structural material, leading to increased losses, reduced confinement of electric field distributions, and a degradation in symmetry.

Table 4 compares the performance of the proposed semitransparent antenna with that of other state-of-the-art transparent antennas. Most showcased works feature patch designs at frequencies similar to ours, with mesh-based patches discussed in [14,17,54] and a stacked configuration reported in [9]. In [31], a micromesh-based stacked patch achieved the highest gain of 6 dBi among all results, boasting a large 19% impedance bandwidth and 70% transparency. However, the micromesh significantly blurs images, obstructing clear views through it, and it is notably larger than our proposed design. We also compared our design with that proposed in [55], the only non-transparent patch based on mesh but using FR4 substrate on PCB at 2.45 GHz, yielding a gain close to 3 dBi, which is notably lower than our outcome. Some transparent patches incorporate water inside a plastic container, as evidenced in [12], achieving a 4 dBi gain at 2.4 GHz but with larger antenna sizes. Additional radiating elements include a slot in SIW technology, achieving 4.8 dBi at 26.3 GHz [27]; a dipole loaded with a split-ring resonator, gaining 5 dBi at 5 GHz [10]; and a meandering monopole with 75% transparency but only 0.74 dBi gain at 2.44 GHz [15]. Upon reviewing the results, we conclude that the cost-effective semitransparent antenna performs exceptionally well in terms of high gain. While its impedance bandwidth is limited compared to other non-patch-type antennas, it aligns well with frequency-sharing patches. This highlights the feasibility of designing low-cost mesh patch antennas with high transparency and strong electromagnetic performance. Additionally, our design prioritizes low complexity, facilitating sustainability in materials and enhancing recyclability.

Table 4. Performance comparison with other reported transparent antennas.

Refs.	Element	Structure/ Substrate	Processing Method	Freq. (GHz)	OT	BW (%)	Gain (dBi)	Size (λ_0^3)	Complexity/ Cost
[17]	Patch	Wire mesh/ ceramic	PCB + cutting	2.73	60-65%	2.2	4.8	0.41×0.34	High
[27]	Slot + SIW	TCM /PC	-	26.3	71%	17.3	4.8	$1.59 \times$ 1.39×0.04	High
[12]	Patch	Water/plexiglass container	CNCM	2.4	-	35	4	$2.39 \times$ 2.39×0.312	Medium
[9]	Stacked patch	TCM/ PC	-	3.45	70%	39.8	4.1	$0.63 \times$ 0.63×0.07	High
[31]	Stacked patch	Conductive film /PMM	Metal alloy printing	2.65	70%	19	6	$0.88 \times$ 0.88×0.08	High
[15]	Meandering monopole	MMF/ glass	SNT	2.44	75%	3.3	0.74	0.34×0.34	High
[55]	Patch	Metal mesh Cu/ FR4	PCB	2.45	non OT	4	2.95	-	Low
[54]	Patch	MMF/ acrylic	Phys. deposition	2.45	60%	narrow	2.63	$0.41 \times$ 0.41×0.008	Medium
[14]	Patch	Micro MM/ acrylic	Phys. deposition	2.44	68.6%	narrow	5.28	-	Medium
[10]	Dipole + split ring	Metal grid/glass	PCB	5	69.8%	64.6	5	$0.67 \times$ 0.83×0.019	Medium
This work	Patch	Painted mesh/ air	PLA 3D printing+ SCP	2.64	60%	2.7	5.4	$0.56 \times$ 0.56×0.043	Low

An illustrative image of the solution proposed in this work is included in Figure 23. It exemplifies the potential application of the proposed semitransparent antennas. For this purpose, ideal array factors combined with the designed antenna were obtained using CST Microwave Studio. These radiating systems, the patch, and two arrays of 2×2 and 4×4 patch elements operating at 2.6 GHz, are placed on the windows of a smart building, as depicted in Figure 23. For each case, the calculated theoretical 3D radiation pattern is shown, obtaining gain values of 7.6 dBi, 12.5 dBi, and 18 dBi for the three systems. The graphic representation in Figure 23 also includes a photograph of the proposed antenna placed on a window, showcasing the achieved transparency.

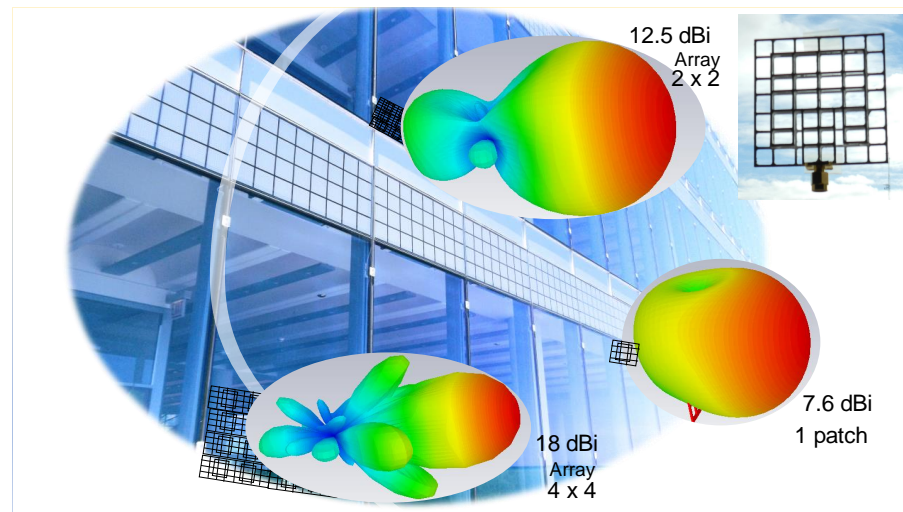


Figure 23. Graphic representation of the proposed application for semitransparent antenna systems. It showcases theoretical 3D radiation patterns for a patch, a 2×2 array, a 4×4 array, and the manufactured prototype placed on a window.

5. Conclusions

This article introduces a cost-effective method for creating semitransparent antennas suitable for integration into building or vehicle windows. The study presents a substrate-

less 3D printed mesh patch antenna, achieving a 2.7% bandwidth and a realized gain of 5.4 dBi at 2.6 GHz. This antenna design utilizes any dielectric material for the support structure, eliminating the need for a substrate, and can employ eco-friendly printing materials to reduce the carbon footprint. The impact of the surface roughness and conductivity of the metallic coating on antenna performance was assessed. The performance of the proposed semitransparent antenna reaches levels comparable to those of opaque patches but with 60% transparency in the optical range, allowing for the passage of most light and minimizing visual impact. Furthermore, by foregoing a substrate, the proposed radiating device minimizes losses and costs, optimizes recycling, and offers significant mass reduction. These semitransparent 3D printed meshed antennas are envisioned for sub-6GHz systems utilizing windows in smart buildings, offering advanced 5G/6G urban radio communication infrastructure.

Funding: This research was partially funded by the Spanish State Research Agency under projects PID2022-141055NB-C22 and PDC2022-133811-C22 from MCIN/AEI/10.13039/501100011033.

Institutional Review Board Statement: Not applicable.

Informed Consent Statement: Not applicable.

Data Availability Statement: Data are contained within the article.

Conflicts of Interest: The author declares no conflicts of interest.

Abbreviations

The following abbreviations are used in this manuscript:

ABS	Acrylonitrile butadiene styrene
AgHT	Ag coated polyester
AM	Additive manufacturing
AZO	Aluminum zinc oxide
CNCM	Computer numerical control machining
DLP	Digital (direct) light processing
FDM	Fused deposition modeling
FBW	Fractional bandwidth
FFF	Fused filament fabrication
FTB	Front to back ratio
ITO	Indium tin oxide
IZTO	Indium zinc thin oxide
MIMO	Multiple-input multiple output
MMF	Metal mesh film
OT	Optical transparency
PCB	Printed circuit board
PC	Polycarbonates
PET	Polyethylene terephthalate
PIFA	Planar inverted folded antenna
PLA	Polylactic acid
PMM	Polymethyl methacrylate
PVD	Physical vapor deposition
SCP	Silver conductive paint
SIW	Substrate integrated waveguide
SLS	Selective laser sintering
SLA	Stereolithography
SNT	Self-assembling nanoparticle technology
TCM	Transparent conductive mesh
TCO	Transparent conducting oxides
WMM	Wired metal mesh
ZnO	Doped zinc oxide

References

1. Bariah, L.; Mohjazi, L.; Muhaidat, S.; Sofotasios, P.C.; Kurt, G.K.; Yanikomeroğlu, H.; Dobre, O.A. A Prospective Look: Key Enabling Technologies, Applications and Open Research Topics in 6G Networks. *IEEE Access* **2020**, *8*, 174792–174820. [CrossRef]
2. López, O.L.A.; Alves, H.; Souza, R.D.; Montejo-Sánchez, S.; Fernández, E.M.G.; Latva-Aho, M. Massive Wireless Energy Transfer: Enabling Sustainable IoT Toward 6G Era. *IEEE Internet Things J.* **2021**, *8*, 8816–8835. [CrossRef]
3. Ikram, M.; Sultan, K.; Lateef, M.F.; Alqadami, A.S.M. A Road towards 6G Communication-A Review of 5G Antennas, Arrays, and Wearable Devices. *Electronics* **2022**, *11*, 169. [CrossRef]
4. Green, R.B.; Guzman, M.; Izyumskaya, N.; Ullah, B.; Hia, S.; Pitchford, J.; Timsina, R.; Avrutin, V.; Ozgur, U.; Morkoc, H.; et al. Optically Transparent Antennas and Filters: A Smart City Concept to Alleviate Infrastructure and Network Capacity Challenges. *IEEE Antennas Propag. Mag.* **2019**, *61*, 37–47. [CrossRef]
5. Freni, A.; Beccaria, M.; Mazzinghi, A.; Massaccesi, A.; Pirinoli, P. Low-Profile and Low-Visual Impact Smart Electromagnetic Curved Passive Skins for Enhancing Connectivity in Urban Scenarios. *Electronics* **2023**, *12*, 4491. [CrossRef]
6. Silva, Z.J.; Valenta, C.R.; Durgin, G.D. Optically Transparent Antennas: A Survey of Transparent Microwave Conductor Performance and Applications. *IEEE Antennas Propag. Mag.* **2021**, *63*, 27–39. [CrossRef]
7. Fang, X.S.; Leung, K.W. Design of Wideband Omnidirectional Two-Layer Transparent Hemispherical Dielectric Resonator Antenna. *IEEE Trans. Antennas Propag.* **2014**, *62*, 5353–5357. [CrossRef]
8. Clasen, G.; Langley, R. Meshed patch antennas. *IEEE Trans. Antennas Propag.* **2004**, *52*, 1412–1416. [CrossRef]
9. Shi, Y.; Wang, W.J. A Transparent Wideband Dual-Polarized Antenna for Sub-6 GHz Application. *IEEE Antennas Wirel. Propag. Lett.* **2022**, *21*, 2020–2024. [CrossRef]
10. Sun, Y.X.; Wu, D.; Fang, X.S.; Ren, J. On-Glass Grid Structure and Its Application in Highly-Transparent Antenna for Internet of Vehicles. *IEEE Trans. Veh. Technol.* **2023**, *72*, 93–101. [CrossRef]
11. Sun, J.; Luk, K.M. A Wideband and Optically Transparent Water Patch Antenna With Broadside Radiation Pattern. *IEEE Antennas Wirel. Propag. Lett.* **2020**, *19*, 341–345. [CrossRef]
12. Sun, J.; Luk, K.M. A Wideband Low Cost and Optically Transparent Water Patch Antenna With Omnidirectional Conical Beam Radiation Patterns. *IEEE Trans. Antennas Propag.* **2017**, *65*, 4478–4485. [CrossRef]
13. Saberlin, J.R.; Furse, C. Challenges with Optically Transparent Patch Antennas. *IEEE Antennas Propag. Mag.* **2012**, *54*, 10–16. [CrossRef]
14. Kang, S.H.; Jung, C.W. Transparent Patch Antenna Using Metal Mesh. *IEEE Trans. Antennas Propag.* **2018**, *66*, 2095–2100. [CrossRef]
15. Li, Q.L.; Cheung, S.W.; Wu, D.; Yuk, T.I. Optically Transparent Dual-Band MIMO Antenna Using Micro-Metal Mesh Conductive Film for WLAN System. *IEEE Antennas Wirel. Propag. Lett.* **2017**, *16*, 920–923. [CrossRef]
16. Clasen, G.; Langley, R.J. Gridded circular patch antennas. *Microw. Opt. Technol. Lett.* **1999**, *21*, 311–313. [CrossRef]
17. Ryan, C.G.M.; Eleftheriades, G.V. Single- and Dual-Band Transparent Circularly Polarized Patch Antennas with Metamaterial Loading. *IEEE Antennas Wirel. Propag. Lett.* **2015**, *14*, 470–473. [CrossRef]
18. Li, W.; Yarali, E.; Bakytbekov, A.; Anthopoulos, T.D.; Shamim, A. Highly transparent and conductive electrodes enabled by scalable printing-and-sintering of silver nanowires. *Nanotechnology* **2020**, *31*, 395201. [CrossRef]
19. Yao, Y.; Shao, Y.; Zhang, J.; Zhang, J. A Transparent Antenna Using Metal Mesh for UWB MIMO Applications. *IEEE Trans. Antennas Propag.* **2023**, *71*, 3836–3844. [CrossRef]
20. Yazdani, R.; Yousefi, M.; Aliakbarian, H.; Oraizi, H.; Vandenbosch, G.A.E. Miniaturized Triple-Band Highly Transparent Antenna. *IEEE Trans. Antennas Propag.* **2020**, *68*, 712–718. [CrossRef]
21. Xi, B.; Liang, X.; Chen, Q.; Wang, K.; Geng, J.; Jin, R. Optical Transparent Antenna Array Integrated With Solar Cell. *IEEE Antennas Wirel. Propag. Lett.* **2020**, *19*, 457–461. [CrossRef]
22. Yekan, T.; Baktur, R. Conformal Integrated Solar Panel Antennas: Two effective integration methods of antennas with solar cells. *IEEE Antennas Propag. Mag.* **2017**, *59*, 69–78. [CrossRef]
23. Hong, W.; Lim, S.; Ko, S.; Kim, Y.G. Optically Invisible Antenna Integrated Within an OLED Touch Display Panel for IoT Applications. *IEEE Trans. Antennas Propag.* **2017**, *65*, 3750–3755. [CrossRef]
24. Morimoto, Y.; Shiu, S.; Huang, I.W.; Fest, E.; Ye, G.; Zhu, J. Optically Transparent Antenna for Smart Glasses. *IEEE Open J. Antennas Propag.* **2023**, *4*, 159–167. [CrossRef]
25. Wagih, M.; Weddell, A.S.; Beeby, S. Meshed High-Impedance Matching Network-Free Rectenna Optimized for Additive Manufacturing. *IEEE Open J. Antennas Propag.* **2020**, *1*, 615–626. [CrossRef]
26. Lin, Y.M.; Wu, H.W.; Hung, C.Y.; Chang, S.J.; Liu, R. Dual-Polarized Transparent Antenna and Its Application for Capsule Endoscopy System. *Electronics* **2023**, *12*, 3124. [CrossRef]
27. Shi, Y.; Wang, W.J.; Hu, T.T. A Transparent SIW Cavity-Based Millimeter-Wave Slot Antenna for 5G Communication. *IEEE Antennas Wirel. Propag. Lett.* **2022**, *21*, 1105–1109. [CrossRef]
28. Lee, I.G.; Yoon, Y.J.; Choi, K.S.; Hong, I.P. Design of an Optical Transparent Absorber and Defect Diagnostics Analysis Based on Near-Field Measurement. *Sensors* **2021**, *21*, 3076. [CrossRef]
29. Wan, S.; Lu, P.; Yin, D.; Guan, X.; Ni, W. A compact hybrid solar and electromagnetic energy harvester at 2.45 GHz microstrip rectenna. *AEU Int. J. Electron. Commun.* **2023**, *172*, 154941. [CrossRef]

30. Hu, H.T.; Chen, B.J.; Chan, C.H. A Transparent Proximity-Coupled-Fed Patch Antenna With Enhanced Bandwidth and Filtering Response. *IEEE Access* **2021**, *9*, 32774–32780. [CrossRef]
31. Ding, C.; Liu, L.; Luk, K.M. An Optically Transparent Dual-Polarized Stacked Patch Antenna With Metal-Mesh Films. *IEEE Antennas Wirel. Propag. Lett.* **2019**, *18*, 1981–1985. [CrossRef]
32. Fernandez, A.; Touchard, G.; Sanchez, L.I.; Iglesias, E.R. ANTENNA, 2018. EP 3 584 884. Available online: <https://data.epo.org/publication-server/document?iDocId=6118369&iFormat=0> (accessed on 26 December 2023).
33. Inclán-Sánchez, L. Analysis of a Semitransparent PIFA Element for MIMO Applications. In Proceedings of the 2022 16th European Conference on Antennas and Propagation (EuCAP), Madrid, Spain, 27 March–1 April 2022; pp. 1–5.
34. Yaqoob, I.; Hashem, I.A.T.; Mehmood, Y.; Gani, A.; Mokhtar, S.; Guizani, S. Enabling Communication Technologies for Smart Cities. *IEEE Commun. Mag.* **2017**, *55*, 112–120. [CrossRef]
35. Medina, W.; Novillo, F.; Chancay, E.; Romero, J. Mechanism to Estimate Effective Spectrum Availability Inside Smart Buildings. *Electronics* **2020**, *9*, 1244. [CrossRef]
36. Rani, S.; Mishra, R.K.; Usman, M.; Kataria, A.; Kumar, P.; Bhambri, P.; Mishra, A.K. Amalgamation of Advanced Technologies for Sustainable Development of Smart City Environment: A Review. *IEEE Access* **2021**, *9*, 150060–150087. [CrossRef]
37. Dionigi, M.; Tomassoni, C.; Venanzoni, G.; Sorrentino, R. Simple High-Performance Metal-Plating Procedure for Stereolithographically 3-D-Printed Waveguide Components. *IEEE Microw. Wirel. Components Lett.* **2017**, *27*, 953–955. [CrossRef]
38. Kuosmanen, M.; Ala-Laurinaho, J.; Holopainen, J.; Viikari, V. Antenna Array Based on 3D-printed Plastic BoR Elements Coated with Conductive Paint. In Proceedings of the 2023 17th European Conference on Antennas and Propagation (EuCAP), Florence, Italy, 26–31 March 2023; pp. 1–5. [CrossRef]
39. Whittaker, T.; Zhang, S.; Powell, A.; Stevens, C.J.; Vardaxoglou, J.Y.C.; Whittow, W. 3D Printing Materials and Techniques for Antennas and Metamaterials: A survey of the latest advances. *IEEE Antennas Propag. Mag.* **2023**, *65*, 10–20. [CrossRef]
40. Golhin, A.P.; Tonello, R.; Frisvad, J.R.; Grammatikos, S.; Strandlie, A. Surface roughness of as-printed polymers: A comprehensive review. *Int. J. Adv. Manuf. Technol.* **2023**, *127*, 987–1043. [CrossRef]
41. Gold, G.; Helmreich, K. A Physical Surface Roughness Model and Its Applications. *IEEE Trans. Microw. Theory Tech.* **2017**, *65*, 3720–3732. [CrossRef]
42. Sepaintner, F.; Scharl, A.; Jakob, J.; Schmalzbauer, M.; Röhr, F.; Bogner, W.; Zorn, S. An Effective Surface Impedance Concept to Model Arbitrary Roughness Profiles on Printed Circuit Boards up to 110 GHz. *IEEE Microw. Wirel. Technol. Lett.* **2023**, *33*, 783–786. [CrossRef]
43. Gold, G.; Helmreich, K. Surface impedance concept for modeling conductor roughness. In Proceedings of the 2015 IEEE MTT-S International Microwave Symposium, Phoenix, AZ, USA, 17–22 May 2015; pp. 1–4. [CrossRef]
44. Ahn, D.; Kweon, J.H.; Kwon, S.; Song, J.; Lee, S. Representation of surface roughness in fused deposition modeling. *J. Mater. Process. Technol.* **2009**, *209*, 5593–5600. [CrossRef]
45. Yang, L.; Li, S.; Li, Y.; Yang, M.; Yuan, Q. Experimental Investigations for Optimizing the Extrusion Parameters on FDM PLA Printed Parts. *J. Mater. Eng. Perform.* **2019**, *28*, 169–182. [CrossRef]
46. Reddy, V.; Flys, O.; Chaparala, A.; Berrimi, C.E.; V, A.; Rosen, B. Study on surface texture of Fused Deposition Modeling. *Procedia Manuf.* **2018**, *25*, 389–396. [CrossRef]
47. Rizwan, M.; Khan, M.W.A.; Sydänheimo, L.; Virkki, J.; Ukkonen, L. Flexible and Stretchable Brush-Painted Wearable Antenna on a Three-Dimensional (3-D) Printed Substrate. *IEEE Antennas Wirel. Propag. Lett.* **2017**, *16*, 3108–3112. [CrossRef]
48. RS Components. RS Pro Silver Conductive Paint. Available online: <https://www.rs-components.com> (accessed on 20 September 2023).
49. Zhong, T.; Jin, N.; Yuan, W.; Zhou, C.; Gu, W.; Cui, Z. Printable Stretchable Silver Ink and Application to Printed RFID Tags for Wearable Electronics. *Materials* **2019**, *12*, 3036. [CrossRef] [PubMed]
50. Kim, Y.J.; Kim, G.; Kim, H.K. Study of Brush-Painted Ag Nanowire Network on Flexible Invar Metal Substrate for Curved Thin Film Heater. *Metals* **2019**, *9*, 1073. [CrossRef]
51. Chang, Y.C.; Lu, Y.C.; Hung, Y.J. Controlling the Nanoscale Gaps on Silver Island Film for Efficient Surface-Enhanced Raman Spectroscopy. *Nanomaterials* **2019**, *9*, 470. [CrossRef]
52. Claus, N.; Verhaevert, J.; Rogier, H. Cost-Driven Design of Printed Wideband Antennas with Reduced Silver Ink Consumption for the Internet of Things. *Sensors* **2022**, *22*, 7929. [CrossRef]
53. Aragbaiye, Y.M.; Isleifson, D. Mass Reduction Techniques for Short Backfire Antennas: Additive Manufacturing and Structural Perforations. *Sensors* **2023**, *23*, 8765. [CrossRef]
54. Hong, S.; Kim, Y.; Won Jung, C. Transparent Microstrip Patch Antennas With Multilayer and Metal-Mesh Films. *IEEE Antennas Wirel. Propag. Lett.* **2017**, *16*, 772–775. [CrossRef]
55. Silva, Z.J.; Hunter, C.P.; Valenta, C.R.; Durgin, G.D. 2.5 GHz Meshed Inset-Fed Patch Antenna. In Proceedings of the 2019 IEEE International Symposium on Antennas and Propagation and USNC-URSI Radio Science Meeting, Atlanta, GA, USA, 7–12 July 2019; pp. 843–844. [CrossRef]

Disclaimer/Publisher’s Note: The statements, opinions and data contained in all publications are solely those of the individual author(s) and contributor(s) and not of MDPI and/or the editor(s). MDPI and/or the editor(s) disclaim responsibility for any injury to people or property resulting from any ideas, methods, instructions or products referred to in the content.

Article

A Multi-Band Circularly Polarized-Shared Aperture Antenna for Space Applications at S and X Bands

Syed Salman Kabir, Mehedi Hassan Khan and Saeed I. Latif * 

Department of Electrical and Computer Engineering, University of South Alabama, Mobile, AL 36688, USA

* Correspondence: slatif@southalabama.edu

Abstract: In this article, a compact multiband antenna design and analysis is presented with a view of ensuring efficient uplink/downlink communications at the same time from a single antenna for CubeSat applications. This design shares the aperture of an S-band slot antenna to accommodate a square patch antenna operating in the X-band. Shared aperture antennas, along with an air gap and dielectric loading, provided good gain in both frequency bands. The S-band patch had an $S_{11} = -10$ dB bandwidth of 30 MHz (2013–2043 MHz, 1.5%), and the X-band antenna demonstrated a bandwidth of 210 MHz (8320–8530 MHz, 2.5%). The Axial Ratio (<3 dB) bandwidth of the slot antenna in the S-band is 7 MHz (2013–2020 MHz, 0.35%), and it is 67 MHz (8433–8500 MHz, 0.8%) in the case of patch antenna in the X-band. While the maximum gain in the S-band reached 7.7 dBic, in the X-band, the peak gain was 12.8 dBic. This performance comparison study shows that the antenna is advantageous in terms of high gain, maintains circular polarization over a wideband, and can replace two antennas needed in CubeSats for uplink/downlink, which essentially saves space.

Keywords: CubeSat; shared aperture antenna; multiband; high gain; circular polarization



Citation: Kabir, S.S.; Khan, M.H.; Latif, S.I. A Multi-Band Circularly Polarized-Shared Aperture Antenna for Space Applications at S and X Bands. *Electronics* **2023**, *12*, 4439. <https://doi.org/10.3390/electronics12214439>

Academic Editor: Hristos T. Anastassiou

Received: 16 September 2023

Revised: 24 October 2023

Accepted: 25 October 2023

Published: 28 October 2023



Copyright: © 2023 by the authors. Licensee MDPI, Basel, Switzerland. This article is an open access article distributed under the terms and conditions of the Creative Commons Attribution (CC BY) license (<https://creativecommons.org/licenses/by/4.0/>).

1. Introduction

At the beginning of space exploration, satellites were large and heavy and delivered a multi-functional payload. These satellites used high power and needed a long development time and a huge budget. Satellite development skills were inaccessible to students and researchers in most cases. Also, there were many scientific questions that required attention but could not justify the large cost of satellite development to resolve them. The technological advances in low-power microelectronics, micro-electromechanical systems, and digital signal processing paved the way for the development of small satellites with a low cost and short development time yet with a lot of advanced functionality [1–3]. These small satellites are lighter and cheaper compared to conventional satellites, which makes them suitable for applications in academia and amateur projects. CubeSat, a special type of small satellite made of one or multiple $10 \times 10 \times 10$ cm³ cubic structures, rapidly gained popularity in different sectors due to its flexible design and capacity for custom development. A CubeSat with a dimension of 10 cm on each side is called 1 U, which is the standard unit of the CubeSat size. A CubeSat can be 1 U, 2 U, 3 U and even increases up to 12 U and 16 U if required by the mission. CubeSat was first developed and standardized in 1999 by Jordi Puig-Suari and Bob Twiggs at Stanford University's Space Systems Development Laboratory (SSDL) [4]. The goal behind CubeSat's development was to provide a platform to help students and researchers develop skills related to the design, manufacture, and testing of small satellites at a lower earth orbit for various science missions while reducing the cost and development time. With time, CubeSats gained a lot of attention and found its way into academia, industry, and government projects.

A CubeSat comprises different subsystems (e.g., electrical power, communication, attitude determination and control, propulsion, etc.) with numerous components. Antennas are integral and one of the most important passive components of a CubeSat communication

subsystem. The antenna design for CubeSats originated from analyzing the link budget of the communication system and identifying antenna requirements, such as gain, bandwidth, polarization, etc. The operating frequency of the antenna depends on frequency licensing and the availability of the ground station. The required bandwidth from the antenna depends on modulation and the data rate of the communication system. Before designing an antenna, requirements for gain, bandwidth, polarization, and other antenna performance metrics must be identified. Designing an antenna for CubeSats is challenging due to space limitations and mission requirements. Reliability is the most important aspect of a CubeSat antenna as it cannot be changed once the CubeSat is launched. CubeSat antennas must also survive mechanical vibration, radiation, out-gassing, atomic oxidation, and wide temperature variations. Like other satellite communication systems, CubeSats prefer circularly polarized antennas [5]. Linearly polarized antennas radiate along a single axis and require the strict orientation matching of the transmitting and receiving antennas. On the other hand, circularly polarized antennas do not require the orientation matching of transmitting and receiving antennas. It also reduces the fading effect caused by the Faraday rotation effect in the ionosphere [6]. Linearly polarized antennas also experience the same Faraday rotation effect, as the polarization vector is rotated by charged particles in the ionosphere. Consequently, keeping strict orientation matching between linearly polarized receiving and transmitting antennas becomes difficult. The CP antennas are not prone to this Faraday rotation effect, as the strict orientation of transmit and receive antennas is not required. Antennas of different sizes, shapes, and performance have been used in CubeSats. Commonly used CubeSat antennas are wire antennas (dipole/monopole/quad-pole) [7,8], reflector antennas [9], reflect-array antennas [10], membrane antennas [11], microstrip patch antennas [12], horn and waveguides [13], etc. These antennas have their advantages and disadvantages based on performance, ease of integration, shape and size, mass, deployable mechanisms, etc. Developers select antennas from these options and customize the design to suit the purpose of the mission. Moreover, the widespread practice is to use dedicated antennas on CubeSats to serve the following purposes:

- Telemetry, tracking and command (TT&C) for uplink and downlink communications with the ground station;
- High speed downlink communication for large payload data when downloaded;
- GNSS (GPS, Galileo, etc.);
- Inter-satellite communication.

Normally, CubeSats are equipped with 3–4 antennas or even more if required by the mission. The placement of these antennas is also challenging due to several issues. CubeSats must fulfill mass and size requirements and pass the vibration test before launching. The designed antennas must withstand shock and vibration during launch and deployment. Most of the CubeSat's antennas are placed on the outside surface of the structure. CubeSats also have solar cells placed on the outside surface of their structure for power generation from solar energy. If multiple antennas with a large form factor are placed on these sides, CubeSats suffer from a lack of space for solar panels. Developers then struggle to accommodate enough solar cells to maintain power positivity in the total period of the satellite operation. A reduction in size is one of the major challenges faced by the antenna designers of CubeSats. An advancement in commercial-off-the-shelf products, rapid prototyping, and testing have made it possible to develop high-frequency radios with a high data rate for application in small satellites with low power. As a result, CubeSats are collecting more scientific payload data than ever before. However, CubeSats have a very short ground pass duration while orbiting at lower earth orbits. This means that the time for downlinking payload data using a line-of-sight communication channel to the ground station is very short. For the fast and efficient downlink of the payload data from a CubeSat, a transmitter system with large bandwidth and high data rate is required. Hence, CubeSat's payload data downlink system requires an antenna with a large bandwidth and high gain [14,15]. Shared aperture antennas (SAA) have the potential to resolve the current issues and future challenges of recent CubeSat antennas [16–19]. The concept of

structure reuse can reduce the size of the antenna and combine multiple antennas in one single structure. Moreover, multiple antennas can be fabricated into a single structure and make a multiband antenna system. This could play a vital role for CubeSats as they struggle to accommodate multiple antennas due to lack of space and volume. In addition to this, planer antennas do not need any deployment. In 1991, when the STS-37 launch of the Gamma Ray Observatory was happening, the high gain antenna did not deploy as per the initial command [20]. The proposed high-gain antenna has an upper hand in reliability in addition to saving more space.

In this article, a microstrip patch-based and shared aperture antenna is proposed for multiband operation. A dual-band-shared aperture antenna operating in L1 and X bands is presented in [21]. The antenna discussed in this paper has two microstrip patches that operate at S-band and X-band frequencies. It has two printed elements that share the same ground plane and dielectric aperture. The antenna system uses a single aperture yet operates in two frequency bands and, thus, saves space on the CubeSat's sides. The sense of polarization of the proposed antenna is Right Hand Circularly Polarized (RHCP). The performance of the patches is further improved by placing an additional dielectric layer that acts as a partial reflective surface (PRS) [22]. The S-band patch can be used as a TT&C antenna, while the X-band patch can be used to downlink the payload data collected by a CubeSat. This paper is organized as follows: Section 2 presents the detailed antenna geometry along with the design parameters. Simulated and measured results from the fabricated antenna are presented in Section 3. The performance of the proposed antenna is compared with other related work in Section 4. Section 5 has some concluding remarks.

2. Proposed Antenna Geometry

The proposed shared aperture antenna comprises three square-shaped dielectric layers and two square-shaped microstrip printed elements for the S-band and X-band operation. The S-band antenna is designed for use with the uplink/downlink communication system for telemetry, tracking, and command (TT&C) data reception and transmission. The sole objective of the X-band antenna is to downlink large mission data gathered by the CubeSat to the ground station within a short ground pass. To serve the same purposes, CubeSats are normally equipped with two separate conventional antennas. This proposed antenna is compact in size, and due to its planer ground shape, it can be easily integrated with the CubeSat structure.

Figure 1 shows the structure of the proposed antenna. The dielectric layer-1 of the antenna is h mm thick Rogers RT/duroid 5880. The square-shaped copper ground plane of the antenna has a length of g mm and thickness of $35 \mu\text{m}$ and is placed at the bottom of the dielectric layer-1. The X-band patch is placed on the upper surface of the dielectric layer-1. The X-band square patch antenna has a length of L_3 mm with a negative perturbation of q_c mm. The dielectric layer-2 is stacked on top of the dielectric layer-1. This layer also has h mm-thick Rogers RT/duroid 5880 material. Any copper cladding from the bottom of the dielectric layer-2 is removed. On top of the dielectric layer-2, a slotted square-ring patch with a crossed strip at the center is etched, which operates as the S-band antenna [23]. It has a length of L_1 mm and negative corner perturbation of p_c mm, as shown in Figure 2. Four equal-sized square-shaped slots or perforations are present inside the S-band square ring antenna. An X-band patch antenna can be placed in the middle of any of these four slots, making sure that the S-band ring patch does not block the radiation of the X-band patch antenna. A patch antenna operating in the X-band is placed in the bottom-left slot, as shown in Figure 2. Two separate 50Ω coaxial probes are used to feed the S-band and X-band patch antennas. The dielectric layer-3 is made of h_u mm-thick Rogers RT/duroid 6010. It is placed on top of the second dielectric layer using nonconductive bolts. An air gap of h_a mm separates the dielectric layers 2 and 3. Dielectric layer-3 works as a partial reflective surface (PRS) for the X-band patch antenna. Placing the PRS at an approximate $0.5\lambda_x$ (λ_x is the wavelength at the resonance frequency of the X-band patch antenna) distance away

from the X-band antenna means that a Fabry–Perot Resonator Cavity Antenna (FPRA) [24] is formed. FPRAs can exhibit high gain compared to normal patch antennas.

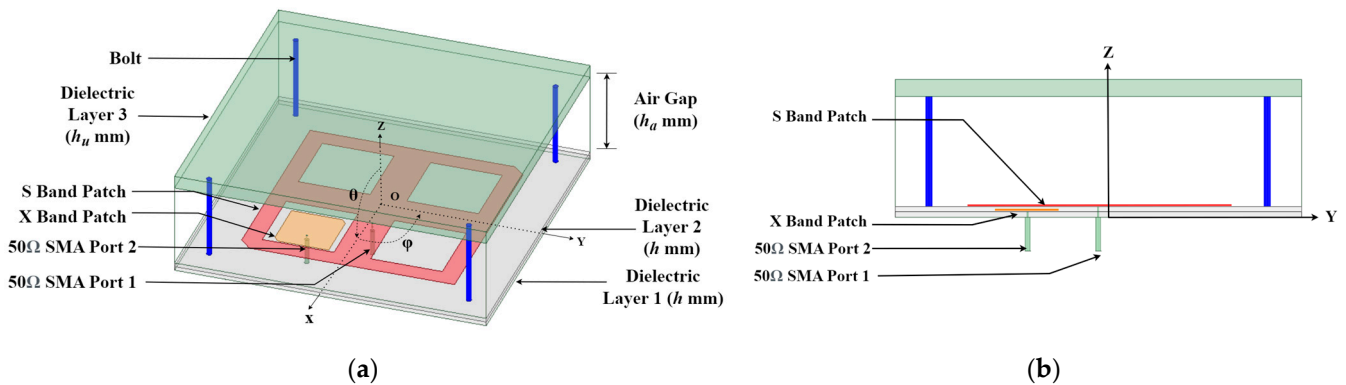


Figure 1. Proposed S- and X-band shared aperture antenna (a) Antenna structure in isometric view; (b) Side view of the antenna.

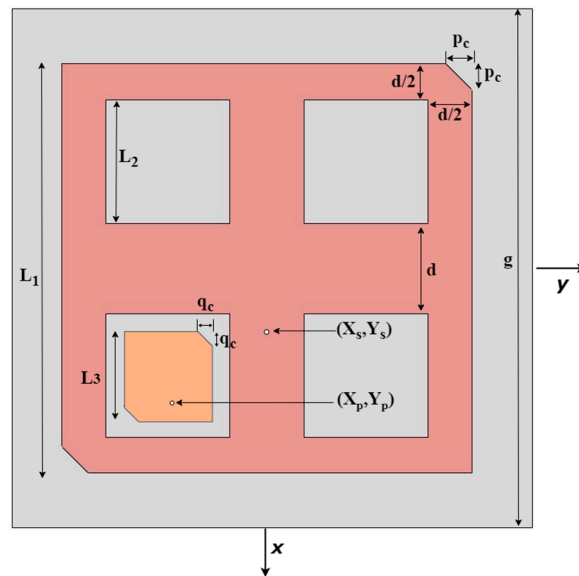


Figure 2. Geometry of the proposed S- and X-band patches.

The center of the antenna is placed at the origin of the coordinate system, as shown in Figure 2. The feed location of the S-band patch and the X-band patch is given with respect to the origin. The antenna has a total volume of $60 \times 60 \times 20 \text{ mm}^3$. Table 1 describes the parameters of Figures 1 and 2 and their optimized values for the proposed antenna.

Table 1. The design parameters of the S- and X-band-shared aperture antenna.

Antenna Parts	Parameters	Symbol	Value (mm)
Antenna Main Structure	Dielectric Layer-1 height	h	0.787 mm
	Dielectric Layer-2 height	h	0.787 mm
	Air gap distance	h_a	16.2 mm
	Dielectric Layer-3 height	h_u	2.5 mm
	All dielectric layers and ground Plane length	g	60 mm

Table 1. Cont.

Antenna Parts	Parameters	Symbol	Value (mm)
S-band Patch	Square Ring antenna length	L_1	41.7 mm
	Square Ring antenna slot length	L_2	13.8 mm
	Square Ring patch corner perturbation length	p_c	2.2 mm
	Distance between slots	d	7.05 mm
	Square Ring antenna feed location	(X_s, Y_s)	(5.7, 0) mm
X-band Patch	X-band square patch length	L_3	10.8 mm
	X-band square patch corner perturbation length	q_c	1 mm
	X-band patch feed location	(X_p, Y_p)	(12.3, -10.4) mm

3. Results

The proposed antenna was modeled and optimized using the finite element method-based full-wave electromagnetic solver Ansys HFSS 2022. Based on the simulation results from HFSS, a prototype of the antenna was built. The measured results from the antenna prototype are compared below with the simulated results.

3.1. Simulated Results

Figure 3 shows the simulated performance of the S-band patch for the proposed shared aperture antenna. The $S_{11} < -10$ dB bandwidth of the S-band patch is 30 MHz (from 2013 MHz to 2043 MHz, 1.5%). The Axial Ratio (AR) of the proposed antenna is measured in the boresight (+z axis in Figure 1) direction. The simulated AR < 3 dB bandwidth starts from 2013 MHz to 2020 MHz (7 MHz, 0.35%), as shown in Figure 3b. It has a minimum AR value of 1.9 dB at 2016 MHz. Figure 3c,d show the polar plots of the RHCP and LHCP radiation patterns for the patch in the $\varphi = 0^\circ$ and $\varphi = 90^\circ$ planes, respectively. It is clear in the plot that the RHCP is more dominant, and the maximum RHCP gain is 7.7 dBic at 2016 MHz. From the radiation patterns of the S-band antenna, it is evident that the antenna has a peak RHCP gain at the boresight. Due to the partial reflective surface, the antenna has a slightly higher gain compared to conventional S-band patch antennas.

Figure 4 depicts the simulated results of the X-band patch of the proposed antenna. The $S_{11} < -10$ dB bandwidth of the proposed X-band FPRA starts from 8320 MHz and ends at 8530 MHz (210 MHz, 2.5%). It has an AR < 3 dB bandwidth that ranges from 8433 MHz to 8500 MHz (67 MHz, 0.8%), as shown in Figure 4b, measured in the boresight (+z axis in Figure 1) direction. A simulated maximum RHCP gain of 12.8 dBic was achieved from the single X-band patch antenna. This increased gain from a single radiating patch is close to the gain achieved for a 4-element antenna array [25]. The minimum AR = 0.9 dB of the X-band patch occurred at 8460 MHz. Figure 4c,d show the RHCP and LHCP gain patterns of the proposed antenna in the $\varphi = 0^\circ$ and $\varphi = 90^\circ$ planes, respectively. These patterns occurred at the frequency 8460 MHz, where the Axial Ratio is the lowest (0.9 dB). The RHCP beam of the X-band patch antenna was more direct due to the PRS being placed at an approximate $0.5\lambda_x$ (λ_x being the free-space wavelength at X-band frequency) distance away from the X-band patch. From the simulated results, it can be concluded that the proposed dual-band shared aperture antenna is an excellent option to replace two antenna systems of a CubeSat and to cover two bands. The S-band patch has a narrow bandwidth, but it is sufficient to perform as the uplink/downlink antenna for TT&C due to the fact that the data speed required to send/receive commands to the CubeSat is not that high. The X-band patch shows a high RHCP gain, which is desirable for establishing a fast downlink connection. The 67 MHz Axial Ratio bandwidth of the proposed antenna can establish Megabits per second (Mbps) and a speed communication link with a ground station.

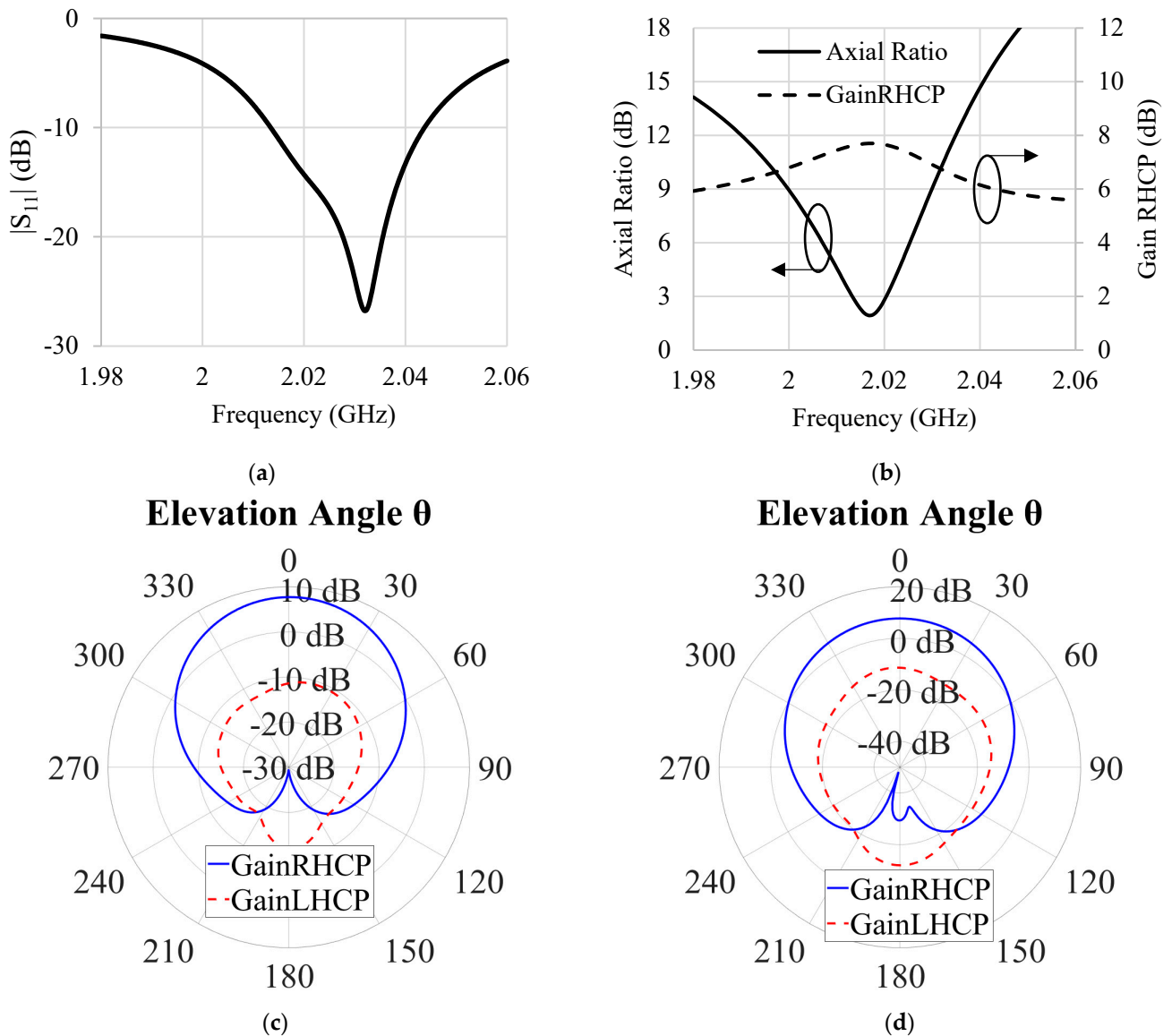


Figure 3. Performance of the S-band patch of the proposed antenna, (a) Return loss (b) Axial Ratio and peak RHCP gain vs. frequency (c) RHCP gain and LHCP gain patterns at 2016 MHz in the $\varphi = 0^\circ$ plane (d) RHCP gain and LHCP gain patterns at 2016 MHz, in the $\varphi = 90^\circ$ plane.

3.2. Antenna Prototype Fabrication and Measurement

A prototype of the proposed antennas was developed in the Applied Electromagnetics Research Lab at the University of South Alabama, and reflection coefficients were measured using an Anritsu 37369A Vector Network Analyzer (VNA). Figure 5 shows the fabricated prototype of the proposed antenna. Figure 5a,b show the S-band and X-band microstrip patches etched on two separate dielectric substrates. These two dielectric layers were placed on top of each other, and four nonconductive screws and bolts were used to ensure that there were no air gaps between them. Nonconductive spacers ensured that a uniform distance between the patch and the partially reflective surface was maintained.

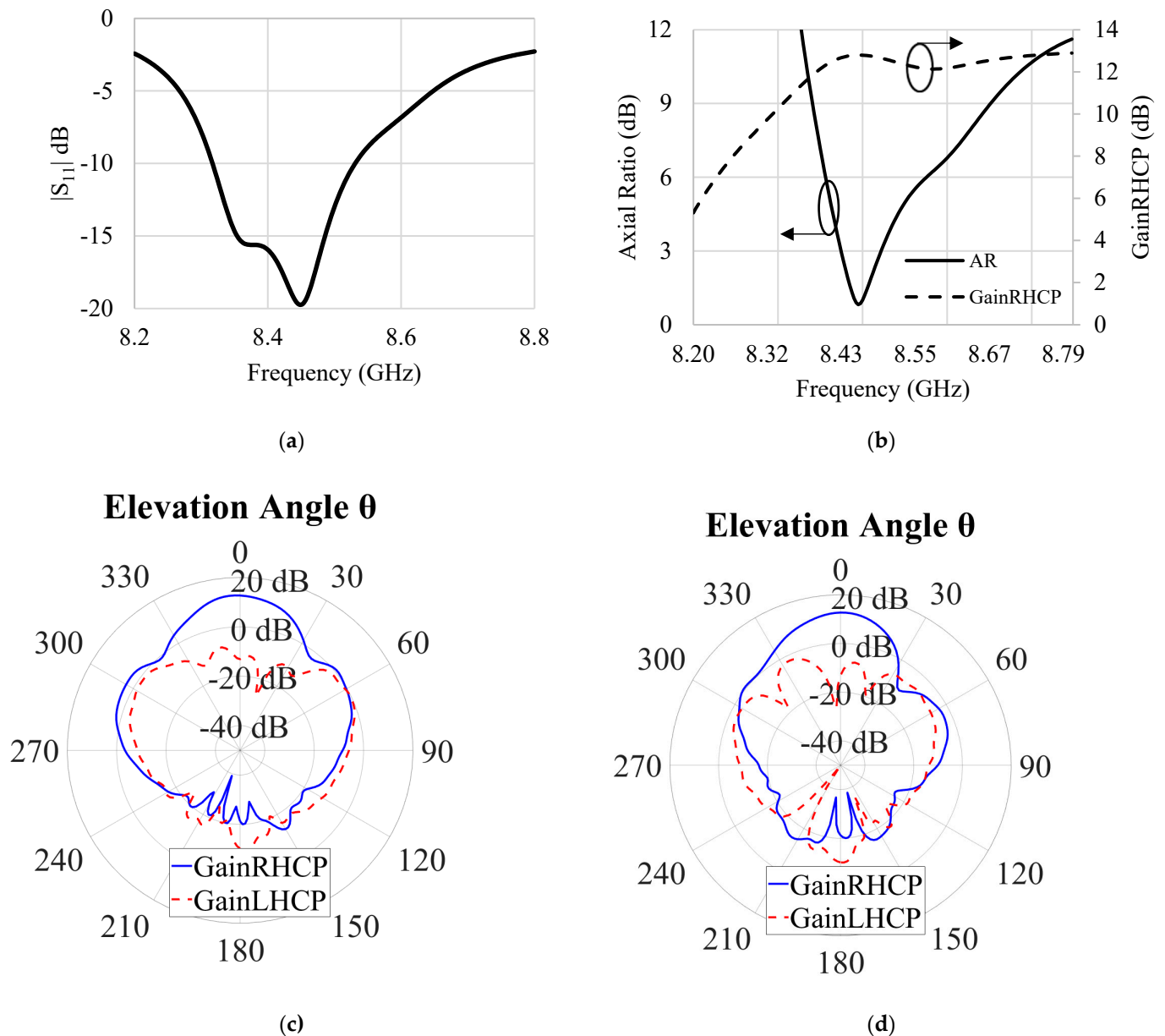


Figure 4. X-band patch antenna simulated results, (a) return loss (b) AR and peak RHCP gain vs. frequency (c) RHCP, LHCP gain patterns at 8460 MHz in the $\phi = 0^\circ$ plane (d) RHCP, LHCP gain patterns at 8460 MHz in the $\phi = 90^\circ$ plane.

Figure 6 compares the return loss from measurement and simulation results. From the return loss graphs, it appears that the fabricated antenna prototype produced similar results. The measured $S_{11} < -10$ dB bandwidth in the S-band was 16 MHz, which was 30 MHz in the simulation. This difference was due to the slightly higher reflection coefficient of the fabricated antenna compared to the simulated one. In the case of the X-band patch, the measured return loss bandwidth was 270 MHz, whereas the simulation showed a 210 MHz bandwidth. The differences in the simulation and measurement results could be attributed to some fabrication errors, including the misalignment of various layers of this antenna and maybe the presence of some air gaps between layers. The fabricated prototype exhibited good isolation between ports of the S-band and X-band patches (below -20 dB in the S-band and -15 dB in the X-band).

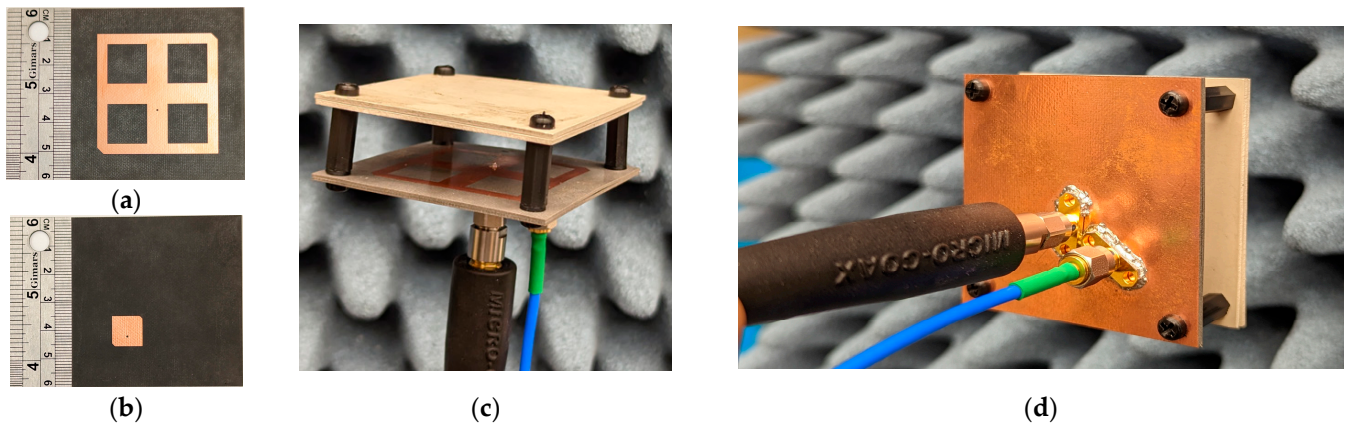


Figure 5. Fabricated prototype of the proposed antenna, (a) S-band patch (b) X-band patch (c) Proposed antenna (Isometric view) (d) Ground plane and SMA probes (viewing from bottom).

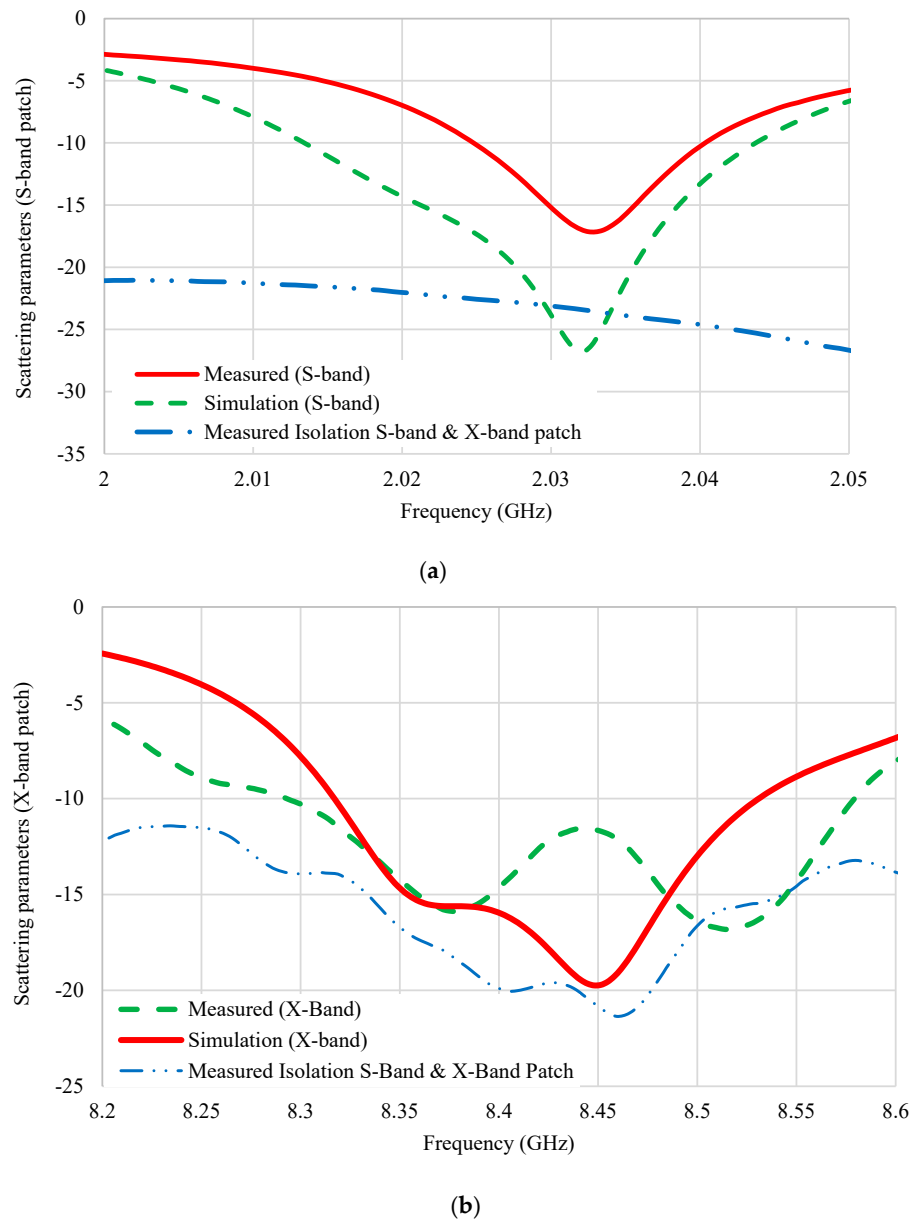


Figure 6. Comparison of measured and simulated return loss of the proposed antenna and measured isolation between two ports: (a) S-band patch; (b) X-band patch.

4. Discussion

The proposed antenna shows a way to design a shared aperture antenna by etching microstrip patches in different layers of dielectric materials and, thus, reuse the aperture for the size reduction in the antenna. The lower and higher operating bands of the proposed shared aperture antenna had a frequency ratio of four. Having a high frequency ratio means that the antenna can be used for two separate communication systems that require two antennas. As CubeSats have a very small form factor and different design restrictions, the proposed antenna can be an excellent option for CubeSat missions that have difficulties accommodating multiple antennas. Table 2 compares the performance of the proposed antenna with recent published works on shared aperture antennas for CubeSat application [26–28].

Table 2. Performance comparison of the proposed antenna with other related work.

Ref.	Freq. Bands	AR BW (%)	Gain (dBic)	Antenna Volume (mm ³)	Polarization
[26]	S-/X-band	NA	8/11.5	140 × 140 × 9.4	Linear
[27]	S-/X-band	1/1.4	6.55/12.5	82 × 82 × 4	RHCP
[28]	S-/X-band	NA	7.2/12.4	100 × 100 × 1.6	Linear
Proposed work	S-/X-band	0.35/0.8	7.7/12.8	60 × 60 × 20	RHCP

From the Table, it is evident that the proposed antenna achieved similar or better performances while keeping the antenna size compact. Both S/X-band antennas in [25,26] had an array of patch antennas for high gain in the X-band, which required a feed network. The dual-band antenna in [28] consisted of a 1 × 3 linear array antenna for the X-band operation, which had 6 ports in total for dual-polarization. Our proposed antenna has only two ports and provides a high gain due to the dielectric loading. Moreover, the proposed antenna uses coaxial probe feeding, which is desirable for CubeSat developers due to the low complexity of cable placement from the radio to the antenna in a concise space.

5. Conclusions

This paper showcases a patch antenna operating in the X-band frequency range with 12.8 dbic gain, positioned between two substrates, with another S bands slotted on a crossed-strip microstrip patch located above, generating a gain of 7.7 dBic. A notable reduction in the size was observed, replacing two antennas next to one antenna system, which could be handy in a CubeSat limited in space. This antenna can be used for S-band uplink/downlink and X-band high-speed data downlink in CubeSats. As more CubeSat projects are looking at high-frequency operations for deep space communication with increased data download requirements, this antenna can be used in CubeSats for use with NASA's Near-Earth Network (NEN) and Deep Space Network (DSN) for high-speed data transmission in the X-band, and TT&C operation in the S-band.

Author Contributions: Conceptualization, S.S.K. and S.I.L.; methodology, S.S.K.; software, S.S.K.; validation, S.S.K., M.H.K. and S.I.L.; formal analysis, S.S.K.; investigation, S.S.K.; resources, S.I.L.; data curation, S.S.K.; writing—original draft preparation, S.S.K. and M.H.K.; writing—review and editing, S.I.L.; visualization, S.S.K. and S.I.L.; supervision, S.I.L.; project administration, S.I.L.; funding acquisition, S.I.L. All authors have read and agreed to the published version of the manuscript.

Funding: This research has received partial external funding provided by the National Science Foundation (Award Number: AGS 1936537).

Data Availability Statement: Not Applicable.

Conflicts of Interest: The authors declare no conflict of interest.

References

1. Gao, S.; Clark, K.; Unwin, M.; Zackrisson, J.; Shiroma, W.A.; Akagi, J.M.; Maynard, K.; Garner, P.; Boccia, L.; Amendola, G.; et al. Antennas for Modern Small Satellites. *IEEE Antennas Propag. Mag.* **2009**, *51*, 40–56. [CrossRef]
2. Liddle, J.D.; Holt, A.P.; Jason, S.J.; O'Donnell, K.A.; Stevens, E.J. Space Science with CubeSats and Nanosatellites. *Nat. Astron.* **2020**, *4*, 1026–1030. [CrossRef]
3. Cappelletti, C.; Battistini, S.; Malphrus, B. (Eds.) *Cubesat Handbook: From Mission Design to Operations*; Academic Press: Cambridge, MA, USA, 2020.
4. *The CubeSat Program, California Polytechnic State University—San Luis Obispo “CubeSat Design Specification Rev. 13”*; California Polytechnic State University: San Luis Obispo, CA, USA, 2014.
5. Imbriale, W.A.; Boccia, L. *Space Antenna Handbook*; Wiley Online Library: Hoboken, NJ, USA, 2012.
6. Le Vine, D.M.; Jacob, S.D.; Dinnat, E.P.; De Matthaeis, P.; Abraham, S. The Influence of Antenna Pattern on Faraday Rotation in Remote Sensing at L-Band. *IEEE Trans. Geosci. Remote Sens.* **2007**, *45*, 2737–2746. [CrossRef]
7. Deshpande, M.; Piepmeier, J. Design and Development of VHF Antennas for Space Borne Signal of Opportunity Receivers for CubeSat Platforms. In Proceedings of the IEEE International Symposium on Antennas and Propagation and North American Radio Science Meeting, Vancouver, BC, Canada, 19–24 July 2015.
8. Joseph, A.T.; Deshpande, M.; O'Neill, P.E.; Miles, L. Development of VHF (240–270 MHz) antennas for SoOp (Signal of Opportunity) Receiver for 6U CubeSat Platforms. In Proceedings of the 2016 Progress in Electromagnetic Research Symposium (PIERS), Shanghai, China, 8–11 August 2016; pp. 2530–2531.
9. Chahat, N.; Sauder, J.; Thomson, M.; Hodges, R.; Rahmat-Samii, Y. CubeSat deployable ka-band reflector antenna for deep space missions. In Proceedings of the 2015 IEEE International Symposium on Antennas and Propagation & USNC/URSI National Radio Science Meeting, Vancouver, BC, Canada, 19–24 July 2015; pp. 2185–2186.
10. Hodges, R.E.; Radway, M.J.; Toorian, A.; Hoppe, D.J.; Shah, B.; Kalman, A.E. ISARA-integrated solar array and reflectarray cubesat deployable ka-band antenna. In Proceedings of the 2015 IEEE International Symposium on Antennas and Propagation & USNC/URSI National Radio Science Meeting, Vancouver, BC, Canada, 19–24 July 2015; pp. 2141–2142.
11. Warren, P.A.; Steinbeck, J.W.; Minelli, R.J.; Mueller, C. Large, Deployable S-band antenna for a 6U CubeSat. In Proceedings of the 29th Annual American Institution Aeronautics and Astronautics/Utah State University Conference Small Satellites, Santa Clara, CA, USA, 8–13 August 2015; pp. 1–7.
12. Tubbal, F.E.; Raad, R.; Chin, K.W. A Survey and Study of Planar Antennas for Pico-Satellites. *IEEE Access* **2015**, *3*, 2590–2612. [CrossRef]
13. Vouch, C.J.; Drysdale, T.D. Inter-CubeSat communication with V-Band ‘Bull’s Eye’ antenna. In Proceedings of the 8th European Conference on Antennas and Propagation (EuCAP 2014), Hague, The Netherlands, 6–11 April 2014; pp. 3545–3549.
14. Hossain, M.M.; Kabir, S.S.; Latif, S.I.; Spencer, E.; Qudrat-E-Maula, M. A wideband stacked patch-patch antenna with hybrid perturbations for circular polarization. In Proceedings of the 2021 IEEE International Symposium on Antennas and Propagation and USNC-URSI Radio Science Meeting (AP-S/URSI), Singapore, 4–10 December 2021; pp. 55–56.
15. Liu, S.; Theoharis, P.I.; Raad, R.; Tubbal, F.; Theoharis, A.; Iranmanesh, S.; Abulgasem, S.; Khan, M.U.A.; Matekovits, L. A Survey on CubeSat Missions and Their Antenna Designs. *Electronics* **2022**, *11*, 2021. [CrossRef]
16. Axness, T.A.; Coffman, R.V.; Kopp, B.A.; O'Haver, K.W. Shared Aperture Technology Development. *Johns Hopkins APL Tech. Dig.* **1996**, *17*, 285–294.
17. Wang, S.; Zhang, L.; Zhu, K.; Sun, H. Multi-band shared aperture circularly polarized antenna with metal isolation columns. In Proceedings of the 2022 IEEE MTT-S International Wireless Symposium (IWS), Harbin, China, 12–15 August 2022; pp. 1–3.
18. Xie, M.; Wang, Z.; Sun, L.; Zhu, S.; Deng, G.; Cao, Z. An L/S multi-band shared-aperture circularly polarized antenna. In Proceedings of the 2021 13th International Symposium on Antennas, Propagation and EM Theory (ISAPE), Zhuhai, China, 1–4 December 2021; pp. 1–3.
19. Gaffar, M.; Zaman, M.A.; Choudhury, S.M.; Matin, M.A. Design and Optimisation of a Novel Dual-Band Circularly Polarised Microstrip Antenna. *IET Microw. Antennas Propag.* **2011**, *5*, 1670–1674. [CrossRef]
20. Rivera, A.; Stewart, A. Study of spacecraft deployables failures. In Proceedings of the European Space Mechanisms and Tribology Symposium, Virtual, 20–24 September 2021.
21. Kabir, S.S.; Latif, S. Multi-band shared aperture antenna for satellite communications. In Proceedings of the 2022 IEEE International Symposium on Antennas and Propagation and USNC-URSI Radio Science Meeting (AP-S/URSI), Denver, CO, USA, 10–15 July 2022; pp. 1814–1815.
22. Rao, S.; Shafai, L.; Sharma, S.K. (Eds.) *Handbook of Reflector Antennas and Feed Systems Volume III: Applications of Reflectors*; Artech House: Norwood, MA, USA, 2013.
23. Chen, W.-S.; Wu, C.-K.; Wong, K.-L. Square-Ring Microstrip Antenna with a Cross Strip for Compact Circular Polarization Operation. *IEEE Trans. Antennas Propag.* **1999**, *47*, 1566–1568. [CrossRef]
24. Orr, R.; Goussetis, G.; Fusco, V. Design Method for Circularly Polarized Fabry–Perot Cavity Antennas. *IEEE Trans. Antennas Propag.* **2013**, *62*, 19–26. [CrossRef]
25. Abbak, M.; Tekin, I. RFID Coverage Extension Using Microstrip-Patch Antenna Array. *IEEE Antennas Propag. Mag.* **2009**, *51*, 185–191. [CrossRef]

26. Mathur, P.; Kumar, G. Dual-Frequency Microstrip Antenna at S and X Bands with Higher-Order Mode Suppression Technique. *IET Microw. Antennas Propag.* **2018**, *12*, 583–587. [CrossRef]
27. Serup, D.E.; Williams, R.J.; Zhang, S.; Pedersen, G.F. Shared aperture dual S- and X-band antenna for nano-satellite applications. In Proceedings of the 2020 14th European Conference on Antennas and Propagation (EuCAP), Copenhagen, Denmark, 15–20 March 2020; pp. 1–4.
28. Bandi, R.B.; Kothapudi, V.K.; Pappula, L.; Kalimuthu, R.; Gottapu, S.K. A Single-Layer S/X-Band Shared Aperture Antenna with MIMO Characteristics at X-Band for Airborne Synthetic Aperture Radar Applications. *Int. J. Antennas Propag.* **2023**, *2023*, 1384388. [CrossRef]

Disclaimer/Publisher’s Note: The statements, opinions and data contained in all publications are solely those of the individual author(s) and contributor(s) and not of MDPI and/or the editor(s). MDPI and/or the editor(s) disclaim responsibility for any injury to people or property resulting from any ideas, methods, instructions or products referred to in the content.

Article

Design of Antenna Polarization Plane for Concurrent Uplink/Downlink Drone Networks

Gia Khanh Tran *  and Takuma Okada

Department of Electrical and Electronic Engineering, School of Engineering, Tokyo Institute of Technology, Meguro, Tokyo 152-8550, Japan; okada@mobile.ee.titech.ac.jp

* Correspondence: khanhtg@mobile.ee.titech.ac.jp

Abstract: In recent years, drones have been used in a wide range of fields, such as agriculture, transportation of goods, and security. Drones equipped with communication facilities are expected to play an active role as base stations in areas where ground base stations are unavailable, such as disaster areas. In addition, asynchronous operation is being considered for local 5G, in order to support all kinds of use cases. In asynchronous operation, cross-link interference between base stations is an issue. This paper attempts to reduce the interference caused by the drone network by introducing circularly polarized antennas against the conventional system using linearly polarized antennas. Numerical analyses are conducted to validate the effectiveness of the proposed system, where Signal-to-Interference Ratios (SIRs) are shown to be improved significantly as the numerical evaluation results. Specifically, for the scenario of only access links, in the region where conventional antenna architecture can only achieve an SIR of less than 20 dB, our proposed system applying circularly polarized antennas can almost realize an SIR of more than 40 dB. Significant improvement can be also observed in the scenario with the existence of backhaul links, where the conventional system had difficulty achieving our system design goal SIR of 16.8 dB, while the proposed antenna architecture could easily attain this goal in most regions of our evaluation ranges.

Keywords: aerial base station; multiple drones; circular polarization; two-ray model; antennas



Citation: Tran, G.K.; Okada, T. Design of Antenna Polarization Plane for Concurrent Uplink/Downlink Drone Networks. *Electronics* **2023**, *12*, 3045. <https://doi.org/10.3390/electronics12143045>

Academic Editors: Raad Raad, Ladislau Matekovits and Faisal Tubbal

Received: 3 June 2023

Revised: 9 July 2023

Accepted: 10 July 2023

Published: 12 July 2023



Copyright: © 2023 by the authors. Licensee MDPI, Basel, Switzerland. This article is an open access article distributed under the terms and conditions of the Creative Commons Attribution (CC BY) license (<https://creativecommons.org/licenses/by/4.0/>).

1. Introduction

Drones are a type of unmanned aircraft achieving significant attention in recent years for both civilian and commercial applications, due to their hovering capability, flight capacity, ease of deployment, and low operation and maintenance costs. Drones or Unmanned Aerial Vehicles (UAVs) have many use cases, since they have been used in a wide range of applications, such as disaster rescue operations, smart agriculture, emergency medical services, and aerial photography [1]. In addition, recent advances in drone technology have made it possible to widely deploy drones for wireless communication. This allows drones to be used as aerial base stations to support the connection of existing terrestrial wireless networks, such as cell phones and broadband networks.

Unlike conventional ground base stations, aerial base stations have the advantage that they can adjust their flight altitude and avoid obstacles to increase the possibility of connecting with ground users by establishing Line-of-Sight (LoS) communications. The LoS connection can improve coverage and data rate performance. In addition, it is possible to construct the network flexibly because it can be freely deployed in the air. On the other hand, wireless data communication has exploded in the last few years due to the rapid spread of the Internet of Things (IoT) and their various new applications. However, conventional wireless drone networks operate in the microwave frequency band below 6 GHz, where the spectrum resources are already heavily utilized. Despite the rapid increase in the demand for data capacity, there is a growing concern that the available spectrum is limited. Several techniques have been proposed to improve the network capacity and to

achieve high frequency efficiency in future cellular systems. For example, Multiple-Input and Multiple-Output (MIMO), Non-Orthogonal Multiple Access (NOMA), and cooperative relaying. However, these technological advances do not provide a solution to solve the spectrum scarcity problem. Therefore, a solution may be to expand using higher frequencies in the radio spectrum. In this paper, communication links between user and drone, and between drone and drone are considered using millimeter-wave communication. The expanding use of millimeter-wave frequencies can provide multiple gigabit data transmission rates by ensuring a wide range of available spectrum resources [2]. Hence, millimeter-wave communication should be leveraged in 5G wireless communication systems that require very high data throughput, wide bandwidth, high communication speed, and low latency. In addition to the sufficient bandwidth, the short wavelength of millimeter-wave communication makes it possible to design physically small circuits and antennas. Moreover, it is easy to achieve sharper directivity by miniaturizing the antenna. On the other hand, millimeter-wave communications suffer from large free space attenuation. In addition to the expected application of drone to wireless networks, the possibility of transmitting multiple gigabits of data using 5G millimeter-wave communications has led to the idea of combining wireless network support by drone with millimeter-wave communications [3].

In this paper, we propose a scenario for a disaster area where ground base stations are out of service. In fact, during the Great East Japan Earthquake in 2011, about 29,000 cell phone base stations and PHS (Personal Handy-phone System) base stations of five major companies, NTT docomo, KDDI, Softbank Mobile, EMOBILE, and WILLCOM were out of service [4]. The first 72 h after a disaster occurs are considered the most critical, and it is necessary to deploy wireless networks quickly to restore communication connectivity in order to aid rescue teams in the disaster area. Establishing a wireless network using drones in the damaged area where ground base stations are malfunctioned is an effective and fast method to support different rescue operations at the disaster area. We assume that the drone networks are deployed into post-disaster areas in mild weather conditions, especially after thunderstorms had left.

Figure 1 shows the overall architecture [5] of our disaster-resilient millimeter-wave drone networks. As aforementioned, UAV networks have several advantages because of their ability to place base stations in the sky. The first is that they can move regardless of the constraints on the ground. This allows for the rapid deployment of base stations when needed and allows for the optimal placement of base stations for a particular distribution of users. The other point is the ability to provide data from the sky. This reduces the probability of being blocked by buildings, etc., and increases the probability that the propagation path between the UAV and the user is in line-of-sight condition. These advantages make UAV networks attractive applications for many use cases, but in this study, we mainly consider disaster-stricken areas as our target use case. Moreover, for the selection of the types of UAVs, this study assumes the use of a multirotor UAV rather than a fixed-wing UAV for our temporary base stations. Unlike fixed-wing UAVs, multirotor UAVs have a higher degree of freedom of movement, enabling the optimization of not only the placement, but also the UAV's trajectories [6]. Our proposed system consists of two types of UAVs: access UAVs and backhaul UAVs. The backhaul UAV is responsible for relaying the traffic sent from the base station on the ground and other backhaul UAVs to other UAVs. If the distance between the access UAV and the neighboring base station is fixed, by using backhaul UAVs as relays in between base stations and access UAVs, the transmission distances between these links are effectively shortened. The shorter communication distance between UAVs alleviates the effects of distance attenuation and rain attenuation, which are problems in the millimeter-wave band. This allows for a longer communication distance between the access UAV and the ground base station, which can be used for various use cases. The access UAV provides the traffic sent from the backhaul UAV to the user on the ground. Since the access UAV provides data directly to the user, its placement has a significant impact on the data rate provided.

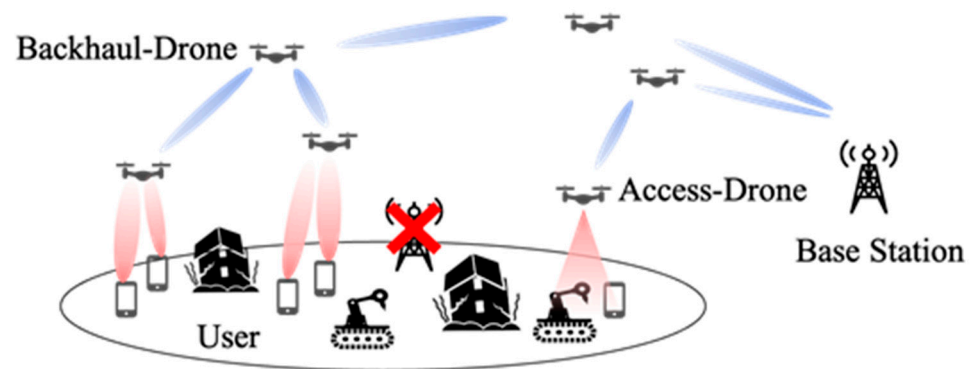


Figure 1. Overall architecture. (Red x in picture means the conventional base station goes out of service due to the influence of disasters).

Our previous work in [5] had been dealing with the optimization of the access UAVs' placements and the corresponding coverages against varying user traffic distribution. The work found that owing to the moving freedom of UAVs, our optimal UAV placement can offer significant system throughput gain. For the fixed location of access UAVs, our work in [7] revealed that the backhaul drones can construct optimal routes to offload traffic to the central macro base station, owing to the effect of multi-hop communications and multi-route multiplexing over backhaul drone networks. We also constructed a Proof-of-Concept system and partially demonstrated the effectiveness of our proposed system via outdoor experiment [8].

For future deployment of our proposed system, we aim to develop our system at the 28 GHz band assigned for local 5G [9], with a bandwidth of 100 MHz ready for use in outdoor environments. One of our current problems is that when multiple drones communicate with the user, the uplink (UL) that sends data from the user to the aerial base station and the downlink (DL) that sends data from the aerial base station to the user cause interference. Such scenarios are common in the asynchronous operation of the local 5G system assigned at the 28 GHz band in Japan [10]. In this paper, as opposed to the conventional system using linearly polarized antennas, we investigate the improvement of SIR by using the characteristics of circular polarization whose rotation direction changes before and after the ground reflection. For the propagation model, we apply the two-ray model to calculate the received power and SIR, and show the effectiveness of the proposed method. This paper extends from the authors' previous work in [11], where only a system of access drones communicating directly to ground users was investigated. In this paper, we thoroughly investigate the overall system under the existence of backhaul drones that cause more intra/inter-system interference. By the way, since comparison between the conventional microwave-band system and the proposed system employing millimeter-wave band is not the main focus of this paper, readers might refer to [5] for the comparison of these two systems. Solutions for powering the aerial drones as discussed in [12] are also out of this paper's scope.

The rest of this paper is organized as follows. In Section 2, we present the related work about our research and the overall architecture of our research. In Section 3, we show the system model and design using different antenna polarization when there are only access drones and ground users. Section 4 furthermore investigates the SIR performance of the system when there is the existence of backhaul drones. Finally, we conclude our work and discuss our future works in Section 5.

2. Related Works

The overall architecture of this research is shown in Figure 1. The roles of drones are assumed to be divided into the access-drones and the backhaul-drones to provide data to users. The access-drones communicate directly with the user, while the backhaul-drones act as a relay between the access-drones and the ground base station. By relaying

the backhaul-drones, the communication distance between drones becomes shorter. This reduces the effect of distance attenuation and rainfall attenuation, which are concerns in millimeter-wave communication. On the other hand, since the access-drones provide data directly to users, it is important to know how to deploy these drones. If drones are efficiently deployed, it is expected to provide LoS communication to the ground users, which is important in millimeter-wave communications, and to expand the coverage with fewer base stations.

Authors in [13] show the minimum transmit power required to have a certain coverage radius as a function of the altitude of the drones. At lower altitudes, the shadowing effect reduces the probability of LoS connection between the transmitter and the receiver, resulting in a decrease in the coverage radius. On the other hand, at high altitudes, the probability of LoS connection is high. However, due to the large distance between the transmitter and the receiver, the path loss increases, and as a result, the coverage performance decreases. In [14], the optimal deployment of multiple drones equipped with directional antennas as aerial base stations was investigated. Based on the circle packing theory, an efficient placement method was proposed in which each drone can obtain the maximum coverage with the minimum transmission power. As a result, the optimal altitude and position of drones were determined based on the number of available drones, antenna gain, and beam-width. In [5], a deployment method that combines the K-means method with the minimum envelope problem was considered to maximize the data rate that can be provided to users in DL. There have been many studies of deployment methods that give priority to DL connections, but few studies have been conducted in environments where DL and UL concurrently exist. In this paper, we propose a method to reduce the interference to UL caused by DL in the communication between adjacent concurrent UL/DL drone networks via the introduction of circularly polarized antennas, against the conventional system applying linearly polarized antennas.

3. Access Link Analysis

In this section, we describe the system model and the proposed method considered in this research. For simplicity, we consider an UL-DL pair system as shown in Figure 2. The structure of this section is as follows. Section 3.1 describes the overall system model with the considered arrangement of the drone and the user. In Section 3.2, the analysis is applied for conventional cases when drones employ linearly polarized antennas. In Section 3.3, the analysis is applied for our proposed system design when drones are proposed to be equipped with circularly polarized antennas.

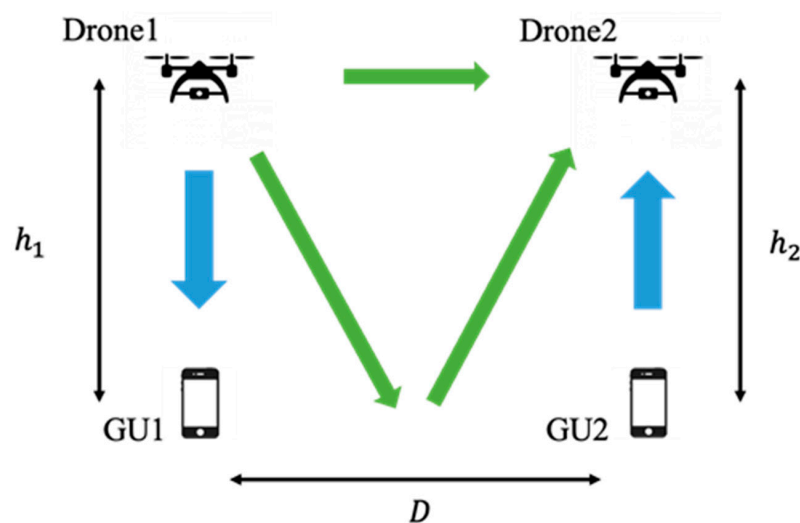


Figure 2. System model (GU1 and GU2 represent the Ground User 1 and 2, respectively). Arrows mean possible propagation paths between these transmitters and receivers.

3.1. System Model

Figure 2 shows the system model used in this research. Here, h_1 is the height of Drone 1 from the ground surface, h_2 is the height of Drone 2 from the ground surface, and D is the distance between Drone 1 and Drone 2 (GU1 and GU2). The blue arrow represents the desired signal; the green one represents the interference signal. We considered an environment in which the user and the drone are communicating one-to-one. The communication between Drone 1 and GU1 is assumed to be DL, and that between Drone 2 and GU2 is assumed to be UL. It is assumed that the communication between Drone 1-GU1 and Drone 2-GU2 is DL, and that the communication between Drone 1-GU1 and Drone 2-GU2 is UL. Considering the receiving power of Drone 2, the signal transmitted from GU2 can be treated as a desired signal, and the other signals are treated as interference signals. During the communication between Drone 1 and GU1, a part of the radio wave transmitted from Drone 1 is reflected from the ground and is received by Drone 2 as an interference component. It is considered that the shorter D is, the larger the influence of the ground reflection. The direct wave from Drone 1 without ground reflection is also received by Drone 2 as an interference component.

3.2. Conventional Linearly Polarized Antenna Case

In this section, we apply the two-ray model to the system model described in Section 3.1, and calculate the received power and SIR from Friis's formula. The received signal in Drone 2 consists of two components, i.e., the direct wave transmitted from Drone 1 through free space and the reflected wave from the ground. The distance of the direct wave and the reflected wave is shown as follows.

$$D_d = \sqrt{D^2 + |h_1 - h_2|^2}, \tag{1}$$

$$D_r = \sqrt{D^2 + (h_1 + h_2)^2}. \tag{2}$$

The phase difference φ between the direct wave and the reflected wave is shown as follows.

$$\varphi = 2\pi(D_r - D_d)/\lambda. \tag{3}$$

The received power, which is the interference signal at Drone 2, is shown as follows by applying the two-ray model [15] as shown in Figure 3.

$$P_{I_{uav}} = P_{t_{uav}} \left(\frac{\lambda}{4\pi} \right)^2 \left| \frac{\sqrt{G_{dir}}}{D_d} + R \frac{\sqrt{G_{ref}} e^{-j\Delta\varphi}}{D_r} \right|^2, \tag{4}$$

$$\sqrt{G_{dir}} = \sqrt{G_b G_d}, \tag{5}$$

$$\sqrt{G_{ref}} = \sqrt{G_a G_c}, \tag{6}$$

where $P_{t_{uav}}$ denotes the transmit power of Drone 1, R denotes the reflection coefficient, $\sqrt{G_{dir}}$ denotes the product of the antenna field patterns along the LoS direction, $\sqrt{G_{ref}}$ denotes the product of the antenna field patterns along the reflected path. The antenna model is based on the following Equation (7).

$$\begin{aligned} G(\theta) &= 10^{G_0 - 3.01 \frac{2\theta}{\theta_B}} \left(-\frac{\theta_{ml}}{2} \leq \theta \leq \frac{\theta_{ml}}{2} \right) \\ &= 10^{-0.411 \ln \theta_B - 10.6} \left(0 < -\frac{\theta_{ml}}{2}, \frac{\theta_{ml}}{2} < \theta \right), \end{aligned} \tag{7}$$

$$G_0 = 20\log_{10}\left(\frac{1.62}{\sin\frac{\pi}{180}\frac{\theta_B}{2}}\right), \tag{8}$$

$$\theta_{ml} = 2.58\theta_B, \tag{9}$$

where θ_B denotes the half-width angle, θ_{ml} denotes the main lobe width, and G_0 denotes the antenna gain.

The power of the desired signal transmitted from GU2 is shown as follows [16].

$$P_{up} = P_t\left(\frac{\lambda}{4\pi}\right)^2\frac{G_tG_0}{h_2^2}, \tag{10}$$

where P_t denotes the terminal ground power, and G_t denotes the terminal antenna gain. From the above, SIR can be shown as follows.

$$\text{SIR} = \frac{P_{up}}{P_{I_{uav}}}, \tag{11}$$

where P_{up} denotes the desired power received from GU2 to Drone 2 and $P_{I_{uav}}$ denotes the interference power received from Drone 1 to Drone 2. Figure 4 shows the SIR when D is varied from 5 m to 125 m in the system model with $h_1 = 50$ m and $h_2 = 25$ m. The green curve shows the SIR of the direct wave only, and the red curve shows the SIR of the two-ray model that combines the direct and reflected waves. From the figure, we can see that the red curve is less than 30 dB for the range from 5 m to 60 m, which is affected by the ground reflection. The closer the distance between the drones is, the stronger the interference becomes, and the more remarkably SIR performance degrades. Therefore, it is necessary to improve the SIR performance for this target communication range. Under the same conditions, the proposed method investigates the usage of circular polarization to resolve the aforementioned issue as shown in the next section.

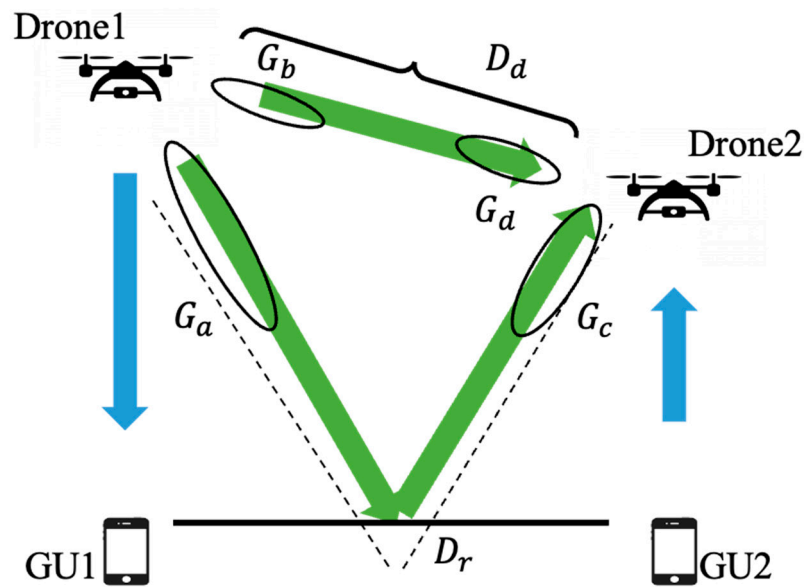


Figure 3. Two-ray model. Arrows mean possible propagation paths between these transmitters and receivers.

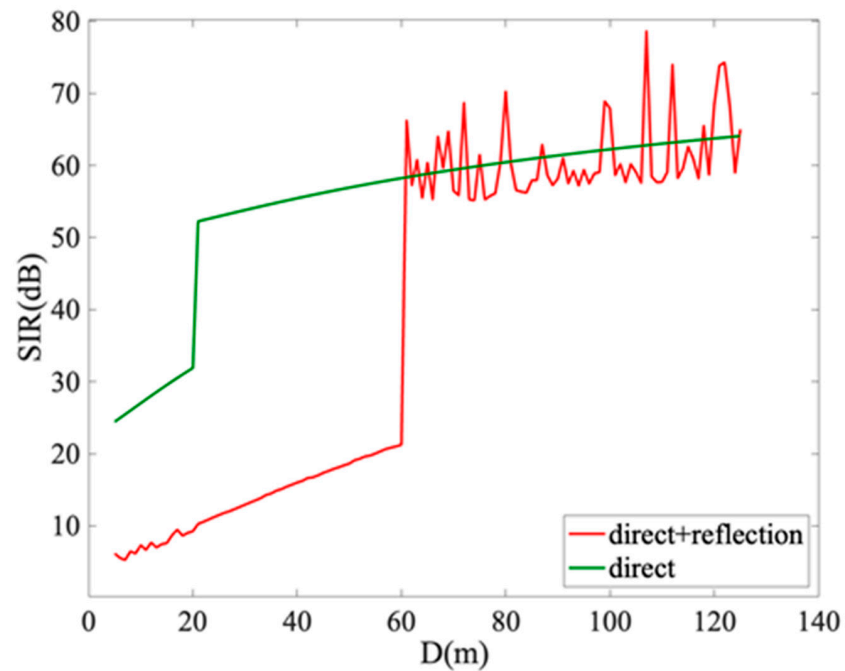


Figure 4. SIR performance with linearly polarized antenna.

3.3. Proposed Circularly Polarized Antenna Case

In the system model shown in Figure 2, we considered the adoption of circular polarization. A circular polarization wave is a polarized wave in which the electric field propagates in a rotation like a circle. There are two advantages of using the circular polarization. The first is that the alignment angle of the transmitting and receiving antennas in the wave-front can be set freely because the electric field component propagates in a rotating pattern. The second is that the direction of rotation of the electric field after reflection can be reversed if the angle of incidence of the electric field is within the Brewster angle, thereby reducing multipath fading [17]. In our system model shown in Figure 2, Drone 1 and Drone 2 are equipped with antennas that can transmit and receive right-handed circular polarization, and GU1 and GU2 are equipped with antennas that can transmit and receive linearly polarized waves. The right-handed circular polarization transmitted from Drone 1 is converted to left-handed circular polarization after reflection from the ground, and Drone 2, which is equipped with an antenna capable of receiving right-handed circular polarization, cannot receive the left-handed circular polarization. With this principle, we considered how to improve the SIR of Drone 2 by preventing the influence of ground reflection. On the other hand, it should be noted that the desired signal transmitted from GU2 is linearly polarized waves, so the power is only half when it is received by Drone 2. As to be shown in our numerical analyses summarized in Appendix A, regardless of this power loss of 3 dB, the proposed system employing circularly polarized antennas is still superior compared to conventional linearly polarized antennas in terms of achieved SIR. Next, we apply the circular polarization to the system model and explain how to calculate the electric field after reflection. The polarization plane that is vertical to the ground is called a vertical polarization (TM wave), and that which is horizontal is called a horizontal polarization (TE wave). The reflection coefficients for incident vertical and horizontal polarization waves [15] are shown as follows.

$$\rho_V = \frac{(\epsilon_r - jx)\sin\phi - \sqrt{(\epsilon_r - jx) - \cos^2\phi}}{(\epsilon_r - jx)\sin\phi + \sqrt{(\epsilon_r - jx) - \cos^2\phi}}, \quad (12)$$

$$\rho_H = \frac{\sin\phi - \sqrt{(\epsilon_r - jx) - \cos^2\phi}}{\sin\phi + \sqrt{(\epsilon_r - jx) - \cos^2\phi}}, \quad (13)$$

where ϵ_r denotes the relative dielectric constant of the earth fields, σ denotes conductivity, ϵ_0 denotes the dielectric constant of free space, and ϕ denotes grazing angle, where x is defined as follows.

$$x = \frac{\sigma}{\omega\epsilon_0}. \tag{14}$$

The reflection coefficient is determined by the shape and material of the ground and is expressed as a complex number. In our research, we adopted the value for an average ground in [18]. Assuming that the wave propagates in the z -axis direction, the right-handed circular polarization can be expressed as follows.

$$E_R = E_0 e^{j\omega t} \left\{ \mathbf{i} + j e^{j(-\frac{\pi}{2})} \right\} e^{-jk_0 z}. \tag{15}$$

When the phase is 90° behind, the circular polarization is right-handed, and when the phase is 90° ahead, the circular polarization is left-handed. Since the circular polarization can be decomposed into TM wave and TE wave, the electric field of TM wave and TE wave can be shown as follows.

$$E_{TM} = E_0 \mathbf{i} \left(e^{j\omega t} \right) e^{-jk_0 z}, \tag{16}$$

$$E_{TE} = E_0 j e^{j(-\frac{\pi}{2})} \left(e^{j\omega t} \right) e^{-jk_0 z}, \tag{17}$$

$$k_0 = \frac{2\pi f}{c}, \tag{18}$$

where E_0 denotes amplitude of electric field, \mathbf{i} denotes the unit vector in the x -axis direction, j denotes the unit vector in the y -axis direction, k_0 denotes a wave number, and c denotes the speed of light.

Based on the reflection coefficient and the incident wave, the TM and TE waves after ground reflection are expressed as follows.

$$\begin{bmatrix} E_{TM}^r \\ E_{TE}^r \end{bmatrix} = \begin{bmatrix} \rho_V & 0 \\ 0 & \rho_H \end{bmatrix} \begin{bmatrix} E_{TM}^i \\ E_{TE}^i \end{bmatrix}, \tag{19}$$

where E_{TM}^i denotes TM wave before reflection, E_{TE}^i denotes TE wave before reflection, E_{TM}^r denotes TM wave after reflection, and E_{TE}^r denotes TE wave after reflection.

By matrix calculation, the right- and left-handed circular polarization after ground reflection are shown as follows.

$$\begin{bmatrix} E_L^r \\ E_R^r \end{bmatrix} = \frac{1}{\sqrt{2}} \begin{bmatrix} 1 & j \\ 1 & -j \end{bmatrix} \begin{bmatrix} E_{TM}^r \\ E_{TE}^r \end{bmatrix}, \tag{20}$$

where E_L^r denotes left-handed circular polarization, and E_R^r denotes right-handed circular polarization.

The desired power to be received from GU2 to Drone 2 is shown as follows.

$$P_{up1} = \frac{1}{2} \left| E_{up} \times \sqrt{P_t \times G_0 \times 1 \times \left(\frac{c}{4\pi f h_2} \right)^2} \right|^2, \tag{21}$$

where E_{up} denotes the amplitude of linear polarization, P_t denotes the transmit power of the terminal, and G_0 denotes the gain of receiving antenna (Drone 2). The reason for the factor of a half in Equation (21) is that a circularly polarized antenna can receive only half the power of a linearly polarized transmission. The power is calculated as the square of the absolute value of the electric field.

3.4. Numerical Analysis

Numerical analyses are conducted to evaluate the SIR of the conventional and proposed UAV's antennas. The parameters used in our numerical analyses are listed in Table 1. Figure 5 shows the SIR of the system with $h_1 = 50$ m and $h_2 = 25$ m, while D is varied from 5 m to 125 m.

Table 1. Numerical parameters.

Parameter	Value [Unit]
Carrier frequency	28 [GHz]
Bandwidth	100 [MHz]
Transmit power (drone)	13 [dBm]
Transmit power (terminal)	23 [dBm]
Transmit antenna half-width	30 [°]
Receive antenna gain	0 [dBi]
Conductivity	5×10^{-3} [S]
Relative dielectric constant	15

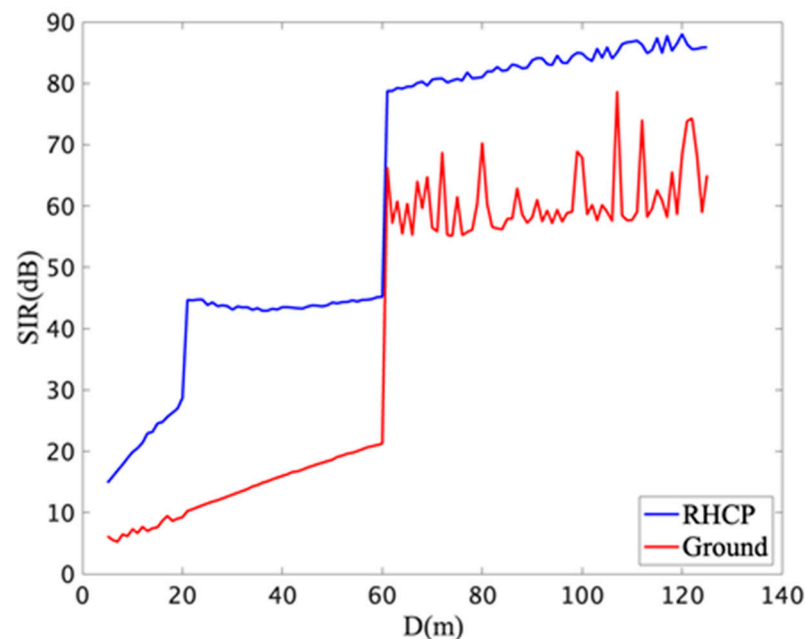


Figure 5. SIR performance with circularly polarized antenna.

The blue curve shows the SIR of the right-handed circular polarization transmitted from Drone 1. The red curve is the same curve as Figure 4 and is shown for the sake of comparison. The SIR is less than 20 dB when the circularly polarized antenna is not applied for the range 20 m and 60 m, which is affected by the ground reflection. On the other hand, the SIR of more than 40 dB can be achieved in the case of circular polarization. However, when the distance between the users is closer, e.g., from 5 m to 20 m, the SIR is less than 30 dB even in the case of circular polarization. The reason for this phenomenon is that Drone 2 is placed within the main lobe of Drone 1's antenna. In order to improve the SIR in these specific distance ranges, it is preferred to introduce antennas of narrower beam-width. When the separation of the drones is more than 60 m, we can see a significant increase in the SIR. This is owing to the fact that the reflected wave is received with side lobes at the receiver.

4. Backhaul Link Analysis

In this section, the system model in Section 3 is further extended to the scenarios with the existence of backhaul drones. Section 4.1 describes the extended system model with the existence of backhaul drones. In Section 4.2, the SIR performance at the access drones is evaluated. Furthermore, Section 4.3 evaluates the SIR performance at the backhaul drones.

4.1. System Model

A system model with backhaul drones is shown in Figure 6. In this system, a backhaul drone Drone3 is placed on top of the access drone Drone1 providing DL services to the user GU1. Similarly, a backhaul drone Drone4 is placed above the access drone Drone2 providing UL services to the user GU2. Let h_3 be the height of the backhaul drone Drone3, and h_4 be the height of the backhaul drone Drone4, respectively. Focusing on Drone2, the desired signal is the signal transmitted from GU2, and the signals received from other sources are interference signals. Similarly, the desired signal for Drone4 is the signal transmitted from Drone2, and the signals received from other drones are interference signals. The access drone plays the role of a Decode-and-Forward (DF) relay station transferring DL or UL data between the ground user and the backhaul drone. For that purpose, each access drone is assumed to be equipped with two antenna interfaces, each facing its corresponding user and backhaul drone, respectively. For the user-facing interface, an antenna of wide beam-width is desired to cover users distributed on the ground. On the other hand, for the backhaul drone-facing interface, an antenna of narrow beam-width is preferred [19].

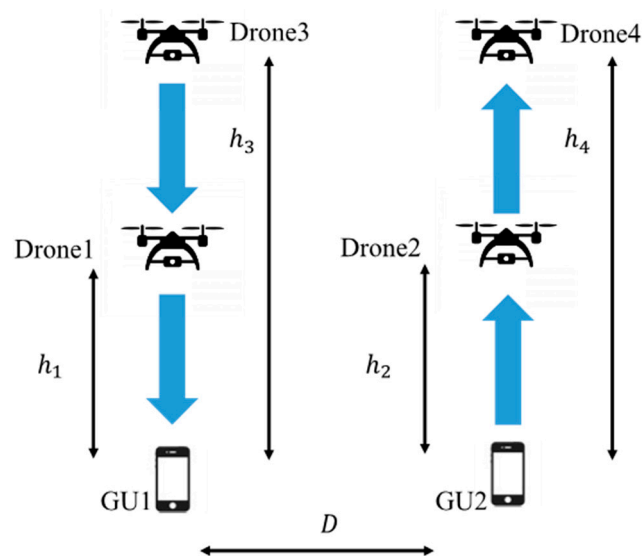


Figure 6. System model with backhaul drones. Arrows mean communication links established between these transmitters and receivers.

Similar to Section 3, the SIR performance at different types of drones of the system is investigated in the next two subsections, assuming that circularly polarized antennas are employed at these drones. The difference from Section 3 is that the polarization plane can be selected for the access link and the backhaul link. One such example pattern is to use right-handed circularly polarized antennas for access links and left-handed circularly polarized antennas for backhaul links, etc. Such combinations of polarization planes will be investigated in the following parts of the paper, in terms of achieved SIR.

4.2. SIR Performance at the Access Drones

In this subsection, the SIR at Drone2, which is receiving signals will be analyzed. Figure 7 shows the signal reception model at Drone2 when linearly polarized antennas are used in both backhaul and access links as a conventional system. The blue signal represents the desired signal and the green signal represents the interference signal. In this case of

linear polarization, the interference signals received by Drone2 are the direct and reflected waves from Drone1, and the direct and reflected waves from Drone3.

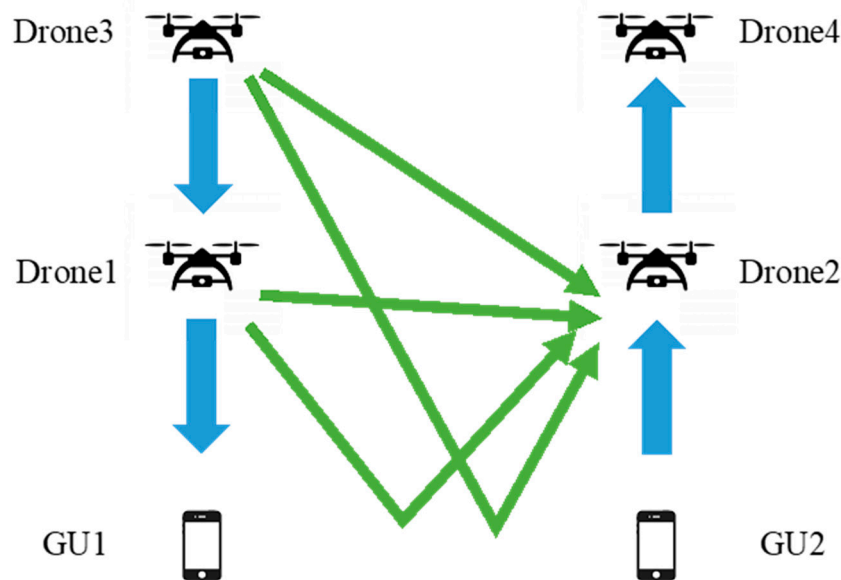


Figure 7. Signal reception model at Drone2 (linear polarization case). Blue arrows mean communication links established between these transmitters and receivers. Green arrows mean interference links between these transmitters and receivers. Similar for the other mentioned figures.

Figure 8 shows the signal reception model at Drone2 when the backhaul link and access link employ the same polarization plane, e.g., right-handed circularly polarized antennas, as depicted in the figure. The dashed line represents an inversed polarization plane with a different rotation direction, i.e., left-handed circular polarization plane in this figure. As for the interference signal as a whole, the influence of the reflected wave is reduced, owing to the polarization plane inversion at ground reflection. Thus, the influence of the direct wave becomes dominant in this proposed model.

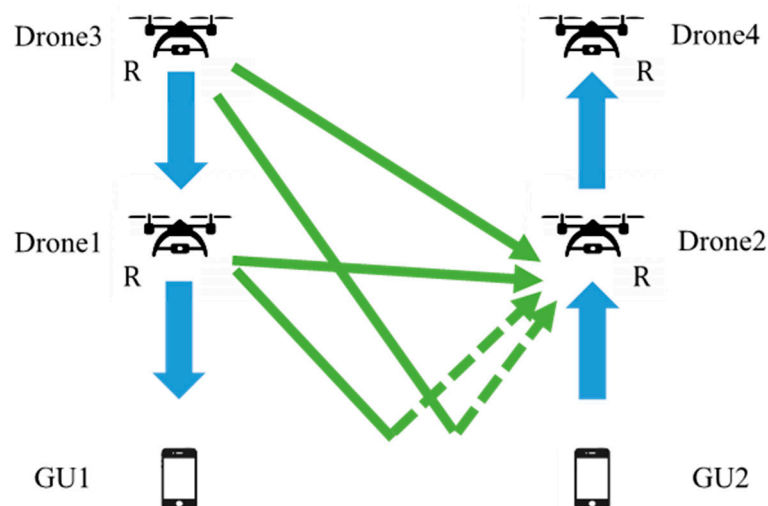


Figure 8. Signal reception model at Drone2 (same polarization antennas are used at both access and backhaul links, dashed line represents the inversion of polarization plane due to ground reflection).

Figure 9 shows the signal reception model at Drone2 when the backhaul link and access link employ antennas of different polarization planes. Since the left-handed circularly polarized wave is transmitted from Drone3, it becomes a right-handed circularly polarized wave after reflection to be received at Drone2. Therefore, the reflected wave from the

backhaul drone and the direct wave from the access drone dominate the entire interference signal in the model of Figure 9.

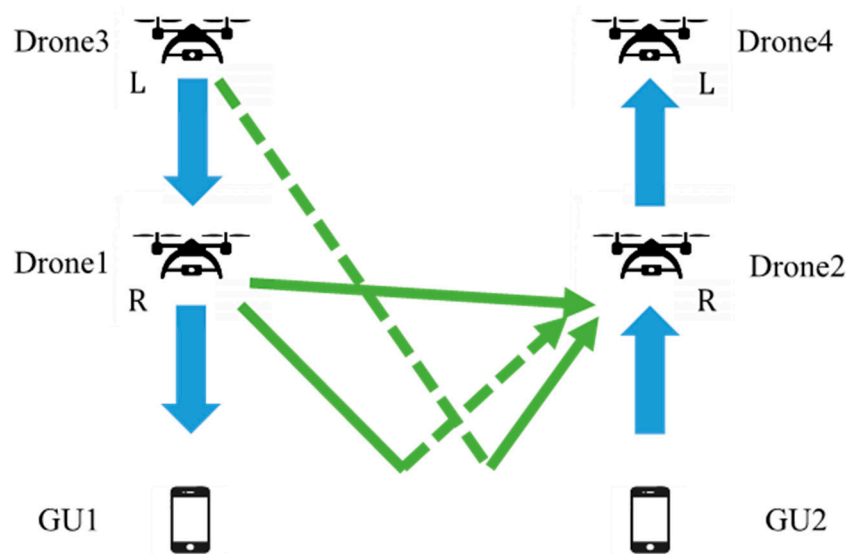


Figure 9. Signal reception model at Drone2 (different polarization antennas are used at access and backhaul links).

Figure 10 shows the signal reception model at Drone2 when the same polarization plane is employed at each uplink or downlink communication link, but different polarization planes are used at these two adjacent UL/DL systems. From the figure, the influence of reflected waves from neighboring backhaul drones and neighboring access drones dominates the interference signal as a whole.

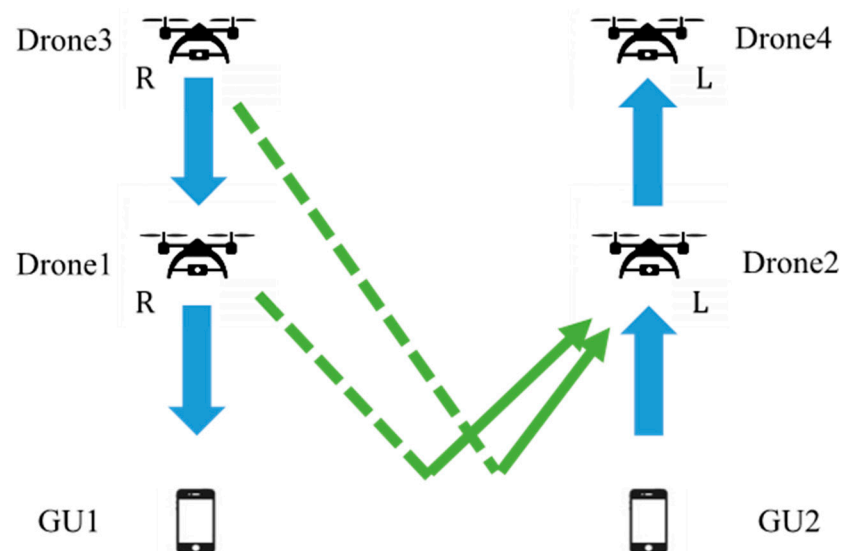


Figure 10. Signal reception model at Drone2 (different polarization antennas are used at adjacent UL/DL communication links).

Figure 11 shows the SIR characteristics of Drone2 when D is varied from 10 m to 100 m, with both h_1 and h_2 fixed at 25 m, and h_3 and h_4 both fixed at 75 m for the above four patterns of polarization combinations, knowing that these drones' altitudes were empirically selected based on our own experiences in realistic outdoor environments [8]. The green curve shows the performance of the conventional linear polarization case in Figure 7, just for the sake of comparison. The red line shows the case of Figure 8 where

the backhaul link and access link use same plane of polarization. Since the influence of direct wave is dominant, the SIR performance of this case almost outperforms other cases even when the distance between adjacent drones is shorten. It can be seen that D must be separated by approximately 13 m or more to satisfy our system requirement of 16.8 dB [20]. Compared to the case without the existence of backhaul drones in Figure 5, the new result reveals the necessity of increasing the separation distance between these adjacent UL/DL communication links to achieve a system's target SIR under the existence of backhaul drones.

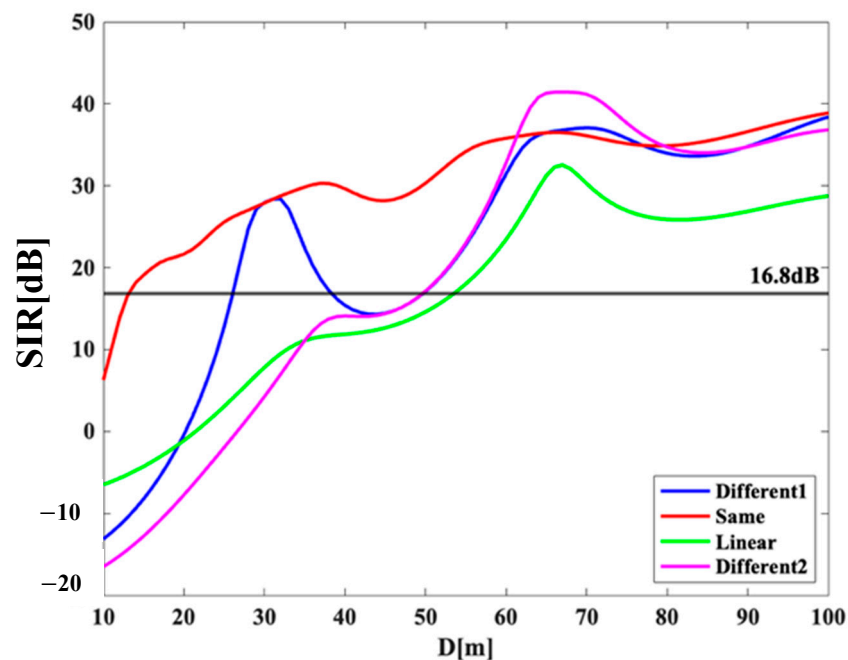


Figure 11. SIR performance at Drone 2 under the existence of backhaul drones.

The blue line indicates the case where the backhaul link and access link employ antennas of different polarization planes as in Figure 9 (denoted as “Different1” in the legend). It can be seen that D must be separated by about 26 m or more to satisfy the system requirement for this type of polarization selection. The SIR performance of the blue curve temporarily takes a high value when D is about 30 m and 68 m. These can be explained by the nulls of the employed antennas.

The magenta line shows the performance when using different planes of polarization for uplink/downlink links separately as in Figure 10 (denoted as “Different2” in the legend). It can be seen that D must be separated by about 55 m or more to satisfy the system requirement. For this scenario, since the interference is dominated by the ground-reflected waves from both Drone1 and Drone3, the separation requirement is even stricter compared to the two aforementioned cases. We can also remark that there is no significant difference in the SIR characteristics when D is sufficiently large, regardless of different circular polarization choices. Overall, as red curve shows the best performance, it is recommended to use antennas of a same type of circular polarization for all access/backhaul and UL/DL links. Such selection also simplifies the system design.

4.3. SIR Performance at the Backhaul Drones

SIR for Drone4, which is receiving signals, can be calculated in the same way as in Section 4.1. Figure 12 shows the signal reception model at Drone4 when using linearly polarized antennas at both the backhaul and access links as a comparison scheme. The blue signal represents the desired signal and the green signal represents the interference signal. In the case of linear polarization, the interference signals received by Drone4 are the

direct and reflected waves from Drone1, the direct and reflected waves from Drone3, and the signal from GU2.

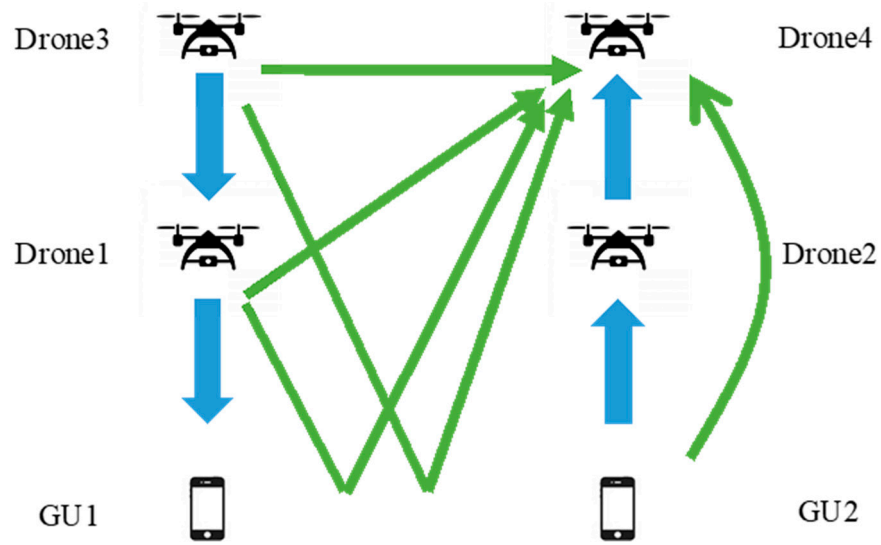


Figure 12. Signal reception model at Drone4 (linear polarization case).

Figure 13 shows the signal reception model at Drone4 when the same circular polarization plane is used at both the access and backhaul links. Among all the interference signals, only the direct waves are dominant, owing the polarization plane inversion of the ground reflected paths.

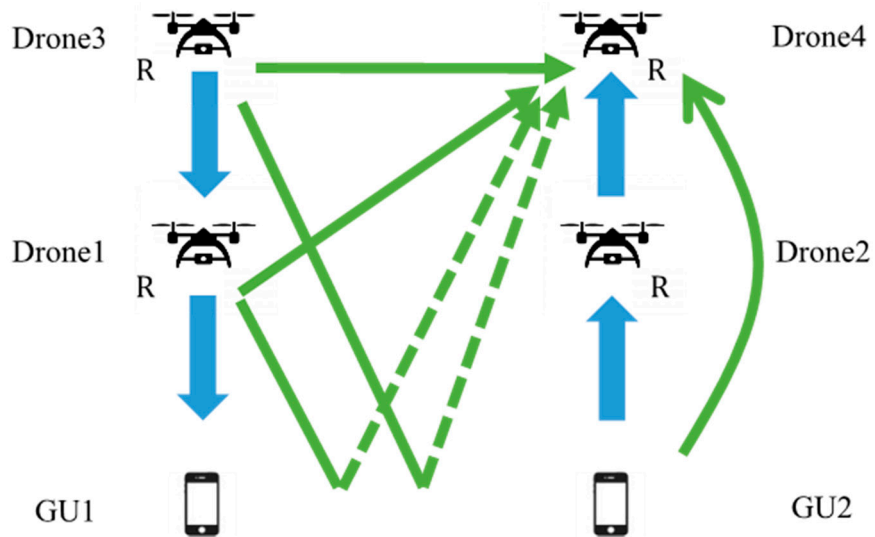


Figure 13. Signal reception model at Drone4 (same polarization antennas are used at both access and backhaul links).

Figure 14 shows the signal reception model at Drone4 when different circular polarization planes are assigned to the backhaul and access link, respectively. The interference signals received by Drone4 are the direct wave from Drone3, the reflected wave from Drone1, and the signal from GU2.

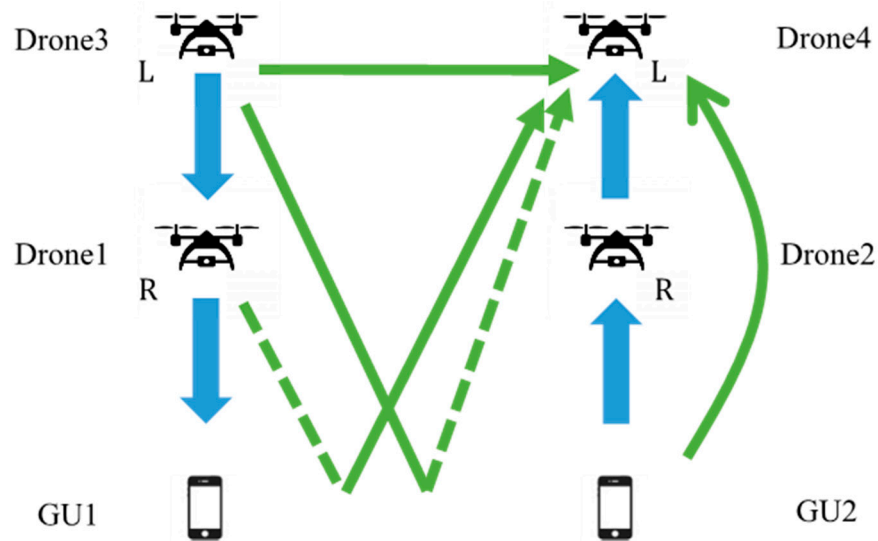


Figure 14. Signal reception model at Drone4 (different polarization antennas are used at access and backhaul links).

Figure 15 shows the signal reception model at Drone 4 when adjacent UL/DL drones communicate using different planes of polarization. In this model, the influence of reflected waves from adjacent access and backhaul drones is dominant due to the polarization plane inversion effect.

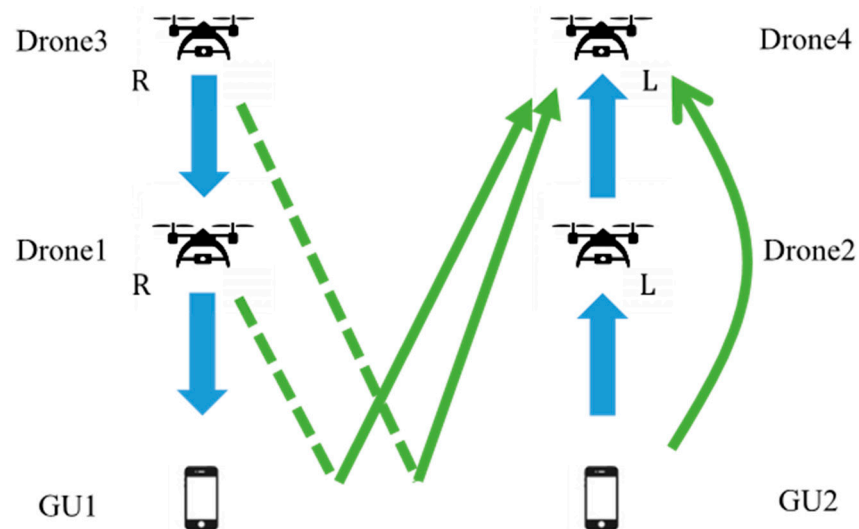


Figure 15. Signal reception model at Drone4 (different polarization antennas are used at adjacent UL/DL communication links).

Figure 16 shows the SIR characteristics of Drone4 when D is moved from 10 m to 100 m, with both h_1 and h_2 fixed at 25 m, and h_3 and h_4 both fixed at 75 m, as in Section 4.2 for the aforementioned four patterns. The red line shows the case where the backhaul link and access link employ antennas of the same plane of polarization, as shown in Figure 13. Regardless of D , the SIR takes a nearly constant value of 45 dB, much higher than the system requirement of 16.8 dB. Such superior performance is owing to the fact that the polarization planes of the interference paths caused by ground reflection were inverted such that the only dominant interference source is from GU2, transmitting at lower transmit power.

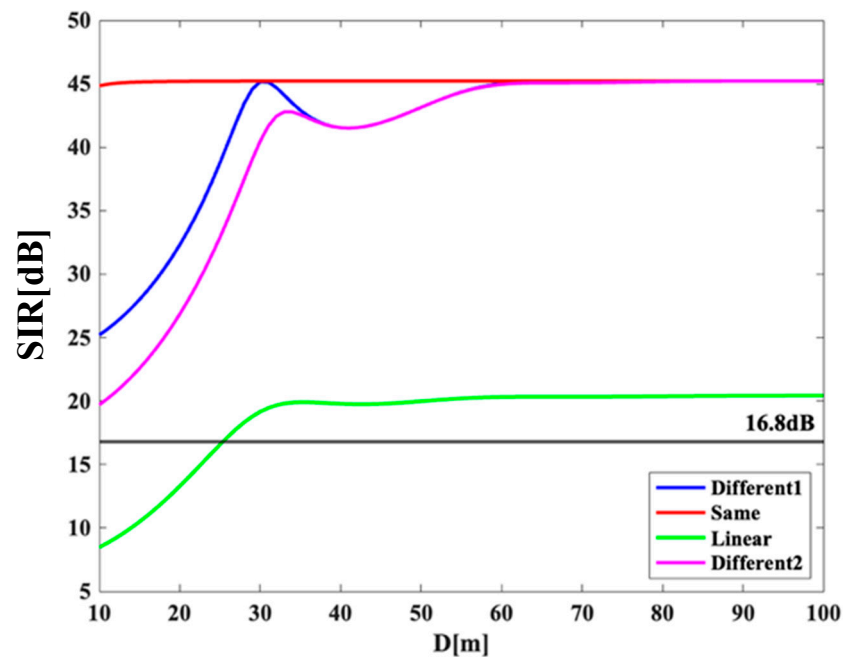


Figure 16. SIR performance at Drone 4 under the existence of backhaul drones.

The blue line shows the performance where different polarization planes are assigned to the backhaul and access drones, respectively, as shown in Figure 14 (denoted as “Different1” in the legend). As the dominant interference source in this case is due to the ground reflection path from Drone1, the SIR performance gradually increases against larger separation D and achieves the peak when D is about 30 m, which corresponds to the null of the receive antenna pattern at Drone4.

The magenta line shows the performance when different polarization planes are assigned for adjacent UL/DL drones, as shown in Figure 15 (denoted as “Different2” in the legend). Similar to the previous scenario, the dominant interference sources are from the ground reflection paths from both Drone1 and Drone3. It results in almost the same SIR performance trend as that of “Different1”, but at a lower value of SIR.

In the overall, the performance of applying circular polarization is superior to the conventional scheme of linear polarization, shown by the green curve of Figure 16. For the proposed schemes, the SIR performance of all curves converges at the value of 45 dB when enough D separation (larger than 60 m) is attained. It means that in these regions, the effect of inter-drone interference is negligible and the only remaining interference source is from the ground user GU2. Among all of the comparisons schemes, similar to the analysis in Section 4.2, applying the same circular polarization plane to all the drones’ access and backhaul interfaces yields the best SIR performance.

5. Conclusions

In this research, as a wireless network system for disaster areas using drones, we proposed a system that transmits data in the 28 GHz band with a bandwidth of 100 MHz used in local 5G. Asynchronous operation has been considered in response to the demand for increasing uplink data capacity, such as sending videos from smartphones. We attempted to reduce the intra/inter-system interference by properly introducing antennas of circular polarization against a conventional system employing linearly polarized antennas. In Section 3, the two-wave model was applied to analyze the SIR performance between the access drone and the ground user. A comparison was made using different combination planes of polarization, and our numerical result revealed that the SIR characteristics were improved when antennas of the same kind of circular polarization were employed. In Section 4, we furthermore evaluated the SIR of the system in the existence of backhaul drones. Similarly, it was found that deploying antennas of the same kind of

circular polarization to all the access and backhaul links of both UL/DL yields the best performance. Overall, the introduction of circular polarization antennas in our system helped to reduce interference significantly compared to the conventional approach of using linearly polarized antennas. Therefore, we plan to use this type of antenna architecture in our own system in the future. For reference, the findings of our numerical analyses are summarized in Appendix A. We have constructed a Proof-of-Concept (PoC) system and partially demonstrated the effectiveness of our proposed system (mainly access links) via outdoor experiment in [8]. Our future topics include extending this PoC system [8] for the backhaul links and conducting outdoor experiments to demonstrate the effectiveness of introducing circularly polarized antennas in our drone communication networks.

Author Contributions: Conceptualization, T.O. and G.K.T.; methodology, T.O. and G.K.T.; software, T.O.; validation, T.O. and G.K.T.; formal analysis, T.O.; investigation, T.O. and G.K.T.; resources, T.O. and G.K.T.; data curation, T.O.; writing—original draft preparation, T.O. and G.K.T.; writing—review and editing, G.K.T.; visualization, T.O.; supervision, G.K.T.; project administration, G.K.T.; funding acquisition, G.K.T. All authors have read and agreed to the published version of the manuscript.

Funding: This research was funded by MIC SCOPE, grant number JP235003015.

Data Availability Statement: Not applicable.

Acknowledgments: We would like to thank the anonymous reviewers for their careful reading of our manuscript, and their many insightful comments and suggestions to improve the quality of the manuscript. We would also like to acknowledge the Telecommunications Advancement Foundation for its financial support to complete part of this research.

Conflicts of Interest: The authors declare no conflict of interest.

Appendix A. Summary of Our Numerical Investigations

The below table summarizes the numerical findings of different antenna architectures in this paper, in terms of achieved SIR measured in dB. Type A denotes the scenarios of only access links as observed from Figure 5. Type B and Type C denote the scenarios with the existence of backhaul links, where SIRs are investigated at the access layer (Figure 11) and the backhaul layer (Figure 16), respectively. The “All Linear” column shows the performance of the conventional scheme where all antenna interfaces employ linear polarization, while the other columns show those of our proposed system employing circularly polarized antennas. “All Circular” means that all the drones employ the same direction of circularly polarized antennas that is applicable for scenarios. “Counter Circular”, that can be applied for only Type B and Type C scenarios, means that opposite directions of circularly polarized antennas are employed for different layers of drones. More specifically, “Counter Circular 1” means that different polarization antennas are used at access and backhaul links, while “Counter Circular 1” means that different polarization antennas are used at adjacent UL/DL communication links.

Type	D	All Linear (Figure 7)	All Circular (Figure 8)	Counter Circular 1 (Figure 9)	Counter Circular 2 (Figure 10)
A	10 m	6 dB	20 dB	-	-
	40 m	15 dB	42 dB	-	-
	100 m	60 dB	80 dB	-	-
B	10 m	-7 dB	7 dB	-12 dB	-17 dB
	40 m	11 dB	30 dB	15 dB	14 dB
	100 m	29 dB	39 dB	38 dB	35 dB
C	10 m	8 dB	44 dB	25 dB	20 dB
	40 m	19 dB	45 dB	42 dB	42 dB
	100 m	20 dB	45 dB	45 dB	45 dB

References

1. Hayat, S.; Yanmaz, E.; Muzaffar, R. Survey on unmanned aerial vehicle networks for civil applications: A communications viewpoint. *IEEE Commun. Surv. Tutor.* **2016**, *18*, 2624–2661. [CrossRef]
2. Ghosh, A.; Thomas, T.A.; Cudak, M.C.; Ratasuk, R.; Moorut, P.; Vook, F.W.; Rappaport, T.S.; MacCartney, G.R.; Sun, S.; Nie, S. Millimeter-wave enhanced local area systems: A high-data-rate approach for future wireless networks. *IEEE J. Sel. Areas Commun.* **2014**, *32*, 1152–1163. [CrossRef]
3. Zhang, L.; Zhao, H.; Hou, S.; Zhao, Z.; Xu, H.; Wu, X.; Wu, Q.; Zhang, R. A survey on 5G millimeter wave communications for UAV-assisted wireless networks. *IEEE Access* **2019**, *7*, 117460–117504. [CrossRef]
4. Ministry of Internal Affairs and Communications Japan. [WHITE PAPER] *Information and Communications in Japan*; Ministry of Internal Affairs and Communications Japan: Tokyo, Japan, 2011.
5. Tran, G.K.; Ozasa, M.; Nakazato, J. NFV/SDN as an Enabler for Dynamic Placement Method of mmWave Embedded UAV Access Base Stations. *Network* **2022**, *2*, 479–499. [CrossRef]
6. Amrallah, A.; Mohamed, E.M.; Tran, G.K.; Sakaguchi, K. UAV Trajectory Optimization in a Post-Disaster Area Using Dual Energy-Aware Bandits. *Sensors* **2023**, *23*, 1402. [CrossRef] [PubMed]
7. Hirata, K.; Tran, G.K.; Sakaguchi, K. *Design of Dynamic mmWave Mesh Backhaul with UAVs*; IEICE Technical Report; No. 238, SR2020-38; IEICE: Tokyo, Japan, 2020; Volume 120, pp. 100–107. (In Japanese)
8. Masaoka, R.; Tran, G.K. Construction and Demonstration of Access Link for Millimeter Wave UAV Base Station Network. In Proceedings of the 14th International Conference on Ubiquitous and Future Networks ICUFN 2023, Paris, France, 4–7 July 2023; IEEE: Piscataway, NJ, USA, 2023.
9. National Institute of Information and Communications Technology. Local 5G Current Status and Future Prospects. 2020. Available online: https://www.jstage.jst.go.jp/article/bplus/14/3/14_246/_pdf (accessed on 7 July 2023). (In Japanese)
10. Qualcomm Japan. About Local 5G Asynchronous Operation. 2020. Available online: https://www.soumu.go.jp/main_content/000676472.pdf (accessed on 7 July 2023). (In Japanese)
11. Okada, T.; Tran, G.K. A Study on Antenna Polarization Plane for UL/DL Drone Access Network. In Proceedings of the 12th International Conference on Ubiquitous and Future Networks ICUFN 2021, Jeju Island, Republic of Korea, 17–20 August 2021; IEEE: Piscataway, NJ, USA, 2021; pp. 334–338.
12. Boukoberine, M.N.; Zhou, Z.; Benbouzid, M. A critical review on unmanned aerial vehicles power supply and energy management: Solutions, strategies, and prospects. *Appl. Energy* **2019**, *255*, 113823. [CrossRef]
13. Mozaffari, M.; Saad, W.; Bennis, M.; Debbah, M. Drone Small Cells in the Clouds: Design, Deployment and Performance Analysis. In Proceedings of the IEEE Global Communications Conference, San Diego, CA, USA, 6–10 December 2015.
14. Mozaffari, M.; Saad, W.; Bennis, M.; Debbah, M. Efficient Deployment of Multiple Unmanned Aerial Vehicles for Optimal Wireless Coverage. *IEEE Commun. Lett.* **2016**, *20*, 1647–1650. [CrossRef]
15. Salous, S. *Radio Propagation Measurement and Channel Modelling*; Wiley: Hoboken, NJ, USA, 2013.
16. Karasawa, Y. *Radiowave Propagation Fundamentals for Digital Mobile Communications*; Corona, Inc.: Sanjo, Japan, 2003; pp. 21–23.
17. Fukusako, T. *Basics of Circularly Polarized Antenna*; Corona, Inc.: Sanjo, Japan, 2018.
18. Parsons, J.D. *The Mobile Radio Propagation Channel*, 2nd ed.; John Wiley & Sons, Inc.: Hoboken, NJ, USA, 2000.
19. Chia, S.; Gasparroni, M.; Brick, P. The next challenge for cellular networks: Backhaul. *IEEE Microw. Mag.* **2009**, *10*, 54–66. [CrossRef]
20. Okada, T. Research on Antenna Polarization in Drone Access Network with Uplink and Downlink. Master's Thesis, Tokyo Institute of Technology, Tokyo, Japan, 2022.

Disclaimer/Publisher's Note: The statements, opinions and data contained in all publications are solely those of the individual author(s) and contributor(s) and not of MDPI and/or the editor(s). MDPI and/or the editor(s) disclaim responsibility for any injury to people or property resulting from any ideas, methods, instructions or products referred to in the content.

Article

Gain Enhancement of Microstrip Patch Array Antennas Using Two Metallic Plates for 24 GHz Radar Applications

Junho Yeo ^{1,*}  and Jong-Ig Lee ²¹ School of Artificial Intelligence, Daegu University, Gyeongsan 38453, Republic of Korea² Department of Electronics Engineering, Dongseo University, Busan 47011, Republic of Korea

* Correspondence: jyeo@daegu.ac.kr; Tel.: +82-53-850-6642

Abstract: In this paper, a method of enhancing gain in a microstrip patch array antenna using two metallic plates for 24 GHz radar applications is presented. A 4×1 linear microstrip square patch array antenna covering the 24.0 to 24.25 GHz frequency range and using a shunt-connected series feed network with a tapered power distribution was first designed with a measured maximum gain of 9.8 dBi and dimensions of 30 mm \times 12 mm. Two metallic plates were appended along the array axis of the antenna to double the gain in the 4×1 array antenna. Effects on performance from varying the tilting angle and length of the metallic plates, such as the input reflection coefficient, the radiation patterns, and gain, were investigated through simulation. Gain enhancement in the 4×1 patch array antenna with metallic plates was highest when the tilting angle was around 70° , and gain kept increasing as the length of the metallic plates increased. A prototype of the 4×1 patch array antenna was fabricated with plates at a tilting angle of 70° , a length of 50 mm, and a measured maximum gain of 16.8 dBi. Therefore, a gain enhancement of about 7 dB was achieved by adding the metallic plates along the array axis of the 4×1 patch array antenna.

Keywords: microstrip patch array antenna; gain enhancement; metallic plates; tilting angle; radar



Citation: Yeo, J.; Lee, J.-I. Gain Enhancement of Microstrip Patch Array Antennas Using Two Metallic Plates for 24 GHz Radar Applications. *Electronics* **2023**, *12*, 1512. <https://doi.org/10.3390/electronics12071512>

Academic Editors: Faisal Tubbal, Ladislau Matekovits and Raad Raad

Received: 27 February 2023

Revised: 22 March 2023

Accepted: 22 March 2023

Published: 23 March 2023



Copyright: © 2023 by the authors. Licensee MDPI, Basel, Switzerland. This article is an open access article distributed under the terms and conditions of the Creative Commons Attribution (CC BY) license (<https://creativecommons.org/licenses/by/4.0/>).

1. Introduction

Radar measures the distance, direction, angle, and speed of an object or a target by using reflected electromagnetic waves that return from the object after transmitting them [1]. Radar was developed during World War II for air defense applications to detect German aircraft. Its usage has progressively widened to civilian and commercial applications, such as airports and harbor traffic control, weather forecasting, and Earth remote sensing [2]. Recently, it has been widely used for automotive and industrial applications, such as collision avoidance and adaptive cruise control in advanced cars, for traffic monitoring, level sensing, and motion detection because of low-cost single-chip solutions from semiconductor integration [3].

Radar, in general, is divided into continuous-wave (CW) radar and pulse radar based on the waveform of the transmitted signals [4]. Pulse radar transmits and receives a pulse signal; the shorter the pulse width, the better the distance resolution. Since pulse radar uses pulse waveforms, it has high instantaneous power and requires a wide frequency bandwidth. Therefore, it is challenging to implement in hardware, expensive, and mainly used for military purposes. CW radar is divided into three types: single-tone CW, frequency shift keying (FSK), and frequency-modulated CW (FMCW). In single-tone CW, the object's speed can be detected by the frequency change due to the Doppler from the object's movement, when the object reflects the electromagnetic wave. However, this type of radar cannot measure the distance to the object or the velocity of a stationary object. FSK can measure the speed and distance of a moving object by using two or more discrete transmission frequencies but cannot measure the distance to a stationary object. FMCW uses a voltage-controlled oscillator (VCO) to calculate the shift between the received

frequency and the transmitted frequency using the linear frequency modulated transmitted frequency to measure the speed and distance of a moving object as well as the distance to a stationary object. Hence, FMCW is the most accurate and widely used method because of its advantages.

Three main operating frequency bands exist for automotive millimeter-wave radar: 24 GHz, 77 GHz, and 79 GHz [5]. The 24 GHz frequency band (24.0 GHz to 24.25 GHz) is allocated to short-ranges up to 30 m and is used in blind-spot detection, rear cross-traffic alerts, and collision avoidance, whereas the 77 GHz frequency band (76 GHz to 77 GHz) is allocated to long ranges up to 250 m and is used in adaptive cruise control and forward collision warning systems. The 79 GHz frequency band (77 GHz to 81 GHz) is allocated to high-resolution short-range applications. The upper millimeter wave band (100 GHz to 300 GHz) or the sub-terahertz band (100 GHz to 1000 GHz) is expected to be used for higher-resolution radar applications shortly [6,7].

A radar system usually consists of transmitter circuitry producing high-frequency signals, a transmitting antenna sending the signals toward the target, a receiving antenna capturing the signal reflected from the target, and a receiver circuitry extracting the information of interest from the received signal [4]. High-gain directional antennas are required for radar systems. Generally, the antennas used for radar systems can be classified into reflector antennas, lens antennas, and array antennas [8,9]. Reflector antennas consist of a feed antenna and a parabolic reflector. The feed antenna, placed at the reflector's focal point, is the source of the transmitted waves and is the collection point for the received waves. The reflector reflects the transmitted waves in the direction of its axis to make plane waves and reflects the received waves coming from the axis direction to the focal point. Types of reflector antennas used for radar systems are the parabolic reflector antenna, the Cassegrain reflector antenna with dual reflectors, and the offset feed reflector antenna. Lens antennas have been used for radar systems because they can convert a spherical wave into a plane wave to produce high gain. A convex-plane lens using low-loss dielectric material with a relative permittivity greater than 1 can be used. A Luneburg lens, a spherical dielectric lens with a graded index of refraction (increasing toward the center), can create multiple beams using multiple feed antennas. Lens antennas offer several advantages, such as a wide scan angle, a very low sidelobe, and low feed blockage, compared to reflector antennas. Still, they are very thick and heavy at microwave frequencies, and the attenuation caused by the loss tangent of the dielectric material is significant. Various array antennas using different array elements, such as dipoles, waveguide slots, horns, and microstrip patches, have also been widely used to achieve high gain for radar systems. Various planar microstrip patch array antennas are mainly used for commercial semiconductor-integrated radar sensors.

The microstrip patch array antenna configurations are based on the feed network [10,11]. There are three types of feed networks for the microstrip patch array antennas: series, parallel (or corporate), and series-parallel combination. In the parallel feed network, input power is distributed to all radiating elements using power dividers. Larger frequency bandwidths can be achieved, and the configuration is modular. Since the path length to each array element is the same, each element has the same power and phase. However, the parallel feed network requires a very large space; a long length in the feed network causes high feed losses, and discontinuity between line corners causes large mutual coupling effects that distort the radiation patterns resulting in a high cross-polarization level. In the series feed network, array elements are serially fed from a single transmission line, and the total lengths of the feed line can be minimized with reduced losses and lower sidelobes. The series feed network can be divided into in-line and shunt-connected. For the in-line series feed network, array elements are placed in series and are connected by an intervening transmission line. Therefore, it is most compact in size and efficient in space usage. For the connection between array elements, direct connection or coupled connection can be employed. Since the electrical length of the transmission line between the elements changes as the frequency changes, the main beam direction changes and can be used for frequency beam scanning. In addition, the frequency bandwidth of the in-line series feed network is narrower, compared to the corporate network.

The shunt-connected series feed network is the same as the in-line series feed network, but the array elements branch out from the transmission line, and each element has only one transmission line. The lengths of the paths between the elements can be adjusted to make the array insensitive to frequency variation. The series-parallel combination feed network can compensate for the disadvantages of series and parallel feed networks.

According to the radar equation, maximum detection range varies as a square root of the antenna gain. Therefore, we can double the maximum detection range by increasing the antenna gain by four times (6 dB) [8]. Various gain enhancement methods for microstrip patch antennas have been attempted. Fabry–Perot cavity (FPC) antennas, formed by the ground plane of the feed patch antenna and a partially reflective surface (PRS) located above the ground plane with some spacing, have been extensively studied for gain enhancement [12–16]. The PRS is also called the superstrate, and it consists of arrays of periodic metallo-dielectric or pure dielectric elements. Gain in the FPC antenna is proportional to the reflection magnitude and the dimensions of the PRS. Hemispherical, extended hemispherical with a cylinder, elliptical, or planar graded index dielectric lenses have been used for gain enhancement [17–20]. Another method to increase gain is the use of a metallic horn structure mounted on the surface of the patch radiator [21–25]. Gain from the antennas integrated with a surface-mounted horn structure depends on the dimensions and slant angle. For the horn structure, a pyramidal horn, a conical horn, or two side wings can be used.

In this paper, a gain-enhanced 4×1 microstrip patch array antenna with metallic plates for 24 GHz radar applications is proposed. First, a reference 4×1 microstrip square patch array antenna with a shunt-connected series feed network using a tapered power distribution was designed to cover the 24.0 to 24.25 GHz frequency range. As the tilting angle and length of the metallic plates were varied, variations in the input reflection coefficient (S_{11}), radiation patterns, and gain characteristics of the microstrip patch array antenna with the metallic plates were investigated in order to find the optimum design parameters for gain enhancement. Full-wave simulations were performed using CST Studio Suite (Dassault Systèmes Co., Vélizy-Villacoublay, France) [26].

2. Designing the 4×1 Microstrip Square Patch Array Antenna

2.1. The Single Microstrip Square Patch Antenna

First, an inset-fed microstrip square patch antenna to be used as an element of the 4×1 microstrip patch array antenna was designed to cover the 24.0 to 24.25 GHz frequency range on an HF-350F substrate ($\epsilon_r = 3.5$, $h = 0.254$ mm, $\tan \delta = 0.0029$), as shown in Figure 1a. Initially, the length of square patch antenna was calculated as follows [27]:

$$L_1 = 0.48\lambda_g \quad (1)$$

$$\lambda_g = \frac{c}{f_r \sqrt{\epsilon_{\text{reff}}}} \quad (2)$$

$$\epsilon_{\text{reff}} = \frac{(\epsilon_r + 1)}{2} + \frac{(\epsilon_r - 1)}{2\sqrt{1 + \frac{(12h)}{W}}} \quad (3)$$

$$W = \frac{c}{2f_r \sqrt{\frac{\epsilon_r + 1}{2}}} \quad (4)$$

in which L_1 is the side length of the square patch antenna; λ_g is the guided or effective wavelength considering the relative permittivity of the substrate; f_r is the desired resonant frequency of the square patch antenna; c is the speed of light; ϵ_r is the relative permittivity of the substrate; ϵ_{reff} is the effective relative permittivity; h is the substrate thickness; and W is the width of the microstrip line.

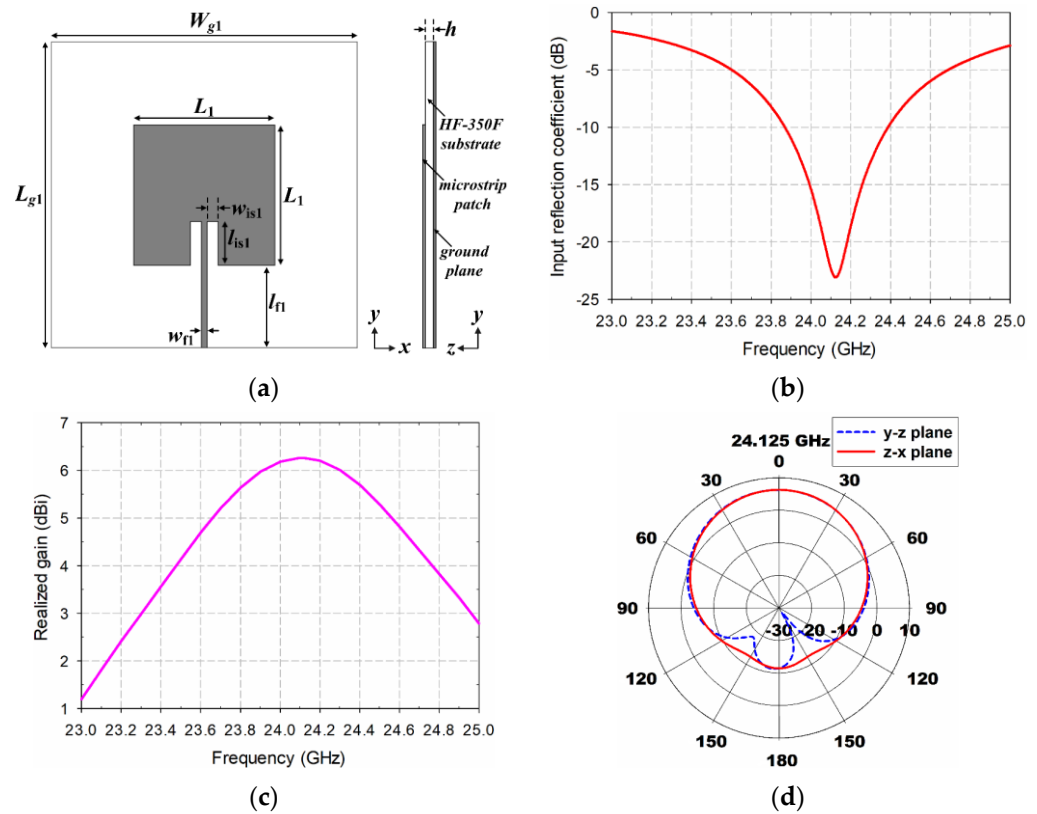


Figure 1. Design and performance of the single microstrip patch antenna: (a) the geometry, (b) the input reflection coefficient, (c) realized gain in the +z-axis direction, and (d) radiation patterns on the y–z and z–x planes at 24.125 GHz.

The calculated length of the square patch using Equations (1) to (4) is $L_{1, \text{calculated}} = 3.34$ mm. By using this information, the length of the inset-fed square patch was then adjusted through simulation by varying the width and length of the inset in order to make the patch resonate at 24.125 GHz, as shown in Figure 1b. The final length of the square patch was $L_1 = 3.22$ mm. For the simulation, the length of the square ground plane was set at $L_{g1} = W_{g1} = 7$ mm, and a 100Ω microstrip feed line with a width of $w_{f1} = 0.125$ mm was used. The final width and length of the inset were $w_{is1} = 0.25$ mm and $l_{is1} = 1.0$ mm, respectively. The simulated frequency bandwidth for a voltage standing wave ratio (VSWR) less than 2 in the input reflection coefficient was 23.853 to 24.404 GHz (2.28%), which covers the 24.0 to 24.25 GHz frequency band.

Simulated realized gain in the +z-axis main lobe direction as a function of frequency and radiation pattern at 24.125 GHz are plotted in Figure 1c,d, respectively. Gain in the 24.0 to 24.25 GHz band ranged from 6.18 dBi to 6.26 dBi with maximum gain at 24.125 GHz. Half power beam width (HPBW) for the y–z plane was 88.7 degrees, whereas for the z–x plane, it was 85.3 degrees.

2.2. Designing 4×1 Shunt-Connected Series Feed Networks Using Uniform and Tapered Power Distributions

In this subsection, 4×1 shunt-connected series feed networks using uniform and tapered power distributions are designed, and theoretical and simulated scattering parameters of the networks are compared.

2.2.1. Uniform Power Distribution

Figure 2 shows the geometry and scattering parameter characteristics of the 4×1 shunt-connected series feed network using a uniform power distribution. Port 1 is connected by a 50Ω subminiature version A (SMA) connector for measurement, and the characteristic impedance, length, and width of the microstrip line connected to port 1 are

$Z_{c1} = 50 \Omega$, $l_1 = 1.87$ mm, and $w_1 = 0.54$ mm, respectively. Port 1 feeds ports 2 to 5 where four inset-fed square patches are connected. The input impedance of ports 2 to 5 was set to 100Ω , with the characteristic impedance and width of the microstrip line connected to ports 2 to 5 at $Z_{c2} = 100 \Omega$ and $w_2 = 0.125$ mm, respectively. The spacing among ports 2 to 5 was set to $l_2 = 7.49$ mm, which is about one guided wavelength of the microstrip line at 24.125 GHz. If the power loss in the microstrip line is ignored, the input power to port 1 is the sum of the power delivered to ports 2 to 5:

$$P_1 = P_2 + P_3 + P_4 + P_5 \tag{5}$$

where P_1, P_2, P_3, P_4 , and P_5 denote the power delivered to ports 1, 2, 3, 4, and 5, respectively.

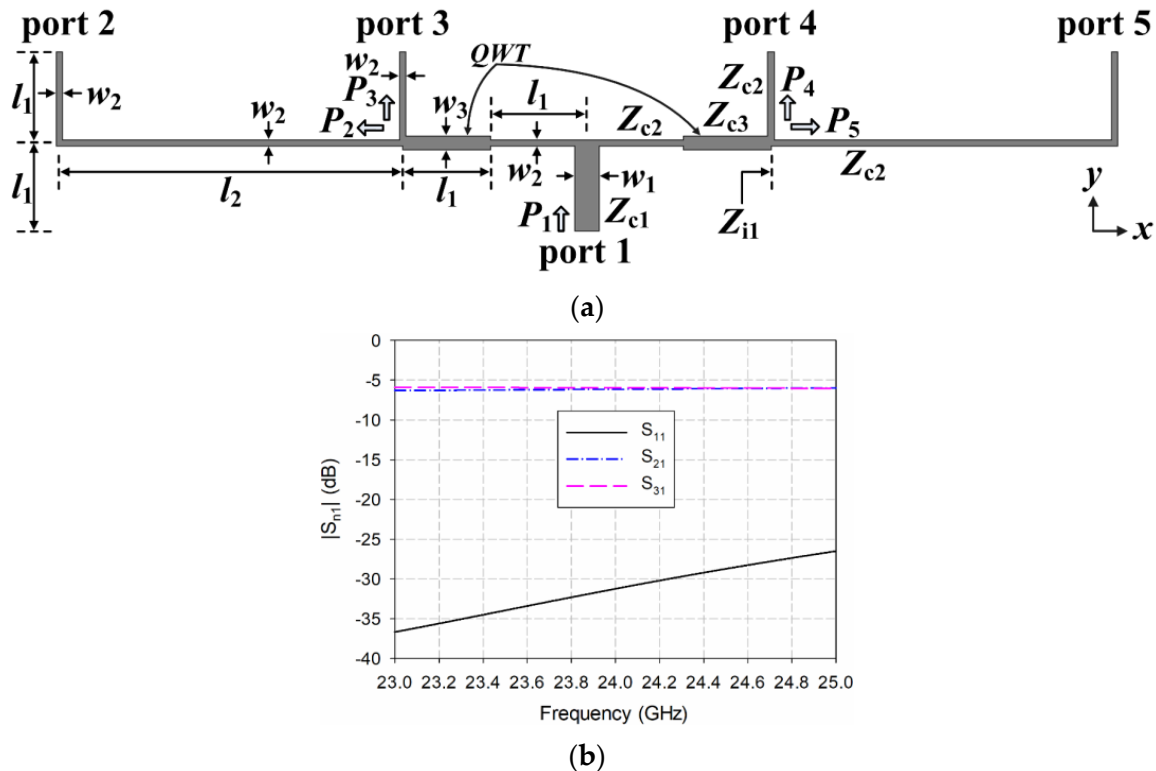


Figure 2. Geometry and scattering parameter characteristics of the 4×1 shunt-connected series feed network using a uniform power distribution: (a) the geometry and (b) scattering parameters.

Port 1 is located between ports 3 and 4, and two 100Ω microstrip lines branch out to the left and right symmetrically at the end of the 50Ω microstrip line connected to port 1. Two T-junction structures connect the two branched microstrip lines to ports 2 to 5. A quarter-wavelength transformer (QWT) is used at the input microstrip line of the T-junction structure for impedance matching. For instance, since the characteristic impedance of the microstrip lines to ports 4 and 5 is $Z_{c2} = 100 \Omega$, the impedance seen at the junction of the microstrip lines toward ports 4 and 5 is $Z_{i1} = Z_{c2} / Z_{c2} = 50 \Omega$, which is the parallel impedance of the characteristic impedance of the microstrip lines to ports 4 and 5. Therefore, the impedance of the QWT can be calculated as follows:

$$Z_{c3} = \sqrt{Z_{c2} \times Z_{i1}} = \sqrt{100 \times 50} = 70.71 \Omega \tag{6}$$

The corresponding length and width of the QWT are $l_1 = (1/4 \times l_2) = 1.87$ mm and $w_3 = 0.29$ mm, respectively.

For uniform power distribution, the input power at port 1 is delivered equally to ports 2 to 5. Therefore, the power distribution among ports 2 to 5 is 1:1:1:1, and the power delivered to ports 2 to 5 is one quarter of P_1 or $P_2 = P_3 = P_4 = P_5 = (1/4 \times P_1)$. Since the power at

a port is proportional to the square of the voltage, and scattering parameters are defined as the input–output voltage ratio between ports, the scattering parameters between port 1 (input) and ports 2 to 5 (output) should theoretically be $S_{21} = S_{31} = S_{41} = S_{51} = 1/2 = -6$ dB. The 4×1 shunt-connected series feed network with uniform power distribution in Figure 2a was simulated using CST Studio Suite, and the simulated scattering parameters between port 1 (input) and ports 2 to 5 (output) at 24.125 GHz were $S_{21} = S_{51} = -6.13$ dB, $S_{31} = S_{41} = -5.96$ dB, respectively. The simulated scattering parameters at 24.125 GHz were close to -6 dB, and this validates the uniform power delivery from port 1 to ports 2 to 5.

2.2.2. Tapered Power Distribution

To reduce sidelobe levels in the radiation patterns of the 4×1 array antenna, a 4×1 shunt-connected series feed network using a tapered power distribution ratio of 1:5:5:1 was designed, and the geometry and scattering parameter characteristics are shown in Figure 3. In this case, the characteristic impedance, length, and width of the microstrip line connected to port 1 are $Z_{c1} = 50 \Omega$, $l_1 = 1.87$ mm, and $w_1 = 0.54$ mm, respectively. Similarly, the input impedance of ports 2 to 5 was set to 100Ω with the characteristic impedance and width of the microstrip line connected to ports 2 to 5 at $Z_{c2} = 100 \Omega$ and $w_2 = 0.125$ mm, respectively. For a tapered power distribution with a power ratio of 1:5:5:1, the power delivered to the two center ports (3 and 4) is five times that delivered to edge ports (2 and 5). Therefore, the power delivered to center ports 3 and 4 is $P_3 = P_4 = (5/12 \times P_1)$, whereas the power delivered to edge ports 2 and 5 is $P_2 = P_5 = (1/12 \times P_1)$.

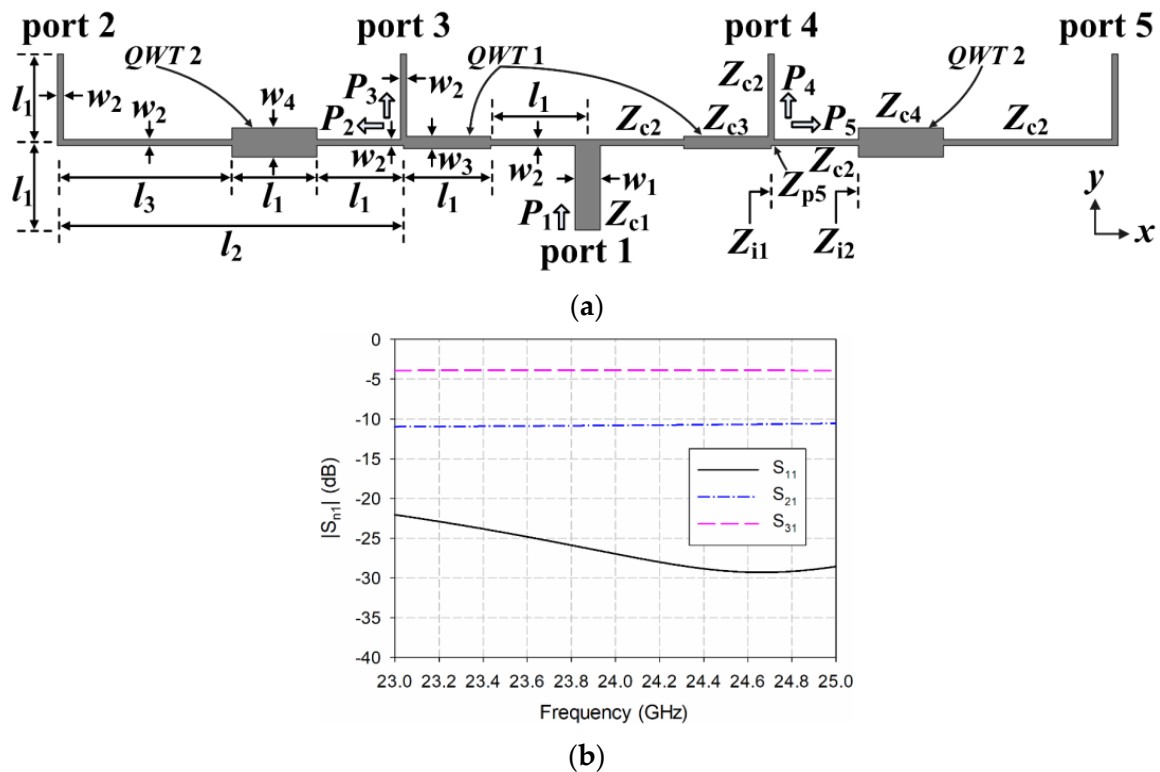


Figure 3. Design and scattering parameter characteristics of the 4×1 shunt-connected series feed network using tapered power distribution: (a) the geometry and (b) scattering parameters.

Two QWTs were used for impedance matching: one at the input microstrip line of the T-junction structure, and the other in the middle of the microstrip line of edge ports 2 and 5. For QWT 1 at the input microstrip line of the T-junction structure, different power distributions connected to the input microstrip line need to be considered. For instance, since the power delivered to port 4 (P_4) is five times the power delivered to port 5 (P_5), and the power ratio of the microstrip line is inversely proportional to the impedance ratio, the impedance of port 5 (Z_{p5}) should be five times the impedance of port 4 (Z_{p4}). If we

assume the impedance of port 4 as $Z_{c2} = 100 \Omega$, the impedance toward port 5 should $Z_{p5} = 5 \times Z_{c2} = 500 \Omega$. The input impedance at the junction of the microstrip lines toward ports 4 and 5 was $Z_{i1} = Z_{c2}/Z_{p5} = 83.33 \Omega$. Therefore, the characteristic impedance of the QWT 1 can be calculated as follows:

$$Z_{c3} = \sqrt{Z_{c2} \times Z_{i1}} = \sqrt{100 \times 83.33} = 91.29 \Omega \quad (7)$$

The length and width of QWT 1 are $l_1 = 1.87 \text{ mm}$ and $w_3 = 0.16 \text{ mm}$, respectively.

For QWT 2 in the middle of the microstrip line of edge ports 2 and 5, impedance transformation of Z_{p5} ($=500 \Omega$) to Z_{c2} ($=100 \Omega$) needs to be considered. For example, if a QWT is directly used to transform $Z_{p5} = 500 \Omega$ to $Z_{c2} = 100 \Omega$, the impedance of the QWT became 223.61Ω , where the corresponding microstrip line width is extremely small and hard to implement. To avoid this problem, a 100Ω microstrip line with a quarter-wavelength was located first, followed by the QWT. In this case, the impedance seen at the input of the QWT 2 becomes:

$$Z_{i2} = \frac{Z_{c2}^2}{Z_{p5}} = \frac{100^2}{500} = 20 \Omega \quad (8)$$

Therefore, the impedance of QWT 2 can be calculated as follows:

$$Z_{c4} = \sqrt{Z_{c2} \times Z_{i2}} = \sqrt{100 \times 20} = 44.72 \Omega \quad (9)$$

The corresponding length and width of QWT 2 are $l_1 = 1.87 \text{ mm}$ and $w_4 = 0.65 \text{ mm}$, respectively.

For tapered power distribution with a power ratio of 1:5:5:1, the scattering parameter between port 1 (input) and ports 2 and 5 (output) is theoretically $S_{21} = S_{51} = \sqrt{1/12} = -10.79 \text{ dB}$, whereas the scattering parameter between port 1 (input) and ports 3 and 4 (output) is $S_{31} = S_{41} = \sqrt{5/12} = -3.8 \text{ dB}$. The 4×1 shunt-connected series feed network with a tapered power distribution of 1:5:5:1 in Figure 3a was simulated using CST Studio Suite. The simulated scattering parameters between port 1 (input) and ports 2 and 5 (output) at 24.125 GHz were $S_{21} = S_{51} = -10.79 \text{ dB}$, whereas the simulated scattering parameters between port 1 (input) and ports 3 and 4 (output) at 24.125 GHz were $S_{31} = S_{41} = -3.88 \text{ dB}$. The simulated scattering parameters at 24.125 GHz are close to the theoretical scattering parameters, and this validates the tapered power delivery from port 1 to ports 2 to 5.

2.3. Performance of the 4×1 Microstrip Square Patch Array Antenna Combined with Shunt-Connected Series Feed Networks Using Uniform and Tapered Power Distributions

This subsection compares the performance of the 4×1 microstrip square patch array antenna when combined with shunt-connected series feed networks using uniform and tapered power distributions.

First, the 4×1 microstrip square patch array antenna combined with a shunt-connected series feed network using a uniform power distribution was designed by adding four square patches at ports 2 to 5 from Figure 2a, as shown in Figure 4a.

Note that the location of port 1 is between ports 3 and 4 to reduce the size of the array antenna, compared to Figure 2a, and a circular disk was appended to port 1 for impedance matching with a coaxial feed to the SMA connector. The final radius of the circular disk was $r_1 = 0.45 \text{ mm}$. The width and length of the inset in the patch are $w_{is2} = 0.25 \text{ mm}$ and $l_{is1} = 1.1 \text{ mm}$, respectively. The width and length of the ground plane were set at $W_{g2} = 30 \text{ mm}$ and $L_{g2} = 12 \text{ mm}$, respectively. The values of other parameters were the same as those in Figure 2a. Figure 4b shows the electric field distribution of the 4×1 microstrip square patch array antenna combined with the shunt-connected series feed network using uniform power distribution at 24.125 GHz. We observed that the electric fields were almost equally distributed on the four patches corresponding to the uniform power distribution.

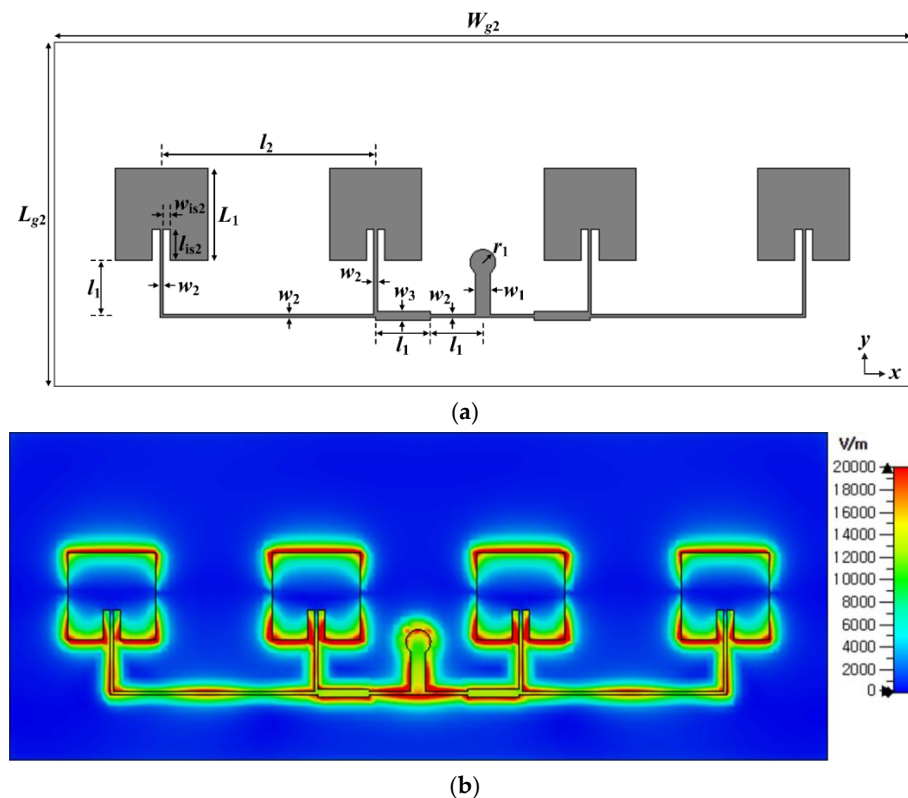


Figure 4. Design and electric field distribution of the 4×1 microstrip square patch array antenna combined with a shunt-connected series feed network using a uniform power distribution: (a) the geometry and (b) the electric field distribution at 24.125 GHz.

Next, the 4×1 microstrip square patch array antenna combined with a shunt-connected series feed network using a tapered power distribution ratio of 1:5:5:1 was designed by adding four square patches at ports 2 to 5 from Figure 3a, as shown in Figure 5a. The parameter values are the same as those in Figures 3a and 4a. Figure 5b shows the electric field distribution of the 4×1 microstrip square patch array antenna combined with the shunt-connected series feed network using tapered power distribution at 24.125 GHz. The electric fields on the two center patches were much higher than those on the two edge patches, which confirmed the tapered power distribution.

Figure 6 compares performance characteristics such as input reflection coefficient, realized gain in the $+z$ -axis main lobe direction, and the radiation patterns of the 4×1 microstrip square patch array antennas combined with the shunt-connected series feed networks using uniform and tapered power distributions. For the 4×1 patch array antenna using uniform power distribution, the simulated frequency bandwidth for a VSWR less than 2 in the input reflection coefficient was 23.805 to 24.429 GHz (2.59%), which is slightly larger than that of the single patch antenna. The frequency bandwidth for a VSWR less than 2 in the 4×1 patch array antenna using the tapered power distribution was 23.836 to 24.402 GHz (2.35%), which is slightly less than the uniform power distribution. Realized gain in the $+z$ -axis direction of the antenna using uniform power distribution ranged from 11.44 dBi to 11.64 dBi in the 24.0 to 24.25 GHz band with maximum gain at 24.125 GHz, whereas it ranged from 10.94 dBi to 11.11 dBi in the 24.0 to 24.25 GHz band with maximum gain at 24.125 GHz in the 4×1 patch array antenna using the tapered power distribution. Therefore, maximum gain at 24.125 GHz was decreased by 0.53 dB when the tapered power distribution was employed instead of the uniform power distribution. For the 4×1 patch array antenna using uniform power distribution, HPBW for the y - z plane was 76.7 degrees at 24.125 GHz, whereas for the z - x plane, it was 22.0 degrees with a sidelobe level of -13.4 dB.

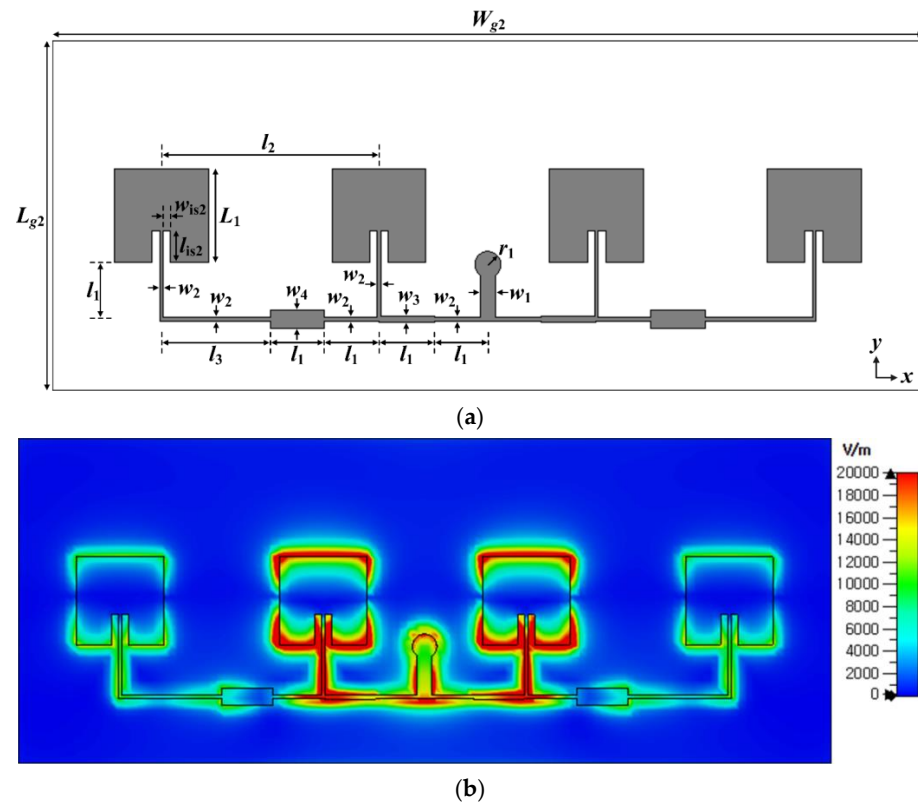


Figure 5. Design and electric field distribution of the 4×1 microstrip square patch array antenna combined with a shunt-connected series feed networks using a tapered power distribution: (a) the geometry and (b) the electric field distribution at 24.125 GHz.

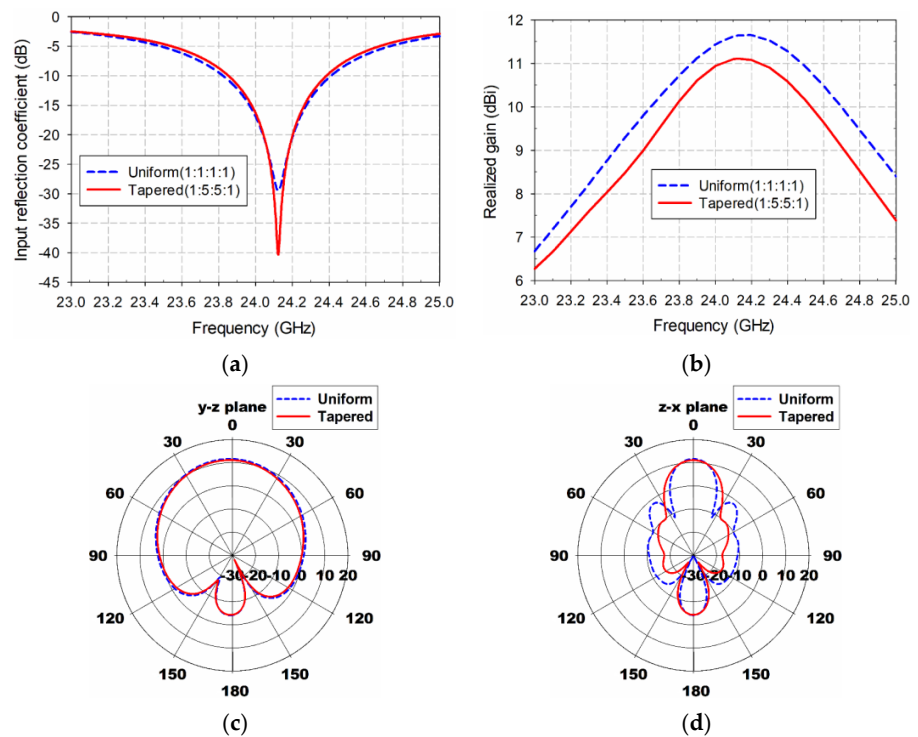


Figure 6. Performance comparison of the 4×1 microstrip square patch array antenna combined with shunt-connected series feed networks using uniform and tapered power distributions: (a) the input reflection coefficient, (b) the realized gain in the $+z$ -axis direction, (c) the radiation patterns on the y - z plane at 24.125 GHz, and (d) the radiation patterns on the z - x plane at 24.125 GHz.

For the 4×1 patch array antenna using a tapered power distribution, the HPBW for the y - z plane was 75.5 degrees at 24.125 GHz, whereas for the z - x plane, it was 26.6 degrees with a side-lobe level of -21.3 dB. We observed that although the HPBW for the z - x plane increased by 4.6 degrees with a resulting maximum gain reduction, the sidelobe level for the z - x plane decreased by 7.9 dB when the tapered power distribution was used instead of the uniform power distribution.

3. Design of 4×1 Microstrip Square Patch Array Antenna Appended with Two Metallic Plates

3.1. Effects from the Tilting Angle when the Metallic Plate Length Is 10 mm

To increase gain in the 4×1 patch array antenna using tapered power distribution, two metallic plates were appended along the array axis (x -axis), as shown in Figure 7a. The width of the metallic plates, w_m , is the same as the ground plane width of the 4×1 patch array antenna. The effects on performance from varying tilting angle θ of the metallic plates were investigated. In this case, the tilting angle was varied from 0° to 90° at increments of 10° when the length of the metallic plates was fixed at $l_m = 10$ mm. Figure 7b,c shows the input reflection coefficients, and the frequencies and magnitudes at the minimum of the input reflection coefficients. The minimum frequency of the input reflection coefficients decreased from 24.106 GHz to 24.02 GHz as θ increased from 0° to 60° . When θ increased to 70° and 80° , the minimum frequency increased to 24.072 GHz and 24.164 GHz, respectively. The minimum frequency decreased to 23.918 GHz when θ increased to 90° . The magnitude at the minimum frequency ranged from -24.59 dB to -33.52 dB except for $\theta = 60^\circ$ and 90° . For $\theta = 60^\circ$, the value decreased to -51.08 dB, whereas it increased to -16.66 dB for $\theta = 90^\circ$. Figure 7d,e shows the realized gain characteristics in the $+z$ -axis direction, and the frequencies and values of maximum gain. The maximum gain frequency ranged from 24.1 GHz to 24.2 GHz when θ ranged from 0° to 80° , whereas it decreased to 23.9 GHz at $\theta = 90^\circ$.

When θ increased from 0° to 30° , the maximum gain value decreased from 10.12 dBi to 4.05 dBi owing to the null on the $+z$ -axis direction. As θ increased from 40° to 70° , the value increased from 8.57 dBi to 13.12 dBi. However, it decreased in the range 11.24 dBi to 11.52 dBi, when θ increased to 80° and 90° . Figure 7f,g compares the radiation patterns on the y - z and z - x planes in the $+z$ -axis direction, whereas Figure 7h,i compares 3D radiation patterns when $\theta = 30^\circ$ and $\theta = 70^\circ$, respectively. We observed a null on the $+z$ -axis direction when $\theta = 30^\circ$, and maximum gain was highest when the tilting angle was $\theta = 70^\circ$. Therefore, $\theta = 70^\circ$ was chosen for maximum gain enhancement. Note that this tilting angle is similar to that of a standard pyramidal horn antenna.

3.2. Effects from the Length of the Metallic Plates when $\theta = 70^\circ$

Next, the effects on performance from length l_m of the metallic plates were investigated, as shown in Figure 8. In this case, the length of the metallic plates was varied from 5 mm to 50 mm in increments of 5 mm when the tilting angle was fixed at $\theta = 70^\circ$ for maximum gain enhancement. Figure 8b,c shows the input reflection coefficients, and the frequencies and magnitudes at the minimum of the input reflection coefficients. The minimum frequency of the input reflection coefficients increased from 23.894 GHz to 24.156 GHz as l_m increased from 5 mm to 15 mm. When l_m increased from 20 mm to 50 mm, the minimum frequency decreased to within the 24.054 GHz to 24.094 GHz range. The magnitude at the minimum frequency ranged from -21.96 dB to -26.08 dB except for $l_m = 20$ mm. For $l_m = 20$ mm, the magnitude increased to -19.6 dB.

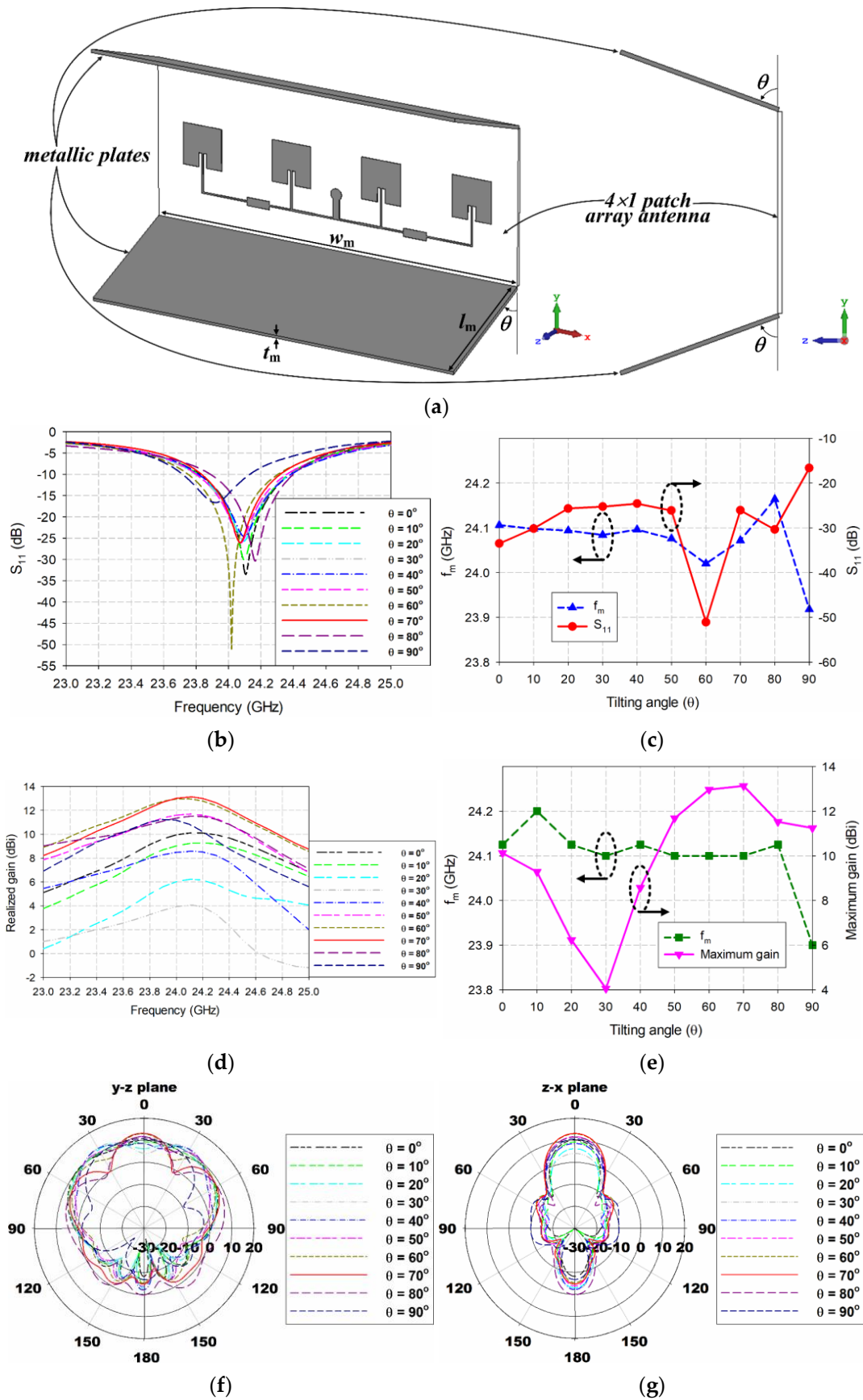


Figure 7. Cont.

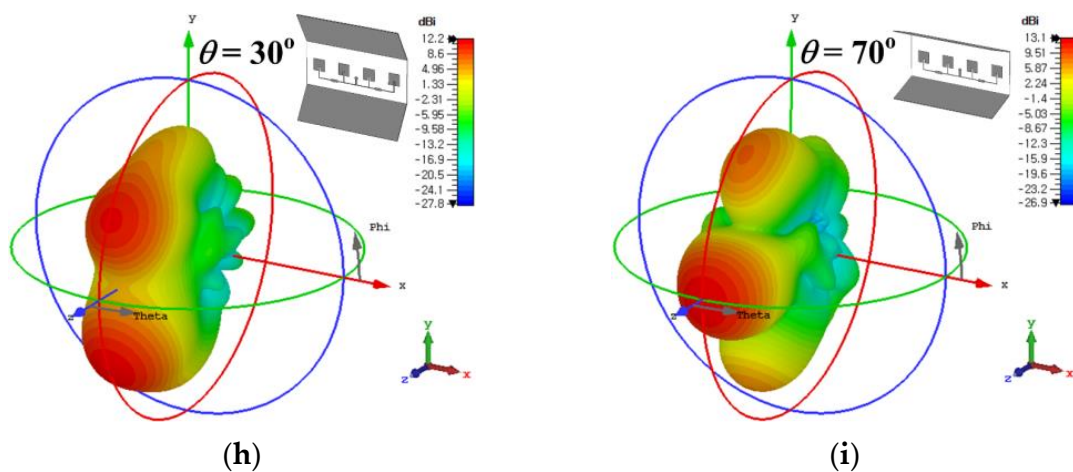


Figure 7. Effects from tilting angle θ of the 4×1 array antenna appended with two metallic plates when $l_m = 10$ mm: (a) the geometry, (b) S_{11} , (c) the frequencies and magnitudes at the minimum of S_{11} , (d) realized gain, (e) the frequencies and values of maximum gain, (f) radiation patterns on the y - z plane for maximum gain frequency, (g) radiation patterns on the z - x plane for maximum gain frequency, (h) 3D radiation pattern at $\theta = 30^\circ$, and (i) 3D radiation pattern at $\theta = 70^\circ$.

Figure 8d,e shows the realized gain characteristics in the $+z$ -axis direction, and the frequencies and values of maximum gain. The maximum gain frequency ranged from 23.9 GHz to 24.1 GHz, whereas the maximum gain value increased gradually from 12.33 dBi to 18.29 dBi. Figure 8h shows the 3D radiation patterns for $l_m = 50$ mm. As mentioned earlier, the maximum detection range can be doubled by increasing antenna gain by four times (6 dB) according to the radar equation. In this work, a 7 dBi gain enhancement was selected to double the maximum detection range in consideration of additional losses and errors occurring during fabrication. Therefore, a metallic plate length of $l_m = 50$ mm was chosen for gain enhancement of more than 7 dBi, compared to the 4×1 patch array antenna without the metallic plates where maximum gain was 11.11 dBi.

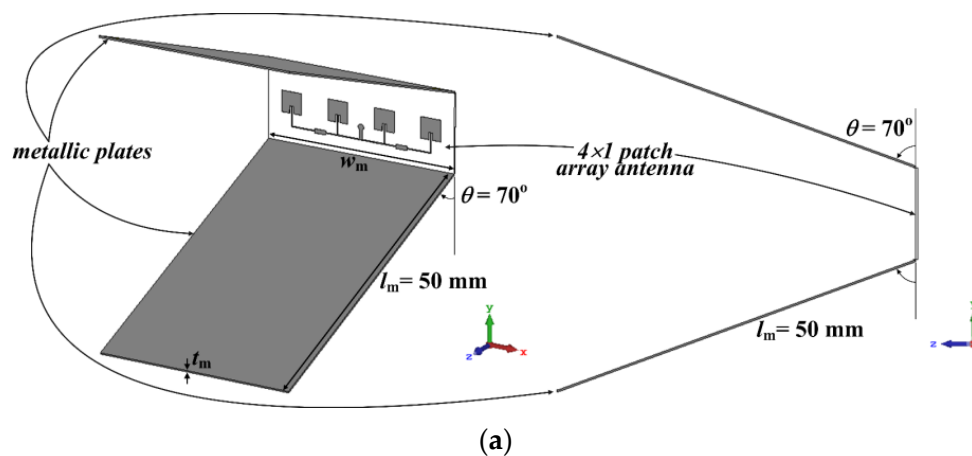


Figure 8. Cont.

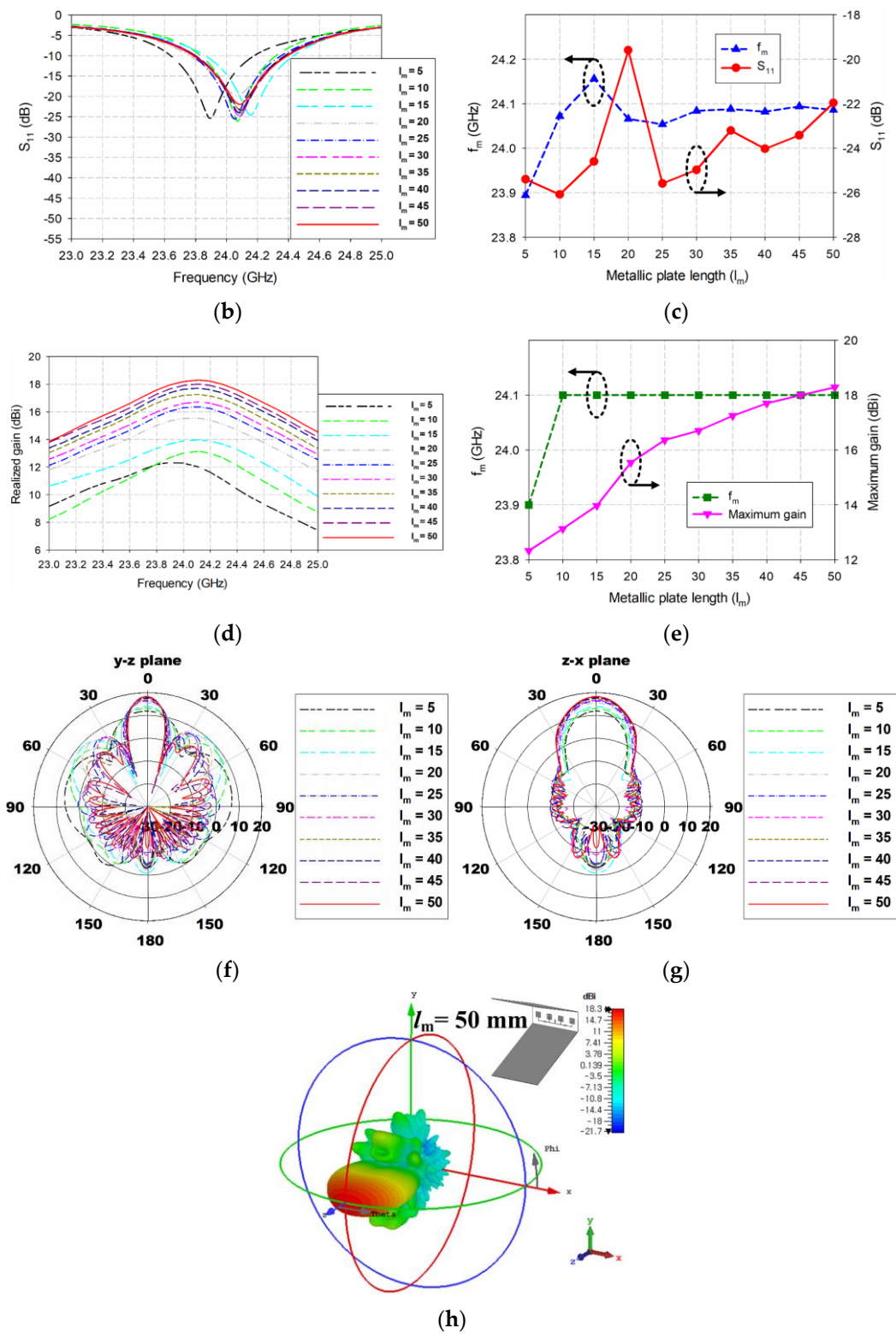


Figure 8. Effects from length l_m of the two metallic plates on the 4×1 microstrip square patch array antenna when $\theta = 70^\circ$: (a) the geometry for $l_m = 50$ mm, (b) S_{11} , (c) the frequencies and magnitudes at the minimum of S_{11} , (d) realized gain, (e) the frequencies and values of maximum gain, (f) radiation patterns on the y–z plane at maximum gain frequency, (g) radiation pattern at z–x planes at maximum gain frequency, and (h) the 3D radiation pattern for $l_m = 50$ mm.

4. Experiment Results and Discussion

To validate the simulated results, the prototypes of the 4×1 patch array antennas using uniform and tapered power distributions and the 4×1 patch array antenna using a tapered power distribution appended with two metallic plates at the tilting angle $\theta = 70^\circ$ and metallic plate length $l_m = 50$ mm were fabricated, as shown in Figure 9. A high-performance SMA connector (PSF-S00-000, GigaLane Co., Ltd., Hwaseong, Korea) designed for applications up to 26.5 GHz, was used. A support structure made of acrylic ($\epsilon_r = 2.56$) was designed and fabricated using the VLS 3.50 model laser cutting system (Universal Laser Systems, Scottsdale, AZ, USA), as shown in Figure 9c. The dimensions of the support structure are shown in Figure 9d. A $36 \mu\text{m}$ -thick copper tape (1181, 3M Co., Ltd., Saint Paul, MN, USA) was used to make the two metallic plates.

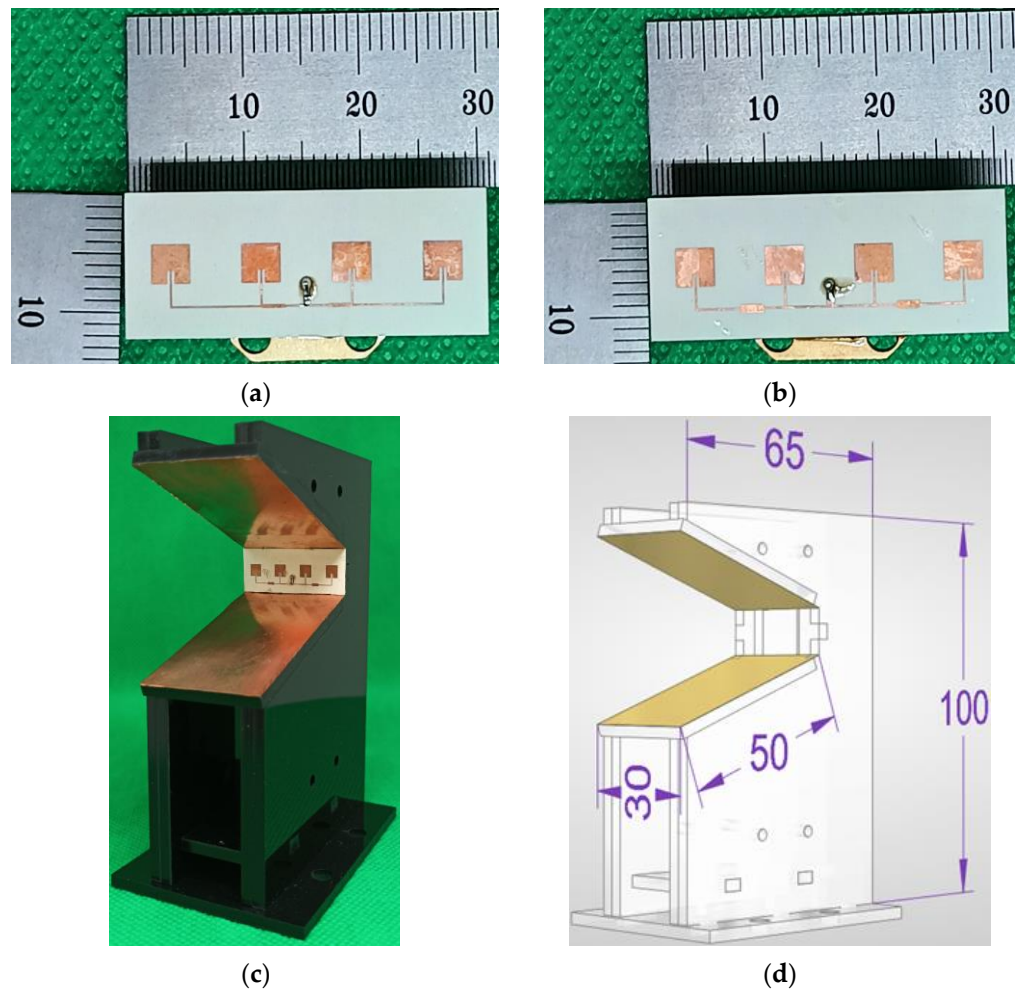


Figure 9. Photographs and dimensions of the fabricated antennas: (a) the 4×1 array antenna using uniform power distribution, (b) the 4×1 array antenna using tapered power distribution, (c) the 4×1 array antenna using tapered power distribution with metallic plates, and (d) the dimensions of the acrylic support structure for the metallic plates. (All units are in millimeters).

The simulated and measured results of the fabricated antennas are compared in Figure 10. An Anritsu 37397C vector network analyzer (Anritsu Co., Ltd., Morgan Hill, CA, USA) was used to measure input reflection coefficient and realized gain characteristics. For the 4×1 patch array antenna using a uniform power distribution, the simulated and measured frequency bands for a VSWR less than two were 23.805 to 24.429 GHz (2.59%) and 23.851 to 24.840 GHz (4.06%), respectively, and were 23.836–24.402 GHz (2.35%) and 23.819–24.381 GHz (2.33%), respectively, for the 4×1 patch array antenna using a tapered

power distribution. Note that the measured frequency band for the 4×1 patch array antenna using uniform power distribution moved toward a high frequency with a bandwidth increase, whereas the measured frequency band shifted toward a low frequency with a similar bandwidth. For the 4×1 patch array antenna using a tapered power distribution appended with two metallic plates, the simulated and measured frequency bands for a VSWR less than two were 23.767 to 24.414 GHz (2.69%) and 23.725 to 24.365 GHz (2.66%), respectively, and, therefore, the measured frequency band shifted toward a low frequency with a similar bandwidth.

For the 4×1 patch array antenna using uniform power distribution, the simulated and measured realized gain in the 24.0 to 24.25 GHz band were 11.44 to 11.64 dBi and 10.3 to 10.5 dBi, respectively, with maximum gain decreasing by 1.14 dB. The simulated and measured realized gain in the 24.0 to 24.25 GHz band was 10.94 to 11.11 dBi and 9.7 to 9.8 dBi, respectively, for the 4×1 patch array antenna using tapered power distribution, with maximum gain decreasing by 1.31 dB.

For the 4×1 patch array antenna using a tapered power distribution appended with two metallic plates, the simulated and measured realized gain in the 24.0 to 24.25 GHz band were 18.19 to 18.29 dBi and 16.7 to 16.8 dBi, respectively, with maximum gain decreasing by 1.49 dB.

The measured radiation patterns of the fabricated antenna on the y - z and z - x planes at 24.125 GHz are compared with the simulated results in Figure 10c–h. The measured radiation patterns agreed quite well with the simulated results. For the 4×1 patch array antenna using uniform power distribution, the simulated and measured sidelobe levels for the z - x plane were -13.4 dB and -9.5 dB, respectively, and the measured sidelobe level increased by 3.9 dB. The simulated and measured sidelobe levels for the z - x plane were -21.3 dB and -17.83 dB, respectively, for the 4×1 patch array antenna using a tapered power distribution, and the measured sidelobe level increased by 3.47 dB. For the 4×1 patch array antenna using a tapered power distribution appended with two metallic plates, the simulated and measured sidelobe levels for the z - x plane were -26.65 dB and -33.66 dB, respectively, and the sidelobe level decreased by 7.01 dB. For the y - z plane, the simulated and measured sidelobe levels were -15.04 dB and -16.17 dB, respectively, and the sidelobe level decreased by 1.13 dB. Note that the sidelobe levels for both the y - z and z - x planes were decreased by appending the two metallic plates.

Table 1 compares the dimensions and performance of the proposed 4×1 patch array antenna using a tapered power distribution appended with two metallic plates with other antennas in the literature. Electrical dimensions of the antennas were calculated using the freespace wavelength of the center frequency for the antennas. We can see that the volume of the proposed antenna is the smallest among the antennas in Table 1.

Table 1. Comparison of dimensions and performance of the proposed antenna with other antennas in the literature.

References	Antenna Type	Physical Dimensions (mm ³)	Electrical Dimensions (λ_0^3)	Bandwidth (GHz) for VSWR < 2	Maximum Gain (dBi)
[19]	Patch antenna + Hemispherical lens	$65 \times 60 \times 49$	$5.18 \times 4.78 \times 3.90$ ($96.57 \lambda_0^3$)	23.35–24.45 ($f_c = 23.9$)	15.2
[20]	Waveguide antenna + Planar graded index lens	$89 \times 89 \times 32$	$10.09 \times 10.09 \times 3.63$ ($369.56 \lambda_0^3$)	28.0–40.0 ($f_c = 34.0$)	25.7
[24]	27×1 slot array antenna + Two wing reflectors	$260 \times 74 \times 54$	$22.33 \times 6.36 \times 4.64$ ($658.97 \lambda_0^3$)	24.94–26.60 ($f_c = 25.77$)	30.5
[28]	2×1 series-fed patch array antenna + PRS	$50 \times 30 \times 10$	$10.79 \times 6.48 \times 2.16$ ($151.03 \lambda_0^3$)	62.5–67.0 ($f_c = 64.75$)	20.1
This Work	4×1 patch array antenna + Two metallic plates	$30 \times 46.2 \times 47$	$2.40 \times 3.70 \times 3.77$ ($33.48 \lambda_0^3$)	23.35–24.45 ($f_c = 24.045$)	16.8

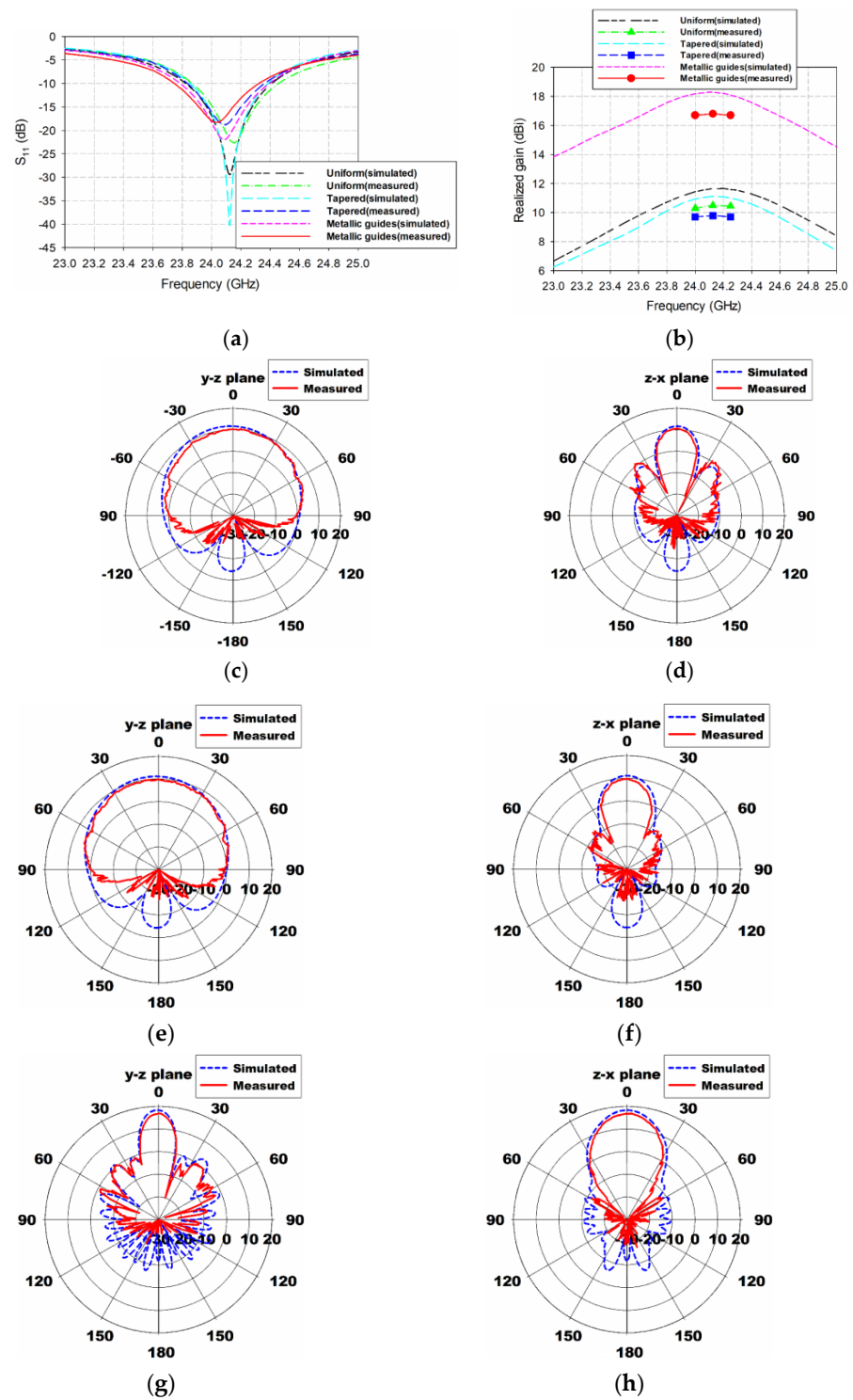


Figure 10. Performance comparison of the fabricated antennas: (a) input reflection coefficients, (b) realized gain, (c) y-z plane radiation patterns at 24.125 GHz for the 4×1 array antenna using uniform power distribution, (d) z-x plane radiation patterns at 24.125 GHz for the 4×1 array antenna using uniform power distribution, (e) y-z plane radiation patterns at 24.125 GHz for the 4×1 array antenna using tapered power distribution, (f) z-x plane radiation patterns at 24.125 GHz for the 4×1 array antenna using tapered power distribution, (g) y-z plane radiation patterns at 24.125 GHz for the 4×1 array antenna using tapered power distribution appended with two metallic plates, and (h) z-x plane radiation patterns at 24.125 GHz for the 4×1 array antenna using tapered power distribution appended with two metallic plates.

5. Conclusions

We proposed a simple method of enhancing gain in a linear microstrip patch array antenna by appending two metallic plates on the array axis along with adjustment of the tilting angle and the length of the metallic plates for 24 GHz radar applications. First, an inset-fed microstrip square patch antenna with a $100\ \Omega$ microstrip feed line, which is used as an element for a 4×1 microstrip patch array antenna, was designed to cover the 24.0–24.25 GHz frequency range on an HF-350F substrate.

Next, 4×1 shunt-connected series feed networks using uniform power distribution with a power ratio of 1:1:1:1 and tapered power distribution with a power ratio of 1:5:5:1 were designed. Their performance as a power divider was validated through a comparison of the theoretical and simulated results. The input reflection coefficients, realized gain, and radiation patterns of the 4×1 microstrip square patch array antennas combined with shunt-connected series feed networks using uniform and tapered power distributions were compared. Maximum gain of the 4×1 array antenna with the tapered power distribution decreased 0.53 dB with an increased HPBW, but the sidelobe level of the z–x plane was reduced by 7.9 dB.

Two metallic plates were appended along the array axis to increase gain in the 4×1 patch array antenna using the tapered power distribution. The effects on the array antenna performance from the tilting angle and the length of the metallic plates were investigated. We found that maximum gain was highest when the tilting angle was around 70° , and it increased gradually as the length of the two metallic plates increased. To achieve 7 dB gain enhancement (doubling the maximum detection range), a metallic plate length of 50 mm was selected.

Measured maximum gain of the 4×1 patch array antenna using the tapered power distribution without metallic plates was 9.8 dBi at 24.125 GHz, whereas the measured maximum gain of the antenna appended with metallic plates was 16.8 dBi. Therefore, a 7 dB gain enhancement can be achieved by adding two metallic plates along the array axis.

Maximum gain might be slightly enhanced by appending two more metallic plates along the axis perpendicular to the array to surround the whole four sides of the array antenna, but the cost and complexity of the fabrication might be considerably increased.

The proposed method can be applied to various radar and millimeter wave applications. It can also be used for satellite communications and future mobile communication systems (5G and 6G). In future work, we plan to conduct research on the production of integrated antennas by using 3D printers.

Author Contributions: J.Y. contributed the idea, the simulation, the analysis, and the overall research. J.-I.L. contributed fabrications and measurements. All authors have read and agreed to the published version of the manuscript.

Funding: This research was supported by Daegu University Research Grant 2019.

Data Availability Statement: Not applicable.

Conflicts of Interest: The authors declare they have no conflict of interest.

References

1. Skolnik, F.; Merrill, I. *Introduction to Radar: Radar Handbook*; McGraw-Hill: New York, NY, USA, 1962.
2. James, R.J. A history of radar. *IEE Rev.* **1989**, *35*, 343–349. [CrossRef]
3. Greco, M.S.; Li, J.; Long, T.; Zoubir, A. Advances in radar systems for modern civilian and commercial applications: Part 1 [From the Guest Editors]. *IEEE Signal Process. Mag.* **2019**, *36*, 13–15. [CrossRef]
4. Lin, J.; Li, C.; Chang, C.C.; Tsai, T.; Zito, D.; Chang, S.F. Review—Semiconductor integrated radar for sensing applications. *ECS J. Solid State Sci. Technol.* **2018**, *7*, 3126–3142. [CrossRef]
5. Chipengo, U.; Krenz, P.M.; Carpenter, S. From antenna design to high fidelity, full physics automotive radar sensor corner case simulation. *Model. Simul. Eng.* **2018**, *2018*, 4239725. [CrossRef]
6. Sabery, S.M.; Bystrov, A.; Navarro-Cía, M.; Gardner, P.; Gashinova, M. Study of low terahertz radar signal backscattering for surface identification. *Sensors* **2021**, *21*, 2954. [CrossRef]

7. Xiao, L.; Xie, Y.; Gao, S.; Li, J.; Wu, P. Generalized radar range equation applied to the whole field region. *Sensors* **2022**, *22*, 4608. [CrossRef] [PubMed]
8. Edde, B. *RADAR: Principles, Technology, Applications*; Prentice Hall, Inc.: Englewood Cliffs, NJ, USA, 1993.
9. Menzel, W.; Moebius, A. Antenna concepts for millimeter-wave automotive radar sensors. *Proc. IEEE* **2012**, *100*, 2372–2379. [CrossRef]
10. Aydemir, A.E. Development of K Band Microstrip Patch Antenna Array for Traffic Radars. Master's Thesis, Middle East Technical University, Ankara, Turkey, 13 November 2017.
11. Errifi, H.; Baghdad, A.; Badri, A.; Sahel, A. Design and analysis of directive microstrip patch array antennas with series, corporate and series-corporate feed network. *Int. J. Electr. Electron. Eng.* **2015**, *3*, 416–423. [CrossRef]
12. Trentini, G.V. Partially reflecting sheet arrays. *IRE Trans. Antennas Propag.* **1956**, *4*, 666–671. [CrossRef]
13. Nguyen, T.K.; Park, I. Design of a low-profile, high-gain Fabry-Perot cavity antenna for Ku-band applications. *J. Electromagn. Eng. Sci.* **2014**, *14*, 306–313. [CrossRef]
14. Goudarzi, A.; Honari, M.M.; Mirzavand, R. Resonant cavity antennas for 5G communication systems: A review. *Electronics* **2020**, *9*, 1080. [CrossRef]
15. Aqlan, B.; Vettikalladi, H.; Alkanhal, M. Millimeter wave antenna with frequency selective surface (FSS) for 79 GHz automotive radar applications. *Int. J. Microw. Wirel. Technol.* **2017**, *9*, 281–290. [CrossRef]
16. Yang, X.X.; Tan, G.N.; Han, B.; Xue, H.G. Millimeter wave Fabry-Perot resonator antenna fed by CPW with high gain and broadband. *Int. J. Antennas Propag.* **2016**, *2016*, 3032684. [CrossRef]
17. Nguyen, N.T.; Rolland, A.; Boriskin, A.V.; Valerio, G.; Le Coq, L.; Sauleau, R. Size and weight reduction of integrated lens antennas using a cylindrical air cavity. *IEEE Trans. Antennas Propag.* **2012**, *60*, 5993–5998. [CrossRef]
18. Malik, B.T.; Doychinov, V.; Zaidi, S.A.R.; Robertson, I.D.; Somjit, N. Antenna gain enhancement by using low-infill 3D-printed dielectric lens antennas. *IEEE Access.* **2019**, *7*, 102467–102476. [CrossRef]
19. Ahmad, W.; Dayi, F.; Rehman, H.; Khan, W. Low-cost and small size millimeter wave (24 GHz) extended hemispherical lens antenna for automotive and industrial applications using FR408HR substrate. *Prog. Electromagn. Res. Lett.* **2021**, *100*, 73–80. [CrossRef]
20. Poyanco, J.M.; Pizarro, F.; Rajo-Iglesias, E. Cost-effective wideband dielectric planar lens antenna for millimeter wave applications. *Sci. Rep.* **2022**, *12*, 4204. [CrossRef] [PubMed]
21. Ranga, Y.; Verma, A.K.; Esselle, K.P.; Weily, A.R. Gain enhancement of UWB slot with the use of surface mounted short horn. In Proceedings of the 2010 IEEE Antennas and Propagation Society International Symposium, Toronto, ON, Canada, 2 September 2010; pp. 1–4.
22. Ononchimeg, S.; Otgonbaatar, G.; Bang, J.H.; Ahn, B.C. A new dual-polarized horn antenna excited by a gap-fed square patch. *Prog. Electromagn. Res. Lett.* **2011**, *21*, 129–137. [CrossRef]
23. Sethi, W.H.; Vettikalladi, H.; Alkanhal, M.A. Millimeter wave antenna with mounted horn integrated on FR4 for 60 GHz Gbps communication systems. *Int. J. Antennas Propag.* **2013**, *2013*, 834314. [CrossRef]
24. Boas, E.C.V.; Ferrero, M.A.S.; Nasri, A.; Mittra, R.; Sodré, A.C. 31 dBi-gain slotted waveguide antenna array using wing-based reflectors. *IEEE Access.* **2022**, *10*, 57327–57338. [CrossRef]
25. Jung, Y.B.; Park, D.Y.; Jung, C.W. Low cost 24GHz patch array antenna for high sensitivity EM sensor. In Proceedings of the 2010 Asia-Pacific Microwave Conference, Yokohama, Japan, 7–10 December 2010; pp. 2208–2211.
26. Electromagnetic Simulation Solvers, CST Studio Suite. Available online: <https://www.3ds.com/products-services/simulia/products/cst-studio-suite/solvers/> (accessed on 28 February 2023).
27. Ahmad, S. A Linear Array Design Based on Non-Uniform Chebyshev Distribution for High Gain Low Sidelobe Level Millimetre Wave 5G Applications. Master's Thesis, Universitat Politècnica de Catalunya-BarcelonaTech, Barcelona, Spain, 31 August 2020.
28. Rabbani, M.S.; Churm, J.; Feresidis, A.P. Fabry-Perot beam scanning antenna for remote vital sign detection at 60 GHz. *IEEE Trans. Antennas Propag.* **2021**, *69*, 3115–3124. [CrossRef]

Disclaimer/Publisher's Note: The statements, opinions and data contained in all publications are solely those of the individual author(s) and contributor(s) and not of MDPI and/or the editor(s). MDPI and/or the editor(s) disclaim responsibility for any injury to people or property resulting from any ideas, methods, instructions or products referred to in the content.

Article

Eight-Port Modified E-Slot MIMO Antenna Array with Enhanced Isolation for 5G Mobile Phone

Hassan Sani Abubakar ¹, Zhiqin Zhao ^{1,*}, Boning Wang ¹, Saad Hassan Kiani ², Naser Ojaroudi Parchin ^{3,*} and Bandar Hakim ⁴

¹ School of Electronics Science and Engineering, University of Electronics Science and Technology of China, Chengdu 610056, China

² Smart Systems Engineering Lab, College of Engineering, Prince Sultan University, Riyadh 11786, Saudi Arabia

³ School of Engineering and the Built Environment, Edinburgh Napier University, Edinburgh EH10 5DT, UK

⁴ Electrical and Computer Engineering Department, Faculty of Engineering, King Abdulaziz University, Jeddah 21589, Saudi Arabia

* Correspondence: zqzhao@uestc.edu.cn (Z.Z.); n.ojaroudiparchin@napier.ac.uk (N.O.P.)

Abstract: An eight-element antenna system operating at sub 6 GHz is presented in this work for a future multiple-input multiple-output (MIMO) system based on a modified E-slot on the ground. The modified E-slot significantly lowers the coupling among the antenna components by suppressing the ground current effect. The design concept is validated by accurately measuring and carefully fabricating an eight-element MIMO antenna. The experimentation yields higher element isolation greater than -21 dB in the 3.5 GHz band and the desired band is achieved at -6 dB impedance bandwidth. The E-shape slot occupies an area of $17.8 \text{ mm} \times 5.6 \text{ mm}$ designed on an FR-4 substrate with dimensions of $150 \text{ mm} \times 75 \text{ mm} \times 0.8 \text{ mm}$. We fed the I-antenna element with an L-shape micro-strip feedline, the size of the I-antenna is $20.4 \times 5.2 \text{ mm}^2$, which operates in the (3.4–3.65 GHz) band. Moreover, our method obtained an envelope correlation coefficient (ECC) of <0.01 and an ergodic channel capacity of 43.50 bps/Hz. The ECC and ergodic channel capacity are important metrics for evaluating MIMO system performance. Results indicate that the proposed antenna system is a good option to be used in 5G mobile phone applications.

Keywords: antenna systems; 5G; MIMO; ECC



Citation: Abubakar, H.S.; Zhao, Z.; Wang, B.; Kiani, S.H.; Parchin, N.O.; Hakim, B. Eight-Port Modified E-Slot MIMO Antenna Array with Enhanced Isolation for 5G Mobile Phone.

Electronics **2023**, *12*, 316.

<https://doi.org/10.3390/electronics12020316>

Academic Editor: Andrea Randazzo

Received: 13 December 2022

Revised: 30 December 2022

Accepted: 4 January 2023

Published: 7 January 2023



Copyright: © 2023 by the authors. Licensee MDPI, Basel, Switzerland. This article is an open access article distributed under the terms and conditions of the Creative Commons Attribution (CC BY) license (<https://creativecommons.org/licenses/by/4.0/>).

1. Introduction

In a communication system, the use of the multiple-input multiple-output (MIMO) antenna technique significantly enhances the channel capacity, spectral efficiency, and reliability link without the additional requirement of increased bandwidth and power [1–3]. As compared to the existing infrastructure of 4G devices which uses at most four radiating elements, the 5G system utilizes a minimum of six to eight elements for efficient transmission [4–7]. The increased demand for faster data rates with exceptionally low latency is outpacing the present LTE advanced technology [8–12]. This results in the adoption of the 5G communication systems, which can deliver data throughput with a much lower latency of <1 ms in comparison to 4G-LTE [13] and intra-band contiguous carrier aggregation to increase the data throughput. Arranging multiple antennas in a size-limited environment is challenging since the radiation among antenna elements disturbs the radiating environment of the neighboring antennas, thus reducing the overall performance of the system. To achieve promising outcomes of such a design, the level of isolation among the elements needs to be greater than 12 dB [14]. Several techniques do exist in most of the recent literature to alleviate the effect of coupling among closely packed antenna elements [15,16]. These isolating structures include neutralization lines [17,18], decoupling networks [19,20], electromagnetic band gap [21], parasitic elements [22], orthogonal modes [23], pattern diversity arrangement [24], and multi-mode decoupling schemes [25].

Table 1. Proposed antenna dimensions.

Parameter	<i>a</i>	<i>b</i>	<i>d</i>	<i>g</i>	<i>h</i>	<i>I</i>	<i>L</i>	<i>m</i>	<i>p</i>	<i>t</i>	<i>w</i>
Value (mm)	1.2	3.3	3	5.2	5.6	20.6	17.8	1	2.2	2.8	1.5

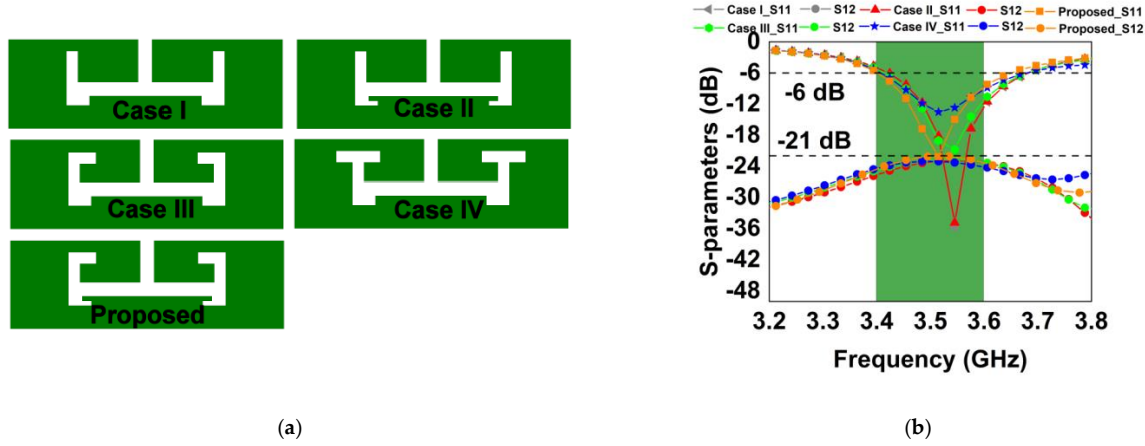


Figure 2. (a) Design evolution (b) S-parameters of design evolution.

The final proposed E-shaped slot was achieved by combining the concepts from case I–III to come up with the final layout, with the desired center frequency of 3.5 GHz and a superior isolation level of 21 dB. Figure 2b shows the corresponding S-parameters obtained from the evolved E-shaped slot etched on the ground plane. Considering the plotted scattering parameters in Figure 2b, we can conclude that in the case of I to IV, the ground current effect is considerably less, leading to higher isolation. In the final proposed design, it is clear that the introduction of the bent sections resulted in shifting the center frequency to the desired one 3.5 GHz. However, the isolation level is less when compared to the previous cases I to IV. That is to say, the bent section has a direct effect on the S11 result. All the isolation levels are found to be below -21 dB. The result demonstrates that the proposed antenna is a suitable candidate to be employed in smartphone applications in the LTE frequency band 42.

Figure 3 shows the current distribution on the ground when Ant. 1 is energized while all others are terminated to 50-ohm impedance. A little current spreads across Ant. 2, which is non-desirable and leads to lowering the isolation level. For this reason, we employ an E-shaped resonator to restrict undesirable currents, as illustrated in Figure 3b. With no decoupling structure, the isolation is -19 dB, while the isolation improves to more than -21 dB with the decoupling structure. The advantage of the decoupling structure can further be deduced by looking at Figure 4a,b.

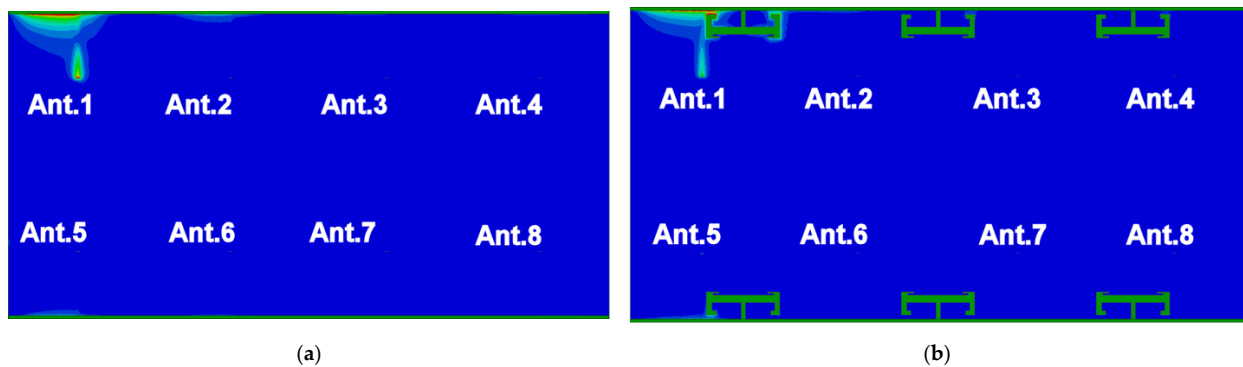


Figure 3. Antenna surface current distribution at 3.5 GHz with Ant.1 excited (a) with no decoupling element and (b) with the decoupling element.

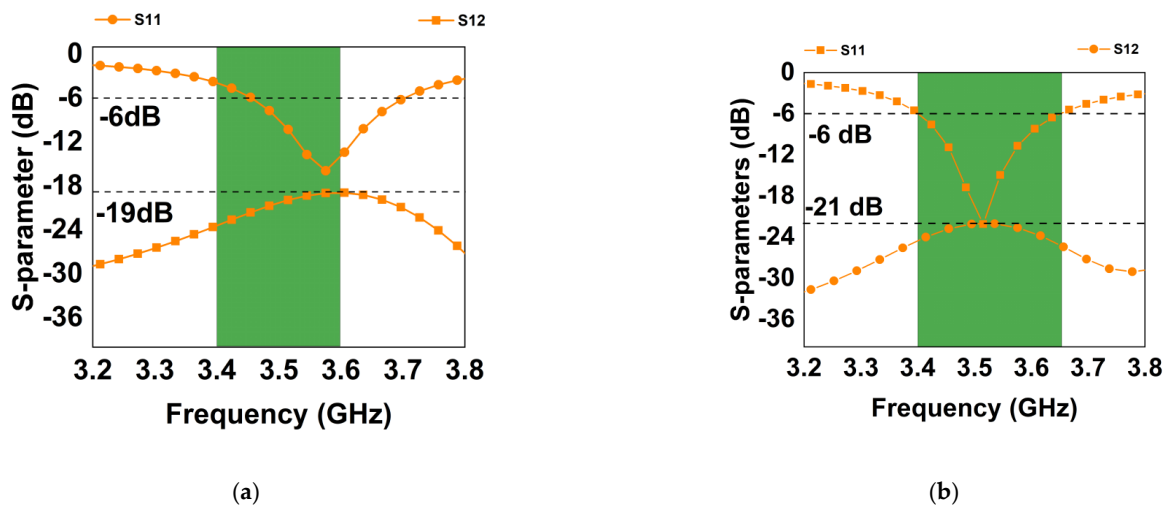


Figure 4. Simulated S-parameter (a) with no decoupling element (b) with the decoupling element.

3. Results and Discussions

The proposed eight-element array antenna simulation results, such as parametric analysis, envelope correlation coefficient (ECC), S-parameters, overall efficiency, antenna gain, and radiation pattern, are presented in this section.

3.1. Parametric Analysis, S-Parameters, Gain, and Efficiency

Variations of some design parameters were investigated in this study. Figure 5a–e shows the plots of the scattering parameters as a dependent variable on L , t , d , g , and I , respectively. Sweeps were performed to validate the impact of the aforementioned factors on system performance. From Figure 5a, it is clear that with the initial parameter value of 15 mm, the first resonance is at 3.53 GHz, so also all other values remain at that frequency. The only effect here is that the magnitude of the resonance increases with an increase in the L value.

Figure 5b is a plot of t variation, which indicates how the frequency resonance varies with an increase in the t parameter. The resonance point moved toward the higher frequency band with an increase in the t value, so also the magnitude increased with the increase in the parameter. The variation of the d parameter in Figure 5c shows little effect when the value is varied from 2 to 4 mm; at an interval of 0.5. Similarly, the g parameter was also varied, and the effect can be seen in Figure 5d. Figure 5e shows the experimental results of the I -shape variation on the antenna frame. As can be seen from the simulated scattering parameters in Figure 5e, the S11 shifts to a lower resonance frequency with an increase in the length of the I parameter.

Figure 6a depicts both the simulated values as well as the measured reflection coefficient plot for Ant 1 through Ant 4. This work achieved a magnitude better than 18 dB for the four antennas, covering the (3.4–3.65) GHz. Figure 6b shows the port isolation plots between the neighboring antennas, for which we obtained isolation better than 21 dB in all possible combinations. From the depicted measured antenna efficiency in Figure 7a, it is clear that our system achieved an efficiency value between 34–76% within the frequency of interest with antenna 8 having the maximum efficiency of 70%. We consider the minimum and maximum efficiencies of the antennas as quoted in Table 2. Figure 7b indicates the gain of the antenna. A gain value higher than 3.1 dB is obtained with a maximum value of around 4.8 dBi. Note that the maximum value of the gain is quoted as provided in Table 2.

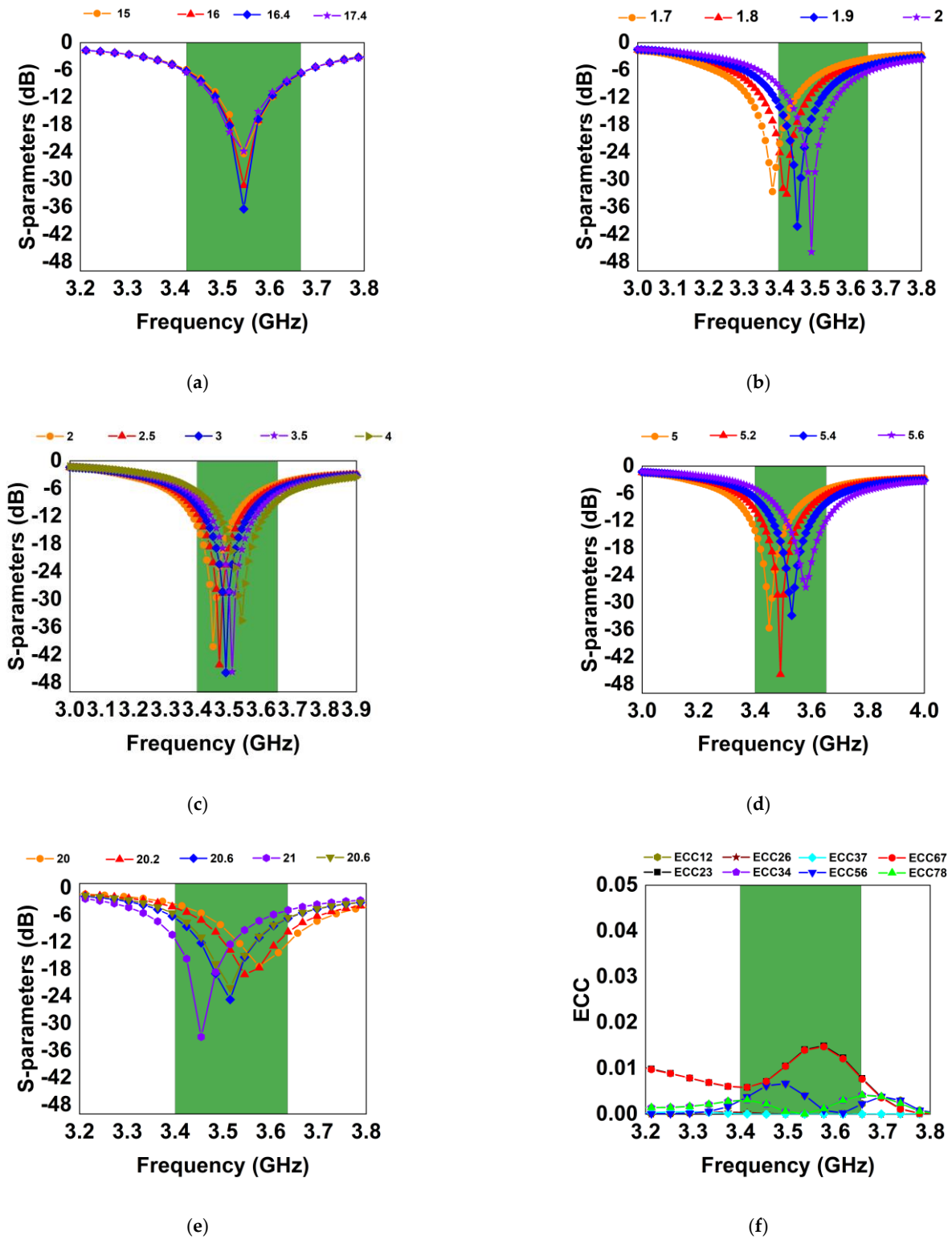


Figure 5. Scattering parameter plots (a) parametric study of the parameter L (b) parametric study of t parameter (c) parametric study of d parameter (d) parametric study of g parameter (e) parametric study of l parameter (f) envelope correlation coefficient.

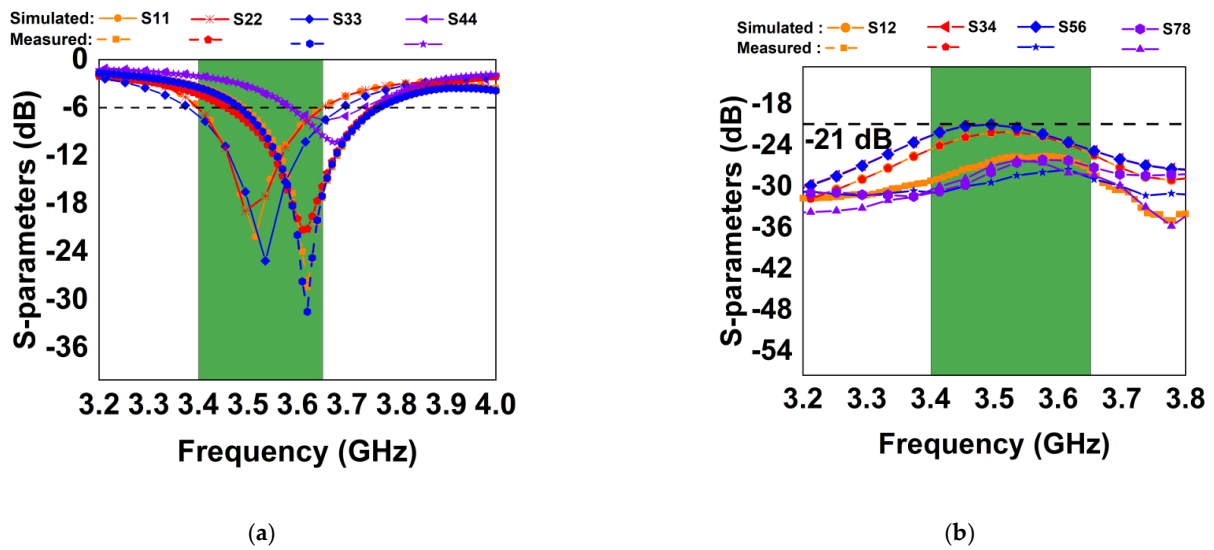


Figure 6. Simulated and measured scattering parameters (a) reflection parameters and (b) transmission parameters value.

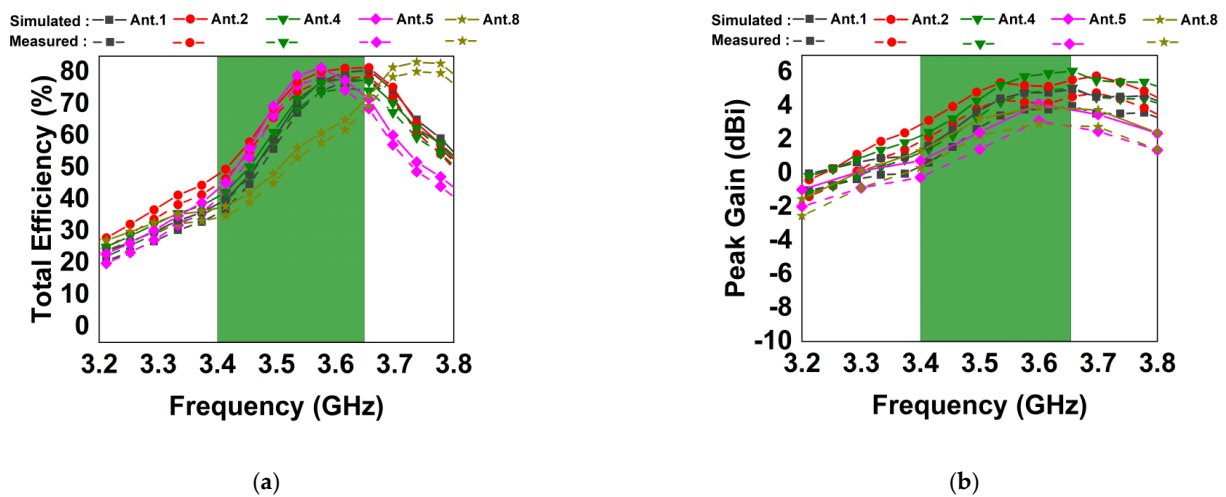


Figure 7. Measured (a) antenna total efficiency and (b) antenna gain.

3.2. Radiation Performance

The 3.5 GHz band 2D radiation patterns for Ant. 1–4 are shown in Figure 8. The solid lines denote the simulated results, while the dotted lines are the measured results. It is quite evident that antenna 1–4, at both $\Phi = 90^\circ$ and $\theta = 0^\circ$, have strong radiation in almost all the planes. Despite minor differences between the measured and simulated results, there is a general trend between the two findings, and the tiny discrepancy is related to the test settings. In conclusion, variation in maximum radiation orientations results in a diverse pattern, which contributes to the general diversity performance of the MIMO antenna.

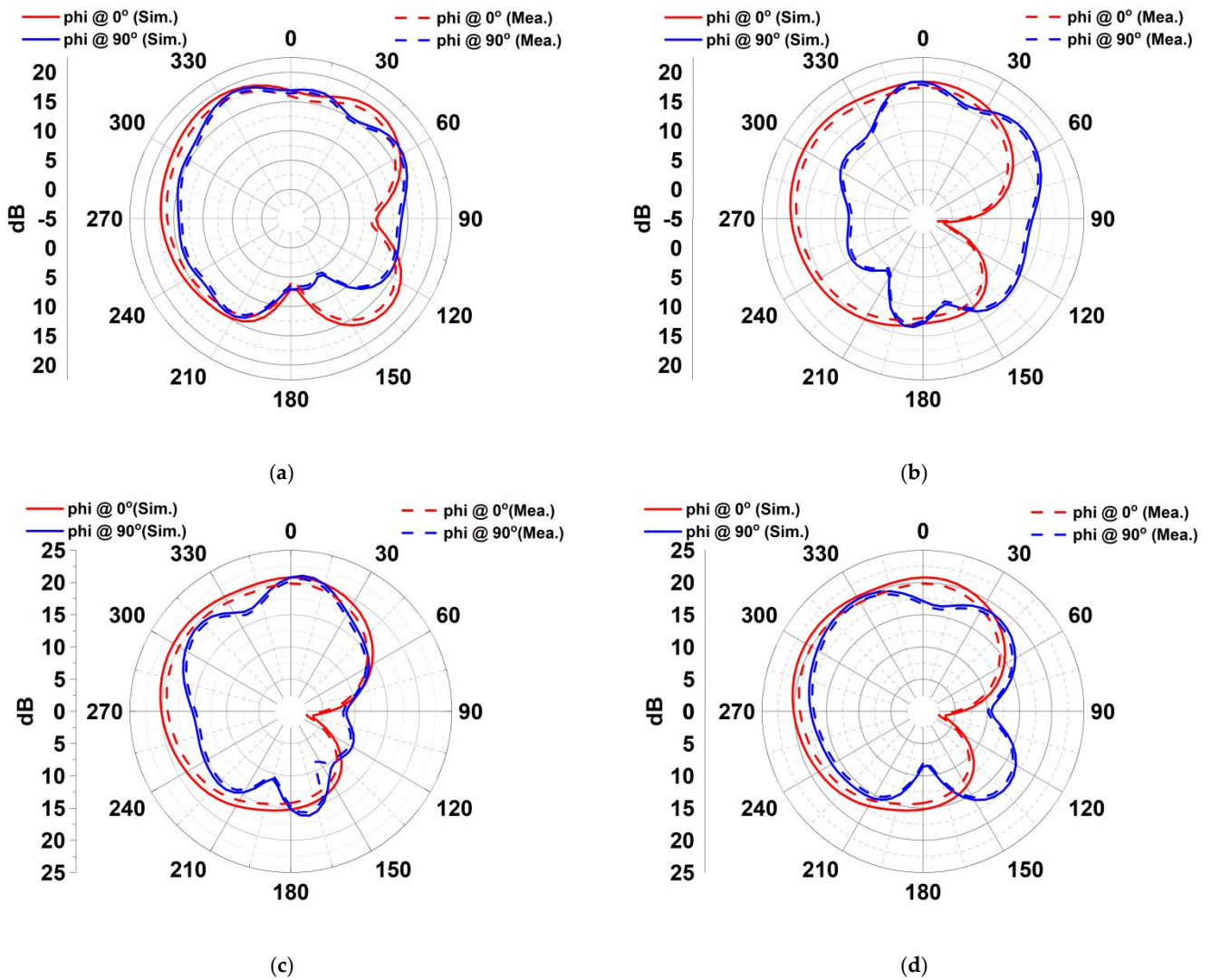


Figure 8. Simulated and measured radiation patterns of the MIMO antenna at 3.5 GHz (a) Ant 1 $\theta = 0^\circ$ and 90° (b) Ant 2 $\theta = 0^\circ$ and 90° (c) Ant 3 $\theta = 0^\circ$ and 90° (d) Ant 4 $\theta = 0^\circ$ and 90° .

3.3. MIMO Channel Capacity and ECC

The channel capacity and envelope correlation coefficient are the key criteria for assessing a MIMO antenna diversity and multiplexing capability. Although zero is the ideal value for ECC, in practice the acceptable limit must be less than 0.5 ($ECC < 0.5$). The value of the ECC can be calculated from the S-parameter or from the far-field radiation pattern [29,30]. This work uses a far-field radiation pattern [31] to calculate the ECC value as expressed in [32,33] (1). From Figure 6f, this work obtained an ECC value lower than 0.01 across the desired band of interest. Figure 9 is the channel capacity plot of the design. The fabricated prototype and measurement set up is shown in Figure 10.

$$ECC = \frac{\left| \int \int_{4\pi} (\vec{D}_i(\theta, \varphi)) \times (\vec{D}_j(\theta, \varphi)) d\Omega \right|^2}{\int \int_{4\pi} \left| (\vec{D}_i(\theta, \varphi)) \right|_2^2 d\Omega \times \int \int_{4\pi} \left| (\vec{D}_j(\theta, \varphi)) \right|_2^2 d\Omega} \quad (1)$$

where $\vec{D}_i(\theta, \varphi)$ and $\vec{D}(\theta, \varphi)$ represent the radiation pattern when antenna i and j are energized, while Ω is the solid angle.

$$DG = 10(dB) \times \sqrt{1 - |ECC|^2} \tag{2}$$

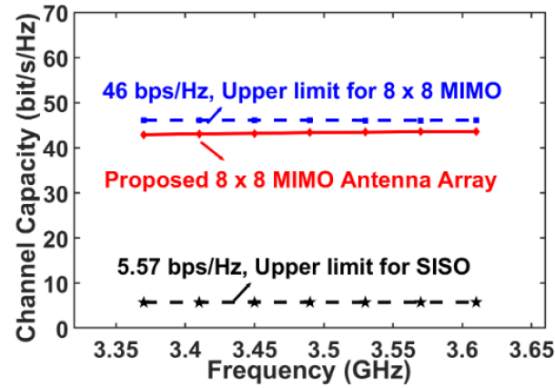


Figure 9. Calculated channel capacity of proposed system.

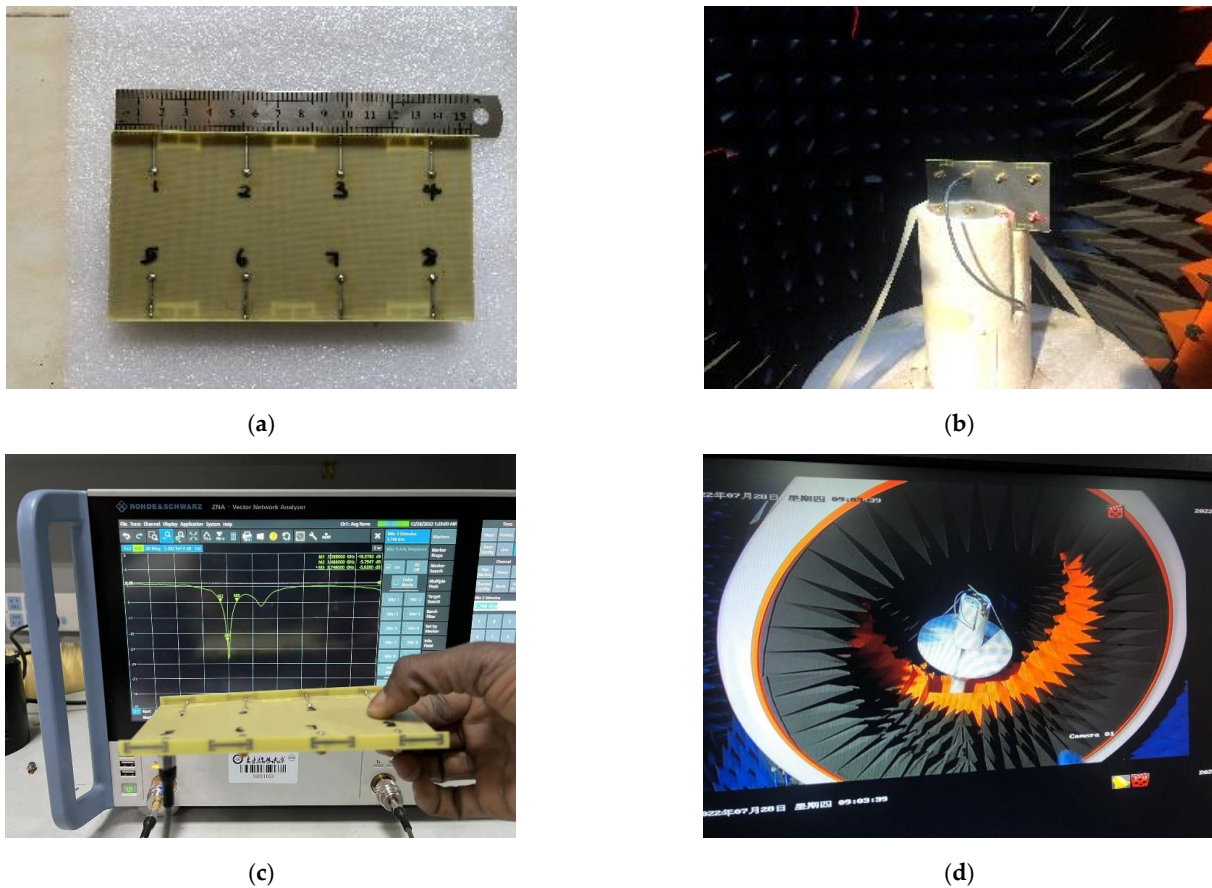


Figure 10. (a) Proposed MIMO system fabricated prototype (b) measurement set-up (c) S-parameter measurement by the VNA (d) antenna under measurement in the chamber room.

The diversity gain plot of the antenna elements is shown in Figure 11, while Equation (2) is used to calculate the DG from the ECC value. It could be seen that for all the possible combinations, a gain of more than 9.99 dB is achieved over the operation band.

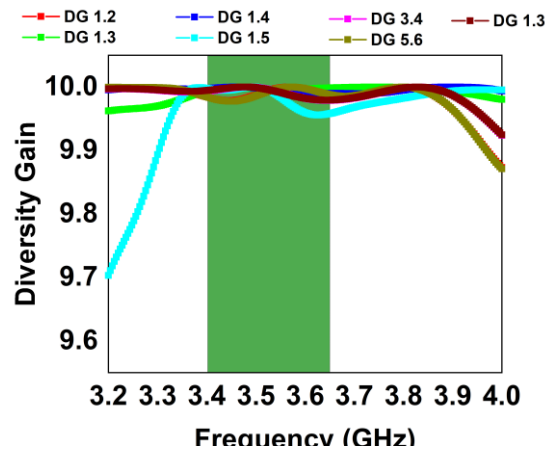


Figure 11. Diversity gain.

Based on antenna efficiency and ECC, the ergodic channel capacity is obtained by averaging 100,000. Rayleigh fading channel realizations with the Kronecker channel model by considering SNR of 20 dB [34,35]. The value varies from 40.95 to 43.50 bps/Hz. The highest peak channel capacity (PCC) is (43.5 b/s/Hz), which is satisfactory in performance with SISO (5.57 b/s/Hz) and close in value for 8 × 8 MIMO (46 b/s/Hz). These values demonstrate unequivocally that the presented antenna system is suitable for use in 5G mobile terminal applications due to its high diversity and multiplexing capabilities. Figure 10 shows the proposed antenna fabricated prototype, far-field measurement set-up, S-parameters measurement using Vector Network Analyzer (VNA), and the antenna in the anechoic chamber room under measurement. From the obtained results, it can be easily concluded that the proposed design is highly competitive in comparison to the most recent advancements in this field, as presented in Table 2.

Table 2. Comparison table.

Ref.	BW (GHz)	S _{ij} (dB)	ECC	Eff. (%)	PCC (bps/Hz)	Elements	Gain (dB)
[1]	3.4–3.7 (−6 dB)	>15	<0.1	50–75	38.1	8 × 8	4
[5]	3.4–3.6 (−6 dB)	>12	<0.1	47–65	37.5	8 × 8	3.2
[14]	3.4–3.6 (−6 dB)	>17.5	<0.05	62–76	40.8	8 × 8	Not Given
[18]	3.4–3.6 (−6 dB)	>15	<0.15	45–60	35	8 × 8	4.8
[36]	3.4–3.6 (−10 dB)	>19.1	<0.012	59–98	Not Given	8 × 8	Not Given
[37]	3.4–3.6 (−10 dB)	>12.7	<0.13	39–50	Not Given	4 × 4	Not Given
Proposed	3.4–3.65 (−6 dB)	>21	<0.01	34–76	43.5	8 × 8	4.8

4. Conclusions

In this paper, an eight-element antenna array incorporating an I-shaped frame and a modified E-slot etched on the ground is presented. The proposed antenna is simple to design and easy to fabricate. An impedance bandwidth of more than 250 MHz under −6 dB conditions is achieved in this work. The ECC for the entire frequency range is less than 0.01, and the level of element isolation is well below −21 dB. This work achieves these better performances since we etched the modified E-slot on the ground. The antenna system channel capacity obtained is 43.5 b/s/Hz, while the efficiency is more than 76%.

Author Contributions: Conceptualization, H.S.A. and Z.Z.; methodology, H.S.A., B.W. and S.H.K.; software, N.O.P. and Z.Z.; validation, B.H. and S.H.K.; formal analysis, N.O.P.; investigation, H.S.A.; resources, B.W. and B.H.; data curation, S.H.K. and N.O.P.; writing—original draft preparation, B.H. and Z.Z.; writing—review and editing, B.H. and B.W.; visualization, S.H.K. and B.W.; supervision, Z.Z.; project administration, Z.Z.; funding acquisition, Z.Z. All authors have read and agreed to the published version of the manuscript.

Funding: The Deanship of Scientific Research (DSR) at King Abdulaziz University, Jeddah, funded this project under grant no. RG-14-135-43.

Data Availability Statement: All data have been included in the study.

Acknowledgments: The authors are thankful to the Deanship of Scientific Research, King Abdulaziz University for providing financial support via grant number (RG-14-135-43).

Conflicts of Interest: The authors declare no conflict of interest.

References

1. Abdullah, M.; Altaf, A.; Anjum, M.; Arain, Z.; Jamali, A.; Alibakhshikenari, M.; Falcone, F.; Limiti, E. Future smartphone: MIMO antenna system for 5G mobile terminals. *IEEE Access* **2021**, *9*, 91593–91603. [CrossRef]
2. Abdullah, M.; Kiani, S.H.; Abdulrazak, L.F.; Iqbal, A.; Bashir, M.A.; Khan, S.; Kim, S. High-performance multiple-input multiple-output antenna system for 5G mobile terminals. *Electronics* **2019**, *8*, 1090. [CrossRef]
3. Abdullah, M.; Kiani, S.H.; Iqbal, A. Eight-element multiple-input multiple-output (MIMO) antenna for 5G mobile applications. *IEEE Access* **2019**, *7*, 134488–134495. [CrossRef]
4. Kiani, S.H.; Altaf, A.; Abdullah, M.; Muhammad, F.; Shoaib, N.; Anjum, M.R.; Damaševičius, R.; Blažauskas, T. Eight element side edged framed MIMO antenna array for future 5G smartphones. *Micromachines* **2020**, *11*, 956. [CrossRef] [PubMed]
5. Kiani, S.H.; Altaf, A.; Anjum, M.R.; Afridi, S.; Arain, Z.A.; Anwar, S.; Limit, E. MIMO Antenna System for Modern 5G Handheld Devices with Healthcare and High Rate Delivery. *Sensors* **2021**, *21*, 7415. [CrossRef] [PubMed]
6. Huang, D.; Du, Z.; Wang, Y. A quad-antenna system for 4G/5G/GPS metal frame mobile phones. *IEEE Antennas Wirel. Propag. Lett.* **2019**, *18*, 1586–1590. [CrossRef]
7. Sultan, K.; Ikram, M.; Nguyen-Trong, N. A Multiband Multibeam Antenna for Sub-6 GHz and mm-Wave 5G Applications. *IEEE Antennas Wirel. Propag. Lett.* **2022**, *21*, 1278–1282. [CrossRef]
8. Lin, Z.; Niu, H.; An, K.; Wang, Y.; Zheng, G.; Chatzinotas, S.; Hu, Y. Refracting RIS aided hybrid satellite-terrestrial relay networks: Joint beamforming design and optimization. *IEEE Trans. Aerosp. Electron. Syst.* **2022**, *58*, 3717–3724. [CrossRef]
9. Lin, Z.; An, K.; Niu, H.; Hu, Y.; Chatzinotas, S.; Zheng, G.; Wang, J. SLNR-based secure energy-efficient beamforming in Multibeam Satellite Systems. *IEEE Trans. Aerosp. Electron. Syst.* **2022**. [CrossRef]
10. An, K.; Lin, M.; Ouyang, J.; Zhu, W.P. Secure transmission in cognitive satellite terrestrial networks. *IEEE J. Sel. Areas Commun.* **2016**, *34*, 3025–3037. [CrossRef]
11. An, K.; Liang, T.; Zheng, G.; Yan, X.; Li, Y.; Chatzinotas, S. Performance limits of cognitive-uplink FSS and terrestrial FS for Ka-band. *IEEE Trans. Aerosp. Electron. Syst.* **2018**, *55*, 2604–2611. [CrossRef]
12. Lin, Z.; Lin, M.; De Cola, T.; Wang, J.B.; Zhu, W.P.; Cheng, J. Supporting IoT with rate-splitting multiple access in satellite and aerial-integrated networks. *IEEE Internet Things J.* **2021**, *8*, 11123–11134. [CrossRef]
13. Chen, H.; Tsai, Y.; Kuo, C. Broadband eight-antenna array design for sub-6 GHz 5G NR bands metal-frame smartphone applications. *IEEE Antennas Wirel. Propag. Lett.* **2020**, *19*, 1078–1082. [CrossRef]
14. Li, Y.; Luo, Y.; Yang, G. High-isolation 3.5 GHz eight-antenna MIMO array using balanced open-slot antenna element for 5G smartphones. *IEEE Trans. Antennas Propag.* **2019**, *67*, 3820–3830. [CrossRef]
15. Chen, X.; Zhang, S.; Li, Q. A review of mutual coupling in MIMO systems. *IEEE Access* **2018**, *6*, 24706–24719. [CrossRef]
16. Sun, L.; Li, Y.; Zhang, Z. Decoupling between extremely closely spaced patch antennas by mode cancellation method. *IEEE Trans. Antennas Propag.* **2020**, *69*, 3074–3083. [CrossRef]
17. Wong, K.; Lu, J.; Chen, L.; Li, W.; Ban, Y. 8-antenna and 16-antenna arrays using the quad-antenna linear array as a building block for the 3.5-GHz LTE MIMO operation in the smartphone. *Microw. Opt. Technol. Lett.* **2016**, *58*, 174–181. [CrossRef]
18. Jiang, W.; Liu, B.; Cui, Y.; Hu, W. High-isolation eight-element MIMO array for 5G smartphone applications. *IEEE Access* **2019**, *7*, 34104–34112. [CrossRef]
19. Zhao, L.; Yeung, L.; Wu, K. A coupled resonator decoupling network for two-element compact antenna arrays in mobile terminals. *IEEE Trans. Antennas Propag.* **2014**, *62*, 2767–2776. [CrossRef]
20. Li, M.; Jiang, L.; Yeung, K. Novel and efficient parasitic decoupling network for closely coupled antennas. *IEEE Trans. Antennas Propag.* **2019**, *67*, 3574–3585. [CrossRef]
21. Lee, J.; Kim, S.; Jang, J. Reduction of mutual coupling in planar multiple antenna by using 1-D EBG and SRR structures. *IEEE Trans. Antennas Propag.* **2015**, *63*, 4194–4198. [CrossRef]
22. Li, Z.; Du, Z.; Takahashi, M.; Saito, K.; Ito, K. Reducing mutual coupling of MIMO antennas with parasitic elements for mobile terminals. *IEEE Trans. Antennas Propag.* **2011**, *60*, 473–481. [CrossRef]
23. Zhang, S.; Lau, B.; Tan, Y.; Ying, Z.; He, S. Mutual coupling reduction of two PIFAs with a T-shape slot impedance transformer for MIMO mobile terminals. *IEEE Trans. Antennas Propag.* **2011**, *60*, 1521–1531. [CrossRef]
24. Sun, L.; Feng, H.; Li, Y.; Zhang, Z. Compact 5G MIMO mobile phone antennas with tightly arranged orthogonal-mode pairs. *IEEE Trans. Antennas Propag.* **2018**, *66*, 6364–6369. [CrossRef]
25. Ding, C.; Zhang, X.; Xue, C. Novel pattern-diversity-based decoupling method and its application to multi-element MIMO antenna. *IEEE Trans. Antennas Propag.* **2018**, *66*, 4976–4985. [CrossRef]

26. Xu, H.; Zhou, H.; Gao, S.; Wang, H.; Cheng, Y. Multimode decoupling technique with independent tuning characteristic for mobile terminals. *IEEE Trans. Antennas Propag.* **2017**, *65*, 6739–6751. [CrossRef]
27. Ren, Z.; Zhao, A.; Wu, S. MIMO antenna with compact decoupled antenna pairs for 5G mobile terminal. *IEEE Antennas Wirel. Propag. Lett.* **2019**, *18*, 1367–1371. [CrossRef]
28. Li, M.; Ban, Y.; Xu, Z.; Guo, J.; Yu, Z. Tri-polarized 12-antenna MIMO array for future 5G smartphone applications. *IEEE Access* **2017**, *6*, 6160–6170. [CrossRef]
29. Sharma, P.; Tiwari, R.N.; Singh, P.; Kumar, P.; Kanaujia, B.K. MIMO Antennas: Design Approaches, Techniques, and Applications. *Sensors* **2022**, *22*, 7813. [CrossRef]
30. Peng, H.; Zhi, R.; Yang, Q.; Cai, J.; Wan, Y.; Liu, G. Design of a MIMO antenna with high gain and enhanced isolation for WLAN applications. *Electronics* **2021**, *10*, 1659. [CrossRef]
31. Sharawi, M.S.; Hassan, A.; Khan, M.U. Correlation coefficient calculations for MIMO antenna systems: A comparative study. *Int. J. Microw. Wireless Technol.* **2017**, *9*, 1991–2004. [CrossRef]
32. Agarwal, S.; Rafique, U.; Ullah, R.; Ullah, S.; Khan, S.; Donelli, M. Double Overt-Leaf Shaped CPW-Fed Four Port UWB MIMO Antenna. *Electronics* **2021**, *10*, 3140. [CrossRef]
33. Zahid, M.N.; Gaofeng, Z.; Kiani, S.H.; Rafique, U.; Abbas, S.M.; Alibakhshikenari, M.; Dalarsson, M. H-shaped eight-element dual-band MIMO antenna for sub-6 GHz 5G smartphone applications. *IEEE Access* **2022**, *10*, 85619–85629. [CrossRef]
34. Tian, R.; Lau, B.; Ying, Z. Multiplexing efficiency of MIMO antennas. *IEEE Antennas Wirel. Propag. Lett.* **2011**, *10*, 183–186. [CrossRef]
35. Ali, H.; Ren, X.-C.; Hashmi, A.M.; Anjum, M.R.; Bari, I.; Majid, S.I.; Jan, N.; Tareen, W.U.K.; Iqbal, A.; Khan, M.A. An eight-element dual band antenna for future 5G smartphones. *Electronics* **2021**, *10*, 3022. [CrossRef]
36. Zhao, A.; Ren, Z. Size reduction of self-isolated MIMO antenna system for 5G mobile phone applications. *IEEE Antennas Wirel. Propag. Lett.* **2018**, *18*, 152–156. [CrossRef]
37. Chang, L.; Yu, Y.; Wei, K.; Wang, H. Polarization-orthogonal co-frequency dual antenna pair suitable for 5G MIMO smartphone with metallic bezels. *IEEE Trans. Antennas Propag.* **2019**, *67*, 5212–5220. [CrossRef]

Disclaimer/Publisher’s Note: The statements, opinions and data contained in all publications are solely those of the individual author(s) and contributor(s) and not of MDPI and/or the editor(s). MDPI and/or the editor(s) disclaim responsibility for any injury to people or property resulting from any ideas, methods, instructions or products referred to in the content.

Article

Programmable Beam-Steering Capabilities Based on Graphene Plasmonic THz MIMO Antenna via Reconfigurable Intelligent Surfaces (RIS) for IoT Applications

Sherif A. Khaleel ^{1,2,*} , Ehab K. I. Hamad ^{2,*} , Naser Ojaroudi Parchin ^{3,*}  and Mohamed B. Saleh ¹ 

- ¹ College of Engineering and Technology, Arab Academy for Science, Technology and Maritime Transport, Aswan 81511, Egypt
- ² Electrical Engineering Department, Faculty of Engineering, Aswan University, Aswan 81542, Egypt
- ³ School of Engineering and the Built Environment, Edinburgh Napier University, Edinburgh EH10 5DT, UK
- * Correspondence: sherif.abdalla@aast.edu (S.A.K.); e.hamad@aswu.edu.eg (E.K.I.H.); n.ojaroudiparchin@napier.ac.uk (N.O.P.)

Abstract: The approaching sixth-generation (6G) communication network will modernize applications and satisfy user demands through implementing a smart and reconfigurable system with a higher data rate and wider bandwidth. The controllable THz waves are highly recommended for the instantaneous development of the new technology in wireless communication systems. Recently, reconfigurable intelligent surfaces (RIS), also called coded/tunable programmable metasurfaces, have enabled a conspicuous functionality for THz devices and components for influencing electromagnetic waves (EM) such as beam steering, multi-beam-scanning applications, polarization variation, and beam focusing applications. In this article, we proposed a graphene plasmonic two-port MIMO microstrip patch antenna structure that operates at a 1.9 THz resonance frequency. An E-shape MTM unit cell is introduced to enhance the isolation of the antenna from -35 dB to -54 dB. An implementation of controllable and reconfigurable surfaces based on graphene meta-atoms (G-RIS) placed above the radiating patches with a suitable separated distance to control the radiated beam to steer in different directions ($\pm 60^\circ$). The reconfigurable process is carried out via changing the (ON/OFF) meta-atoms states to get a specific code with a certain beam direction. The gain enhancement of the antenna can be implemented through an artificial magnetic conductor (AMC) based on graphene material. The G-AMC layer is located underneath the (MIMO antenna, G-RIS layer) to improve the gain from 4.5 dBi to 10 dBi. The suggested antenna structure results are validated with different techniques CST microwave studio and ADS equivalent circuit model. The results have asymptotic values. So, the proposed design of the MIMO antenna that is sandwiched between G-RIS and G-AMC is suitable for IoT applications.

Keywords: 6G communication; reconfigurable intelligent surfaces (RIS); graphene meta-atoms (G-RIS); artificial magnetic conductor (AMC)



Citation: Khaleel, S.A.; Hamad, E.K.I.; Parchin, N.O.; Saleh, M.B. Programmable Beam-Steering Capabilities Based on Graphene Plasmonic THz MIMO Antenna via Reconfigurable Intelligent Surfaces (RIS) for IoT Applications. *Electronics* **2023**, *12*, 164. <https://doi.org/10.3390/electronics12010164>

Academic Editor: Dal Ahn

Received: 15 November 2022

Revised: 23 December 2022

Accepted: 27 December 2022

Published: 29 December 2022



Copyright: © 2022 by the authors. Licensee MDPI, Basel, Switzerland. This article is an open access article distributed under the terms and conditions of the Creative Commons Attribution (CC BY) license (<https://creativecommons.org/licenses/by/4.0/>).

1. Introduction

The presently used frequency spectrum (e.g., microwave, millimeter wave) is insufficient to meet the demands of wireless communication due to the exponential development of data traffic in sixth-generation (6G) applications. The terahertz frequency spectrum is ranging from 0.1 THz to 10 THz, which provides large bandwidth and achieves an extremely high-speed data rate of up to several terabit per second (Tbps). So, it has attracted great attention all over the world. Recently, the THz spectrum opened the door for researchers from both industry and academicians to use it in numerous applications such as wireless communications, biomedical applications, imaging, spectroscopy, and aerospace applications [1–3]. The THz wireless communications are preferable for short-distance indoor applications due to the free space path loss, which is relevant at THz frequencies

compared to mm-Wave. The THz band offers a lot of potential for future 6th-generation wireless communication technologies. In a wireless medium, EM waves are attenuated by material absorption loss and wave dispersion owing to reflection, refraction, and diffraction, leading to many propagation pathways between devices. So, the system gets uncontrollable due to the multipath fading problem. By the way, introducing metasurfaces (Artificial magnetic conductor structures) layer is a good candidate to overcome these limitations. The metasurface is a type of MTM with an artificial unit cell structure that repeated in a periodic manner. Due to their versatile qualities and properties, metasurfaces have found widespread use in recent years. It also has a wide range of applications such as perfect absorption applications [3], wireless power transfer [4], wave fronts with reflectionless sheets [5], polarization controllability [6], beam splitting and forming [7,8], total reflection or transmission layers [9,10], and its gained the researcher attentions in the wireless communications because of the total controllability and tunability of the wave propagations and its directions [11]. This tunability means that all the meta-atoms (unit cells) are controlled by switching it from ON to OFF state (modulated) by changing the external biasing gate voltage. This tunability or in another word reconfigurability can be realized electrically, optically, thermally, mechanically, or chemically. This property can change the response of the meta-atoms from the absorption mode to the reflection or transmission mode of operations by controlling the biasing voltage [12]. The tunable Metasurfaces or the reconfigurable capability of the meta-atoms is named in many research papers as a reconfigurable intelligent surface (RIS) or intelligent reflecting surfaces (IRS). Additionally, it could be considered as a special kind of the artificial magnetic conductors (AMC). The RIS is a good candidate in the new revolution of the 6G wireless communications systems and the Terahertz (THz) frequency band applications.

The conventional metasurfaces in the microwave band are implemented using copper material as a conducting element to make the tunability and reconfigurability process. In the THz band, the copper material is like the reconfigurability and the adaptability property. Additionally, copper material is not stable in the THz band and its behavior may be changed in this band. The electrical conductivity of copper is excellent in the radio frequency (RF) and microwave (MW) ranges, but it degrades in the terahertz (THz) region. Lower THz frequency ranges cause a reduction in copper's skin depth and conductivity. As a result, the ohmic resistance contributes more to the copper's surface impedance than anything else. This presents a considerable difficulty for antenna design in the THz frequency range. Copper's low conductivity and shallow skin cause significant propagation losses in the terahertz frequency range, reducing the material's overall radiation efficiency [13]. So, the graphene material has great potential for the design of meta-atoms because of its tunable and reconfigurable properties. Graphene is a prominent material that gives the opportunity in making reconfigurable devices, especially in the THz band [14,15]. Graphene is a single-layer material with remarkable capabilities in a wide range of areas, including electricity, mechanics, heat, and light. Supporting the propagation of surface plasmon polariton (SPP) waves in the THz frequency band is the most significant property of graphene. Graphene's conductivity and chemical potential are both dynamically influenced by an external electric field applied through a gate voltage [16]. The reconfigurability or tunability of the graphene material pushes the researchers to go forward in the usage of the graphene material as a RIS in THz communications [17]. Recently, reconfigurable antennas have attracted the researchers' attention in 6G wireless communications. The beam scanning or beam forming types are widely studied in the last few years, due to their critical role in phased array systems. The reconfigurable property of the antenna can be implemented by different techniques of electrical or mechanical switches such as p-i-n diodes, varactor diodes, and micro-electromechanical system switches (MEMS) [14,18]. Unfortunately, these types of switches cannot be used in the microscale of the THz spectrum. So, the graphene-based antenna structures reveal many advantages for tunable THz devices due to the tunable graphene conductivity.

The MIMO antenna structure is a good candidate for the usage of the graphene based RIS for THz applications. The isolation between the MIMO antenna patches is considered the harmful parameter that reduces the antenna's efficiency. So, introducing the graphene material as a conducting element in the MIMO structure has a good impact on reducing the mutual coupling problem. This impact is due to the short SPP wavelength of the graphene due to the SPP wave's sluggish transmission. As a result, the graphene- MIMO antenna structure gives a fewer mutual coupling effect than the metallic one at the same preparation conditions. The MTM structure is a good way used to reduce the mutual coupling. It's considered a band-stop filter between the radiating elements. The existence of the MTM reduces mutual coupling, which in turn increases diversity gain (DG), decreases channel capacity loss (CCL), and improves antenna efficiency.

Herein the article is organized as follows and depicted in the flowchart in Figure 1. The following Section 2 depicts the material properties of graphene that are important from the MIMO antenna and RIS point of view. Section 3 is summarized as follows; it starts by designing single and two-port MIMO graphene-based antennas and reducing their mutual coupling via E-shape MTM. It also discusses placing a G-RIS superstrate layer above the MIMO antenna to reconfigure the gain and produce beam steering in different directions. There also a G-AMC layer is introduced to increase the gain of the antenna. Finally, the last Section 4 introduced the paper's conclusion. The novelty in this paper can be summarized as follows:

- Design a graphene plasmonic MIMO antenna to be operated at 1.9 THz.
- Introduced the E-shaped MTM structure between the MIMO element to increase the isolation between the elements and enhance the MIMO antenna performance.
- The graphene reconfigurable intelligent surfaces (G-RIS) used as a superstrate layer to control the beam direction from $+60^\circ$ to -60° . The beam-steering capability is used in indoor THz applications, so this antenna is a good candidate for these applications.
- As the gain of the proposed design of the MIMO antenna + GRIS layer is small, so an artificial magnetic conductor layer from the graphene material (G-AMC) is introduced. This layer is used beneath the antenna structure at a certain height.

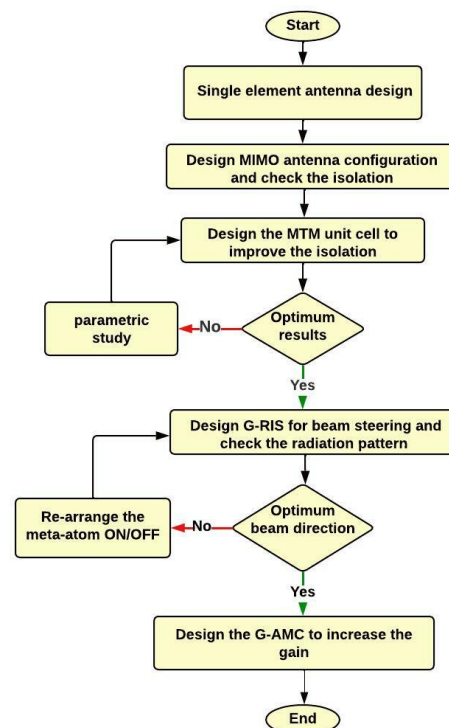


Figure 1. Flowchart of the proposed design.

2. Graphene Material Properties

The graphene nanomaterial is a two-dimensional infinitesimal thin monolayer of carbon atoms arranged in a highly ordered manner in a hexagonal lattice unit cell. The extraordinary properties of the graphene material especially in the THz frequency band open plenty of applications in several fields [19]. The plasmonic wave propagation in the THz band depends on the graphene material with low losses and good tunability. The conductivity of graphene is characterized using the Drude model [20]. It is consisting of two main terms due to the interband and intraband contributions and it is given by:

$$\sigma_s(\omega, \mu_c, \tau, T) = \sigma_{inter} + j\sigma_{intra} \tag{1}$$

$$\sigma_{s,inter}(\omega, \mu_c, \tau, T) = -\frac{je^2}{4\pi\hbar} \ln \left[\frac{2|\mu_c| - \hbar(\omega - j\tau^{-1})}{2|\mu_c| + \hbar(\omega - j\tau^{-1})} \right] \tag{2}$$

$$\sigma_{s,intra}(\omega, \mu_c, \tau, T) = -j\frac{e^2K_B T}{\pi\hbar^2(\omega - j\tau^{-1})} \left[\frac{\mu_c}{K_B T} + 2 \ln \left(e^{-\mu_c/K_B T} + 1 \right) \right] \tag{3}$$

where ω is the angular frequency, μ_c is the chemical potential, τ is the relaxation time, T is the temperature, K_B is Boltzmann's constant, and \hbar is the reduced Planck's constant. The graphene conductivity is controlled by adjusting the chemical potential which depends on the free carrier density. It can be changed by varying the gate voltage, electric field, magnetic field, and/or chemical doping. The chemical potential, given in terms of the biasing voltage V_g looks similar to that in [21,22]:

$$\mu_c = \hbar v_f \sqrt{\frac{\pi C_{ox} V_g}{e}}, \text{ and } C_{ox} = \frac{\epsilon_0 \epsilon_r}{t} \tag{4}$$

where C_{ox} is the gate capacitance, ϵ_r is the relative permittivity, ϵ_0 free space permittivity, v_f is the Fermi velocity of Dirac fermions in graphene $v_f = 10^6$ m/s, and t is the height of the substrate. The graphene permittivity can be obtained by its conductivity [23].

$$\epsilon_g = 1 + j\frac{\sigma_s}{t_g \epsilon_0 \omega} \tag{5}$$

where t_g is the thickness of graphene layer. From the presented equations we can conclude that Graphene's characteristics, including its conductivity and permittivity, are dynamically influenced by an applied gate voltage. This property enables the reconfigurability process of graphene-based devices. Figure 2 shows the variations of the graphene surface conductivity with frequency for different chemical potential values and $\tau = 1$ ps at $T = 300$ K.

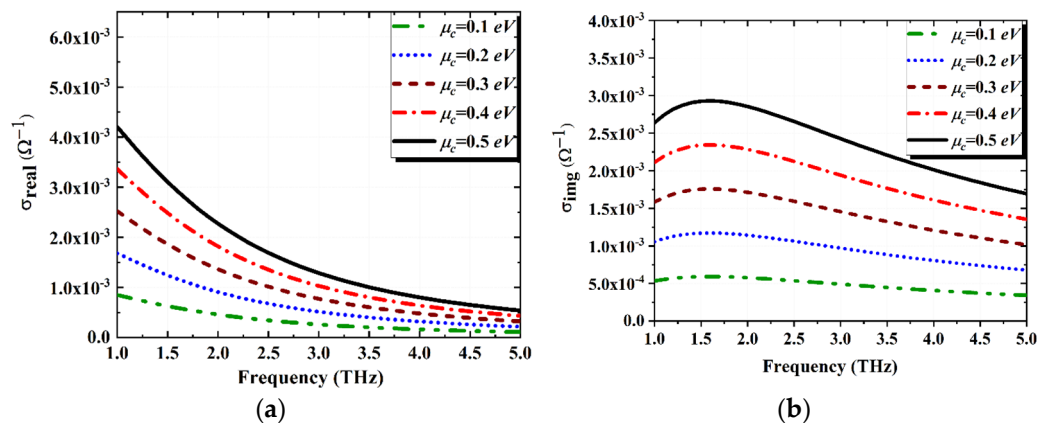


Figure 2. Surface conductivity of graphene for different chemical potentials (a) real part and (b) imaginary part.

3. Antenna Design

3.1. Graphene MIMO Antenna Configurations

In recent years, MIMO configuration systems have received a lot of attention due to their usefulness in boosting data rates despite the existence of signal fading, multipath fading, and interference. To transmit more data over a farther distance while maintaining acceptable MIMO characteristics, a MIMO system is developed. In MIMO antennas, mutual coupling is the key issue that needs to be considered. Therefore, it is desirable to minimize it as much as possible to improve system performance. Figure 2 demonstrated the proposed two configurations of the MIMO elements. The first one is side-by-side, while the other configuration is the orthogonal one as shown in Figure 3a,b. The antenna is designed using a polyamide substrate with a thickness and dielectric constant of 10 μm and 3.5, respectively. Also, the proposed antenna parameters are listed in Table 1. The graphene material is used as the conducting layer. Surface plasmon polariton (SPP) waves propagate more easily via graphene material compared to other plasmonic materials such as gold or silver. The CST microwave studio suite (2021) is used to analyze the performance of the proposed graphene MIMO antenna. It is considered the most powerful multilayer 3D full-wave electromagnetic solver, which accurately solves the Maxwell equations using the Finite Element Method (FEM) technique. For modelling graphene, the CST software includes both a graphene and a graphene-Eps model. The graphene model expressed in the CST with a thickness of 0.345 nm is considered a single layer of graphene, while the graphene-EPS is expressed as a multilayer of graphene sheets with a suitable thickness. In our proposed antenna design, we introduced the graphene model with a different chemical potential value from 0.1 eV to 0.5 eV and relaxation time of 0.1 psec, and a room temperature of 300 K. Figure 4a shows how changing the chemical potentials affects the frequency response of the graphene plasmonic antenna. This figure reveals that the antenna resonance frequency increases by increasing the chemical potential value. So, the design of the proposed is dynamically controlled and reconfigurable, which is a plethora of THz antenna technology. Figure 4b illustrates the S_{11} and S_{21} of the graphene MIMO antenna configurations, which resonate at 1.9 THz. The reflection coefficient S_{11} of the two configurations is almost the same, while the isolation coefficient S_{21} between antenna elements is better in the case of the side-by-side orientation than the orthogonal one. The S_{21} of the orthogonal one is reached -25 dB in the desired bandwidth, while this value is reached -35 dB in the side-by-side configuration. So, side-by-side orientation is suggested in the MIMO antenna design.

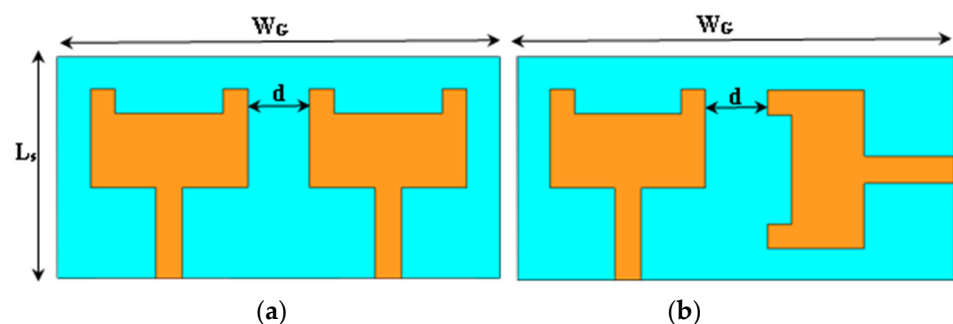


Figure 3. The proposed MIMO configurations; (a) side-by-side orientation and (b) orthogonal orientation.

3.2. E-Shaped Metamaterial Unit Cell for Mutual Coupling Reduction

Mutual coupling is the main problem facing MIMO configuration structures. The degree of coupling is determined by the distance between the components. So, the metamaterial structure is a good candidate that is to be used to increase the isolation between the graphene MIMO patches [24]. The new E-shaped metamaterial unit cell introduced between the patches has a band rejection feature (Band-Stop Filter) as presented in Figure 5a. The S-parameters

of the metamaterial structure as illustrated in Figure 5b, reveals that the proposed E-shaped metamaterial has a high band-stop characteristic in the desired bandwidth. The metamaterial unit cell has been printed above the substrate between the two patches with a negative value of the relative permittivity and permeability (ϵ_r and μ_r) in the desired bandwidth, which is considered the main condition for the metamaterial design procedure as illustrated in Figure 5c,d.

Table 1. The proposed antenna parameters.

Par.	Value (μm)	Par.	Value (μm)
W_s	120	L_s	90
W_p	65	L_p	40
W_f	10	L_f	35
W_a	8	L_a	8
W_b	49	W_G	180
d	25		
Two Element Parameters of ADS Circuit			
$R_1 = R_3 = R_6 = R_7$	25.8 Ω	$L_1 = L_3$	7.15 pH
$C_1 = C_3$	0.7 fF	$L_2 = L_4$	10 pH
$C_2 = C_4$	1.48 fF	$R_2 = R_4 = R_5$	60.3 Ω
L_5	0.8 pH	C_5	0.5 fF

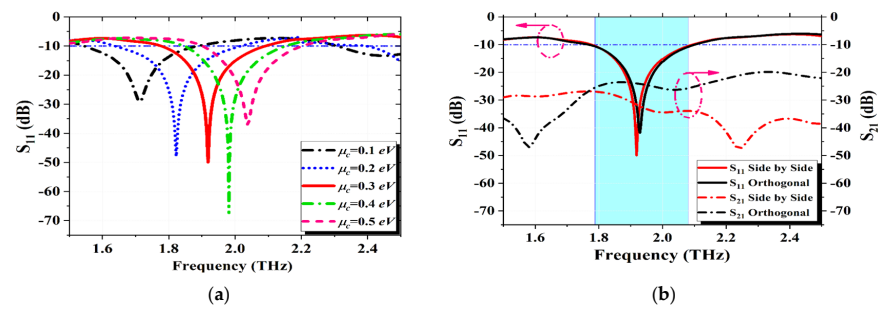


Figure 4. (a) The S_{11} of the proposed antenna with different chemical potential and (b) The S_{11} and S_{21} of the proposed graphene MIMO configurations.

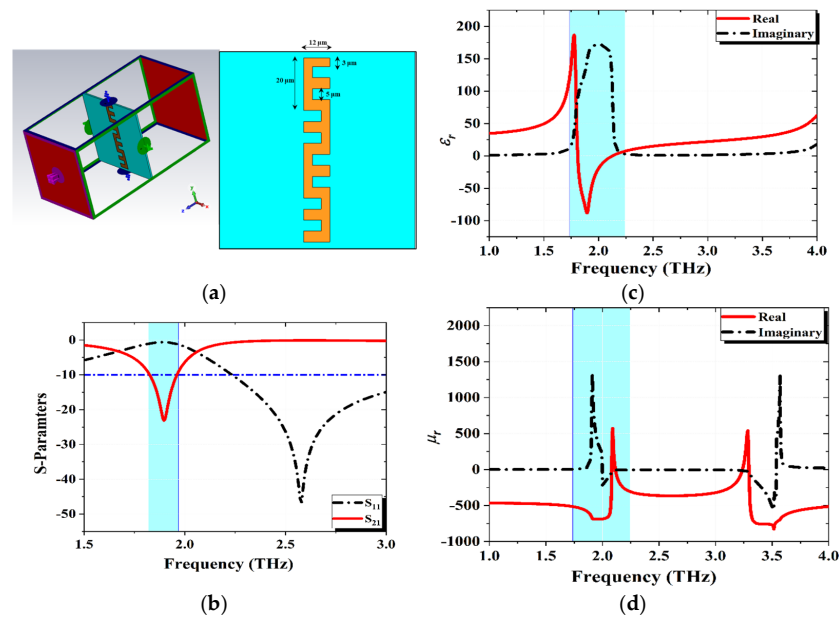


Figure 5. The parameters of the MTM unit cell, (a) MTM structure of E-shape, (b) S-parameters of the unit cell, (c) relative permittivity, and (d) relative permeability.

The proposed E-shaped metamaterial unit cell incorporated between the radiating patches consists of a series four elements connected in opposite manner as indicated in Figure 6a. The E-shaped series has a good impact on the isolation between the elements and, reduces the mutual coupling as shown in Figure 6b. This figure presents a comparison with and without the usage of the E-shaped metamaterial unit cell. It is revealed that the S_{21} of the antenna (isolation coefficient) decreased from -35 dB to -54 dB. The equivalent circuit model (ECM) of the proposed graphene plasmonic MIMO antenna design with the E-shaped metamaterial unit cell is designed using the ADS software. The ECM is used to validate the results of the CST and compare them. The proposed circuit design of the antenna and S-parameters are listed in Figure 7a,b. The ECM of the antenna consists of a two-input port with 50Ω input impedance and is separated by the RLC that represents the E-shaped metamaterial resonator. The S-parameters of the antenna reveals that ADS circuit model results are in good agreement and coincide with the CST results with a small deviation due to the values of the RLC components.

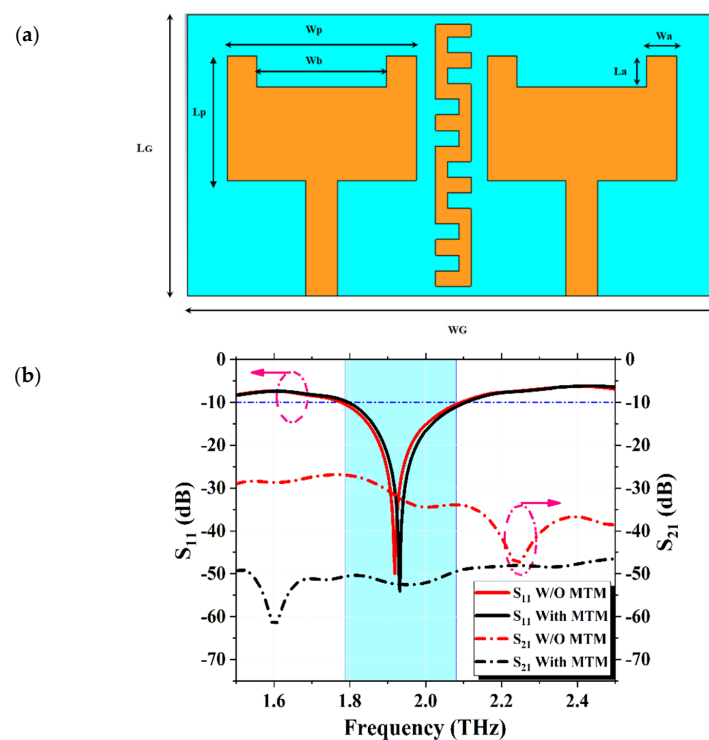


Figure 6. (a) The proposed structure of the MIMO antenna with metamaterial unit cell and, (b) The S-parameters of the antenna in the presence and absence of metamaterial unit cell.

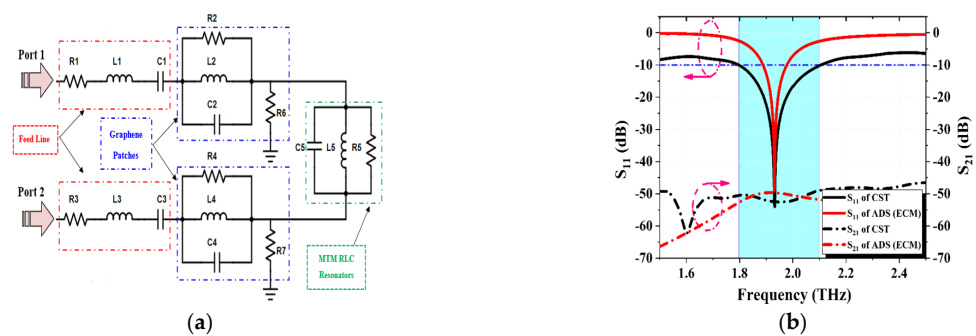


Figure 7. (a) The ADS equivalent circuit model and, (b) The S-parameters of the antenna using CST and ADS.

3.3. MIMO Antenna Performance Analysis

Herein in this part, we introduced a discussion and analysis of the most important parameters of the graphene plasmonic MIMO antenna. The envelope correlation coefficient (ECC), diversity gain (DG), and channel capacity loss (CCL) are very crucial parameters in the MIMO systems which reported and discussed in different research papers [16,25]. The ECC indicates the correlation between the parts of the MIMO antenna configuration. A greater MIMO performance is associated with a smaller amount of ECC between the MIMO components; this value may be determined by the extraction of the S-parameters, as described in [26].

$$ECC = \rho_{ij} = \frac{|S_{11}^* S_{12} + S_{21}^* S_{22}|^2}{(1 - (|S_{11}|^2 + |S_{21}|^2))(1 - (|S_{22}|^2 + |S_{12}|^2))} \quad (6)$$

where S_{11}^* and S_{21}^* represent the conjugate of S_{11} and S_{21} , respectively. The ECC threshold should be below 0.5 to be considered acceptable. The ECC is computed and shown in Figure 8a for the proposed graphene plasmonic MIMO antenna. In this figure, the value of ECC presented in the absence of the E-shaped metamaterial unit cell has a value of 0.00059, while it has a value of 0.000023 in the presence of the metamaterial through the desired bandwidth. Good MIMO performance of the proposed antenna is ensured by its low ECC value. Diversity gain (DG) reflects power losses in transmission and is another metric that may be used to analyze and assess MIMO antenna performance. The DG can be calculated by using the ECC of the MIMO antenna by following relation [27].

$$DG = 10\sqrt{1 - (ECC)^2} \quad (7)$$

In the ideal case, in which the value of the $ECC = 0$, introducing a $DG = 10$ dB. Consequently, for the real case, the ECC value should be extremely small so that the DG must be approximately reached to 10 dB for our proposed MIMO design that is presented in Figure 8b, the diversity gain value is 9.93 dB and 9.999 dB in the presence and absence the MTM unit cell., respectively.

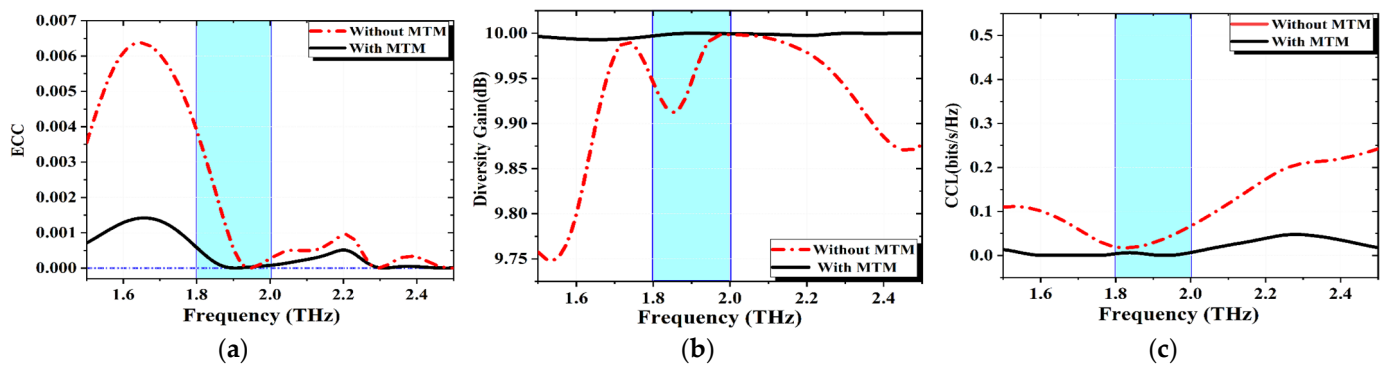


Figure 8. (a) Envelop correlation coefficient (ECC), (b) Diversity gain (DG), and (c) channel capacity loss (CCL) of the proposed antenna in the presence and absence the metamaterial unit cell.

The channel capacity loss (CCL) an essential characteristic for MIMO antenna setups is the channel capacity loss (CCL). The channel impairments caused by inter-MIMO correlation are being revealed. Within the working frequency range, a well-designed MIMO arrangement will have a value of less than 0.5 (bits/s/Hz). As mentioned in, the CCL may be found in Equation (8) [28]:

$$CCI = -\log_2(\varphi^R) \quad (8)$$

$$\varphi^R = \begin{bmatrix} \rho_{11} & \rho_{12} \\ \rho_{21} & \rho_{22} \end{bmatrix} \quad (9)$$

$$\rho_{ii} = \left(1 - \left(|S_{ii}|^2 + |S_{ij}|^2\right)\right) \text{ and } \rho_{ij} = -\left(S_{ii}^*S_{ij} + S_{ij}^*S_{jj}\right) \quad (10)$$

where φ^R indicates the correlation matrix at the receiving antenna. A comparison between the CCL curves in the presence and absence the E-shaped metamaterial unit cell is illustrated in Figure 8c. Its value varying from of 0.0014 and 0.028, respectively. It can be confirmed that the suggested design of graphene plasmonic MIMO configuration increases transmission data rates in any scattering environment. The mean effective gain (MEG) is one of the MIMO antenna parameters that is used to measure the average power that is received by the antenna in the fading environment relative to the sum of the average power that can be gained from two isotropic antennas, MEG is calculated from the following relation [29].

$$\text{MEG} = 0.5 \left(1 - \sum_{j=1}^M |S_{ij}|^2\right) \quad (11)$$

where M is the number of MIMO elements. The value of MEG should be less than -3 dB and should be greater than -12 dB. Figure 9a illustrates that the value of MEG is in an acceptable range in the presence and absence of the MTM unit cell. The radiation performance of the MIMO antenna is represented by the total active reflection coefficient (TARC) [30]. It can be calculated using the following relation and introduced in Figure 9b:

$$\text{TARC} = \sqrt{\frac{|S_{11} + S_{12}e^{j\theta}|^2 + |S_{21} + S_{22}e^{j\theta}|^2}{2}} \quad (12)$$

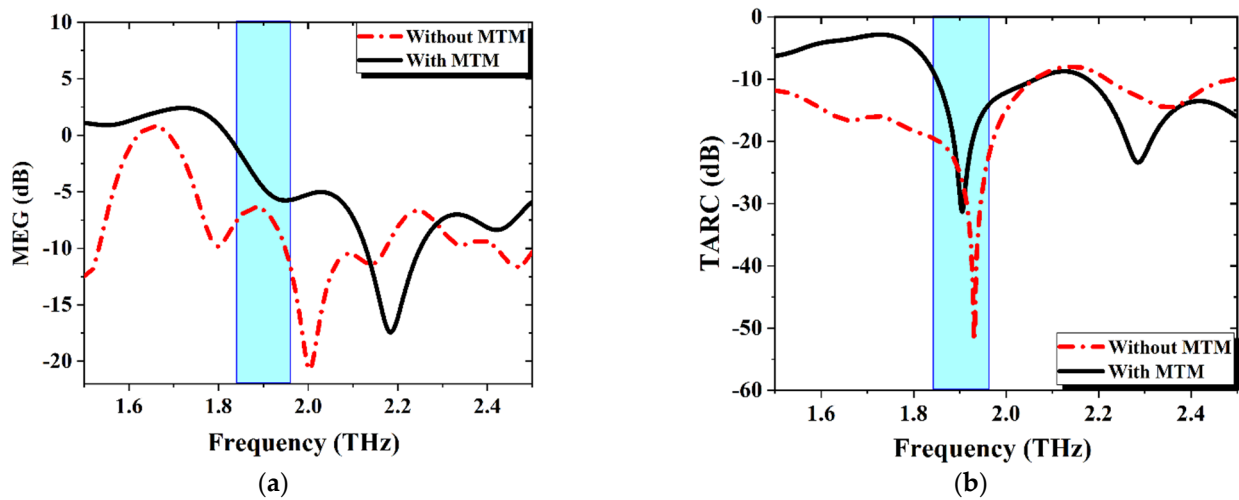


Figure 9. (a) Mean effective gain (MEG) and (b) total active reflection coefficient (TARC) parameters.

3.4. THz Graphene Reconfigurable Intelligent Surfaces (G-RIS) Design and Analysis

The importance of the RIS appeared in a plethora of applications, especially in the 6G (THz) wireless communication systems. The RIS consists of a periodic structure of meta-atoms (unit cells) that can impose an independent phase shift/amplitude on the impinging THz electromagnetic signal in a fully customized. The phase shift imposed on the THz signal can be adjusted by variations in the wireless propagation environment. By judiciously tuning the phase shifts of the RIS, the signals which reradiated from the RIS layer can be added to other signal paths in a constructive way to enhance the received signal power at the desired users or can be combined in a destructive way to mitigate the unwanted signals at the eavesdroppers. These functionalities push the researcher in the last few years to use the RIS in the 6G wireless communication in the THz frequency band to improve the channel rank, mitigate the channel interference, enhance the system reliability, and position accuracy improvement [31].

A graphene plasmonic meta-atoms as a smart conducting RIS layer is investigated to operate in the THz frequency band. The usage of the graphene material with the reconfigurable intelligent surfaces (G-RIS) added a new degree of freedom in the reconfigurability process. The reconfigurability of the proposed structure of G-RIS in this work is easily achievable by modifying artificially the meta-atoms geometry. An ON/OFF switching behavior of the graphene material is induced by the external gate voltage V_g . High conductivity in the graphene layer follows the higher biasing voltage. In contrast, the lower biasing voltage reducing interns the graphene conductivity. The dichotomy between the higher and lower conductivity of the graphene is conceived as an ON/OFF switching state, respectively. The proposed implemented design of the G-RIS is called a reprogrammable meta-tom or a coding meta surface due to its reconfigurability. The G-RIS design consists of a 2D graphene meta-atoms periodic array structure placed upon a polyamide material with a substrate height (h) of $5\ \mu\text{m}$. The proposed graphene material is modeled in CST microwave studio with a specific parameter. It's modeled as a thin conductive sheet with a thickness of $t_g = 0.345\ \text{nm}$, at room temperature of $300\ \text{K}$, fermi energy velocity $v_f = 10^6\ \text{m/s}$, and free carrier mobility of $\mu_g = 10000\ \text{cm}^2/\text{Vs}$ [32]. The G-RIS is easily reconfigured by applying the biasing gate voltage V_g throughout the graphene chemical potential that ranges from $\mu_c = [0.1 - 0.5]\ \text{eV}$.

The geometry of the proposed G-RIS is schematically shown in Figure 10a,b in which the top layer of the graphene meta-atoms is periodically arranged with a period of $D = 12\ \mu\text{m}$ and a gap of $g = 4\ \mu\text{m}$ separated the meta-atoms conductive patches. The G-RIS unit cell shown in Figure 8, illustrates that the bottom layer is a perfect electric conductor (PEC) that is used as a ground plate with a thickness of $t_p = 0.345\ \text{nm}$. The whole structure of the G-RIS can be modeled as an electrical circuit element based on the transmission line theory. In pursuit of presenting the circuit model description, the graphene meta-atoms are modeled as a thin sheet with a surface impedance of $Z_s = \frac{1}{\sigma_s}$. The surface conductivity of the graphene layer listed in Equation (1) can be expressed in the Drude model form:

$$\sigma_s = \frac{\sigma_o}{1 + j\omega\tau} \tag{13}$$

where:

$$\sigma_o = \frac{e^2 K_B T}{\pi \hbar^2} \left[\frac{\mu_c}{K_B T} + 2 \ln \left(e^{-\mu_c / K_B T} + 1 \right) \right] \tag{14}$$

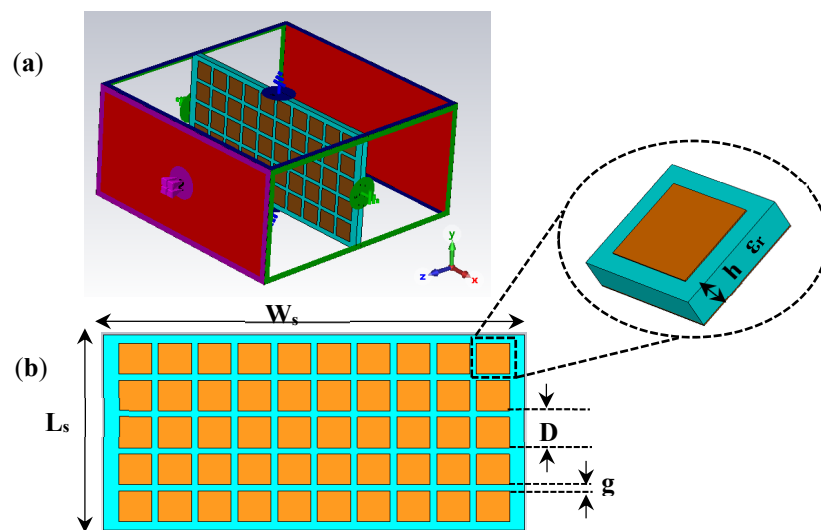


Figure 10. (a) RIS boundary condition, and (b) RIS with geometrical parameters.

In Figure 11, the equivalent circuit diagram is consisting of (R-L-C) that represents the Z_s of the array of graphene meta-atoms, Z_d is the impedance of the dielectric layer,

$Z_0 = 120 \pi \Omega$ which indicates the impedance of the free space, Z_c is the impedance of the ground layer of (PEC) that has a conductivity high enough to be considered a short circuit in the THz frequency band so $Z_c = 0$ [33] Based on the electromagnetic wave theory, the reflection coefficient S_{11} of the proposed G-RIS can be numerically calculated using the following relation:

$$\Gamma_{in} = S_{11} = \frac{Z_{in} - Z_0}{Z_{in} + Z_0} \quad (15)$$

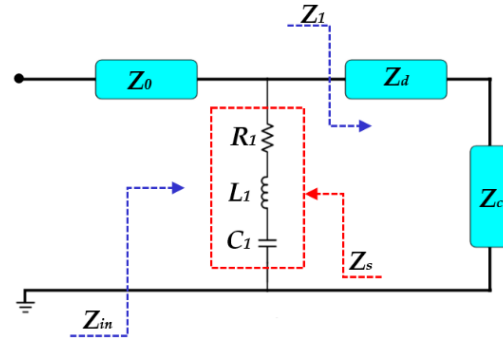


Figure 11. The equivalent circuit model of G-RIS structure.

The total impedance Z_{in} can be identified by calculating at first the value of the Z_1 with the normal incident THz wave which can be derived in:

$$Z_1 = Z_d \frac{Z_c + jZ_d \tan(\beta_d h)}{Z_d + jZ_c \tan(\beta_d h)} \quad (16)$$

where Z_d is the dielectric impedance, β_d is the propagation constant of the propagating THz wave through the dielectric substrate, and h , is the height of the substrate layer. In the absence of the PEC impedance $Z_c = 0$, so this relationship can be modified to be:

$$Z_1 = jZ_d \tan(\beta_d h) \quad (17)$$

The total input impedance of the proposed G-RIS can be calculated as $Z_{in} = (Z_s \parallel Z_1)$. So, the surface impedance of the array graphene patch can be calculated as in:

$$Z_s = \frac{D}{(D - g)\sigma_s} - j \frac{\pi}{\omega \epsilon_0 (\epsilon_r + 1) D \ln \left[\csc \left(\frac{\pi h}{2D} \right) \right]} \quad (18)$$

where D is the G-RIS periodicity, g is the distance between the meta-atoms, ϵ_r is the relative permittivity of a substrate. The above equation can be rewritten as [34]:

$$Z_s = \frac{D}{(D - g)\sigma_s} - j \frac{1}{\omega C_{eff}} \quad (19)$$

where C_{eff} is the effective capacitance established from the gaps between the meta-atoms of graphene [35]

$$C_{eff} = \frac{1}{\pi} \epsilon_0 (\epsilon_r + 1) D \ln \left[\csc \left(\frac{\pi h}{2D} \right) \right] \quad (20)$$

By insertion of the Drude model of graphene conductivity and substitution in Equation (19), so the graphene surface impedance will be in the following form [34]:

$$Z_s = \frac{D}{(D - g)} \frac{1 + j\omega\tau}{\sigma_0} - j \frac{1}{\omega C_{eff}} \quad (21)$$

$$Z_s = \frac{D}{(D - g)\sigma_0} + j \left[\frac{\omega\tau D}{(D - g)\sigma_0} - \frac{1}{\omega C_{eff}} \right] \quad (22)$$

The G-RIS structure can be modeled as (R-L-C) circuit. The resistive and conductive part in Equation (22) is due to the graphene meta-atoms while, the capacitive part is due to the gap between the patches, so this part can be concluded as [35]:

$$R = \frac{D}{(D - g)\sigma_0}, \quad L = \frac{\omega\tau D}{(D - g)\sigma_0}, \quad C = C_{eff} \quad (23)$$

So, the total impedance can be calculated from the following relation:

$$\frac{1}{Z_{in}} = \frac{1}{Z_s} + \frac{1}{Z_1} \quad (24)$$

According to the (R-L-C) value and the setup parameters of the G-RIS structure, the reflection coefficient S_{11} can be calculated analytically using the *MATLAB* program and compared with the results with the electromagnetic solver CST microwave studio. The S-parameter curves are depicted in Figure 12. It reveals that the analytical method has very close results with the CST. So, according to the high impact of the G-RIS structure, it will be a good candidate to be immersed in the whole structure of the superstrate MIMO antenna as illustrated in the next section.

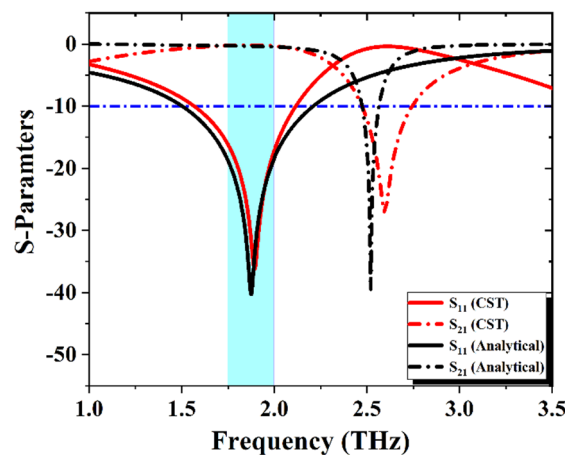


Figure 12. The S-parameters of the proposed G-RIS structure and compared the results with CST and analytical methods.

3.5. MIMO Antenna with G-RIS Superstrate Structure

Recent years have witnessed immense research efforts dedicated to improving the overall performance of the RIS to be used in the new technology of the 6G. For the high-demand IoT which hoped to be the internet of intelligence. So, RIS is a good candidate that obeys its requirements. The artificial intelligence RIS is used in a plethora of applications such as healthcare, robotics, unmanned aerial vehicles (UAVs), smart sensors, smart agriculture, self-driving cars, and IoT smart home systems [36]. In this section, we introduced the conventional plasmonic graphene MIMO antenna structure with the addition of a smart and reconfigurable (Coded) superstrate layer of G-RIS meta-atoms. The reconfigurability of the graphene-based intelligent structure layers provokes the G-RIS is suitable for a wide variety of communication scenarios. This layer is placed upon the MIMO antenna as depicted in Figure 13. Herein, we studied the behavior of the G-RIS on the performance of the MIMO antenna structure. The reconfigurability process of the G-RIS is studied and presented from the point of view of frequency and radiation pattern. Firstly, reconfiguring the operating frequency of the main structure (MIMO antenna metasurface G-RIS). The presence of the graphene material gives us the chance to reconfigure the operating frequency of the antenna by varying the graphene chemical potential $\mu_c = [0.1 - 0.5]$ eV throughout changing the electrical gate voltage. As mentioned before, increasing the value of the chemical potential leads to shifting the operating frequency to higher values. Secondly, the reconfigurable

process for the radiation pattern of the antenna. The main functionalities of the G-RIS consist of the beam-steering reconfiguration to provide the line of sight (LOS) user to be used in indoor IoT applications. This property is achieved by modifying the state of the graphene meta-atoms from ON/OFF states ("0" and "1") that constitute the G-RIS reconfigurable metasurfaces as illustrated in Figure 13. The ON/OFF states of the graphene meta-atoms can be handled by external control of field programmable gate array (FPGA) by dynamically controlling the applying graphene biasing voltage. The programmable G-RIS for a beam steering in a certain direction. So, the order of the meta-atoms must be changed in a specific sequence to achieve the desired direction, so the optimal coding arrangement gives a maximum gain in the optimal direction.

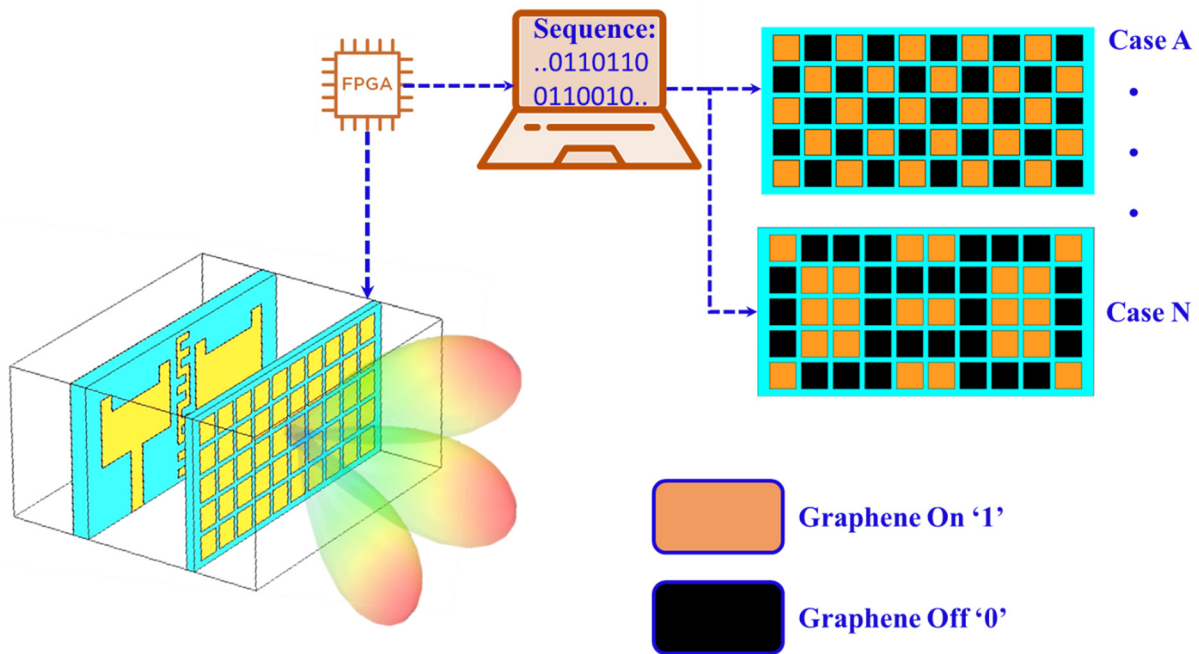


Figure 13. MIMO antenna structure with the G-RIS superstrate meta-atoms.

According to our proposed G-RIS programmable meta surface, there are a lot of structures that can be achieved by changing the meta surface code to get the desired radiation pattern to the suitable direction. For this property, the G-RIS is a good candidate for point-to-multipoint applications which need high directive and narrow beam width patterns. The directive beams will reduce power consumption, especially in the THz IoT applications. The main functionality of the G-RIS beam steering is employed to extend the coverage area of the antenna to increase the number of communication devices. Additionally, it is requisite for alleviating the path interference, in contrast, increasing the gain and directivity of the antenna. The reconfigurability process of the beam steering has a vital role in averting obstacles in the communication system by mitigating noise and interference, improving the security system, increasing the gain, and reducing the power consumption (power saving problems) by directing the transmitted signals to only the desired direction. In our proposed design, the beam-steering mechanism depends on the meta surface operating code. There are many coded G-RISs which produce a variety of paths according to the angle orientation. These different paths are used in smart IoT applications as illustrated in Figure 14 [37]. Figure 15 illustrates the suitable configuration of the G-RIS after a parametric analysis to get the three configurations namely zero-degree orientation, right, and left orientation. All these configurations depend on the (ON/OFF) states of the graphene meta-atoms which interns, which position the radiation pattern in a certain direction. In our proposed structure, the beam steering is approximately from ($\pm 60^\circ$). This can be noticed well in Figure 16 which illustrates the dependency of the beam steering on the different angle orientation.



Figure 14. G-RIS for indoor wireless IoT applications.

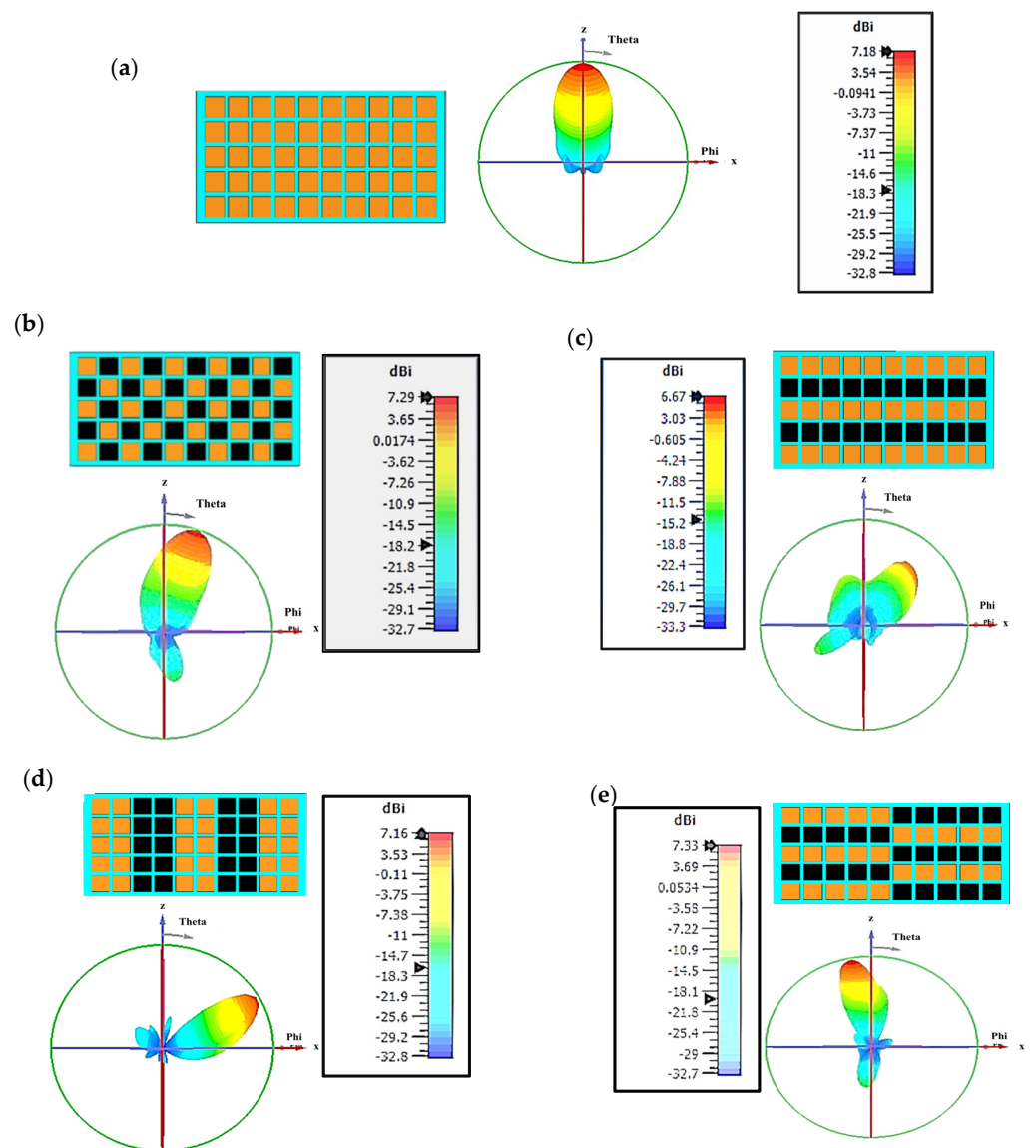


Figure 15. Cont.

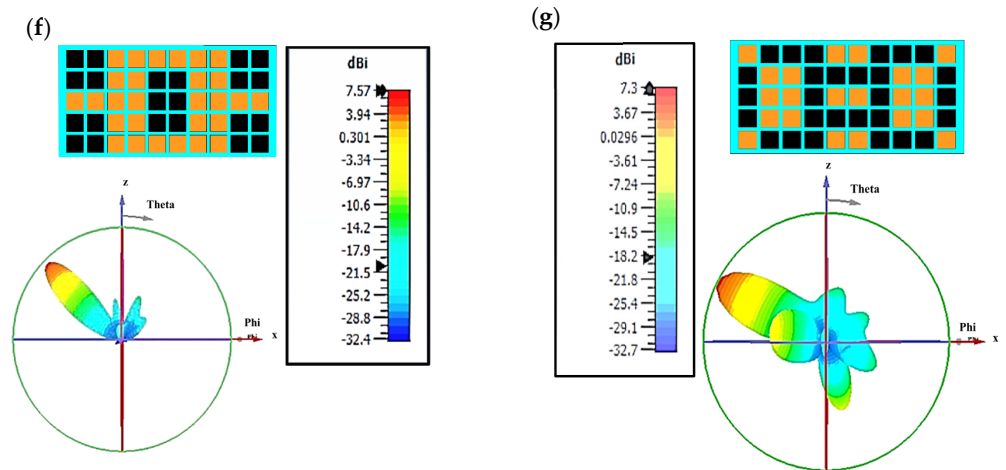


Figure 15. Gain orientation of the proposed MIMO antenna with different configurations of G-RIS meta-atoms (a) Zero-degree orientation, (b–d) Positive orientation and (e–g) Negative orientation.

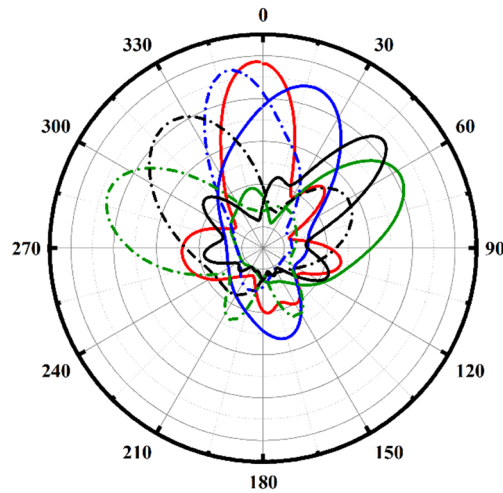


Figure 16. Beam-steering orientation with different angles value.

Although the idea of coding metamaterials was first proposed for use with microwaves, it has now been effectively applied to other frequencies, including THz and acoustic waves. The beam-steering capability throughout the G-RIS meta-atoms is introduced by the far-field radiation pattern $F(\theta, \Phi)$ which can be expressed as [38].

$$F(\theta, \Phi) = f_E(\theta, \Phi) \times AF(\theta, \Phi) \tag{25}$$

where θ and Φ are the elevation and azimuth angle of a certain direction, respectively. $f_E(\theta, \Phi)$ is the pattern function of a lattice and $AF(\theta, \Phi)$ is the array factor for a 2D configuration [38].

$$AF(\theta, \Phi) = \sum_{n=1}^N \sum_{m=1}^M A_{nm} e^{-j\beta_{nm}} \cdot e^{-jK_o(x_{nm} \sin\theta \cos\Phi + y_{nm} \sin\theta \sin\Phi)} \tag{26}$$

where the double summation indicates the positions of row and column meta-atom of 2D array configuration, $n = [1, 2, \dots, N]$ and $m = [1, 2, \dots, M]$ represent the number of elements in row and column, respectively, A_{nm} is the amplitude of each cell, $K_o = 2\pi/\lambda_o$ is the free space wave number, β_{nm} represents phase excitation between the elements, x_{nm} and y_{nm} denote the position of the unit cell along the x-axis and y-axis, respectively. Herein we consider the graphene coded RIS possibility to characterize the states ON and OFF the

graphene meta-atoms that match the bits 0 and 1 digitally. The beam-steering scenario according to the variation of the angle from ($\pm 60^\circ$) can be adjusted by varying the code of the meta-atom unit cells. According to MATLAB code (1001100) and the far-field radiation pattern, we can demonstrate the efficiently coded metasurfaces in the proposed direction which can be verified by the CST microwave studio and indicates the optimum order of the G-RIS unit cell for the beam-steering mechanism.

3.6. Suggested MIMO/G-RIS Antenna with AMC Layer

Our proposed design of the graphene plasmonic MIMO antenna configuration with the RIS meta surface has a low operating gain of around 4.5 dB. To enhance the gain of the structure with a directional pattern without increasing the antenna size (conventional methods), an artificial magnetic conductor (AMC) is introduced. The proposed AMC unit cell is illustrated in Figure 17a,b. It is composed of a square patch with an internal square slotted on its center to make a resonance frequency at 1.9 THz on the top layer while a full ground plane is incorporated in the bottom. The resonance frequency of the AMC changes by varying the size of the unit cell. The substrate material is the same used in the MIMO antenna with a thickness of $5\ \mu\text{m}$. The conducting material of the AMC is carried out by graphene (G-AMC). Figure 17c indicates that the S_{11} reflection phase of the G-AMC is around 0° throughout the operating frequency of the antenna. For the MIMO antenna structure, the G-AMC layer is at the bottom with a $15\ \mu\text{m}$ separated distance between them. The array size is chosen based on a high-parametric study.

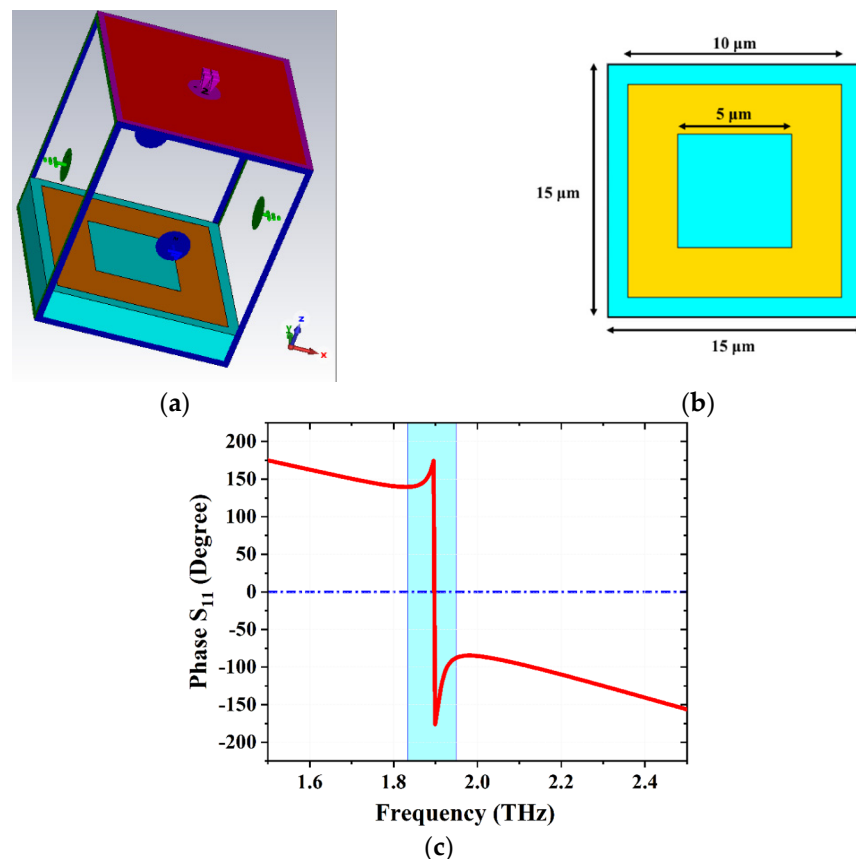


Figure 17. AMC unit cell (a) The applied boundary condition (b) 2D layout with optimized dimensions, and (c) the Simulated S_{11} reflection phase of the AMC unit cell.

The graphene MIMO antenna structure with the G-RIS superstrate layer is placed above the G-AMC layer. There are three suggested arrays 12×12 , 10×10 , and 8×8 of unit cells. These three designs are selected and studied to cover the suggested antenna. The main target from the usage of the G-AMC layer is to increase the gain of the MIMO antenna

by increasing the array size while the reflection coefficient S_{11} is not affected due to the array size. The 3D radiation pattern of the proposed design is illustrated in Figure 18. The 12×12 G-AMC layer recorded a high gain of 10 dBi, while the 10×10 , and 8×8 structures give a gain of 8.6 and 7.3 dBi, respectively. The 2D curves of the gain assure the same results as depicted in Figure 19. The back surface field direction of the MIMO antenna structure is reflected due to the presence of the G-AMC unit cells through the operating frequency. The reflected waves are collected and added in phase with the main radiated antenna waves which intern enhances the overall gain of the antenna.

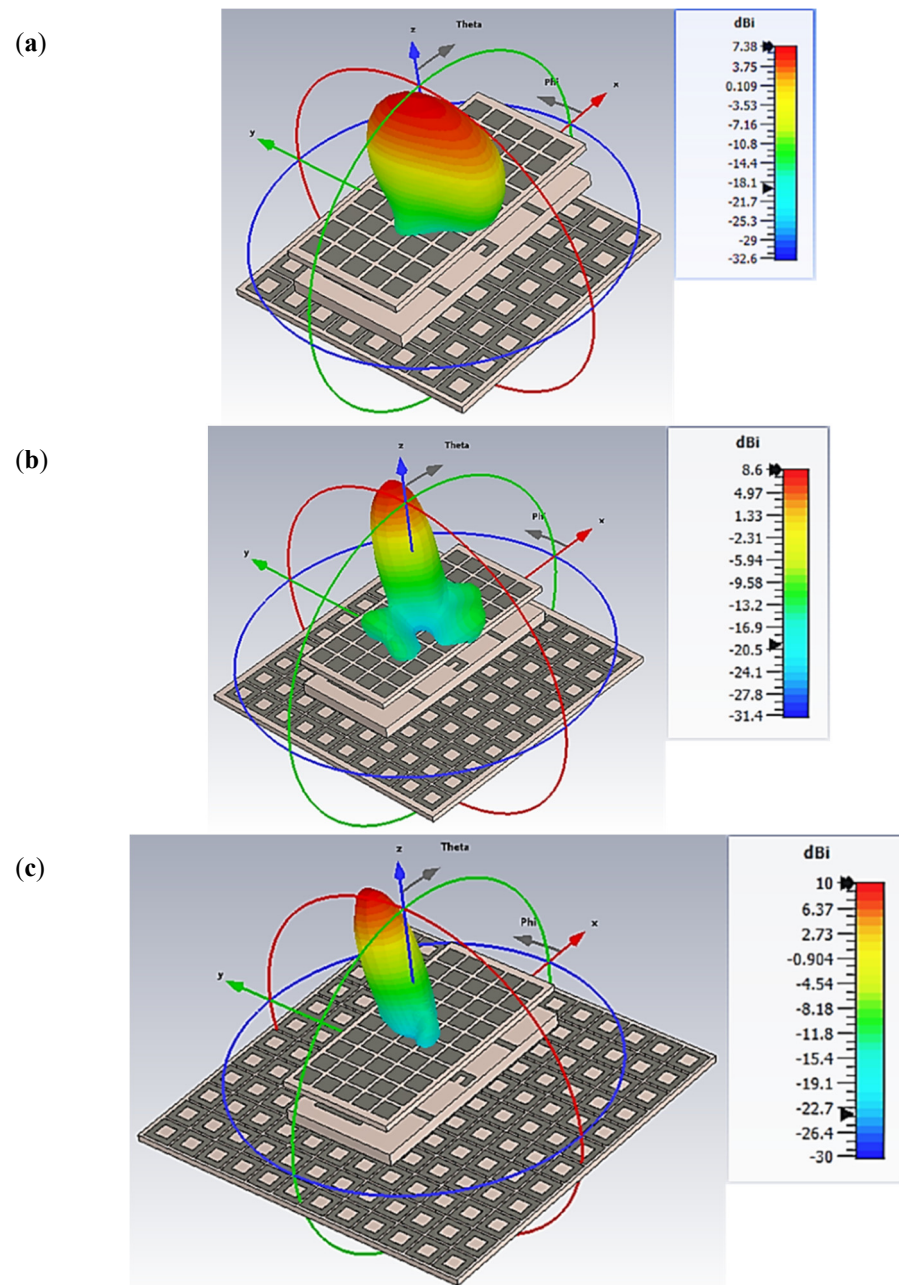


Figure 18. Different AMC configurations (a) 8×8 , (b) 10×10 , and (c) 12×12 -unit cells with different gain values.

The proposed graphene plasmonic MIMO antenna is sandwiched between the G-RIS superstrate layer (at the top) and the G-AMC layer (at the bottom). This mechanism is considered the best choice to enhance the overall gain of the MIMO antenna, furthermore, make the reconfigurability process at the same time. The results of the final proposed

design of the three parts (Antenna, G-RIS, and G-AMC) are compared with the states of the arts of the latest published papers on this point. This reveals that the proposed design of the MIMO antenna has a good impact with a suitable result that can be used in different applications such as IoT. The comparison of the proposed antenna with the states of the is of different resent papers are tabulated in Table 2 which reveals that the proposed antenna structure is interested and can be used in different applications of the THz frequency band.

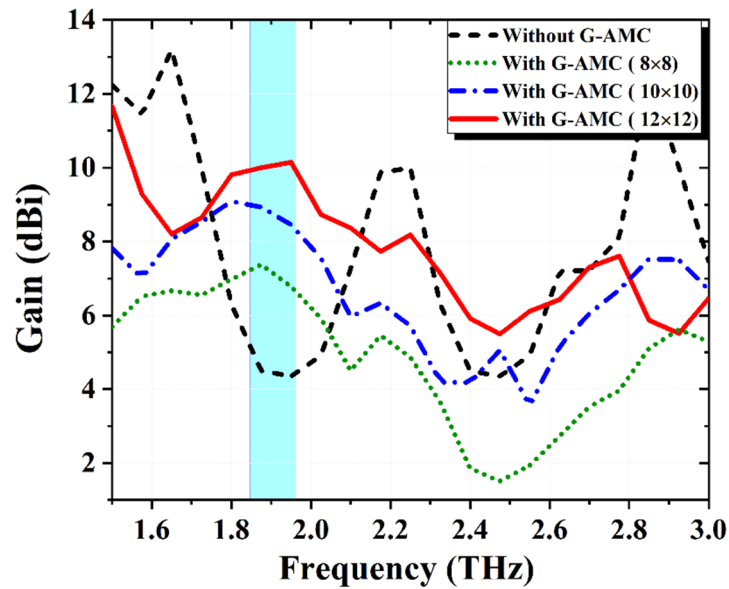


Figure 19. The 2D gain values of the MIMO antenna for different AMC configurations.

Table 2. Comparison with the state-of-the-art works.

Ref.	Freq. (THz)	Size (μm^2)	Decoupling Method	Max. Isolation Improvement (dB)	Gain (dBi)	ECC/DG (dB)	CCL	Reconfigurability	Antenna Configuration
[39]	0.4935	600×300	Separated Distance	-40	4.74	0.001/9.95	0.00018	-	MIMO
[16]	3.5	130×85	MTM + Elements Arrangement	-55	7.23	0.000168/9.999	0.006	-	MIMO
[40]	1.2	192×192	-	-	4.26	-	-	Gain reconfigurable + Metasurfaces ($\pm 35^\circ$)	Single element
[41]	2.02	256×216	-	-	8.91	-	-	Gain reconfigurable + Graphene Metasurfaces ($\pm 50^\circ$)	Single element
[38]	1.47	422×359	-	-	4.88–7.68	-	-	Gain reconfigurable + Graphene ribbons ($30^\circ:150^\circ$)	Single element
[42]	0.51	600×300	Separated Distance	-54	5.49	0.015/9.99	-	Frequency reconfigurable + Graphene chemical potential	MIMO
Proposed Work	1.9	120×90	MTM+ AMC	-54	4.5–10	0.000023/9.99	0.0014	Frequency reconfigurable + Graphene chemical potential. —Gain reconfigurable + Graphene RIS ($\pm 60^\circ$)	MIMO

4. Conclusions

Herein In this paper, a graphene MIMO microstrip patch antenna has been introduced for THz wireless communication applications. E-shaped metamaterial unit cells have been placed between the radiating patches to enhance the isolation from -35 dB to -54 dB. The proposed RIS layer based on graphene meta-atoms is placed above the radiating patches

to configure the gain to steer at a specific angle ($\pm 60^\circ$). Another layer based on graphene material is employed to increase the gain of the antenna from 4.5 dBi to 10 dBi, namely G-AMC layers. This layer is placed underneath the antenna at a suitable separated distance. The proposed MIMO antenna is considered a good candidate to be used in a plethora of applications. Due to the high performance of the proposed antenna design it can be used in the high-speed short-distance indoor communication applications (IoTs) which can be used in smart home which need a high gain, high data rate, and beam-steering property to reconfigure the different devices in the smart IoT application. Additionally, this proposed antenna can be used in the radar applications which need a wide scanning angle (beam-steering property) to detect the objects in addition to the higher data rate. So, the proposed structure is very interesting design for the THz applications.

Author Contributions: S.A.K. came up with the idea, drafted the paper, and ran the simulations, E.K.I.H. and N.O.P. reviewed the article and carried out the theoretical analysis; N.O.P. and M.B.S. analyzed the numerical findings. S.A.K. and E.K.I.H. enhanced the updated version of the manuscript and contributed to the simulation result and the validation. All authors have read and agreed to the published version of the manuscript.

Funding: This research received no external funding.

Institutional Review Board Statement: Not applicable.

Informed Consent Statement: Not applicable.

Data Availability Statement: All the data have been included in the study.

Conflicts of Interest: No conflict of interest.

References

1. Krishan, R.J.T.W.C.C.; Technologies, S. Terahertz Band for Wireless Communication—A Review. In *Terahertz Wireless Communication Components and System Technologies*; Ghzaoui, M.E., Das, S., Lenka, T.R., Biswas, A., Eds.; Springer: Singapore, 2022; pp. 153–161. [CrossRef]
2. Malhotra, I.; Singh, G. Terahertz Technology for Biomedical Application. In *Terahertz Antenna Technology for Imaging and Sensing Applications*; Springer: Cham, Switzerland, 2021; pp. 235–264. [CrossRef]
3. Civas, M.; Akan, O.B. Terahertz wireless communications in space. *ITU J. Futur. Evol. Technol.* **2021**, *2*, 31–38. [CrossRef]
4. Ranaweera, A.L.A.K.; Pham, T.S.; Bui, H.N.; Ngo, V.; Lee, J.-W. An active metasurface for field-localizing wireless power transfer using dynamically reconfigurable cavities. *Sci. Rep.* **2019**, *9*, 11735. [CrossRef]
5. Pfeiffer, C.; Grbic, A. Metamaterial Huygens' Surfaces: Tailoring Wave Fronts with Reflectionless Sheets. *Phys. Rev. Lett.* **2013**, *110*, 197401. [CrossRef] [PubMed]
6. Abouelatta, M.A.A.; Obayya, S.S.A.; Hameed, M.F.O. Highly efficient transmissive metasurface for polarization control. *Opt. Quantum Electron.* **2021**, *53*, 87. [CrossRef]
7. Wu, C.-T.M.; Chen, P.-Y. Low-Profile Metamaterial-Based Adaptive Beamforming Techniques. In *Modern Printed-Circuit Antennas*; IntechOpen: London, UK, 2020. [CrossRef]
8. Zhang, X.; Deng, R.; Yang, F.; Jiang, C.; Xu, S.; Li, M. Metasurface-Based Ultrathin Beam Splitter with Variable Split Angle and Power Distribution. *ACS Photon.* **2018**, *5*, 2997–3002. [CrossRef]
9. Zhu, X.-F.; Lau, S.-K. Perfect anomalous reflection and refraction with binary acoustic metasurfaces. *J. Appl. Phys.* **2019**, *126*, 224504. [CrossRef]
10. Wang, X.; Ding, J.; Zheng, B.; An, S.; Zhai, G.; Zhang, H. Simultaneous Realization of Anomalous Reflection and Transmission at Two Frequencies using Bi-functional Metasurfaces. *Sci. Rep.* **2018**, *8*, 1876. [CrossRef]
11. Liaskos, C.; Nie, S.; Tsioliaridou, A.; Pitsillides, A.; Ioannidis, S.; Akyildiz, I. A New Wireless Communication Paradigm through Software-Controlled Metasurfaces. *IEEE Commun. Mag.* **2018**, *56*, 162–169. [CrossRef]
12. Li, Y.; Lin, J.; Guo, H.; Sun, W.; Xiao, S.; Zhou, L. A Tunable Metasurface with Switchable Functionalities: From Perfect Transparency to Perfect Absorption. *Adv. Opt. Mater.* **2020**, *8*, 1901548. [CrossRef]
13. Dash, S.; Patnaik, A.; Letters, O.T. Material selection for THz antennas. *Microw. Opt. Technol. Lett.* **2018**, *60*, 1183–1187. [CrossRef]
14. Ghaffar, A.; Li, X.J.; Awan, W.A.; Hussain, N. Reconfigurable Antenna: Analysis and Applications. In *Wideband, Multiband, and Smart Antenna Systems*; Springer: Berlin/Heidelberg, Germany, 2021; pp. 269–323. [CrossRef]
15. Karthika, K.; Kavitha, K. Reconfigurable Antennas for Advanced Wireless Communications: A Review. *Wirel. Pers. Commun.* **2021**, *120*, 2711–2771. [CrossRef]
16. Khaleel, S.A.; Hamad, E.K.I.; Parchin, N.O.; Saleh, M.B. MTM-Inspired Graphene-Based THz MIMO Antenna Configurations Using Characteristic Mode Analysis for 6G/IoT Applications. *Electronics* **2022**, *11*, 2152. [CrossRef]

17. Ojaroudi, M.; Loscri, V. Graphene-Based Reconfigurable Intelligent Meta-Surface Structure for THz Communications. In Proceedings of the 2021 15th European Conference on Antennas and Propagation (EuCAP), Düsseldorf, Germany, 22–26 March 2021; pp. 1–5. [CrossRef]
18. Fazaelifar, M.; Jam, S.; Basiri, R. A circular polarized reflectarray antenna with electronically steerable beam and interchangeable polarizations. *Int. J. Microw. Wirel. Technol.* **2020**, *13*, 198–210. [CrossRef]
19. Geim, A.K.; Novoselov, K.S. The rise of graphene. In *Nanoscience and Technology*; Co-Published with Macmillan Publishers Ltd.: British, UK, 2009; pp. 11–19.
20. Beiranvand, B.; Sobolev, A.S.; Sheikholeh, A. A proposal for a dual-band tunable plasmonic absorber using concentric-rings resonators and mono-layer graphene. *Optik* **2020**, *223*, 165587. [CrossRef]
21. Gómez-Díaz, J.S.; Perruisseau-Carrier, J. Graphene-based plasmonic switches at near infrared frequencies. *Opt. Express* **2013**, *21*, 15490–15504. [CrossRef]
22. Khaleel, S.A.; Hamad, E.K.I.; Saleh, M.B. High-performance tri-band graphene plasmonic microstrip patch antenna using superstrate double-face metamaterial for THz communications. *J. Electr. Eng.* **2022**, *73*, 226–236. [CrossRef]
23. Vakil, A.; Engheta, N. Transformation Optics Using Graphene. *Science* **2011**, *332*, 1291–1294. [CrossRef]
24. Roshani, S.; Shahveisi, H. Mutual Coupling Reduction in Microstrip Patch Antenna Arrays Using Simple Microstrip Resonator. *Wirel. Pers. Commun.* **2022**, *126*, 1665–1677. [CrossRef]
25. Khan, M.I.; Khan, S.; Kiani, S.H.; Parchin, N.O.; Mahmood, K.; Rafique, U.; Qadir, M.M. A Compact mmWave MIMO Antenna for Future Wireless Networks. *Electronics* **2022**, *11*, 2450. [CrossRef]
26. Zahra, H.; Awan, W.; Ali, W.; Hussain, N.; Abbas, S.; Mukhopadhyay, S. A 28 GHz Broadband Helical Inspired End-Fire Antenna and Its MIMO Configuration for 5G Pattern Diversity Applications. *Electronics* **2021**, *10*, 405. [CrossRef]
27. Naqvi, S.I.; Hussain, N.; Iqbal, A.; Rahman, M.; Forsat, M.; Mirjavadi, S.S.; Amin, Y. Integrated LTE and Millimeter-Wave 5G MIMO Antenna System for 4G/5G Wireless Terminals. *Sensors* **2020**, *20*, 3926. [CrossRef] [PubMed]
28. Hussain, N.; Jeong, M.-J.; Abbas, A.; Kim, N. Metasurface-Based Single-Layer Wideband Circularly Polarized MIMO Antenna for 5G Millimeter-Wave Systems. *IEEE Access* **2020**, *8*, 130293–130304. [CrossRef]
29. Hussain, N.; Awan, W.A.; Ali, W.; Naqvi, S.I.; Zaidi, A.; Le, T.T. Compact wideband patch antenna and its MIMO configuration for 28 GHz applications. *AEU—Int. J. Electron. Commun.* **2021**, *132*, 153612. [CrossRef]
30. Raj, U.; Sharma, M.K.; Singh, V.; Javed, S.; Sharma, A. Easily extendable four port MIMO antenna with improved isolation and wide bandwidth for THz applications. *Optik* **2021**, *247*, 167910. [CrossRef]
31. Pan, C.; Zhou, G.; Zhi, K.; Hong, S.; Wu, T.; Pan, Y.; Ren, H.; Di Renzo, M.; Swindlehurst, A.L.; Zhang, R.; et al. An Overview of Signal Processing Techniques for RIS/IRS-Aided Wireless Systems. *IEEE J. Sel. Top. Signal Process.* **2022**, *16*, 883–917. [CrossRef]
32. Novoselov, K.S.; Geim, A.K.; Morozov, S.V.; Jiang, D.; Zhang, Y.; Dubonos, S.V.; Grigorieva, I.V.; Firsov, A.A. Electric field effect in atomically thin carbon films. *Science* **2004**, *306*, 666–669. [CrossRef]
33. Aghaee, T.; Orouji, A.A. Reconfigurable multi-band, graphene-based THz absorber: Circuit model approach. *Results Phys.* **2019**, *16*, 102855. [CrossRef]
34. Padooru, Y.R.; Yakovlev, A.B.; Kaipa, C.S.R.; Hanson, G.W.; Medina, F.; Mesa, F. Dual capacitive-inductive nature of periodic graphene patches: Transmission characteristics at low-terahertz frequencies. *Phys. Rev. B* **2013**, *87*, 115401. [CrossRef]
35. Liu, Z.; Guo, L.; Zhang, Q. Design of Dual-Band Terahertz Perfect Metamaterial Absorber Based on Circuit Theory. *Molecules* **2020**, *25*, 4104. [CrossRef]
36. Das, S.K.; Benkhelifa, F.; Sun, Y.; Abumarshoud, H.; Abbasi, Q.H.; Imran, M.A.; Mohjazi, L. Comprehensive Review on ML-based RIS-enhanced IoT Systems: Basics, Research Progress and Future Challenges. *TechRxiv* **2022**. [CrossRef]
37. IoT—Internet of Things. Things. Interactive Demos of the Smart Connected Kitchen of the Future at NRF 2017. 2017. Available online: <https://iot.do/interactive-demos-smart-connected-kitchen-nrf-2017-01> (accessed on 14 November 2022).
38. Babu, K.V.; Das, S.; Varshney, G.; Sree, G.N.J.; Madhav, B.T.P. A micro-scaled graphene-based tree-shaped wideband printed MIMO antenna for terahertz applications. *J. Comput. Electron.* **2022**, *21*, 289–303. [CrossRef]
39. Jarchi, S. Radiation pattern direction control of THz antenna with applying planar graphene metasurface. *Optik* **2021**, *243*, 167458. [CrossRef]
40. Shubham, A.; Samantaray, D.; Ghosh, S.K.; Dwivedi, S.; Bhattacharyya, S. Performance improvement of a graphene patch antenna using metasurface for THz applications. *Optik* **2022**, *264*, 169412. [CrossRef]
41. Basiri, R.; Zareian-Jahromi, E.; Aghazade-Tehrani, M. A reconfigurable beam sweeping patch antenna utilizing parasitic graphene elements for terahertz applications. *Photon. Nanostructures Fundam. Appl.* **2022**, *51*, 101044. [CrossRef]
42. Babu, K.V.; Das, S.; Sree, G.N.J.; Madhav, B.T.P.; Patel, S.K.K.; Parmar, J. Design and optimization of micro-sized wideband fractal MIMO antenna based on characteristic analysis of graphene for terahertz applications. *Opt. Quantum Electron.* **2022**, *54*, 281. [CrossRef]

Disclaimer/Publisher’s Note: The statements, opinions and data contained in all publications are solely those of the individual author(s) and contributor(s) and not of MDPI and/or the editor(s). MDPI and/or the editor(s) disclaim responsibility for any injury to people or property resulting from any ideas, methods, instructions or products referred to in the content.

Article

Eight-Element Antenna Array with Improved Radiation Performances for 5G Hand-Portable Devices

Atta Ullah ¹, Naser Ojaroudi Parchin ^{2,*} , Ahmed S. I. Amar ^{1,3} and Raed A. Abd-Alhameed ^{1,4} ¹ Faculty of Engineering and Informatics, University of Bradford, Bradford BD7 1DP, UK² School of Engineering and the Built Environment, Edinburgh Napier University, Edinburgh EH10 5DT, UK³ Air Defense College, Alexandria University, Alexandria 21568, Egypt⁴ Department of Information and Communication Engineering, Basrah University College of Science and Technology, Basra 61004, Iraq

* Correspondence: n.ojaroudiparchin@napier.ac.uk

Abstract: This study aims to introduce a new phased array design with improved radiation properties for future cellular networks. The procedure of the array design is simple and has been accomplished on a low-cost substrate material while offering several interesting features with high performance. Its schematic involves eight air-filled slot-loop metal-ring elements with a 1×8 linear arrangement at the top edge of the 5G smartphone mainboard. Considering the entire board area, the proposed antenna elements occupy an extremely small area. The antenna elements cover the range of 21–23.5 GHz sub-mm-wave 5G bands. Due to the air-filled function in the configurations of the elements, low-loss and high-performance radiation properties are observed. In addition, the fundamental characteristics of the introduced array are insensitive to various types of substrates. Moreover, its radiation properties have been compared with conventional arrays and better results have been observed. The proposed array appears with a simple design, a low complexity profile, and its attractive broad impedance bandwidth, end-fire radiation mode, wide beam steering, high radiation coverage, and stable characteristics meet the needs of 5G applications in future cellular communications. Additionally, the smartphone array design offers sufficient efficiency when it comes to the appearance and integration of the user's components. Thus, it could be used in 5G hand-portable devices.

Keywords: 5G; beam steering; cellular networks; linear phased array; smartphone applications; substrate insensitive



Citation: Ullah, A.; Ojaroudi Parchin, N.; Amar, A.S.I.; Abd-Alhameed, R.A. Eight-Element Antenna Array with Improved Radiation Performances for 5G Hand-Portable Devices. *Electronics* **2022**, *11*, 2962. <https://doi.org/10.3390/electronics11182962>

Academic Editor: Massimo Donelli

Received: 27 June 2022

Accepted: 15 September 2022

Published: 19 September 2022

Publisher's Note: MDPI stays neutral with regard to jurisdictional claims in published maps and institutional affiliations.



Copyright: © 2022 by the authors. Licensee MDPI, Basel, Switzerland. This article is an open access article distributed under the terms and conditions of the Creative Commons Attribution (CC BY) license (<https://creativecommons.org/licenses/by/4.0/>).

1. Introduction

The current generation (4G) wireless cellular systems are not able to meet the demand for a high data-rate transfer for future communications [1]. Therefore, the 5th generation (5G) of mobile networks or wireless communications has been established to meet these challenges and provide several enhanced services on the internet of things (IoT), mobile broadband, massive multiple-input multiple-output (MIMO), machine-to-machine (M2M), and ultra-reliable communications [2–4]. The 5G spectrum is categorized in two broad regions as the Sub-6 GHz, ranging under 6 GHz frequency, and the millimeter-wave (mm-wave) region in which frequencies 24 GHz and above are adopted. In 5G networks, the mm-wave and sub-mm-wave spectrums play an important role in providing broadband communications that can support multiple sensing devices to demonstrate the performance of 5G service requirements [5–7]. Small antennas can be formed in linear or planar array schematics to overcome high attenuation and propagation losses and provide point-to-point communications. As represented in Figure 1, in the frequency range of 20–50 GHz, several candidate bands, such as 22.25, 26, 28, and 42 GHz, were determined by academia and industrial researchers to be considered efficient in 5G networks [8–12]. Apart from the cited frequencies, several bands (beyond 10 GHz), such as 15 and 21 GHz, were studied

for 5G applications [13–15]. It is also evident that compared with 4G, significant frequency shifting to the higher bands is expended for 5G communications.

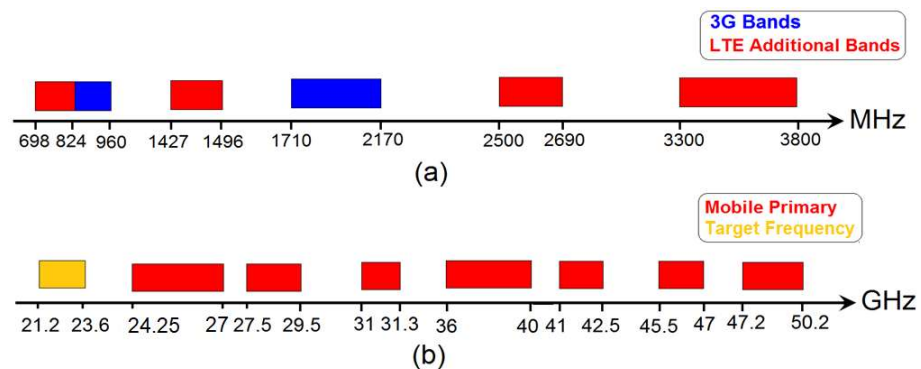


Figure 1. (a) Frequency spectra of 4G, (b) some candidate bands for 5G.

Linear phased arrays with compact resonators and broad frequency operation are desired for smartphone applications. Recently, several designs have been proposed to be integrated into handheld platforms [16–18]. One of the challenges in antenna design is to accomplish high-efficient antenna arrays which require careful consideration because it could increase the complexity of the design and material and implementation cost [19,20]. Therefore, in order to address these limitations and challenges, we introduce here a simple and straightforward design idea that can create high-efficiency and wide scanning radiations on a single substrate material and can be easily applied for smartphone applications. An additional selling point of the introduced design is its insensitivity to a wide range of substrate materials. In particular, this is due to the air-filled loop-ring resonators used as the radiation elements, which have a similar thickness to the FR4 substrate. Therefore, for different substrate types, the air acts as the main substrate and provides constant radiation properties with very low losses in terms of antenna gain and efficiency [21,22]. Unlike the reported design which needs a multi-layer configuration or complex feeding or high-cost materials, the proposed antenna array can be arranged on a single-layer cheap FR4 substrate and still provide sufficient radiations. The antenna elements can be easily fed using discrete or microstrip-line techniques. The presented antenna array is designed using the commercially available CST software package [23]. The array was manufactured on a standard smartphone board with FR4 material, and the properties of the single element have been experimentally measured. The design and fundamental characteristics of the single radiator and its phased array are elaborated below.

2. Antenna Design

The presented phased array is designed on a low-cost FR-4 dielectric with properties of $h_{\text{sub}} = 0.8$ mm, permittivity (ϵ_r) = 4.3, and loss tangent (δ) = 0.025. The schematic diagram of the design is represented in Figure 2. As depicted, eight elements of the air-filled/substrate-insensitive elements are adopted to form a 1×8 linear array at the edge of the smartphone board with an overall size of $W_{\text{sub}} \times L_{\text{sub}} = 55 \times 110$ mm². The employed linear array has a compact size of 8.5×43 mm². In order to obtain full radiation coverage in 5G mobile communication, another set of the presented phased array can be deployed at the bottom edge of the mainboard. The parameter values of the array design are specified in Table 1.

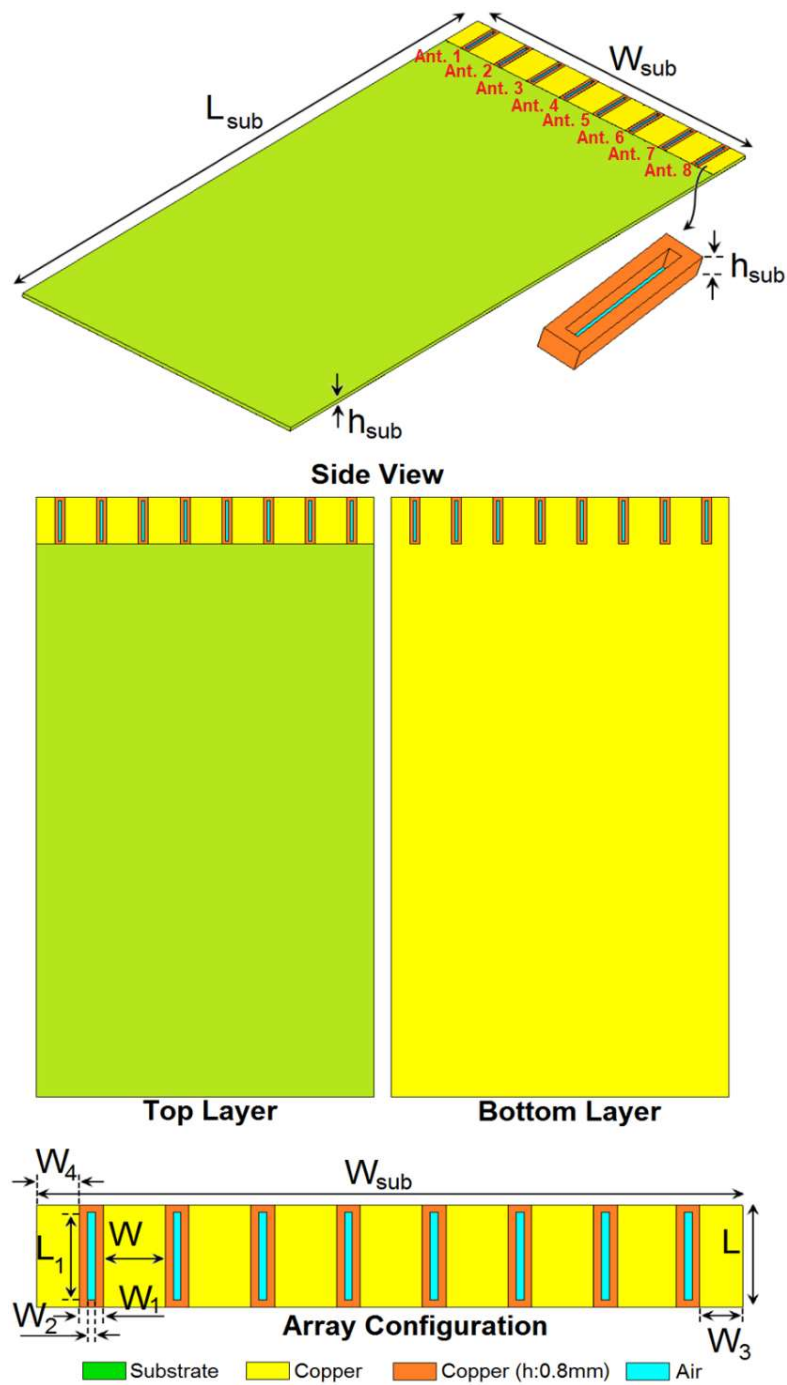


Figure 2. Details of the introduced array's configuration and design.

Table 1. Final dimensions of the 5G antenna parameters.

Parameter	W_{sub}	L_{sub}	h_{sub}	W	W_1
Value (mm)	55	110	0.787	5.25	1.5
Parameter	W_2	W_3	W_4	L	L_1
Value (mm)	0.5	3.125	3.125	8.3	7.8

Figure 3a depicts an ideal system architecture that can be used for a linear phased array antenna system. The feeding network of the phased array design is one of the critical issues to obtain a functional antenna array set. A 1×8 uniform linear array could be employed, on another thin substrate above the elements, for the presented array design.

It should be noted that each antenna radiator must be excited with equal magnitude and different phases [24,25]. The shape of the radiation beams can be defined by applying the relative phase amplitudes to each antenna radiator as below:

$$\varphi = 2\pi (d/\lambda) \sin \theta \quad (1)$$

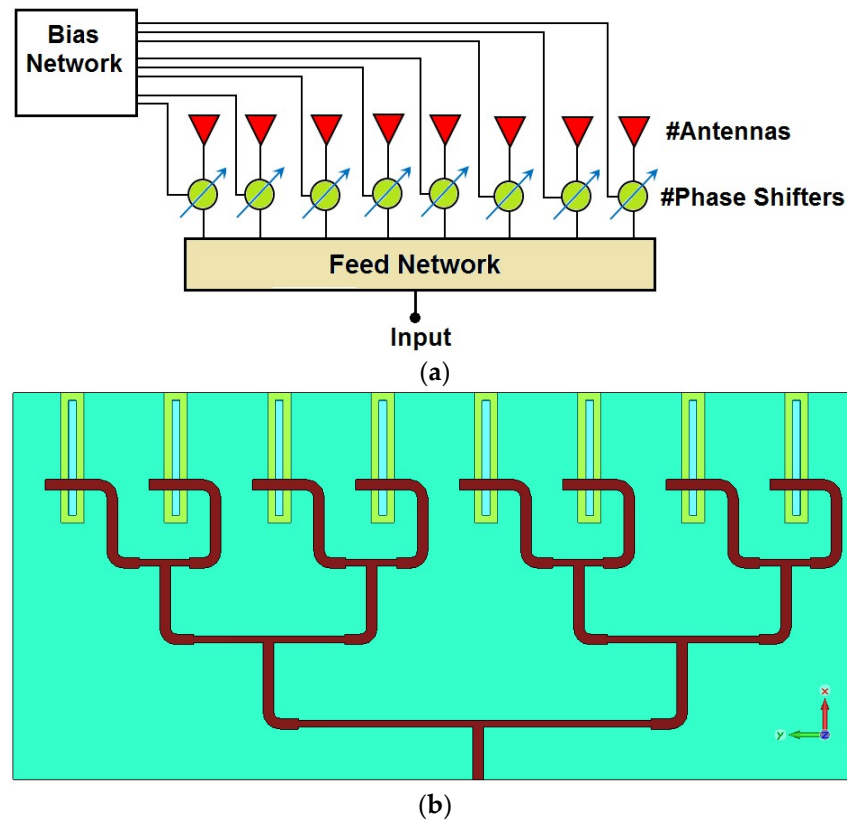


Figure 3. (a) Phased array architecture and (b) typical 1:8 feed network for the array design.

There are various techniques of feed network design for this purpose: parallel (Figure 3b), series, etc. The power dividers (such as Wilkinson) divide the power equally 1: N and also unequally by changing the input and output [26]. In general, in the microstrip-line power dividers, the number of junctions from the input to each output is controlled for tapering amplitude. Moreover, the overall performance of the power divider mainly depends on the power-split level for each output; therefore, the design process can be simple, and the fabrication sensitivity can be insignificant [27].

3. Single-Element Antenna

In general, the microstrip printed slot antenna is a resonator that can be easily formed by cutting a thin slot in a metal-sheet plane. Its size is a half-wavelength ($\lambda/2$) of the antenna operation frequency [28–30]. It can exhibit different polarizations (vertical/circular/horizontal polarizations) depending on its placement, feeding, and antenna configuration. This work has been started by designing a typical slot antenna operation at 21–23.5 GHz. In this study, a rectangular slot radiator is converted into a rectangular metal-ring radiator of the same thickness as the substrate in order to improve the radiation performance and eliminate the impact of high-loss FR-4 dielectric (h_{sub}). The design evaluation and structures of the conventional slot and rectangular metal-ring antennas are depicted in Figure 4a,b. It can be also observed that the discrete feeding technique is employed to feed the radiator in the simulations.

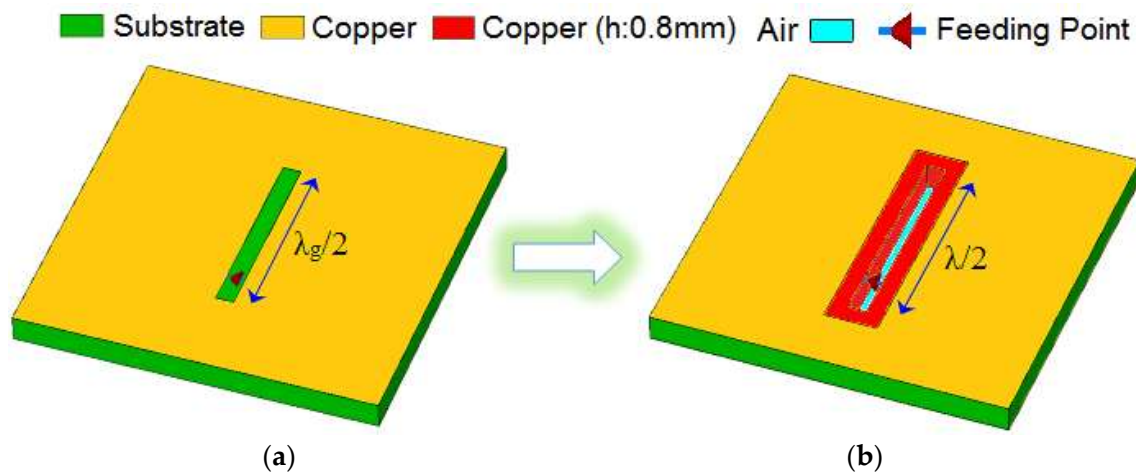


Figure 4. (a) Conventional $\lambda/2$ slot resonator and (b) the configuration of the proposed metal-ring/air-filled slot.

As shown in Figure 5, the proposed design is flexible and by changing the size of the main radiator (L_1), the antenna operating frequency can be easily tuned to the desired band. Figure 6a plots the distributions and densities of the surface currents at the resonating frequency in the top and back layers of the suggested antenna, respectively. It can be observed that the currents are significantly distributed around the slot resonator. Moreover, the embedded metal-ring loop appeared highly active with the surface currents flowing around it. The 3D radiation of the introduced design has been plotted in Figure 6b. Observations have shown that the metal-ring/air-filled resonator provided good radiation, supporting substrate sides at the top and bottom. Moreover, the element provides a high gain level of 5 dB at 22.25 GHz. Furthermore, it is worth mentioning that the -0.35 and -0.38 (radiation and total) efficiencies are discovered for the element at the resonating frequency.

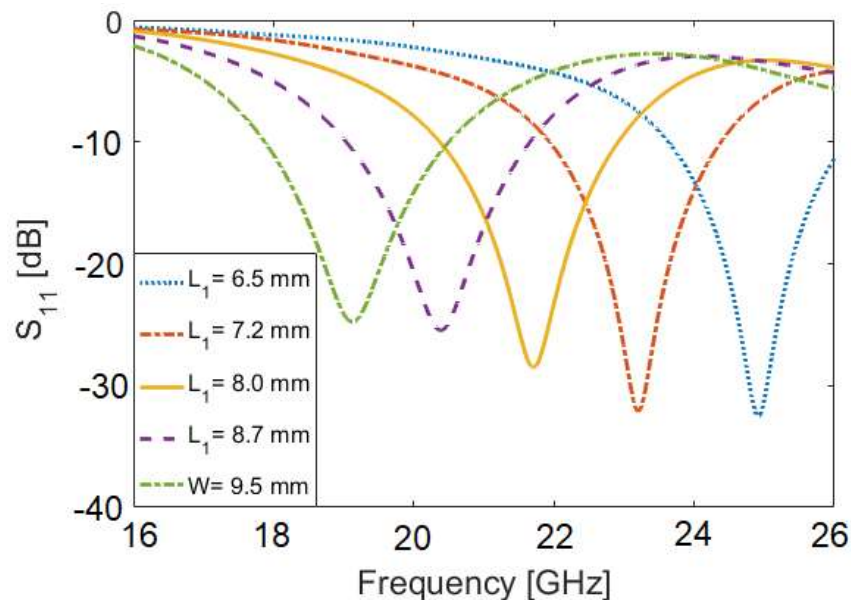


Figure 5. Operation-frequency tuning of the designed antenna for different lengths of the slot resonator.

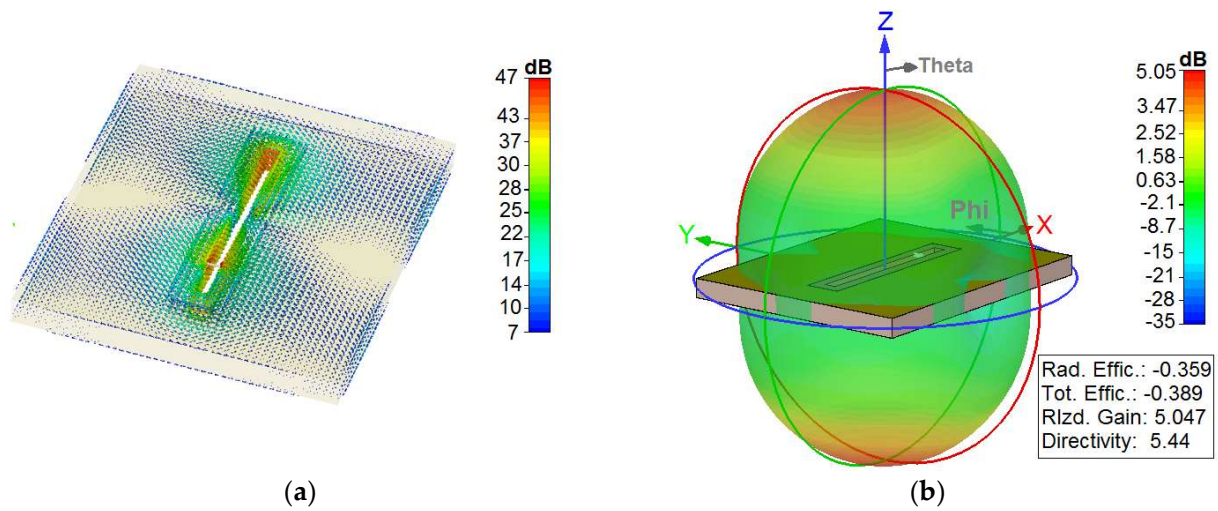


Figure 6. (a) The current densities and (b) radiation at 22.25 GHz.

4. Characteristics of the 5G Smartphone Antenna Array

This section describes and examines the main properties and radiation parameters of the represented array and its beam-tuning capabilities. The S parameters ($S_{11} \sim S_{81}$) of the introduced linear array design are represented in Figure 7. As shown, the design offers 2.5 GHz operational bandwidth with a single resonance at 22.5 GHz, and with lower than -17 dB couplings of the slot radiators. The current distribution at 22.25 GHz is plotted in Figure 8. As can be observed, the currents have mainly concentrated on the top portion of the mainboard. It can be seen that the employed metal-ring radiator is very active and the current flows are mainly distributed around them [31,32].

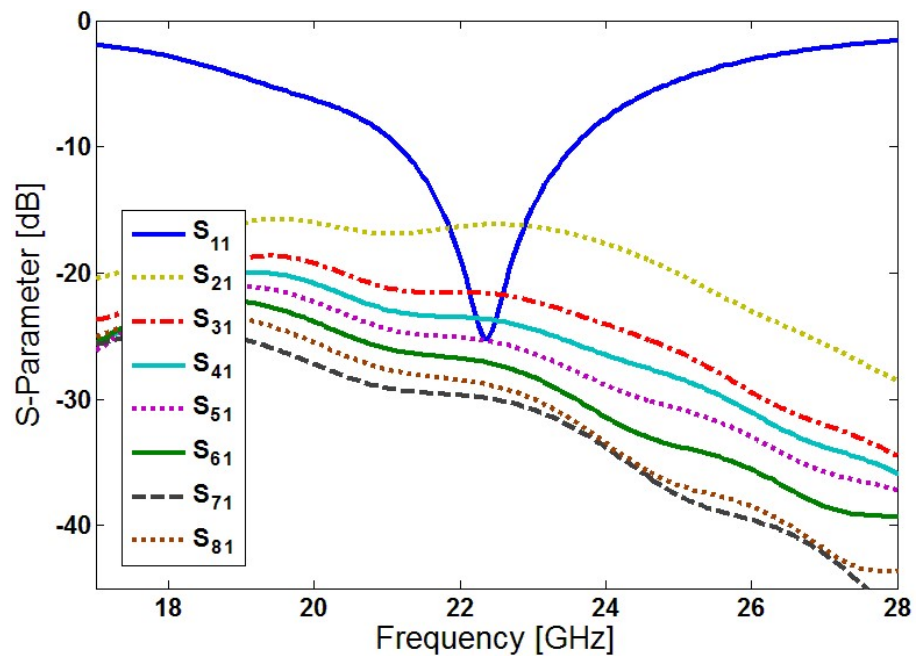


Figure 7. S parameters for the proposed phased array.

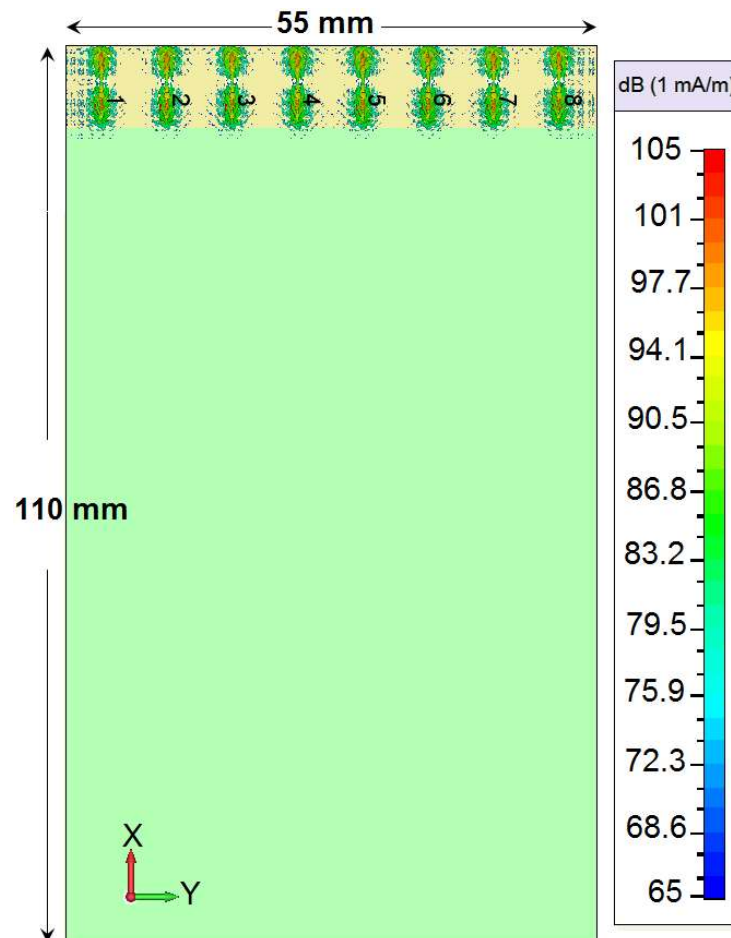


Figure 8. Current distribution at 22.25 GHz for 0° beam of the phased array.

Figure 9 shows the 3D beams of the introduced array radiations for various tuning angles at 22.25 GHz. As can be noticed, the array beams exhibit a wide scanning property over 0° – 70° . On the other hand, we observe well-defined end-fire radiations and quite sufficient gains and directivity over the scanning angles. As represented, the array offers an end-fire radiation mode at the selected scanning angle (0° , 15° , 30° , 45° , 60° , and 70°) which could provide half-space radiation coverage with point-to-point scanning possibility at a different desired angle. As mentioned earlier, to acquire full radiation coverage, another set of the introduced antenna can be located at the bottom side of the mainboard PCB.

Figure 10 shows the simulated 2D-cartesian gain levels of the suggested array beam steering at minus/plus scanning angles. It is shown that the antenna provides wide scan and high-gain beam steering. At 0° to $\pm 50^\circ$ scanings, the array gains are almost constant and offer greater than 11 dB gains. The critical characteristics of the design radiations, such as the directivities and efficiencies for the various radiation beams of the suggested smartphone array at 22.25 GHz, have been represented in Figure 11. Across the range of 0° – 60° , the array efficiencies are greater than 90%. In addition, for the angles below $\pm 50^\circ$, the directivity value varies from 10 to 12 dBi. The efficiency characteristics of the introduced array in the operating frequency range at the 0° scanning angle are plotted in Figure 12. It is discovered that the designed 5G smartphone antenna provides good efficiencies over the frequency band. As represented, a more than -0.15 (97%) radiation efficiency and -1 (80%) total efficiencies have been achieved for the array at the operation band of 21–23.5 GHz. Moreover, the design exhibits sufficient gain values over the targeted frequency band. It was realized that the maximum gain improves while moving to the higher frequencies.

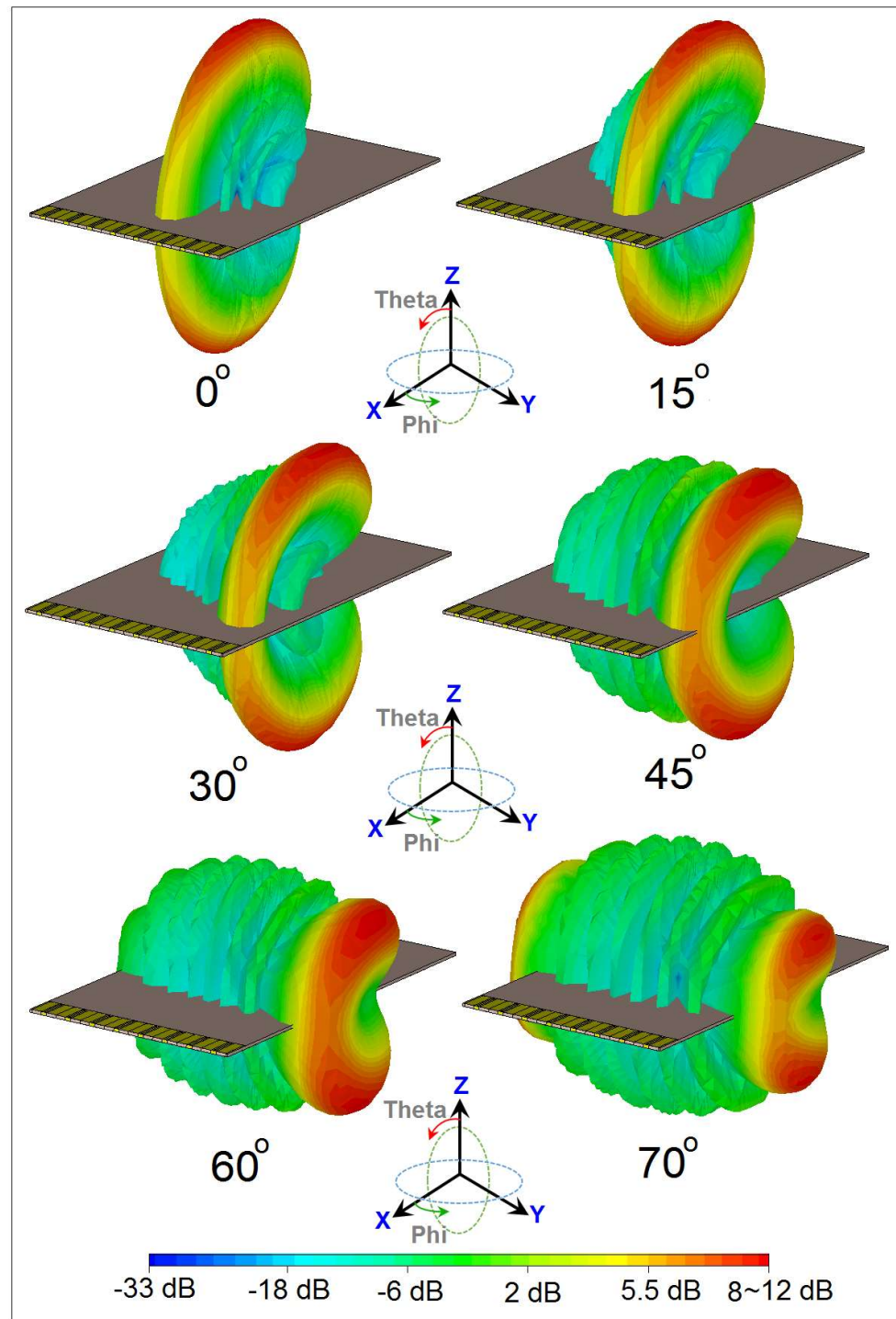


Figure 9. Transparent views of the array beams.

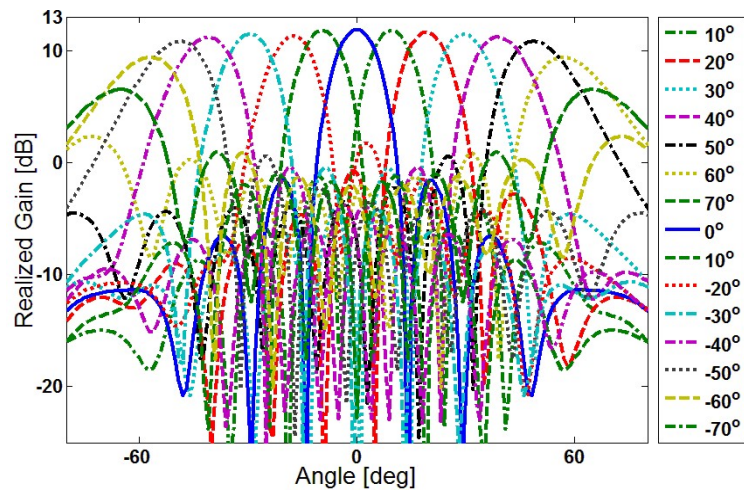


Figure 10. Array gain levels for the scanning radiation beams.

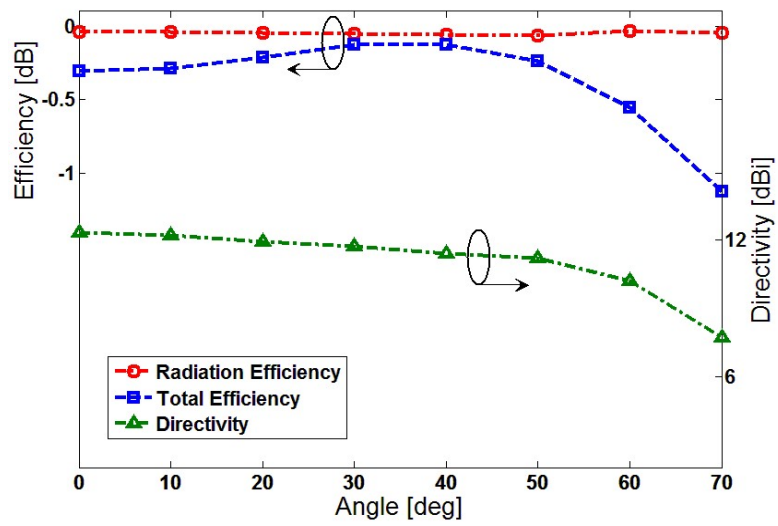


Figure 11. Simulated fundamental radiation parameters at 22.25 GHz.

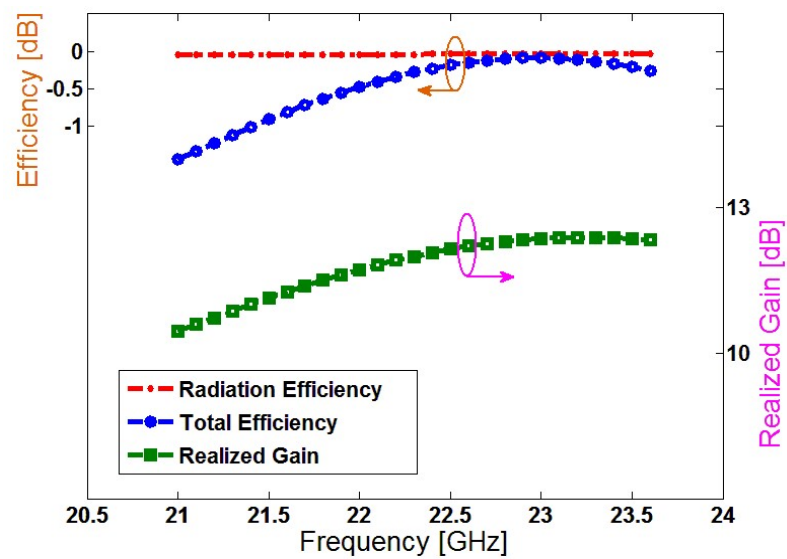


Figure 12. Fundamental radiation parameters over the array impedance bandwidth.

5. Comparison of the Proposed Design with the Conventional Arrays

In order to clarify the improved and higher performance of the introduced phased array compared with the conventional arrays (such as patch and slot antenna arrays), the main properties have been compared and discussed in this section. All designed arrays with eight resonators and a distance of 6.75 mm ($\lambda/2$) are placed in identical smartphone mainboards with FR4 substrate materials to operate at the target frequency of 22.25 GHz. The radiations, beam steering, S parameters, and efficiencies are studied. Figure 13 illustrates the schematics of the cited 5G array antennas.

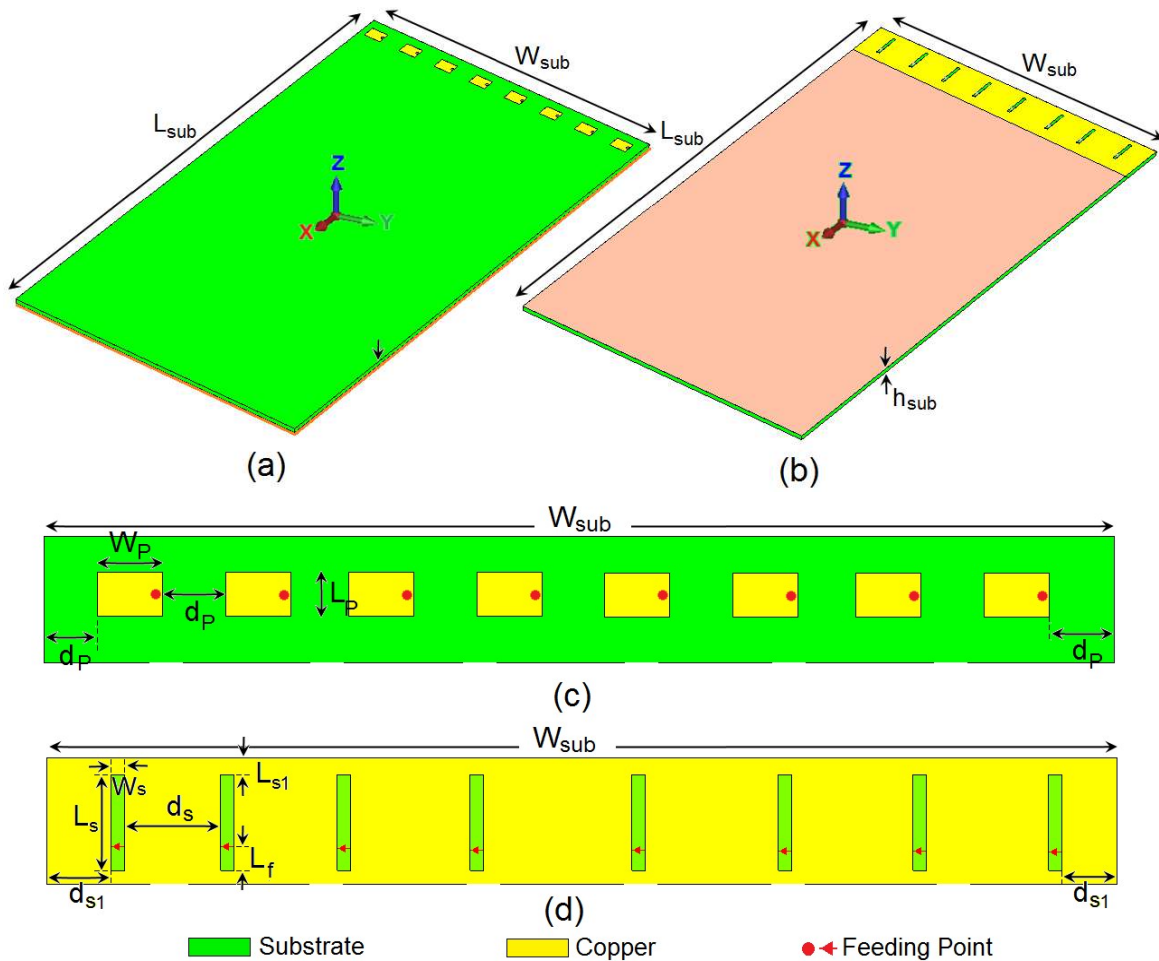


Figure 13. Side views of the smartphone mainboard with conventional (a) patch and (c) slot array antenna, (b) the detailed (c) patch, and (d) slot array arrangements.

Both conventional arrays have been designed to resonate at 22 GHz. Figure 14 depicts their S parameters. As shown, the antennas exhibit good behavior with sufficient couplings. Compared with the S parameters of the proposed design (in Figure 7), the conventional arrays provide sufficient and almost similar S-parameter results. Therefore, they can be good candidates for radiation comparison. Figure 15 compares the radiation efficiency of the designed arrays for various angles of 0° to 60° . It can be seen that compared with the conventional slot and patch array, the introduced array offers very high efficiency. It should be noted that using $\alpha = 10\log_{10}k$, the percentage (linear) value of the antenna efficiency can be converted to dB (logarithmic) [33]. Therefore, as clearly observed, even though the proposed antenna is designed on a lossy substrate (FR4), it offers a much higher efficiency (almost 100%) compared to the conventional designs (80–85%). This is mainly due to the employed design technique which eliminates the loss of the substrate material.

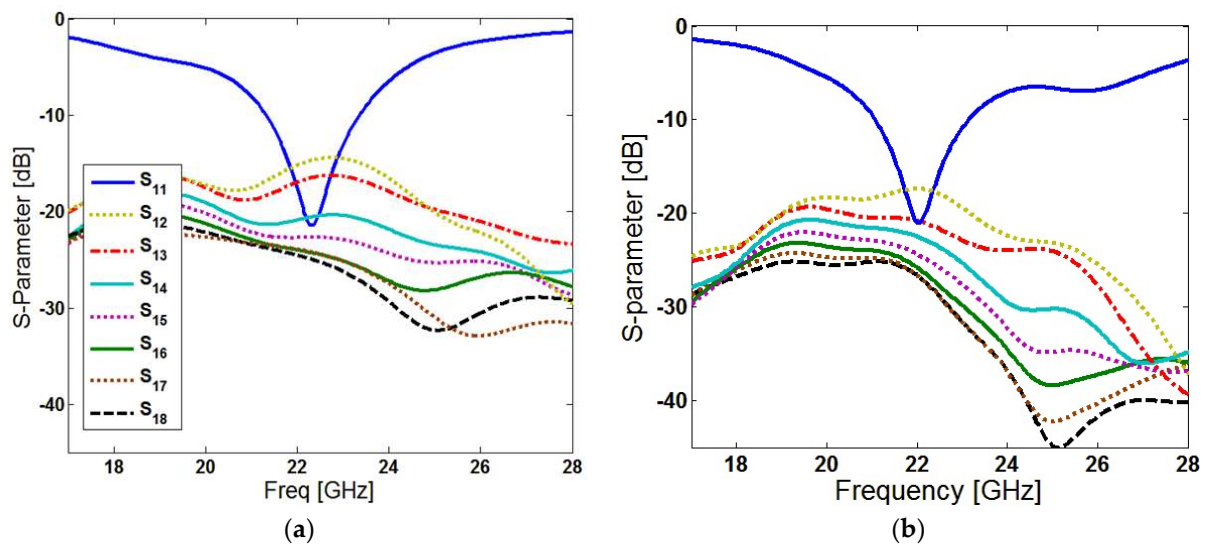


Figure 14. S parameters of the conventional array antennas, (a) slot antenna and (b) patch antenna.

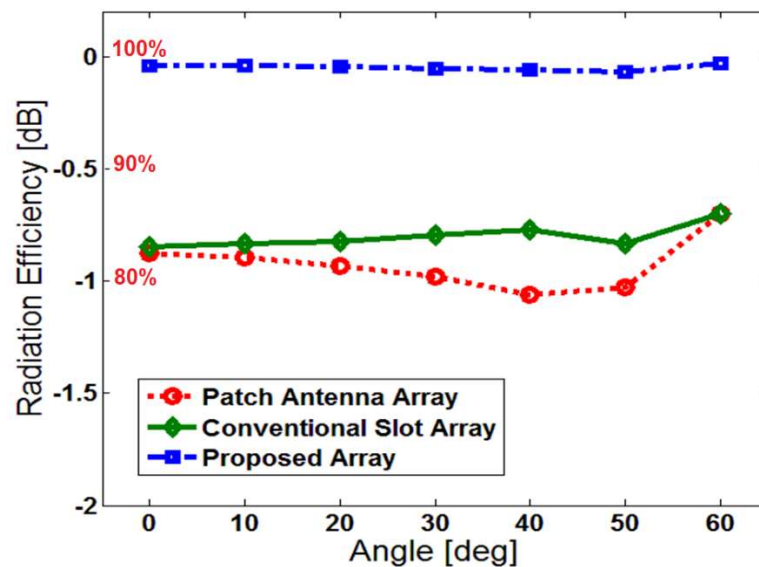


Figure 15. Comparison between the radiation efficiencies of the arrays illustrated in Figure 12 and the proposed design.

Figure 16 plots and compares the 3D beam-steering radiations of the selected antenna arrays with gain levels in the range of 0–60 degrees. As represented, compared with the conventional antenna arrays [Figure 16a,b], the suggested array design offers improved and almost constant radiation gains at various degrees. The simulations and efficiency/gain calculations for each radiation beam were carried out using computer simulation technology (CST) software. As shown, the efficiency values of the proposed design are better than -0.5 dB (90%), while for the conventional design, the parameter is less than -1 dB (80%). In addition, higher efficiency results are discovered for the proposed design. Despite the fact that the conventional patch antenna is higher at 0 degrees, when moving the scanning to higher levels, both conventional arrays (patch and slot) have significantly lower gain levels. Moreover, for the patch array placed at the top side of the mainboard, the radiation coverage will be limited, and achieving full coverage would be challenging. Meanwhile, as shown in Figure 16c, the introduced array design generates end-fire beams with increased radiation coverage. Therefore, using the proposed design technique and applying the

air-filled metal resonators, the antenna’s critical properties can be improved for better communications [34,35].

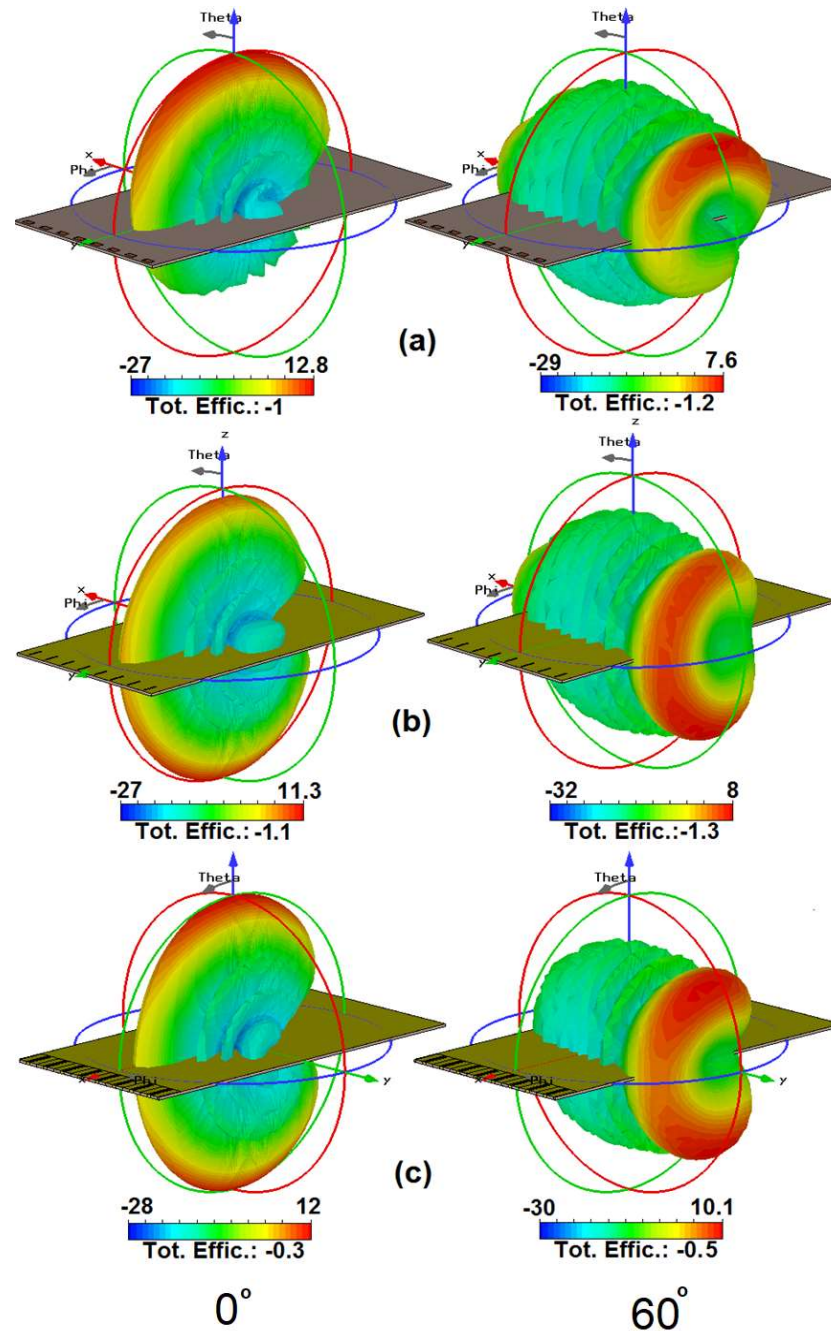


Figure 16. Three-dimensional radiation beams of the antennas are shown in Figure 8 and the proposed design.

6. Insensitivity Function of the Proposed Array Design

As mentioned above, the fundamental properties of the introduced array design are insensitive to different substrate characteristics. The properties of the dielectric substrate, including the permittivity and loss tangent, are critical parameters to control the radiation and performance of the small antennas. In order to clarify this property, the array coefficient reflection (S_{nn}) for various dielectric constant (ϵ_r) values are studied in Figure 17. For the conventional slot antenna array plotted in Figure 13b, when the value of the antenna permittivity (ϵ_r) increases from 2 to 6, the resonating frequency of the conventional slot

antenna (S_{11}) decreases from 28 to 18 GHz. However, as can be observed from Figure 17, unlike the conventional array design, the introduced air-filled array offers similar S_{11} results for various values of the substrate permittivity. From this result, it can be concluded that the array design is insensitive, and its reflection coefficient remains constant for various types of substrates.

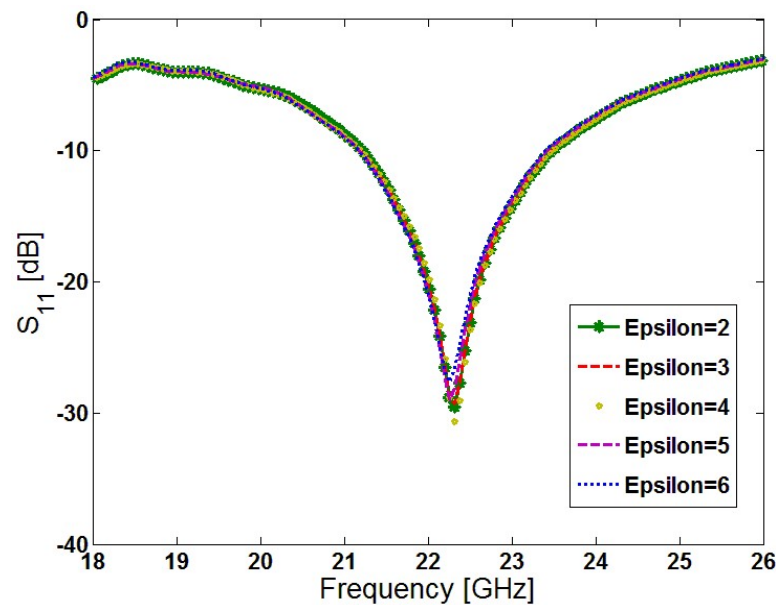


Figure 17. S_{11} results of the array for various values of Epsilon (ϵ_r).

The loss tangent (δ) is another substrate characteristic that should be considered for the insensitivity function of the proposed array design [36]. It plays a vital role and can affect both the cost and radiation characteristics of an antenna design. The fundamental radiation properties of the introduced array design, including the realized gain, radiation, and efficiencies at different scanning degrees at 22.25 GHz of the presented array design for various loss tangent values, are illustrated in Figure 18. The studied loss tangent varies from 0.005 to 0.5. As shown, changing the value of δ does not affect the radiation properties of the phased array. The design exhibits similar behavior with high efficiencies. It can be found that the designed phased array offers almost the same values of efficiencies (radiation and total) and very insignificant variation. In addition, at different degrees, the gain characteristic of the introduced array does not change. The radiation characteristics of the introduced design with various lengths of the ground plane have been studied in Figure 19. As illustrated, as the array elements are the insensitive slot-loop radiators with the air substrates, the ground-plane impact on the array performance is insignificant. However, as can be seen, using different lengths for the ground plane, different values of the fundamental radiation properties can be obtained.

Table 2 exhibits a comparative summary of the antenna characteristics for the proposed design with the recently reported smartphone 5G phased arrays available in the literature [37–45]. As depicted in the table, the suggested design can support wide scanning angles with better gain and efficiency characteristics. In addition, different from the reported designs, the gain and efficiency characteristics of the design are almost constant over the main scanning angles (0–60 degrees). In addition, the antenna elements have more than 17 dB isolation. Furthermore, unlike the reported design, the proposed antenna is insensitive to different substrate materials which is a unique function and can be demonstrated in low-cost substrates. Its performance is also almost constant for different ground-plane lengths as discussed in Figure 19.

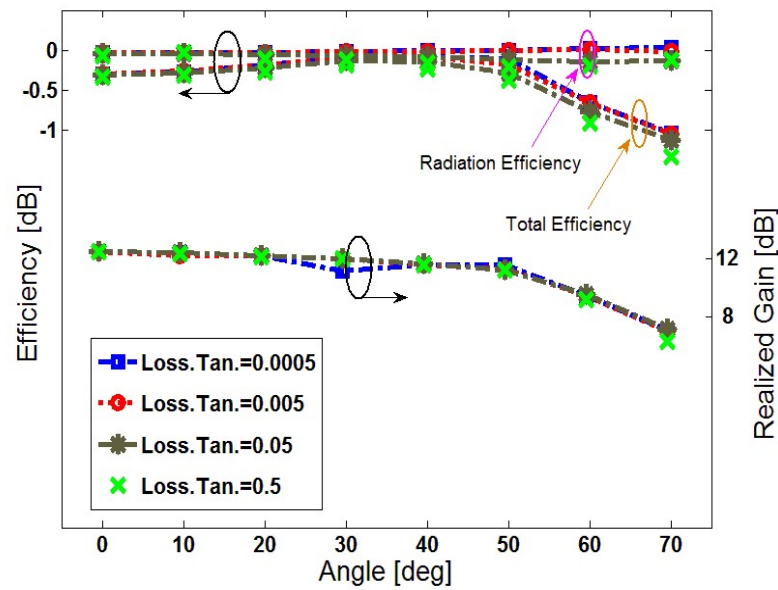


Figure 18. Efficiencies and gain results for different loss tangents (δ) at 22.25 GHz for different scanning angles.

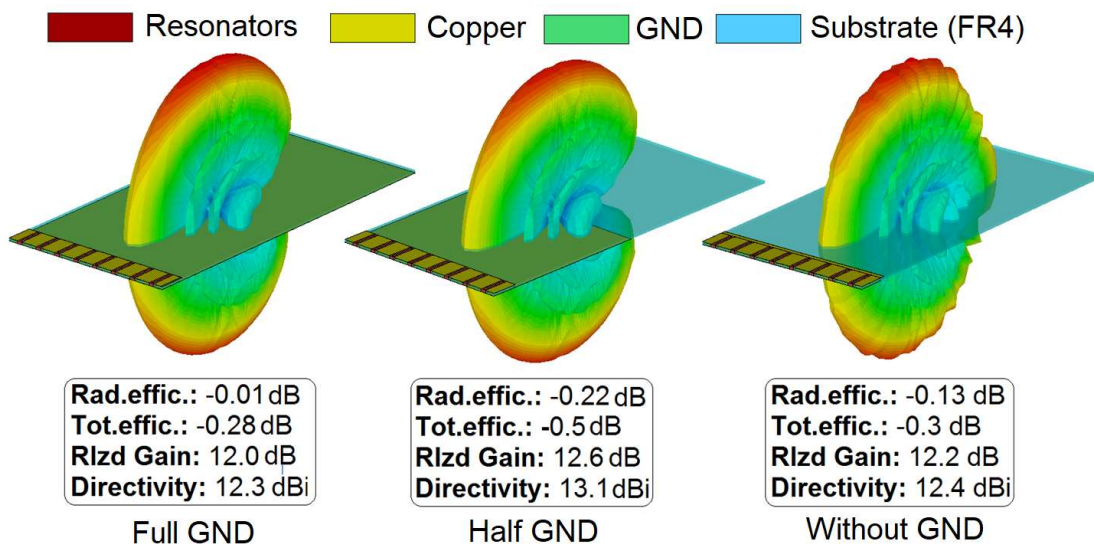


Figure 19. Fundamental radiation properties of the antenna with different sizes of the ground plane.

Table 2. Comparison between the proposed and the reported mobile handset antennas.

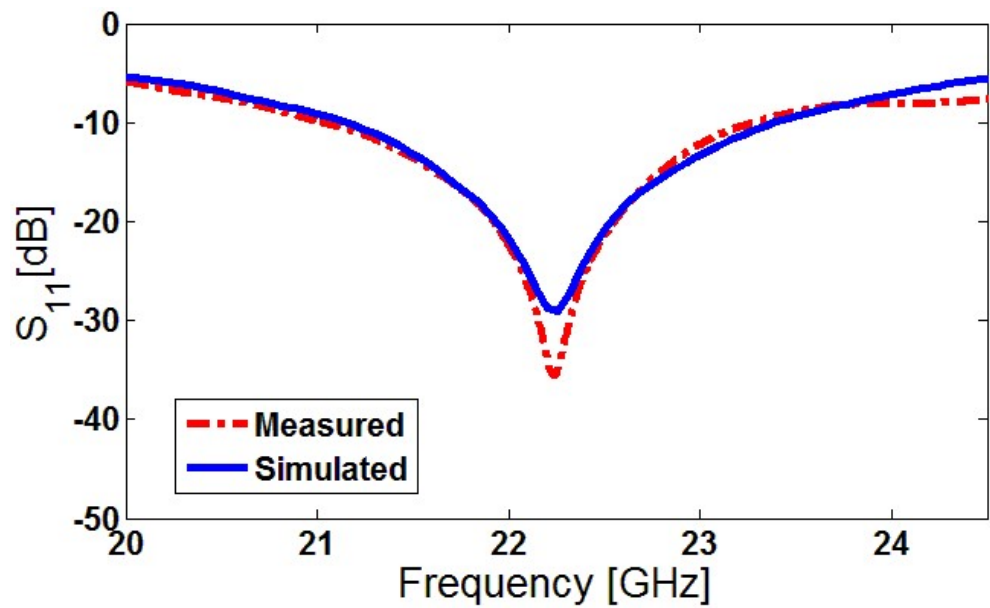
Reference	Bandwidth (GHz)	Efficiency (%)	Gain (dB)	Isolation (dB)	Scanning Range	Insensitivity Function
[37]	21–22	-	8–12	14	0°~75°	No
[38]	27.5–28.5	70	7–11	11	0°~60°	No
[39]	21–23	85	9–11.5	12	0°~60°	No
[40]	27.4–28.8	-	7–11	16	0°~60°	No
[41]	27–29	80	5–9.5	13	0°~75°	No
[42]	27.5–28.5	-	8–11.5	15	0°~60°	No
[43]	27.75–28.25	-	10–13	20	0°~50°	No
[44]	25–29	75–90	8–11	15	0°~75°	No
[45]	27.5–29.5	-	6–8	20	0°~30°	No
Proposed	21–23.5	80–95	10–12.5	17	0°~75°	YES

7. Fabricated Prototype and Experimental Results

The proposed substrate-insensitive phased array was fabricated in a standard FR-4 dielectric. Figure 20a shows the front/back views of the prototype sample. During the fabrication process, eight-slot holes with a distance of $\lambda/2$ have been made to hold the metal-ring resonators. In the next step, the metal-ring resonators were made separately and then inserted into the slot holes on the PCB. Due to some restrictions in terms of equipment and also due to the fact that the antenna elements exhibit almost identical frequency/radiation behavior, the S_{11} and radiation pattern of one antenna element placed at the corner is measured for the introduced phased array.



(a)



(b)

Figure 20. (a) Fabricated prototype sample with the coaxial feeding mechanism of the element and (b) measured/simulated comparison for the antenna reflection coefficient (S_{11}).

However, it should be noted that the mutual coupling effects are not considered in this experimental approach. As can be observed from Figure 20a, in order to measure the S_{11} characteristic of the single-element resonator, the inner conductor of a coaxial cable was extended across the ring resonator and soldered on the PCB ground plane. The simulated/measured S_{11} results of the single-element radiator placed on the mainboard are also plotted and compared in Figure 20b. As evident from the figure, the antenna element exhibits a sufficient measured/simulated S_{11} . In addition, a good agreement is observed between the experimental and simulation results. It is worth mentioning that due to the flexibility of the employed feeding method and also in order to acquire the best possible measured result and also eliminate the SMA connector/cable losses, the feeding point of the antenna element can be slightly adjusted to obtain a better result.

The radiation patterns (including the E and H planes) of the single-element antenna are also measured. Figure 21a plots the measured 2D polar patterns for the element under experiment. As shown, the single-resonator exhibits a quasi omnidirectional radiation shape in the E-plane, while in the H-plane, the radiation's main direction ended in the end-fire mode. Furthermore, in order to study the beam-steering potential of the proposed design with a general perspective, using the measured radiation data of the single antenna, the beam patterns of the introduced array have been synthesized and simulated [46]. The calculated results in the scanning range of $0^\circ \sim 70^\circ$ were illustrated in Figure 21b. As can be observed, a well-defined beam-steering function is obtained for the synthesized beams in the range from 0° to 70° . It is worth mentioning that in the realist approach (where all the elements are measured and mutual couplings and phase shifting are included), the obtained results might be slightly different.

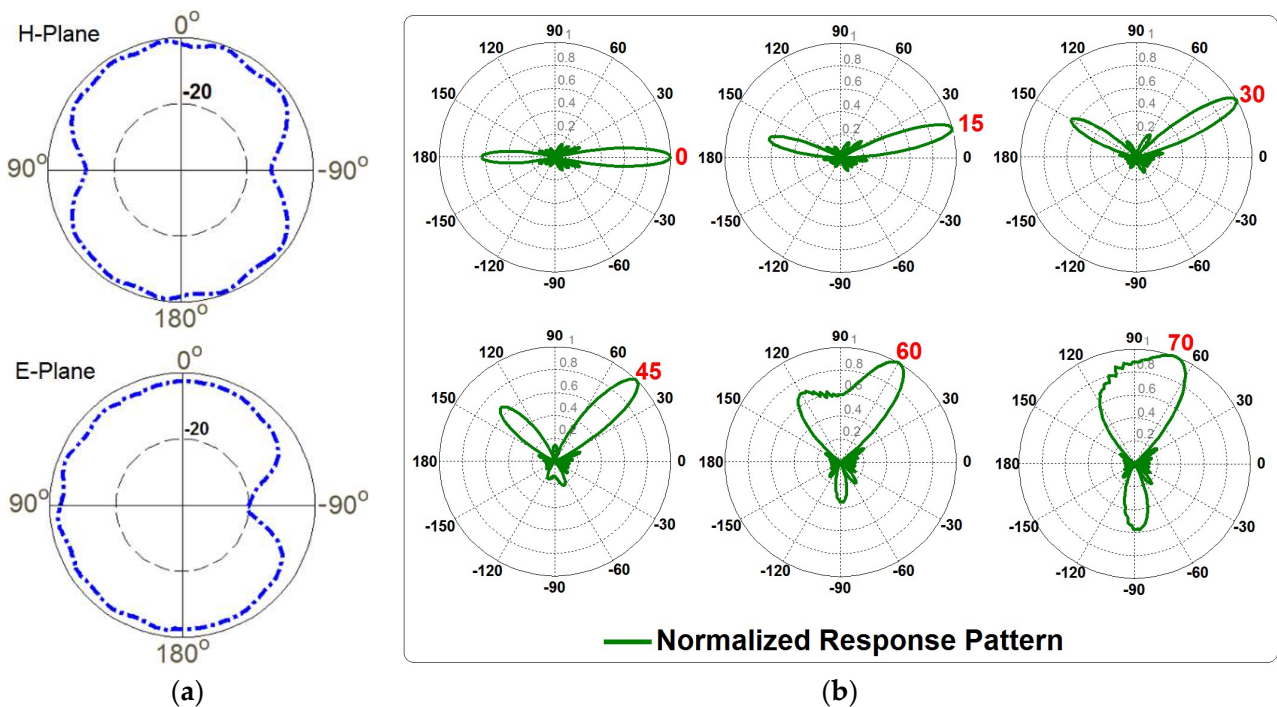


Figure 21. (a) Measured radiation patterns and (b) synthesized array beams using the single-element experiments.

8. Effect of User Hand in Data-Mode

The user-hand effect is a critical part of smartphone applications on handheld platforms and usually creates negative impacts on the radiation and properties of the smartphone antennas [47–50]. This section studied and compared the radiation beams, antenna gain, and efficiencies of the introduced array in the appurtenance of the user hand for the Data-Mode scenario. Figure 22 represents the array beams at different scanning degrees

($0^\circ \sim 75^\circ$). It is clearly shown that the introduced array design offers well-defined radiations with sufficient gains and radiation coverage in quasi-end-fire radiation mode. However, as mentioned before, due to the negative impact of the user-hand phantom, a slight reduction in the array performance was observed. Figure 23 illustrates and compares the losses of the performances of the phased array design in terms of the realized gain and efficiencies in the Data-Mode (DM) compared with Free-Space (FS). As seen, the total losses of the designed array parameters for the antenna gain are around 0.5 to 1.5 dB. In addition, in the scanning range of 0° to 50° , the efficiency reduction is less than 0.25 dB (5%). However, as expected, by moving to the higher scanning angles ($60^\circ \sim 70^\circ$), an about 15–20% reduction is observed in the antenna efficiency. Therefore, it can be concluded that the effect of the user’s hand is not significant.

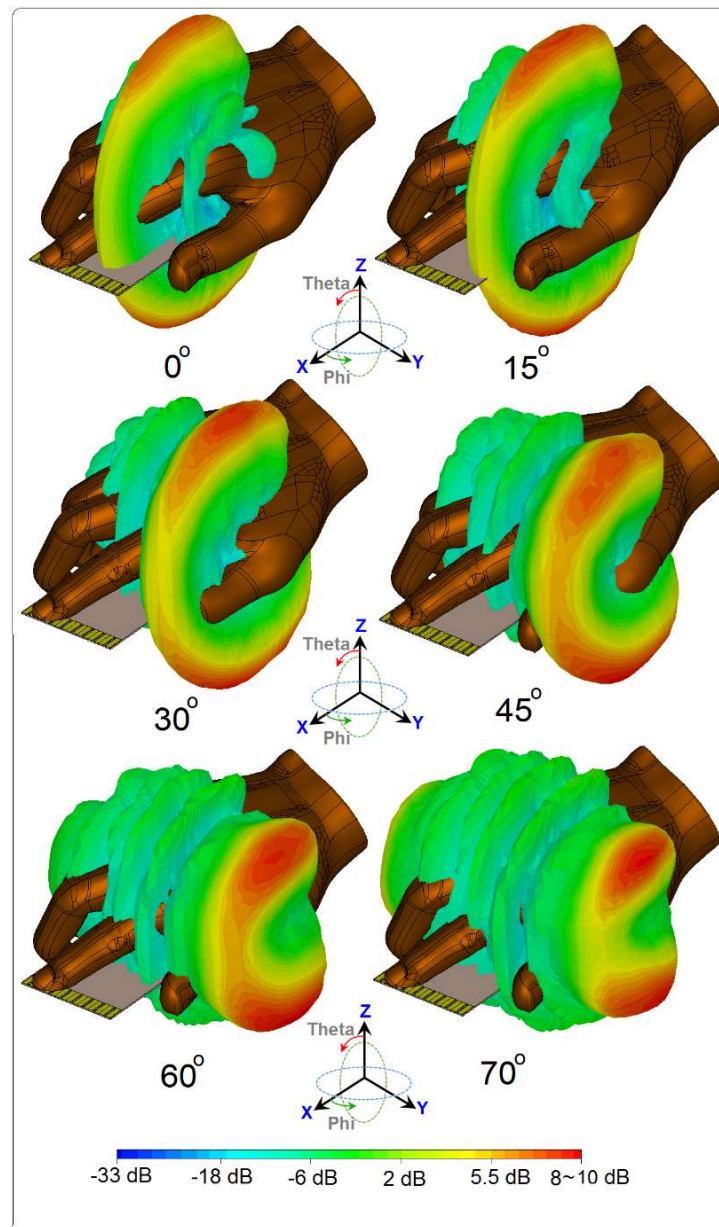


Figure 22. Three-dimensional beams of the array radiation in Data-Mode.

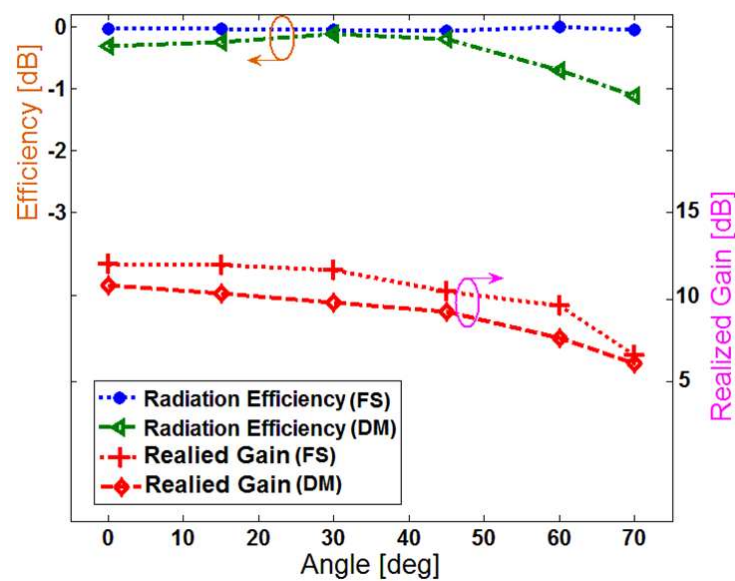


Figure 23. Comparison between the characteristics of the array in FS and DM.

9. Conclusions

This manuscript proposes a new beam-steerable array antenna design with improved performance and substrate insensitivity for modern 5G smartphones. The antenna array is designed on the FR-4 dielectric and its configuration contains eight slot-loop/metal-ring resonators with the air-filled substrate in a 1×8 array form located at the edge of the smartphone board. The usefulness of the introduced array for 5G applications is validated through simulations and measurements. The proposed design provides a wide impedance bandwidth of 21–23.5 GHz. It also exhibits constant radiation properties with very low losses in terms of the antenna gain, S parameters, and efficiency for different substrate materials. It also offers high gains and efficiencies at frequencies different from its operating band. In addition, sufficient radiation is observed in the presence of the user's hand in Data-Mode. Considering these advantages, the array is highly suitable for modern 5G smartphones.

Author Contributions: Writing—original draft preparation, A.U., N.O.P. and R.A.A.-A.; writing—review and editing, N.O.P., A.S.I.A. and R.A.A.-A.; investigation, N.O.P. and A.U.; resources, N.O.P. and A.S.I.A.; for other cases, all authors have participated. All authors have read and agreed to the published version of the manuscript.

Funding: This research received no external funding.

Data Availability Statement: All the data have been included in the study.

Conflicts of Interest: The authors declare no conflict of interest.

References

- Gupta, P. Evolution of mobile generations: 1G to 5G. *Int. J. Technol. Res. Eng.* **2013**, *1*, 152–157.
- Rappaport, T.S.; Sun, S.; Mayzus, R.; Zhao, H.; Azar, Y.; Wang, K.; Wong, G.N.; Schulz, J.K.; Samimi, M.; Gutierrez, F. Millimeter wave mobile communications for 5G cellular: It will work! *IEEE Access* **2013**, *1*, 335–349. [CrossRef]
- Rappaport, T.S.; Gutierrez, F.; Ben-Dor, E.; Murdock, J.N.; Qiao, Y.; Tamir, J.I. Broadband millimeter-wave propagation measurements and models using adaptive-beam antennas for outdoor urban cellular communications. *IEEE Trans. Antennas Propag.* **2013**, *61*, 1850–1859. [CrossRef]
- Liu, D.; Pfeiffer, U.; Grzyb, J.; Gaucher, B. *Advanced Millimeter-Wave Technologies*; John Wiley and Sons: Hoboken, NJ, USA, 2009.
- Yarali, A. Fifth Generation (5G) Cellular Technology. In *Public Safety Networks from LTE to 5G*; Wiley: Hoboken, NJ, USA, 2020; pp. 171–188.
- Narayan, C.P. *Antennas and Propagation*; Technical Publications: Pune, Maharashtra, India, 2007.

7. Roh, W.; Seol, J.-Y.; Park, J.; Lee, B.; Lee, J.; Kim, Y.; Cho, J.; Cheun, K.; Aryanfar, F. Millimeter-wave beamforming as an enabling technology for 5G cellular communications: Theoretical feasibility and prototype results. *IEEE Commun. Mag.* **2014**, *52*, 106–113. [CrossRef]
8. Rajagopal, S.; Abu-Surra, S.; Pi, Z.; Khan, F. Antenna array design for multi-gbps mmwave mobile broadband communication. In Proceedings of the 2011 IEEE Global Telecommunications Conference—GLOBECOM 2011, Houston, TX, USA, 5–9 December 2011; pp. 1–6.
9. Siddiqui, Z.; Sonkki, M.; Chen, J.; Berg, M.; Leinonen, M.E.; Pärssinen, A. Dual-band dual-polarized antenna for mm-wave 5G base station antenna array. In Proceedings of the 2020 14th European Conference on Antennas and Propagation (EuCAP), Copenhagen, Denmark, 15–20 March 2020; pp. 1–4.
10. Parchin, N.O.; Abdalhameed, R.A. A compact Vivaldi antenna array for 5G channel sounding applications. In Proceedings of the 12th European Conference on Antennas and Propagation (EuCAP 2018), London, UK, 9–13 April 2018.
11. Daigle, B. Printed circuit board material and design considerations for wireless applications. In Proceedings of the 46th Electronic Components and Technology Conference, Orlando, FL, USA, 28–31 May 1996; pp. 354–357.
12. Chen, Q.; Gong, Z.; Yang, X.; Wang, Z.; Zhang, L. Design considerations for millimeter wave antennas within a chip package. In Proceedings of the IEEE International Workshop on Anti-Counterfeiting, Security and Identification, Xiamen, China, 16–18 April 2007; pp. 13–17.
13. Nielsen, J.Ø.; Pedersen, G.F. Performance of Beamforming for a Handheld Device in Measured 21.5 GHz Indoor Channels. *IEEE Trans. Antennas Propag.* **2022**, *70*, 5725–5735. [CrossRef]
14. Sani Yahya, M.; Rahim, S. 15 GHz grid array antenna for 5G mobile communications system. *Microw. Opt. Technol. Lett.* **2016**, *58*, 2977–2980. [CrossRef]
15. Helander, J.; Zhao, K.; Ying, Z.; Sjöberg, D. Performance Analysis of Millimeter-Wave Phased Array Antennas in Cellular Handsets. *IEEE Antennas Wirel. Propag. Lett.* **2016**, *15*, 504–507. [CrossRef]
16. Sun, W.; Li, Y.; Chang, L.; Li, H.; Qin, X.; Wang, H. Dual-band dualpolarized microstrip antenna array using double-layer gridded patches for 5G millimeter-wave applications. *IEEE Trans. Antennas Propag.* **2021**, *69*, 6489–6499. [CrossRef]
17. Seo, J.; Yoon, I.; Jung, J.; Ryoo, J.; Park, J.; Lee, W.; Ko, D.; Oh, J. Miniaturized dual-band broadside/endfire antenna-in-package for 5G smartphone. *IEEE Trans. Antennas Propag.* **2021**, *69*, 8100–8114. [CrossRef]
18. Ojaroudi, N.; Ghadimi, N. UWB small slot antenna with WLAN frequency band-stop function. *Electron. Lett.* **2013**, *49*, 1317–1318. [CrossRef]
19. Sethi, W.T.; Vettikalladi, H.; Minhas, B.K.; Alkanhal, M.A. High gain and wide-band aperture-coupled microstrip patch antenna with mounted horn integrated on FR4 for 60 GHz communication systems. In Proceedings of the IEEE Symposium on Wireless Technology and Applications (ISWTA), Kuching, Malaysia, 22–25 September 2013; pp. 359–362.
20. Hong, W.; Baek, K.; Lee, Y.; Kim, Y.G. Design and analysis of a low-profile 28 GHz beam steering antenna solution for future 5G cellular applications. In Proceedings of the IEEE International Microwave Symposium, Tampa, FL, USA, 1–6 June 2014.
21. Salman, J.W.; Ameen, M.M.; Hassan, S.O. Effects of the loss tangent, dielectric substrate permittivity and thickness on the performance of circular microstrip antennas. *J. Eng. Dev.* **2006**, *10*, 1–13.
22. Salokhe, B.T.; Mali, S.N. Effect of substrate material variations on RMSA, CMSA and NLMSA. *Int. J. Adv. Res. Electr. Electron. Instrum. Eng.* **2014**, *3*, 14009–14015.
23. CST Microwave Studio, Version 2020; CST: Framingham, MA, USA, 2020.
24. Amitay, N.; Galindo, V.; Wu, C.P. *Theory and Analysis of Phased Array Antennas*; Wiley-Interscience: New York, NY, USA, 1972.
25. Xu, R.; Chen, Z.N. A Compact Beamsteering Metasurface Lens Array Antenna with Low-Cost Phased Array. *IEEE Trans. Antennas Propag.* **2021**, *69*, 1992–2002. [CrossRef]
26. Guo, J.; Xiao, S.; Liao, S. A Low-Cost Feeding Network with Simple Phase Shift Structures. In Proceedings of the 2018 IEEE International Conference on Computational Electromagnetics (ICCEM), Chengdu, China, 26–28 March 2018; pp. 1–3.
27. Roshani, S.; Koziel, S.; Roshani, S.; Jamshidi, M.B.; Parandin, F.; Szczepanski, S. Design of a Patch Power Divider with Simple Structure and Ultra-Broadband Harmonics Suppression. *IEEE Access* **2021**, *9*, 165734–165744. [CrossRef]
28. Parchin, N.O. Dual-Band Phased Array 5G Mobile-Phone Antenna with Switchable and Hemispherical Beam Pattern Coverage for MIMO-Diversity Communications. *ACES J.* **2022**, *36*, 1602–1609. [CrossRef]
29. Nakano, H.; Yamauchi, J. Printed slot and wire antennas: A Review. *Proc. IEEE* **2012**, *100*, 2158–2168. [CrossRef]
30. Kim, D.-Y.; Lim, Y.; Yoon, H.-S.; Nam, S. High-Efficiency W-Band Electroforming Slot Array Antenna. *IEEE Trans. Antennas Propag.* **2015**, *63*, 1854–1857. [CrossRef]
31. Ojaroudi, N. Application of protruded strip resonators to design an UWB slot antenna with WLAN band-notched characteristic. *Prog. Electromagn. Res. C* **2014**, *47*, 111–117. [CrossRef]
32. Hong, W.; Ko, S.-T.; Lee, Y.; Baek, K.-H. Compact 28 GHz antenna array with full polarization flexibility under yaw, pitch, roll motions. In Proceedings of the 2015 9th European Conference on Antennas and Propagation (EuCAP), Lisbon, Portugal, 13–17 April 2015; pp. 1–3.
33. Available online: <https://www.lasercalculator.com/db-percent-converter/> (accessed on 14 September 2022).
34. Hong, W.; Baek, K.-H.; Ko, S. Millimeter-wave 5G antennas for smartphones: Overview and experimental demonstration. *IEEE Trans. Antennas Propag.* **2017**, *65*, 6250–6261. [CrossRef]

35. Ide, T.; Kanaya, H. 28 GHz one-sided directional slot array antenna for 5G application. In Proceedings of the 2019 IEEE 21st Electronics Packaging Technology Conference (EPTC), Singapore, 4–6 December 2019; pp. 440–443.
36. Chen, C.-N.; Lin, Y.-H.; Hung, L.-C.; Tang, T.-C.; Chao, W.-P.; Chen, C.-Y.; Chuang, P.-H.; Lin, G.-Y.; Liao, W.-J.; Nien, Y.H. 38-GHz Phased Array Transmitter and Receiver Based on Scalable Phased Array Modules with Endfire Antenna Arrays for 5G MMW Data Links. *IEEE Trans. Microw. Theory Tech.* **2021**, *69*, 980–999. [CrossRef]
37. Ojaroudiparchin, N.; Shen, M.; Pedersen, G.F. Beam-steerable microstrip-fed bow-tie antenna array for fifth generation cellular communications. In Proceedings of the 2016 10th European Conference on Antennas and Propagation (EuCAP), Davos, Switzerland, 10–15 April 2016.
38. Zhang, J.; Zhang, S.; Li, Y.; Pedersen, G.F. Printed vertically-polarized quasi-endfire beam steering array with full ground plane for 5g mobile applications. In Proceedings of the 13th European Conference on Antennas and Propagation (EuCAP), Krakow, Poland, 31 March–5 April 2019.
39. Ojaroudiparchin, N.; Shen, M.; Zhang, S.; Pedersen, G.F. A switchable 3-D-coverage-phased array antenna package for 5G mobile terminals. *IEEE Antennas Wirel. Propag. Lett.* **2016**, *15*, 1747–1750. [CrossRef]
40. Zhang, J.; Zhang, S.; Lin, X.; Fan, Y.; Pedersen, G. 3D radiation pattern reconfigurable phased array for transmission angle sensing in 5G mobile communication. *Sensors* **2018**, *18*, 4204. [CrossRef] [PubMed]
41. Parchin, N.O.; Shen, M.; Pedersen, G.F. Small-size tapered slot antenna (TSA) design for use in 5G phased array applications. *Appl. Comput. Electromagn. Soc. (ACES) J.* **2017**, *3*, 1054–4887.
42. Zhao, A.; Ai, F. 5G mm-wave antenna array based on T-slot antenna for mobile terminals. In Proceedings of the 2018 IEEE Asia-Pacific Conference on Antennas and Propagation (APCAP), Auckland, New Zealand, 5–8 August 2018.
43. Ojaroudi Parchin, N.; Al-Yasir, Y.; Abdulkhaleq, A.M.; Elfergani, I.; Rayit, A.; Noras, J.M.; Rodriguez, J.; Abd-Alhameed, R.A. Frequency reconfigurable antenna array for mm-Wave 5G mobile handsets. In Proceedings of the 9th International Conference on Broadband Communications, Networks, and Systems, Faro, Portugal, 19–20 September 2018.
44. Tatomirescu, A.; Oprian, A.; Zhekov, S.; Pedersen, G.F. Beam-steering array for handheld devices targeting 5G. In Proceedings of the 2015 International Symposium on Antennas and Propagation (ISAP), Hobart, TAS, Australia, 9–12 November 2015.
45. Park, E.; Yoon, Y.J.; Kim, H. Dual Polarization L-Shaped Slot Array Antenna for 5G Metal-Rimmed Mobile Phone. In Proceedings of the 2018 International Symposium on Antennas and Propagation (ISAP), Busan, Korea, 23–26 October 2018; pp. 1–2.
46. Rafique, U.; Dalal, P.; Abbas, S.M.; Khan, S. Phased Array Antenna for Millimeter-Wave 5G Mobile Phone Applications. In Proceedings of the 2022 IEEE Wireless Antenna and Microwave Symposium (WAMS), Rourkela, India, 5–8 June 2022; pp. 1–4. [CrossRef]
47. di Paola, C.; Zhao, K.; Zhang, S.; Pedersen, G.F. Hybrid Switchable Phased Array with p-i-n Diodes for 5G Mobile Terminals. In Proceedings of the 2021 15th European Conference on Antennas and Propagation (EuCAP), Dusseldorf, Germany, 22–26 March 2021; pp. 1–5. [CrossRef]
48. Parchin, N.O.; Zhang, J.; Abd-Alhameed, R.A.; Pedersen, G.F.; Zhang, S. A planar dual-polarized phased array with broad bandwidth and quasi-endfire radiation for 5G mobile handsets. *IEEE Trans. Antennas Propag.* **2021**, *69*, 6410–6419. [CrossRef]
49. Ilvonen, J.; Kivekas, O.; Holopainen, J.; Valkonen, R.; Rasilainen, K.; Vainikainen, P. Mobile terminal antenna performance with the user's hand. *IEEE Antenna Wirel. Propag. Lett.* **2011**, *10*, 772–775. [CrossRef]
50. Alshamaileh, M.H.; Alja'afreh, S.S.; Almajali, E. Nona-band, hybrid antenna for metal-rimmed smartphone applications. *IET Microw. Antennas Propag.* **2019**, *13*, 2439–2448. [CrossRef]

Article

Design of a Flat-Panel Metasurface Reflectarray C-Band Antenna

Gyoungdeuk Kim ¹, Myeongha Hwang ¹, Hyunmin Jeong ¹ , Chul-Min Lim ², Kyoung Youl Park ²
and Sangkil Kim ^{1,*} 

¹ Department of Electronics Engineering, Pusan National University, Busan 26241, Korea

² Defense Space Technology Center, Agency for Defense Development, Daejeon 34186, Korea

* Correspondence: ksangkil3@pusan.ac.kr; Tel.: +82-51-510-2375; Fax: +82-51-515-5190

Abstract: This paper presents the design of a flat-panel metasurface reflectarray antenna fed by a circular horn antenna for satellite applications. A metasurface-based reflectarray antenna is similar to a flat-panel reflector and is characterized by a reflection angle adjustment that is free from the well-known Snell's law. This was done by compensating the angle of the incident wave using the structure of each unit cell. A unit cell of the designed metasurface is composed of a dual-ring resonator. Many satellites use a reflectarray antenna due to its flat-panel structure and the capability of steering the reflection angle of the incident wave. This paper presents the detailed design procedure using a commercial 3D EM simulator and the operation principle of the flat-panel metasurface reflectarray antenna, including the simulation setup, design environment and automation. The proposed design method is scalable to any EM solvers for numerical analysis. A reflectarray composed of a 16×16 -unit cell array at 5.8 GHz (C-band) was designed and validated by measurement as a proof of concept. It is excited by a low-cost linearly polarized circular horn antenna. The measured antenna gain and radiation patterns show good agreement with the simulation. The measured antenna gain of the reflectarray was 22.4 dBi (cross-pol suppression level: 36 dB), and the reflection angle was 15° at normal incidence.

Keywords: metasurface; reflectarray; high gain antenna; array antenna; C-band



Citation: Kim, G.; Hwang, M.; Jeong, H.; Lim, C.-M.; Park, K.Y.; Kim, S. Design of a Flat-Panel Metasurface Reflectarray C-Band Antenna. *Electronics* **2022**, *11*, 2729. <https://doi.org/10.3390/electronics11172729>

Academic Editors: Massimo Donelli, Faisal Tubbal, Ladislau Matekovits and Raad Raad

Received: 18 July 2022

Accepted: 10 August 2022

Published: 30 August 2022

Publisher's Note: MDPI stays neutral with regard to jurisdictional claims in published maps and institutional affiliations.



Copyright: © 2022 by the authors. Licensee MDPI, Basel, Switzerland. This article is an open access article distributed under the terms and conditions of the Creative Commons Attribution (CC BY) license (<https://creativecommons.org/licenses/by/4.0/>).

1. Introduction

The concept of a reflectarray was proposed in the 1960s using a short-circuited waveguide array composed of different lengths [1]. Early reflectarray designs have not received much attention due to their impractical structures, but the development of a printed flat-panel microstrip reflectarray paved a new way in the late 1980s [2]. The breakthrough of printed microstrip circuit technology has contributed significantly to the innovation of reflectarray antennas, which have emerged as high-gain antennas for long-distance communications, such as nano-/cube-satellite communications.

Dish-type parabolic reflector antennas are widely used in satellite communications for the space-Earth link because of their high-gain property. Small satellite platforms such as CubeSat have extremely limited payload, so it is challenging to mount bulky high-gain reflector antennas on them for the space-Earth link [3]. The advance of resonator-based metamaterial technology has expedited the progress of the metamaterial-based antennas. The metasurface consisting of resonator arrays is widely adopted for antenna, absorber, power-splitter and reflector designs [4–8]. It is because the negative constitutive parameters at desired frequency can be easily obtained by utilizing the planar resonator array structures. For the high gain antenna applications, a flat-panel metasurface reflectarray antenna is a good candidate for the high-gain foldable antenna of CubeSats because of their flat reflectors fabricated from a multi-layer PCB [9–11].

The operation principle and structure of a reflectarray are similar to those of a parabolic reflector antenna [12–14]. Both antennas reflect an incident wave from a source feeding antenna to focus or steer the wave's direction. The direction of the reflected wave is

determined by the shape or phase response of the reflector. A conventional parabolic reflector antenna has a bulky curved metallic surface as a reflector, whereas a reflectarray has a flat planar antenna or resonator array, which results in a low profile, low mass, ease of fabrication and low cost.

Reflectarrays are also different from conventional phased antenna arrays because they do not have a beamforming/steering network, such as a power dividing circuit and phase shifters. The phase response of each unit cell of a reflectarray works as a phase shifter, which results in high reliability due to the relatively simple feeding and passive phase shifting property. Unlike traditional active phased antenna arrays, designing large arrays of thousands of elements is much easier.

This paper discusses a generalized design procedure for a planar reflectarray antenna design and presents a high-gain reflectarray in the C-band as a design example. It shows detailed simulation setup, design environment and automation of a reflectarray antenna. The detailed design procedure of a unit-cell and array analysis using a commercially available full-wave EM solver are discussed. The presented design procedure is demonstrated by a flat-panel reflectarray antenna consisting of a dual-ring resonator fed by a circular horn antenna. Measured experimental data agree well with the proposed design and analysis. It should be noted that the proposed design method is scalable to any EM solvers for numerical analysis.

The measured antenna has a high co-pol gain value of 20.0–22.2 dBi with a cross-pol suppression level of 26–39 dB at the operation frequency. There was an error of 1–2° for the beam steering direction between the simulated data and the measured data. The size of the designed 16×16 reflectarray is $400 \times 400 \text{ mm}^2$, whereas the distance between the source horn antenna and the reflectarray is 200 mm. The proposed design procedure is scalable to any frequency band.

This article is organized as follows. Section 2 presents the detailed operation principle of the reflectarray antenna, its geometry, antenna design parameters and dimensions. Pictures of planar, folded and inactive modes of the antenna are also included in this section.

The measured antenna performance parameters in the C-band, such as the antenna gain, $|S_{11}|$, polarization, source horn antenna are presented in Section 3. The conclusion is given in Section 4.

2. Operation Principle of the Reflectarray Antenna

The operation principle of a flat-panel metasurface reflectarray is shown in Figure 1.

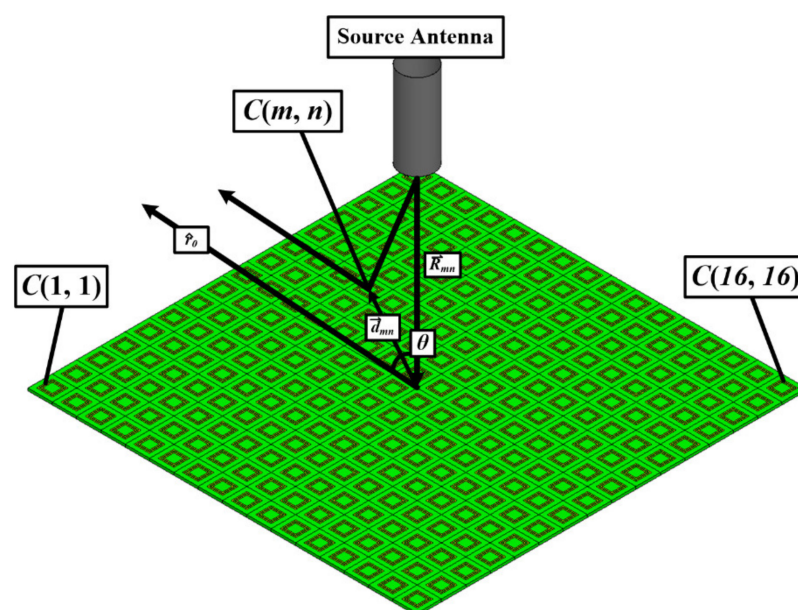


Figure 1. Operation principle of a flat-panel metasurface reflectarray antenna.

The incident electromagnetic waves radiated from a source antenna are reflected by the flat-panel metasurface. The metasurface consists of an array of unit cells, each of which shifts the phase of the incident waves in order to propagate them in the desired direction. The array factor $AF(\theta, \phi)$ of a flat-panel metasurface reflector array with $M \times N$ unit-cells can be written as (1) and (2) when the metasurface reflector is located on the xy -plane [15]:

$$AF(\theta, \phi) = \sum_{m=0}^{M-1} \sum_{n=0}^{N-1} A_{mn} e^{jk_0(md_x u + md_y v)} \tag{1}$$

$$\begin{cases} u = \sin \theta \cos \phi + \beta_x \\ v = \sin \theta \sin \phi + \beta_y \end{cases} \tag{2}$$

where A_{mn} is the complex excitation of the (m, n) -th unit cell, $C(m, n)$ and k_0 is the free space wavenumber. β_x and β_y are the progressive phase shift between the adjacent unit-cells in the x and y directions, respectively. The progressive phase shifts can be expressed as (3) in order to create reflected waves focused in the (θ_r, ϕ_r) direction. d_x and d_y are the period of the unit cell in the x and y directions, respectively.

$$\begin{cases} \beta_x = -\sin \theta_0 \cos \phi_0 \\ \beta_y = -\sin \theta_0 \sin \phi_0 \end{cases} \tag{3}$$

The phase shift $(\Delta\phi_{mn})$ on the mn -th unit cell, $C(m, n)$, can be calculated by using the period of unit cell, β_x , and β_y . It is critical to compensate the phase of the incident waves using the unit-cell structure to control the reflection angle. The phase of the reflected wave at $C(m, n)$ can be calculated by adding the phase of the incident wave to the relative phase shift due to the unit cell. The required phase shift distribution $\Delta\phi$ to obtain a desired reflection angle can be analytically calculated by (4):

$$\Delta\phi_{mn} = 2N\pi + k_0 \left(\left| \vec{R}_{mn} \right| - \vec{d}_{mn} \cdot \hat{r}_0 \right) \quad (N = 0, 1, 2, \dots) \tag{4}$$

where \vec{R}_{mn} is the position vector from the source antenna to $C(m, n)$, \vec{d}_{mn} is the position vector from the center of the metasurface reflector to $C(m, n)$, k_0 is the wavenumber and \hat{r}_0 is the unit vector in the direction of the reflected waves.

The unit cell of the flat-panel reflectarray, which operates at 5.8 GHz (C-band), is composed of dual square rings, as shown in Figure 2. The dual square rings are printed on a widely used commercially available 0.8-mm-thick (Ts) FR4 substrate ($\epsilon_r = 4.4$ and $\tan \delta = 0.04$). The unit cell is placed above a solid metal GND plane, as shown in Figure 2. The width and length (W_{ring}) of the outer ring vary from 6 to 16 mm, whereas the unit cell size (D_{cell}) is fixed at 25 mm. The widths of the inner and outer rings (T_{r1}, T_{r2}) and the gap between the rings (G_1) are also fixed to 1 mm for design simplicity. The metal thickness and the air gap (G_2) between the GND plane and the dual square ring are 18 μm and 2.76 mm, respectively. All the detailed unit cell dimensions are summarized in Table 1.

The phase of the reflected wave changes as the size of the double square ring changes because the impedance of the unit cell is a function of the length and width of the square ring [16,17]. To analyze the phase response of the unit cell according to the size of the dual square rings, an infinite array condition was assumed, and calculation was done by a commercial 3D full-wave simulator, Ansys HFSS. The master-slave boundary condition and Floquet port setup were applied to build an infinite unit cell array simulation environment. The phase response depending on the size of the double ring and incident angle at 5.8 GHz is shown in Figure 3. It is clear that the relative phase shift strongly depends on the size of the ring resonator. The relative phase shift according to the incident angle is very small when the angle of incidence is less than $\pm 15^\circ$. The incidence/reflection angle of $\pm 15^\circ$ is wide enough for the LEO satellite applications because of the mission altitude of the LEO satellites. The mission altitude of the LEO satellite is typically 2000 km or less. It can cover

a circular area with a diameter of 709 km. It is wide enough to cover a small country of a city.

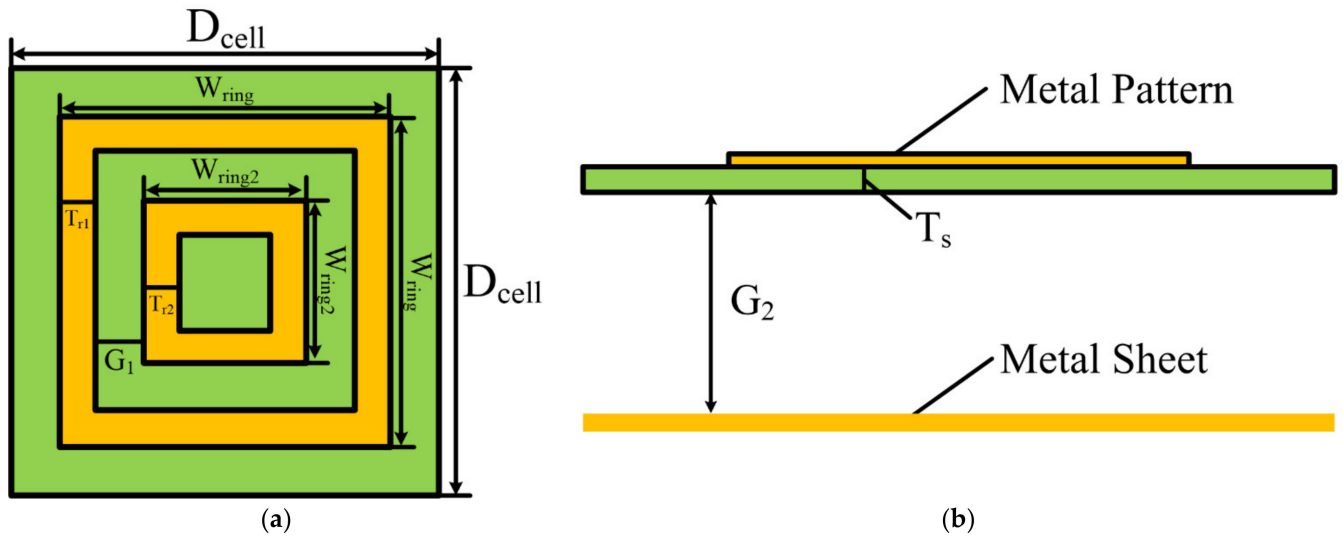


Figure 2. Unit-cell geometry: (a) top and (b) side views.

Table 1. Unit-cell Design Parameters in mm.

D_{cell}	25	W_{ring}	10–20
W_{ring2}	6–16	T_{r1}	1
T_{r2}	1	G_1	1
G_2	2.76	T_s	0.8

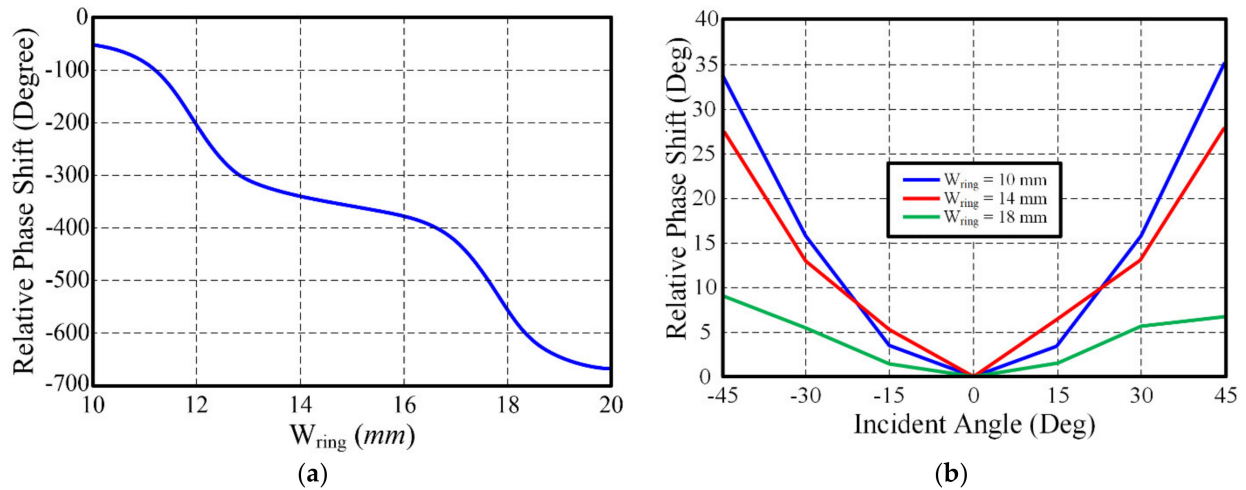


Figure 3. The relative phase shift of the reflected wave depending on (a) the size of the dual-square ring and (b) incident angle.

In this parametric analysis, the size of the unit cell (D_{cell}) was fixed at 25 mm, the length of the outer ring (W_{ring}) was varied from 10 to 20 mm and the width (T_{r1} , T_{r2} , G_1) and gap between the square rings were fixed. The observed relative phase shifts in the unit cell ranged from -50° to -670° at 5.8 GHz. The obtained phase shifting range of 620° is wide enough to compensate the incident waves because only a phase shifting range of 360° is required to set any reflection angle. The proper dimension of the dual square ring

resonator (W_{ring}) is 10–16 mm because it covers phase shifts of 0–360° at the operation frequency of 5.8 GHz. A 16 × 16-unit cell array was designed based on the phase response of the unit cell shown in Figure 2 and Equation (4).

The source horn antenna is aligned to the center of the flat panel metasurface, and the distance between the source antenna and the metasurface is 200 mm. The size of the dual square ring can be determined by calculating the required phase to compensate the incident wave on the metasurface according to (4). The size of the dual square rings and their associated phase shifting value were tabulated, and the 16 × 16-unit cell array was placed automatically by utilizing custom-built Python code for Ansys HFSS. The design procedure is shown in Figure 4a.

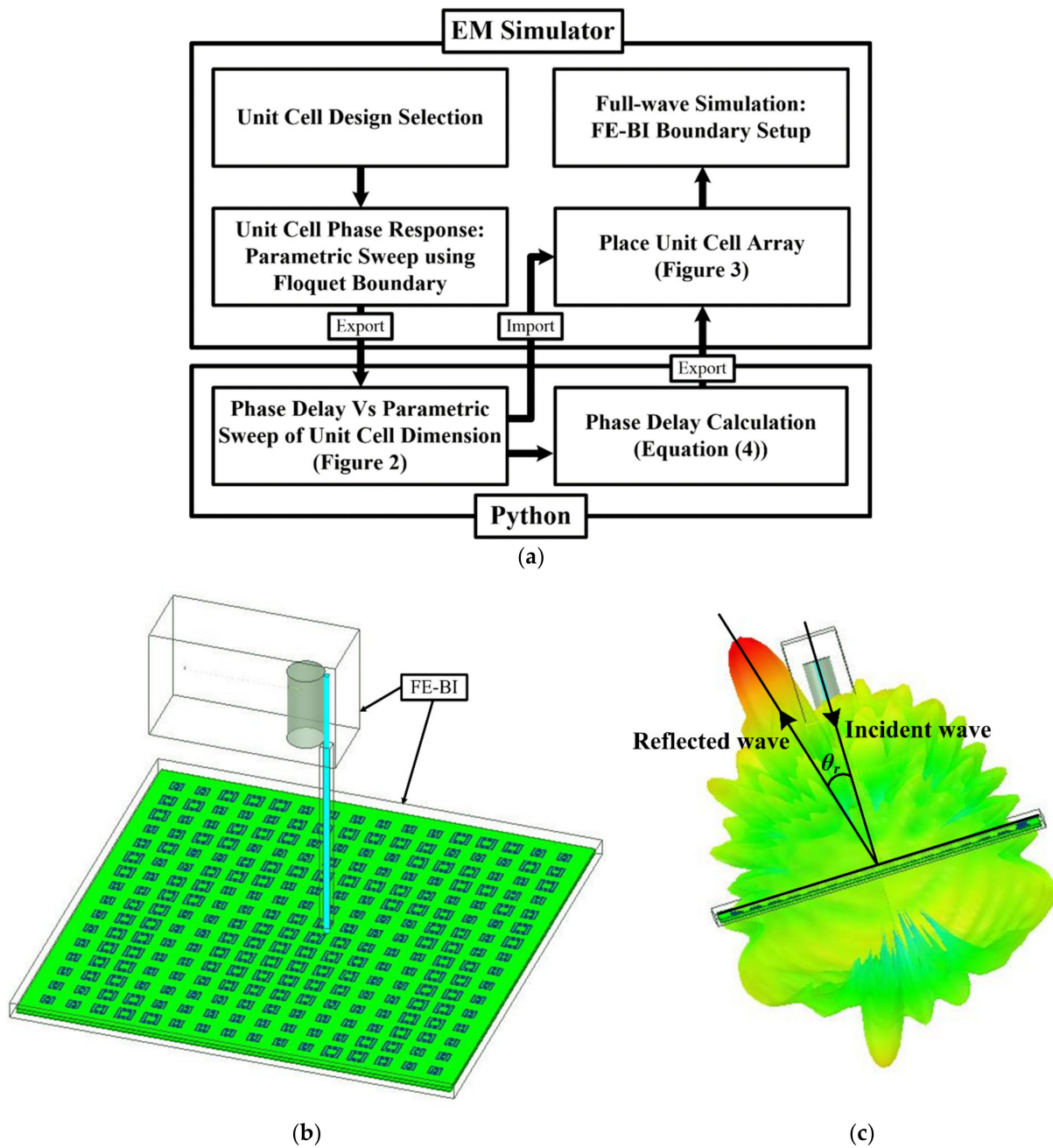


Figure 4. (a) Overall design procedure of the proposed reflectarray, (b) FE-BI domain decomposition simulation setup and (c) simulated radiation pattern of the designed reflectarray antenna.

A simulation was run in Ansys HFSS electromagnetic simulator to verify the performance of the designed metasurface reflectarray antenna. To save computation resources and simulation time, the finite-element and the boundary integral (FE-BI) domain decomposition method was applied in this work, as shown in Figure 4b [18–21]. The integration boundaries were set up around the source horn and the designed flat-panel reflectarray. The field information near the source horn antenna was integrated and applied to the reflectarray to calculate the reflected waves. The simulation result of the reflected wave is shown in Figure 4c. The designed reflection angle (θ_r) of 15° is clearly observed.

3. Reflectarray Antenna Measurement

3.1. Source Antenna: Circular Waveguide Antenna

A cylindrical horn antenna was designed for the feeding antenna based on dominant mode analysis [22]. The size of the cylindrical can is $35 \times 88 \text{ mm}^2$ (diameter \times height), and it has a single dominant TM_{11} mode in the band of 5.0–6.6 GHz, which is broad enough to cover the whole operation frequency of the proposed metasurface reflector. The length of a feeding probe is 12 mm, and the distance between the probe and the metal wall is 20 mm. The fabricated source horn antenna and its measurement data are shown in Figure 5.

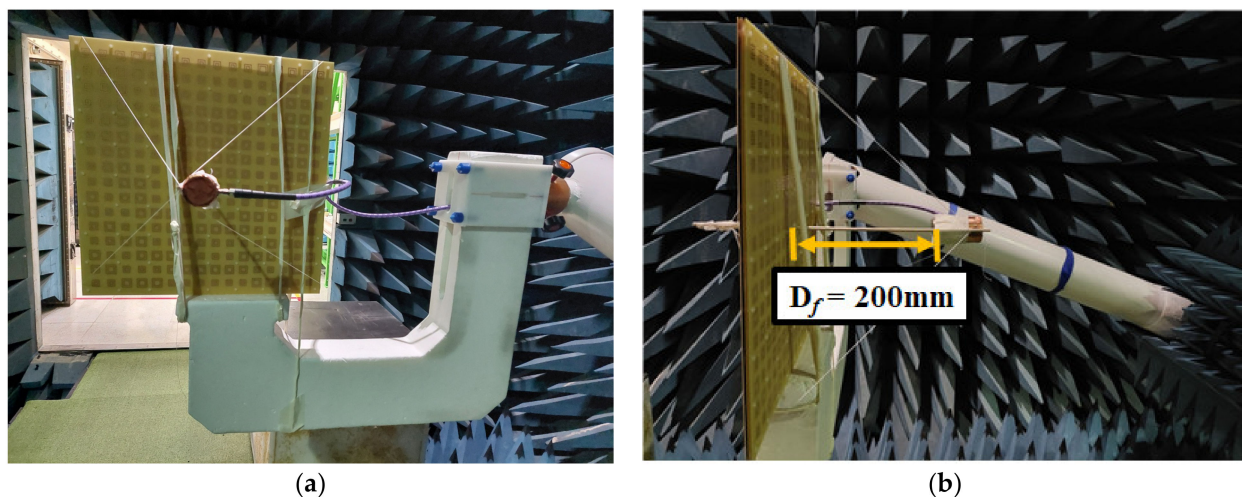


Figure 5. Fabricated 16×16 reflectarray in the anechoic chamber: (a) front and (b) side views.

All antenna parameters were measured in an anechoic chamber. The designed antenna has a broad impedance bandwidth of 5.8–6.0 GHz (Figure 6a) and high antenna gain value of 6.8–7.8 dBi (Figure 6b). The measured cross-pol suppression level was higher than 20 dB at the operation frequency band. All the simulation results show good agreement with the measurement data.

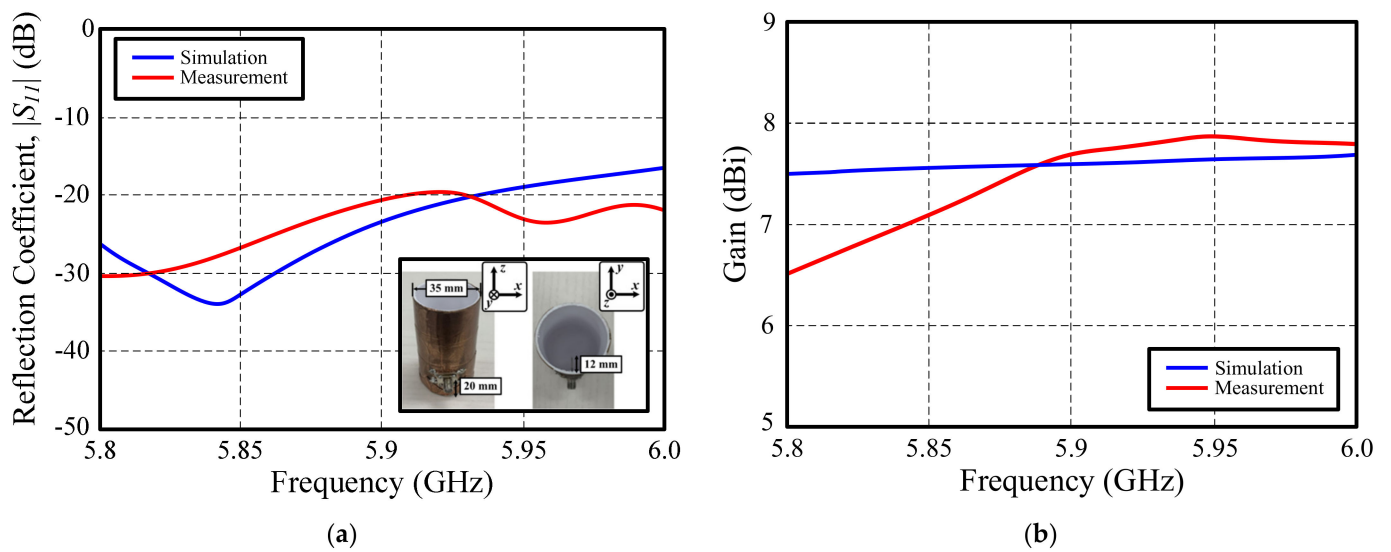


Figure 6. Designed circular horn antenna: (a) S -parameter and (b) antenna gain.

3.2. Flat-Panel Metasurface Reflectarray Antenna

The designed flat panel reflectarray antenna was printed on an FR4 PCB board. The air gap between the dual square ring metasurface and the GND plane was maintained by cylindrical PCB spacers made of polyester. The source horn antenna was tied to a wooden pole to keep a distance of 200 mm from the metasurface reflector, as shown in Figure 5 ($F/D = 0.35$). The far-field response of the fabricated flat panel metasurface reflectarray antenna was measured in an anechoic chamber. The measured far-field co-pol and cross-pole gain patterns are shown in Figure 7. The results show good agreement between the measurement and simulation. The measured peak co-pol gain value was 20~22.2 dBi, the cross-pol gain value was $-3.6\sim-0.6$ dBi, and the side-lobe level was 16~18 dB. There was less than 1 dB of difference between the simulated and measured co-pol peak gain values. The measured radiation directions of the reflected waves were $12\sim14^\circ$, which were very close to the designed radiation direction of $14\sim16^\circ$. The small discrepancy of $1\sim3^\circ$ in the reflection angle can be considered as fabrication error such as misalignment of the mounted source horn antenna. The measured 1-dB and 3-dB beamwidth values are 5° and 10° , respectively. Figure 7 shows 1-dB and 3-dB bandwidth of the proposed reflectarray antenna. The 1-dB and 3-dB bandwidth are 500 MHz (5.6~6.1 GHz, 8.5%) and 860 MHz (5.4~6.26 GHz, 14.8%), respectively. The aperture efficiency (ϵ_A) can be calculated from the measurement data because $\epsilon_A = A_e/A_p = \lambda_0^2 G / (4\pi A_p)$ where A_e is effective area of antenna, A_p is physical area of antenna, λ_0 is a wavelength and G is antenna gain [14]. The measured aperture efficiency of the proposed antenna is 21.1%. The performance comparison table is shown in Tables 2 and 3. Those reported reflectarray antennas at the C-band have multi band or tunable capability, but they also have relatively high loss due to active components, such as varactors or PIN diodes. The proposed reflectantenna features high gain and a low-profile.

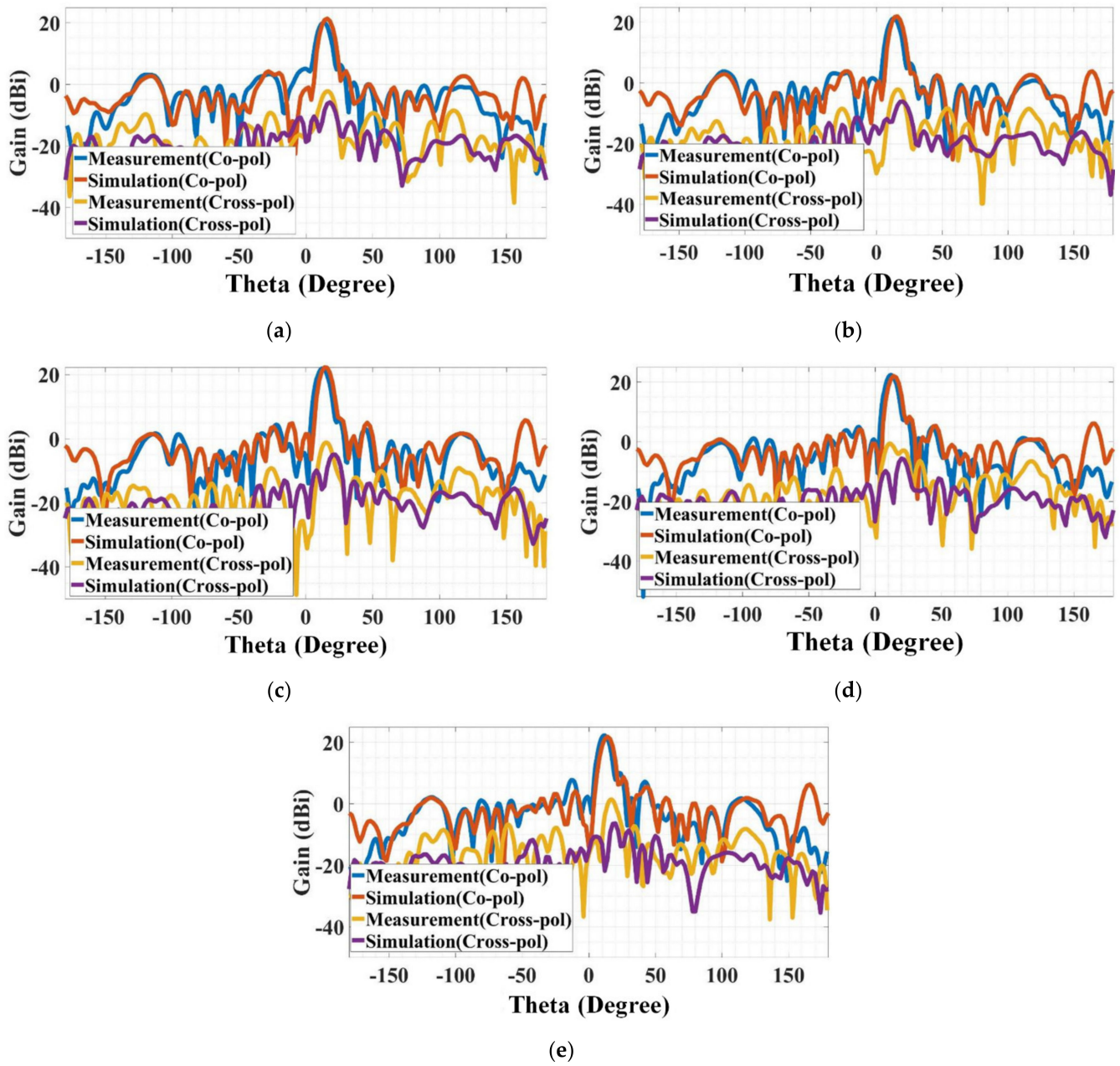


Figure 7. Measured gain patterns of the designed reflectarray antenna: (a) 5.6 GHz, (b) 5.7 GHz, (c) 5.8 GHz, (d) 5.9 GHz and (e) 6.0 GHz.

Table 2. Simulation and Measurement Data.

	Co-pol Gain (dBi)		Cross-pol Gain (dBi)		Radiation Angle (θ , $^{\circ}$)	
	Sim.	Mea.	Sim.	Mea.	Sim.	Mea.
5.6 GHz	21.3	20.0	-6.0	-2.7	16	14
5.7 GHz	21.9	21.3	-7.0	-3.5	16	13
5.8 GHz	22.2	22.0	-14.0	-1.9	14	13
5.9 GHz	22.0	22.4	-14.0	-0.6	14	13
6.0 GHz	21.8	22.2	-17.0	-3.6	14	12

Table 3. Performance Comparison.

Ref	Peak Gain (dBi)	Reflector Size (mm ³)	Frequency Band
[23]	18.1	300 × 400 × 5.0	C-band
[24]	19.0	350 × 350 × 5.6	C-band
[25]	12.9	300 × 210 × 1.5	C-band
This work	22.4	400 × 400 × 3.6	C-band

4. Conclusions

This paper presented a detailed design process for a flat-panel metasurface reflectarray and a design example operating in the C-band for satellite applications. A detailed automated design procedure based on the phase compensation and the proposed design method was demonstrated. The designed metasurface reflectarray was composed of a 16 × 16 dual-ring unit-cell array. The designed reflectarray structure was simulated using the FE-BI domain decomposition method to save computation resources such as time and memory. The measured antenna gain and radiation patterns were in good agreement with the proposed design method.

The proposed automated design method is scalable to any other frequency band. This work could pave a new way for fast design and prototyping of a metasurface reflectarray that has a broad application spectrum. For instance, artificial satellites or mobile communication areas could be good applications for the proposed reflectarray antenna.

Author Contributions: Conceptualization, S.K. and K.Y.P.; methodology, G.K.; validation, C.-M.L.; writing—original draft preparation, G.K.; writing—review and editing, M.H. and H.J.; supervision, S.K.; project administration, K.Y.P.; funding acquisition, C.-M.L. All authors have read and agreed to the published version of the manuscript.

Funding: This research was funded by Agency for Defense Development, Republic of Korea (grant number: UD210003ED).

Institutional Review Board Statement: Not applicable.

Informed Consent Statement: Not applicable.

Data Availability Statement: All data have been included in the paper.

Conflicts of Interest: The authors declare no conflict of interest.

References

- Berry, D.G.; Malech, R.G.; Kennedy, W.H. The Reflectarray Antenna. *IEEE Trans. Antennas Propag.* **1963**, *11*, 645. [CrossRef]
- Huang, J.; Encinar, J.A. *Reflectarray Antennas*, by Institute of Electrical and Electronics Engineers; John Wiley & Sons: Hoboken, NJ, USA, 2008.
- Pozar, D.M.; Targonski, S.D.; Syrigos, H.D. Design of Millimeter Wave Microstrip Reflectarrays. *IEEE Trans. Antennas Propag.* **1997**, *45*, 287. [CrossRef]
- Tamim, A.M.; Hasan, M.M.; Faruque, M.R.I.; Islam, M.T.; Nebhen, J. Polarization-independent Symmetrical Digital Metasurface Absorber. *Results Phys.* **2021**, *24*, 103985. [CrossRef]
- Ahamed, E.; Hasan, M.M.; Faruque, M.R.I.; Islam, M.T. Double negative bend headed I-shaped metamaterial based Terahertz optical power splitter. *Results Phys.* **2021**, *27*, 104492. [CrossRef]
- Hasan, M.M.; Faruque, M.R.I.; Islam, M.T. Compact Left-Handed Meta-Atom for S-, C- and Ku-Band Application. *Appl. Sci.* **2017**, *7*, 1071. [CrossRef]
- Hasan, M.M.; Rahman, M.; Faruque, M.R.I.; Islam, M.T.; Khandaker, M.U. Electrically Compact SRR-Loaded Metamaterial Inspired Quad Band Antenna for Bluetooth/WiFi/WLAN/WiMAX System. *Electronics* **2019**, *8*, 790. [CrossRef]
- Hasan, M.M.; Faruque, M.R.I.; Islam, M.T. Dual Band Metamaterial Antenna for LTE/Bluetooth/WiMAX System. *Sci. Rep.* **2018**, *8*, 1240. [CrossRef]
- Abulgasem, S.; Tubbal, F.; Raad, R.; Theoharis, P.I.; Lu, S.; Iranmanesh, S. Antenna Designs for CubeSats: A Review. *IEEE Access* **2021**, *9*, 45289. [CrossRef]
- Pelletier, E.C.; Lecourt, C.M.; Laurin, J.J. Reflectarray Antenna Concept for a Snow Mass Measurement SAR Mission in Ku-Band on a Nanosatellite Platform *IEEE Antennas Wirel. Propag. Lett.* **2021**, *20*, 2085.

11. Hodges, R.E.; Chahat, N.; Hoppe, D.J.; Vacchione, J.D. A Deployable High-Gain Antenna Bound for Mars. *IEEE Antennas Propag. Mag.* **2017**, *59*, 39. [CrossRef]
12. Montero, J.S.; Lopez, J.I.M.; Cuevas, J.R.; Martynyuk, A.E. Spiraphase-Type Reflectarray for Large Reflection Elevation Angles. *IEEE Trans. Antennas Propag.* **2015**, *63*, 4342. [CrossRef]
13. Javor, R.D.; Wu, X.D.; Chang, K. Design and Performance of a Microstrip Reflectarray Antenna. *IEEE Trans. Antennas Propag.* **1995**, *43*, 932. [CrossRef]
14. Balanis, C.A. *Antenna Theory: Analysis and Design*, 4th ed.; John Wiley & Sons: Hoboken, NJ, USA, 2016.
15. Wang, T.; Zhang, Y.; Zhang, H.; Cao, M. Dual-controlled Switchable Broadband Terahertz Absorber Based on a Graphene-vanadium Dioxide Metamaterial. *Opt. Express* **2020**, *10*, 369–386. [CrossRef]
16. Ma, B.; Lu, F.; Zhi, G.; Xue, X.; Zhao, X.; Ma, C.; Fan, Y.; Yang, M. Development of an X-Band Reflectarray Antenna for Satellite Communications. *Sci. Rep.* **2021**, *11*, 6530. [CrossRef]
17. Ma, B.; Xia, M.Y.; Yan, L.B. Design of a K-band Reflectarray Antenna using Double Square Ring Elements. *Microw. Opt. Technol. Lett.* **2012**, *54*, 394. [CrossRef]
18. Zhang, Y.; Wang, Z.; Ren, Y.; Pan, C.; Zhang, J.; Jia, L.; Zhu, X. A Novel Metasurface Lens Design for Synthesizing Plane Waves in Millimeter-Wave Bands. *Electronics* **2022**, *11*, 1403. [CrossRef]
19. Niccolai, A.; Grimaccia, F.; Mussetta, M.; Zich, R.; Gandelli, A. Optimization Environment Definition for Beam Steering Reflectarray Antenna Design. *Mathematics* **2021**, *10*, 33. [CrossRef]
20. Tienda, C.; Encinar, J.A.; Barba, M.; Arrebola, M. Dual-Polarization Ku-Band Compact Spaceborne Antenna Based on Dual-Reflectarray Optics. *Sensors* **2018**, *18*, 110. [CrossRef]
21. Soliman, S.A.M.; Eldesouki, E.M.; Attiya, A.M. Analysis and Design of an X-Band Reflectarray Antenna for Remote Sensing Satellite System. *Sensors* **2022**, *22*, 1166. [CrossRef]
22. Jeong, H.; Kim, S. Educational Low-Cost C-Band FMCW Radar System Comprising Commercial Off-the-Shelf Components for Indoor Through-Wall Object Detection. *Electronics* **2021**, *10*, 2758. [CrossRef]
23. Borgese, M.; Costa, F.; Genovesi, S.; Monorchio, A. An Iterative Design Procedure for Multiband Single-Layer Reflectarrays: Design and Experimental Validation. *IEEE Trans. Antennas Propag.* **2017**, *65*, 4595–4606. [CrossRef]
24. Alsath, M.G.N.; Kanagasabai, M.; Arunkumar, S. Dual-Band Dielectric Resonator Reflectarray for C/X-Bands. *IEEE Antennas Wirel. Propag. Lett.* **2012**, *11*, 1253–1256. [CrossRef]
25. Hum, S.V.; Okoniewski, M.; Davies, R.J. Modeling and Design of Electronically Tunable Reflectarrays. *IEEE Trans. Antennas Propag.* **2007**, *55*, 2200–2210. [CrossRef]

MDPI AG
Grosspeteranlage 5
4052 Basel
Switzerland
Tel.: +41 61 683 77 34

Electronics Editorial Office
E-mail: electronics@mdpi.com
www.mdpi.com/journal/electronics



Disclaimer/Publisher's Note: The title and front matter of this reprint are at the discretion of the Guest Editors. The publisher is not responsible for their content or any associated concerns. The statements, opinions and data contained in all individual articles are solely those of the individual Editors and contributors and not of MDPI. MDPI disclaims responsibility for any injury to people or property resulting from any ideas, methods, instructions or products referred to in the content.



Academic Open
Access Publishing

mdpi.com

ISBN 978-3-7258-3631-4